WILEY-VCH

Edited by
S. Schlemmer, T. Giesen, H. Mutschke, and C. Jäger

Laboratory Astrochemistry

From Molecules through Nanoparticles to Grains

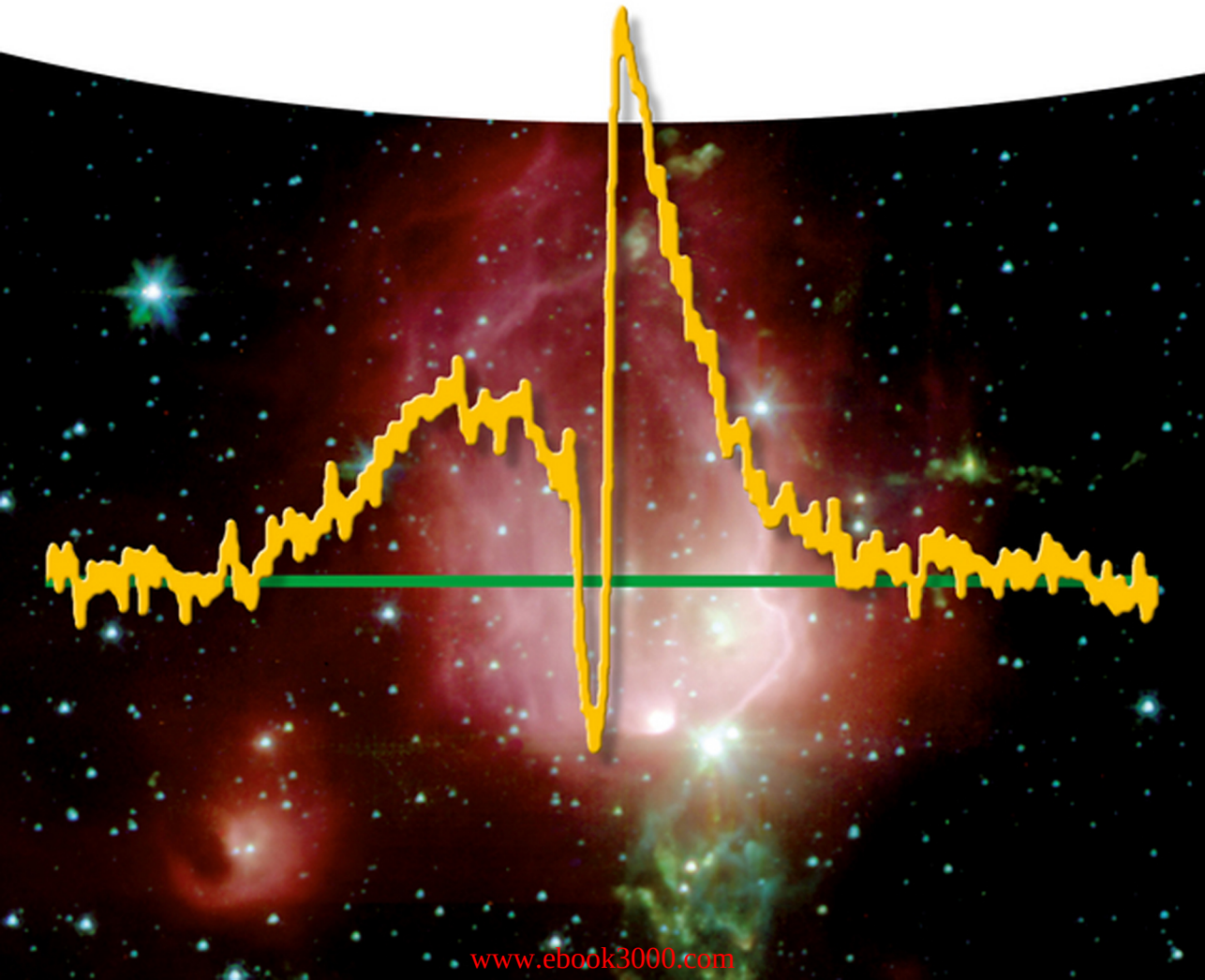

Edited by
Stephan Schlemmer, Thomas Giesen,
Harald Mutschke, and Cornelia Jäger

Laboratory Astrochemistry

Related Titles

Meierhenrich, Uwe

Comets And Their Origin

The Tool To Decipher A Comet

2014

Print ISBN 978-3-527-41281-5

Foukal, Peter V.

Solar Astrophysics

2013

Print ISBN 978-3-527-41174-0

Kwok, Sun

Organic Matter in the Universe

2011

Print ISBN 978-3-527-40986-0

Rehder, D.

Chemistry in Space

From Interstellar Matter to the Origin of Life

2010

Print ISBN: 978-3-527-32689-1

Edited by Stephan Schlemmer, Thomas Giesen,
Harald Mutschke, and Cornelia Jäger

Laboratory Astrochemistry

From Molecules through Nanoparticles to Grains

WILEY-VCH
Verlag GmbH & Co. KGaA

Editors

Prof. Stephan Schlemmer
Universität zu Köln
I. Physikalisches Institut
Zülpicher Straße 77
50937 Köln
Germany

Dr. Harald Mutschke
Friedrich-Schiller-Universität Jena
Astrophysikalisches Institut und
Universitäts-Sternwarte
Schillergäßchen 2-3
D-07745 Jena
Germany

Prof. Thomas Giesen
Universität Kassel
Fachbereich 10 - Physik
Fachgruppe Laborastrophysik
Heinrich-Plett-Str. 40
34132 Kassel
Germany

Dr. Cornelia Jäger
Friedrich Schiller University Jena
Max Planck Institute for Astronomy
Laboratory Astrophysics Group
Helmholtzweg 3
D-07743 Jena
Germany

Cover Design

Infrared image of the NGC 7129 nebula obtained with the Spitzer Space Telescope (Credit: NASA/JPL-Caltech/T. Megeath). The cluster of young stars and associated nebula are located at a distance of 3300 light years in the constellation Cepheus. This image is a color composite of images at 3.6 (blue), 4.5 (green), and 8.0 micron (red). The yellow superposed spectrum is the 988 GHz line of water observed toward this source with the HIFI instrument onboard the Herschel Space Observatory (Johnstone et al. 2010, A&A 521, L41). The broad line wings are due to fast-moving hot water in outflows from the young star, whereas the narrow absorption feature indicates the presence of cold quiescent water associated with the protostellar envelope. Montage by L. Kristensen.

Library of Congress Card No.: applied for

British Library Cataloguing-in-Publication Data
A catalogue record for this book is available from the British Library.

Bibliographic information published by the Deutsche Nationalbibliothek
The Deutsche Nationalbibliothek lists this publication in the Deutsche Nationalbibliografie; detailed bibliographic data are available on the Internet at <http://dnb.d-nb.de>.

Print ISBN: 978-3-527-40889-4
ePDF ISBN: 978-3-527-65316-4
ePub ISBN: 978-3-527-65315-7
Mobi ISBN: 978-3-527-65314-0
oBook ISBN: 978-3-527-65313-3

Cover Design Grafik-Design Schulz, Fußgönheim, Germany
Typesetting Laserwords Private Limited, Chennai, India
Printing and Binding Markono Print Media Pte Ltd, Singapore

Printed on acid-free paper

Contents

List of Contributors

Oskar Asvany
Universität zu Köln
I. Physikalisches Institut
Zülpicher Straße 77
50937 Köln
Germany

Yvain Carpentier
Friedrich Schiller University Jena
Laboratory Astrophysics Group
of the Max Planck Institute for
Astronomy
Helmholtzweg 3
D-07743 Jena
Germany

and

Laboratoire de Physique des
Lasers
Atomes et Molécules Université
de Lille 1
F-59655 Villeneuve d'Ascq Cedex
France

Mark Collings
Heriot-Watt University
Institute of Chemical Sciences
Riccarton
Edinburgh EH14 4AS
UK

Olivier Debieu
Max-Planck-Institut für
Astronomie
Laborastrophysik- und
Clusterphysikgruppe
am Institut für Festkörperphysik
Friedrich-Schiller-Universität Jena
Helmholtzweg 3
D-07743 Jena
Germany

and

CIRIMAT-ENSIACET
4, allee Emile Monso
BP 44362
31030 Toulouse CEDEX 4
France

Ewine F. van Dishoeck
Leiden University
Leiden Observatory
Niels Bohrweg 2
NL-2333 CA Leiden
The Netherlands

Francois Dulieu
Cergy-Pontoise University
LERMA
5, mai Gay Lussac
95031 Cergy Pontoise
France

Jean-Hugues Fillion
UPMC
LERMA
4 Place Jussieu
75252 Paris
France

Hans-Peter Gail
Institut für Theoretische Astrophysik
Zentrum für Astronomie
Ruprecht-Karls-Universität
Universität Heidelberg
D-69120 Heidelberg
Albert-Ueberle-Str. 2
Germany

Wolf Geppert
Stockholm University
Department of Molecular Physics
Roslagstullsbacken 21C
106 91 Stockholm
Sweden

Thomas Giesen
Universität Kassel
Institut für Physik
Fachbereich 10 - Physik
Fachgruppe Laborastrophysik
Heinrich-Plett-Str. 40
34132 Kassel
Germany

Juraj Glosik
Charles University
Department of Surface and Plasma Science
Faculty of Mathematics and Physics
V Holešovičkách 2
18000 Prague
Czech Republic

Olivier Guillois
Service des Photons
Atomes et Molécules
CEA Saclay
F-91191 Gif/Yvette Cedex
France

Thomas Henning
Max Planck Institute for Astronomy
Königstuhl 17
D-69117 Heidelberg
Germany

Eric Herbst
University of Virginia
Departments of Chemistry and Astronomy
Charlottesville
VA 22904
USA

Liv Hornekær
Aarhus University
Department of Physics and Astronomy
Ny Munkegade 1520
8000 Aarhus C
Denmark

Friedrich Huisken
Friedrich Schiller University Jena
Laboratory Astrophysics Group of the Max Planck Institute for Astronomy
Helmholtzweg 3
D-07743 Jena
Germany

Sergio Ioppolo
Radboud University Nijmegen
Nijmegen Institute for Molecules and Materials
P.O. Box 9010
NL-6500 GL Nijmegen
The Netherlands

and

California Institute of Technology
Division of Geological and Planetary Sciences
1200 E. California Blvd.
Pasadena, California 91125
USA

Cornelia Jäger
Max-Planck-Institut für Astronomie
Laborastrophysik- und Clusterphysikgruppe
am Institut für Festkörperphysik
Friedrich-Schiller-Universität Jena
Helmholtzweg 3
D-07743 Jena
Germany

Chiyoe Koike
Ritsumeikan University
Department of Physics
Kusatsu
Shiga 525-8577
Japan

Holger Kreckel
Max-Planck-Institut for Nuclear Physics
Saupfercheckweg 1
69117 Heidelberg
Germany

Harold Linnartz
University of Leiden
Leiden Observatory
Sackler Laboratory for Astrophysics
PO Box 9513
2300 RA Leiden
The Netherlands

John P. Maier
University of Basel
Department of Chemistry
Klingelbergstrasse 80
4056 Basel
Switzerland

Martin McCoustra
Heriot-Watt University
Institute of Chemical Sciences
Riccarton
Edinburgh EH14 4AS
UK

Vito Mennella
INAF-Osservatorio Astronomico di Capodimonte
Via Moiariello 16
80131 Napoli
Italy

Holger S.P. Müller
Universität zu Köln
I. Physikalisches Institut
Zülpicher Strasse 77
50937 Köln
Germany

Harald Mutschke
Friedrich-Schiller-Universität Jena
Astrophysikalisches Institut und Universitäts-Sternwarte
Schillergäßchen 2-3
D-07745 Jena
Germany

Joseph A. Nuth
NASA Goddard Space Flight Center
Mail Code 691
Greenbelt, MD 20771
USA

Karin I. Öberg
Harvard Smithsonian Center for Astrophysics
60 Garden Street
Cambridge, MA 02138
USA

Jos Oomens
Radboud University
Institute for Molecules and Materials
FELIX Facility
Toernooiveld 7
6525 ED Nijmegen
The Netherlands

and

University of Amsterdam
Van't Hoff Institute for Molecular Sciences
Science Park 904
1098 XH Amsterdam
The Netherlands

Maria Elisabetta Palumbo
Osservatorio Astrofisico di Catania - INAF
Via Santa Sofia 78
95123 Catania
Italy

David Parker
Radboud University Nijmegen
Department of Molecular and Laser Physics
Institute for Molecules and Materials
Heijendaalseweg 135
6525 AJ Nijmegen
The Netherlands

Olivier Pirali
Institut des Sciences Moléculaires d'Orsay
UMR8214 CNRS – Université Paris-Sud
Bât. 210
91405 Orsay cedex
France

and

AILES Beamline
Synchrotron SOLEIL
L'Orme des Merisiers
Saint-Aubin
91192 Gif-sur-Yvette CEDEX
France

Thomas Posch
Universität Wien
Institut für Astrophysik
Türkenschanzstraße 17
A-1180 Vienna
Austria

Karsten Potrick
Friedrich Schiller University Jena
Laboratory Astrophysics Group of the Max Planck Institute for Astronomy
Helmholtzweg 3
D-07743 Jena
Germany

Stephen D. Price
University College London
(UCL)
Chemistry Department
20 Gordon Street
London WC1H 0AJ
UK

Frans J. M. Rietmeijer
University of New Mexico
Department of Earth and
Planetary Sciences
221 Yale Boulevard NE
Albuquerque
NM 87131.0001
USA

Corey A. Rice
University of Basel
Department of Chemistry
Klingelbergstrasse 80
4056 Basel
Switzerland

Gaël Rouillé
Friedrich Schiller University Jena
Laboratory Astrophysics Group
of the Max Planck Institute for
Astronomy
Helmholtzweg 3
D-07743 Jena
Germany

Daniel Wolf Savin
Columbia University,
Astrophysics Laboratory
MC 5247
550 West 120th Street
New York, NY 10027-6601
USA

Stephan Schlemmer
Universität zu Köln
I. Physikalisches Institut
Zülpicher Straße 77
50937 Köln
Germany

Torsten Schmidt
Friedrich Schiller University Jena
Laboratory Astrophysics Group
of the Max Planck Institute for
Astronomy
Helmholtzweg 3
D-07743 Jena
Germany

and

Royal Institute of Technology
(KTH)
Material Physics
ICT School
Electrum 229
SE-164 40 Kista-Stockholm
Sweden

Mathias Steglich
Friedrich Schiller University Jena
Laboratory Astrophysics Group
of the Max Planck Institute for
Astronomy
Helmholtzweg 3
D-07743 Jena
Germany

and

University of Basel
Department of Chemistry
Klingelbergstrasse 80
CH-4056 Basel
Switzerland

Akemi Tamanai
Universität Heidelberg
Kirchhoff-Institut für Physik
Im Neuenheimer Feld 227
D-69120 Heidelberg
Germany

Alexander G.G.M. Tielens
Leiden University
Leiden Observatory
PO Box 9513
2300 RA Leiden
The Netherlands

Ruud Visser
University of Michigan
Department of Astronomy
1085 S. University Ave
Ann Arbor, MI 48109–1107
USA

Malcolm Walmsley
INAF
Osservatorio Astrofisico di
Arcetri
Largo E. Fermi 5
50125 Firenze
Italy

and

Dublin Institute of Advanced
Studies (Cosmic Physics)
31 Fitzwilliam Place
Dublin 2
Ireland

Laurent Wiesenfeld
Laboratoire d'Astrophysique de
l'Observatoire de Grenoble
414, Rue de la Piscine
Domaine Universitaire
BP 53
38041 Grenoble Cedex 09
France

Andreas Wolf
Max-Planck-Institut for Nuclear
Physics
Saupfercheckweg 1
69117 Heidelberg
Germany

Simon Zeidler
Friedrich-Schiller-Universität
Jena
Astrophysikalisches Institut und
Universitäts-Sternwarte
Schillergäßchen 2-3
D-07745 Jena
Germany

and

National Astronomical
Observatory of Japan
Gravitational Wave Project
Office
Osawa 2-21-1
Mitaka
Tokyo 181-8588
Japan

Preface

The field of laboratory astrophysics is well established and developing various branches of dedicated research in laboratories to provide astronomy with elementary data for the interpretation of their observations. Over the past 20 years, the branch that deals with molecular physics, chemical physics, and the physics and chemistry of dust particles became very active. As a result, laboratory astrochemistry is an important area of research around the globe. In view of today's needs to interpret the richness of observations in the era of the Herschel or ALMA obersvatories, much of the atomic and molecular data is stored in a growing number of databases like those for chemical reaction rates and those for molecular spectroscopy. In recent years, even a common framework for these databases has been developed in order to access many databases at the same time as this is needed for the interpretation of the vast information from the detailed astronomical observations.

A concerted development of laboratory astrochemistry became possible through continuous funding on national and international levels and through a strong exchange between the groups active in this field of research. Especially, the different European training networks and COST activities as well as the establishment of a Laboratory Astrophysics Division (LAD) within the American Astronomical Society helped scientists to create awareness of this new and growing discipline and to attract students to work in this field. In the course of these developments, we felt that it could be helpful for new graduate students or fellow scientists to be introduced to the very different approaches of laboratory astrochemistry. The field is already too wide that one book could address all topics in great detail. Instead the idea of this book was to compile chapters on molecular spectroscopy, photodissociation, gas-phase processes, surfaces of grains, dust formation, and their spectroscopic properties.

In order to fit into one book, each chapter has an introductory section which is followed by a small set of contributions summarizing some recent advances. This attempt could by no means be comprehensive. Instead our intention is that reading the various chapters guides and encourages newcomers to then look up original work.

We would like to thank the chapter authors for their activities to bring together a number of coauthors contributing to the individual chapters. We are grateful to those authors for their participation and, in particular, for the patience to finish this work. Especially, we want to thank Malcom Walmsley for the introductory chapter to this book where he highlights the need of laboratory astrochemistry for the interpretation of astronomical observations. Several other people helped to prepare this work and we want to thank them and all coauthors for the patience and endurance to complete this work.

October 2014

Stephan Schlemmer, Thomas Giesen,
Harald Mutschke and Cornelia Jäger

1
The Astrophysical Background

Malcolm Walmsley

Astrophysics is a parasite science in some ways. It borrows from the work of others and often adapts results from the physical or chemical literature for its own purposes. Of course, the reverse situation can also occur, where astrophysical observations provide insight into physical or chemical processes both in space and elsewhere. Either way, this requires understanding both from the astronomers and the physicists or chemists about the aims and claims on the other side of the fence. This book aims at facilitating such understanding.

The book is a compendium of articles discussing laboratory and theoretical work relevant for astrophysicists and will be useful for specialists of the interstellar medium (ISM) and circumstellar envelopes. It may also provide insight into basic physical and chemical processes. In this introduction, I will give a short overview of the interplay between interstellar astronomy and the study of fundamental physical processes. I will also review briefly some current questions of interest in the light of results from the HERSCHEL satellite as well as of the prospects of what may or may not be found with Atacama Large Millimeter Array (ALMA). Finally, I give a brief summary of the subjects treated in this volume.

One reason why astronomical observations can occasionally contribute to basic physics is that it is difficult to achieve in the laboratory pressures comparable to those found in the interstellar medium. A classical example was the discovery by Bowen in 1927 [1] that a series of unidentified lines from nebulae (originally discovered by Huggins in the nineteenth century, the so-called nebulium lines) were in fact forbidden (i.e., electric-dipole-forbidden) transitions of various ionization stages of O and N. These were strong in nebulae (but not in the laboratory) because the densities in ionized interstellar (HII) regions are sufficiently low that radiative decay is faster than collisions. Although they had not been detected in the laboratory, the wavelengths expected for such magnetic dipole transitions could be inferred from combinations with a third level (and thus the laboratory input was indeed critical) and compared with the astronomical results. The agreement was perfect!

Another astronomical identification was the discovery of interstellar molecular ions such as HCO^+ (the former "X-ogen") in interstellar molecular clouds. This

Laboratory Astrochemistry: From Molecules through Nanoparticles to Grains, First Edition.
Edited by Stephan Schlemmer, Thomas Giesen, Harald Mutschke and Cornelia Jäger.

was first detected at 3 mm (the 1-0 transition) in 1970 by Buhl and Snyder [2], and almost immediately Klemperer [3] realized what it must be. He estimated the bond lengths for HCO^+ (from HCN and CO^+) and the rotation constant which corresponded to a prediction for the 1-0 transition differing by 56 MHz from the observed astronomical frequency. I have always been amazed at the insight needed to make that equivalence. In any case, that astronomical result was rapidly confirmed by Woods *et al.* [4] in the laboratory. Moreover, Klemperer's work led to two landmark papers on interstellar chemistry from Solomon and Klemperer [5] and from Herbst and Klemperer [6]. This was the start of ion–molecule chemistry, which had great success in explaining many of the questions brought up by the astronomers exploiting millimeter-wavelength telescopes. Some of this early work is summarized in the review by Winnewisser *et al.* [7].

Astrochemistry has come a long way since the initial phases almost a century ago. One realizes this on reading some of the first papers on the topic. An example of this is the note by Swings and Rosenfeld in 1937 [8] entitled "Considerations regarding interstellar molecules". They were discussing the "new interstellar lines of rather diffuse origin" discovered by Merrill. Others who had contributed to the subject and whom they cite included Russell, Eddington, and Saha! Swings and Rosenfeld discuss a suggestion by Saha [9] that a band at 6283 Å (which later turned out to be a DIB (or diffuse interstellar band and just what these are is still a puzzle) could be due to Na_2 and attempt a calculation (using a modified Saha equation) of the likely abundance of interstellar diatomics. They concluded that CH, OH, NH, CN, and C_2 seem "promising" and make the case for the identification of a line at 4300 Å with CH (which turned out to be correct). They also note the pitfalls in using a Saha-type equation as well as the uncertainties in their estimates of the interstellar radiation density. It was, all in all, a very prescient article based on our present-day knowledge.

From an astronomer's standpoint, however, it may be that the biggest mystery of all is that of the nature, composition, formation, and destruction of dust grains (see Draine [10], Henning [11]). Because of their extinction and scattering properties, but also because of the processes that take place on their surfaces, they cannot be ignored. In different regions, the grains take on different forms; for example, there is good evidence that they grow to centimeter size in the pre-main-sequence (T Tauri) disks. At the other end of the scale, it is clear that nanometer-sized grains and PAHs (polycyclic aromatic hydrocarbons) make a large contribution to the observed extinction in the optical and UV as well as giving rise to spectacular emission features in the near- and mid- infrared (IR). In spite of this, it is clear that there are many gaps in our understanding of interstellar dust, and it may be interesting to mention some of them here. There are also several "mysteries" that need to be resolved before one can say that our grain models are realistic.

One of these concerns the "large grains." Are there big (1 μm or larger) grains or "pebbles" out there? Models of the interstellar grain size distribution typically have a power-law size distribution with a cutoff at around 0.5 μm. Much of the mass is in the largest grains with sizes in the range 0.1–0.5 μm. However, the Ulysses and Galileo satellites have been directly detecting grains of apparent interstellar origin

with sizes as large as 1 μm or more (see Draine [12] for a summary). The number of these grains seems to be much larger that what is needed to explain interstellar extinction as well as the limits inferred from the amount of heavy elements depleted from the gas phase. Thus there is a problem, and resolving the controversy will not be easy. At face value, one needs fundamental changes to our generally accepted interstellar grain model, an error in the interpretation of the Ulysses and Galileo measurements, or a large inhomogeneity in the dust distribution close to the heliosphere. Clearly, new measurements of these micrometer-sized particles are needed.

The discrepancy, however, may just be part of our general lack of comprehension about how interstellar grains form and evolve. Why, after all, should there be an upper limit to the interstellar grain size distribution? The answer must lie in how grains are formed, are destroyed, and evolve. We think that grains have their origins in mass loss from giants and planetary nebulae, but it has been known for some time that this cannot compete directly with the grain destruction rate because of supernova shocks. Thus grains are not simply "stardust" but they manage to absorb refractory elements during their roughly billion-year lifetime in the ISM. Presumably, they accomplish this trick in molecular clouds where it also seems likely that they coagulate to form larger grains causing a "flattening" of the UV extinction curve. The details of how this happens are obscure, but it is surely true that finding out the answer will require an improved knowledge of grain surface processes as well as of the processes that destroy grains (sputtering, shattering in shocks, etc.). The complex physics of PAHs and of a variety of "organic grains" must also be part of the answer. It is any case encouraging to learn in the last chapter of this book (Jäger *et al.* 7) of the progress made in the study of dust formation in giant envelopes.

It is certainly also true that a real advance in our understanding of interstellar dust grain properties will come only with a solution of some of the unsolved puzzles that have bedeviled the subject for the best part of a century (see the recent article by Tielens [13] as well as this volume). One of these puzzles is to find a convincing identification for the well-known 220-nm feature in the extinction curve. It is fairly clear that it is due to a substance or molecular family with aromatic properties, and a possibility is that a family of PAH-type molecules similar to those causing the IR emission features (3.3, 7.6, 11.3 μm, etc.) is also responsible for the 220-nm absorption. However, convincing proof of this is lacking, and small graphitic grains are still a possible contender. The identification of the PAH features themselves is less controversial, but there are still some doubters and one still wonders whether the identification of an individual PAH may prove possible. Could one identify interstellar Coronene and, if so, how?

Another unsolved puzzle is, of course, that of the DIBs. These have resisted identification for almost a century despite the best efforts of many talented people. Again, it seems likely that the solution has to do with large organic molecules and that a large fraction of interstellar carbon is involved. The article by Rice and Maier in this volume discusses possible solutions. These questions are not simply amusing conundrums posed by Mother Nature but questions whose solution

has consequences for the makeup and evolution of interstellar grains. They also probably affect the carbon budget with likely consequences for gas-phase chemistry. One question that has been slightly "forgotten" in recent years is the origin of long-chain carbon compounds such as the cyanopolyynes which are abundant in certain (but not all) dark clouds in the vicinity of the Sun. Their abundance is certainly dependent on the C/O gas phase abundance ratio, and variations in this quantity are likely responsible for variations in the cyanopolyyne abundances. The suspicion is that all these questions are connected.

Will some useful input to these questions come from ALMA, HERSCHEL, Stratospheric Observatory for Infrared Astronomy (SOFIA), and other new instruments? HERSCHEL has already been and gone, and some of its answers were unexpected. Perhaps most unexpected were the results on the ions OH^+, H_2O^+, and so on, from HERSCHEL with important contributions from the Atacama Pathfinder Experiment (APEX) (see Gupta *et al.* [14] and Wyrowski *et al.* [15]). Figure 1.1 taken from Gerin *et al.* [16] gives a flavor of the first HERSCHEL results. These ions react with H_2 and hence have a short lifetime in molecular clouds. They, nevertheless, are detectable in diffuse gas (in absorption) and in some photon-dominated regions (PDRs). Their abundance is clearly related to the cosmic ray ionization rate as well as to the relative abundance of atomic and molecular hydrogen. It is amusing (and to some extent unexpected) that some of the main advances brought by HERSCHEL was to diffuse cloud science.

Of course, the unique contribution made by HERSCHEL to our understanding of interstellar chemistry has been that of providing reliable information on the distribution and abundance of water. It was already known from the Infrared Space Observatory (ISO), Submillimeter Wave Astronomy Satellite SWAS, and ODIN, as well as from ground-based studies, that gas-phase water H_2O usually contains a minor fraction of the available oxygen (e.g., Bergin *et al.* [17]). On the other hand, it is clear from fairly basic theory that in all molecular regions with temperatures above a threshold of around 300 K, any available atomic oxygen gets converted into water. One knows that such hot molecular regions exist. That is convincingly demonstrated by observations of hot molecular hydrogen seen in both pure rotational transitions (for example, by SPITZER) and in vibrotational lines seen by ground-based work in the near-IR. Does HERSCHEL confirm this?

The jury is still out on this, but the available evidence to date suggests not. The derived water abundance in the hottest layers traced in outflows is often only a few percent of reasonable estimates of the free oxygen abundance. There are, however, considerable uncertainties caused by complex geometry and radiative transport. It is also true that such hot molecular layers in shocked gas associated with outflows are subject to UV radiation fields capable of destroying the water just produced. It certainly seems to be true that the water abundance rises precipitously in shocks even if not to the level expected, and, also, estimating the column density of hydrogen in the water-line-emitting layers is not easy. One thing that has become clear is that photodesorption of water ice caused by incident UV radiation is a key process

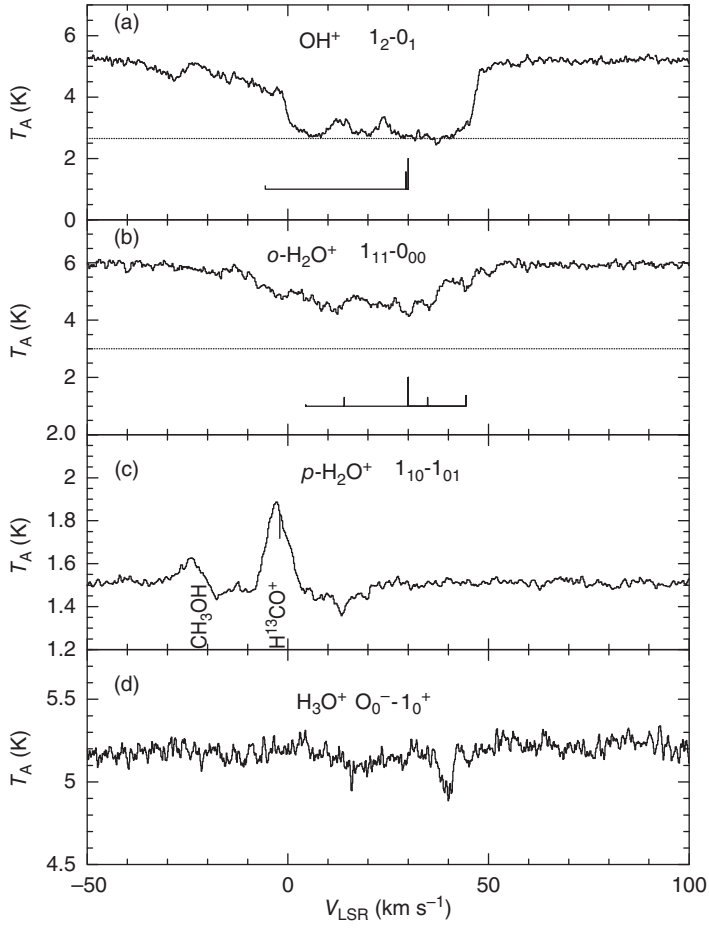

Figure 1.1 HIFI spectra [Reproduced with permission © ESO] of (a) OH^+, (b) *o*-H_2O^+, (c) *p*-H_2O^+, and (d) H_3O^+ toward the millimeter continuum source G10.6-0.4. The hyperfine structure of the OH^+ and *o*-H_2O^+ lines is indicated on the upper two panels.

in determining the water abundance as is the (possibly associated) water photodissociation. Of course, H_2O is almost always the major ice constituent and hence this is of more importance for water than for other species. Nevertheless, it seems likely that photodesorption can influence the abundance of methanol and related species, and hence more precise rates for such processes will be needed. The work discussed by Linnartz and collaborators in this volume highlights recent developments in the area.

An example of the importance of understanding photodesorption is provided by the detection of ground-state water transitions toward the nearby (55 pc) disk around the 10 Myr old T Tauri star TW Hya (Hogerheijde *et al.* [18]) using the

HIFI (Heterodyne instrument for the Far Infrared) spectrometer on HERSCHEL. The detected water lines are narrow (1 km s^{-1}) (see Figure 1.2) and are likely from the outer disk at a radius of about 100 astronomical units (AUs) from the central K7 star. This is well beyond the water "snow line" (the radius in the disk outside which water is frozen out onto grain surfaces) and thus the observed lines are likely formed in an outer layer where water can be photodesorbed (more precisely an intermediate layer between the height at which water is photodissociated and that at which it is photodesorbed). The inferred ice reservoir is several thousand times the mass of the Earth's oceans and is thus consistent with suggestions that comets delivered the oceans to Earth. These inferences, however, depend sensitively on the assumed photodesorption yields as well as on grain settling.

TW Hya has been the subject of intense study with HERSCHEL, and another surprise was the detection by Bergin *et al.* [19] using the Photodetector Array Camera and Spectrometer (PACS) of the 1-0 rotational transition of hydrogen deuteride (HD) at 112 μm. This is important because it provides constraints on the disk gas mass (and hence on the gas-to-dust ratio). One knows much more about dust than about gas in such young disks, and what one does know about the

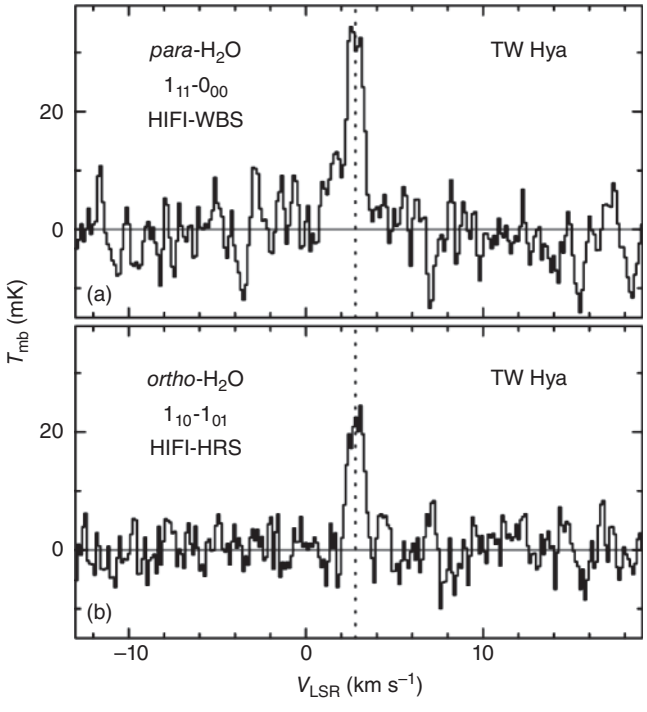

Figure 1.2 HIFI spectra [from [18], copyright 2011 © permission from American Association for the Advancement of Science] of water ground-state lines toward the nearby pre-main-sequence disk TW Hya. The observed gas-phase water suggests the presence of an ice reservoir of several thousand Earth oceans in this object.

gas (as in the case of water mentioned above) often just concerns a thin surface layer. This is partly true also for HD (the $J = 1$ level is 128 K above ground) and most of the emission comes from inside 80 AU. However, the conclusion seems to be that the disk is relatively massive and that the gas-to-dust ratio may not be far from the canonical ISM value of 100. But certainly this is an area where SOFIA can potentially make important discoveries.

Another interesting result from HERSCHEL has come from the work on the 69-μm Forsterite feature in the emission from circumstellar disks around Herbig Ae stars by Sturm *et al.* [20]). Interstellar silicate dust is essentially amorphous, and the silicate emission from pre-main-sequence star disks is mainly from amorphous silicates. However, features from crystalline dust were found with ISO, and much work on shorter wavelength features was carried out with the SPITZER spectrometer. All of this, together with the HERSCHEL observations, puts limits both on the temperature and the iron-to-magnesium abundance ratio in the emitting grains. One finds that the crystalline silicates are iron-poor and magnesium-rich and this is found also in the emission from débris disks such as β Pic. If this is true for the crystalline silicates, it may also hold for the amorphous silicates. Where is the iron if it is not in the silicates? Could a large fraction of interstellar dust be in the form of "iron filings"?

Results using ALMA are beginning to arrive, but we surely have had only a taste of what is to come. As one perhaps should expect, the first results have focused on protostellar disks and inner envelopes. For example, it is becoming possible to establish the location of the "CO snow line" in some nearby disks such as that around TW Hya. This has now been imaged by Qi *et al.* [21] in the N_2H^+(4-3) transition showing a ring of about 20–30 AU in radius (see Figure 1.3).

Since N_2H^+ is known to react rapidly with CO, it is thought that this ring must be due to CO freeze-out onto grain surfaces and consequently to N_2H^+ enhancement. CO itself is seen at much smaller radii. This observation will certainly be surpassed when full ALMA is in operation, but we are already seeing signs of what can be achieved.

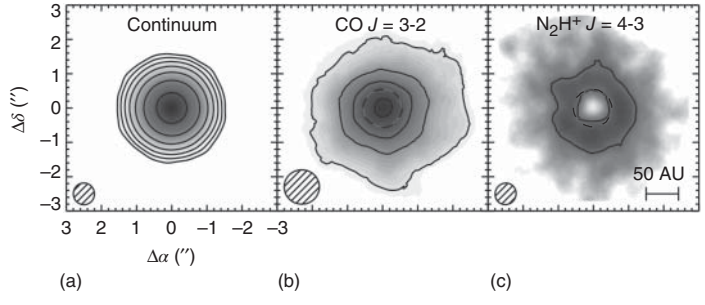

Figure 1.3 Images taken with ALMA (a,c) and with the sub-millimeter array (SMA (b)) of disk emission from the young pre-main-sequence star TW Hya. (a) shows the 372-GHz dust continuum emission and (b) emission in the CO(3-2) line. (c) shows an image in N_2H^+ (4-3) where the dashed circle marks the best fit inner radius of the N_2H^+ ring (the hypothesized CO snow line). (Reprinted with permission from AAAS, Ref. [21].)

ALMA will impinge upon our understanding in a variety of ways, and it is beyond the scope of this short foreword to discuss all of them. The fact that one can get linear resolutions of better than 100 AU in some nearby objects suggests [21] a host of possible observations. It is also true that the increased sensitivity will allow fundamental advances in diffuse cloud chemistry using the well-honed techniques (absorption toward background quasi-stellar objects (QSOs, etc.) which have been used so effectively with the Institut de Radioastronomie Millimeterique IRAM instruments. Gravitational lenses seen in absorption at high redshift will certainly be another source of interesting results. And, of course, there will be surprises. All of these will certainly need new input from physicists and chemists.

What sort of input would astronomers like to have from the laboratory? Modern astrophysics needs both high-quality measurements of physical processes and high-quality simulations of the chemical processes that affect the abundances of the observed interstellar molecules. One also needs laboratory measurements of the optical properties and other characteristics of interstellar grains. The latter is a vast topic but it is worth noting that our understanding of the formation of the first galaxies depends critically on the characteristics of the grains observed at high redshift and their differences with the modern Milky Way variety. Molecular hydrogen forms (as a rule) on grain surfaces, and its formation is critically dependent on grain characteristics as well as on physical conditions (gas and grain temperature, for example). All of these topics are covered in the present volume, which explores recent advances in laboratory astrochemistry spanning a large range from molecular spectroscopy via gas-phase chemistry to grain formation processes and grain properties.

1.1 The Contents of this Volume

This book brings us up to date with some of the puzzles that have inspired laboratory spectroscopists over the years. The most ancient concerns the origin of the DIBS, which, as mentioned earlier, were discovered roughly 90 years ago and are still unidentified despite a plethora of suggestions. The contribution by Rice and Maier in Section 2.1 in this volume discusses some possible solutions to this conundrum. There are other puzzles, such as the dissociative recombination rate of the ion H_3^+, that are crucial for the chemistry and appears now to have been resolved (see the contribution of Geppert, Wolf, and Glosik in Section 3.2). The latter question affects our understanding of how ion chemistry works and of to what extent ions are responsible for processes such as deuterium fractionation (see discussion by Asvany and Schlemmer in Section 3.4). A combination of astronomical observation and laboratory work is surely the way to proceed in this area.

But the most fundamental puzzles perhaps involve surface science and, in particular, molecular hydrogen formation. First, one should note that molecular hydrogen is not always formed on grain surfaces, and, indeed, in the early universe

(where initially there are no grains) H_2 presumably has to form in the gas phase (see the discussion of negative ion chemistry by Kreckel and Savin in Section 3.5). However, once dust has formed, there seems little doubt that molecular hydrogen forms on grains, but how it does it and on which sort of grains (or nanoparticles) has been the source of much controversy. The best astronomical measurements (see the discussion of Hornekaer in Section 5) give some guidance, but the main conclusion one draws is that the estimates of Salpeter and coworkers in the 1960s and 1970s were very prescient. Getting beyond that to understand, for example, the relative importance of the Eley–Rideal and Langmuir–Hinshelwood mechanisms in various astrophysical situations has proven difficult (see contributions by Hornekaer and Price in Section 5.2 as well as by Herbst in Section 5.5). Another aspect is the effect of the different surfaces (ice or silicate or carbonaceous), which becomes important in differing locales (see contribution by McCoustra *et al.* in Section 5.3).

Of course, molecular hydrogen is not the only species which forms on dust grain surfaces although for many years, it was assumed tacitly that this was the case. That assumption was made for the "lack of a better" alternative, or because it was unclear what rates were applicable on grain surfaces (though the early work of Allen and Robinson [22] provided a guide). These days it is clear that, for example, water, methanol, and carbon dioxide can form on grain surfaces (see the contribution of Isokoski and collaborators who also discuss some of the early ideas in this area). Can complex organic molecules (e.g., prebiotic species) form in this manner? Relatively complex species such as glycolaldehyde are found in the "hot core" region SgrB2(N), and the circumstances (high temperature such that ices desorb) are suggestive of surface formation. The models to date are consistent with this, but there is presently no convincing explanation of the patterns of complex species observed.

One essential input for the millimeter astronomers interpreting observations of sources like SgrB2(N) is reliable spectroscopic data. The increasing sensitivity of modern telescopes (in particular the potential of ALMA) has had the consequence that one reaches the confusion limit where line-blending dominates the spectrum and where many of the observed transitions are due to vibrationally excited states. Separating out the "weeds" due to species such as methanol and ethyl cyanide from the "transitions of interest" has rendered clear identification of emission from new molecules extremely challenging. The contribution by Müller in Section 2.4 describes some of what has been done both in the laboratory and astronomically. I might add that in all of this the availability of the CDMS (Cologne Database for Molecular Spectroscopy) database has been invaluable.

Molecular line intensities and profiles are used as probes of the physical characteristics of the clouds and stellar envelopes where the lines are formed. As in the case of the forbidden lines from ionized gas, level populations are non-Boltzmannian and are determined by competition between collisional excitation and radiative decay. Thus one needs accurate computations of state-to-state rates for the observed species, and this in turn requires accurately determined potential energy surfaces as well as computations of the various cross sections. One also

needs laboratory measurements of the cross sections to verify the computations, and some recent experimental results are described in the contribution by Parker and Wiesenfeld in Section 3.3.

Another fundamental input for our understanding of interstellar chemistry is a set of credible photodissociation rates. It is, of course, a challenge to understand how one forms interstellar molecules, but equally important is to know how they are destroyed. In the diffuse interstellar gas, but also in the so-called PDRs, the main destruction process is often photodissociation by the ambient UV field (in the case of the PDRs, the UV photons originate in nearby hot stars). In practice, most photodissociation rates are computed at least for small species but, of course, laboratory work has provided important checks on theory. van Dishoeck and Visser in Chapter 4 provide a useful overview of the techniques used as well as some insight into some of the complications that occur in the astrophysical context (an example is line self-shielding in cases such as CO). In this context, the databases provided by the Leiden group have been invaluable to the community.

In all of the discussions of molecular complexity in the interstellar medium, the role played by the PAHs is clearly of great importance. It is worth stressing that the PAH's near- and mid-IR features dominate the spectra of many well-studied galactic and extragalactic objects (planetary nebulae, galactic nuclei, PDRs, young stellar objects, etc.). Nanoparticles matter! PAH characteristics are described in the contribution by Oomens, Pirali, and Tielens in Section 2.3 and UV spectroscopy by Carpentier *et al.* in Section 2.2. Their importance is underlined by the fact that they are thought in many situations to take up a large fraction (several percent) of the available carbon. How is it possible for one single family to do this? There is no good answer to this, but certainly good laboratory data on both ionized PAHs and various PAH modifications are needed. One of the interesting questions is whether PADs (deuterated PAHs) are abundant and can affect the amount of deuterium in atomic or molecular (HD) form.

If carbon-based nanoparticles exist, why not also Si-based nanoparticles? Huisken and collaborators in Section 6.7 discusses the possibility that photoluminescence from such particles may be observable. It might even account for the "extended red emission" or ERE seen toward some reflection nebulae.

For astronomers, however, the properties of the classical 0.1-μm-sized dust particles are of primary importance. This is because of both the importance of extinction in the visible and near-IR and the observed dust emission at wavelengths ranging from the far-IR to 1 mm. In particular, the results from the PLANCK and HERSCHEL satellites have led to increased interest in the long-wavelength emissivity. Such measurements often give us our most reliable estimates of cloud masses and column densities. It is, therefore, appropriate that Chapters 6 and 7 of this volume are devoted to studies of classical dust.

A description of our present knowledge of ISM, circumstellar, protoplanetary, and solar system dust is given in the contribution by Henning in Section 6.1, while laboratory techniques for measuring grain optical properties are discussed by Mutschke in Section 6.2. Laboratory techniques for measuring the IR spectra of amorphous silicates are considered by Mutschke and Zeidel in Section 6.3 and

for crystalline silicates by Koike in Section 6.4. Crystalline silicates are found in comets and protoplanetary disks, and we have seen earlier the potential of the observations of crystalline features for understanding grain composition.

The apparent predominance of silicate dust brings up the question of the role played by other oxides in the formation and evolution of cosmic dust. This is discussed in the contribution by Posch and Zeidler in Section 6.5, who point out the role a variety of oxides (SiO, FeO, Al_2O_3, etc.) can play as intermediaries in the formation of silicate dust in circumstellar shells. Some hints about how this might work are given by observations of inclusions in meteorites. A large fraction of interstellar dust, however, is formed of either graphite or HACs (hydrogenated amorphous carbon) and it is clear that one therefore needs accurate optical constants for such substances. Mutschke's second chapter (Section 6.6) deals with this topic as well as with the characteristics of related species such as SiC. An open question here is whether one of these materials can account for the prominent "bump" at 220 nm seen in the interstellar extinction curve; some of the proposed solutions to this problem are discussed.

A clear need is a comprehensive model of the formation, evolution, and destruction of interstellar dust particles. A partial answer to this is given in Section 7.1 by Gail, who reviews present knowledge of the formation of dust in the shells surrounding asymptotic-giant-branch (AGB) stars and supergiants. This requires separate discussion of the oxygen-rich stars producing silicates and of the carbon stars forming soot and other carbon-rich solids. Can one mimic grain formation processes in the laboratory? Such possibilities are discussed in Sections 7.2, 7.4 by Jaeger and Section 7.3 by Rietmeijer and Nuth. The grains that one actually observes in the ISM have, however, been subject to shocks as well as irradiation by cosmic rays and UV. These processes are discussed in Section 7.5 by Jaeger and Mennella. The spectroscopic characteristics of the grains change under irradiation, for example, the 220-nm feature shifts. One is surprised at the relative constancy of the band wavelength in the observed extinction curves.

This compendium will be useful to both students and experts. It serves both as an introduction to several topics and as a summary of recent results in the field. Most importantly perhaps, it gives different points of view on some of the open questions both from the astrophysical standpoint and from that of the laboratory physicist.

References

1. Bowen, I.S. (1927) *Nature*, **120**, 473.
2. Buhl, D. and Snyder, L.E. (1970) *Nature*, **228**, 267–269.
3. Klemperer, W. (1970) *Nature*, **227**, 1230.
4. Woods, R.C., Dixon, T.A., Saykally, R.J., and Szanto, P.G. (1975) *Phys. Rev. Lett.*, **35**, 1269–1272.
5. Solomon, P.M. and Klemperer, W. (1972) *Astrophys. J.*, **178**, 389–422.
6. Herbst, E. and Klemperer, W. (1973) *Astrophys. J.*, **185**, 505–534.
7. Winnewisser, G., Churchwell, E., and Walmsley, C.M. (1979) *Modern Aspects of Microwave Spectroscopy* (ed. G.W. Chantry), Academic Press, pp. 313–503.

8. Swings, P. and Rosenfeld, L. (1937) *Astrophys. J.*, **86**, 483–486.
9. Saha, M.N. (1937) *Nature*, **139**, 840.
10. Draine, B.T. (2003) *Annu. Rev. Astron. Astrophys.*, **41**, 241–289.
11. Henning, T. (2010) *Annu. Rev. Astron. Astrophys.*, **48**, 21–46.
12. Draine, B.T. (2009) *Space Sci. Rev.*, **143** (1-4), 333.
13. Tielens, A.G.G.M. (2013) *Rev. Mod. Phys.*, **85**, 1021–1081.
14. Gupta, H., Rimmer, P., Pearson, J.C. *et al.* (2010) *Astron. Astrophys.*, **521**, L47.
15. Wyrowski, F., Menten, K.M., Güsten, R., and Belloche, A. (2010) *Astron. Astrophys.*, **518**, A26.
16. Gerin, M., de Luca, M., Black, J. *et al.* (2010) *Astron. Astrophys.*, **518**, L110.
17. Bergin, E.A., Melnick, G.J., Stauffer, J.R. *et al.* (2000) *Astrophys. J. Lett.*, **539**, L129–L132.
18. Hogerheijde, M.R., Bergin, E.A., Brinch, C. *et al.* (2011) *Science*, **334**, 338–33.
19. Bergin, E.A., Cleeves, L.I., Gorti, U. *et al.* (2013) *Nature*, **493**, 644–646.
20. Sturm, B., Bouwman, J., Henning, T. *et al.* (2013) *Astron. Astrophys.*, **553**, A5.
21. Qi, C., Öberg, K.I., Wilner, D.J. *et al.* (2013) *Science*, **341**, 630–632.
22. Allen, M. and Robinson, G.W. (1977) *Astrophys. J.*, **212**, 396–415.

2
Molecular Spectroscopy

Thomas Giesen

High-resolution spectroscopy applied to gas-phase molecules is a powerful tool to derive and to analyze molecular properties from spectral line profiles and transition frequencies. In a simplified scheme, the visible and ultraviolet spectral range (UV–vis) reveals the valence-electronic structure of molecules in ground and excited vibronic states. Spectroscopy in the mid-infrared (IR) reveals the vibrational molecular dynamics, whereas at millimeter/submillimeter wavelengths the molecular structure can be derived from rotational transitions. The spectral resolution is limited by the Doppler effect and – especially in the UV–vis region – by lifetime broadening rather than by instrumental constraints. Because the Doppler width scales linearly with frequency, details of the rotational and hyperfine structures are often resolved only at low frequencies corresponding to millimeter/submillimeter wavelengths.

Since the first discovery of molecules in space by the detection of optical spectra of CN and CH, spectroscopy has successfully been applied to astronomy, not only for identification of new molecular species but also to derive physical conditions, for example, gas excitation temperatures, heat transfer and cooling conditions in star-forming regions, and turbulences and shocks of interstellar gas flow. The amount of accurate spectral data from astronomical observations over the accessible frequency range (from the UV–vis to the millimeter and centimeter wavelength region) has been significantly improved over the last two decades thanks to remarkably enhanced receiver techniques, the access to excellent observation sites on satellites, airplanes, and high-altitude platforms, and through improved angular resolution of interferometrically coupled telescope arrays, such as the Atacama Large Millimeter Array (ALMA) and Atacama Submillimeter Array in Chile.

Laboratory spectroscopic studies of gas-phase molecules allow a direct comparison with astronomical data and have significantly contributed to the interpretation of astrophysical observations. Most of the 180 interstellar molecules known to date have been identified by rotational transitions in the millimeter/submillimeter wavelength region. In the mid- and far-IR region, ro-vibrational transitions, especially of nonpolar molecules which have no pure rotational spectra, have been observed. Examples of recent detections are

Laboratory Astrochemistry: From Molecules through Nanoparticles to Grains, First Edition.
Edited by Stephan Schlemmer, Thomas Giesen, Harald Mutschke and Cornelia Jäger.

benzene (C_6H_{12}) and the fullerenes (C_{60}, and C_{70}). A series of characteristic mid-IR absorption features has been assigned to polycyclic aromatic hydrocarbons (PAHs), consisting of a few ten to a few hundred atoms. Comparison to laboratory data reveals a complex organic interstellar chemistry of medium-sized molecules. In the UV–vis region, the spectra observed in either absorption or emission contain valuable information on electronic states of molecules present in diffuse interstellar clouds. A large number of yet-unidentified spectral lines have been reported up to now. These diffuse interstellar bands (DIBs) still await the assignment to molecular carriers, and, if this ever happens, evidence will come from laboratory measurements.

In recent years, laboratory methods have been developed or further improved to study gas-phase spectra of molecules relevant to astrophysics. Technically speaking, each spectral region has developed specific spectroscopic tools for most sensitive detections and characterization of molecular species, including molecular ions and radicals as well. These techniques comprise resonant two-photon excitation, multiphoton dissociation, fragmentation and electron detachment, laser-induced fluorescence (LIF), and four-wave mixing (FWM) techniques, as well as multipass enhanced absorption and emission spectroscopy in high-Q resonators, multipass optics, and cavity ringdown spectroscopy (CRDS). In addition to powerful, narrow-bandwidth radiation sources, such as frequency-stabilized lasers and synthesizer-driven multiplier chains, intense monochromatic light of large spectral coverage is generated by free-electron lasers and synchrotron facilities, which can cover the entire electromagnetic spectrum from the UV region to the low frequencies of submillimeter wavelengths. For spectroscopic studies on astrophysically relevant molecules, efficient devices to produce short-lived neutral and ionic molecular species, for example, electrical discharges or laser ablation sources, have been developed. In some cases, cooling of these usually short-lived molecules in supersonic jets, in cold rare gas matrixes, or in cold ion traps leads to a significant enhancement of spectroscopic sensitivity.

Although our understanding of the physics and chemistry of the interstellar gas has improved thanks to laboratory studies, a number of fundamental questions still remain. In this chapter, we address current topics of laboratory astrophysics and present strategies for finding the answers. In Sections 2.1 and 2.2, recent laboratory studies in the UV–vis region are presented, which aim at characterization and possible identification of carriers of the diffuse interstellar bands. Section 2.1 summarizes laboratory work on unsaturated carbon chains and rings as possible carriers of the DIBs and presents experimental methods of how to get the optical spectra of short-lived radicals and ions. Metal-containing carbon chains are also considered because of the atomic abundance within the interstellar medium (ISM) of magnesium and aluminum, for example. Section 2.2 is a systematic investigation of PAHs in the visible spectral region and gives details on the experimental methods to gain gas-phase spectra of these mostly nonvolatile species. Experimental studies of PAHs in the mid-IR and their relevance to the characteristic mid-IR absorption features are presented in Section 2.3. Finally, Section 2.4 is an

inventory of current laboratory work on complex molecules studied in the millimeter/submillimeter wavelength region and a status report on their astrophysical detection.

2.1
Electronic Spectroscopy of Potential Carriers of Diffuse Interstellar Bands

Corey A. Rice and John P. Maier

2.1.1
Introduction

The major element of the Universe is hydrogen, but heavier atoms, such as carbon, are produced in nuclear reactions in the interiors of stars. When a star dies, ejected material collides, cools, and recombines. These processes form part of the complex chemistry of the interstellar medium (ISM). Limited knowledge is compiled on rates of reactions, spectroscopic information, and composition of the ISM; however, in the last decades, considerable progress and new developments of techniques for the preparation, isolation, and characterization of unstable neutral, radical, and charged molecular species have been made.

A long-standing enigma in observational astronomy is the identification of some of the species causing the diffuse interstellar bands (DIB). Observations of these absorption features date back a century [1, 2]. There are regions of space containing not only dust grains but also molecular species absorbing light along the line of sight [3]. These features now number close to 400 [1, 4]; they have different widths and intensities, asymmetric shapes, and even some band structure, similar to the unresolved rotational profiles of gas-phase molecules. Identification of DIBs will come from a match of laboratory and DIB wavelengths. Within the band shape and width of the spectral features lies information about the rotational temperature and excited-state lifetime of the absorbing species; however, the astronomical features are also broadened by the velocity distribution of $\sim$10 km s^{-1}. For many years, the possible carriers in the ISM were hypotheses based on conjectured spectral and photophysical properties of certain molecular types. Prominent considerations have been carbon chains and polycyclic aromatic cations [5]. Measurements of the gas-phase electronic spectra of smaller carbon chains such as C_4 and C_5, of their derivatives with hydrogen, nitrogen, and metals, and of some of their ions have given a wealth of spectroscopic information to the field, allowing a search for these species in the diffuse medium [6]. Important were the first direct identification of C_3 (Figure 2.1) [7] and the possibility of H_2CCC to be a DIB carrier [8]; however, in all other cases, only upper limits could be inferred [9].

This chapter considers some of the techniques and molecules that bring insight into the spectroscopic information needed for astronomical comparisons. The experimental gas-phase methods and spectral observations have led to the first-time possibility of testing these by direct comparison of laboratory and astronomical data. In particular, because the electronic spectra in the gas phase could be

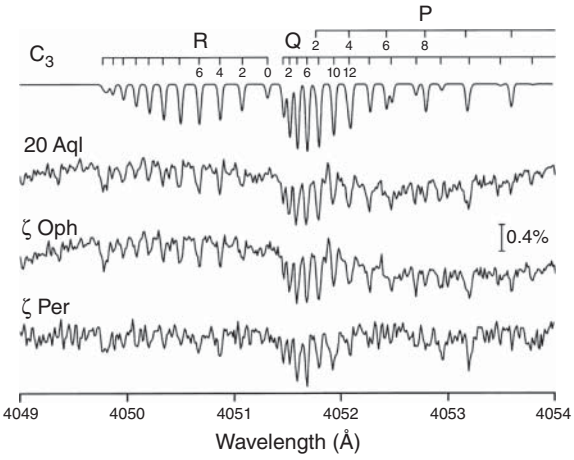

Figure 2.1 A comparison between the simulation at 80 K (top trace) and astronomical observations for the origin band of C_3 $A\,^1\Pi_u - X\,^1\Sigma_g^+$, measured toward three different stars. (Reproduced from [7], copyright 2001 © permission from AIP Publishing.)

obtained for a number of carbon-containing species, it could be concluded that the proposals that bare carbon chains of sizes containing up to a handful of atoms are good candidates as DIB carriers should be excluded [6]. This has been an important advance after all the years of speculations, and, in turn, the results have pointed out promising candidates for future laboratory studies, in particular, odd-numbered carbon chains from sizes C_{15} onwards.

2.1.2
Laboratory Methods

There are difficulties in trying to measure the electronic spectra of transient species in the gas phase. These problems arise whenever the production of a radical, neutral, or charged species is not of sufficient concentration or the sensitivity of the experimental approach is not high enough to measure a spectrum, and some knowledge of the energy region of the transition should be known. The combination of mass selection and matrix-isolation spectroscopy [10] has made the identification of the absorbing species within the electronic spectrum obtainable, and the development of gas-phase techniques couples the two for an unperturbed characterization and comparison with astronomical observations.

The following section outlines the experimental methods that are used to generate and measure the electronic spectra of unstable molecular species. These laboratory approaches include resonant two-color, two-photon ionization (R2C2PI), resonant two-color photodetachment (R2CPD), resonant two-color, two-photon fragmentation (R2C2PF), cavity ringdown spectroscopy (CRDS), four-wave mixing (FWM) technique, and laser-induced fluorescence (LIF).

2.1.2.1 Resonant Two-Color Two-Photon Ionization

To overcome the spectral overlap that is present in CRDS and LIF, mass-selective techniques become advantageous in gas-phase studies to assist in the unambiguous assignment of absorption features. One such gas-phase experimental approach for neutral radicals is R2C2PI [11]. The experimental setup consists of a molecular beam combined with a linear time-of-flight mass spectrometer (TOF-MS). Laser vaporization or pulsed discharge sources are incorporated with supersonic jet expansions, resulting in the production of neutrals, radicals, and ions. The expanded jet is passed through a skimmer, forming a collimated molecular beam. The species of interest enter the interaction region of the TOF-MS, where they are first excited to a resonant state and then, following a short time delay, ionized by the 157-nm radiation from an F_2 laser. Ions are extracted into the TOF-MS, and the separation of ions in the drift tube after resonant excitation allows the different masses to be monitored simultaneously, which is profitable whenever survey searches are performed.

2.1.2.2 Resonant Two-Color Photodetachment

To obtain the electronic spectra of negatively charged carbon chains, a R2CPD method was implemented. This approach is similar to that of R2C2PI and incorporates a molecular beam with a TOF-MS [12]. Carbon anion species are produced in a pulsed gas discharge, and the resulting supersonic expansion is skimmed to ensure collimation. Anions are passed into the extraction region of the TOF-MS and injected into the drift tube, where the ions are focussed to intersect the two laser beams. R2CPD is a pump–probe technique, where the first laser is scanned over the electronic transition and the second one is of a fixed frequency, such that a single photon has sufficient energy to detach an electron after resonant excitation but not enough from the ground state of an anion. The neutrals are detected following photodetachment.

2.1.2.3 Resonant Two-Color, Two-Photon Fragmentation

A challenge related to the comparison of astronomical data with laboratory spectra is the equilibration of the vibrational and rotational degrees of freedom to low temperatures as present in the ISM. Techniques employing free-jet expansions produce rotationally cold radicals and ions; however, vibrational modes are not completely relaxed, though slit-jet expansions are much better than pinhole ones [13]. By confining charged molecular species within an ion trap, buffer gas cooling can be used to relax the ions into the vibrational ground state.

Cations are created using electron impact on an effusive beam of gas. The ions produced are deflected by a magnetic field, separating neutrals from charged species, into a hexapole ion guide, which transmits them into the first quadrupole for mass selection. Mass resolution is ± 0.5 u, and a 36-mm-long 22-pole ion trap is filled with ions for 20 ms [14–16]. Thousands of stored cations are collisionally cooled with a continuous flow or pulse of cryogenic helium (about 10 K), thermalizing the internal degrees of freedom. Cold ions are then probed using the R2C2PF technique, where the first color is the tunable radiation from

a dye laser, and, following a short time delay, probed by a fixed wavelength from another laser. The frequency of the second color is chosen in such a way that the energy of the two photons exceeds the fragmentation threshold. After resonant excitation, the photodissociation products are released from the ion trap by lowering the exit potential. The second quadrupole is tuned to the fragment mass. Spectra are obtained by monitoring the dissociation products while scanning the first color over an electronic transition.

2.1.2.4 Cavity Ringdown Spectroscopy

CRDS is a sensitive absorption technique [17]. The sample, created using a slit-jet expansion discharge, is produced inside an optical cavity consisting of two highly reflective mirrors. A fraction of the laser light is coupled into the cavity and reflected back and forth, where a small percentage of the light envelope leaks out, causing an exponential decay. The ringdown time is related to the absorbance of sample present within the cavity. A major advantage of CRDS is the considerable path length achieved, which can be on the order of kilometers. Another benefit of the setup employed is the fact that the radicals are produced in a 30 mm × 1 mm supersonic slit discharge. When the propagation of the probing laser is along the length of the slit, the Doppler profile is reduced. An absorption spectrum is obtained by measuring the ringdown time as a function of wavelength.

2.1.2.5 Four-Wave Mixing Technique

Absorption methods such as CRDS result in the overlapping of electronic transitions from the different species produced in the plasma. This problem can be circumvented by the FWM technique [18]. This spectroscopic approach is background-free, producing coherent light which is discriminated from laser scatter and plasma emission from the pulsed-discharge source. For degenerate four-wave mixing (DFWM), one of the lasers is split into three components of equal intensity by beamsplitters and sent in a BOXCARS configuration [19] into the interaction region. To increase spectral sensitivity and selectivity, a variant of DFWM, namely two-color resonant four-wave mixing (TC-RFWM) [20, 21], is used. In the case of TC-RFWM, the third beam (probe or dump) is replaced by the output of a second laser and the frequency is scanned as the pump laser remains at a fixed wavelength. Nonlinearity of these techniques enables the disentanglement of overlapping absorptions, for example, C_4H and C_3 (Figure 2.2). Both the amplification of concentration changes and the nanoseconds rather than microseconds of CRDS time structure are advantages.

2.1.2.6 Laser-Induced Fluorescence

LIF is a method that uses the excitation of an absorbing species whereby the emission of light from the molecule is detected. The signal-to-noise ratio of the fluorescence signal is high, providing good sensitivity for detection. LIF has been employed for studying combustion and plasma [22], where transient species are produced similar to that in the ISM. Jet-cooled radicals are produced using laser vaporization of a pure sample rod, such as carbon, in argon gas (10 bar) provided

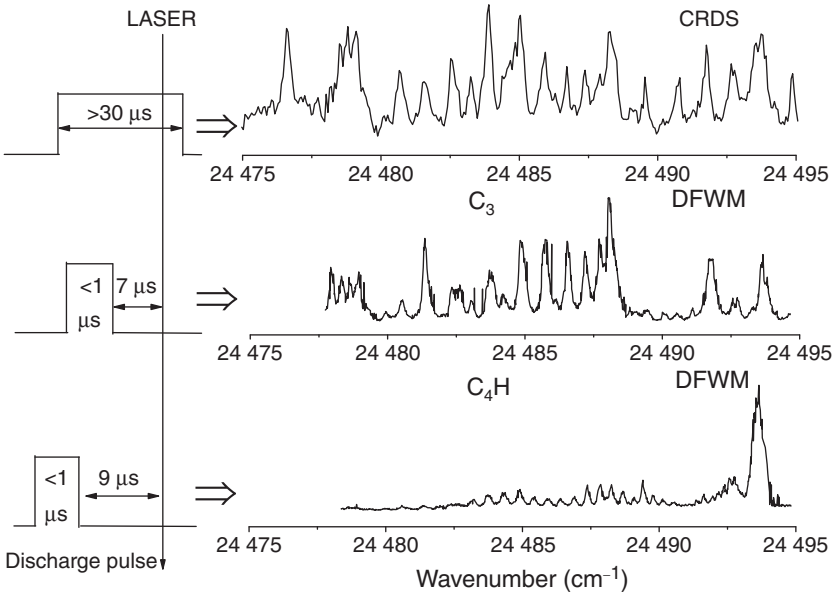

Figure 2.2 Selectivity offered by DFWM combined with a short and intense discharge pulse (<1 μs). The delay between the plasma generation and the laser pulse was increased by 2 μs, enabling disentanglement of the $B\,^2\Pi_i - X\,^2\Sigma^+$ (5^3_0) spectrum of C_4H and a hot band of C_3 ($A\,^1\Pi_u$-$X\,^1\Sigma^+_g$ electronic transition). The cavity ringdown spectrum (top) is with a discharge period of at least 20 μs, resulting in absorptions of C_3 and C_4H to overlap.

by an 0.3-mm orifice pulsed valve. Different species are generated by changing the sample and/or by adding a small percentage of acetylene, diacetylene, or methane to the argon gas mixture. The vaporization plume flows with the carrier gas in an interaction region before undergoing a free-jet expansion. The cold radicals are then probed through LIF using a tunable laser and the fluorescence is collected; the detection is perpendicular to the supersonic expansion and laser radiation.

2.1.3 Species of Astrophysical Interest

2.1.3.1 Molecular Ions

Almost all organic molecules will be ionized in diffuse molecular clouds by the UV radiation field because their ionization potentials (IPs) are lower than that of hydrogen (13.6 eV) and the photon flux is high. Monohydrogenated carbon chain anions and positive variations thereof have been detected in dark clouds, particularly carbon-rich envelopes (e.g., TCM-1 and IRC+10216), by radio astronomy [23, 24]. These charged species are shielded from the intense UV radiation by the outer perimeter of the dense ISM. A famous example for the photostability of an anion is the presence of H^-, causing opacity of the sun. The importance

of molecular ions that are of astrophysical interest are based on millimeter-wave identifications and models of the ISM. Gas-phase electronic spectra of charged species provide a means of their identification within the ISM and a direct comparison to DIB observations. Presented here are examples for carbon chain cations and anions.

Cations Linear polyacetylene cations $HC_{2n}H^+$ have a ground state symmetry $X\,^2\Pi_{g/u}$, g if n = even and u if n = odd. The first excited-state $A\,^2\Pi_{u/g}$ comes from the promotion of an inner-shell electron to the singly occupied molecular orbital (MO). The $B\,^2\Pi_{u/g}$, $C\,^2\Pi_{u/g}$, and $D\,^2\Pi_{u/g}$ excited states are derived by electron excitation from the latter MO to lowest unoccupied MO, giving rise to higher energy transitions. $HC_{2n}H^+$ have been investigated in terms of combustion [25] and astrophysical relevance for some time [26]. The origin bands of the $A\,^2\Pi \leftarrow X\,^2\Pi$ transition were studied for $n = 2$–8 in the gas phase for this purpose [27, 28], and the trend as n increases can be seen in Figure 2.3. However, rotationally resolved origin bands of the $A \leftarrow X$ transitions were obtained only for the chains $n = 2$–4 [29–33], and larger ones ($n = 5$–8) were measured using the R2C2PF technique [27]. Attempts to fit the relevant laboratory measurements to astrophysical spectra have thus far been unsuccessful [9, 27]; however, the upper limit for interstellar abundance was inferred.

A general phenomenon is that the lowest energy dipole-allowed electronic transitions of carbon chains shift systematically to the red with increasing size of the system (Figure 2.3). Thus, only a limited number of members of a homologous series will fall in the window of DIB observations (4000–9000 Å). For example, with polyacetylene cations $HC_{2n}H^+$, the $A\,^2\Pi \leftarrow X\,^2\Pi$ origin bands ($\Omega = 3/2$) lie at 5068.7 Å ($n = 2$), 6001.1 Å ($n = 3$), 7067.8 Å ($n = 4$), and 8156.3 Å ($n = 5$). However, the longer chains, $n = 4, 5, 6$, with the $A\,^2\Pi \leftarrow X\,^2\Pi$ transition in the red or near-infrared, would have excitations to higher states in the visible region [34]. The higher excited states should be considered, provided that the full width at half-maximum (FWHM) of the band is comparable to the DIBs (<0.1–6 Å), which corresponds to excited state lifetimes of ~0.2–50 ps [34].

The $A\,^2\Pi \leftarrow X\,^2\Pi$ origin band of dicyanodiacetylene NC_4N^+ is shown in Figure 2.4. This cation and the isoelectronic species HC_6H^+ are centrosymmetric, having no permanent electric dipole moment, and are inaccessible to radio astronomy. For the case of NC_4N^+, the origin band shows a resemblance to that of the DIB at 5959.5 Å, where the rotational profile of the DIB has the structure of an unresolved P, Q, and R branch contour similar to that of the observed gas-phase spectrum; however, the wavelengths differ by 0.9 Å [9].

The rotational profile of the origin band of the $A\,^2\Pi \leftarrow X\,^2\Pi$ transition of NC_4N^+ changes as the temperature increases from 3 to 150 K. This is due to the $\Omega = 1/2$ spin–orbit component and higher rotational levels becoming populated. The band maximum of the R-branch blue-shifts, while the P-branch fades to the red. As NC_4N^+ is a nonpolar molecule, it is expected that its rotational temperature is similar to that of H_3^+ and C_3, ~50–80 K.

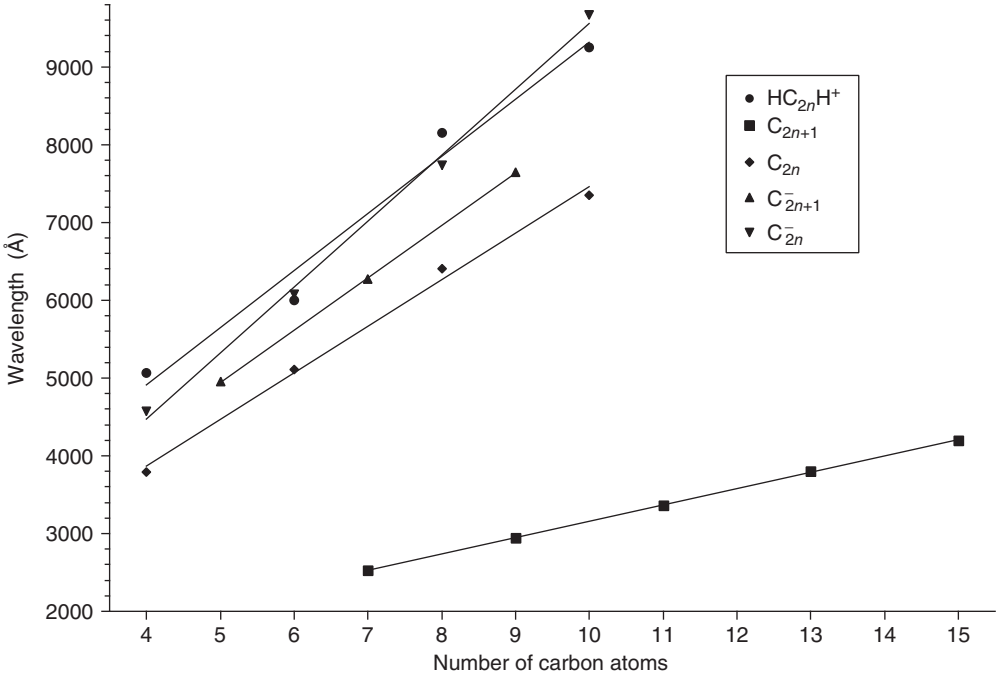

Figure 2.3 Wavelength (Å) of the origin band maxima in the electronic transitions of $HC_{2n}H^+$ ($A\,^2\Pi - X\,^2\Pi$), C_{2n} ($^3\Sigma_u^- - X\,^3\Sigma_g^-$), C_{2n+1} ($^1\Sigma_u^+ - X\,^1\Sigma_g^+$), C^-_{2n} ($^2\Pi - X\,^2\Pi$), and C^-_{2n+1} ($A\,^2\Pi - X\,^2\Pi$) versus the number of carbon atoms.

Another class of positive molecular ions of chemical and astrophysical significance is protonated polyacetylenes. Unsaturated hydrocarbons have been shown to be present in the ISM, and models predict the presence of large polyacetylenic chains [35, 36]. As many chemical reactions in the ISM are of the ion–molecule type, protonated polyacetylenes stand out as important intermediates bridging the gap in the chemistry of carbon chains and cumulenes [37]. $HC_{2n}H_2^+$ ($n = 3, 4$) have been observed in the gas phase using the R2C2PF method [38]; however, only the $B\,^1A_1 - X\,^1A_1$ electronic transition of $HC_8H_2^+$ lies within DIB range at 4672.9 Å. Larger protonated polyacetylenic chains have not yet been measured in the gas phase.

Anions Odd carbon chain anions (C^-_{2n+1}, $n = 1$–4) are open-shell systems, and theoretical studies predicted linear equilibrium structures, corresponding to $\cdots\sigma_g^2\sigma_u^2\pi_{u/g}^4\pi_{g/u}^1$ electronic configuration and $^2\Pi_{g/u}$ ground states. The neutral linear carbon chains have high electron affinities (EAs) of ∼3–5 eV [39], resulting in at least one bound excited state below the photodetachment threshold. C_3^-, which has an EA of 1.99 eV, is the only anion in the $2n + 1$ series that does not have a bound excited state but possesses longer lived Feshbach states, lying above the electron detachment.

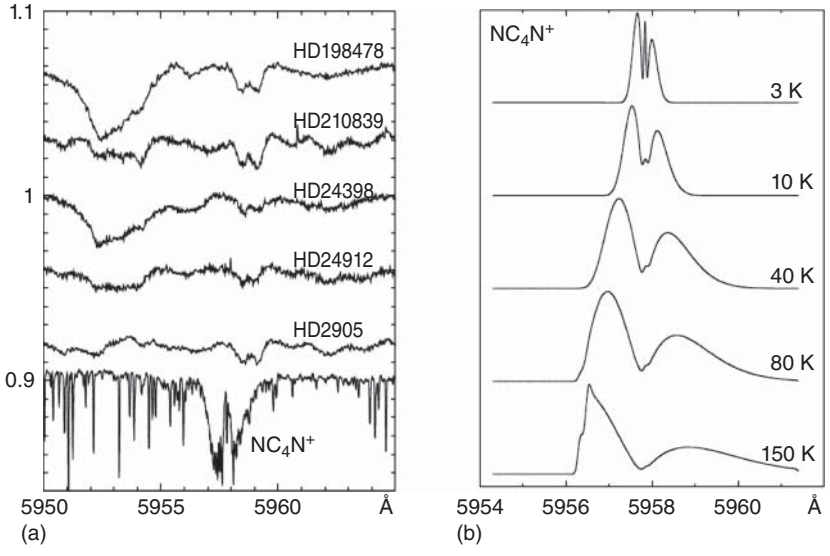

Figure 2.4 (a) Origin band of the $A\,^2\Pi \leftarrow X\,^2\Pi$ transition of NC_4N^+ measured in the laboratory (bottom) compared to absorptions toward the indicated reddened stars. (b) Change in the rotational contour as the temperature is increased from 3 to 150 K.

The maxima of the origin and several other bands in the $A\,^2\Pi_u \leftarrow X\,^2\Pi_g$ transition of C_7^- were found to be close to some DIBs [40]. To test the C_7^- matches, astronomical measurements were recorded from reddened and unreddened stars [41] and the 0_0^0, 3_0^1, and $1_0^2 3_0^1$ bands were found to be in good agreement with DIBs in both relative intensities and wavelength. Several problems were later revealed [42] by higher resolution DIB observations, including that the rotational contour of the 0_0^0 band showed additional features not present in the 6270 Å DIB, and the 1_0^1 peak was red-shifted from 5610 Å DIB by ~2 Å. Thus, as close as the wavelength match may appear at first sight, stringent spectroscopic criteria are required for the confirmation of a carrier. In a similar manner, the transitions of ℓ-$C_3H_2^-$ were found to be close to DIBs [43], though once again a detailed investigation showed small wavelength differences [44].

The electronic transition origins of C_{2n}^- ($^2\Pi - X\,^2\Pi$) and C_{2n+1}^- ($A\,^2\Pi - X\,^2\Pi$) $n = 2$–5 are seen in Figure 2.3. Even-carbon-chain anions C_{2n}^- have the first excited state in the near-IR; however, higher excitations lie in the 4000–9000 Å region. In the C_{2n+1}^- series, the $A\,^2\Pi - X\,^2\Pi$ transition red-shifts as n increases and absorptions occur in the DIB window. When the negative species are larger in size, the photodetachment threshold is lower in energy; however, intramolecular vibrational relaxation stabilizes the anions as the chain length increases.

2.1.3.2 **Bare Carbon Chains**

In Figure 2.5, the origin band of the energetically lowest allowed electronic transition of C_{18} at 5930.5 Å is presented, which was recorded in the laboratory using

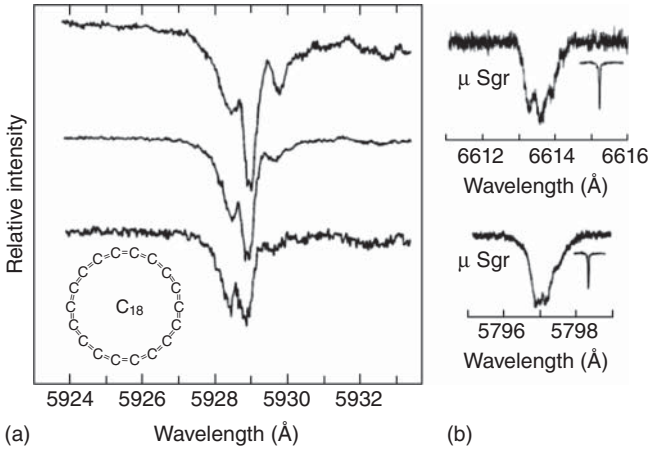

Figure 2.5 (a) Experimentally measured origin band of an electronic transition of cyclic C_{18} located near 5929 Å at a rotational temperature ranging from ~100 K (top trace) to 20 K (bottom). (b) Two diffuse interstellar absorption features measured toward μ Sgr at comparable resolution as for the laboratory C_{18} spectrum. (Reproduced from [46, 47], copyright 1995, 2006 © permission from Wiley & IOP Publishing respectively)

the R2C2PI technique [45]. As seen in the figure, different rotational temperatures are achieved by varying the expansion conditions, where it drops from about 100 K (top trace) to 20 K (bottom). An analysis of the spectra based on experimental evidence, that is, the known position of the transition for the linear C_{18} chain, showed the lack of correlation with the band system of $HC_{18}H$ that appears in the presence of hydrogen in the supersonic discharge expansion, and reasonable agreement with the vertical excitation energies obtained from density functional theory (DFT) calculations on the minimum energy cyclic structures led to the conclusion that the cyclic isomers are the absorbing species. Spectroscopy is currently unable to determine whether the cyclic structures have alternating single and triple bonds (acetylenic C_{9h} symmetry) or equal bond lengths among the carbons (cumulenic D_{9h}).

Particularly striking is the comparison of the 5930.5 Å origin band in the electronic transition of the C_{18} ring with the high-resolution measurements of DIBs, though at different spectral regions [47]. In Figure 2.5, two such results have been selected: the triplet structure observed for the 6614 Å and the doublet for the 5797 Å DIB, measured toward μ Sgr with a resolving power of 300 000 [46]. It is seen that the triplet DIB structure, when shifted to the same wavelength as the C_{18} absorption and at ≈100 K, is almost superimposable as is the case with the doublet peak in the bottom trace for the laboratory spectrum at 20 K. Therefore, it is tempting to suggest that the two observed DIBs are due to plate-like molecules with sizes on the order of C_{18} or larger, with the requirement that the electronic transition responsible has a considerable oscillator strength, which the transition of C_{18} at 5930.5 Å does not have. The central peak would be the origin band, and

the accompanying bands on both sides could be the sequence transitions involving the lowest frequency (skeleton) modes, which remain populated even at low interstellar temperatures.

The C_{2n} chains have $^3\Sigma_g^-$ ground state symmetry, whereas C_{2n+1} chains have a $^1\Sigma_g^+$ closed-shell configuration. In Figure 2.3, the dependence of chain length as a function of wavelength is shown. The open-shell system of C_{2n} chains have their first electronic transition in the visible, whereas the C_{2n+1} series would have to be larger than C_{15}.

Small bare carbon chains, such as C_2 and C_3, may undergo reactions with atomic and molecular hydrogen in interstellar clouds producing, for example, C_2H, C_3H, C_2H_2, and C_3H_2. These unsaturated hydrocarbons have mainly been observed in the ISM using radio astronomy [48–50]. Recently, there is spectroscopic evidence in the optical region for ℓ-C_3H_2 as a possible DIB carrier [8]. Two absorption bands in the $B\,^1B_1 \leftarrow X\,^1A_1$ electronic spectrum of ℓ-C_3H_2 measured in the laboratory in the gas phase by CRDS match the 4881 and 5450 Å DIBs in profile and wavelength.

2.1.3.3 Metal-Containing Carbon Chains

Metal-containing molecules, such as MgCN, have been detected in the circumstellar envelopes of carbon-rich stars by pure rotational spectroscopy [51], and given the fact that Al and Mg are among the elements found in the ISM, some of the DIBs might be due to metal-containing carbon chains. Metal-capped carbon-containing species, which have absorptions in the DIB region (4000–9000 Å) with large enough oscillator strengths, could be feasible candidates.

The $MgC_{2n}H$ ($n = 1$–3) series have been studied because they absorb in the DIB region (Figure 2.6), using the LIF and R2C2PI techniques [82, 83]. As the carbon chain increases in length, the $A\,^2\Pi \leftarrow X\,^2\Sigma^+$ electronic transition red-shifts (Table 2.1), similar to that of other open-shell radicals, such as $C_{2n}H$. MgCCCN and MgC_4H have been considered as carriers for the unassigned B1395 millimeter-wave lines detected in the envelope of IRC+10216 (carbon-rich star) [89]. In particular, the features observed are proposed to originate from an unidentified linear $^2\Sigma$ species with $B_0 = 1.3946$ GHz. MgCCCN and MgC_4H have identical ground state $^2\Sigma$ symmetries and similar rotational constants ($B_0 \approx 1.3925$ and ~1.3972 GHz for MgCCCN and MgC_4H, respectively, and the latter has a ground state rotational constant of 1.3847 GHz, determined from fitting the $A\,^2\Pi \leftarrow X\,^2\Sigma^+$ electronic transition [83]). In the same star, Mg- and Al-containing species, such as MgNC [90], MgCN [51], AlNC [91], AlCl [92], and AlF [93], have all been observed using radio astronomy. However, the absence of the smaller MgC_2H radical in IRC+10216 seems to hint at even lower abundances of MgC_4H [89]. Another characteristic of the $MgC_{2n}H$ chains is that, even though their $A\,^2\Pi \leftarrow X\,^2\Sigma^+$ transitions occur in the DIB range, the oscillator strength f falls off as a function of n. A comparison of $MgC_{2n}H$ ($n = 1$–3) with the DIB absorption features has resulted in no matches [1]; however, the $A\,^2\Pi \leftarrow X\,^2\Sigma^+$ excitation is not the most intense transition. Calculations of the vertical excitation energies of MgC_4H using time dependent

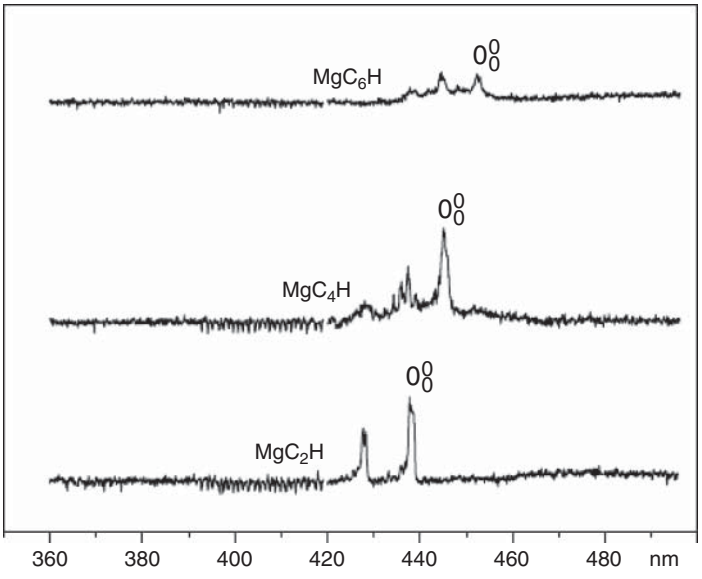

Figure 2.6 The $A\,^2\Pi \leftarrow X\,^2\Sigma^+$ electronic transition of $MgC_{2n}H$ (n = 1–3) measured by a resonant two-color, two-photon ionization technique. (Reproduced from [82], copyright 2008 © permission from IOP Publishing.)

density functional theory (TD-DFT) have shown that there are two higher lying transitions: $A\,^2\Pi - X\,^2\Sigma^+$ (2.79 eV, $f = 0.09$), $B\,^2\Pi - X\,^2\Sigma^+$ (3.05 eV, $f = 0.02$), and $C\,^2\Sigma^+ - X\,^2\Sigma^+$ (4.49 eV, $f = 0.29$) [82]; the B and C excited states have not yet been detected.

In the case of aluminum monoacetylide (AlC_2H), calculations have predicted two stable structures, where the linear form is energetically favored by 41 kJ mol^{-1} over the cyclic isomer [86]. The electronic ground state configuration of linear AlC_2H is $\cdots 4\pi^4 9\sigma^2 5\pi^0$ and $\cdots 7a_1^2 8a_1^2 4b_2^0$ for cyclic $HAlC_2$, giving symmetries of $X\,^1\Sigma^+$ and $X\,^1A_1$. Promotion of an electron from $9\sigma \rightarrow 5\pi$ results in a $^1\Pi$ state; however, for the cyclic $HAlC_2$, $8a_1 \rightarrow 4b_2$ excitation produces the $^1B_1$ state. The electronic spectrum of AlC_2H was obtained using the R2C2PI technique, and based on a rotational analysis, the origin band at 3478.2 Å [86] (Table 2.1) was assigned to the $A\,^1\Pi \leftarrow X\,^1\Sigma^+$ transition of linear AlC_2H.

Another metal-containing carbon chain with known optical transitions is AlC_2, which has a T-shaped cyclic structure (C_{2v}) with the Al situated over the C≡C triple bond, corresponding to an $X\,^2A_1$ ground state. The linear isomer ($X\,^2\Sigma^+$) is higher in energy by 33 kJ mol^{-1} [94]. A rotational and vibrational analysis of the $C\,^2B_2 \leftarrow X\,^2A_1$ (4524.3 Å) and $D\,^2B_1 \leftarrow X\,^2A_1$ (3833.9 Å) electronic transitions, using LIF and R2C2PI (Figure 2.7 and Table 2.1), has been carried out [87, 88]. The lowest electronic excitation $A\,^2A_1 \leftarrow X\,^2A_1$, according to the photoelectron spectrum of AlC_2, lies in the near-infrared (~0.98 eV) [95] outside of the DIB region.

Table 2.1 Summary of measured electronic transitions. q is for cumulenic structures, ac for acetylenic compounds, and *c* for a cyclic arrangement of the carbon atoms.

Species	Transition	Origin (Å)	Method	Reference
C_4	$^3\Sigma_u^- - X\,^3\Sigma_g^-$	3790.0	CRDS	[52]
C_5	$^1\Pi_u - X\,^1\Sigma_g^+$	5110.8	CRDS	[53]
C_5	$A\,^1\Pi_u - X\,^1\Sigma_g^+$	5109.4	R2C2PI	[54]
C_5	$^1\Sigma_u^+ - X\,^1\Sigma_g^+$	4450.4	R2C2PI	[54]
C_6	$2\,^3\Sigma_u^- - X\,^3\Sigma_g^-$	5113.0	R2C2PI	[54]
C_4^-	$C\,^2\Pi_u - X\,^2\Pi_g$	4572.0	R2CPD	[55]
C_6^-	$C\,^2\Pi_g - X\,^2\Pi_u$	6069.4	R2CPD	[56]
C_5^-	$A\,^2\Pi_g - X\,^2\Pi_u$	4959.3	R2CPD	[12]
C_7^-	$A\,^2\Pi_u - X\,^2\Pi_g$	6272.3	R2CPD	[12]
C_7^-	$B\,^2\Pi_u - X\,^2\Pi_g$	4926.6	R2CPD	[12]
C_9^-	$A\,^2\Pi_g - X\,^2\Pi_u$	7645.3	R2CPD	[12]
C_9^-	$B\,^2\Pi_g - X\,^2\Pi_u$	6077.2	R2CPD	[12]
C_{13}^-	$B\,^2\Pi - X\,^2\Pi$	8849.6	R2CPD	[57]
C_2^+	$B\,^4\Sigma_u^- - X\,^4\Sigma_g^-$	5088.5	LIF	[58]
C_6H	$^2\Pi - X\,^2\Pi$	5266.0	CRDS	[59]
C_8H	$^2\Pi - X\,^2\Pi$	6260.4	CRDS	[60]
$C_{10}H$	$^2\Pi - X\,^2\Pi$	7142.9	CRDS	[60]
C_5H	$A\,^2\Delta - X\,^2\Pi$	5321.6	R2C2PI	[61]
C_5H	$B\,^2\Sigma^- - X\,^2\Pi$	4852.4	R2C2PI	[61]
C_7H	$A\,^2\Delta - X\,^2\Pi$	5945.5	R2C2PI	[61]
C_7H	$B\,^2\Sigma^- - X\,^2\Pi$	5396.0	R2C2PI	[61]
C_7H	$C\,^2\Sigma^+ - X\,^2\Pi$	4848.0	R2C2PI	[61]
C_9H	$C\,^2\Sigma^+ - X\,^2\Pi$	5319.2	R2C2PI	[61]
C_3H	$A\,^2A' - X\,^2\Pi$	5210.4	R2C2PI	[62]
C_3H	$B\,^2A'' - X\,^2\Pi$	4867.7	R2C2PI	[62]
C_3H	$C\,^2A'' - X\,^2\Pi$	4314.5	R2C2PI	[62]
C_6H^+	$^3\Pi - X\,^3\Pi$	5131.9	CRDS	[63]
q-$C_{14}H^-$	$^1\Sigma^+ - X\,^1\Sigma^+$	4208.2	R2CPD	[64]
ac-$C_{14}H^-$	$^1\Sigma^+ - X\,^1\Sigma^+$	4208.2	R2CPD	[64]
q-$C_{16}H^-$	$^1\Sigma^+ - X\,^1\Sigma^+$	4576.2	R2CPD	[64]
ac-$C_{16}H^-$	$^1\Sigma^+ - X\,^1\Sigma^+$	4711.2	R2CPD	[64]
q-$C_{18}H^-$	$^1\Sigma^+ - X\,^1\Sigma^+$	4962.3	R2CPD	[64]
ac-$C_{18}H^-$	$^1\Sigma^+ - X\,^1\Sigma^+$	5201.3	R2CPD	[64]
q-$C_{20}H^-$	$^1\Sigma^+ - X\,^1\Sigma^+$	5364.5	R2CPD	[64]
ac-$C_{20}H^-$	$^1\Sigma^+ - X\,^1\Sigma^+$	5684.4	R2CPD	[64]
$C_{11}H^-$	$^3\Sigma^- - X\,^3\Sigma^-$	4117.3	R2CPD	[65]
$C_{13}H^-$	$^3\Sigma^- - X\,^3\Sigma^-$	4504.5	R2CPD	[65]
$C_{15}H^-$	$^3\Sigma^- - X\,^3\Sigma^-$	5145.6	R2CPD	[65]
$C_{13}H^-$	$^1A' - X\,^1A'$	4044.3	R2CPD	[65]
$C_{15}H^-$	$^1A' - X\,^1A'$	4294.8	R2CPD	[65]
C_3H^-	$^3A'' - X\,^3A''$	6773.0	R2CPD	[66]
HC_7H	$^3\Sigma_u^- - X\,^3\Sigma_g^-$	5044.5	CRDS	[67]

(*continued over leaf*)

Table 2.1 (*Continued*).

Species	Transition	Origin (Å)	Method	Reference
HC_9H	$^3\Sigma_u^- - X\,^3\Sigma_g^-$	5817.6	CRDS	[67]
$HC_{11}H$	$^3\Sigma_u^- - X\,^3\Sigma_g^-$	6536.3	CRDS	[67]
$HC_{13}H$	$^3\Sigma_u^- - X\,^3\Sigma_g^-$	7183.8	CRDS	[67]
HC_7H	$A\,^3\Sigma_u^- - X\,^3\Sigma_g^-$	5045.9	R2C2PI	[68]
HC_9H	$A\,^3\Sigma_u^- - X\,^3\Sigma_g^-$	5818.9	R2C2PI	[68]
$HC_{11}H$	$A\,^3\Sigma_u^- - X\,^3\Sigma_g^-$	6538.8	R2C2PI	[68]
$HC_{13}H$	$A\,^3\Sigma_u^- - X\,^3\Sigma_g^-$	7185.6	R2C2PI	[68]
HC_4H^+	$A\,^2\Pi_u - X\,^2\Pi_g$	5068.7	CRDS	[29]
HC_6H^+	$A\,^2\Pi_g - X\,^2\Pi_u$	6001.1	CRDS	[30, 31, 33]
HC_8H^+	$A\,^2\Pi_u - X\,^2\Pi_g$	7067.8	CRDS	[32]
HC_8H^+	$B\,^2\Pi_u - X\,^2\Pi_g$	5662.2	R2C2PF	[34]
HC_8H^+	$C\,^2\Pi_u - X\,^2\Pi_g$	4945.6	R2C2PF	[34]
$HC_{10}H^+$	$A\,^2\Pi_g - X\,^2\Pi_u$	8156.3	CRDS	[28]
$HC_{10}H^+$	$B\,^2\Pi_g - X\,^2\Pi_u$	6466.6	R2C2PF	[34]
$HC_{10}H^+$	$C\,^2\Pi_g - X\,^2\Pi_u$	5661.2	R2C2PF	[34]
$HC_{12}H^+$	$D\,^2\Pi_u - X\,^2\Pi_g$	5357.9	R2C2PF	[34]
$HC_8H_2^+$	$B\,^1A_1 - X\,^1A_1$	4672.9	R2C2PF	[38]
$C_4H_3^+$	$^3E - X\,^3E$	4083.1	CRDS	[69]
HC_6N	$A\,^3\Sigma^- - X\,^3\Sigma^-$	4715.1	CRDS	[70]
HC_5N^+	$A\,^2\Pi - X\,^2\Pi$	5821.4	CRDS	[71]
HC_7N^+	$A\,^2\Pi - X\,^2\Pi$	6699.9	CRDS	[72]
NC_5N	$A\,^3\Sigma_u^- - X\,^3\Sigma_g^-$	4379.7	CRDS	[73]
$NCCN^+$	$B\,^2\Sigma_u^+ - X\,^2\Pi_g$	8886.5	R2C2PF	[16]
$NCCN^+$	$C\,^2\Pi_u - X\,^2\Pi_g$	5759.0	R2C2PF	[74]
NC_4N^+	$A\,^2\Pi_g - X\,^2\Pi_u$	5959.4	CRDS	[71]
NC_6N^+	$A\,^2\Pi_u - X\,^2\Pi_g$	6559.1	CRDS	[75]
HCCS	$A\,^2\Pi - X\,^2\Pi$	4132.7	LIF	[76]
HC_4S	$^2\Pi - {}^2\Pi$	5004.8	LIF	[77]
HC_6S	$^2\Pi - {}^2\Pi$	5895.9	LIF	[78]
HC_8S	$A\,^2\Pi - X\,^2\Pi$	6739.5	CRDS	[79]
$HC_{10}S$	$A\,^2\Pi - X\,^2\Pi$	7499.6	CRDS	[79]
c-C_{14}		5213.7	R2C2PI	[80]
c-C_{18}		5930.5	R2C2PI	[45]
c-C_{22}		6205.8	R2C2PI	[45]
MgC_2H	$A\,^2\Pi - X\,^2\Sigma^+$	4384.2	LIF	[81]
MgC_4H	$A\,^2\Pi - X\,^2\Sigma^+$	4454.3	R2C2PI,LIF	[82, 83]
MgC_6H	$A\,^2\Pi - X\,^2\Sigma^+$	4526.3	R2C2PI,LIF	[82, 83]
CaCCH	$A\,^2\Pi_{1/2} - X\,^2\Sigma^+$	6457.0	LIF	[84]
CaCCH	$A\,^2\Pi_{3/2} - X\,^2\Sigma^+$	6426.7	LIF	[84]
SrCCH	$A\,^2\Pi_{1/2} - X\,^2\Sigma^+$	7054.2	LIF	[85]
SrCCH	$A\,^2\Pi_{3/2} - X\,^2\Sigma^+$	6919.9	LIF	[85]
AlCCH	$A\,^1\Pi - X\,^1\Sigma^+$	3478.2	R2C2PI	[86]
AlC_2	$C\,^2B_2 - X\,^2A_1$	4524.3	R2C2PI,LIF	[87, 88]

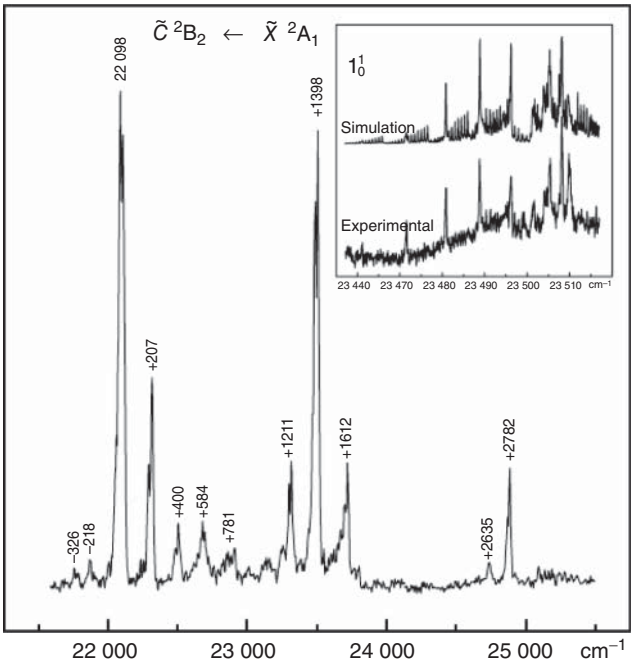

Figure 2.7 Low-resolution 5 cm^{-1} laser bandwidth spectrum of the $B\,^2B_2 \leftarrow X\,^2A_1$ electronic transition for the T-shaped AlC_2 radical recorded using a resonant two-color two-photon ionization technique. (Reproduced from [88], copyright 2009 © permission from AIP Publishing.) The inset shows the 1_0^1 vibronic band measured with 0.15 cm^{-1} laser bandwidth.

2.1.4 Outlook

Over the years, different experimental techniques have been employed to record the electronic spectra of a variety of carbon-containing species, which has generated a wealth of knowledge within this area. Survey measurements carried out on mass-selected ions in argon and neon matrices have been a guide for gas-phase studies. The latter have been obtained using supersonic jet expansions or by buffer gas cooling within ion traps, which is mandatory for direct comparisons with astronomical observations. The possibility of ℓ-C_3H_2 as a DIB carrier illustrates this: the match of two gas-phase absorption bands measured in the laboratory by CRDS with the 4881 and 5450 Å DIBs. In connection with the DIBs, electronic spectra obtained from the studies presented in this chapter exclude bare carbon chains and their derivatives of sizes up to a dozen or more atoms as carriers; however, larger species, such as carbon chains and rings, should be considered if the oscillator strength is of a considerable magnitude. Another criterion is that the radicals and molecular ions should have excited-state lifetimes on the order of tens of picoseconds. Therefore, higher excited states of these species, having electronic

transitions in the DIB range (4000–9000 Å), should not be dismissed. These findings help in refining the types of molecules that should be focused on in future laboratory characterizations.

Acknowledgments

This research was made possible by the continued financial support of the Swiss National Science Foundation (current project 200020-124349/1) and concerted efforts of many postdoctoral fellows and PhD students.

2.2
UV–Vis Gas-Phase Absorption Spectroscopy of PAHs

Yvain Carpentier, Gaël Rouillé, Mathias Steglich, Cornelia Jäger, Thomas Henning, and Friedrich Huisken

2.2.1
Introduction

The diffuse interstellar bands (DIBs) are currently the oldest unsolved puzzle of astronomical spectroscopy. Based on observational data, it is known today that gas-phase molecules, rather than dust particles, are the carriers of the DIBs; but their definite identification is still lacking. In the 1980s, polycyclic aromatic hydrocarbons (PAHs) were proposed as particularly attractive candidates not only for the carriers of the DIBs but also for the unidentified infrared (UIR) bands [96, 97]. The existence of PAHs in various astrophysical environments, ranging from planetary nebulae, reflection nebulosities, circumstellar disks to even active galactic nuclei, has actually been inferred from the detection of infrared (IR) emission bands related to aromatic C–H and C–C vibrations [98, 99]. However, the identification of a specific molecule based on these vibrational mid-IR bands is not possible. Only information about the size and charge state distributions, as well as the ratio between aliphatic and aromatic carbon, can be obtained [100]. Based on energetic arguments, the IR emission bands are attributed to aromatic molecules containing about 50 carbon atoms [101]. After H_2 and CO, PAHs are probably the most abundant molecules in the interstellar medium (ISM) [102]. It is possible that they are also responsible for various other still-unexplained features like the extended red emission (ERE) [103], the blue luminescence [104], the UV extinction bump at 217.5 nm [105], and especially the DIBs [1, 106, 107]. For recent reviews on PAHs, see, for example, the publications by Tielens [101] and Salama [108].

Models show that PAHs play a major role in interstellar chemistry and physics. Giving rise to photoelectric heating, they are important for the energy balance of the ISM, and they affect the charge state of interstellar clouds. This shows that, in addition to their spectroscopic properties, many other properties and interactions with the surroundings (photoionization, electron recombination, photodissociation, chemical reactions, cluster formation, etc.) must be studied.

In general, the size of PAHs may range from small molecules containing a few rings, such as the three-ring species anthracene and phenanthrene, to large units that can be considered as fragments of graphene, in which the peripheral carbon atoms are passivated by hydrogen. To further add to the diversity, PAHs can be partly dehydrogenated and/or they can be charged. These species may be produced as a result of the interaction with the interstellar radiation field.

In order to prove whether observational spectra contain features that can be attributed to PAHs, we have to compare them with laboratory spectra. To make this comparison meaningful, laboratory measurements must be carried out under astrophysical conditions, that is, at low temperature and in an interaction-free environment in the gas phase. The most elegant method where these requirements are ideally met is the supersonic jet technique. A rare gas (mostly He or Ar) is seeded with the vapor of the PAH species to be studied and expanded through a small nozzle into a high vacuum. The expansion provides an extremely rapid cooling of the molecules down to temperatures between ~2 and 50 K, depending on what internal degree of freedom is considered (translation, rotation, or vibration). Moreover, at a distance of a few nozzle diameters, the density has decreased so much that the PAH molecules fly freely without interacting with each other or with the rare gas atoms. Owing to the low density, the spectroscopic technique applied to investigate their optical properties must be extremely sensitive, a requirement which calls for the application of laser spectroscopy.

A very sensitive method, often applied to perform electronic spectroscopy in molecular beams, is laser-induced fluorescence (LIF). In this technique, the resonant excitation of molecules by the radiation of a tunable laser is detected indirectly by measuring the fluorescence emitted by the excited molecule. Of course, it can be applied only if the molecule does fluoresce. Moreover, care must be taken if one wants to compare the intensities of absorption bands involving different upper states as the fluorescence yields may be different. On the other hand, the method is extremely sensitive because the signal is measured on a very low background.

A direct absorption technique, yielding proper intensity ratios and being better adapted to astrophysical applications, is provided by the so-called cavity ring-down spectroscopy (CRDS) [109]. The first applications of CRDS to the study of jet-cooled PAHs were reported in the late 1990s [110, 111]. In this technique, the tunable laser beam is injected into a cavity of extremely high quality (high reflectance of the mirrors) containing the supersonic jet expansion, and the decay of the transmitted laser beam is measured as a function of the laser wavelength. The resonant absorption of the PAH molecules in the jet causes a faster decay of the signal, which can be correlated with the absorption cross section at this particular wavelength. To determine the absolute absorption cross sections is very difficult, however, as the density of PAH molecules in the jet is not known and as it is not homogeneous along the cavity axis.

Another technique to obtain spectroscopic information on molecules at cryogenic temperature – however not in the gas phase – is matrix isolation spectroscopy (MIS). It is based on the incorporation of the molecules to be studied

into a solid rare gas matrix and their spectroscopic characterization with a conventional spectrometer. Although the method does not supply gas-phase data which can be directly compared with astrophysical observations, it is nevertheless extremely useful as it delivers overview spectra spanning the entire region from the UV to the near-IR. These overview spectra can then be used to estimate the corresponding transitions in the gas phase and to define the spectral region where the more sophisticated supersonic jet CRDS measurements are to be carried out. Moreover, MIS consumes very small amounts of sample so that it may be the proper choice if the PAHs are available only in small quantities.

For a complete comparison between astronomical and laboratory-based spectra, it is important to know, besides the position, width, and line shape of an absorption band, also its line strength or absorption cross section. This information is required if one wants to derive column densities from astrophysical observations or upper limits of column densities if the spectral features do not appear in the astrophysical spectrum. As discussed before, this absolute data is difficult to obtain. However, it is possible to provide sufficiently good estimates of absorption cross sections if the absorption spectra measured in a supersonic jet or in a cryogenic matrix can be correlated with solution spectra which are usually given in absolute units.

In this chapter, we present an overview of the efforts carried out in our laboratory to obtain low-temperature gas-phase spectra of PAHs in the UV and visible (vis) and to determine absolute absorption cross sections for the measured spectra. The respective PAH samples were either purchased or obtained through cooperations. Finally, we describe a method for synthesizing large PAHs in the laboratory under astrophysically relevant conditions. It is based on the CO_2-laser-assisted pyrolysis of hydrocarbons. First results will be presented.

Although we are going to focus on recent results obtained in our laboratory, we would like to give a short account of what has been achieved by other researchers. Table 2.2 lists the electronic transitions of PAHs that have been measured by other groups in the gas phase at low temperature. Owing to the limited space, this list cannot be exhaustive. Therefore, if a PAH molecule has been studied by more than one laboratory, we decided to cite only the work of highest relevance. Priority was given first to the study covering the largest wavelength range or, second, to the study with the highest accuracy. Note that in this table we have not included the molecules that were studied in our laboratory, as they are discussed in more detail below and in the original literature quoted. The smallest molecule listed in Table 2.2 is naphthalene ($C_{10}H_8$) and the largest hexabenzocoronene ($C_{42}H_{18}$). The positions of the origin bands of the respective transitions are given in the fourth column. We chose to quote them as wavelengths in nanometer for air because most astronomical observations of DIBs are reported in this unit. Unfortunately, in the original literature it is not always clearly stated whether the given band positions are referred to air or vacuum. Therefore, we applied the following rule: If no explicit statement was made, we assumed that wavelength positions were given for air and the wavenumber positions for vacuum. The latter values were converted to wavelengths in nanometer according to $\lambda = 10^7\,\tilde{\nu}^{-1}$ and

Table 2.2 Spectroscopic studies of electronic transitions of PAHs by other authors.

Molecule	Formula	Transition	Origin[a] (nm)	Technique	Reference
Naphthalene	$C_{10}H_8$	$S_1 \leftarrow S_0$	312.212*	LIF	[112]
Azulene	$C_{10}H_8$	$S_1 \leftarrow S_0$	699.925*	CRDS	[111]
Azulene	$C_{10}H_8$	$S_2 \leftarrow S_0$	347.62*	LIF	[113]
Azulene	$C_{10}H_8$	$S_3 \leftarrow S_0$	293.08*	LIF	[114]
Azulene	$C_{10}H_8$	$S_4 \leftarrow S_0$	281.53*	LIF	[114]
Pyrene	$C_{16}H_{10}$	$S_1 \leftarrow S_0$	367.49*	LIF	[115]
Tetracene	$C_{18}H_{12}$	$S_1 \leftarrow S_0$	446.355†	HB[b]	[116]
Triphenylene	$C_{18}H_{12}$	$S_1 \leftarrow S_0$	334.748*,‡	LIF	[117]
Benzo[*a*]anthracene	$C_{18}H_{12}$	$S_1 \leftarrow S_0$	376.683*	LIF	[118]
Benzo[*a*]anthracene	$C_{18}H_{12}$	$S_3 \leftarrow S_0$	293.853*	LIF	[118]
Chrysene	$C_{18}H_{14}$	$S_1 \leftarrow S_0$	375.90*	LIF	[119]
Benzo[*a*]pyrene	$C_{20}H_{12}$	$S_1 \leftarrow S_0$	395.80	LIF	[120]
Benzo[*a*]pyrene	$C_{20}H_{12}$	$S_2 \leftarrow S_0$	~365	LIF	[120]
Benzo[*ghi*]perylene	$C_{22}H_{12}$	$S_2 \leftarrow S_0$	368.46*	CRDS	[121]
Pentacene	$C_{22}H_{14}$	$S_1 \leftarrow S_0$	536.9	LIF	[122]
Coronene	$C_{24}H_{12}$	$S_1 \leftarrow S_0$	415.37‡	LIF	[123]
Coronene	$C_{24}H_{12}$	$S_2 \leftarrow S_0$	333.78*,‡	LIF	[124]
Terrylene	$C_{30}H_{16}$	$S_1 \leftarrow S_0$	519.667	LIF	[125]
Ovalene	$C_{32}H_{14}$	$S_1 \leftarrow S_0$	466.22	LIF	[126]
Ovalene	$C_{32}H_{14}$	$S_2 \leftarrow S_0$	425–430	LIF	[126]
Hexabenzocoronene[c]	$C_{42}H_{18}$	$S_1 \leftarrow S_0$	433.40†,‡	R2C2PI[d]	[127]

[a] Wavelength positions λ_{air} expressed in nanometer. * The origin position was given by the authors in wavenumbers and converted by us to wavelength (see text). † Wavelength position explicitly given for vacuum and converted to air (see text). ‡ The origin band could not be observed as the transition is strongly forbidden. The position of the vibrational band with the longest wavelength is reported.
[b] Hole-burning technique derived from LIF.
[c] Full name: Hexa-*peri*-hexabenzocoronene.
[d] Resonant two-color, two-photon ionization.

then corrected to apply to air. When the wavelengths were explicitly given for vacuum, we transformed them to wavelengths in air. It is interesting to note that, in the wavelength range considered here (280–700 nm), the difference between λ_{vacuum} and λ_{air} varies from 0.08 to 0.19 nm, respectively.

2.2.2 Experimental

2.2.2.1 Supersonic Jet Cavity Ringdown Spectrometer

In order to study the spectroscopy of PAHs in a supersonic jet, the molecules to be studied have to be transferred into the gas phase and expanded, together with a carrier gas (typically He or Ar), into a vacuum. At room temperature, the PAHs are generally in the solid phase in the form of a powder. As far as small PAHs

are concerned, their vapor pressure can be increased to a useful level simply by heating the powder in a small reservoir attached to the supersonic jet source close to its nozzle. As the PAHs increase in size, the temperature that has to be applied to achieve a given vapor pressure also increases. But the high temperature may cause the decomposition of the molecule, making the method inappropriate. As an alternative, laser vaporization can be applied, as has been done for the case of hexabenzocoronene [127]. However, laser vaporization is difficult to combine with CRDS because the molecular beam pulse is very short [128].

We have developed heated pulsed sources to generate supersonic jets of rare gases seeded with PAHs. Details are given in Ref. [129]. In contrast to continuous sources, pulsed nozzles may be operated at higher stagnation pressures, so that the densities of molecules in the jet are sufficient to carry out absorption spectroscopy. Each source consists of a pulsed solenoid valve that controls the opening of a pinhole nozzle in the heated reservoir containing the PAH sample. An electrode assembly can be mounted at the nozzle exit to generate an electrical discharge in the jet and to produce a beam of PAH cations [130].

In conventional laser absorption spectroscopy, the attenuation of a tunable laser beam is measured when it is directed through the material under study. The sensitivity can be significantly enhanced with a multipass arrangement based on reflection optics. However, it is always limited by the noise of the radiation source.

In contrast, the principle of CRDS is to measure the decay of a laser pulse trapped in a high-quality optical cavity containing the absorbing sample. The latter must be optically thin and can be, for example, a supersonic jet. A schematic view of our supersonic jet CRDS is shown in Figure 2.8. Pulses emitted by a tunable laser source are injected into an optical cavity formed by two high-reflectance mirrors M1 and M2. While the pulses are reflected back and forth, each time a small portion of the light is transmitted through M2 resulting in a decaying signal, which can be measured with a photomultiplier detector. Finally, the photomultiplier signal is recorded by a digital oscilloscope, which transfers

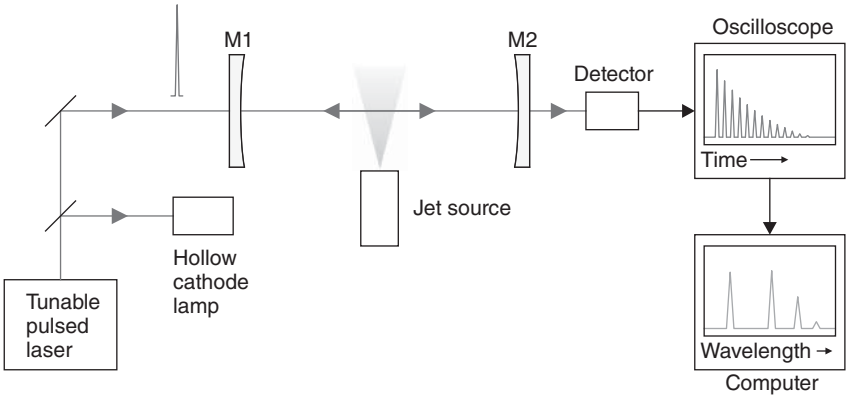

Figure 2.8 Schematic of the supersonic jet cavity ringdown spectrometer setup.

the waveform to a computer. A dedicated program fits an exponential decay to the experimental data, yielding the time constant τ.

The decay rate τ^{-1} can be expressed by

$$\tau^{-1} = c\,L_c^{-1}\left(\sigma N L_s - \ln R\right) \tag{2.1}$$

where c is the speed of light in vacuum, L_c is the length of the cavity, σ is the absorption cross section of the molecules present in the beam path, N is the number density of the molecules in the jet, L_s is the length of the sample along the cavity axis, and R is the reflectance of the mirrors. Thus, by measuring τ^{-1} while varying the wavelength of the light beam, absorption spectra can be obtained with backgrounds that depend on R and not on the intensity of the laser beam. The photon losses due to scattering are not included in Eq. (2.1), as they can be considered by taking an effective value of R.

Interestingly, molecular absorption cross sections can be measured by CRDS provided that the other parameters of Eq. (2.1) are known. In the case of a supersonic jet seeded with PAH molecules, it is, however, difficult to evaluate N with sufficient accuracy. Therefore, we will employ another method to derive absolute absorption cross sections based on calibrated solution spectra (Section 2.2.3.1).

Details of our CRDS setup have already been published [129–131]. Briefly, we use a wavelength-tunable pulsed dye laser as the light source. The linewidth is ~0.1 cm^{-1}, and the pulses have a duration of 5 ns. A frequency doubling system allows us to extend the range of the laser source to the UV. A pinhole and a converging lens are employed to form a collimated beam with near-Gaussian geometry. It is injected into an optical cavity defined by two high-reflectance mirrors. Typical reflectances are in the range 0.9995–0.9999. The decay signal is detected by a fast photomultiplier protected with optical filters, averaged by a digital oscilloscope, and the resulting waveform is transferred to a computer. A fit is carried out to determine the decay time constant τ. In accordance with Eq. (2.1), by plotting $\tau^{-1}c^{-1}L_c$ as a function of wavelength, an absorbance spectrum ($\sigma N L_s$) is obtained superimposed on a background that depends on R.

In order to obtain a wavelength calibration for the measured absorption spectra, a fraction of the laser beam is directed into a hollow-cathode lamp filled with neon gas. The optogalvanic spectrum of Ne I is measured simultaneously with the CRDS spectrum, providing absolute wavelength references. As the number of Ne I lines is in general limited within the range of the CRDS spectrum, several lines are also measured individually over a broader region immediately before proceeding with the CRDS scan.

For a review on CRDS, the reader is referred to Ref. [132]. Finally, it is worthwhile to mention the development of broadband CRDS techniques. The multiplex integrated cavity output spectroscopy (MICOS) technique was applied in a study on the cations of naphthalene ($C_{10}H_8^+$), acenaphthene ($C_{12}H_{10}^+$), and pyrene ($C_{16}H_{10}^+$) [133]. The incoherent broadband cavity-enhanced absorption spectroscopy (IBBCEAS) technique was demonstrated for azulene [134].

2.2.2.2 Matrix-Isolation Spectroscopy

Absorption spectroscopy in supersonic jets is usually applied in a very narrow wavelength range and requires rather large amounts of sample. In contrast, MIS allows the exploration of a wide range of wavelengths simultaneously while consuming only very little sample. This technique consists in the preparation of a solid transparent matrix in which the molecules under study are kept isolated from each other, usually at cryogenic temperatures.

Because of the interactions taking place between the molecules and the surrounding matrix material, the bands in MIS spectra are broadened and shifted in comparison with jet-cooled gas-phase measurements. For this reason, MIS spectra should not be compared with the results of astrophysical observations. However, MIS is efficient in providing approximate band positions, which is very useful for determining the scan parameters for a measurement in supersonic jets. Moreover, gas-phase band positions can be estimated by extrapolation if MIS data for different matrix materials are available (Section 2.2.3.2). Provided that this is possible, in some cases the MIS data could be sufficient to demonstrate that a particular molecule is not responsible for a given interstellar feature.

We routinely carry out MIS studies using either Ne or Ar as matrix material. This choice is determined by the fact that the lighter rare gases provide an environment with the weakest interaction so that broadening and line-shift effects are minimized. Our setup has already been described in detail elsewhere [135–137]. Figure 2.9 depicts the components relevant for an MIS experiment. A CaF_2 substrate transparent to UV and visible wavelengths is mounted on the cold finger

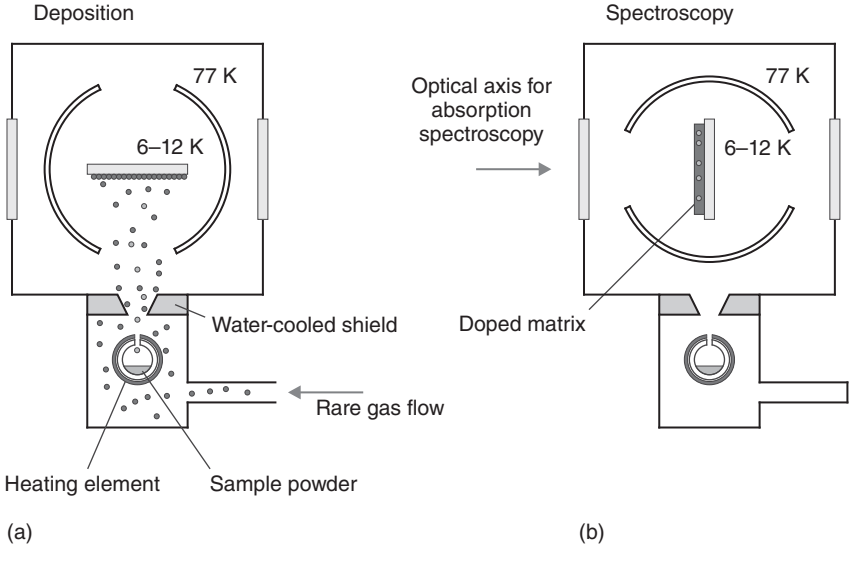

Figure 2.9 Matrix-isolation spectroscopy setup. (a) Molecules exit the oven and are deposited on a cold substrate with an excess of rare gas atoms. (b) After the doped matrix is formed, the substrate and heat shield are rotated by 90° to carry out absorption spectroscopy in transmission.

of a closed-cycle cryostat incorporated into a high-vacuum chamber and cooled down to cryogenic temperatures (6.5 K for Ne and 12 K for Ar). The substrate can be rotated together with its heat shield (~77 K). The sample is prepared in the configuration depicted in Figure 2.9a. At first, a pure layer of rare-gas atoms is deposited on the cold substrate to prevent the deposition of molecules directly on the substrate. Next, the oven that contains the PAH sample is heated up in a separate chamber. During this heating-up period, the heat shield is in the position shown in Figure 2.9b, in order to prevent the PAH molecules from forming a film on the substrate. When the temperature of the oven is stable, the rare-gas flow is started and the matrix deposition can proceed. The deposition is stopped when the matrix is thick enough for absorption measurements, and the substrate is rotated into the position shown in Figure 2.9b. Absorption spectra are recorded by measuring the transmission through the matrix and substrate with a commercial spectrophotometer.

Note that laser vaporization can be used if large PAH molecules are difficult to transfer into the vapor phase. Finally, it should be mentioned that it is also possible to study PAH ions in matrixes. The simplest method to produce them is by irradiating the previously prepared neutral matrix with UV light at $\lambda = 121.6$ nm from a hydrogen discharge lamp (Ly-α line).

2.2.3 Data Analysis

2.2.3.1 Derivation of Absorption Cross Sections

The photoabsorption cross sections of PAHs in the gas phase are of particular interest for astronomers who want to derive the abundance of such molecules in space or at least quote an upper limit of their concentration relative to H if no spectral match is found [138]. These values are also required for the refinement of models that attempt to simulate the IR emission of PAHs after the absorption of UV–vis photons [139].

The absorption cross section of a free-flying molecule is difficult to determine experimentally since one needs to know accurately the number density of the species interacting with the laser beam. On the other hand, for such large molecules as the PAHs, theoretical calculations do not provide a reliable alternative to experiments since the results highly depend on the level of theory and on the geometry used for the calculation.

To derive estimates of the absorption cross sections of PAHs, one can resort to the solution spectra of such molecules which can be measured quantitatively in the laboratory [140]. Compared to those of the gas phase, the spectral features of a solution spectrum are affected by a shift of the band positions and a broadening of the band profiles. Both effects result from the interaction of the solute with the surrounding solvent molecules. These effects can be reduced by the use of a nonpolar solvent such as cyclohexane. To a first approximation, one can neglect the solvent effect and assign to a transition in the gas phase the same absorption cross section as measured in solution. This approximation has already been used

in the astrophysical literature to calibrate the matrix spectra of coronene and ovalene against solution spectra [141] and to estimate the oscillator strength of a weak band of hexabenzocoronene in a jet spectrum [127]. Unfortunately, a single band in a solution spectrum often corresponds to several bands in the jet spectrum, and the jet spectrum generally covers only a short wavelength range. Both circumstances make a one-to-one assignment very difficult. In this situation, the measurement of an MIS spectrum in a cryogenic rare gas matrix may overcome the problem. The perturbation induced by the neighboring rare gas atoms is much smaller than in a solution at 25 °C and, therefore, the individual vibronic features are much better resolved. At first, the MIS spectrum is calibrated against the solution spectrum, and then the narrow features of the jet spectrum are calibrated against the MIS data.

We resort to Figure 2.10 to describe the complete procedure for a specific example for which we chose perylene. The room-temperature solvent spectrum (perylene in cyclohexane), the MIS spectrum (perylene in neon at 6.5 K), and the jet spectrum are displayed by the dash-dotted, dashed, and solid curves, respectively. Note that the features in the solution spectrum are much broader than in the Ne matrix spectrum, and these again are much broader compared to the jet spectrum. Further, note that the matrix spectrum is red-shifted from the jet spectrum, and the solution spectrum again is red-shifted from the matrix spectrum. All spectral features appearing between 350 and 450 nm are assigned to the $S_1 \leftarrow S_0$ transition, which is the electronic transition with the lowest energy. The arrows plotted above the curves start at the respective origin positions and point to the range where the vibronic transitions evolve. Another electronic

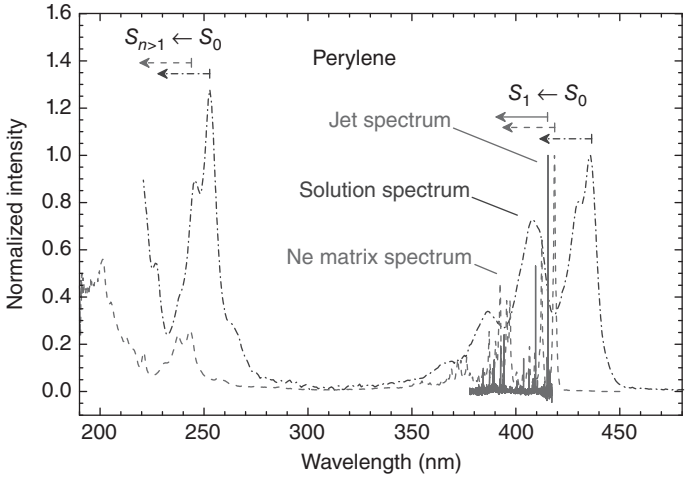

Figure 2.10 Absorption spectra of perylene measured in a supersonic jet around 10 K (solid curve) in a neon matrix at 6.5 K (dashed curve) and in cyclohexane at room temperature (dash-dotted curve). All spectra were normalized according to their $S_1 \leftarrow S_0$ origin band located between 400 and 450 nm.

transition is observed around 250 nm. It involves an electronic state S_n ($n > 1$), not specified here, with higher energy. The fact that the matrix and solution shifts depend on the specific electronic transition can be exploited to distinguish between different electronic states.

Within the first electronic transition ($S_1 \leftarrow S_0$), one can easily distinguish between three different vibronic band groups. This becomes more apparent in Figure 2.11, where the same data are plotted as a function of wavenumber. To compensate for the matrix and solution shifts, the corresponding spectra were shifted by 177 and 1130 cm^{-1}, respectively, to higher energy. (Expressed in wavelengths, these shifts correspond to 3.1 and 19.6 nm, respectively.) It can be seen that all vibronic bands have experienced the same shift, suggesting that they belong to the same electronic transition. It is also interesting to note that, for most narrow features observed in the jet spectrum, we can find a broader counterpart in the matrix spectrum. Finally, it becomes clear that the solution spectrum is indeed too broad to establish a correlation with the jet spectrum and that the matrix spectrum can take the role to mediate between solution and jet spectra.

Figure 2.11 allows us to establish the spectral ranges for which the calibration is performed. At first, the matrix spectrum is calibrated against the solution spectrum given in absolute units by integrating both spectra from 22 000 to 32 000 cm^{-1} and equating the areas. In this way, the absorption cross section of each band of the Ne matrix spectrum is obtained. In a second step, we perform the same procedure, however, for a much smaller spectral range (from 23 800 to 24 250 cm^{-1} in the case of perylene) to calibrate the jet spectrum against the

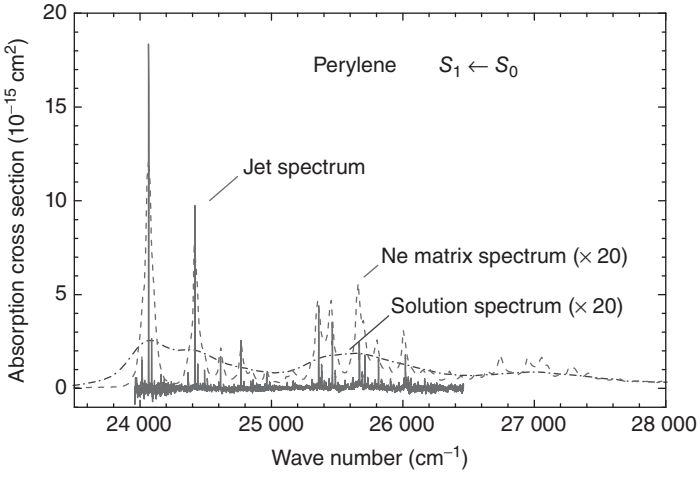

Figure 2.11 Same absorption spectra of perylene as in Figure 2.10 but now plotted as a function of wavenumber. To allow a proper comparison and calibration, the matrix and solution spectra were shifted, compared to the jet spectrum, by 177 and 1130 cm^{-1}, respectively, to higher energy.

matrix spectrum. It is interesting to note that the maximum absorption cross section of the $S_1 \leftarrow S_0$ origin band in the jet spectrum is more than 20 times larger than the corresponding band in the Ne matrix. This is because the origin band is this much narrower in the jet than in the matrix.

2.2.3.2 Extrapolation of Gas-Phase Transitions from MIS Data

We have already mentioned that the absorption bands of molecules measured in rare gas matrixes are broadened and shifted with respect to the gas phase. These effects are due to the interactions that take place between the molecules and the rare gas atoms surrounding them. As a consequence, MIS data are not relevant for a close comparison with DIB spectra. Still, they can be exploited to estimate the band positions in the gas phase. These approximate positions are useful for preparing measurements in jets, and they may compensate for the lack of jet-cooled data.

The dominating mechanism in the interaction between a PAH molecule and the surrounding rare gas atoms is the dispersion effect. It arises between polarizable species and is proportional to the product of their mean static dipole polarizabilities [142]. As the polarizability of the molecule changes upon electronic excitation, the dispersion interaction energy changes as well, thus causing the matrix-induced band shift. If different electronic states are associated with different polarizabilities, the band shift may vary for each electronic transition. In general, a red shift is observed since the dispersion effect tends to lower the energy of the system and because the polarizability of a PAH normally increases upon electronic excitation. Since the dispersion effect also depends on the polarizability of the matrix material, a given electronic transition is found at different positions if the spectra are measured in different matrixes.

Various models have been proposed to evaluate the dispersion interaction energy. In addition to the polarizabilities of the interacting species, they include a factor that depends on the relative distances between the molecule and the rare gas atoms. As the structural details are difficult to assess, we assume that this factor does not significantly change whether we consider a Ne or Ar matrix. With this assumption, we obtain the result that the matrix shift $\Delta\tilde{\nu}$ should be proportional to the polarizability of the matrix material (α_{Ne} and α_{Ar}) with the same proportionality factor.

Thus, provided that spectra measured in Ne and Ar matrixes are available, the gas-phase position $\tilde{\nu}_{\mathrm{gas}}$ of a band, in terms of wavenumber, can be calculated from the respective band positions $\tilde{\nu}_{\mathrm{Ne}}$ and $\tilde{\nu}_{\mathrm{Ar}}$ in the matrixes according to

$$\tilde{\nu}_{\mathrm{gas}} = \tilde{\nu}_{\mathrm{Ne}} + \frac{1}{R_\alpha - 1}\left(\tilde{\nu}_{\mathrm{Ne}} - \tilde{\nu}_{\mathrm{Ar}}\right). \tag{2.2}$$

In this formula, $R_\alpha = \alpha_{\mathrm{Ar}}/\alpha_{\mathrm{Ne}} = 4.13$ is the ratio of the polarizabilities of Ar to Ne [143]. Making use of Eq. (2.2) is equivalent to a determination of the gas-phase band position by extrapolating the respective positions in Ar and Ne matrixes to a "matrix" with zero polarizability.

As an example, let us discuss with Figure 2.12 the application of this simple rule to the origin band of the $S_1 \leftarrow S_0$ transition of 2,3-benzofluorene. The vertical axis at the left-hand side gives a measure of the polarizability of the matrix

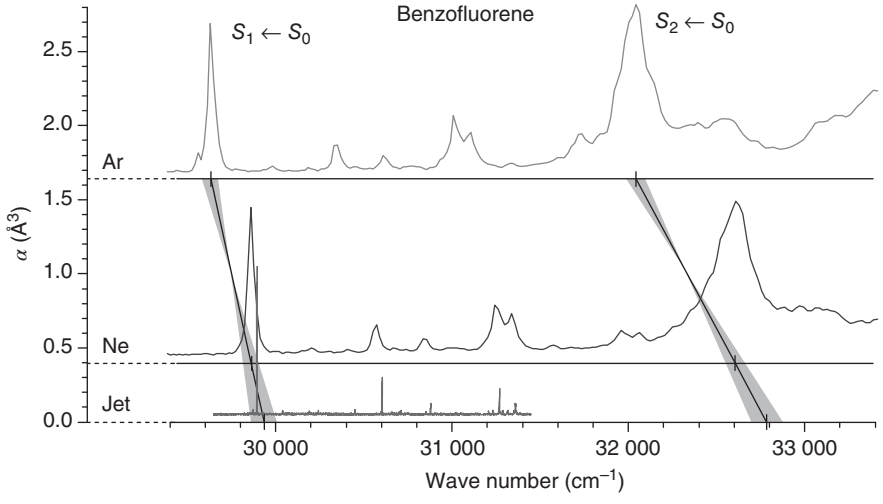

Figure 2.12 Determination of the gas-phase positions of the origin bands of the $S_1 \leftarrow S_0$ and $S_2 \leftarrow S_0$ transitions of 2,3-benzofluorene by extrapolation of matrix data.

material. Normalized spectra recorded in Ar and Ne matrixes are plotted above the horizontal solid lines drawn at the levels of the respective rare gas polarizabilities. The jet-cooled spectrum is associated with zero polarizability. The solid lines connecting the positions of the origin bands measured in both matrixes are extrapolated to $\alpha = 0$. They yield the gas-phase positions of the origin bands according to Eq. (2.2). For $S_1 \leftarrow S_0$, the figure shows that the extrapolated value (29 933 cm^{-1}) falls very close to the true gas-phase band position (29 894.3 cm^{-1} [144]). Applying the same procedure to the $S_2 \leftarrow S_0$ transition, we find the gas-phase position at 32 786 cm^{-1}. The fact that this extrapolation has a weaker slope demonstrates that, compared to the $S_1 \leftarrow S_0$ transition, the matrix-induced red shifts are larger for the $S_2 \leftarrow S_0$ transition. Taking into account the possible errors in the determination of the matrix band positions, mainly resulting from the given accuracy of the spectrometer (0.3 nm) and the wavelength step of the scan (0.2 nm), the gray shaded areas demonstrate the uncertainty of the extrapolations.

We applied the extrapolation to several PAHs for which jet-cooled as well as matrix spectra in Ar and Ne are available, and we could confirm that the method works quite well. Analyzing the results for seven transitions of six different PAHs, we found that the accuracy of the procedure is ±50 cm^{-1}.

2.2.4
Results and Discussion

Applying the CRDS technique described in Section 2.2.2, we have studied the spectroscopy of several PAHs in the gas phase at low temperature as provided in the expansion of a supersonic jet. Figure 2.13 presents an overview of all absorption spectra measured in our laboratory and compares them with

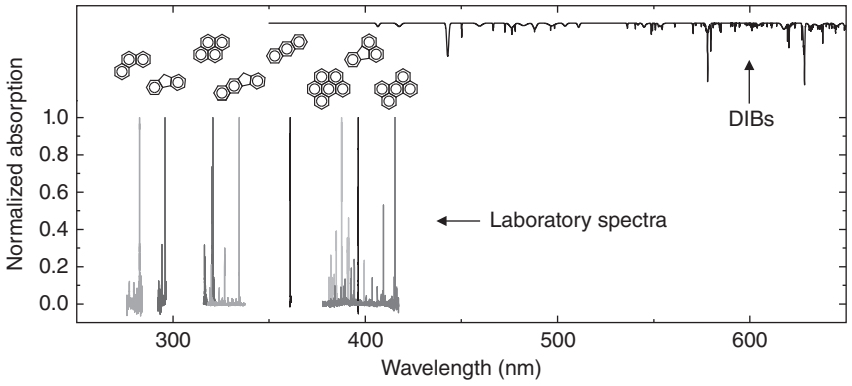

Figure 2.13 Absorption spectra of jet-cooled PAHs measured by cavity ringdown spectroscopy. The synthetic DIB spectrum displayed at the top for comparison is based on the data compiled by Jenniskens (http://leonid.arc.nasa.gov/DIBcatalog.html).

a synthetic spectrum representing the DIBs [1]. In the order of increasing wavelength, the laboratory spectra include those for phenanthrene [145], fluorene [145], pyrene [146], 2,3-benzofluorene [144], anthracene [129], benzo[*ghi*]perylene [131], fluoranthene [145], and perylene [131]. They cover a wavelength range from 280 to 420 nm. Comparison with the DIB spectrum shows that there are no coincidences. Moreover, it is seen that major DIBs are located at larger wavelength. Because high-quality astrophysical observations are missing for the range where the laboratory spectra were taken, new high-resolution spectra were recorded from five different heavily reddened supergiants, using the Ultraviolet and Visual Echelle Spectrograph (UVES) at the Very Large Telescope (VLT) on Cerro Paranal in Chile [138]. However, this high-quality observational data also did not reveal any coincidence with the PAH spectra obtained in our laboratory. A similar study carried out by Salama *et al.* [147] came to the same conclusion.

In order to draw further conclusions from the nonobservation of PAH features in the astrophysical spectra and to derive upper limits of column densities for the PAHs whose absorption bands were measured in the laboratory, absolute absorption cross sections are needed. We applied the method, described in Section 2.2.3.1 for the case of perylene, to all PAH molecules whose normalized spectra are displayed in Figure 2.13. The results are summarized in Table 2.3.

The table includes the assignment to the electronic transition, the central wavelength in air (λ_{air}) of the origin band, its full width at half-maximum (FWHM), the integrated absorption cross section for the origin band, its oscillator strength, and the upper limit of the column density (N_{max}) assuming a detection limit of 1 mÅ equivalent width. For the case where the origin band consists of a two-component rotational profile, we quote as band position the position of the minimum between the two branches. Owing to a vibronic interaction between the S_2 and S_1 states, the spectrum of the $S_2 \leftarrow S_0$ transition of pyrene is composed of band clusters.

Therefore, in Table 2.3, we report for pyrene only the position of the strongest component.

The oscillator strength f was calculated in the approximation of a weak transition using the expression [148]

$$f = \frac{4\epsilon_0 mc^2}{e^2 \lambda_0^2} \int \sigma_\lambda d\lambda \tag{2.3}$$

where ϵ_0, m, c, e, and λ_0 are the vacuum permittivity, the electron mass, the speed of light in vacuum, the charge of the electron, and the central wavelength of the absorption band, respectively. It is important to note that the $S_1 \leftarrow S_0$ oscillator strengths, determined for the PAH transitions considered here, cover more than two orders of magnitude (from 8.0×10^{-5} to 1.6×10^{-2}). This implies that some molecules would be seen more easily than others if their concentrations were comparable. In many cases, the $S_2 \leftarrow S_0$ is stronger than the $S_1 \leftarrow S_0$ transition.

The integrated cross section can be taken to derive the column density N of a molecule toward a line of sight using the relation

$$N = \frac{W_\lambda}{\int \sigma_\lambda d\lambda}. \tag{2.4}$$

In this equation, W_λ is the equivalent width of the band of interest in an astrophysical spectrum. In the case where the absorption band is not observed, the same formula can be used to determine an upper limit of the column density, $N_{\max}$. Then we have to insert for W_λ the detection limit in units of the equivalent width. Assuming that a value of 1 mÅ is quite realistic, we calculated upper limits of the column density and quote them in the last column of Table 2.3. This equivalent width is consistent with recent high signal-to-noise astrophysical observations [138, 149]. For example, depending on the line of sight, Gredel *et al.* [138] report equivalent widths between 1 and 7 mÅ for the spectral ranges where anthracene, pyrene, and 2,3-benzofluorene absorb. For the specific case of perylene, a column density of 1.4×10^{11} cm^{-2} would be needed to be able to detect this molecule in an astrophysical cloud with a detection limit of 1 mÅ equivalent width. Similar upper limit values were derived by Salama *et al.* [147].

Various errors, including experimental, data processing, and methodological, may affect the accuracy of our cross-section determination. The major source of experimental uncertainty is the difficulty to accurately measure the PAH concentration in the solution, which directly affects the derivation of the absorption cross section. From repeated solution preparations with subsequent absorption measurements, we estimate this error to be smaller than 10%. In the data analysis, the integration is not always straightforward since the spectra in solution and in the matrix may be affected by scattering, giving rise to a continuum in the spectra. Another difficulty may arise from the overlapping of vibronic bands belonging to different electronic transitions. However, when we apply the calibration to the first electronic transition, these effects are less pronounced.

Finally, in our procedure, the solution and matrix effects on the band intensities, which were already discussed, are completely neglected. In the literature, one

Table 2.3 Spectral properties (assignment, position, width, integrated cross section, and oscillator strength) of the origin bands of the PAH transitions considered in this chapter.

Molecule	Electronic transition	Band position (nm)	FWHM (nm)	Reference	$\int \sigma d\lambda$ (10^{-16} cm^2 nm)	Oscillator strength	$N_{max}^{a)}$ (cm^{-2})
Fluorene	$S_1 \leftarrow S_0$	295.989	0.017	[145]	2.0	0.026	4.9×10^{11}
Anthracene	$S_1 \leftarrow S_0$	361.073	0.034	[129]	1.9	0.016	5.3×10^{11}
Phenanthrene	$S_1 \leftarrow S_0$	340.921	0.020	[145]	0.016	0.00016	6.2×10^{13}
	$S_2 \leftarrow S_0$	282.642	0.090	[145]	9.8	0.14	1.0×10^{11}
Pyrene	$S_2 \leftarrow S_0$	320.822	0.55	[146]	8.9	0.097	1.1×10^{11}
Fluoranthene	$S_1 \leftarrow S_0$	396.416	0.043	[145]	0.043	0.00031	2.3×10^{13}
2,3-Benzofluorene	$S_1 \leftarrow S_0$	334.416	0.018	[144]	0.84	0.0085	1.2×10^{12}
Perylene	$S_1 \leftarrow S_0$	415.529	0.022	[131]	7.4	0.048	1.4×10^{11}
Benzo[*ghi*]perylene	$S_1 \leftarrow S_0$	399.454	0.038	[131]	0.011	0.00008	9.1×10^{13}

[a)] An upper limit of the column density toward a hypothetical astrophysical object is calculated assuming a detection limit of 1 mÅ equivalent width.

can find various studies carried out with the aim of correlating integrated band intensities of solution spectra with those of gas-phase spectra. Unfortunately, no general rule can be applied because the spectral perturbation strongly depends on the nature of both solvent and solute molecules. Quantum mechanical approaches exist, but the expressions are not in a form to be conveniently applied to experiments. On the other hand, a classical model may be useful for giving an estimate of the correction. Within the model of Chako [150], the ratio of the oscillator strengths in the gas phase and in solution can be written as

$$\frac{f_{\text{gas}}}{f_{\text{sol}}} = \frac{9n}{(n^2+2)^2} \tag{2.5}$$

where n is the refractive index of the solvent. For cyclohexane, this factor is 0.77–0.79 in the wavelength range between 280 and 420 nm. However, as the Chako factor is controversial, we abstained from applying any correction. Taking into account all uncertainties, we estimate that the gas-phase values given in Table 2.3 for the integrated absorption cross section and the oscillator strength are accurate to within 50%.

To strengthen the arguments for the validity of our method and to be able to give an estimate for the error that we make in the first step of the calibration, we can test whether, for a specific example, the relative absorption cross sections of PAHs are conserved from the solution to the matrix. For this purpose, we have prepared a Ne matrix containing three different PAHs by evaporating a three-component mixture at constant temperature. Provided that the vapor pressures of the three components are precisely known at the given temperature, we also know the relative concentrations of the three species in the matrix. As an example, we have studied a matrix containing the three PAHs perylene, benzo[*ghi*]perylene, and coronene. The results are displayed in Figure 2.14 and summarized in Table 2.4.

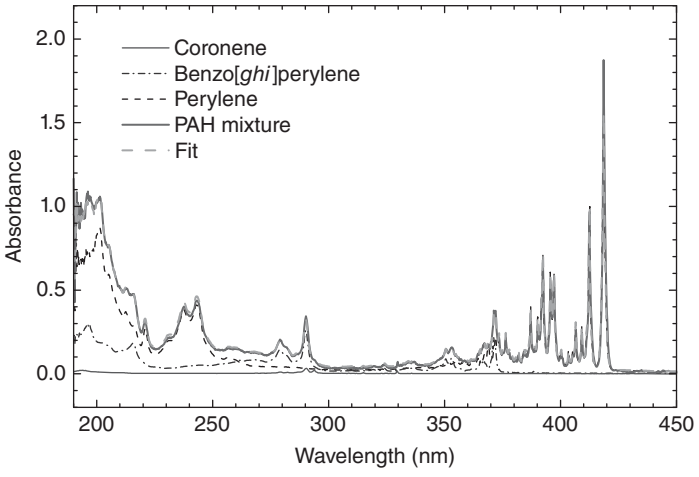

Figure 2.14 Ne matrix spectrum of a mixture of PAHs compared with the spectra of the individual molecules. A linear combination of the three individual spectra (light dashed curve) reproduces the mixture spectrum fairly well.

The three-component mixture evaporated at 130 °C and embedded into the Ne matrix at 6.5 K gives rise to the absorption spectrum plotted by the thick solid curve. The individual components, measured separately, are given by the dashed (perylene), dash-dotted (benzo[*ghi*]perylene), and thin solid (coronene) curves. Using the calibrated cross sections for the three species given in Table 2.3, we can perform a least-squares fit to derive the individual contributions of each species to the three-component matrix spectrum. While the fit is displayed in Figure 2.14 by the light dashed curve, the individual contributions are given in Table 2.4 in the fourth column. Ideally, these values should be equal to the molar fractions derived from the vapor pressures (third column). The relative deviations between the fitted results and those obtained from the vapor pressure are given in the last column. These figures give an idea of how accurate our calibration procedure might be. Note that a possible error in the vapor pressure determination [151, 152] will also affect this comparison.

Table 2.4 Vapor pressures at 130 °C and relative contributions of the three PAH molecules studied in Figure 2.14.

Molecule	Vapor pressure at 130 °C[a] (Pa)	Molar fraction[b]	Molar fraction from fit	Relative deviation (%)
Perylene	0.02047	0.682	0.774	13
Benzo[*ghi*]perylene	0.00920	0.307	0.217	−29
Coronene	0.00034	0.011	0.009	−18

[a] From Refs [151, 152].
[b] Derived from vapor pressures.

To conclude the discussion on the assignment of absolute absorption cross sections to the measured PAH jet spectra, we present the final result of this procedure in Figure 2.15. The figure contains the same spectra as in Figure 2.13, except that they are now calibrated. From the molecules studied, the $S_1 \leftarrow S_0$ transition of perylene with its origin band at 415.529 nm clearly dominates the long-wavelength region of the composite spectrum. It is also interesting to note that the $S_1 \leftarrow S_0$ transitions of fluoranthene and phenanthrene are so weak that they had to be emphasized by arrows.

As discussed in Sections 2.2.1 and 2.2.3.2, MIS spectra are very useful for the purpose of obtaining an overview and to estimate the positions of the absorption bands in the gas phase. For different reasons, we could not yet measure the absorption spectra of some interesting larger PAHs (corannulene, coronene, dibenzorubicene, and hexabenzocoronene) in supersonic jets. However, we were able to characterize them in Ne matrixes. The results are displayed in Figure 2.16. In order to prepare the matrixes, the PAH samples were vaporized by heating them in an oven, except for coronene which was vaporized with a laser.

Panel (a) shows the spectrum of corannulene, which looks very similar to an earlier spectrum measured by us in an Ar matrix and which has been discussed in detail in Ref. [135]. The spectrum is dominated by the strong origin band of the $S_6 \leftarrow S_0$ transition near 250 nm. At longer wavelengths, the broad features belong to the $S_4 \leftarrow S_0$ and $S_5 \leftarrow S_0$ transitions. Because of the symmetry properties of the molecule, the one-photon absorptions from S_0 to S_1, S_2, and S_3 are forbidden and could not be detected.

In panel (b), the spectrum of coronene, which was already presented in Ref. [137], shows two remarkable electronic transitions in the near-UV region. The strongest bands near 290 nm mark the origin region of the $S_\beta \leftarrow S_0$ transition. Between 300 and 350 nm, one can see narrower features attributed to the $S_2 \leftarrow S_0$

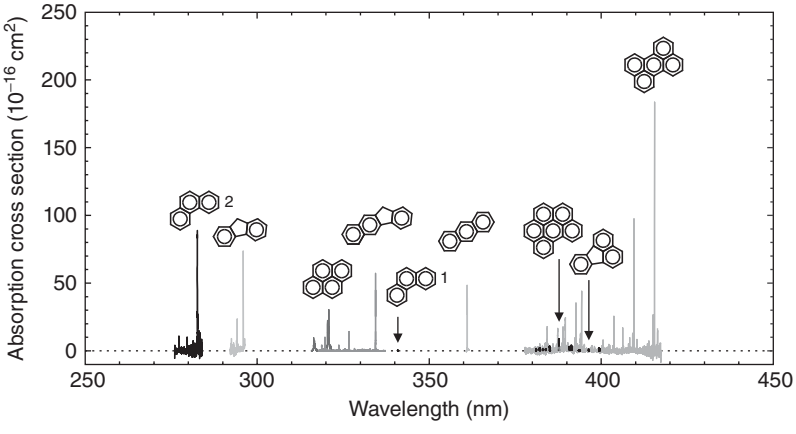

Figure 2.15 Absorption spectra of jet-cooled PAHs measured by cavity ringdown spectroscopy and calibrated against the respective solution and Ne matrix spectra. Weak transitions are emphasized by arrows pointing to them.

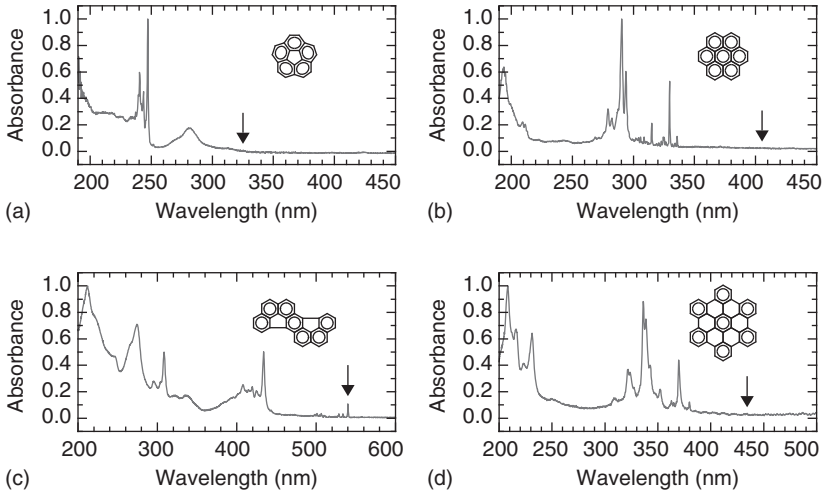

Figure 2.16 Normalized absorption spectra of corannulene (a), coronene (b), dibenzorubicene (c), and hexabenzocoronene (d) isolated in Ne matrixes at 6 K. The arrows point to the positions of the $S_1 \leftarrow S_0$ origin bands except for corannulene where the arrow marks the $S_4 \leftarrow S_0$ transition.

transition. The peak pattern in the $S_\beta \leftarrow S_0$ transition reflects a level structure arising from the interaction between the S_2 and S_β states. Although the $S_1 \leftarrow S_0$ transition is forbidden and cannot be seen in this spectrum, it is possible to observe it near 400 nm under optimized experimental conditions [141].

The spectrum of dibenzorubicene, plotted in panel (c), shows numerous features, narrow and broad. The bands in the visible wavelength range are of particular interest since they lie in a region where DIBs have been observed. In a recent article [153], we assigned the weak band at 540.0 nm to the origin of the $S_1 \leftarrow S_0$ transition. The strong peak at 434.4 nm was attributed to $S_2 \leftarrow S_0$.

Finally, panel (d) depicts the spectrum of hexabenzocoronene which we analyzed in Ref. [136]. It is very similar to the coronene spectrum of panel (b). The $S_2 \leftarrow S_0$ and $S_\beta \leftarrow S_0$ transitions are shifted to longer wavelengths, and the energy difference between the two excited states is smaller. This likely contributes to the fact that the bands are broader than in the coronene spectrum. Although it is too weak to be seen in the figure, we also measured the forbidden $S_1 \leftarrow S_0$ transition marked by an arrow [136].

Only three of the transitions mentioned above have been studied in the gas phase at low temperature. These are the $S_1 \leftarrow S_0$ and $S_2 \leftarrow S_0$ transitions of coronene and the $S_1 \leftarrow S_0$ transition of hexabenzocoronene (Table 2.2). Since the spectra of corannulene, dibenzorubicene, and hexabenzocoronene are now available for Ne and Ar matrixes, band positions in the gas phase can be extrapolated with the method described in Section 2.2.3.2. Table 2.5 lists the extrapolated air wavelength positions for some selected bands. In the case of hexabenzocoronene, the extrapolated position for the $S_1(\nu \neq 0) \leftarrow S_0(0)$ band (433.2 nm) is in good

Table 2.5 Extrapolation of gas-phase positions for vibronic bands of corannulene, dibenzorubicene, and hexabenzocoronene.

Molecule	Band	Ar matrix (nm)	Ne matrix (nm)	Gas phase extrapolated (nm)
Corannulene	$S_6(0) \leftarrow S_0(0)$	249.5	247.2	246.5
Dibenzorubicene	$S_1(0) \leftarrow S_0(0)$	548.4	540.0	537.4
Dibenzorubicene	$S_2(0) \leftarrow S_0(0)$	441.6	434.0	431.6
Hexabenzocoronene	$S_1(\nu \neq 0) \leftarrow S_0(0)$	438.3	434.4	433.2
Hexabenzocoronene	$S_\beta(\nu \neq 0) \leftarrow S_0(0)$	342.0	336.2	334.4

agreement with the cold beam measurement reported in Ref. [127]. The authors gave a vacuum wavelength position of 433.52 nm, which corresponds to 433.4 nm in air.

Figure 2.13 reveals that the wavelengths of PAHs that we have investigated so far in the gas phase do not match the wavelength range in which most of the DIBs are observed. This is because the molecules that we have studied are rather small. To access the longer wavelength region, one has to go to larger PAHs. This could be shown with the matrix spectra of some particular PAHs presented in Figure 2.16.

Unfortunately, it is difficult to have access to large PAHs for spectroscopic studies. Therefore, we decided to synthesize samples of PAHs in our own laboratory employing CO_2-laser-induced pyrolysis of ethylene in a gas-flow reactor. Details are reported elsewhere [154]. Aside from being able to produce PAH mixtures containing large molecules, the technique offers the advantage that it provides gas-phase condensation conditions similar to those encountered in astrophysical environments where PAHs are likely to be produced [155].

Our studies showed that, depending on the laser power which affects the temperature in the reaction zone, different carbonaceous nanomaterials can be obtained. Low temperatures ($T \leq 1700$ K) favor the production of PAHs, whereas at comparatively higher temperatures fullerene- or onion-like nanoparticles are formed. Using a continuous-wave CO_2 laser with a power of 60 W, we realized low-temperature synthesis conditions resulting almost exclusively in the formation of PAHs [154]. The thus-obtained PAH mixture was extracted from the filter by dissolution in dichloromethane (DCM) and subsequent evaporation of the solvent. Furthermore, an enrichment of the sample with the heavier PAH molecules was achieved by washing the sample with methanol which dissolves only the lighter species. Finally, in order to prepare the Ne matrix for spectroscopy, the remaining dried sample was evaporated in an oven kept at 400 °C (Section 2.2.2.2).

Figure 2.17 shows the absorption spectrum of the PAH mixture just described and already reported in Ref. [137]. The spectrum reveals many small features in the UV, for example, the $S_2 \leftarrow S_0$ origin band of pyrene at 323.5 nm, but also various absorption bands in the visible between 380 and 500 nm, as can be clearly seen in

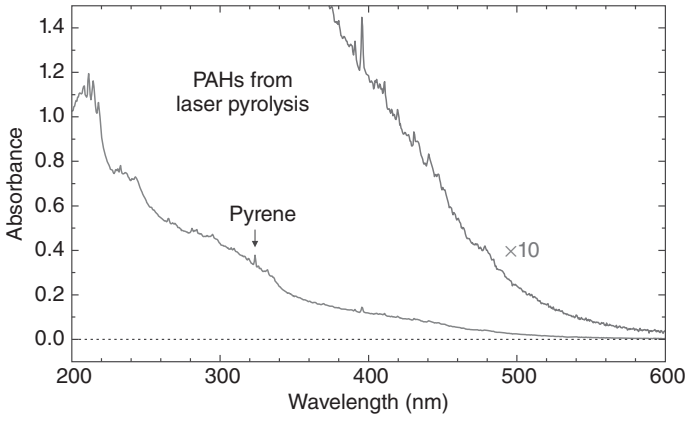

Figure 2.17 Ne matrix spectrum of a mixture of PAHs produced by laser pyrolysis of ethylene. The lighter PAH species have been removed by washing the sample in methanol.

the spectral part magnified by a factor of 10. These features fall well into the range where the density of DIBs is rather high (Figure 2.13), even though a matrix shift of $\lesssim$3 nm is considered. Hence, it can be concluded that laser pyrolysis is a suitable technique to produce PAHs that are sufficiently large to reveal absorption features in the region where DIBs are prominent. As discussed before, the matrix spectrum displayed in Figure 2.17 cannot be directly compared with astrophysical observations. To make a proper comparison, gas-phase spectra must be measured, which, however, is still a difficult task as the concentration of the individual molecules in the mixture is rather low. Finally, it is worthwhile to mention that Figure 2.17 also reveals a strong absorption band with a maximum just below 220 nm, which is very close to the interstellar UV extinction bump at 217.5 nm. The possible contribution of grains composed of PAHs to the UV bump is discussed in Ref. [137].

2.2.5
Conclusion

In this chapter, we reviewed laboratory experiments devoted to the UV–vis spectroscopy of PAHs. The goal of these studies was to provide a database of PAH gas-phase absorption bands that could be compared with astronomical observations for the identification of DIBs. Until now, no agreement has been found. Nevertheless, the laboratory data can be used to derive upper limits for the column densities of the respective PAHs in the astrophysical object considered [138]. In order to do so, one has to know the absolute absorption cross sections. We presented here a practical method of obtaining rather good estimates for the absorption cross section. In addition, we showed that gas-phase band positions of PAHs can be estimated fairly well even if jet-cooled spectra are not available. However, it must be emphasized that gas-phase measurements are mandatory if one needs to know exact band positions and if detailed knowledge of the line shapes is required.

Although attempts to correlate DIBs with PAH features have been unsuccessful up to now, the possibility that PAHs may be responsible for some of the interstellar bands should not be rejected. From the discussion presented in Section 2.2.4, it becomes clear that further laboratory studies should concentrate on larger PAHs which have absorption bands in the spectral range above 425 nm where the density of DIBs is much higher. Attempts to synthesize samples with PAHs absorbing in this spectral range and to characterize them are in progress.

Acknowledgments

This work was supported by the Deutsche Forschungsgemeinschaft (DFG). The authors are grateful to Prof. H.-J. Knölker (TU Dresden) for the synthesis of corannulene and dibenzorubicene and to Prof. K. Müllen (MPI for Polymer Research, Mainz) for providing the sample of hexabenzocoronene.

2.3
Laboratory IR Spectroscopy of PAHs

Jos Oomens, Olivier Pirali, and Alexander G.G.M. Tielens

2.3.1
Introduction

Over the past three decades, satellite observations have opened up the infrared (IR) spectral window for systematic studies of the molecular composition of the interstellar medium (ISM), and IR emission studies have become a major tool in these studies. These studies revealed that the mid-IR spectra of most objects – including HII regions, reflection nebulae, the surface of molecular clouds, young stellar objects, post-asymptotic giant branch objects, planetary nebulae, galactic nuclei, the ISM of galaxies, and the nuclei of ultraluminous infrared galaxies – are dominated by emission features at 3.3, 6.2, 7.7, and 11.2 μm, which are collectively known as the *IR emission features*[1] (for a recent review, see Ref. [101]).

The composite IR emission spectrum of the ISM shown in Figure 2.18 presents a typical example. This spectrum is characterized by a broad emission peak at long wavelengths (≃150 μm) due to cold dust ($T \simeq 15$ K). In addition to this bright far-IR peak, the spectrum also shows mid-IR emissions [156] in the form of broad and strong features. The mid-IR emission spectrum is incredibly rich in detail with a host of weaker features – at 3.4, 3.5, 5.25, 5.75, 6.0, 6.9, 7.5, 10.5, 11.0, 12.7, 13.5, 14.2, 16.4, 17.4, and 18.9 μm – and underlying plateaus – from 3.2 to 3.6, 6 to 9, 11 to 14, and 15 to 19 μm [157]. These are perched on a (quasi-)continuum emission which rises rapidly toward longer wavelengths.[2] The spectral characteristics of the

1) In the older literature, these features are also referred to as the *unidentified infrared (UIR) bands*.
2) At present, features have been detected out to 20 μm, but the Herschel Space Observatory may extend this into the far-IR and even the sub-millimeter range.

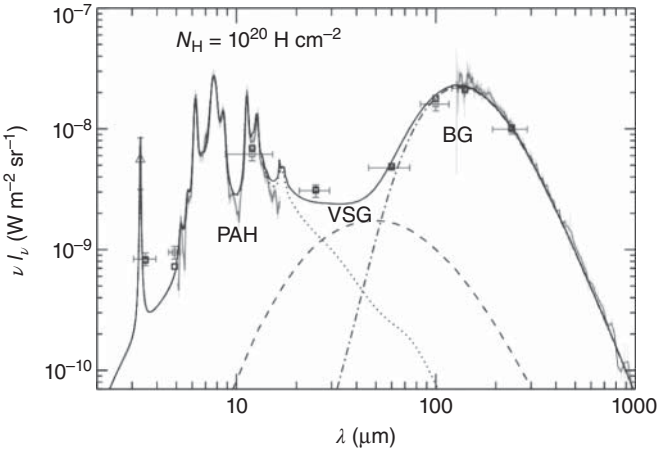

Figure 2.18 Emission of dust in the diffuse high galactic latitude medium normalized for $N_H = 10^{20}$ H cm^{-2}. Gray symbols and curves display the emission spectrum observed with the AROME balloon experiment, ISOCAM/CVF on board ISO, and DIRBE and FIRAS on board COBE. Black lines are the DUSTEM model output (Adapted from the original model developed by Dèsert *et al.* [162].) and black squares the modeled DIRBE points taking into account instrumental transmissions and color corrections. The fit (Based upon the original model of Ref. [162].) consists of (carbonaceous and silicate) big grains in radiative equilibrium responsible for the far-infrared (FIR) and submillimeter emission, (carbonaceous) very small grains that fluctuate stochastically, responsible for the mid-IR continuum, and PAH molecules fluorescing in mid-IR emission bands. See Ref. [156] for details and references.

IR emission features show subtle variations in profile, peak position, and relative strength within sources, as well as from one source to another, but globally the spectrum is remarkably similar; if you see one feature, you see them all. The peak positions of these spectral features are very characteristic of aromatic hydrocarbon materials and they are generally ascribed to IR fluorescence of UV-pumped large polycyclic aromatic hydrocarbon (PAHs) molecules. There are three pieces of evidence for the predominance of these large molecules over "bulk" materials (e.g., 10–300-nm grains): (i) In order to emit in the mid-IR, the carrier(s) of the IR emission features must be much hotter than the 15 K that characterizes the far-IR emission due to 10–300-nm grains in radiative equilibrium with the interstellar radiation field. Instead, the mid-IR emission is thought to arise in small species that, because of their limited heat capacity, are instantaneously heated to a high temperature (∼1000 K) by the absorption of a single UV photon [158]. In absence of collisions, the highly excited species then cools rapidly (∼1 s) through IR emission. The species remains very cold until the absorption of another UV photon, in the ISM typically about a year later but near a bright star once every hour. This is a solid-state description of what is essentially a molecular fluorescence process: a molecule absorbs a UV photon and this electronic energy is quickly transferred to the vibrational manifold of a lower lying, electronic state (e.g., internal conversion). This excitation then decays through emission in the molecular vibrational

bands (the IR emission features). When working out the energetics of this process, taking the heat capacity into account and adopting a typical UV absorption energy of 10 eV, a size of ~50 C atoms is implied for the carrier of the IR emission bands. The other emission components observed in the interstellar spectra are carried by somewhat cooler and therefore larger species: The plateaus and the continuum in the 5–20 μm range are due to clusters of PAHs (~400 C atoms) and the continuum longward of ~20 μm to very small (nano-sized, 1–10 nm) carbonaceous grains. (ii) Several of the IR emission features (e.g., the 6.2 and 11.2 μm features) show a pronounced red-shaded profile. Such a profile is produced by anharmonicity, again characteristic of emission by highly vibrationally excited molecules [159–161]. (iii) The feature to continuum ratio is very high, exceeding 20 in many sources. This is quite typical for molecular compounds; bulk (carbonaceous) materials, in contrast, invariably have intrinsic feature-to-continuum ratios that are much lower.

Over the years, a consensus has arisen in the field with regard to a number of key characteristics of interstellar PAHs, although not all of these are firmly established [101]. (i) The emission appears to be carried by a diverse family of related species. Indeed, no single (small) molecular spectrum measured in the laboratory or quantum chemically calculated has been able to reproduce the spectral complexity of the interstellar spectra [163]. Moreover, many of the emission bands show a substructure that varies independently, indicative of the contribution from many different species whose relative abundance varies with the local physical conditions [157]. Furthermore, PAHs are apparently linked to the 10–300 nm sized dust grains through the PAH clusters (carriers of the plateaus) and the 1–10 nm sized very small grains (carriers of the continuum emission) in an interstellar grain size distribution that reaches down to molecular sizes. (ii) Theoretical and experimental studies have revealed that the charge state of a PAH molecule has a profound influence on the spectra: neutral PAHs have strong CH modes and weak CC modes, while cationic PAHs have weak CH modes and strong CC modes [164]. Interstellar spectra show strong emission in both the CH stretching (3.3 μm) and bending (11–14 μm) and the CC stretching (6–9 μm) modes and hence a mixture of charge states is implied [165]. Since the charge state of the PAHs is determined by a balance of photoionization and electron recombination, the observed interstellar spectra provide a convenient tool to probe the local physical conditions (e.g., the ratio of the strength of the UV field and the electron density) [166]. (iii) The emission process is pumped predominantly by UV photons. Visible photons may contribute as well, but are much less efficient [167]. (iv) Interstellar PAHs are constantly "cooked" in the harsh environment of the ISM and only the most stable species will survive the onslaught of energetic processes. Over their lifetime in the ISM, perhaps some 100 Myr, interstellar PAH molecules absorb some hundred million UV photons. So, even a photodissociation process that has a probability of only ~1 in 10^8 can still be important for the destruction of interstellar PAHs. On a similar timescale, interstellar PAHs will typically encounter one 100 km s^{-1} and four 50 km s^{-1} shocks. PAHs are likely exposed to energetic atoms colliding at several tens to hundreds of electronvolts in the post-shock gas. Likewise, energetic

cosmic rays (>100 MeV) can also process PAHs on similar timescales [168–170]. Driven by this hypothesis, it has recently been suggested that the interstellar PAH family may actually be dominated by so-called grand PAHs, which are extremely stable, large PAHs that can withstand the rigors of space much better [101]. (v) Inside dense clouds, PAH molecules may readily cluster with each other. These clusters are thought to be the carriers of the broader plateaus as well as the 5–20 μm continuum. In addition, this aggregation process may be at the base of the formation of the very small grains responsible for the emission in the 25–60 μm range. While there is theoretical support for the importance of this process and observational indications of a change of spectral behavior of the IR emission spectra deep inside dense clouds [171, 172], direct laboratory studies of PAH clusters are still lacking. Complex formation of metal atoms such as Fe with PAHs has also been considered in this regard [173].

Laboratory studies and quantum chemical calculations are of key importance in understanding the characteristics of the interstellar PAH family and in relating the observed spectra to the local physical conditions in order to be used later by astronomers as a simple "toolbox." In this chapter, we review the different experimental techniques that have been used over the years to measure the IR spectra of PAHs. We then summarize the intrinsic spectroscopic properties of astrophysically relevant PAHs, paying particular attention to the effects of charge state because of its influence on the spectra. In view of the launch of the Herschel Space Observatory in 2009, which has opened up the FIR spectral range for systematic studies of the ISM, we summarize recent studies on the spectroscopic properties of PAHs at these long wavelengths. Finally, we discuss recent studies of the spectroscopic properties of PAH derivatives that may be of relevance such as Fe-PAH complexes.

2.3.2 Laboratory Spectroscopic Methods

In the 1980s, when the PAH hypothesis was originally formulated, IR spectroscopic data on PAH species was limited to spectral databases of pellet and solution-phase spectra obtained using grating instruments. One of the original papers suggesting that the UIRs are carried by PAH species [99] used a Raman spectrum of a car exhaust sample as the reference PAH spectrum. The hypothesis that PAHs are the carriers of the UIR emission bands [98, 99] inspired spectroscopists around the world to record IR spectra of these species under conditions relevant to those in interstellar clouds, that is, the species should be isolated, gaseous, and cold. Such conditions are not easily realized in the laboratory because of the low vapor pressure of PAH molecules. In addition, most laboratory methods yield absorption spectra, while the interstellar spectra are observed in emission.

2.3.2.1 Neutral PAHs

In order to reduce the effects of the medium, such as the salt pellet or the solvent, on the IR spectra, matrix isolation spectroscopy (MIS) as originally developed by Pimentel [174] was used to record PAH spectra. In MIS, the PAH molecule is thermally evaporated and condensed onto a cryogenically cooled IR-transparent substrate together with an excess amount of a noble gas (mostly Ar or Ne). MIS has been widely applied to study the spectroscopy of reactive species [175], which are stabilized by the cold, inert environment of the noble gas matrix. IR spectra recorded using MIS feature narrow vibrational bands (typically around 1 cm^{-1}) as a consequence of the quenching of rotational motion of the molecules, collapsing the rotational contour to a sharp peak at the band origin. While it was known that IR frequencies measured by MIS reproduce gas-phase frequencies very closely, significant deviations in relative intensities may occur, even up to a factor of five for PAHs [176].

The low vapor pressure of typical medium-sized PAHs impedes the study of their spectra in the gas phase. On the other hand, the high stability of PAHs enables the use of relatively high temperatures to vaporize most of them without inducing dissociation. Gas-phase absorption spectra were thus recorded in a heatpipe oven for PAHs up to the size of ovalene, $C_{32}H_{14}$, [176]. While the spectra recorded at high temperatures appear to be less relevant from an astrophysical point of view, one should bear in mind that the emitting PAHs in interstellar environments are believed to be transiently heated to vibrational temperatures on the order of 1000 K [177]. Moreover, spectra recorded at different oven temperatures provide direct experimental data on the anharmonic shifting of vibrational bands, which is an important parameter in modeling PAH emission spectra [160, 161, 178, 179] that is not easily obtained with other experimental or theoretical methods.

Gas-phase IR spectra at low temperature provide the most accurate values for line positions and intensities so that methods based on supersonic molecular beam expansions [180] are attractive. However, the low number densities that prevail in molecular beam expansions require the use of laser-based spectroscopic methods, which have indeed been widely applied to aromatic species in the UV–vis spectral range. In the astrophysically most interesting IR range of the spectrum, namely 5–15 μm, the only studies reported thus far make use of a tunable IR free electron laser (FEL). Only some of the smallest members of the PAH family have been investigated [181].

Interstellar UIR spectra are observed in emission rather than in absorption, and hence various researchers have reported IR emission spectra of (UV) excited PAH molecules, particularly in the 3 μm spectral range [182, 183]. At longer wavelengths, it becomes increasingly difficult to distinguish the PAH emission from the blackbody radiation of the environment. Using thermally excited PAHs greatly increases the number densities of the emitting sample so that IR emission spectra deeper into the IR could be recorded [177], although UV excitation leading to a rotationally cold but vibrationally hot ensemble resembles the astrophysical situation more closely.

Mid-IR emission spectra of UV excited gas-phase PAH molecules were first recorded by Saykally and coworkers, who employed a Czerny–Turner monochromator equipped with an extremely sensitive IR photon detector [160, 184, 185]. To distinguish the weak IR emission of the low-density gas-phase PAH molecules from the blackbody radiation of the instrument, the detector, the monochromator, and all elements in the line of sight were cryogenically cooled. Although the spectra thus obtained probably approach the interstellar situation most closely, this method turned out to be very demanding experimentally, so that only a few emission spectra of relatively small PAHs have been recorded.

2.3.2.2 **Cationic PAHs**

It was recognized already early on [178] that PAHs may be easily photoionized under interstellar conditions because of their relatively low ionization potentials of typically 7–8 eV. The dramatic change in the relative intensities of the various IR absorption bands upon ionization as first revealed by calculations of the naphthalene cation spectrum [164] initiated a surge in the laboratory spectroscopy of cationic PAHs. These methods are described below and sketched in Figure 2.19.

The first experimental PAH^+ IR spectrum was reported for the naphthalene radical cation [186]. To obtain this spectrum, Vala and coworkers modified their matrix-isolation setup to include an electron gun, so that the sublimed naphthalene was electron-ionized on the way to the cryogenically cooled substrate (see Figure 2.19a). Carbon tetrachloride was added to the Ar stream and co-deposited in order to sequester the electrons and thus to reduce reneutralization of the naphthalene cations once trapped in the matrix. An IR spectrum of this matrix revealed additional IR absorptions as compared to the spectrum taken with the electron gun turned off. Though relatively weak, these additional bands were assigned to ionized naphthalene and confirmed the altered relative intensities as predicted by the calculations [164]. Many variations of this method have since been applied. For example, instead of using electron ionization, matrix-isolated neutral PAH molecules may be irradiated with a UV lamp to induce *in situ* ionization of the embedded PAHs. As a drawback of these methods, it was realized that apart from ionization the PAHs may undergo fragmentation or otherwise be chemically modified, which could also give rise to new spectral bands. To mitigate these problems, externally generated ions have been mass-selected using a quadrupole mass filter prior to deposition on to the matrix. This method has, among others, been used to record the first IR spectra of ionized C_{60} and other fullerenes [189, 190].

MIS has now been employed to obtain IR spectra for a large number of cationic PAHs, mainly by the groups at the University of Florida [191] and at NASA Ames in California [192–194]. These spectra are included in an extensive database maintained by the group at NASA Ames[3)] [195]. This collection of PAH cation spectra provided the laboratory spectroscopic basis for the hypothesis that a substantial fraction of the interstellar PAHs is ionized [165, 196].

3) See www.astrochem.org/pahdb.

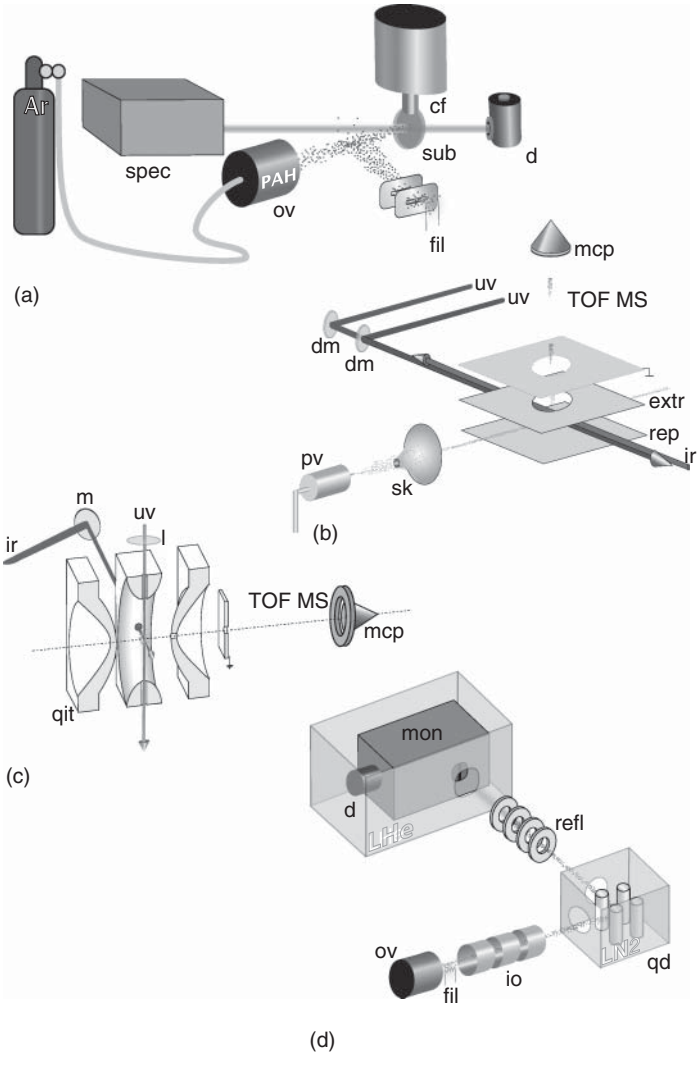

Figure 2.19 Simplified schematics of different methods used to obtain infrared PAH cation spectra: (a) Matrix-isolation spectroscopy; (b) messenger-atom spectroscopy; (c) IR multiple photon dissociation spectroscopy; (d) IR emission spectroscopy. cf, cold finger; d, detector; dm, dielectric mirror; extr, extractor electrode; fil, filament; ir, IR laser beam; l, lens; m, mirror; mcp, multichannel plate detector; mon, monochromator; io, ion optics; ov, oven; pv, pulsed valve; qd, quadrupole deflector; qit, quadrupole ion trap; refl, reflectron; rep, repeller electrode; sk, skimmer; spec, FTIR spectrometer; sub, substrate; uv, UV laser beam. (Illustrations adapted from Refs [181, 186–188] with permission.)

Despite the success of MIS in obtaining IR spectral information on PAHs and their ions, true gas-phase spectra remained highly relevant because of the possible unknown effects of the matrix on the spectra. Comparison of the MIS spectra with gas-phase spectra could directly verify the accuracy of MIS spectra. The extremely low number densities of gas-phase (mass-selected) ions, however, make the application of conventional spectroscopic methods based on direct absorption spectroscopy impossible. The so-called action spectroscopy methods, where the effect of the (laser) light on the PAH ion is monitored rather than the effect of the ion on the light, form a viable alternative [197]. Action spectroscopy methods generally require light sources with sufficient power to induce the "action" and must be tunable over the wavelength range of interest, that is, here the mid-IR to FIR range. Therefore, IR FELs [198] as well as laser sources based on parametric downconversion (see, for instance, Ref. [199]) of the output of powerful YAG lasers have been mainly employed.

A commonly applied laser-based method to obtain IR spectra of gas-phase ions makes use of IR-induced predissociation of a complex consisting of the ion of interest with a weakly bound "messenger" atom. In this method, as originally developed in the group of Lee [200, 201], the ionic complexes are typically generated by expansion cooling in a molecular beam and are then mass-selected. Resonant IR excitation of the ion and subsequent intramolecular redistribution of the energy lead to dissociation of the complex, detaching the weakly bound messenger, which is detected in a mass analyzer. Recording the dissociation yield as a function of the IR frequency of the laser produces an IR spectrum of the ion, or, in fact, of the ionic complex. If the messenger is only weakly attached, its influence on the structure and spectrum of the ion can be assumed to be small. Noble gas atoms are therefore commonly used in messenger-atom spectroscopy.

The group of Meijer at the FEL facility FELIX in The Netherlands [202] recorded IR spectra of cationic benzene [203], naphthalene [204], and phenanthrene [181] using a variant of messenger-atom spectroscopy. Van der Waals complexes of the PAH and Ar were produced in a pulsed molecular beam and ionized by resonant $(1 + 1')$-photon UV excitation (see Figure 2.19b). Subsequent resonant absorption of an IR photon detaches the rare gas atom, which is detected in a time-of-flight mass spectrometer (TOF-MS). The wide wavelength tunability of the FEL allowed recording the spectra over the entire range of astrophysical interest, namely from 6 to 16 μm. Comparison of the experimental spectra with those calculated using density functional theory (DFT) methods confirmed that the influence of the weak interaction with the messenger atom on the spectrum was indeed negligible, except for specific highly symmetric systems [205]. Other variants of messenger-atom spectroscopy have been used to obtain PAH ion spectra in the UV–vis wavelength range [206]. Messenger-atom tagging has also been used recently to obtain spectra of protonated aromatic species [207, 208] including protonated naphthalene [209].

Another method to obtain IR spectra of gas-phase cationic PAHs relies on IR-induced dissociation of the PAH itself through the absorption of multiple (tens to hundreds) IR photons. In the 1980s, various groups explored the application

of infrared multiple photon dissociation (IRMPD) as a spectroscopic tool using mainly line-tunable CO_2 lasers (see Ref. [210] for a recent review). Although various ionic systems were successfully characterized, the CO_2 laser's tuning range of 9–11 μm seriously limited the spectroscopic usefulness of the method. In 2000, it was shown that a widely tunable IR FEL can be used to produce IRMPD spectra of trapped cationic species, in particular PAH ions [187]. The PAHs were vaporized in a small oven and effused to the center of a Paul-type ion trap, where they were ionized with the UV light of an excimer laser (see Figure 2.19c). UV-induced fragments were then removed from the trap by mass-selective axial ejection, and the PAH radical cations were subsequently irradiated with the output of the FEL. The IR-induced fragments as well as the remaining parent ions were then mass-analyzed in a TOF-MS, so that an IR spectrum could be reconstructed by plotting the fragmentation efficiency as a function of the IR wavelength of the FEL. IR spectra of several PAH ions over the astrophysically most interesting range of 6–16 μm were reported [211, 212].

Dissociation of a PAH radical cation requires typically 6–8 eV, corresponding to tens to hundreds of photons in the IR. Absorption of this many IR photons is believed to take place via rapid intramolecular vibrational redistribution (IVR) [213, 214], which occurs on subpicosecond timescales in polyatomic molecules of the size of typical PAHs. IVR removes population from the excited level and dissipates the energy into the background bath of vibrational states, so that very many photons can be sequentially absorbed on the same transition. This IVR-mediated process thus avoids direct ladder climbing in a single vibrational well, which is inefficient because of the anharmonicity of the potential. The multiple photon process reflects itself in the IRMPD spectra particularly in the increased bandwidths observed as compared to, for example, MIS or messenger atom spectra, which are both based on linear absorption processes. The PAH ion spectra recorded using IRMPD display bandwidths of typically 30 cm^{-1} FWHM. Moreover, anharmonic couplings induce a red shift of typically 1–2% of the band center [211].

Both MIS and the gas-phase action spectroscopy methods described above yield IR absorption spectra, whereas the interstellar IR bands are observed in emission. As mentioned above for neutral PAHs, recording IR emission spectra in the 6–16 μm range in the laboratory is, however, complicated, mainly because one has to distinguish the PAH emission from the blackbody radiation of the environment. For ionic PAHs, this is even more difficult because ion densities are inherently lower than neutral PAH number densities. Thus far, only the group of Saykally has managed to record emission spectra of gas-phase PAH ions over the astrophysically interesting IR range [215].

The cryogenically cooled spectrometer [184] was coupled to an electron impact ion source (see Figure 2.19d), which produces ion currents as high as 6 μA [188]. Depending on the electron energy, electron impact ionization produces ions in electronically excited states comparable to those accessed by UV excitation. The IR emission profiles of these PAH ions are thus expected to be similar to those obtained from UV-excited PAH ions, as occur in the ISM. With the use of a quadrupole deflector, the ions are steered into a reflectron, which is mounted in

front of the entrance slit of the IR spectrometer, so as to increase the residence time of the ions in the viewing region of the spectrometer. In order to distinguish the IR emission of the low-density PAH^+ sample, the reflectron and other ion optics in the line of sight needed to be cryogenically cooled (while electrically insulated), which constituted one of the main challenges in the experimental design [188].

Using this apparatus, IR emission spectra were recorded for the pyrene cation ($C_{16}H_{10}^+$) and several of its dehydrogenated product ions [215, 216]. In general, the IR emission spectra are in good accordance with those measured by MIS and IRMPD spectroscopy.

2.3.2.3 Computational

With the advent of modern computers and quantum chemical computational methods, notably DFT methods, IR spectra of PAHs (and many other molecules) can now be accurately calculated. A detailed discussion of the computational methods used to investigate PAH molecules and ions is beyond the scope of this book. However, it is good to note that experimental PAH spectra have been instrumental in verifying the quality of the computed spectra. In some cases, such as cationic phenanthrene [181] and fluoranthene [217, 218], large deviations between experimental and theoretical spectra have been observed and they have been suggested to be due to electronic state mixing, although these effects have not been understood in detail. Nonetheless, the match between experimental and computed spectra is generally very good for relatively small systems, which lends credence to computational methods being applied to PAH species that are not easily accessible experimentally. For instance, the typical size of interstellar PAHs has been estimated to be substantially larger than the largest commercially available PAH molecules, and it is thus of interest to study their spectra with computational methods [217, 219–222]. Large collections of computed PAH spectra are now available in online databases [195, 221, 223], which are used in attempts to fit interstellar UIR profiles as closely as possible.

2.3.2.4 Comparison of Experimental Methods

A description of the various methods to obtain PAH (ion) spectra is not complete without a comparison of the strengths and weaknesses of each of them. Methods based on IR emission spectroscopy, particularly those conducted by the Saykally group, probably approach the interstellar situation most closely. Gaseous PAHs are electronically excited to energies in a range similar to what occurs in the ISM, and the molecules relax by IR fluorescence. The effects of anharmonicity on the bandwidths and shapes [159, 224, 225] are thus naturally incorporated into the observed spectra, avoiding the use of modeling to generate an emission spectrum based on absorption data [161, 226–229]. However, the method is technically challenging, especially for ionic PAHs, and thus far only a handful of cationic PAH IR emission spectra have been reported over the astrophysically most interesting range between 6 and 16 μm [215, 216].

In contrast, MIS has been widely applied, and the majority of experimental PAH spectra reported are based on this method. The merits of this method include its relative ease of use and the narrow bandwidths obtained. On the other hand, the IR spectra may be influenced by unknown matrix interactions, which appear to particularly affect the relative band intensities [176]. In addition, in MIS studies of PAH ions, unknown species may be generated in the matrix apart from the radical cation, possibly producing extraneous bands in the spectrum, so that sophisticated correlation measurements are often necessary [186]. Moreover, the generally weak cation bands may be obscured by overlapping features of the abundantly present neutral species.

PAH ion spectra obtained using messenger-atom spectroscopy probably represent the purest linear absorption spectra of ionic PAHs reported to date. Application of this method requires a tunable IR laser source, and optical parametric oscillators and FELs have thus far been applied. Commercially available IR sources cover the 3 μm range, enabling the study of the H-stretching modes, but more recently also frequencies down to ≈1000 cm^{-1} [209]. Tunable IR FELs are available at (at least) two international research facilities (CLIO in France and FELIX in The Netherlands) and provide access to the entire spectral range of interest. Seeding the low-volatility PAHs into a molecular beam expansion to form weakly bound clusters is an experimental challenge, and so far IR spectra have been reported only for up to three-ring PAHs [181].

IRMPD spectroscopy requires the use of intense and tunable IR sources, and thus far only FELs have been used for these experiments. IRMPD spectroscopy is readily coupled to versatile tandem mass spectrometers, which enables the study of a variety of PAH-related species that are not easily studied with any of the other methods. For example, IR spectra have been obtained for protonated PAHs [230–233], PAHs complexed with iron ions [234, 235] and ion–molecule reaction products involving aromatic species [236]. The spectral resolution of IRMPD spectra is limited because of broadening effects induced by the excitation process [211]. This may result in relatively unresolved spectra, particularly for large, irregularly shaped systems. Note that, on the other hand, broadening due to anharmonic shifting also occurs in IR emission spectra, although the underlying processes of multiple photon absorption and emission are fundamentally different.

Figure 2.20 compares the spectrum of the pyrene cation recorded using three different methods: MIS [193], IRMPD spectroscopy [187], and IR emission spectroscopy [215]. Reported band positions and intensities have been convoluted with a 20 cm^{-1} FWHM line-shape function to facilitate easy comparison. The lower panel shows the pyrene cation spectrum as predicted by DFT calculations. The majority of the bands in the MIS and IRMPD spectra can be directly correlated; relative intensities show some discrepancies. Which of the methods provides the "true" intensities is hard to judge, as both MIS [176] and IRMPD [211] are known to distort relative intensities from their values in a linear gas-phase absorption spectrum (which is only available computationally). Moreover, relative intensities are affected in yet a different way by the IR emission process. The spectrum recorded in emission appears most distinct, especially at 1280–1400 cm^{-1}.

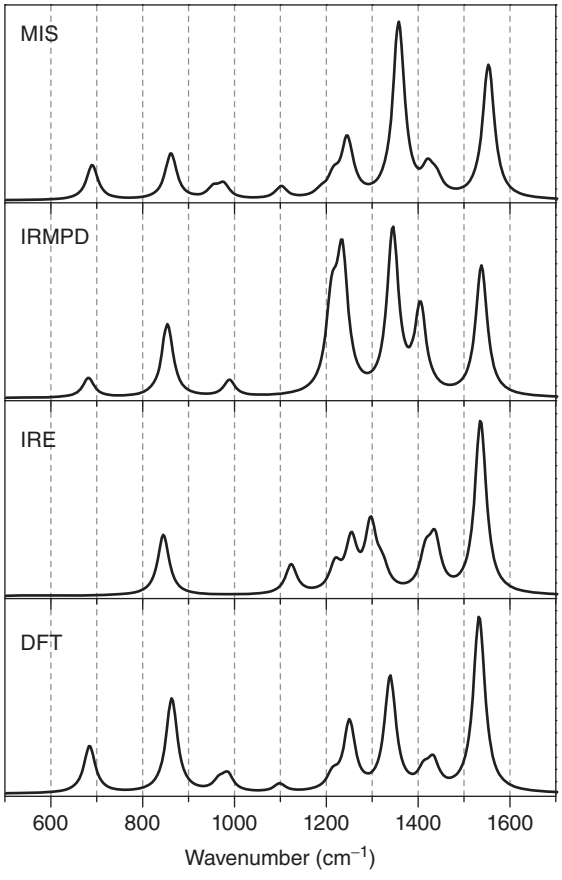

Figure 2.20 IR spectrum of the pyrene cation obtained using three different methods, namely matrix-isolation spectroscopy (MIS), infrared multiple-photon dissociation (IRMPD), and infrared emission (IRE). Reported band positions and intensities have been convoluted with a uniform Lorentzian line shape function for easy comparison. The lower panel shows the calculated spectrum.

The MIS spectrum reproduces the calculated spectrum most closely. Interestingly, both the IRMPD and the emission spectrum show red-shifted bands as compared to their positions in the MIS spectrum (see, e.g., the strong CC stretching band between 1500 and 1600 cm^{-1}), likely due to the influence of anharmoninicity in both emission and multiple-photon excitation processes.

2.3.3
Far-Infrared Spectroscopy

In view of the recent launching of the FIR space observatory "Herschel," there is renewed interest in obtaining laboratory data in this range of the spectrum to guide the observations. The spectral region from 15 to 300 cm^{-1} (30–670 μm,

0.5–10 THz) comprises most of the low-frequency vibrational modes of the PAH molecular family. In contrast to their mid-IR spectra, which mainly probe the CH and CC chemical bonds (through stretching and bending vibrations) and therefore do not permit an unambiguous identification of a single molecule, the FIR spectra of PAHs correlate with vibrational deformations of the entire molecular carbon skeleton, providing a more unique vibrational signature for each species. The FIR modes are, however, of much lower intensity than IR active modes at higher frequencies, generally on the order of only a few km/mol compared to values on the order of 100 km mol^{-1} for intense stretching and bending modes.

A substantial fraction of the emission in the far-IR modes may occur when the molecule is excited to relatively low internal energies. At that point, the modes will decouple, and this leads to vibrational bands with resolved rotational structure. Moreover, bands that are normally not IR active can retain some of the excitation after decoupling and, in the collisionless environment of the ISM, these modes are expected to eventually decay radiatively.

2.3.3.1 Laboratory Results

Early DFT calculations already provided harmonic frequencies for all fundamental vibrational modes of small species [220], which are now available online [195, 221, 223] for a large set of PAH molecules (neutrals, cations, dications, and anions).

The first experimental values for the low-frequency modes (14–40 μm) of a large set of PAHs (40 molecules ranging from 3 to 70 Å in size) were obtained using CsI pellet spectra [237]. More recently, matrix-isolated spectra of relatively large PAH species deeper into the FIR have also been reported [238]. Owing to the low vapor pressure of these large molecules at room temperature and the general difficulties of obtaining experimental spectra in this spectral region, experimental gas-phase spectra have been obtained only for the smallest species [239, 240]. A detailed account of the FIR vibrational assignments was proposed for the five smallest PAHs representing linear (naphthalene, anthracene), nonlinear noncompact (phenanthrene and chrysene), and compact (pyrene) PAHs [240]. From this limited set of data, it was clear that all FIR modes (roughly below 500 cm^{-1}) are associated with skeletal vibrations. For all classes of PAHs, there are far more out-of-plane (oop) modes than in-plane modes in the FIR spectrum. In addition, the oop modes correspond to c-type transitions showing a sharp Q branch. In general, the lowest frequency IR active modes are oop modes, including the so-called drumhead modes, whose frequencies scale inversely with the area of the PAH and largely independent of the molecular geometry [238, 241]. In-plane deformation of the aromatic rings is observed at higher frequencies (around 400–500 cm^{-1} for the molecules studied here), also shifting to lower frequencies with increasing PAH size. For compact molecules, the nature of the FIR modes is different, thus limiting the comparison with other molecules.

PAH species containing only six-membered aromatic rings are planar and very symmetric, which typically results in a very low permanent dipole moment. Laboratory observation of pure rotational transitions in the microwave region of

the spectrum is therefore usually not possible. Ground state rotational constants can be obtained from high-resolution electronic spectroscopy (e.g., Ref. [242]). However, PAHs with defects in the aromatic network present an interesting opportunity for microwave detection in the ISM. For example, molecules containing a pentagonal ring, such as corannulene, can distort to a nonplanar bowl-shaped geometry, giving rise to a permanent dipole moment [243, 244]. Asymmetric PAHs as well as PAHs containing heteroatoms also possess a sizable permanent dipole moment, and their microwave spectra have been investigated in various studies [245, 246].

Little experimental FIR data is presently available for cationic PAHs. A recent extension of the FELIX FEL facility with an intracavity experiment [247] holds the promise that IRMPD can be pushed to longer wavelengths through more efficient multiple-photon IR excitation. IRMPD studies of anthracene, tetracene, pentacene, and coronene cations have revealed IR active modes down to 200 cm^{-1} [248].

Mass-analyzed threshold ionization (MATI) spectra were recorded for phenanthrene [181], and zero-kinetic energy photoelectron spectroscopy (ZEKE-PES) experiments permitted the accurate determination of the FIR frequencies of fluorene [249], tetracene [250], and pentacene [251]. It should be noted, though, that these methods make use of electronic excitation and do not probe the IR spectrum directly; while observed frequencies ought to be accurate, relative intensities may be strongly biased by the vibronic overlap integral and, especially for symmetric species, by the different selection rules that apply as compared to those in a direct IR spectrum.

Several recent studies in the FIR spectral range have experimentally investigated the anharmonicity of low-frequency vibrations of aromatic systems [224, 225]. Anharmonic parameters are important for an accurate modeling of the IR emission process and to predict emission spectra based on data from (calculated) linear absorption spectra [161, 226–229]. Although anharmonic parameters can now be calculated by modern computational chemistry packages, these experiments provide a unique opportunity to verify the computed values.

Whether or not a single specific PAH can be detected in space based on its FIR spectrum remains to be seen, although various limitations seem to apply. The FIR modes are typically of very low intensity as compared to mid-IR vibrations. There is certainly a large diversity among a population of interstellar PAHs, but the extent of this diversity remains largely unknown. If the diversity is too large, the various individual bands may merge into an unresolved emission feature. Finally, the dust emission may hinder the detection of molecular species in this spectral range. Nevertheless, in some favorable cases (low dust emission, relatively intense c-type transition, particularly high abundance of a specific molecule), the high resolution and sensitivity of the Photoconductor Array Camera and Spectrometer (PACS) instrument on board the Herschel satellite is believed to be able to detect specific molecular species [252].

2.3.4
IR Spectral Features of PAHs

The typical features of the IR spectra of PAH molecules and ions and how they relate to the main features of the UIR spectrum have been the subject of various reviews [178, 253]. PAH spectra typically show relatively similar features because the vibrational modes have a collective character; that is, they are delocalized over similar bonds in the PAH molecule, rather than being confined (i.e., localized) to one specific bond. The main vibrational mode characters that are usually distinguished are CH stretching, CC stretching, in-plane CH bending, and out-of-plane CH bending. Using the spectra of coronene as a typical example (Figure 2.21), we give a brief overview of these features and their corresponding vibrational mode

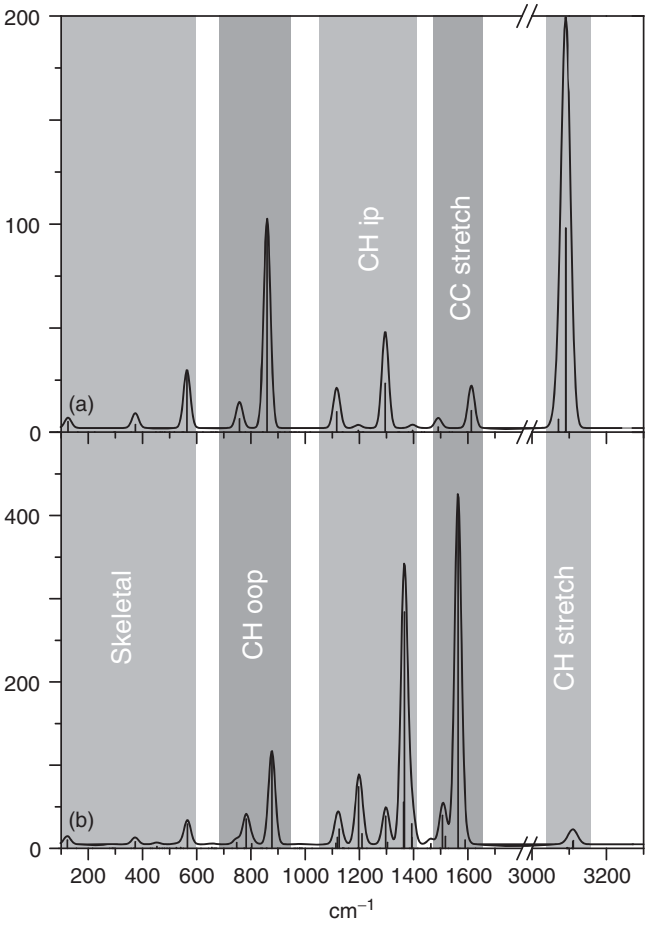

Figure 2.21 Calculated harmonic spectra of neutral (a) and cationic (b) coronene at the B3LYP/cc-pVDZ level. Frequencies are scaled by 0.97.

assignments, which are based on a large number of spectroscopic investigations on neutral [176, 177, 219, 254–256] and cationic PAHs [181, 186, 187, 191–194, 196, 204, 218, 257–266]. Theoretical investigations of PAHs have also been instrumental in the understanding of these spectra [164, 217, 222, 267].

The CH stretching vibrations of PAH molecules are located near 3.3 μm and they are among the strongest bands in the spectra of neutral PAHs. Conversely, they are found to be very weak for PAH radical cations. As for all normal modes in PAHs, these modes do not correspond to the local modes, stretching individual CH bonds, but rather to the collective stretching motions of the CH bonds in the molecules.

The CC aromatic stretching modes of PAHs are typically found somewhat longward of 6 μm and are believed to produce the strong interstellar emission around 6.2–6.3 μm. In-plane CH bending modes are roughly found in the spectral region between 7.5 and 9 μm. It should be noted that PAH normal modes in the 6–9 μm region are not only delocalized modes but also often have strongly mixed CC stretching and in-plane CH bending character. The band intensities in this spectral range are typically 10–100 times higher in the cationic species than in neutral PAHs.

The CH oop modes are found in the 11–13 μm spectral range and their exact position depends on the number of adjacent CH units on an aromatic ring [163]. PAHs of different adjacency classes can thus be identified as follows: solo-CH modes appear near the blue end of the CH oop spectral range, typically between 860 and 900 cm^{-1} ; duet-CH oop modes appear in the range 800–860 cm^{-1}; trio-CH modes appear from 750 to 810 cm^{-1}; and quartet-CH oop modes appear most red-shifted around 735–770 cm^{-1}. These modes are some of the strongest bands in the spectra of neutral PAHs and have slightly lower relative intensities in cationic PAHs.

2.3.5 PAH Derivatives and Related Species

By the end of the 1990s, more and better-quality inter- and circumstellar spectra had become available on account of newly developed instruments, such as the Short Wavelength Spectrometer (SWS) spectrometer on board the ISO satellite. These new data uncovered a wealth of details in the UIR spectra. For example, the CC stretching band around 6.2 μm was deconvoluted into two main components, one closer to 6.2 μm and the other closer to 6.3 μm, and even within these two classes, finer details indicating subclasses were identified [157]. Which of the components is more intense depends on the source. Interestingly, the laboratory PAH spectra (both neutral and cationic) show CC stretching modes at slightly (but definitely) longer wavelengths [268], which turned the scope of many spectroscopists beyond that of the regular series of PAH molecules and their ions. Numerous PAH modifications were suggested to explain the various details in the UIR spectra.

The discrepancy between the interstellar 6.2 μm emission band and the CC stretching modes in laboratory PAH spectra was originally assumed to be related

to PAH size. The CC stretching modes shift to higher frequencies as the PAH size increases [268], so that extrapolation of spectroscopic data on small PAHs suggested that PAHs with 50–100 C atoms would possess CC stretching modes coinciding with the interstellar emission feature. This appeared to make good sense because it was known that, in order to be photostable under interstellar conditions, PAHs need to be larger than about 40 C atoms. Later studies showed, however, that the frequency shift toward higher frequencies levels off at sizes of ~30 C atoms, and that even very large PAHs could at most explain the 6.3 μm feature but not the 6.2 μm feature [157, 269]. The presence of substituted PAHs in the interstellar inventory was put forward as an alternative explanation.

2.3.5.1 Nitrogen-Substituted PAHs

Substitution of a nitrogen atom for a carbon atom in the aromatic PAH framework modifies the bond strengths, charge distribution, and symmetry (and thus IR activity) of the aromatic network, which results in a band blue-shifted from the nonsubstituted PAH CC stretching modes. Computational studies have shown that the blue shift occurs only for endohedrally substituted species, that is, where the N atom replaces a C atom. The computed spectra for these species indeed feature CC stretching modes that are remarkably close to the interstellar 6.2 μm emission band [157, 269]. Exohedral substitution, on the other hand, where the N atom replaces a CH unit on the periphery of the PAH, does not change the spectrum significantly [269]. Experimental studies have unfortunately not been possible for the former class of N-substituted polycyclic aromatic hydrocarbons (PANHs), because endohedral substitution produces odd-electron species, which are therefore not available. Experimental IR spectra of several neutral and cationic exohedrally PANHs trapped in rare-gas matrices are indeed very similar to their unsubstituted PAH analogs, confirming the predictions of quantum chemistry [220, 270].

Gas-phase IR spectra of several small cationic PANHs were recently recorded via IRMPD spectroscopy using the FELIX FEL [233]. The radical cation species, as generated from the exohedral neutral precursors, also show CC stretching modes at positions identical to those in unsubstituted PAHs. Interestingly, however, IR spectra of the protonated exohedral PANHs consistently show a significant blue shift of the CC stretching mode, approaching the interstellar band position [232, 233]. Note that both protonated exohedral PANHs and cationic endohedral PANHs are even-electron species, unlike the radical cation exohedral PANHs, which suggests that the blue shift of the CC stretching mode may be attributed to the closed-shell electronic configuration rather than to the endohedral position of N substitution.

2.3.5.2 Protonated PAHs

Protonation provides experimental access to the class of closed-shell PAHs, which have been suggested as possible UIR carriers based on computed spectra [271]. While regular PAHs have proton affinities that are substantially lower than those of PANHs, various experimental approaches have been successfully applied to

obtain H^+PAH IR spectra, all based on gas-phase action spectroscopy. Protonated naphthalene was generated by chemical ionization with CH_4, and the IR spectrum of $C_{10}H_9^+$ was recorded via IRMPD using the CLIO FEL [230]. Larger protonated PAHs were generated by electrospray ionization from a solution containing the PAH molecule and ammonium acetate, and IRMPD spectra were obtained for species up to the size of protonated coronene [231]. These spectra show a blue shift of the most prominent band in the 6 μm region as compared to radical cation PAHs, analogous to what is observed for PANHs.

Ionic PAHs with a closed-shell electronic structure, and protonated PAHs in particular, thus appear to be interesting candidates to explain the 6.2 μm interstellar emission bands. Band positions with accuracies better than available from IRMPD spectra are thus of great interest, but MIS has thus far not been applied to protonated species. Several variants of IR messenger-atom spectroscopy have been applied to small aromatic species [207, 208], and the group of Duncan [209] recently reported an IR spectrum of protonated naphthalene with a resolution of a few wavenumbers [209].

2.3.5.3 Hydrogenated and Dehydrogenated PAHs

Interstellar PAHs are likely to be chemically transformed in interstellar radiation fields. In the laboratory, photofragmentation of PAHs has been studied using UV and synchrotron light sources [272, 273]. While some, especially smaller PAHs, undergo complete fragmentation of the carbon network, many larger and more stable (i.e., condensed) PAHs show primarily loss of peripheral hydrogen atoms, forming H-deficient PAHs. Interestingly, such PAHs were explicitly suggested as possible carriers of the diffuse interstellar bands [274] and have been related to the "bump" in the UV extinction curve [275]. To date, little is known on the IR spectroscopy of these systems and it is even not known whether the species retain their hexagonal carbon frame or (partially) rearrange to other structures, such as carbon chains or rings. Some computational studies have been carried out on the basis of mass spectrometric results [276]; from a spectroscopic point of view, some bands observed in the IR emission spectrum of the pyrene cation were attributed to dehydrogenated pyrene cations [216].

Hydrogenated PAHs, that is, PAHs having excess H atoms forming CH_2 groups on the periphery, have been suggested as possible members of the interstellar PAH family, particularly because they could explain the weak emission bands near 3.4 and 3.5 μm [277, 278]. The aliphatic CH stretching modes fall close to these wavelengths, although the features have also been suggested to be due to hot band emissions of the aromatic CH stretching modes [159]. PAHs with an even number of CH_2 units are commercially available, and various spectra have been recorded [278]. Spectra of protonated species have also been reported recently using IRMPD spectroscopy. These experiments also revealed that fragmentation occurs through H_2 loss rather than through H loss (as is observed for protonated regular PAHs), which was suggested as an interstellar source of molecular hydrogen [279].

2.3.5.4 Metal–PAH Complexes

The observed depletion of iron in the interstellar medium has been suggested to result from its efficient complexation to, among others, PAHs [280]. The complexes are expected to be stable in dense cloud environments, especially as the PAHs become larger [173]. IR spectroscopic data on the complexes based on solution-phase experiments is complicated by the fact that it is not exactly known which species produce the spectra; there may be several complex structures as well as uncomplexed species present in the solution. Moreover, the solution may strongly affect the structures formed, and solvent adducts may give rise to extraneous features in the spectra. Computational spectra of iron PAH complexes have also been reported [281].

The coupling of tandem mass spectrometers with IR FELs allowed the recording of experimental gas-phase IRMPD spectra of the complexes, which have been mass-selectively prepared [234, 235]. As the PAH increases in size, its ionization potential drops to values below that of atomic Fe. Fe^+–PAH complexes may thus undergo charge transfer depending on the size of the PAH [173], which may have implications for the relative intensities of the various PAH IR bands. Indeed the gas-phase spectra indicate that the CH out-of-plane modes around 12–13 μm become the dominant bands in Fe^+–PAH complexes and that the bands in the 6–9 μm region become less intense. In addition, particularly the position of the out-of-plane modes is seen to be affected by the Fe ion; a blue shift as compared to the uncomplexed PAH is induced by steric hindrance effects. Complexes with other astrophysically abundant metal ions have also been considered, although their IR spectra have been investigated only computationally thus far [282].

2.3.5.5 Other PAH Modifications

In addition to the species discussed above, one can imagine numerous other chemical modifications of pure PAHs. Many of those modified PAHs form stable molecules, which are commercially available and have been studied by IR spectroscopy. In addition, quantum chemical calculations have been applied to a variety of substituted PAHs (e.g., Ref. [220]).

Alkyl-substituted PAHs, and in particular methylated PAHs where one or more peripheral H atoms have been replaced with CH_3 groups, have often been invoked to explain the interstellar 3.40-μm emission band [283]. Note again that this interstellar emission band has also been attributed to the hot band emission of aromatic CH stretches and to the aliphatic CH_2 emission of hydrogenated PAHs. Experimental MIS spectra for several alkyl-substituted PAHs are available [220].

Photoprocessing of interstellar ices containing traces of PAHs has been suggested to induce functionalization of pure PAH molecules. Side-group additions that have been experimentally verified include methyl ($-CH_3$), amino ($-NH_2$), cyano (–CN), hydroxyl (–OH), carboxylic acid (–COOH), methoxy ($-OCH_3$), and ketone (>C=O) groups [284]. As these species can eventually be evaporated from the ice, their spectra could contribute to the interstellar emission bands. IR spectra of some of these species isolated in an Ar matrix have been studied [220].

Fractionation may lead to enrichment of deuterated PAHs [285]. Particularly, the (weak) emission features near 4.40 and 4.65 μm have been attributed to CD stretching modes of partly deuterated aromatic species [286]. Laboratory IR spectra of several perdeuterated PAHs have been reported [181, 192, 193, 257].

Distortions of the hexagonal carbon frame have also been considered. In particular, the inclusion of five-membered rings has received some attention, perhaps because such species may form the link from PAHs to fullerenes, which have been hypothesized to occur in interstellar environments since their discovery [287–289]. PAHs including pentagonal rings have been spectroscopically investigated in the IR range using MIS [218, 263–265] as well as IRMPD spectroscopy [262]. Dedicated theoretical investigations have also been performed [217].

2.3.6
Conclusions

Driven largely by the launch of sensitive IR spectrographs on board of space-based observatories, our observational understanding of the interstellar IR emission features has expanded greatly. Interstellar mid-IR spectra show a bedazzling array of spectral details, which varies from region to region and within regions, reflecting the response of a diverse family of PAHs and PAH derivatives to the local physical conditions. Unraveling this chemical complexity and understanding its implications require a dedicated effort to characterize the IR spectra of such species in the laboratory. Over the past two decades, the concerted efforts of various spectroscopists have been focused on this Herculean feat. Using a variety of experimental techniques – including MIS, gas-phase emission spectroscopy, and action spectroscopy – and supported by DFT quantum chemical studies, the IR spectra of neutral, cationic and anionic, substituted, and complexed PAHs of astrophysical relevance have been characterized. These studies have already led to much insight into the composition of the interstellar PAH family. For the coming decade, we anticipate a focus to be on extending this database to larger species, to clusters of PAHs, to PAH photoproducts, and to the far-IR wavelengths.

2.4
The Spectroscopy of Complex Molecules

Holger S. P. Müller

2.4.1
Introduction

As of May 2010, more than 150 different molecular species have been detected in the interstellar medium (ISM) and in circumstellar envelopes (CSEs) of late-type stars [290]. The up-to-date online version, which is available on the Molecules in Space Web page (http://www.astro.uni-koeln.de/cdms/molecules/) of the

Cologne Database for Molecular Spectroscopy (CDMS), (http://www.astro.uni-koeln.de/cdms/) [291, 292], reveals that by July 2013, this number has risen to around 180. On that Web page, the molecules are sorted according to the number of atoms. Another up-to-date source, but with entirely chronological sorting, is available on the astrochymist Web page (http://www.astrochymist.org/) which is maintained by David E. Woon. The latter provides reference to the principal detection. The former gives information on the detection in various astronomical media for most molecules, including isotopic species or excited vibrational states. A substantial number of di- and triatomic molecules have been detected as well as some larger ones, which include $HC_{11}N$ and, very recently, C_{60} and C_{70}. These molecules are much smaller than what an organic chemist or a biochemist would usually consider to be a complex molecule. Obviously, this is a matter of definition! One may remember that astronomers consider all elements heavier than helium to be metals. Astrochemists and astrophysicists – but also molecular chemists and physicists – view much smaller molecules as complex molecules. I am not aware of a unique definition among these scientists, but the following aspects seem to be met in most instances: (i) the molecule should consist of five or more atoms because it should not be too small and (ii) it should be chemically at least fairly stable; this means it is an organic molecule whose carbon backbone is saturated, or at least nearly so.

Scientists as well as interested amateurs have been interested in the question of whether interstellar chemistry may have contributed to the formation of life on Earth or possibly on a different planet ever since molecules have been identified in space by spectroscopic means, almost all of them in the gas phase; the majority of these have been detected by radio astronomical means, though infrared, visible, and ultraviolet spectroscopy have played a certain role, as well, in particular for molecules which have no rotational spectrum. Most of the molecules detected in space are small – almost 100 molecules contain up to four atoms – and the number of molecules containing 10 or more atoms is, with 12 certain and 1 tentative detection, rather small. On the other hand, a large number of very complex molecules have been found in some carbonaceous meteorites, in particular in the famous Murchison meteorite. Among the molecules identified early were amino acids, albeit after extensive chemical treatment. The presence of some unusual ones and the absence of strong chiral preferences are indicative of a non-biogenic formation and suggest therefore that these molecules may have been formed in space. Also found in this and related meteorites were nucleobases, fullerenes, and considerably larger amounts of aromatic hydrocarbons than aliphatic ones. Therefore, it is of great interest to find out how complex the molecules can get which can be identified unambiguously by spectroscopic, mainly radio astronomical, means.

2.4.2 General Spectroscopic Considerations

The unambiguous identification of spectral features observed by radio astronomical means requires the knowledge of rest frequencies with sufficient accuracy.

These are usually based on laboratory spectroscopic investigations. In this subsection, we will discuss some practical aspects without delving very deeply into the corresponding theory.

The rotational energy $E_{\rm rot}$ of a diatomic or, more generally, a linear molecule is given to lowest order as

$$\frac{E_{\rm rot}}{\hbar} = B \times J(J+1) \tag{2.6}$$

where B is the rotational constant. The $J = 1$–0 transition frequency of CO (unlabeled atoms refer to the most abundant isotopes) has been measured with very high accuracy as 115 271.2018 (5) MHz [293], where the number in parenthesis refers to the 1σ uncertainty in units of the least significant figure. From Eq. (2.6), one would derive for the $J = 2$–1 frequency a value of 230 542.4036 (10) MHz. This value is very different from the experimentally determined value 230 538.0000 (5) MHz [293], the difference being explained by the effect of the quartic centrifugal distortion correction D. A fit of these two transition frequencies to B and D yields values that permit reasonable extrapolations to about 1.5 THz. The predicted uncertainty of the $J = 13$–12 transition is 401 kHz, while the measured frequency is only 196 (12) kHz higher than the calculated one. However, with even larger J, the deviations between the calculated and measured frequencies grow much more rapidly such that the prediction for the $J = 34$–33 transition is 3 890 399.3 (73) MHz, whereas the measured value is 3 890 442.717 (13) MHz. Obviously, at least one further distortion correction is needed to reproduce the experimental data more accurately. The rotational energies of linear molecules are generally expressed as an infinite series whose coefficients usually, but not always, decrease quite rapidly:

$$\frac{E_{\rm rot}}{\hbar} = B \times J(J+1) - D \times J^2(J+1)^2 + H \times J^3(J+1)^3 + \cdots \tag{2.7}$$

The situation is more complex for asymmetric top molecules. Instead of one rotational constant B, three are needed, A, B, and C. Instead of one quartic centrifugal distortion term D, there are five; seven sextic centrifugal distortion terms exist, and so on. Thus, 22 and 30 spectroscopic parameters were used to fit the ground state rotational spectra of the comparatively simple and light molecules H_2CO [294] and SO_2 [295], respectively. Twenty-nine parameters were determined in a recent study of the ground vibrational state of the complex molecule ethyl cyanide (C_2H_5CN) [296].

Additional complications occur if one (or more) large amplitude motions cause non-negligible effects in the rotational spectrum. The simplest case is when tunneling occurs between two equivalent minima, such as in the prototypical NH_3 molecule or its isotopologs. The Hamiltonian consists of a 2×2 matrix in which there are two rotational Hamiltonians on the diagonal, which represent the symmetric and the antisymmetric combinations of the two equivalent minima; the antisymmetric combination is usually higher in energy than the symmetric one in the ground vibrational and all totally symmetric vibrational states. On

the off-diagonal, one finds the interaction Hamiltonian between the two states. It is represented by Coriolis-type operators which have to fulfill certain symmetry constraints. Instructive examples include the recent extensive studies on NH_3 [297] and NHD_2 [298], or on the *aGg′* lowest energy conformer of ethylene glycol, also known as ethanediol ($HOCH_2CH_2OH$) as an example of a complex molecule [299].

Molecules without large amplitude motions or with tunneling as the only large amplitude motion can usually be fitted and predicted with spectroscopy programs such as the widely distributed SPFIT/SPCAT program suite written by Pickett [300], see also Refs [301, 302]. The programs are available on the JPL molecular spectroscopy Web Site (http://spec.jpl.nasa.gov/ftp/pub/calpgm/). Many examples have been provided in the fitting spectra section (http://www.astro.uni-koeln.de/cdms/pickett) of the CDMS.

The situation can become much more complicated when a torsional large-amplitude motion is present. There are examples with two equivalent minima, for example, $HONO_2$ or HSOH. $HOBF_2$ is isoelectronic to $HONO_2$, but not only does it have a large amplitude torsional motion but also the HOB bending mode is of large amplitude. More common, especially among complex molecules, are threefold internal rotors, namely, methyl groups. One methyl group, for example, in methanol requires seven lowest order parameters to describe the rotation–torsional spectrum appropriately: besides the common rotational constants A, B, and C, which are sufficient for a molecule without large amplitude motion, or suitable linear combinations thereof, one has to consider V_3, the barrier to threefold internal rotation, F, the reduced moment of inertia of the internal rotor, ρ, the ratio of the moments of inertia of the rotor and of the frame, and D_{ab}, an axis-rotation term which minimizes certain rotation–torsion interaction terms. General spectroscopy programs are usually suitable only to treat spectra of molecules with internal rotation in cases where the effects of the torsion on the rotational spectrum are comparatively small. Usually, rather specialized programs are needed: a recent review of available programs has been given [303]. Further details will be discussed below based on a few examples.

It is desirable that radio astronomical observations are not hampered by the lack of accurate rest frequencies. Ideally, this means that a sufficient amount of transition frequencies have been measured in the laboratory which cover the whole spectral region in which the molecule may be observable. It is less ideal, but still acceptable, if a number of transition frequencies have been measured in part of the spectral region such that the accuracies of the resulting spectroscopic parameters permit sufficiently accurate predictions across the entire relevant spectral region. This means that a handful to a few tens of transition frequencies, which are usually adequate to determine the basic spectroscopic parameters, are in most cases not enough for radio astronomical observations. Even for a small molecule with no spectroscopic complications, such as fine or hyperfine structure, large amplitude motion, or vibration–rotation interaction, this requires frequently measurements of several tens to a few hundreds of lines. In fact, 31 rotational transitions were reported in Ref. [293] to characterize the ground vibrational state of the rather

light and simple CO molecule. Almost 700 and more than 350 transitions were measured in total for SO_2 in its $\nu_2 = 0$ and 1 states, respectively [295]. In Ref. [294], almost 400 rotational transitions were combined with more than 1600 ground state combination differences (GSCDs) from infrared spectra to determine the ground state spectroscopic parameters for H_2CO.

The availability of broadband sources, see, for example, Ref. [304], has led to spectroscopic investigations covering several very large frequency regions, in particular for complex molecules. In the case of C_2H_5CN in its ground vibrational state, this has led to a line list well in excess of 5000 [296]. And in the case of the slightly smaller C_2H_3CN molecule, such a systematic approach unraveled an interaction between the ground vibrational state and its lowest bending state [305]. Even though such interactions had been identified for other molecules before, previous studies of C_2H_3CN did not find evidence for it.

2.4.3 The Quest for Interstellar Glycine

Among the biotic molecules that are needed for life as we know it – sugars, amino acids, and nucleic bases – aminoacetic acid, also known as *glycine*, has been a frequent object of radio astronomical searches. At least in part this is due to the fact that it is a comparatively small molecule with 10 atoms, 5 of which are heavier than hydrogen. Its parent molecule, acetic acid, has only one less H atom and one less heavy atom (N), and this molecule has been detected.

There are several reports in the literature of unsuccessful searches for glycine, for example, Ref. [306] and references therein. Consequently, a purportedly successful detection of glycine in three hot-core sources [307] created a considerable stir. Hot cores are warm and dense molecular clouds in an advanced state of formation of one or more high-mass stars. The sources that had been studied, Sgr B2(N-LMH), Orion KL, and W51 e1/e2, are known to harbor comparatively large amounts of complex molecules. Moreover, the derived rotational temperatures of 75–140 K and the deduced column densities, on the order of 10^{14} cm^{-2}, together with the large number of transitions studied (27) appeared to constitute a clear-cut case. Fairly soon thereafter, however, these results were questioned quite convincingly [308]. The authors pointed out that the abundance of complex molecules in these hot-core sources is not only an advantage for identifying a new, complex molecule, but also a disadvantage as such complex molecules have very many rotational transitions which can result in frequent overlap of spectral features. Moreover, for the assignment of *all* spectral features, it is often not sufficient to consider the main isotopic species in its ground vibrational state, but knowledge of data for minor isotopologs, in particular species with one ^{13}C, or for excited vibrational states has to be available. The authors of Ref. [308] also pointed some possible misassignments in Ref. [307].

A more serious issue concerns the apparent absence of some strong spectral lines. The comparatively high temperatures and densities in the inner parts of hot-core sources make local thermal equilibrium (LTE) to be a good approximation.

With a derived rotational temperature and column density for a certain molecule in a given source, its entire spectrum can be modeled provided the rest frequencies and the dipole moment components are known sufficiently well. And while overlap with an emission feature of a different molecule can cause a spectral line to appear stronger than has been calculated, a line should not be weaker than has been calculated because absorption features are much rarer than emission features. The absence of spectral features implies, in most instances, that the assumed model has to be revised, usually meaning that the column density has to be lower than the initial assumption.

Up to now, there has been no unambiguous radio astronomical detection of glycine. It is important to keep in mind that this only means that column densities in the gas phase are too low to detect the molecule. It may, nevertheless, be present in the gas phase, albeit at rather low levels. No conclusion can be made about glycine amounts residing in the solid phase. Findings of glycine among other more complex molecules in carbonaceous meteorites, such as the Murchison meteorite (see Section 2.4.1), indicate that some amounts of glycine, other amino acids, and further complex organic molecules should be present in the ISM. It should be pointed out in this context that the detection of a molecule by spectroscopic means in the solid phase is even more complicated than in the gas phase because the spectral features are much broader. Therefore, only species that are very abundant or that have very strong spectral features can be detected.

2.4.4 General Astronomic Considerations

The presence of a new molecular species in space can be established by a single or very few transitions if the spectral features are unique. Usually, this requires the spectral features to be strong or the spectral region to be sufficiently sparse. The recent detection of OH^+ [309] and SH^+ [310] with the Atacama Pathfinder Experiment (APEX) telescope, or of H_2O^+ [311], H_2Cl^+ [312], and HCl^+ [313] with the HIFI instrument on board the Herschel satellite, and finally of SH [314] with GREAT on board the SOFIA airplane serves as examples of new species. However, in general, three or more, at least essentially, nonoverlapping spectral features must be observed for linear or strongly prolate molecules, and more lines should be observed in the case of an asymmetric rotor. In fact, many detections of complex molecules have been recently made in the course of analyzing data from unbiased molecular line surveys.

Complex molecules typically occur in the denser and warmer parts of the ISM, where LTE is frequently a good assumption. Larger and complex molecules are mostly less abundant than smaller ones, making them harder to detect. Furthermore, larger molecules commonly have larger moments of inertia, and thus at a given temperature more rotational levels are populated than in a smaller molecule. Thus, even in the unlikely case that a more complex molecule is as abundant as a less complex one, it will be usually still more difficult to be detected because of the less favorable partition function. Figure 2.22 shows that for heavier

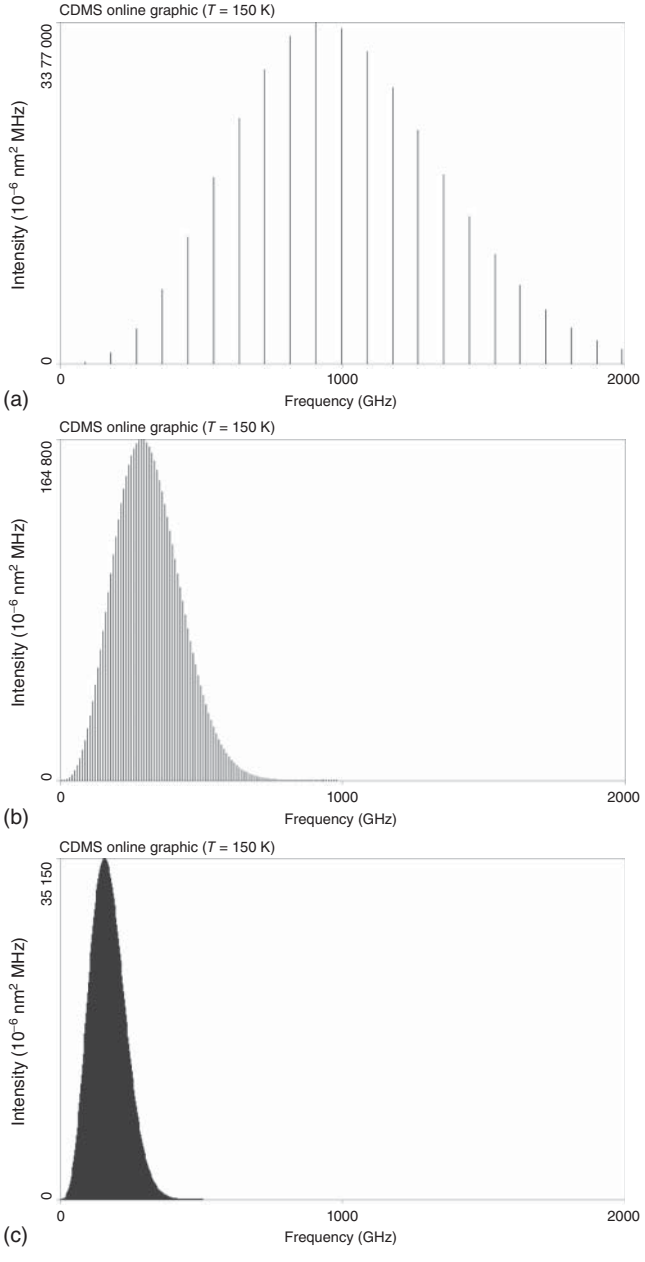

Figure 2.22 Stick spectra of HCN (a), HC_3N (b), and HC_5N (c) at 150 K, demonstrating that for heavier molecules the intensity is distributed over more lines in a narrower frequency range. The maximum intensity drops sharply as a consequence. The stick spectra were generated with the "Search and Conversion" routine of the CDMS catalog.

molecules, more correctly for molecules with larger moments of inertia, the intensity of the lines is distributed over more lines in a much narrower frequency range. Even at the same number densities, the maximum intensity drops sharply. Figure 2.23 shows a similar effect for one molecule, here methanol, at increasing temperatures. Temperatures in dense and dark molecular clouds are usually around 10 K, and warm and dense parts of molecular clouds, heated by the onset of star formation, usually have temperatures of around 100 K to possibly 300 K or higher.

It is worthwhile mentioning that some complex molecules have also been detected in galactic center sources with cold dust and low rotation temperatures (around 10 or 20 K), but with somewhat elevated kinetic temperatures of around 100 K or higher, as for example, in Ref. [315].

As mentioned in Section 2.4.3, spectral features are not allowed to be weaker than calculated, unless clearly overlapped by an absorption feature. That is usually a severe constraint on the calculated abundance of a certain molecular species. Members of the Max-Planck-Institut für Radioastronomie have carried out a line survey with the IRAM 30-m radiotelescope in the entire 3 mm and selected parts of the 2 and 1.3 mm regions toward the prolific high-mass star-forming regions Sagittarius B2(N) and (M) [316]. In particular, with respect to data from the former source, the survey has reached the confusion limit in several sections. A plethora of spectral features are above the 3σ level, but despite thorough investigation of the laboratory spectroscopic literature, dedicated laboratory measurements, and careful modeling, rather many are still unidentified. Nevertheless, a number of new species could be identified. These include aminoacetonitrile [317], the ^{13}C isotopologs of vinyl cyanide [318], and ethyl formate and *n*-propyl cyanide [319]. A number of species could not be identified clearly because too few nonoverlapping features were observed. An important, but maybe not very surprising, aspect became increasingly clear: while it does not matter that much in which spectral region one searches for a molecule with strong emission or absorption lines, it is usually advantageous to search for species with weaker lines at frequencies much lower than the expected Boltzmann peak because line overlap is usually less of a problem there. In fact, the 3-mm region turned out to be ideal for searching for complex molecules such as aminoacetonitrile, ethyl formate, or *n*-propyl cyanide. Less abundant or still heavier molecules should probably be searched for at even lower frequencies, for example, at 7 mm. One should keep in mind, though, that at a lower frequency the chances increase for sampling molecular signals from colder and less dense areas of a molecular cloud which often do not adhere to LTE conditions [320]. It is necessary to point out that the spatial resolution, starting to be available with the Atacama Large Millimeter Array (ALMA) or already available with some interferometers, will reduce the problem of line overlap to some extent, but it is not yet clear if it will suffice to detect many more and maybe still more complex molecules.

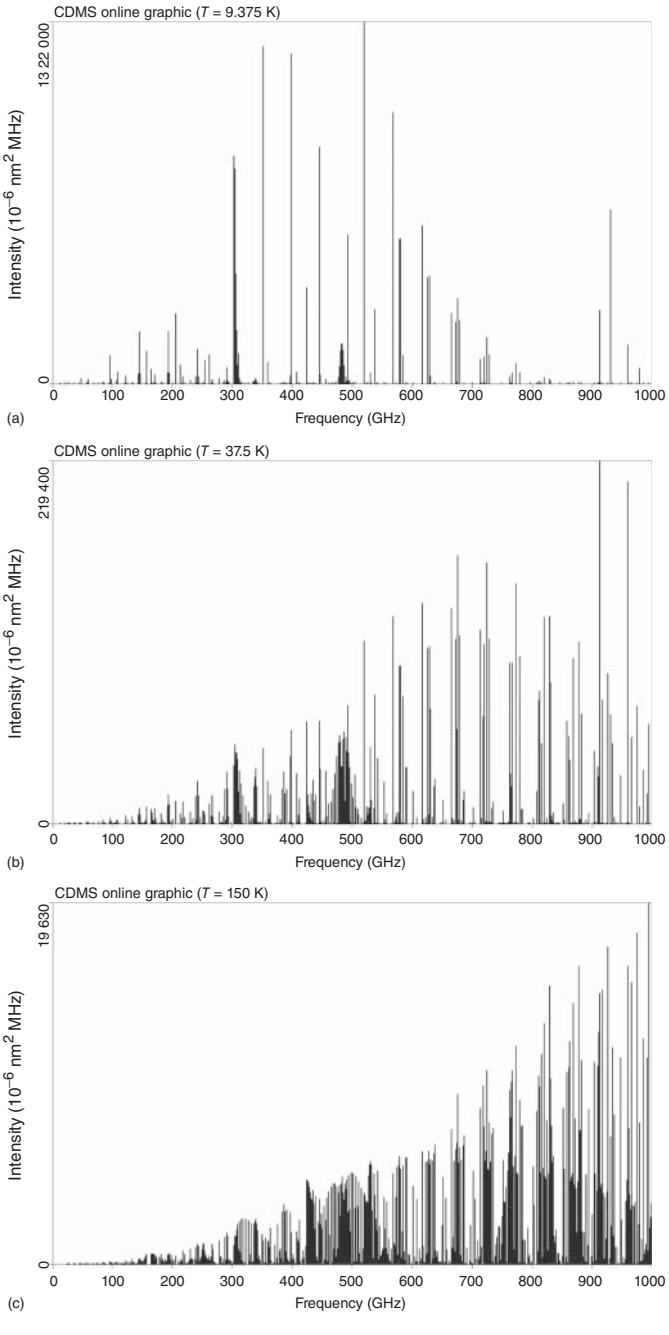

Figure 2.23 Stick spectra of methanol at about 9 K (a), 37.5 K (b), and at 150 K (c), showing that the intensity is distributed over more lines at higher temperature. The maximum intensity drops sharply as a consequence.

2.4.5 Alkyl Alcohols

Alkanols or alkyl alcohols are molecules derived from alkanes, that is, saturated hydrocarbons, in which one or more H atoms have been substituted by a corresponding number of OH groups.

2.4.5.1 Methanol, CH_3OH

Methanol (Figure 2.24a) is one of the most abundant complex molecules in the ISM, and has a fascinating spectroscopy. It is the simplest molecule with a methyl internal rotation; only the hydroxyl group remains as the frame. Obviously, one could also view the OH group as the internal rotor and the CH_3 group as the frame. In fact, the large transition dipole moment of the torsional mode supports this perspective. However, because of the three equivalent minima in the torsional potential, it is much more useful to treat the methyl group as the internal rotor and the hydroxyl group as the frame.

The three equivalent minima lead to rotational transitions belonging to the totally symmetric A symmetry and to the doubly degenerate E symmetry. Levels belonging to different symmetry groups do not interact. The OH frame is only a small obstacle which prevents the CH_3 group from free internal rotation. The experimental barrier, V_3, is 373.555 cm^{-1} [321], corresponding to 4.47 kJ mol^{-1}. In combination with rather large values for F and ρ, this leads to torsional effects, which are still small with respect to the rotational energies, but at low values of K just barely so. Near degeneracies of E symmetry K levels in the ground vibrational state lead to perturbations and to transitions having unusual selection rules and intensities. The first torsionally excited state $\nu_{12} = 1$ straddles the barrier to internal rotation, and $\nu_{12} = 2$ is well above the barrier. As a consequence, torsional effects dominate over rotational effects in states with $\nu_{12} \geq 2$. Accidental near-degeneracies, in particular at higher values of K, lead to perturbations between adjacent torsional levels, starting at $\nu_{12} = 0/1$. An extensive global analysis of CH_3OH data with with $\nu_{12} \leq 2$, $J \leq 30$, and $K \leq 15$ has been presented in Ref. [321]. That work also provides references to recent investigations into methanol isotopologs having symmetrically substituted methyl groups. An extensive comparison of spectroscopic parameters is also given in Ref. [322] for

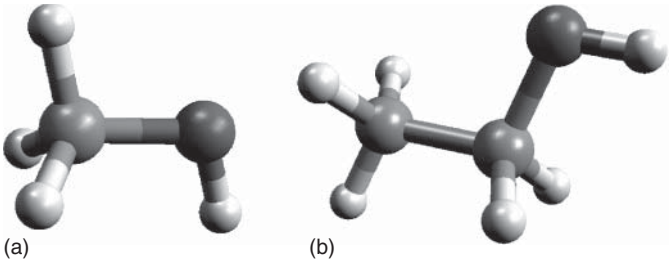

Figure 2.24 Models of the low-energy conformers of (a) methanol and (b) ethanol.

most of these isotopologs. Starting at $\nu_{12} = 3$, additional complications occur as interactions with small amplitude vibrational states, such as the CO stretching state ν_8, become possible. This has been demonstrated, for example, in a study of the rotational spectrum of CH_3OH in its $\nu_{12} = 3$ state [323].

The spectroscopic data of methanol with $\nu_{12} \leq 2$ summarized in Ref. [321] or in references therein were fitted with adapted versions of the BELGI program [303] which takes into account various torsion–rotation interactions within one and between different torsional states. Since interactions with small amplitude vibrations have not yet been included in the program, data from $\nu_{12} = 3$ and other higher states have not been used in the fits to date.

Interestingly, appropriate power series were used for each K stack in Ref. [323] to fit data pertaining to $\nu_{12} = 3$. Effects of perturbations were absorbed in the effective parameters or were dealt with by employing a few interaction parameters and including data for the perturbing K stack from a different vibrational state. Inspection of the magnitudes of perturbations suggested that vibration–rotation interaction is small for states differing in several vibrational quanta, as one would expect. Observations of larger perturbation between such states indicate rather torsion–vibration coupling. However, larger perturbations between states differing only in a few vibrational quanta seem to be caused more by vibration–rotation coupling. It should be emphasized that this discussion was restricted to cases in which one of the interaction states had no or only one quantum of torsion excited. The situation may well be more complicated if more than one quantum of torsion is excited in both interacting states.

An often neglected spectroscopic aspect, the convergence aspect of the Hamiltonian, was briefly alluded to in Ref. [321]. Currently, physically more realistic models for the internal rotation, which have been successfully tested and which are not restricted to a very small quantum number range, are all based on the ρ-axis method (RAM), which is much easier to implement than the internal axis method (IAM). One important set of examples comprises the various versions of the BELGI program [303]. The comparatively simple implementation comes at the expense of folding considerable amounts of torsional contributions into the non-purely torsional parameters. A particularly striking example was the fourth-order purely rotational parameter Δ_K. Its IAM value was derived as 1.67 MHz, which is rather small if one takes into account the value of the A rotational constant, 127.5 GHz; the corresponding values for the smaller H_2CO molecule are 19.4 and 282 GHz, respectively [294]. However, the RAM value for Δ_K of CH_3OH is 255.54 MHz, resulting in $A/\Delta_K = 499$. Hence, for $K > 22$, contributions from Δ_K to the torsion–rotational energy exceed those from A. Already at somewhat lower K, numerical instabilities are likely to occur. Recent infrared measurements [324] should provide insight into this issue.

Another aspect, namely the correct modeling of the intensities of methanol transitions, received some attention only recently [325, 326]. This may be surprising because the intensities are related directly to, for example, the Einstein A values and have a great impact on derived properties, such as rotation temperature, column density, and others. It was found that torsional and rotational

corrections to the permanent dipole moment as well as to the torsional transition moment are required to model the intensities with sufficient accuracy. This result was hardly a surprise given the large internal rotation effects in methanol and the large dipole moment of the OH group, which are strongly affected by the internal rotation. Intensities are also very important in the case of the complicated CH_2DOH spectrum [327, 328].

Methanol was one of the first molecules detected by radio astronomical observations [329]. The isotopic species $^{13}CH_3OH$, CH_2DOH, CH_3OD, and $CH_3^{18}OH$ were also detected. More recently, CHD_2OH and even CD_3OH [330] were detected. It turned out that the abundance of CH_3OH, derived indirectly in that work from that of $^{13}CH_3OH$ and from the known $^{12}C/^{13}C$ ratio, was almost three times higher than that derived directly from CH_3OH observations, presumably because of neglect of opacity. The corrected CH_3OH abundance yielded very high but now consistent deuteration ratios [330].

Many methanol transitions show maser activity [331], and transitions of torsionally excited CH_3OH have also been detected. Even though methanol has been considered by some astronomers as a weed molecule because of its very many observable transitions, it has turned out to be a very good diagnostic for star-formation activity (see, e.g., [332] and references therein).

The question of whether the so-called fundamental constants are in fact constant have attracted great interest of theoreticians and experimentalists. As it turned out, methanol is a particularly sensitive tool to probe the variability of the ratio of the mass of the proton and the mass of the electron [333, 334]. Accurate rest frequencies are necessary for such investigations. A review has been published fairly recently [331], but much more extensive measurements have been obtained in ongoing laboratory measurements. The most accurate test of the variability of the proton to electron mass ratio, carried out with the Effelsberg 100-m radio telescope, suggests no change on the relative level of 10^{-7} [335].

Many isotopologs of methanol have been studied to greatly varying degrees, and for some of them dipole moment components were determined in the ground as well as torsionally excited states. CH_3OH, $^{13}CH_3OH$, and CH_2DOH are among the isotopic species currently under extensive investigation in one or more laboratories. However, the published data are too sparse for isotopic species such as CHD_2OH, $^{13}CH_2DOH$, and $^{13}CH_3^{18}OH$.

2.4.5.2 Ethanol, C_2H_5OH

Ethanol is, strictly speaking, a much more complicated case than methanol because it has two large-amplitude vibrations, namely the internal rotations of the methyl group and of the hydroxyl group. However, the former vibration has a rather high barrier such that frequently no splitting was resolved in the ground vibrational state, and if it was resolved, it amounted usually to only around 1–2 MHz. Most analyses, including the most recent and most extensive one [336], averaged over split transitions and ignored the methyl internal rotation. The internal rotation of the hydroxyl group, however, cannot be ignored. There are three

minima for the hydroxyl internal rotation in ethanol, just as in methanol. However, they are no longer equivalent because of the lower symmetry. Instead, there are two interconvertible conformations. The totally symmetric anti-conformer (a), shown in Figure 2.24, and often also called the trans-conformer (t) because of the trans arrangement of the heavy atoms, can be viewed as corresponding to the totally symmetric *A*-symmetry state of methanol, which in the ground vibrational state is also lowest in energy. Rotation of the OH group by 120° clockwise or counterclockwise leads to the two equivalent *gauche*-conformers, which can be viewed as corresponding to the doubly degenerate *E*-symmetry state of methanol and which manifest themselves spectroscopically as symmetric (g^+) and antisymmetric (g^-) combinations. The latter states are separated by only about 3.3 cm^{-1} and thus strongly interact already at low quantum numbers. In contrast, the separation between *a* on the one side and g^+ and g^- on the other is about 39.5 and 42.8 cm^{-1}, respectively. This means that the *anti*-conformer can be, and has been, treated as an isolated state up to moderate quantum numbers (*J* around 40 and K_a around 7) if one is content with reproducing the transition frequencies to around 100 kHz. At higher values of *J*, and in particular at higher values of K_a, torsion–rotation interaction occurs between all conformers and is, in part, so severe that the assignment of the spectrum is a fairly challenging task.

Up to now, the rotational spectrum of ethanol has been treated quite successfully as an asymmetric rotor with coupled states employing the general spectroscopy programs SPFIT and SPCAT [300]. The torsion–rotation interaction was treated with Coriolis-type operators, though the most recent analysis [336] also contained a Fourier term. More physically realistic models are currently not available. The dipole moments of both conformers have been determined experimentally.

Ethanol was among the first molecules detected in space [337]. Transitions of the higher *gauche*-conformers were also identified [338]. Ethanol is much less abundant than methanol, and its transitions are usually weaker than those of its isomer dimethyl ether (DME), but the molecule has been found readily in many sources. The *anti*-conformers of the two different ^{13}C isotopomers have been studied up to the point at which the interaction with the *gauche* conformers cannot be neglected anymore [339], as indicated two paragraphs above. These measurements are sufficient to identify low to moderately high excited rotational transitions of both isotopomers. It is possible that eventually higher excited rotational levels, including those of the *gauche* conformers, need to be known more accurately. However, preliminary analyses of molecular line surveys suggest that both species will not be detected easily with single-dish radio telescopes. Similar arguments hold for vibrationally excited states. Ethanol has two low-lying vibrational states, namely the methyl torsion and the hydroxyl torsion, both of which are about 240 cm^{-1} above the ground vibrational state. Only very little information is available on the rotational transitions of C_2H_5OH in excited vibrational states. Additional investigations would be useful even though the prospect of detecting vibrationally excited ethanol in space is uncertain. An investigation into the singly

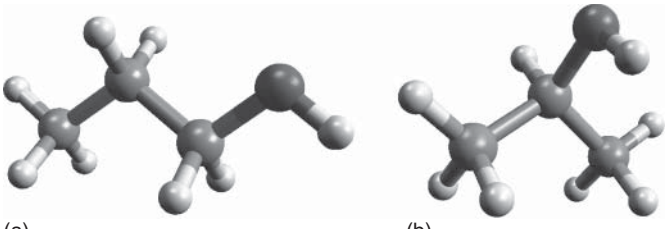

Figure 2.25 One conformer each of (a) n-propanol and (b) i-propanol.

deuterated ethanol isotopomers, similar to the one on the ^{13}C species, has begun fairly recently.

2.4.5.3 **Larger alkanols**

Propanol (C_3H_7OH) is the next larger alkanol. The addition of just one C and two H atoms, however, creates a considerable number of possible structures. As shown in Figure 2.25, the OH group can be attached to carbon atom 1 (atom 3 is equivalent), leading to 1-propanol, also known as normal- or *n*-propanol because of the chain arrangement of the heavy atoms. Attaching the hydroxyl group to C atom 2 results in a completely different branched isomer, 2-propanol, also known as *iso*- or *i*-propanol. Different rotational orientations of the various atom groups in *n*- and *iso*-propanol create a number of conformers for both isomers.

The terminal methyl group and the O atom in *n*-propanol can be attached to the central ethylene unit either in *anti*- or in *gauche*-orientation, leading to the *A* and *G* conformers. In both conformer groups, the OH group can rotate around the CO bond with minima in *anti*- and *gauche*-orientations. The *gauche*-positions are equivalent and different for the *A* and *G* conformers, respectively. The two equivalent *Ag* conformers are observable in the rotational spectrum as symmetric, Ag^+, and antisymmetric, Ag^-, conformers, which are distinguishable. Very extensive spectral recordings and the analysis of several torsion–rotational interactions established very recently that the *Gg* conformer is 47.8 cm^{-1} above the *Ga* conformer, and the *Gg′* conformer is 3.0 cm^{-1} higher still [340]. This energy ordering is quite similar to the one in ethanol, Section 2.4.5.2, with the main difference being that the first energy difference is larger in *n*-propanol. In combination with smaller rotational constants, this has led to a much larger quantum number range in which the *Ga* conformer can be treated as an isolated species [340]. The exact relative energies are not known for the *A* conformers. Theoretical calculations suggest the *Aa* conformer to be higher in energy than *Ga*, but lower than *Gg*. Ag^+ and Ag^- are, according to theoretical calculations, in the vicinity of *Gg′*. The dipole moment components of *Ga*, *Aa*, and *Ag* conformers have been determined experimentally.

2-Propanol, or *iso*-propanol, can occur in two conformers, the *anti*-conformer and the doubly degenerate *gauche*-conformer. The latter occurs again in the rotational spectrum in the distinct symmetric (g^+) and antisymmetric (g^-) combinations. The latter is 1.56 cm^{-1} higher than the former, and the *anti*-conformer is higher still by an amount, not exactly known but probably on the order of a few tens of wavenumbers as judged by intensity measurements [341] and theoretical calculations.

Rotational spectra of both propanol isomers were predicted and fitted with Pickett's SPFIT and SPCAT programs, respectively [300]. It is likely that propanol will be detected in space in the near future.

The detectability of the even heavier alcohol, butanol (C_4H_9OH), is obviously much less certain. The structural complexity of butanol is much greater than that of propanol, as is the number of conformers of each possible structural isomer. Apparently, *tert*-butanol (2-methyl-2-propanol) is the only isomer whose rotational spectrum has been described in detail [342].

2.4.5.4 Alkanediols and -polyols

It is a rule that under "normal" laboratory conditions (STP, standard temperature and pressure), there exist no stable species in which there are two hydroxyl groups at one carbon atom. However, the recent low-temperature solid-state formation of aminomethanol and of carbonic acid suggests that methanediol may also be a species that forms in cold ices. This will be of importance for radio astronomy if these species can be transferred into the gas phase without total decomposition. In the case of carbonic acid, it has been shown that, under favorable conditions, it can be evaporated with only small amounts of decomposition.

As long as methanediol has not been synthesized, ethylene glycol (ethane-1,2-diol) will remain the simplest known alkanediol. There are many possible conformers because of the orientations of the two CH_2 groups with respect to each other (*gauche* (*G*) or *anti* (*A*)), and of the two hydroxyl groups with respect to the respective CH_2 group (*g*, *g′*, or *a*). To date, only two conformers have been identified in the gas phase, and both have been characterized extensively by rotational spectroscopy [299, 343]. The *aGg′* conformer is lowest in energy and the *gGg′* conformer is about 200 cm^{-1} (or about 2.5 kJ mol^{-1}) higher [343]. Both form intramolecular hydrogen bonds between the hydrogen of one OH group and the O atom of the other. Since there are two equivalent configurations for each of these two conformers, extensive tunneling takes place. The barriers to interconversion are moderately high, leading to rotationless tunneling splittings of almost 7.0 and 1.4 GHz for the *aGg′* and *gGg′* conformers, respectively. Extensive Coriolis-type interaction takes place between the symmetric and antisymmetric tunneling states of each conformer, complicating the rotational spectrum significantly. In fact, molecular beam Fourier transform microwave (FTMW) spectroscopy as well as MW–MW and MW–mmW (millimeter wave) double-resonance techniques were required to establish the first few assignments. Moreover, the spectrum of the *gGg′* conformer is so complicated that the fitting had to be truncated, albeit at comparatively high quantum numbers [343].

The analyses of the rotation-tunneling spectra of both conformers were carried out with the SPFIT/SPCAT program suite [300]. The interactions lead to many additional transitions with unusual selection rules and affect the line intensities considerably. As a consequence, it was shown in both studies that the signs of the Coriolis-type terms, which act as axis rotation terms, relative to the signs of the dipole moment components do matter for the proper calculation of intensities. These signs cannot be determined from the fits. The lower energy conformer (*aGg′*) of ethylene glycol has been detected in space in the prolific hot-core Sagittarius B2(N) [344].

Limited information is available on some deuterated isotopologs of ethylene glycol, but apparently no information exists on the astrochemically more important ^{13}C species. Attempts are under way to assign transitions of vibrationally excited states. Unfortunately, such transitions cannot be seen in the FTMW spectra. Thus, only the tedious double-resonance spectroscopy remains a possibility to establish initial assignments. Rotational transitions of the *aGg′* conformer in excited vibrational states may well be detected in space during interferometric observations, in particular with ALMA, since there are several very low lying vibrational states that are lower in energy than those of the *gGg′* conformer.

Two isomers are known for the next heavier molecule propanediol, the 1,2- and the 1,3-isomers. The conformational landscapes of both have been investigated extensively rather recently by FTMW spectroscopy. Seven conformers where identified for propane-1,2-diol, all of which possess unique structures [345]. Millimeter-wave spectroscopy measurements are currently under way. Two chiral forms tunneling between two equivalent minima were identified for propane-1,3-diol, which are separated by rather high barriers [345]. Very recently, extensive millimeter-wave data became available for both conformers [346]. With ethane-1,2-diol already detected, it seems plausible that propanediol may be observed in space in the not too distant future.

So far, heavier alkanediols have been studied to a lesser extent. The conformations of the simplest stable alkanetriol, glycerol, have been studied by FTMW quite recently [347]. Two low-lying conformers were identified, which had been already observed by free-jet millimeter-wave spectroscopy, along with three conformers which are higher in energy. Glycerol has 6 heavy atoms plus 10 H atoms, several conformers, and very likely quite a few low-lying vibrational states. Hence, it has a very unfavorable partition function. In addition, it is much less volatile than lighter alkanols, making it overall less likely to be observed in space any time soon.

2.4.6 Alkyl Ethers

Ethers are molecules in which an O atom connects two organic groups. In this overview, only ethers with saturated alkyl groups will be considered, even though some molecules with unsaturated groups have also been studied in the laboratory.

2.4.6.1 Dimethyl Ether, CH_3OCH_3

DME (CH_3OCH_3), shown in Figure 2.26a, is the simplest possible ether. The study of its rotational spectrum has recently been extended to beyond 2 THz [348]. It was also one of the early detected molecules [349]. It is an abundant species, in particular, in hot cores. In fact, emission features of DME affected two of the three absorption features detected for $H_2^{35}Cl^+$ and $H_2^{37}Cl^+$ with the HIFI instrument on board the Herschel satellite toward the hot-core NGC 6334 [312].

The internal rotation barrier in DME is much higher than in methanol, which makes the analysis of the rotational spectrum more amenable to programs treating internal rotation as a small perturbation of the spectrum. On the other hand, the presence of two (equivalent) methyl groups complicates the situation. The number of internal rotation components of DME can be extrapolated from those of methanol in a straightforward manner. The internal rotation in methanol has three equivalent minima distributed over two symmetry species. In DME, there are nine equivalent minima distributed over four symmetry species; one (*AA*) is totally symmetric and thus nondegenerate, two (*AE* and *EA*) are doubly degenerate, and *EE* is quadruply degenerate. The components usually spread out over few megahertz. If asymmetry and torsional splitting have been fully resolved, somewhat complex spin statistics has to be considered. If asymmetry splitting has not been resolved and the *AE* and *EA* overlap, as is observed frequently, one observes a pattern exhibiting a 1 : 2 : 1 intensity ratio, with the *EE* component in the center and the other two components displaced more or less symmetrically around it. The pattern caused by the internal rotation splitting is very useful for assigning quantum numbers to the observed absorption features.

The ground state rotational spectrum requires Fourier expansions of the spectroscopic parameters to be reproduced within experimental uncertainties. Two programs have been tested, namely ERHAM [350] and SPFIT [300]. The ERHAM program is capable of fitting spectra of molecules containing two 3-fold internal rotors, provided the effects of these internal rotors are only small perturbations of the rotational spectrum. The treatment of SPFIT is very similar, but a small part of the internal rotation has not been accounted for. This part is due to the fact that the internal rotation axis is not exactly on an inertial axis (here the *a*-axis). This has only a small effect for low rotational or torsional quanta but leads to non-negligible deviations at higher quantum numbers.

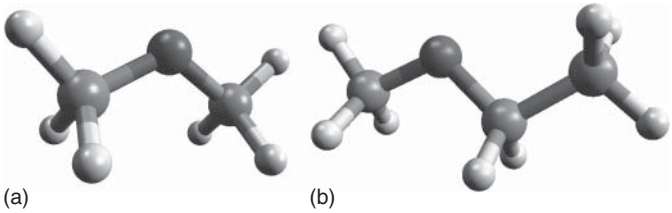

Figure 2.26 (a) Dimethyl ether and (b) ethyl methyl ether.

Studies of DME in excited vibrational states or of isotopic species of DME have been sparse until recently. In the course of the investigation of the ground vibrational state of DME, a study of its first excited torsional states $\nu_{11} = 1$ and $\nu_{15} = 1$ was started and has almost been completed. These states are at vibrational energies of about 200 and 240 cm^{-1}. In spite of this large energy difference, Coriolis interaction occurs between these two torsional states. The good agreement between the experimental first-order Coriolis coupling parameter and its value calculated from an *ab initio* harmonic force field suggests this interaction to be caused by vibration–rotation interaction rather than torsion–vibration interaction. Again, the two programs ERHAM and SPFIT were used to analyze the spectra. While the latter program is capable of treating Coriolis interaction appropriately, the missing torsional parts, mentioned above, caused much more pronounced problems than in the treatment of the ground vibrational state. The former program, ERHAM, on the other hand, currently does not permit fitting Coriolis interaction. A kind of merged fit permits the rotational spectrum in these two states to be predicted sufficiently well for most radio astronomical observations. An extension of ERHAM is under way, which eventually should permit fitting of the Coriolis interaction. Recently, transitions pertaining to these two vibrationally excited states have been detected with a single-dish radio telescope [351].

An extensive investigation into the second excited polyad of DME, $\nu_{11} + \nu_{15} = 2$, has been started. As in the case of $\nu_{11} + \nu_{15} = 1$, Coriolis interaction will take place, between $\nu_{11} = \nu_{15} = 1$ on one side and $\nu_{11} = 2$ or $\nu_{15} = 2$ on the other. Moreover, anharmonic (Darling–Dennison) interaction can occur between $\nu_{11} = 2$ and $\nu_{15} = 2$, but because of the large energy difference the effects are expected to be small and very localized. An additional complication is the lowest bending state $\nu_7 = 1$ which is in the vicinity of $\nu_{11} + \nu_{15} = 1$, permitting rotational (Coriolis-type) interaction to occur. Even though the matrix element connecting a fundamental state with a combination state will usually be smaller than that between two fundamentals, the perturbations may still be substantial because of the proximity of the states. Moreover, Fermi interaction will take place between $\nu_7 = 1$ on one side and $\nu_{11} = 2$ or $\nu_{15} = 2$ on the other.

Fitting these states with SPFIT will fail unless the missing torsional terms are included. Fitting these states with ERHAM will require a considerable number of interaction parameters to be available. If the programs are extended appropriately, they should both be capable of describing the spectrum reasonably well. However, since the $\nu_{11} + \nu_{15} = 2$ states are ~half way up the torsional barrier, it may well be that not all of the torsional effects can be accounted for. In that case, it will be necessary to revert to a program such as BELGI, which employs a more physically realistic model of the torsional problem. It is not known whether an appropriately extended version of such a program will be available in the near future. The polyad involving the $\nu_{11} + \nu_{15} = 2$ and the $\nu_7 = 1$ states is expected to be observable in hot-core sources with interferometers such as ALMA. The prospects of observing the next higher polyad are difficult to judge at present.

Singly deuterated DME has recently been characterized in the laboratory and has been found in space subsequently [352]. The high degree of deuteration

suggests that doubly deuterated isotopomers may well be detectable, at least with ALMA.

Investigations of the ground state rotational spectra of DME isotopologs having one or two ^{13}C atoms have been completed [353]. The spectrum of the species with two ^{13}C atoms is quite similar to that of the main species. One of the main differences is the slightly modified spin-statistic ratios. The spectrum is more different for the species with one ^{13}C atom because the two internal rotors now are different, thus requiring two slightly different sets of torsional parameters. Moreover, the pattern of the torsional splitting is very different since the quadruply degenerate *EE* symmetry species is now split into two doubly degenerate ones, commonly called *EE* and *EE*′.

The isotopic species with one ^{13}C atom has been detected in space [353]; the species with two ^{13}C atoms may be too weak to be observed. Transitions of the isotopolog with one ^{13}C atom in excited vibrational states may well be detectable with ALMA.

2.4.6.2 Larger Ethers

Ethyl methyl ether (EME, $C_2H_5OCH_3$), Figure 2.26b, is the next larger molecule in this family. Like the related ethanol, it occurs in two conformers. The *anti*-conformer is in both cases the lowest in energy. The doubly degenerate *gauche*-conformer is only about 60 K higher in ethanol, whereas the energy difference in EME may be as large as 800 K. The *anti*-conformer has been tentatively detected in a hot-core source, but the *gauche*-conformer has essentially no chance of being observable in space. The ground vibrational state of *anti*-EME has been studied in the laboratory fairly extensively up to 350 GHz [354]. It is not clear whether these observations extend to high enough frequencies for astronomical observations. Assignments to higher quantum numbers are under way. The molecule has two methyl internal rotors. The one attached to the O atom has a barrier very similar to that in DME, and the associated splitting is frequently resolved, in particular at low frequencies. The other one, attached to the C atom, has a slightly higher barrier, comparable to that in ethanol; the splitting caused by this internal motion has been resolved in some instances and, for the most part, not completely. Overall, each rotational transition may be split into five components, as is the case for DME with one ^{13}C atom, but the spectrum is dominated by two-line features, especially at low frequencies, where also some four-line features have been observed. At higher frequencies, the internal rotation splitting is increasingly unresolved.

Since EME has already been tentatively detected in space [355], it appears that it will be only a matter of time before it is detected with certainty. Some information is available for excited vibrational states [356]. In particular, the very low lying skeletal torsion $\nu_{30} = 1$ at a vibrational energy of about 115 cm^{-1} may be detected very soon after the detection of the ground state lines.

Diethyl ether (DEE, $(C_2H_5)_2O$) is the next larger symmetrical ether. Its rotational spectrum has been studied quite extensively up to ∼370 GHz for the lowest two conformers, *aa*-DEE, which is lowest in energy, and *ag*-DEE, which is about 5.4 kJ mol^{-1} higher; *gg*-DEE is another possible conformer but this has

not been identified. Neither conformer shows torsional splitting in the ground vibrational state. Also studied were three low-lying vibrational states of *aa*-DEE. More recently, the investigations into the ground vibrational state rotational spectra have been extended to about 900 and 640 GHz for *aa*- and *ag*-DEE, respectively [357]. As it turned out, extrapolation of the rotational spectrum of *aa*-DEE to 900 GHz worked almost perfectly, whereas the extrapolation to only about 640 GHz was not satisfactory for *ag*-DEE. The latter was not surprising, as many more spectroscopic parameters were already needed for the higher state conformer in the previous study.

It is conceivable that *aa*-DEE will be detected in space in the not too distant future. The detection of *ag*-DEE is much less likely. Moreover, several low-lying vibrational states of *aa*-DEE are lower in energy than *ag*-DEE, so these states should be detected before there is a chance to detect *ag*-DEE.

There are two asymmetric ether isomers to DEE, namely, *n*-propyl methyl ether and *iso*-propyl methyl ether. Both were studied to a limited extent in the microwave region, and several conformers were identified. The corresponding alcohols, *n*-propanol and *iso*-propanol, Section 2.4.5.3, are much simpler molecules which have not yet been identified in space. Hence, the detection of either propyl methyl ether isomer seems to be far away.

2.4.7 Esters

Esters are condensation products of an acid (see Section 2.4.9 for alkyl acids) and an alcohol (see Section 2.4.5) under abstraction of a water molecule. Many esters have fruity or other, in part strong, flavors.

Methyl formate (CH_3OCHO) is the simplest organic ester, derived from methanol and formic acid. With four heavy atoms and four H atoms, we do not consider it to be a small molecule. Even around 100 K, many rotational levels are populated. It was again one of the molecules early detected in space [358]. Moreover, it was observed not only in hot cores [315]. The molecule possesses a low-lying methyl torsional mode. Rotational transitions pertaining even to the second excited methyl torsion have already been detected in space from single-dish observations [359]. Hence, transitions of even higher torsional or other vibrational states should be observable with ALMA.

Methyl formate exists in two conformers, *syn* and *anti*, which are derived from *cis*- and *trans*-formic acid, which differ by the orientation of the methyl group (or H atom) with respect to the carbonyl group. *syn*-Methyl formate is much lower in energy than the *anti*-conformer by an amount which is very similar to the one with which *trans*-formic acid is lower than the *cis*-conformer. The methyl group has a moderately high barrier to internal rotation of 4.46 kJ mol^{-1}, giving rise to well-resolved *A*/*E* splitting in most instances for the ground vibrational state of the *syn*-conformer. This conformer has been subjected to numerous rotational spectroscopic studies. A recent very extensive analysis [360] was able to reproduce the $v_t = 0$ and 1 data within experimental uncertainties by employing a

program similar to BELGI. The ERHAM program was used in an earlier study dealing with states $v_t \leq 2$. While the ground state data could be reproduced satisfactorily, the $v_t = 1$ fit did not reproduce the data within experimental uncertainties, even though a large number of transitions were already not used in the fit. No information is currently available on $v_t = 3$, which is perturbed by interactions with two small-amplitude vibrations. Very recently, an extensive analysis of $v_t = 2$ has been published [361]. A global analysis failed, presumably because of torsion–rotation interaction with the perturbed state $v_t = 3$.

All singly substituted isotopologs have been studied in recent years. The two ^{13}C isotopomers have been detected in space [362]. Very little data have been obtained thus far for the *anti*-conformer [363].

Ethyl formate (C_2H_5OCHO) is also derived from formic acid, but the alcohol is the next heavier ethanol. The conformational landscape can be derived straightforwardly from those of ethanol and methyl formate. Only the conformers in which the ethyl group is oriented *syn* with respect to the carbonyl group of formic acid have been studied; the *anti* conformers are too high in energy. Thus, instead of *anti-syn*-ethyl formate and *gauche-syn*-ethyl formate, one usually finds *anti*-ethyl formate and *gauche*-ethyl formate in the literature. As in ethanol, the latter is higher in energy; the difference of 0.78 ± 0.25 kJ mol^{-1} agrees at the lower limit with the energy difference in ethanol. The rotational spectrum of these conformers in their ground vibrational states has recently been studied up to about 380 GHz [364]. No internal rotation splitting has been resolved in the ground vibrational state, but there appears to be a perturbation at higher K_a between the ground and a low-lying vibrational state of *anti*-ethyl formate. Since the latter conformer had been detected in the massive galactic center hot-core Sagittarius B2(N) [319], there is some chance that the higher lying conformer or transitions of the *anti* conformer in excited vibrational states or of its isotopologs with one ^{13}C can be detected with ALMA.

The ester isomer of ethyl formate, methyl acetate, has two internal methyl rotors. The one attached to an O atom has a moderately high barrier of about 5 kJ mol^{-1} [365], similar to that in methyl formate. The barrier to internal rotation of the acetate methyl group is, at 1.19 kJ mol^{-1}, much lower, even lower than in acetic acid, where the barrier height is 2.04 kJ mol^{-1}. Twenty-five rotational transitions up to $J = 5$ were studied between 8 and 40 GHz [365], providing basic information on the molecule, but this is still insufficient to derive a spectroscopic model that accounts quantitatively for the observed transitions. Very recently, considerably more laboratory data have become available [366], permitting the molecule to be detected in space [367].

Among the esters with four C atoms, ethyl acetate is the one deemed to be most easily observable. Limited information is available on the rotational spectrum of the *anti*-conformer [368]. It is not known whether this or the *gauche*-conformer is lower in energy, nor has its dipole moment been determined experimentally.

2.4.8 Alkyl Cyanides

Alkyl cyanides are characterized by the cyano (–CN) group. Methyl cyanide (CH_3CN) and ethyl cyanide (C_2H_5CN) have been detected in space [369, 370]. Both molecules are particularly abundant in hot-core sources. The lowest energy *anti*-conformer of the next larger *n*-propyl cyanide, C_3H_7CN, has been detected recently in the prolific galactic center hot-core Sgr B2(N) [319]. Interestingly, it was found in that study that, while ethyl cyanide is only slightly less abundant than methyl cyanide, there is a sharp drop in abundance of about two orders of magnitude to *n*-propyl cyanide. It will be interesting to find out whether there is also a sharp drop to the next larger member *n*-butyl cyanide.

Methyl cyanide is a symmetric-top rotor, and thus does not belong to the restrictive definition of complex molecules given in Section 2.4.1. However, many astrochemists do consider it to be complex. It warrants consideration as a model for the heavier alkyl cyanides. A recent laboratory spectroscopic investigation [371] deals with the spectra of six isotopologs studied in their ground vibrational states in natural isotopic composition. Besides the main species, these are two isotopomers with one ^{13}C atom, ones with ^{15}N and D, respectively, and one with two ^{13}C atoms. With the exception of the latter, all have been identified in space. Ref. [371] provides some information on their detection.

There are several low to moderately high lying vibrational states, the lowest one being $\nu_8 = 1$ at 365.0 cm^{-1}. The detection of transitions pertaining to this vibrational state has been published. Laboratory data have been published for states up to $\nu_4 = 1$ [372]. Numerous isotopic species in various excited vibrational states are currently under investigation; some have been detected in space already [316] and more will be observable with ALMA.

Ethyl cyanide (C_2H_5CN) is one of the molecules requiring extensive further laboratory spectroscopic investigations. The ground vibrational state of the main isotopic species has been studied to an extent well beyond the needs of astronomers [296]. Splitting due to the methyl internal rotation is only observable at low frequencies and under favorable circumstances. The three isotopomers with one ^{13}C atom have been studied in the laboratory and have been detected in space subsequently [373]. The three species containing one D and the ^{15}N-containing species have also been studied, but studies on the isotopic species containing two ^{13}C atoms are missing thus far.

Some information has been published on the rotational spectra of ethyl cyanide in vibrationally excited states [374]. The molecule has two low-lying vibrations slightly above 200 cm^{-1}. The torsional state $\nu_{21} = 1$ shows pronounced methyl internal rotation splitting, in particular in *b*-type transitions. The in-plane bending state $\nu_{13} = 1$ also exhibits resolvable internal rotation splitting because of strong Coriolis interaction with the torsional state. Emission features belonging to these states have been detected in hot-core sources.

The situation gets more complicated for the states having $\nu_{13} + \nu_{21} = 2$ since the combination state can show Coriolis interaction with both overtone states, and

the two overtone states can exhibit anharmonic (Darling–Dennison) interaction. In addition, some 20 cm^{-1} below this triad is another vibrational state, the $\nu_{20} = 1$ out-of-plane bending state. It displays methyl internal rotation splitting, which may be facilitated by vibrational mixing (the state may have some torsional character) or by vibration–rotation interaction with one or more of the $\nu_{13} + \nu_{21} = 2$ states. At even higher vibrational energies, the density of states increases rapidly. Besides the four states having $\nu_{13} + \nu_{21} = 3$, there are two combination states involving $\nu_{20} = 1$ and either $\nu_{13} = 1$ or $\nu_{21} = 1$, plus another fundamental state, $\nu_{12} = 1$. The heptad is thus described by $3\nu_{12} + \nu_{13} + 2\nu_{20} + \nu_{21} = 3$. These, as well as even higher states, will be detectable with ALMA (Figure 2.28).

Transitions of the fairly isolated states $\nu_{20} = 1$ and $\nu_{12} = 1$ along with transitions in lower excited vibrational states have been detected recently in Orion KL [375] and in Sagittarius B2(N) [316].

It is difficult to estimate the amount of excited vibrational states that may be detectable for the isotopomers of ethyl cyanide containing one ^{13}C atom, but at least the lowest two states having $\nu_{13} + \nu_{21} = 1$ are expected to be observable.

Propyl cyanide (C_3H_7CN, Figure 2.27) has two structural isomers, the normal *n*-form, with a chain structure, and the *iso* or *i* form with a branched structure. Moreover, *n*-propyl cyanide has two conformers, the *anti*- and the doubly degenerate *gauche* forms. The *anti*-conformer has been detected in space [319]. That work also provides combined analyses of the rotational spectra of both conformers as well as references to previous laboratory work. Only one brief account on vibrationally excited *n*-propyl cyanide is in the literature and apparently none on isotopic species. The prospects of observing such transitions in space are uncertain at the moment.

A very recent report presents detailed information on the ground state rotational spectrum of *iso*-propyl cyanide shown in Figure 2.28 a [376]. Determining the ratio between *i*- and *n*-propyl cyanide, or at least a low upper limit will be very useful to rdetermine how important branched isomers are in astrochemistry. Similarly, *cyclo*- or *c*-propyl cyanide (Figure 2.28b) [377] is a useful probe into the importance of cyclic molecules.

The number of isomers and conformers increases rapidly with each added CH_2 group. There are already four isomers for butyl cyanide (C_4H_9CN). Among them, the *n* form should be the one most likely to be detectable. Three of the five conformers, shown in Figure 2.29, have been characterized quite extensively in the millimeter and lower submillimeter wave regions [378]. There is some

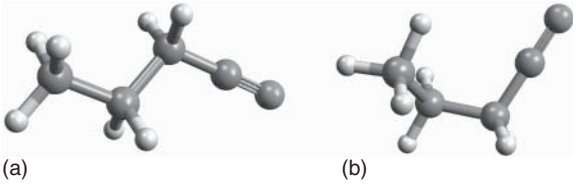

Figure 2.27 The two conformers of *n*-propyl cyanide: (a) *anti* and (b) *gauche*.

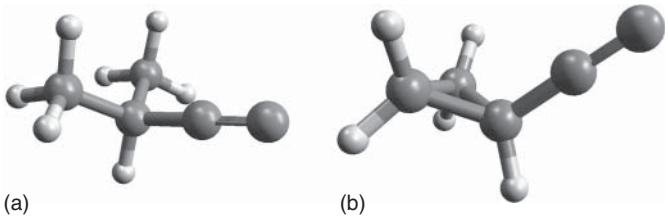

Figure 2.28 Two molecules related to the detected *n*-propyl cyanide: (a) *iso*-propyl cyanide and (b) *cyclo*-propyl cyanide.

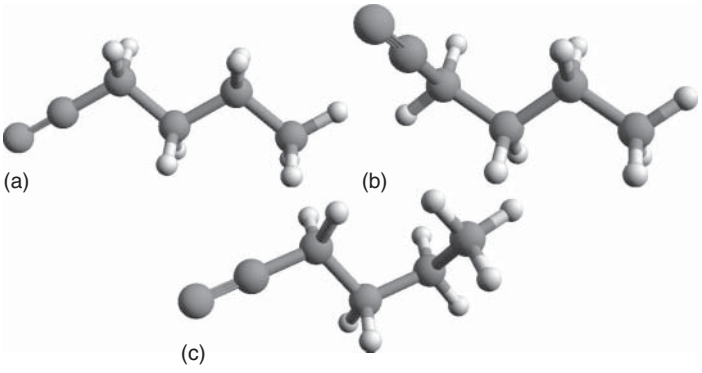

Figure 2.29 The three lowest energy conformers of *n*-butyl cyanide: (a) *anti–anti*, (b) *gauche–anti*, and (c) *anti–gauche*.

information available on the rotational spectrum of *t*-butyl cyanide, which can be derived from methyl cyanide by replacing each of its H atoms with a CH_3 group, but no information is presently available on the rotational spectra of the other two isomers.

2.4.9 Other Complex Molecules

After having provided somewhat detailed information on a selection of related complex molecules, other complex molecules will be mentioned in this section, in particular those that have already been detected; an overview is given in Table 2.6.

Replacement of the O atom in an alkanol with a sulfur atom results in thioalcohols, also known as *mercaptans*. Methyl mercaptan (Figure 2.30a) is the simplest one. It has been detected in space [379], and its rotational spectrum has been characterized fairly extensively [380]. Ethyl mercaptan has not yet been detected in space. Its rotational spectrum has been studied in the microwave region for both the lower *anti*-conformer as well as for the doubly degenerate *gauche*-conformer. Additional measurements are currently under way.

The OH group in an alkanol can also be replaced by an NH_2 group, yielding an amine. Methylamine is the simplest member in this group. It was found in

Table 2.6 Selected families of other complex molecules with light members and status of the laboratory rotational spectroscopy and of its detection in space.

Molecule family Molecule	Status
Thioalcohols	
CH_3SH	Main species fairly well characterized in the laboratory [380]. Found in space [379]. Only a few lines measured for isotopic species.
C_2H_5SH	Microwave spectrum known for *gauche*- and *anti*-conformers; under investigation. Not found in space.
Amines	
CH_3NH_2	Ground vibrational state of main isotopolog well studied [408], detected in space [381].
$C_2H_5NH_2$	Extensive measurements, but only preliminary analyses of complicated spectrum [383]. Not detected in space [383].
Alkanals	
H_2CO	Actually not a complex molecule. Well studied for many isotopologs and excited vibrational states. Many isotopologs detected.
CH_3CHO	Ground and first two torsional states of main isotopolog studied quite well [409] and moderately abundant in space [384] and references therein.
Ethanal	Higher vibrational states and isotopologs not sufficiently studied; under investigation.
C_2H_5CHO	The syn conformer quite well studied; detected in space.
Propanal	The *gauche*-conformer much higher in energy; some data available.
iso-Butanal	Some laboratory data available.
n-Butanal	Some laboratory data in PhD thesis.
Alkanones	
$CH_3C(O)CH_3$	Ground and first two excited states quite well characterized [410] and found in space [411].
Propanone	^{13}C species under investigation; not yet found in space.
$C_2H_5C(O)CH_3$ Butanone	Ground state spectrum well studied. Not yet seen in space.
Alkanoic acids	
HC(O)OH	Ground states of various isotopologs well characterized.
Formic acid	Main species detected in space [386].
$CH_3C(O)OH$	Main species well characterized, including first two excited states [412].
Acetic acid	Detected in space ($v = 0$) [387].
$C_2H_5C(O)OH$	Some microwave data known for low-energy conformer. Not seen in space.

Table 2.6 (Continued).

Molecule family Molecule	Status
Acidamides	
$HC(O)NH_2$	Ground and some excited states well characterized for main species, gs for isotopologs, for example, Ref. [390].
Formamide	Abundant in space [389]; $\nu_{12} = 1$ and ^{13}C species detected.
Acetamide	Spectrum fairly well characterized. Detected in space [391].
Propionamide	Some microwave data available. Not seen in space.
Acyl cyanides	
Formyl cyanide	Spectrum well characterized [392]. Detected in space [394].
Acetyl cyanide	Spectrum well characterized [393]. Not seen in space.
Aminonitriles	
Aminoacetonitrile	Spectrum well characterized [413]. Detected in space [317].
2-Aminopropionitrile	Spectrum well characterized [395]. Not seen in space [395].
3-Aminopropionitrile	Spectrum well characterized, but not yet published. Not seen in space.
Amino acids	
Glycine	Spectrum well characterized. Not seen in space.
Alanine	Spectrum fairly well characterized. Not seen in space.
Glycolaldehyde	Ground [397] and several excited states well to quite well characterized, also singly substituted isotopologs, for example, Ref. [398]. Main species detected in space, also vibrationally excited [399].
Alkenenitriles	
Propenenitrile	Ground vibrational state well studied for many isotopologs. Some low-lying vibrational states for main species [305, 400] additional work in progress, lowest vibrational state for some singly substituted species.
Vinylcyanide	Ground and several excited states detected in space for main species, ^{13}C species in gs [318].
C_3H_5CN	2-, 3-, and *iso*-butenenitrile fairly well studied. Neither detected in space.
Vinyl alcohol	Rotational spectrum reasonably well studied, purportedly detected in space [401].
Vinylamine	Rotational spectrum well studied [404], not seen in space.
Alkanimines	
Methanimine	Main species well studied [403], abundant in space [402] (and references therein). Some minor isotopic species under investigation.
Ethanimine	Rotational spectrum known to some extent and detected in space [414].
Cyanomethanimine	Spectrum fairly well characterized. Detected in space [396].

Table 2.6 (Continued).

Molecule family Molecule	Status
H_2C_2O	Rotational spectrum of ketene known well, abundant in space. Homologs with more C atoms or with S instead of O not seen.
H_2C_2NH	Recently detected in space [406].
Cyclic molecules	Oxirane or ethylene oxide is the only cyclic complex molecule detected in space [407] . For example, aziridine and thiirane (NH or S, respectively, instead of O) well characterized, but not seen in space.

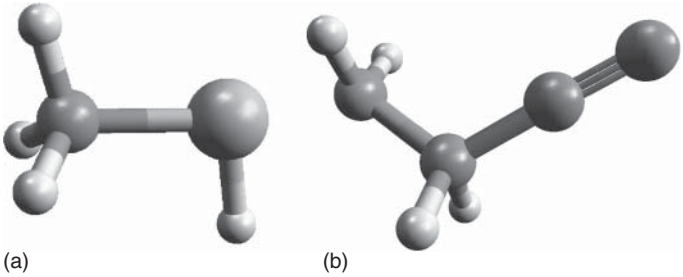

(a) (b)

Figure 2.30 Models of (a) methanethiol and (b) aminoacetonitrile.

space [381], and its rotational spectrum has been studied quite extensively [382]. It appears to be under investigation in at least one group, and these measurements include different isotopic species.

The rotational spectrum of ethylamine is much more complex, so only preliminary analyses have been published [383] even though extensive spectra have been recorded. Searches for this molecule have been unsuccessful thus far [383].

Oxidation of an alkanol RCH_2OH leads to an alkanal RCHO, also known as *alkyl aldehyde*. Methanal (or formaldehyde, H_2CO) is the smallest member in this group, but with four atoms it does not meet the chosen definition of a complex molecule, though some astronomers consider it to be a member of that group. It may be mentioned here that it is a very important molecule in space, and its rotational spectrum has been studied, including those of minor isotopic species or in vibrationally excited states. Ethanal (or acetaldehyde, CH_3CHO) is moderately abundant in space [384] (and references therein). Its rotational spectrum has been studied quite extensively, though publicly available data are sparse at higher frequencies. The molecule is currently under investigation, and this applies also to several of its minor isotopic species. The lower state *syn*-conformer of propanal has been detected in space, and its rotational spectrum has been studies extensively. The doubly-degenerate *gauche*-conformer is much higher in energy; several excited vibrational states of *syn*-propanal are lower. Nevertheless, its spectrum

has been analyzed to some extent. There is some information in the literature on *iso*-butanal, whereas data for *n*-butanal seem to be restricted to a PhD thesis.

Ketones can be considered as structural isomers of alkanals with more than two C atoms. Their general formula is R_1R_2CO, with neither R_1 nor R_2 being an H atom. Propanone, also known as *acetone*, is the smallest one with $R_1 = R_2 = CH_3$. It is comparatively abundant in space, and its rotational spectrum has been studied rather extensively, including its two first excited torsional states. The ERHAM program was quite successfully used for the analysis of the ground vibrational state, but did not perform as well for the symmetric and more so for the asymmetric combination of the two equivalent methyl torsions. Recently, a dedicated two-top program has been developed, which does not only treat the torsion perturbatively. The results obtained for the test case propanone are very promising [385]. Butanone is the next heavier ketone. It has not yet been detected in space. Its rotational spectrum is currently under investigation.

Oxidation of an alkanal, RCHO, leads to an alkanoic acid, RCOOH. The simplest one, formic acid (HCOOH) was detected early in space as far as the lower energy *trans*-conformer is concerned [386]. The *cis*-conformer is very much higher in energy. Rotational spectra of both conformers have been studied very extensively, even for minor isotopic species, which have not yet been detected in space conclusively. Acetic acid (CH_3COOH) has also been detected in space [387], but its lines are much weaker than those of formic acid. Its rotational spectrum has been studied rather extensively [388]. Propionic acid (C_2H_5COOH) has been studied in the microwave region, but it has not yet been detected in space.

Replacing the OH group in an alkanoic acid RCOOH with an NH_2 group yields acidamide $RC(O)NH_2$. R = H yields formamide, which is the simplest one. It was detected early in space [389], and its rotational spectrum has been characterized extensively even for minor isotopologs as well as for excited vibrational states [390] (and references therein). $R = CH_3$ yields acetamide, which was detected in space much more recently [391]. Its rotational spectrum has been studied, and it is currently under investigation. Propionamide, with $R = C_2H_5$, has not yet been detected in space even though some information on its microwave spectrum is available.

Acid cyanides, RC(O)CN, have also been studied. The two simplest ones, formyl and acetyl cyanide, have been studied extensively [392, 393]. Thus far, only the lightest formyl cyanide has been detected by radio astronomy [394].

Amino acids contain a COOH group as well as an NH_2 group. The ones with both groups attached to the same C atom are called α-*amino acids*, those in which they are attached to adjacent C atoms are called β-*amino acids*, and so on. α-Amino acids are most important for life as it occurs on Earth. Glycine (H_2N-CH_2-COOH) is the simplest one. The quest for its detection in space has been summarized briefly in Section 2.4.3. Many other amino acids have been characterized, mostly by FTMW spectroscopy, but several have also been studied in the millimeter region, including glycine and alanine.

Aminoacetonitrile (H_2N-CH_2-CN, Figure 2.30b) is viewed as a potential precursor to glycine in space, since its hydrolysis leads to the amino acid. As

mentioned above, aminoacetonitrile has been detected in space [317]. Rotational spectra of several other acetonitrile derivatives have been reported; in these, one of the H atoms was replaced by groups other than NH_2. These include OH, CH_3O, and CH_2OH; none of these has been observed by radio astronomical means. Aminopropionitrile resembles aminoacetonitrile most, but this may not necessarily mean it has greater chances of detection. Recently, a report on 2-aminopropionitrile appeared [395]; 3-aminopropionitrile has been under investigation. Interestingly, cyanomethanimine has been detected in space, albeit in the cold envelope of Sagittarius B2(N) [396].

Besides ethanediol, which has been dealt with in Section 2.4.5.4, also glycolaldehyde (HOH_2CCHO) has been detected in space. Its rotational spectrum has been characterized extensively [397], even for excited vibrational states. It has been under thorough investigation, including its minor isotopologs [398]. Until quite recently, it was detected only in galactic center sources with fairly low rotational temperatures. However, recently it was detected with ALMA in a molecular cloud surrounding a solar-type protostar with rotational temperature possibly reaching 300 K [399]. Rotational spectra of other related molecules, such as glycolic acid (HOH_2CCOOH) and glyoxilic acid (CHOCOOH), have been studied also, but have not yet been detected in space. Ethanedial, also known as *glyoxal*, $(CHO)_2$, and *oxalic acid*, $(COOH)_2$, will probably not be detected in space by radio astronomical means since the *trans*-conformers are very much lower in energy than the *cis*-conformers, but the former do not possess a pure rotational spectrum. Rotational spectra for the higher lying *cis*-conformers have been recorded.

Thus far, none of the molecules mentioned contained a double or even triple bond between two carbon atoms. Among the complex molecules detected in space, such molecules are much rarer. Among these, vinyl cyanide (C_2H_3CN) is the most important one. Its ^{13}C isotopologs have been detected in space [318] as well as transitions of some low-lying vibrational states of the main isotopolog. The molecule is under investigation [305, 400]. Several isomers exist with the formula C_3H_5CN; among them, there are three butenenitrile isomers known, namely 2-, 3, and *iso*-butenenitrile. Rotational spectra have been recorded for all existing conformers, but none has been detected in space thus far.

Alcohols derived from unsaturated hydrocarbons are energetically disfavored compared to their tautomers or related isomers. For example, vinyl alcohol, also known as *ethenol*, $H_2C{=}CHOH$, is the tautomer of acetaldehyde, also known as *ethanal*, CH_3CHO. While the latter is rather common in space, there has been only one publication on the purported detection of vinyl alcohol [401]. The detection should be viewed with caution because only very few fairly weak transitions were detected, of which some may be overlapped by transitions of other species. Other vinyl derivatives have not been detected, though rotational spectra are known for several species, including, for example, vinylamine.

Methanimine (H_2CNH) is an important molecule in space [402] (and references therein), which has been characterized well [403]. Ethanimine, an isomer of vinylamine [404], was detected by radio astronomy very recently [405].

Among the aldehydes with three carbon atoms, not only the saturated propanal has been detected in Sgr B2(N) but apparently also the less saturated species propenal and propynal.

Ketene (H_2C_2O) is quite abundant in various sources, but none of the related molecules with longer carbon chains has been detected. However, recently there was a report on the detection of ketenimine [406].

Only a few cyclic complex molecules have been detected by radio astronomical means thus far. Ethylene oxide is one of them [407]. Aziridine, in which the O atom of the former molecule has been replaced by the isoelectronic NH group, has not yet been detected.

References

1. Jenniskens, P. and Désert, F.X. (1994) *Astron. Astrophys. Suppl. Ser.*, **106**, 39–78.
2. Snow, T.P. and McCall, B.J. (2006) *Annu. Rev. Astron. Astrophys.*, **44**, 367.
3. Herbig, G.H. (1995) *Annu. Rev. Astrophys.*, **33**, 19.
4. Hobbs, L.M., York, D.G., Snow, T.P. *et al.* (2008) *Astrophys. J.*, **680**, 1256.
5. Snow, T.P. and Witt, A.N. (1995) *Science*, **270**, 1455.
6. Jochnowitz, E.B. and Maier, J.P. (2008) *Annu. Rev. Phys. Chem.*, **59**, 519.
7. Maier, J.P., Lakin, N.M., Walker, G.A.H., and Bohlender, D.A. (2001) *Astrophys. J.*, **553**, 267.
8. Maier, J.P., Walker, G.A.H., Bohlender, D.A. *et al.* (2010) *Astrophys. J.*, **726**, 41.
9. Motylewski, T., Linnartz, H., Vaizert, O. *et al.* (2000) *Astrophys. J.*, **531**, 312.
10. Freivogel, P., Fulara, J., Lessen, D., Forney, D., and Maier, J.P. (1994) *Chem. Phys.*, **189**, 335.
11. Güthe, F., Ding, H.B., Pino, T., and Maier, J.P. (2001) *Chem. Phys.*, **269**, 347.
12. Tulej, M., Kirkwood, D.A., Maccaferri, G., Dopfer, O., and Maier, J.P. (1998) *Chem. Phys.*, **228**, 293.
13. Davis, S., Anderson, D.T., Duxbury, G., and Nesbitt, D.J. (1997) *J. Chem. Phys.*, **107**, 5661.
14. Gerlich, D. (1992) *Adv. Chem. Phys.*, **82**, 1.
15. Dzhonson, A., Gerlich, D., Bieske, E.J., and Maier, J.P. (2006) *J. Mol. Struct.*, **795**, 93.
16. Rudnev, V., Rice, C.A., and Maier, J.P. (2008) *J. Chem. Phys.*, **129**, 134315.
17. Motylewski, T. and Linnartz, H. (1999) *Rev. Sci. Instrum.*, **70**, 1305.
18. Tulej, M., Meisinger, M., Knopp, G. *et al.* (2007) *J. Raman Spectrosc.*, **38**, 1022.
19. Prior, Y. (1980) *Appl. Opt.*, **19**, 1741.
20. Ashfold, M.N.R., Chandler, D.W., Hayden, C.C., McKay, R.I., and Heck, A.J.R. (1995) *Chem. Phys.*, **201**, 237.
21. Chauhan, R., Mazzotti, F.J., Raghunandan, R. *et al.* (2010) *J. Phys. Chem. A*, **114**, 3329.
22. Starikovskaia, S.M. (2006) *J. Phys. D: Appl. Phys.*, **39**, R265.
23. McCarthy, M.C., Gottlieb, C.A., Gupta, H., and Thaddeus, P. (2006) *Astrophys. J.*, **652**, L141.
24. Brünken, S., Gupta, H., Gottlieb, C.A., McCarthy, M.C., and Thaddeus, P. (2007) *Astrophys. J.*, **664**, L43.
25. Homann, K.H. (1998) *Angew. Chem. Int. Ed.*, **37**, 2434.
26. Tielens, A.G.G.M. and Snow, T.P. (1995) *The Diffuse Interstellar Bands*, Kluwer Academic Publishers, Dordrecht.
27. Dzhonson, A., Jochnowitz, E.B., and Maier, J.P. (2007) *J. Phys. Chem. A*, **111**, 1887.
28. Cias, P., Vaizert, O., Denisov, A. *et al.* (2002) *J. Phys. Chem. A*, **106**, 9890.
29. Lecoultre, J., Maier, J.P., and Rösslein, M. (1988) *J. Chem. Phys.*, **89**, 6081.
30. Klapstein, D., Kuhn, R., Maier, J.P., Ochsner, M., and Zambach, W. (1984) *J. Phys. Chem.*, **88**, 5176.

31. Sinclair, W.E., Pfluger, D., Linnartz, H., and Maier, J.P. (1999) *J. Chem. Phys.*, **110**, 296.
32. Pfluger, D., Motylewski, T., Linnartz, H., Sinclair, W.E., and Maier, J.P. (2000) *Chem. Phys. Lett.*, **329**, 29.
33. Pfluger, D., Sinclair, W.E., Linnartz, H., and Maier, J.P. (1999) *Chem. Phys. Lett.*, **313**, 171.
34. Rice, C.A., Rudnev, V., Dietsche, R., and Maier, J.P. (2010) *Astron. J.*, **140**, 203.
35. McCarthy, M.C., Travers, M.J., Kovacs, A., Gottlieb, C.A., and Thaddeus, P. (1997) *Astrophys. J. Suppl. Ser.*, **113**, 105.
36. Shindo, F., Benilan, Y., Guillemin, J.C. *et al.* (2003) *Planet. Space Sci.*, **51**, 9.
37. Turner, B.E., Herbst, E., and Terzieva, R. (2000) *Astrophys. J. Suppl. Ser.*, **126**, 427.
38. Dzhonson, A., Jochnowitz, E.B., Kim, E., and Maier, J.P. (2007) *J. Chem. Phys.*, **126**, 044301.
39. Arnold, D.W. (1991) *J. Chem. Phys.*, **95**, 8753.
40. Tulej, M., Kirkwood, D.A., Pachkov, M., and Maier, J.P. (1998) *Astrophys. J.*, **506**, L69.
41. McCall, B.J., York, D.G., and Oka, T. (2000) *Astrophys. J.*, **531**, 329.
42. McCall, B.J., Thorburn, J., Hobbs, L.M., Oka, T., and York, D.G. (2001) *Astrophys. J.*, **559**, L49.)
43. Güthe, F., Tulej, M., Pachkov, M.V., and Maier, J.P. (2001) *Astrophys. J.*, **555**, 466.
44. McCall, B.J., Oka, T., Thorburn, J., Hobbs, L.M., and York, D.G. (2002) *Astrophys. J.*, **567**, L145.
45. Boguslavskiy, A.E., Ding, H., and Maier, J.P. (2005) *J. Chem. Phys.*, **123**, 034305.
46. Sarre, P.J., Miles, J.R., Kerr, T.H. *et al.* (1995) *Mon. Not. R. Astron. Soc.*, **277**, L41.
47. Maier, J.P., Boguslavskiy, A.E., Ding, H., Walker, G.A.H., and Bohlender, D.A. (2006) *Astrophys. J.*, **640**, 369.
48. Wootten, A., Bozyan, E.P., Garrett, D.B., Loren, R.B., and Snell, R.L. (1980) *Astrophys. J.*, **239**, 844.
49. Thaddeus, P., Gottlieb, C.A., Hjalmarson, A.A. *et al.* (1985) *Astrophys. J.*, **294**, L49.
50. Tenenbaum, E.D., Milan, S.N., Woolf, N.J., and Ziurys, L.M. (2009) *Astrophys. J.*, **704**, L108.
51. Ziurys, L.M., Apponi, A.J., Guelin, M., and Cernicharo, J. (1995) *Astrophys. J.*, **445**, L47.
52. Linnartz, H., Vaizert, O., Motylewski, T., and Maier, J.P. (2000) *J. Chem. Phys.*, **112**, 9777.
53. Motylewski, T., Vaizert, O., Giesen, T.F., Linnartz, H., and Maier, J.P. (1999) *J. Chem. Phys.*, **111**, 6161.
54. Boguslavskiy, A.E. and Maier, J.P. (2006) *J. Chem. Phys.*, **125**, 094308.
55. Zhao, Y.X., de Beer, E., and Neumark, D.M. (1996) *J. Chem. Phys.*, **105**, 2575.
56. Zhao, Y.X., de Beer, E., Xu, C.S., Taylor, T., and Neumark, D.M. (1996) *J. Chem. Phys.*, **105**, 4905.
57. Ohara, M., Kasuya, D., Shiromaru, H., and Achiba, Y. (2000) *J. Phys. Chem. A*, **104**, 8622.
58. Maier, J.P. and Rosslein, M. (1988) *J. Chem. Phys.*, **88**, 4614.
59. Linnartz, H., Motylewski, T., Vaizert, O. *et al.* (1999) *J. Mol. Spectrosc.*, **197**, 1.
60. Linnartz, H., Motylewski, T., and Maier, J.P. (1998) *J. Chem. Phys.*, **109**, 3819.
61. Ding, H., Pino, T., Güthe, F., and Maier, J.P. (2002) *J. Chem. Phys.*, **117**, 8362.
62. Ding, H., Pino, T., Güthe, F., and Maier, J.P. (2001) *J. Chem. Phys.*, **115**, 6913.
63. Raghunandan, R., Mazotti, F.J., and Maier, J.P. (2010) *J. Am. Soc. Mass Spectrom.*, **21**, 694.
64. Kirkwood, D.A., Tulej, M., Pachkov, M.V. *et al.* (1999) *J. Chem. Phys.*, **111**, 9280.
65. Tulej, M., Güthe, F., Schnaiter, M. *et al.* (1999) *J. Phys. Chem. A*, **103**, 9712.
66. Pachkov, M.V., Pino, T., Tulej, M., and Maier, J.P. (2001) *Mol. Phys.*, **99**, 1397.
67. Ball, C.D., McCarthy, M.C., and Thaddeus, P. (2000) *J. Chem. Phys.*, **112**, 10149.

68. Ding, H., Schmidt, T.W., Pino, T. *et al.* (2003) *J. Chem. Phys.*, **119**, 814.
69. Kim, E., Araki, M., Chauhan, R., Birza, P., and Maier, J.P. (2006) *Mol. Phys.*, **104**, 2885.
70. Vaizert, O., Motylewski, T., Wyss, M. *et al.* (2001) *J. Chem. Phys.*, **114**, 7918.
71. Sinclair, W.E., Pfluger, D., and Maier, J.P. (1999) *J. Chem. Phys.*, **111**, 9600.
72. Sinclair, W.E., Pfluger, D., Verdes, D., and Maier, J.P. (2000) *J. Chem. Phys.*, **112**, 8899.
73. Linnartz, H., Vaizert, O., Cias, P., Gruter, L., and Maier, J.P. (2001) *Chem. Phys. Lett.*, **345**, 89.
74. Rice, C.A., Rudnev, V., Chakrabarty, S., and Maier, J.P. (2010) *J. Phys. Chem. A*, **114**, 1684.
75. Linnartz, H., Pfluger, D., Vaizert, O. *et al.* (2002) *J. Chem. Phys.*, **116**, 924.
76. Kohguchi, H., Ohshima, Y., and Endo, Y. (1996) *Chem. Phys. Lett.*, **254**, 397.
77. Nakajima, M., Sumiyoshi, Y., and Endo, Y. (2002) *Chem. Phys. Lett.*, **351**, 359.
78. Nakajima, M., Sumiyoshi, Y., and Endo, Y. (2002) *Chem. Phys. Lett.*, **355**, 116.
79. Denisov, A., Schmidt, T.W., Boguslavskiy, A.E. *et al.* (2004) *Int. J. Mass Spectrom.*, **233**, 131.
80. Boguslavskiy, A.E. and Maier, J.P. (2007) *Phys. Chem. Chem. Phys.*, **9**, 127.
81. Tokaryk, D.W., Adam, A.G., and Hopkins, W.S. (2005) *J. Mol. Spectrosc.*, **230**, 54.
82. Ding, H., Apetrei, C., Chacaga, L., and Maier, J.P. (2008) *Astrophys. J.*, **627**, 348.
83. Chasovskikh, E., Jochnowitz, E.B., and Maier, J.P. (2008) *J. Phys. Chem. A*, **112**, 8686.
84. Li, M.G. and Coxon, J.A. (1996) *J. Mol. Spectrosc.*, **176**, 206.
85. Dick, M.J., Sheridan, P.M., Wang, J.G., and Bernath, P.F. (2005) *J. Mol. Spectrosc.*, **233**, 197.
86. Apetrei, C., Ding, H., and Maier, J.P. (2007) *Phys. Chem. Chem. Phys.*, **9**, 3897.
87. Chasovskikh, E., Jochnowitz, E., Kim, E.B., Navizet, I., and Maier, J.P. (2007) *J. Phys. Chem. A*, **111**, 11986.
88. Apetrei, C., Knight, A.E.W., Chasovskikh, E. *et al.* (2009) *J. Chem. Phys.*, **131**, 064305.
89. Petrie, S., Kagi, E., and Kawaguchi, K. (2003) *Mon. Not. R. Astron. Soc.*, **343**, 209.
90. Kawaguchi, K., Kagi, E., Hirano, T., Takano, S., and Saito, S. (1993) *Astrophys. J.*, **406**, L39.
91. Ziurys, L.M., Savage, C., Highberger, J.L. *et al.* (2002) *Astrophys. J.*, **564**, L45.
92. Cernicharo, J. and Guelin, M. (1987) *Astron. Astrophys.*, **183**, L10.
93. Ziurys, L.M., Apponi, A.J., and Philips, T.G. (1994) *Astrophys. J.*, **433**, 729.
94. Chertihin, G.V., Andrews, L., and Taylor, P.R. (1994) *J. Am. Chem. Soc.*, **116**, 3513.
95. Boldyrev, A.I., Simons, J., Li, X., and Wang, L.S. (1999) *J. Am. Chem. Soc.*, **121**, 10193.
96. Léger, A. and d'Hendecourt, L. (1985) *Astron. Astrophys.*, **146**, 81–85.
97. Van der Zwet, G.P. and Allamandola, L.J. (1985) *Astron. Astrophys.*, **146**, 76–80.
98. Leger, A. and Puget, J.L. (1984) *Astron. Astrophys.*, **137**, L5–L8.
99. Allamandola, L.J., Tielens, A.G.G.M., and Barker, J.R. (1985) *Astrophys. J.*, **290**, L25–L28.
100. Draine, B.T. and Li, A. (2007) *Astrophys. J.*, **657**, 810–837.
101. Tielens, A.G.G.M. (2008) *Annu. Rev. Astron. Astrophys.*, **46**, 289–337.
102. Léger, A., d'Hendecourt, L., and Défourneau, D. (1989) *Astron. Astrophys.*, **216**, 148–164.
103. Rhee, Y.M., Lee, T.J., Gudipati, M.S., Allamandola, L.J., and Head-Gordon, M. (2007) *Proc. Natl. Acad. Sci. U.S.A.*, **104**, 5274–5278.
104. Vijh, U.P., Witt, A.N., and Gordon, K.D. (2005) *Astrophys. J.*, **619**, 368–378.
105. Beegle, L.W., Wdowiak, T.J., Robinson, M.S. *et al.* (1997) *Astrophys. J.*, **487**, 976–982.
106. Salama, F., Galazutdinov, G.A., Krełowski, J., Allamandola, L.J., and Musaev, F.A. (1999) *Astrophys. J.*, **526**, 265–273.

107. Ruiterkamp, R., Halasinski, T., Salama, F. *et al.* (2002) *Astron. Astrophys.*, **390**, 1153–1170.

108. Salama, F. (2008) *Proc. Int. Astron. Union*, **4**, 357–366.

109. O'Keefe, A. and Deacon, D.A.G. (1988) *Rev. Sci. Instrum.*, **59**, 2544–2551.

110. Romanini, D., Biennier, L., Salama, F. *et al.* (1999) *Chem. Phys. Lett.*, **303**, 165–170.

111. Ruth, A.A., Kim, E.K., and Hese, A. (1999) *Phys. Chem. Chem. Phys.*, **1**, 5121–5128.

112. Beck, S.M., Powers, D.E., Hopkins, J.B., and Smalley, R.E. (1980) *J. Chem. Phys.*, **73**, 2019–2028.

113. Lawrance, W.D. and Knight, A.E.W. (1990) *J. Phys. Chem.*, **94**, 1249–1267.

114. Fujii, M., Ebata, T., Mikami, N., and Ito, M. (1983) *Chem. Phys.*, **77**, 191–200.

115. Baba, M., Saitoh, M., Kowaka, Y. *et al.* (2009) *J. Chem. Phys.*, **131**, 224 318/1–224 318/10.

116. Dick, B., Zinghar, E., and Haas, Y. (1991) *Chem. Phys. Lett.*, **187**, 571–578.

117. Kokkin, D.L., Reilly, N.J., Troy, T.P., Nauta, K., and Schmidt, T.W. (2007) *J. Chem. Phys.*, **126**, 084 304/1–084 304/7.

118. Wick, M.T., Nickel, B., and Ruth, A.A. (1993) *Chem. Phys. Lett.*, **215**, 243–250.

119. Yu, H., Joslin, E., and Phillips, D. (1993) *Chem. Phys. Lett.*, **203**, 515–522.

120. Greenblatt, G.D., Nissani, E., Zaroura, E., and Haas, Y. (1987) *J. Phys. Chem.*, **91**, 570–574.

121. Tan, X. and Salama, F. (2005) *J. Chem. Phys.*, **123**, 014 312/1–014 312/7.

122. Amirav, A., Even, U., and Jortner, J. (1980) *Chem. Phys. Lett.*, **72**, 21–24.

123. Bermudez, G. and Chan, I.Y. (1986) *J. Phys. Chem.*, **90**, 5029–5034.

124. Babbitt, R.J., Ho, C.J., and Topp, M.R. (1988) *J. Phys. Chem.*, **92**, 2422–2429.

125. Hoheisel, G. and Hese, A. (2006) *J. Mol. Spectrosc.*, **235**, 211–217.

126. Amirav, A., Even, U., and Jortner, J. (1981) *J. Chem. Phys.*, **74**, 3745–3756.

127. Kokkin, D.L., Troy, T.P., Nakajima, M. *et al.* (2008) *Astrophys. J.*, **681**, L49–L51.

128. Rouillé, G., Arold, M., Staicu, A., Henning, T., and Huisken, F. (2009) *J. Phys. Chem. A*, **113**, 8187–8194.

129. Staicu, A., Sukhorukov, O., Rouillé, G., Henning, T., and Huisken, F. (2004) *Mol. Phys.*, **102**, 1777–1783.

130. Sukhorukov, O., Staicu, A., Diegel, E. *et al.* (2004) *Chem. Phys. Lett.*, **386**, 259–264.

131. Rouillé, G., Arold, M., Staicu, A. *et al.* (2007) *J. Chem. Phys.*, **126**, 174 311/1–174 311/11.

132. Scherer, J.J., Paul, J.B., O'Keefe, A., and Saykally, R.J. (1997) *Chem. Rev.*, **97**, 25–51.

133. Biennier, L., Salama, F., Gupta, M., and O'Keefe, A. (2004) *Chem. Phys. Lett.*, **387**, 287–294.

134. Fiedler, S.E., Hoheisel, G., Ruth, A.A., and Hese, A. (2003) *Chem. Phys. Lett.*, **382**, 447–453.

135. Rouillé, G., Jäger, C., Steglich, M. *et al.* (2008) *ChemPhysChem*, **9**, 2085–2091.

136. Rouillé, G., Steglich, M., Huisken, F., Henning, T., and Müllen, K. (2009) *J. Chem. Phys.*, **131**, 204 311/1–204 311/7.

137. Steglich, M., Jäger, C., Rouillé, G. *et al.* (2010) *Astrophys. J.*, **712**, L16–L20.

138. Gredel, R., Carpentier, Y., Rouillé, G. *et al.* (2011) *Astron. Astrophys.*, **530**, 1–15.

139. Draine, B.T. and Li, A. (2001) *Astrophys. J.*, **551**, 807–824.

140. Karcher, W., Fordham, R.J., Dubois, J.J., Glaude, P.G.J.M., and Ligthart, J.A.M. (1985) *Spectral Atlas of Polycyclic Aromatic Compounds*, Vol. 1, D. Reidel Publishing Company, Dordrecht.

141. Ehrenfreund, P., d'Hendecourt, L., Verstraete, L. *et al.* (1992) *Astron. Astrophys.*, **259**, 257–264.

142. London, F. (1937) *Trans. Faraday Soc.*, **33**, 8–26.

143. Radzig, A.A. and Smirnov, B.M. (1985) *Reference Data on Atoms, Molecules, and Ions, Springer Series in Chemical Physics 31*, Springer-Verlag, Berlin, Heidelberg.

144. Staicu, A., Rouillé, G., Scholz, R. *et al.* (2008) *J. Chem. Phys.*, **129**, 074 302/1–074 302/10.
145. Huisken, F., Rouillé, G., Carpentier, Y., Steglich, M., and Henning, T. (2011) Proceedings of the 27th International Symposium on Rarified Gas Dynamics, Vol. 1333, pp. 819–824.
146. Rouillé, G., Krasnokutski, S., Huisken, F. *et al.* (2004) *J. Chem. Phys.*, **120**, 6028–6034.
147. Salama, F., Galazutdinov, G.A., Krełowski, J. *et al.* (2011) *Astrophys. J.*, **728**, 1–8.
148. Mulliken, R.S. (1939) *J. Chem. Phys.*, **7**, 14–20.
149. Hobbs, L.M., York, D.G., Thorburn, J.A. *et al.* (2009) *Astrophys. J.*, **705**, 32–45.
150. Chako, N.Q. (1934) *J. Chem. Phys.*, **2**, 644–653.
151. Oja, V. and Suuberg, E.M. (1998) *J. Chem. Eng. Data*, **43**, 486–492.
152. Murray, J.J., Pottie, R.F., and Pupp, C. (1974) *Can. J. Chem.*, **52**, 557–563.
153. Rouillé, G., Steglich, M., Jäger, C. *et al.* (2011) *Chem. Phys. Chem.*, **12**, 2131–2137.
154. Jäger, C., Huisken, F., Mutschke, H. *et al.* (2007) *Carbon*, **45**, 2981–2994.
155. Jäger, C., Mutschke, H., Huisken, F. *et al.* (2006) *Astrophys. J. Suppl.*, **166**, 557–566.
156. Compiegne, M., Verstraete, L., Jones, A. *et al.* (2010) *Astron. Astrophys.*, **525**, (A103).
157. Peeters, E., Hony, S., Van Kerckhoven, C. *et al.* (2002) *Astron. Astrophys.*, **390**, 1089–1113.
158. Sellgren, K. (1984) *Astrophys. J.*, **277**, 623–633.
159. Barker, J.R., Allamandola, L.J., Tielens, A.G.G.M. (1987) *Astrophys. J.*, **315**, L61–L65.
160. Cook, D.J., Schlemmer, S., Balucani, N. *et al.* (1998) *J. Phys. Chem. A*, **102**, 1465–1481.
161. Pech, C., Joblin, C., and Boissel, P. (2002) *Astron. Astrophys.*, **388**, 639–651.
162. Désert, F.X., Boulanger, F., and Puget, J.L. (1990) *Astron. Astrophys.*, **237**, 215–236.
163. Hudgins, D.M. and Allamandola, L.J. (1999) *Astrophys. J.*, **516**, L41–L44.
164. Pauzat, F., Talbi, D., Miller, M.D., DeFrees, D.J., and Ellinger, Y. (1992) *J. Phys. Chem.*, **96**, 7882–7886.
165. Allamandola, L.J., Hudgins, D.M., and Sandford, S.A. (1999) *Astrophys. J.*, **511**, L115–L119.
166. Galliano, F., Madden, S.C., Tielens, A.G.G.M., Peeters, E., and Jones, A.P. (2008) *Astrophys. J.*, **679**, 310–345.
167. Uchida, K.I., Sellgren, K., Werner, M.W., and Houdashelt, M.L. (2000) *Astrophys. J.*, **530**, 817–833.
168. Micelotta, E., Jones, A.P., and Tielens, A.G.G.M. (2010) *Astron. Astrophys.*, **510**, A36.
169. Micelotta, E., Jones, A.P., and Tielens, A.G.G.M. (2010) *Astron. Astrophys.*, **510**, A37.
170. Micelotta, E., Jones, A.P., and Tielens, A.G.G.M. (2010) *Astron. Astrophys.*, **526**, (A52).
171. Rapacioli, M., Joblin, C., and Boissel, P. (2005) *Astron. Astrophys.*, **429**, 193–204.
172. Berné, O., Joblin, C., Deville, Y. et al. (2007) *Astron. Astrophys.*, **469**, 575–586.
173. Marty, P., de Parseval, P., Klotz, A., Serra, G., and Boissel, P. (1996) *Astron. Astrophys.*, **316**, 270–274.
174. Becker, E.D. and Pimentel, G.C. (1956) *J. Chem. Phys.*, **25**, 224–228.
175. Frei, H. and Pimentel, G.C. (1985) *Annu. Rev. Phys. Chem.*, **36**, 491–524.
176. Joblin, C., D'Hendecourt, L., Leger, A., and Defourneau, D. (1994) *Astron. Astrophys.*, **281**, 923–936.
177. Joblin, C., Boissel, P., Leger, A., D'Hendecourt, L., and Defourneau, D. (1995) *Astron. Astrophys.*, **299**, 835–846.
178. Allamandola, A.G.G.M., Tielens, L.J., and Barker, J.R. (1989) *Astrophys. J. Suppl. Ser.*, **71**, 733–775.
179. Bakes, E.L.O., Tielens, A.G.G.M., Bauschlicher, C.W., Hudgins, D.M., and Allamandola, L.J. (2001) *Astrophys. J.*, **560**, 261–271.
180. Levy, D.H. (1980) *Annu. Rev. Phys. Chem.*, **31**, 197–225.
181. Piest, J.A., Oomens, J., Bakker, J., von Helden, G., and Meijer, G.

(2001) *Spectrochim. Acta, Part A*, **57**, 717–735.
182. Shan, J., Suton, M., and Lee, L.C. (1991) *Astrophys. J.*, **383**, 459–465.
183. Williams, R.M. and Leone, S.R. (1995) *Astrophys. J.*, **443**, 675–681.
184. Schlemmer, S., Cook, D.J., Harrison, J.A. *et al.* (1994) *Science*, **265**, 1686–1689.
185. Wagner, D.R., Kim, H.S., and Saykally, R.J. (2000) *Astrophys. J.*, **545**, 854–560.
186. Szczepanski, J., Roser, D., Personette, W. *et al.* (1992) *J. Phys. Chem.*, **96**, 7876–7881.
187. Oomens, J., van Roij, A.J.A., Meijer, G., and von Helden, G. (2000) *Astrophys. J.*, **542**, 404–410.
188. Kim, H.S. and Saykally, R.J. (2003) *Rev. Sci. Instrum.*, **74**, 2488–2494.
189. Fulara, J., Jakobi, M., and Maier, J.P. (1993) *Chem. Phys. Lett.*, **206**, 203–209.
190. Fulara, J., Jakobi, M., and Maier, J.P. (1993) *Chem. Phys. Lett.*, **211**, 227–234.
191. Szczepanski, J. and Vala, M. (1993) *Astrophys. J.*, **414**, 646–655.
192. Hudgins, D.M., Sandford, S.A., and Allamandola, L.J. (1994) *J. Phys. Chem.*, **98**, 4243–4253.
193. Hudgins, D.M. and Allamandola, L.J. (1995) *J. Phys. Chem.*, **99**, 3033–3046.
194. Hudgins, D.M. and Allamandola, L.J. (1995) *J. Phys. Chem.*, **99**, 8978–8986.
195. Bauschlicher, C.W., Boersma, C., Ricca, A. *et al.* (2010) *Astrophys. J. Suppl. Ser.*, **189**, 341–351.
196. Szczepanski, J. and Vala, M. (1993) *Nature*, **363**, 699–701.
197. Duncan, M.A. (2000) *Int. J. Mass Spectrom.*, **200**, 545–569.
198. O'Shea, P.G. and Freund, H.P. (2001) *Science*, **292**, 1853–1858.
199. Bosenberg, W.R. and Guyer, D.R. (1993) *J. Opt. Soc. Am. B*, **10**, 1716–1722.
200. Okumura, M., Yeh, L.I., and Lee, Y.T. (1985) *J. Chem. Phys.*, **83**, 3705–3706.
201. Okumura, M., Yeh, L.I., Myers, J.D., and Lee, Y.T. (1990) *J. Phys. Chem.*, **94**, 3416–3427.
202. Oepts, D., van der Meer, A.F.G., and van Amersfoort, P.W. (1995) *Infrared Phys. Technol.*, **36**, 297–308.
203. Satink, R.G., Piest, H., von Helden, G., and Meijer, G. (1999) *J. Chem. Phys.*, **111**, 10750–10753.
204. Piest, H., von Helden, G., and Meijer, G. (1999) *Astrophys. J.*, **520**, L75–L78.
205. Bakker, J.M., Satink, R.G., von Helden, G., and Meijer, G. (2002) *Phys. Chem. Chem. Phys.*, **4**, 24–33.
206. Pino, T., Boudin, N., and Bréchignac, P. (1999) *J. Chem. Phys.*, **111**, 7337–7347.
207. Solca, N. and Dopfer, O. (2002) *Angew. Chem. Int. Ed.*, **41**, 3628–3631.
208. Douberly, G.E., Ricks, A.M., Schleyer, Pv.R., and Duncan, M.A. (2008) *J. Phys. Chem. A*, **112**, 4869–4874.
209. Ricks, A.M., Douberly, G.E., and Duncan, M.A. (2009) *Astrophys. J.*, **702**, 301–306.
210. Eyler, J.R. (2009) *Mass Spectrom. Rev.*, **28**, 448–467.
211. Oomens, J., Tielens, A.G.G.M., Sartakov, B.G., von Helden, G., and Meijer, G. (2003) *Astrophys. J.*, **591**, 968–985.
212. Oomens, J., Sartakov, B.G., Meijer, G., and von Helden, G. (2006) *Int. J. Mass Spectrom.*, **254**, 1–19.
213. Black, J.G., Yablonovitch, E., Bloembergen, N., and Mukamel, S. (1977) *Phys. Rev. Lett.*, **38**, 1131–1134.
214. Grant, E.R., Schulz, P.A., Sudbo, A.S., Shen, Y.R., and Lee, Y.T. (1978) *Phys. Rev. Lett.*, **40**, 115–118.
215. Kim, H.S., Wagner, D.R., and Saykally, R.J. (2001) *Phys. Rev. Lett.*, **86**, 5691–5694.
216. Kim, H. and Saykally, R. (2002) *Astrophys. J. Suppl. Ser.*, **143**, 455–467.
217. Bauschlicher, C.W., Hudgins, D.M., and Allamandola, L.J. (1999) *Theor. Chem. Acc.*, **103**, 154–162.
218. Hudgins, D.M., Bauschlicher, C.W., Allamandola, L.J., and Fetzer, J.C. (2000) *J. Phys. Chem. A*, **104**, 3655–3669.
219. Bauschlicher, C.W., Langhoff, S.R., Sandford, S.A., and Hudgins, D.M. (1997) *J. Phys. Chem. A*, **103**, 2414–2422.

220. Langhoff, S.R., Bauschlicher, C.W., Hudgins, D.M., Sandford, S.A., and Allamandola, L.J. (1998) *J. Phys. Chem. A*, **102**, 1632–1646.
221. Malloci, G., Joblin, C., and Mulas, G. (2007) *Chem. Phys.*, **332**, 353–359.
222. Bauschlicher, C.W., Peeters, E., and Allamandola, L.J. (2008) *Astrophys. J.*, **678**, 316–327.
223. Cami, J., van Malderen, R., and Markwick, A.J. (2010) *Astrophys. J. Suppl. Ser.*, **187**, 409–415.
224. Miani, A., Cane, E., Palmieri, P., Trombetti, A., and Handy, N.C. (2000) *J. Chem. Phys.*, **112**, 248–259.
225. Pirali, O., Vervloet, M., Mulas, G., Malloci, G., and Joblin, C. (2009) *Phys. Chem. Chem. Phys.*, **11**, 3443–3454.
226. Cook, D.J. and Saykally, R. (1998) *Astrophys. J.*, **493**, 793–802.
227. Van-Oanh, N.T., Parneix, P., and Brechignac, P. (2002) *J. Phys. Chem. A*, **106**, 10144–10151.
228. Mulas, G., Malloci, G., Joblin, C., and Toublanc, D. (2006) *Astron. Astrophys.*, **460**, 93–104.
229. Basire, M., Parneix, P., Calvo, F., Pino, T., and Brechignac, P. (2009) *J. Phys. Chem. A*, **113**, 6947–6954.
230. Lorenz, U.J., Solca, N., Lemaire, J., Maitre, P., and Dopfer, O. (2007) *Angew. Chem. Int. Ed.*, **46**, 6714–6716.
231. Knorke, H., Langer, J., Oomens, J., and Dopfer, O. (2009) *Astrophys. J.*, **706**, L66–L70.
232. Vala, M., Szczepanski, J., Dunbar, R., Oomens, J., and Jeffrey, J.D. (2009) *Chem. Phys. Lett.*, **473**, 43–48.
233. Alvaro Galué, H., Pirali, O., and Oomens, J. (2010) *Astron. Astrophys.*, **517**, A15.
234. Szczepanski, J., Wang, H., Vala, M. *et al.* (2006) *Astrophys. J.*, **646**, 666–680.
235. Simon, A., Joblin, C., Polfer, N., and Oomens, J. (2008) *J. Phys. Chem. A*, **112**, 8551–8560.
236. Oomens, J. and Morton, T.H. (2010) *Eur. J. Mass Spectrom.*, **16**, 313–319.
237. Moutou, C., Léger, A., and d'Hendecourt, L. (1996) *Astron. Astrophys.*, **310**, 297–308.
238. Mattioda, A.L., Ricca, A., Tucker, J., Bauschlicher, C.W. Jr., and Allamandola, L.J. (2009) *Astron. J.*, **137**, 4054–4060.
239. Zhang, K., Guo, B., Colarusso, P., and Bernath, P.F. (1996) *Science*, **274**, 582–583.
240. Pirali, O., Van-Oanh, N.T., Parneix, P., Vervloet, M., and Brechignac, P. (2006) *Phys. Chem. Chem. Phys.*, **8**, 3707–3714.
241. Boersma, C., Bauschlicher, C.W., Ricca, A. *et al.* (2011) *Astrophys. J.*, **729**, 64.
242. Kabir, M.H., Kasahara, S., Demtroder, W. *et al.* (2003) *J. Chem. Phys.*, **119**, 3691–3698.
243. Lovas, F.J., McMahon, R.J., Grabow, J.U. *et al.* (2005) *J. Am. Chem. Soc.*, **127**, 4345–4349.
244. Pilleri, P., Herberth, D., Giesen, T.F. *et al.* (2009) *Mon. Not. R. Astron. Soc.*, **397**, 1053–1060.
245. Thorwirth, S., Theule, P., Gottlieb, C.A., McCarthy, M.C., and Thaddeus, P. (2007) *Astrophys. J.*, **662**, 1309–1314.
246. McNaughton, D., Godfrey, P.D., Brown, R.D., Thorwirth, S., and Grabow, J.U. (2008) *Astrophys. J.*, **678**, 309–315.
247. Bakker, J.M., Lapoutre, V.J.F., Redlich, B. *et al.* (2010) *J. Chem. Phys.*, **132**, 074305.
248. Bakker, J.M., Redlich, B., van der Meer, A.F.G., and Oomens, J. (2011) *Astrophys. J.*, **741**, 74.
249. Zhang, X., Pitts, J.D., Nadarajah, R., and Knee, J.L. (1997) *J. Chem. Phys.*, **107**, 8239–8251.
250. Zhang, J., Pei, L.S., and Kong, W. (2008) *J. Chem. Phys.*, **128**, 104301.
251. Zhang, J., Han, F., Pei, L., Kong, W., and Li, A. (2010) *Astrophys. J.*, **715**, 485.
252. Mulas, G., Malloci, G., Joblin, C., and Toublanc, D. (2006) *Astron. Astrophys.*, **456**, 161–169.
253. Tielens, A.G.G.M. (2005) *The Physics and Chemistry of the Interstellar Medium*, Cambridge University Press, Cambridge.
254. Hudgins, D.M. and Sandford, S.A. (1998) *J. Phys. Chem. A*, **102**, 353–360.

255. Hudgins, D.M. and Sandford, S.A. (1998) *J. Phys. Chem. A*, **102**, 344–352.

256. Hudgins, D.M. and Sandford, S.A. (1998) *J. Phys. Chem. A*, **102**, 329–343.

257. Vala, M., Szczepanski, J., Pauzat, F. *et al.* (1994) *J. Phys. Chem.*, **98**, 9187–9196.

258. Szczepanski, J., Drawdy, J., Wehlburg, C., and Vala, M. (1995) *Chem. Phys. Lett.*, **245**, 539–548.

259. Szczepanski, J., Wehlburg, C., and Vala, M. (1995) *Chem. Phys. Lett.*, **232**, 221–228.

260. Hudgins, D.M. and Allamandola, L.J. (1997) *J. Phys. Chem. A*, **101**, 3472–3477.

261. Oomens, J., Sartakov, B.G., Tielens, A.G.G.M., Meijer, G., and von Helden, G. (2001) *Astrophys. J.*, **560**, L99–L103.

262. Oomens, J., Meijer, G., and von Helden, G. (2001) *J. Phys. Chem. A*, **105**, 8302–8309.

263. Szczepanski, J., Banisaukas, J., Vala, M. *et al.* (2002) *J. Phys. Chem. A*, **106**, 63–73.

264. Banisaukas, J., Szczepanski, J., Eyler, J. *et al.* (2003) *J. Phys. Chem. A*, **107**, 782–793.

265. Banisaukas, J., Szczepanski, J., Vala, M., and Hirata, S. (2004) *J. Phys. Chem. A*, **108**, 3713–3722.

266. Wang, H.Y., Szczepanski, J., Hirata, S., and Vala, M. (2005) *J. Phys. Chem. A*, **109**, 9737–9746.

267. Langhoff, S.R. (1996) *J. Phys. Chem.*, **100**, 2819–2841.

268. Hudgins, D.M. and Allamandola, L.J. (1999) *Astrophys. J.*, **513**, L69–L73.

269. Hudgins, D.M., Bauschlicher, C.W., and Allamandola, L.J. (2005) *Astrophys. J.*, **632**, 316–332.

270. Mattioda, A.L., Hudgins, D.M., Bauschlicher, C.W., Rosi, M., and Allamandola, L.J. (2003) *J. Phys. Chem. A*, **107**, 1486–1498.

271. Hudgins, D.M., Bauschlicher, C.W., and Allamandola, L.J. (2001) *Spectrochim. Acta, Part A*, **57**, 907–930.

272. Jochims, H.W., Ruhl, E., Baumgartel, H., Tobita, S., and Leach, S. (1994) *Astrophys. J.*, **420**, 307–317.

273. Ekern, S., Marshall, A., Szczepanski, J., and Vala, M. (1997) *Astrophys. J.*, **488**, L39–L41.

274. Duley, W.W. (2006) *Astrophys. J.*, **643**, L21–L24.

275. Malloci, G., Mulas, G., Cecchi-Pestellini, C., and Joblin, C. (2008) *Astron. Astrophys.*, **489**, 1183–1187.

276. Banisaukas, J., Szczepanski, J., Eyler, J., and Vala, M. (2004) *J. Phys. Chem. A*, **108**, 3723–3726.

277. Schutte, W.A., Tielens, A.G.G.M., and Allamandola, L.J. (1993) *Astrophys. J.*, **415**, 397–414.

278. Bernstein, M.P., Sandford, S.A., and Allamandola, L.J. (1996) *Astrophys. J.*, **472**, L127–L130.

279. Vala, M., Szczepanski, J., Oomens, J., and Steill, J.D. (2009) *J. Am. Chem. Soc.*, **131**, 5784–5791.

280. Klotz, A., Marty, P., Boissel, P. *et al.* (1995) *Astron. Astrophys.*, **304**, 520–530.

281. Simon, A. and Joblin, C. (2007) *J. Phys. Chem. A*, **111**, 9745–9755.

282. Joalland, B., Simon, A., Marsden, C.J., and Joblin, C. (2009) *Astron. Astrophys.*, **494**, 969–976.

283. Joblin, C., Tielens, A.G.G.M., Allamandola, L.J., and Geballe, T.R. (1996) *Astrophys. J.*, **458**, 610–620.

284. Bernstein, M.P., Elsila, J.E., Dworkin, J.P. *et al.* (2002) *Astrophys. J.*, **576**, 1115–1120.

285. Sandford, S.A., Bernstein, M.P., Allamandola, L.J., Gillette, J.S., and Zare, R.N. (2000) *Astrophys. J.*, **538**, 691–697.

286. Peeters, E., Allamandola, L.J., Bauschlicher, C.W. *et al.* (2004) *Astrophys. J.*, **604**, 252–257.

287. Foing, B.H. and Ehrenfreund, P. (1994) *Nature*, **369**, 296–298.

288. Cami, J., Bernard-Salas, J., Peeters, E., and Malek, S.E. (2010) *Science*, **329**, 1180–1182.

289. Sellgren, K., Werner, M.W., Ingalls, J.G. *et al.* (2010) *Astrophys. J.*, **722**, L54–L57.

290. Müller, H.S.P. (2011) *Molecules in Space, in: Encyclopedia of Astrobiology* eds. M. Gargaud *et al.* Springer, Berlin and Heidelberg, pp. 1080–1086.

291. Müller, H.S.P., Thorwirth, S., Roth, D.A., and Winnewisser, G. (2001) *Astron. Astrophys.*, **370**, L49.

292. Müller, H.S.P., Schlöder, F., Stutzki, J., and Winnewisser, G. (2005) *J. Mol. Struct.*, **742**, 215.

293. Winnewisser, G., Belov, S.P., Klaus, T., and Schieder, R. (1997) *J. Mol. Spectrosc.*, **184**, 468.

294. Brünken, S., Müller, H.S.P., Lewen, F., and Winnewisser, G. (2003) *Phys. Chem. Chem. Phys.*, **5**, 1515.

295. Müller, H.S.P. and Brünken, S. (2005) *J. Mol. Spectrosc.*, **232**, 213.

296. Brauer, C.S., Pearson, J.C., Drouin, B.J., and Yu, S. (2009) *Astrophys. J. Suppl. Ser.*, **184**, 133.

297. Yu, S., Pearson, J.C., Drouin, B.J. *et al.* (2003) *J. Chem. Phys.*, **133**, 174317.

298. Endres, C.P., Müller, H.S.P., Brünken, S. *et al.* (2006) *J. Mol. Struct.*, **795**, 242.

299. Christen, D. and Müller, H.S.P. (2003) *Phys. Chem. Chem. Phys.*, **5**, 3600.

300. Pickett, H.M. (1991) *J. Mol. Spectrosc.*, **149**, 371.

301. Drouin, B.J. and Müller, H.S.P. (2008) *J. Mol. Spectrosc.*, **251**, 1.

302. Pearson, J.C., Müller, H.S.P., Pickett, H.M., Cohen, E.A., and Drouin, B.J. (2010) *J. Quant. Spectrosc. Radiat. Transfer*, **111**, 1614.

303. Kleiner, I. (2010) *J. Mol. Spectrosc.*, **260**, 1.

304. Pate, B.H. and De Lucia, F.C. (2012) *J. Mol. Spectrosc.*, **280**, 1.

305. Kisiel, Z., Pszczółkowski, L., Drouin, B.J. *et al.* (2009) *J. Mol. Spectrosc.*, **258**, 26.

306. Hollis, J.M., Pedelty, J.A., Snyder, L.E. *et al.* (2003) *Astrophys. J.*, **588**, 353.

307. Kuan, Y.J., Charnley, S.B., Huang, H.C., Tseng, W.L., and Kisiel, Z. (2003) *Astrophys. J.*, **593**, 848.

308. Snyder, L.E., Lovas, F.J., Hollis, J.M. *et al.* (2005) *Astrophys. J.*, **619**, 914.

309. Wyrowski, F., Menten, K.M., Güsten, R., and Belloche, A. (2010) *Astron. Astrophys.*, **518**, A26.

310. Menten, K.M., Wyrowski, F., Belloche, A. *et al.* (2011) *Astron. Astrophys.*, **525**, A77.

311. Ossenkopf, V., Müller, H.S.P., and Lis, D.C. (2010) *Astron. Astrophys.*, **518**, L111.

312. Lis, D.C., Pearson, J.C., and Neufeld, D.A. (2010) *Astron. Astrophys.*, **521**, L9.

313. De Luca, M., Gupta, H., and Neufeld, D.A. (2012) *Astrophys. J.*, **751**, L37.

314. Neufeld, D.A., Falgarone, E., Gerin, M. *et al.* (2010) *Astron. Astrophys.*, **521**, L9.

315. Requena-Torres, M.A., Martín-Pintado, J., Rodríguez-Franco, A. *et al.* (2006) *Astron. Astrophys.*, **4550**, 971.

316. Belloche, A., Müller, H.S.P., Menten, K.M., Schilke, P., and Comito, C. (2013) *Astron. Astrophys.*, **559**, A47.

317. Belloche, A., Menten, K.M., Comito, C. *et al.* (2008) *Astron. Astrophys.*, **482**, 179.

318. Müller, H.S.P., Belloche, A., Menten, K.M., Comito, C., and Schilke, P. (2008) *J. Mol. Spectrosc.*, **251**, 319.

319. Belloche, A., Garrod, R.T., Müller, H.S.P. *et al.* (2009) *Astron. Astrophys.*, **499**, 215.

320. Faure, A., Remijan, A.J., Szalewicz, K., and Wiesenfeld, L. (2014) *Astrophys. J.*, **783**, 72.

321. Xu, L.H., Fisher, J., Lees, R.M. *et al.* (2008) *J. Mol. Spectrosc.*, **251**, 305.

322. Xu, L.H., Müller, H.S.P., van der Tak, F.F.S., and Thorwirth, S. (2004) *J. Mol. Spectrosc.*, **228**, 220.

323. Pearson, J.C., Brauer, C.S., Drouin, B.J., and Xu, L.H. (2009) *Can. J. Phys.*, **87**, 449.

324. Lees, R.M., Xu, L.H., Billinghurst, B.E., and Appadoo, D.R.T. (2011) *J. Mol. Struct.*, **993**, 269.

325. Brauer, C.S., Sung, K., Pearson, J.C., Brown, L.R., and Xu., L.H. (2012) *J. Quant. Spectrosc. Radiat. Transfer*, **113**, 128.

326. Fortman, S.M., Neese, C.F., and De Lucia, F.C. (2014) *Astrophys. J.*, **782**, 75.

327. Pearson, J.C., Yu, S., and Drouin, B.J. (2012) *J. Mol. Spectrosc.*, **280**, 119.

328. Coudert, L.H., Zemouli, M., Motiyenko, R.A., Margulès, L., and Klee, S. (2014) *J. Chem. Phys.*, **140**, 064307.

329. Ball, J.A., Gottlieb, C.A., Lilley, A.E., and Radford, H.E. (1970) *Astrophys. J.*, **162**, L203.
330. Parise, B., Castets, A., Herbst, E. *et al.* (2004) *Astron. Astrophys.*, **416**, 159.
331. Müller, H.S.P., Menten, K.M., and Mäder, H. (2004) *Astron. Astrophys.*, **428**, 1019.
332. Wang, S., Bergin, E.A., and Crockett, N.R. (2011) *Astron. Astrophys.*, **527**, A95.
333. Levshakov, S.A., Kozlov, M.G., and Reimers, D. (2011) *Astrophys. J.*, **738**, 26.
334. Jansen, P., Kleiner, I., Xu, L.H., Ubachs, W., and Bethlem, H.L. (2011) *Phys. Rev. A*, **84**, 062505.
335. Bagdonaite, J., Jansen, P., Henkel, C. *et al.* (2013) *Science*, **339**, 46.
336. Pearson, J.C., Brauer, C.S., and Drouin, B.J. (2008) *J. Mol. Spectrosc.*, **251**, 394.
337. Zuckerman, B., Turner, B.E., and Johnson, D.R. (1975) *Astrophys. J.*, **196**, L99.
338. Pearson, J.C., Sastry, K.V.L.N., Herbst, E., and De Lucia, F.C. (1997) *Astrophys. J.*, **480**, 420.
339. Bouchez, A., Walters, A., Müller, H.S.P. *et al.* (2012) *J. Quant. Spectrosc. Radiat. Transfer*, **113**, 1148.
340. Kisiel, Z., Dorosh, O., Maeda, A. *et al.* (2010) *Phys. Chem. Chem. Phys.*, **12**, 8329.
341. Maeda, A., Medvedev, I.R., De Lucia, F.L., and Herbst, E. (2006) *Astrophys. J. Suppl. Ser.*, **166**, 650.
342. Cohen, E.A., Drouin, B.J., Valenzuela, E.A. *et al.* (2010) *J. Mol. Spectrosc.*, **260**, 77.
343. Muller, H.S.P. and Christen, D. (2004) *J. Mol. Spectrosc.*, **228**, 298.
344. Hollis, J.M., Lovas, F.J., Jewell, P.R., and Coudert, L.H. (2002) *Astrophys. J.*, **571**, L59.
345. Lovas, F.J., Plusquellic, D.F., Pate, B.H. *et al.* (2009) *J. Mol. Spectrosc.*, **257**, 82.
346. Smirnov, I.A., Alekseev, E.A., Piddyachiy, V.I., Ilyushin, V.V., and Motiyenko, R.A. (2013) *J. Mol. Spectrosc.*, **293**, 33.
347. Ilyushin, V.V., Motiyenko, R.A., Lovas, F.J., and Plusquellic, D.F. (2008) *J. Mol. Spectrosc.*, **251**, 129.
348. Endres, C.P., Muller, H.S.P., Drouin, B.J. *et al.* (2009) *Astron. Astrophys.*, **504**, 635.
349. Snyder, L.E., Buhl, D., Schwartz, P.R. *et al.* (1974) *Astrophys. J.*, **191**, L79.
350. Groner, P. (1997) *J. Chem. Phys.*, **107**, 4483.
351. Bisschop, S.E., Schilke, P., and Wyrowski, F. (2013) *Astron. Astrophys.*, **525**, A122.
352. Richard, C., Margulès, L., Caux, E. *et al.* (2013) *Astron. Astrophys.*, **525**, A122.
353. Koerber, M., Bisschop, S.E., Endres, C.P. *et al.* (2013) *Astron. Astrophys.*, **558**, A112.
354. Fuchs, U., Winnewisser, G., Groner, P., De Lucia, F.L., and Herbst, E. (2003) *Astrophys. J. Suppl. Ser.*, **144**, 277.
355. Fuchs, G.W., Fuchs, U., Giesen, T.F., and Wyrowski, F. (2005) *Astron. Astrophys.*, **444**, 521.
356. Kobayashi, K., Matsui, T., Tsunekawa, S., and Ohashi, N. (2009) *J. Mol. Spectrosc.*, **255**, 64.
357. Walters, A., Müller, H.S.P., Lewen, F., and Schlemmer, S. (2009) *J. Mol. Spectrosc.*, **257**, 24.
358. Brown, R.D., Crofts, J.G., Godfrey, P.D. *et al.* (1975) *Astrophys. J.*, **197**, L29.
359. Takano, S., Sakai, Y., Kakimoto, S., Sasaki, M., and Kobayashi, K. (2012) *Publ. Astron. Soc. Jpn.*, **64**, 89.
360. Ilyushin, V.V., Kryvda, A.V., and Alekseev, E.A. (2009) *J. Mol. Spectrosc.*, **255**, 32.
361. Kobayashi, K., Takamura, K., Sakai, Y. *et al.* (2013) *Astrophys. J. Suppl. Ser.*, **205**, 9.
362. Carvajal, M., Margulès, L., and Tercero, B. (2009) *Astron. Astrophys.*, **500**, 1109.
363. Neill, J.L., Muckle, M.T., Zaleski, D.P. *et al.* (2012) *Astrophys. J.*, **755**, 153.
364. Medvedev, I.R., De Lucia, F.L., and Herbst, E. (2009) *Astrophys. J. Suppl. Ser.*, **181**, 433.
365. Sheridan, J., Bossert, W., and Bauder, A. (1980) *J. Mol. Spectrosc.*, **80**, 1.
366. Tudorie, M., Kleiner, I., Hougen, J.T. *et al.* (2011) *J. Mol. Spectrosc.*, **269**, 211.
367. Tercero, B., Kleiner, I., Cernicharo, J. *et al.* (2013) *Astrophys. J.*, **770**, L13.

368. Jelisavac, D., Gomez, D.C.C., Nguyen, H.V.L. *et al.* (2009) *J. Mol. Spectrosc.*, **257**, 111.

369. Solomon, P.M., Jefferts, K.B., Penzias, A.A., and Wilson, R.W. (1971) *Astrophys. J.*, **168**, L107.

370. Johnson, D.R., Lovas, F.J., Gottlieb, C.A. *et al.* (1977) *Astrophys. J.*, **218**, 370.

371. Müller, H.S.P., Drouin, B.J., and Pearson, J.C. (2009) *Astron. Astrophys.*, **506**, 1487.

372. Cosleou, J., Wlodarczak, G., Boucher, D., and Demaison, J. (1991) *J. Mol. Spectrosc.*, **146**, 49.

373. Demyk, K., Mäder, H., Tercero, B. *et al.* (2007) *Astron. Astrophys.*, **466**, 255.

374. Fukuyama, Y., Omori, K., Odashima, H., Takagi, K., and Tsunekawa, S. (1999) *J. Mol. Spectrosc.*, **193**, 72.

375. Daly, A.M., Bermúdez, C., López, A. *et al.* (2013) *Astrophys. J.*, **768**, 81.

376. Müller, H.S.P., Coutens, A., Walters, A., Grabow, J.U., and Schlemmer, S. (2011) *J. Mol. Spectrosc.*, **267**, 100–107.

377. Bizzocchi, L., Degli Esposti, C., Dore, L., and Kisiel, Z. (2008) *J. Mol. Spectrosc.*, **251**, 38.

378. Ordu, M.H., Müller, H.S.P., Walters, A. *et al.* (2012) *Astron. Astrophys.*, **541**, 121.

379. Linke, R.A., Frerking, M.A., and Thaddeus, P. (1979) *Astrophys. J.*, **234**, L139.

380. Xu, L.H., Lees, R.M., and Crabbe, G.T. (2012) *J. Chem. Phys.*, **137**, 104313.

381. Kaifu, N., Morimoto, M., Nagane, K. *et al.* (1974) *Astrophys. J.*, **191**, L135.

382. Ilyushin, V.V., Alekseev, E.A., Dyubko, S.F., Motiyenko, R.A., and Hougen, J.T. (2005) *J. Mol. Spectrosc.*, **229**, 170.

383. Apponi, A.J., Sun, M., Halfen, D.T., Ziurys, L.M., and Müller, H.S.P. (2008) *Astrophys. J.*, **673**, 1240.

384. Chengalur, J.N. and Kanekar, N. (2003) *Astron. Astrophys.*, **403**, L43.

385. Ilyushin, V.V. and Hougen, J.T. (2005) *J. Mol. Spectrosc.*, **289**, 41.

386. Zuckerman, B., Ball, J.A., and Gottlieb, C.A. (1971) *Astrophys. J.*, **163**, L41.

387. Mehringer, D.M., Snyder, L.E., Miao, Y., and Lovas, F.J. (1997) *Astrophys. J.*, **480**, L71.

388. Ilyushin, V.V., Endres, C.P., Lewen, F., Schlemmer, S., and Drouin, B.J. (2013) *J. Mol. Spectrosc.*, **290**, 31–41.

389. Rubin, R.H. Jr., Swenson, G.W., Benson, R.C., Tigelaar, H.L., and Flygare, W.H. (1971) *Astrophys. J.*, **169**, L39.

390. Kutsenko, A.S., Motiyenko, R.A., Margulès, L., and Guillemin, J.C. (2013) *Astron. Astrophys.*, **549**, 128.

391. Hollis, J.M., Lovas, F.J., Remijan, A.J. *et al.* (2006) *Astrophys. J.*, **643**, L25.

392. Bogey, M., Demuynck, C., Destombes, J.L., and Vallee, Y. (1975) *J. Mol. Spectrosc.*, **172**, 344.

393. Kraśnicki, A., Pszczółkowski, L., and Kisiel, Z. (2010) *J. Mol. Spectrosc.*, **260**, 57.

394. Remijan, A.J., Hollis, J.M., Lovas, F.J. *et al.* (2008) *Astrophys. J.*, **675**, L85.

395. Møllendal, H., Margulès, L., Belloche, A. *et al.* (2012) *Astron. Astrophys.*, **538**, 14.

396. Zaleski, D.P., Seifert, N.A., and Steber, A.L. (2013) *Astrophys. J.*, **765**, L10.

397. Carroll, P.B., Drouin, B.J., and Widicus Weaver, S.L. (2010) *Astrophys. J.*, **723**, 845.

398. Haykal, I., Motiyenko, R.A., Margulès, L., and Huet, T.R. (2013) *Astron. Astrophys.*, **549**, A96.

399. Jørgensen, J.K., Favre, C., Bisschop, S.E. *et al.* (2012) *Astrophys. J.*, **757**, L4.

400. Kisiel, Z., Pszczółkowski, L., Drouin, B.J. *et al.* (2012) *J. Mol. Spectrosc.*, **280**, 134.

401. Turner, B.E. and Apponi, A.J. (2001) *Astrophys. J.*, **561**, L207.

402. Turner, B.E., Terzieva, R., and Herbst, E. (1999) *Astrophys. J.*, **518**, 699.

403. Dore, L., Bizzocchi, L., and Degli Esposti, C. (2012) *Astron. Astrophys.*, **544**, A19.

404. McNaughton, D. and Robertson, E.G. (1994) *J. Mol. Spectrosc.*, **163**, 80.

405. Loomis, R.A., Zaleski, D.P., and Steber, A.L. (2013) *Astrophys. J.*, **765**, L9.

406. Lovas, F.J., Hollis, J.M., Remijan, A.J., and Jewell, P.R. (1999) *Astrophys. J.*, **645**, L137.

407. Dickens, J.E., Irvine, W.M., Ohishi, M. *et al.* (1997) *Astrophys. J.*, **489**, 753.

408. Ilyushin, V.V., Motiyenko, R.A., Drouin, B.J., Yu, S., and Margulès, L. (2014) *Astron. Astrophys.*, **563**, A137.

409. Smirnov, I.A., Alekseev, E.A., Ilyushin, V.V. *et al.* (2014) *J. Mol. Spectrosc.*, **295**, 44.

410. Ilyushin, V.V. and Hougen, J.T. (2013) *J. Mol. Spectrosc.*, **289**, 41.

411. Combes, F., Gerin, M., Wootten, A. *et al.* (1987) *Astron. Astrophys.*, **180**, L13.

412. Ilyushin, V.V., Endres, C.P., Lewen, F., Schlemmer, S., and Drouin, B.J. (2013) *J. Mol. Spectrosc.*, **290**, 31.

413. Motoki, Y., Tsunoda, Y., Ozeki, H., and Kobayashi, K. (2013) *Astrophys. J. Suppl. Ser.*, **209**, 23.

414. Loomis, R.A., Zaleski, D.P., Steber, A.L. *et al.* (2013) *Astrophys. J.*, **765**, L9.

3
Gas Phase Chemistry

Stephan Schlemmer

3.1
Introduction

Atoms and molecules make up a large fraction of the interstellar medium (ISM) and other astrophysical environments. Understanding how they are formed, destroyed, and altered via gas-phase processes is subject of this chapter. The physical process is usually described by a chemical reaction formula such as

$$\mathrm{A} + \mathrm{BC} \rightarrow \mathrm{AB} + \mathrm{C} \tag{3.1}$$

where in this case an atom A is undergoing an exchange reaction with molecule BC to form molecule AB and atom C. The above equation describes the fate of an individual pair of reactants as well as an ensemble of reactants since each collision partner is made up from the same set of atomic nuclei and electrons. If the conditions of the ensemble are well defined, for example, atoms and molecules are in a thermal environment, the rate of change of the concentrations [A], [BC], [AB], and [C] may be written as simple rate equations; for example,

$$-\frac{d[\mathrm{A}]}{dt} = \frac{d[\mathrm{C}]}{dt} = k(T) \cdot [\mathrm{A}] \cdot [\mathrm{BC}] \tag{3.2}$$

with the thermal rate coefficient $k(T)$ (in units of cubic centimeters per second, when [A] is given in per cubic centimeter) as the only number quantifying the rate of reaction. Since this is true under well-prepared laboratory conditions and in appropriate, that is, thermal, astronomical environments, values of $k(T)$ from laboratory studies can be used for astrophysical modeling –they are compiled in a few major data bases [1–3]—and describe rather complex chemical networks provided the environment is truly thermal.

A prototypical network is depicted in Figure 3.1. As can be seen from Eq. (3.2), the chemical evolution of an initial set of atoms and molecules is determined by the rate coefficient for the specific reaction and the concentration of the two collision partners. As a result, the chemical network starts with the most prominent species, which are hydrogen and helium. For simplicity, it is assumed that most of

Laboratory Astrochemistry: From Molecules through Nanoparticles to Grains, First Edition.
Edited by Stephan Schlemmer, Thomas Giesen, Harald Mutschke and Cornelia Jäger.

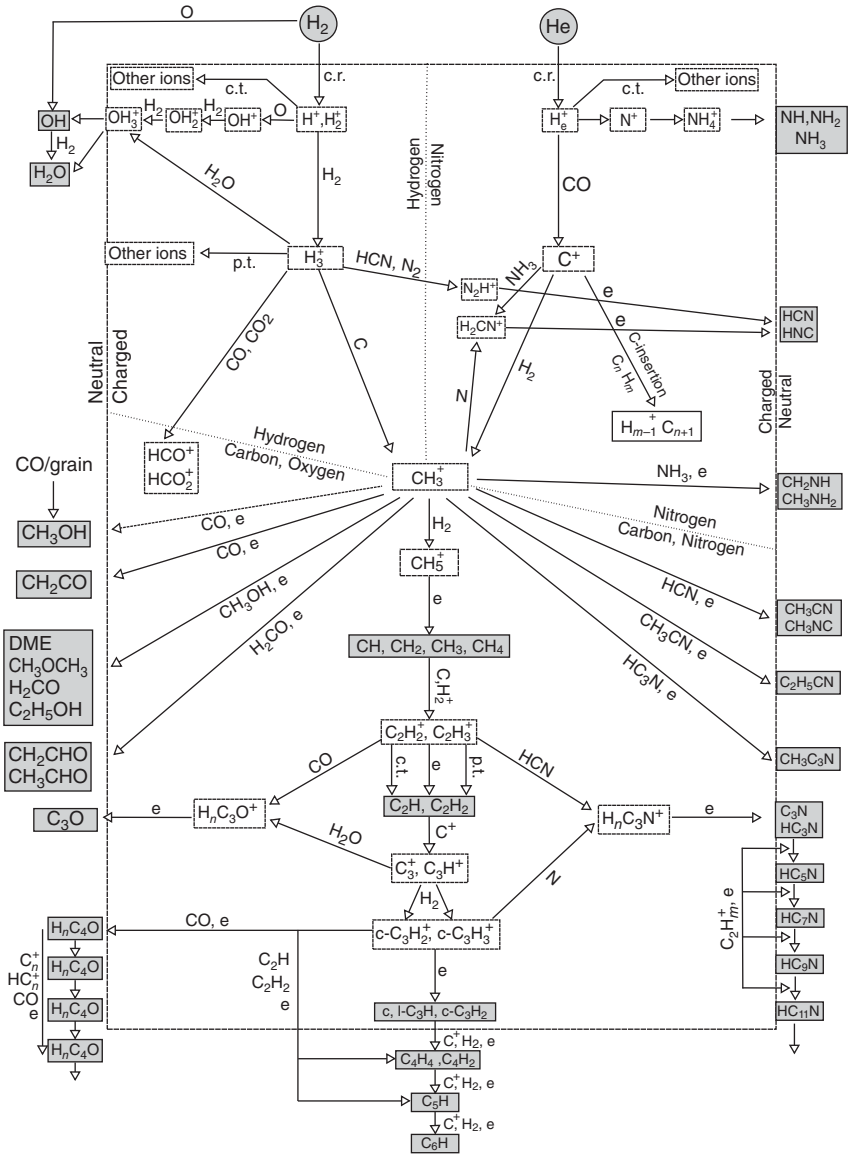

Figure 3.1 Chemical network of some of the most important gas-phase reactions, especially in dense pre-stellar cores, where the temperature remains low. The graphic is updated from an early version by Smith [4]. Important ion–molecule reactions are denoted inside the dashed rectangular box. Neutral molecules emerging from these reactions are shown outside this box. Downward, the number of carbon atoms increases, to the left oxygen and to the right nitrogen is added. (c.r.,cosmic rays; p.t., proton transfer; c.t., charge transfer)

the hydrogen is molecular, as is the case for dense molecular clouds. How the initial conditions vary with the different environments has been discussed in various review articles [4–7].

Figure 3.1 is an updated and modified version of a chemical network already presented 20 years ago by Smith [4], for cold, dense molecular clouds. In fact, the importance of gas-phase processes was first described by Herbst and Klemperer [8] some 40 years ago. Therefore, the gas-phase chemistry is a rather mature field in astrophysics. Many key processes have been identified, and a number of reactions have been studied in the laboratory, providing the relevant data for modeling the chemical evolution of astrophysical environments.

Figure 3.1 is used to illustrate some general aspects that are important to draw such chemical networks and to identify classes of typical processes which are summarized in Table 3.1. Species in rectangular boxes are atoms or molecules that have been identified in space mostly by their rotational lines in radio astronomical observations which are described in Chapter 2. Each arrow connects one important gas-phase species to another key species in a chemical reaction as described in Eq. (3.1). For binary collisions, the second collision partner is given alongside the arrow. It is interesting to see how, besides the dominant hydrogen, the next most abundant elements C, N, and O are entering the chemical network. Carbonaceous species are formed via elementary carbon or via CO, the second most abundant molecule in space. In the network of Figure 3.1, carbonaceous species of growing complexity are appearing top to bottom. Nitrogen is entering the network mainly via N_2, a molecule without a permanent dipole moment and thus without a detectable rotational spectrum, and mainly reprocessed from NH_3, HCN, and other cyanides as indicated. Those nitrogen-bearing species are appearing toward the right of Figure 3.1. Oxygen-bearing species, finally, are appearing to the left.

It might appear suggestive from Figure 3.1 that most of the detected molecules in space (species in boxes) are formed by gas-phase processes. Moreover, the chemistry drawn here appears to be dominated by ion–molecule reactions. However, also heterogeneous chemistry happening mainly on grain surfaces is another important, if not dominant in many cases, route to the formation of the molecules found in space. A prominent example is the case of methanol formation, which today is accepted to be formed by hydrogen addition to CO on grains. Therefore, the corresponding reaction is not part of this network any more (see dashed line). For that reason, the association reactions of CH_3^+ with neutrals shown in this network and the subsequent dissociative recombination (DR) with an electron, e, have to be questioned. In any case, also the rate coefficients of these ion–molecule reactions have to be known to evaluate their role in astrochemistry. The most relevant surface processes are discussed in detail in Chapter 5. The databases for gas-phase processes contain more than 400 species and more than 4000 reactions. As a result of the complex chemical networks, the abundance of many of the currently ~180 molecules detected in the ISM or circumstellar envelopes (CSEs) are predicted in chemical models. Early on, it was a big surprise that molecules could survive the harsh environment of space and that they could grow as large as amino acetonitrile (NH_2CH_2CN), a precursor to the simplest

Table 3.1 Typical (photo)chemical processes occurring in astronomical environments.

	Process	Type of reaction	Typical example	Remarks
Ionic interaction	Cationic	Cation–neutral reactions	$N^+ + H_2 \rightarrow NH^+ + H$	Rearrangement
		Radiative associations (ion)	$C^+ + H_2 \rightarrow CH_2^+ + h\nu$	Bond formation
	Mixed	Chemi-ionization	$O + CH \rightarrow HCO^+ + e$	Bond formation
		Direct cosmic ray processes	$H_2 + \gamma \rightarrow H_2^+ + e^-$	Ionization, Heating
		Radiative recombination	$H_2CO^+ + e^- \rightarrow H_2CO + h\nu$	Neutralization
		Anion–cation recombination	$HCO^+ + H^- \rightarrow H_2 + CO$	Neutralization
		Dissociative recombination	$H_3^+ + e^- \rightarrow H_2 + H, 3H$	Neutralization, Rearrangement
	Anionic	Anion–neutral reactions	$C^- + NO \rightarrow CN^- + O$	Rearrangement
		Associative detachment	$H^- + H \rightarrow H_2 + e^-$	Bond formation
		Electron attachment	$C_6H + e^- \rightarrow C_6H^- + h\nu$	Ionization
	Neutral	Neutral–neutral reactions	$C + C_2H_2 \rightarrow C_3H + H$	Rearrangement
		Photodissociation	$H_2 + h\nu \rightarrow 2H$	Bond dissociation
		External photoprocesses	$C_3N + h\nu \rightarrow C_2 + CN$	Rearrangement
		Internal photoprocesses	$CO + h\nu \rightarrow C + O$	Bond dissociation
		Radiative association (neutral)	$C + H_2 \rightarrow CH_2 + h\nu$	Bond formation
	Nonreactive	Inelastic processes	$C^+(^2P_{1/2}) + M \rightarrow C^+(^2P_{3/2}) \rightarrow C^+(^2P_{1/2}) + h\nu$	Cooling
		Gas–grain interactions	$H + H + \text{grain} \rightarrow H_2 + \text{grain}$	Bond formation

amino acid, glycine (NH_2CH_2COOH), which has been detected in Sgr B2(N) recently [9]. In fact, it is one of the current areas of research in astrochemistry to investigate how complex molecules can grow under the low temperature conditions in space. More discussion of this issue can be found in Section 2.4

A closer look at the chemical network in Figure 3.1 shows that all reactions can be classified into distinct reaction mechanisms, which are distinguished as bond-forming, bond-breaking, and rearrangement reactions. For example, several ions, in particular H_3^+, play a pivotal role in gas-phase chemistry, as depicted in Figure 3.1. In Table 3.1, the various gas-phase processes (type of reaction) are summarized. The upper portion deals with reactions involving ions, the middle part considers processes with uncharged species only, and the lower part deals with nonreactive collisions. For each reaction mechanism, a typical reaction is given as an example in a separate column. In the last column, the effect on the astrophysical environment is described. For example, inelastic collisions of CII (C^+) with a collision partner, denoted as M, are important for the successive cooling via the fine structure transition of CII. In fact, this is the dominant cooling line in the ISM which is important to model quiescent star formation.

The chemical network in Figure 3.1 has been updated on the basis of observational facts. One important example concerns the formation of water. Water is formed in different ways, strongly depending on the temperature of the astrophysical environment. At low temperatures, ion chemistry leads to the formation of OH_n^+ ($n = 1, 2, 3$) by successive hydrogen abstraction in collisions with H_2. All these reactions are exothermic and rather fast, leading to an efficient way of water formation. All OH_n^+ have been detected recently with the Herschel satellite [10, 11], indicating that ion chemistry supplies one possible route to the formation of interstellar water. However, in the presence of grains, atomic oxygen also condenses on the ice, which subsequently is hydrogenated by atomic hydrogen that also arrives at the grain surface. This serves as an alternate route to water formation. At high temperatures, there is also a neutral gas-phase pathway to form water as indicated in Figure 3.1. $O(^1D)$ undergoes hydrogen abstraction in collisions with H_2, and the OH formed can undergo further hydrogen abstraction in collisions with H_2 surpassing an activation barrier as high as some $E_a/k_B \sim 2100$ K, with k_B the Boltzmann constant. This case shows the complexity of the chemical networks. In fact, the search for water as well as the aim to understand the various ways on how it is formed in space was one of the key projects and motivations to build the space observatory Herschel [12–15].

One aim of line observations is to derive the gas density and the temperature of the emitting species such as water as discussed here. In the low density limit, the population of rotational states is dominated by the radiative lifetimes of excited states, thus approaching an equilibrium associated with the local radiation field. In the high density limit, collisions determine the rotational population, and the temperature will be given by the kinetic temperature of the surrounding gas (H_2 as the dominant species). A critical density is defined as the value at which the collision rate $k \cdot [H_2]$ equals the Einstein A coefficient for spontaneous emission. From these considerations, it is clear that accurate values for the dipole moment μ^2 of

the corresponding molecule are needed ($A \sim \mu^2$) as well as accurate values for the rate coefficient k for inelastic collisions and the number density [H_2] in order to convert observations into column densities and temperatures for astrophysical studies. Much progress has been made for the understanding of the inelastic collisions of water with H_2, the most dominant collision partner of water in space. Section 3.3 by Parker and Wiesenfeld describes the detailed measurements in crossed molecular beam arrangements, the analysis of the experimental data, the comparison to state-of-the-art theoretical calculations of cross sections, and rate coefficients in order to provide the necessary data to derive the gas density and temperatures for water observations. In the following, we will introduce the relation between differential cross sections, $d\sigma/d\omega\,(\vartheta, E, i \rightarrow f)$, integral cross sections $\sigma(E)$, and the rate coefficient $k(T)$, of which only the last one was discussed so far.

All the rate coefficients relevant for the chemical network described exemplarily in Figure 3.1 and their temperature dependence have to be known in great detail to set up the chemical models that explain the synthesis of the molecules observed in space. For reactions with different product channels, the branching ratios have to be known as well. Of equal importance are the initial conditions such as the temperature and the initial abundances. For the crucial reactions, the rate coefficients have to be known quite accurately since uncertainties in these rate coefficients will propagate in the chemical model and thus affect also the amount of reaction products of subsequent reactions. For that reason, it is also important to associate uncertainties to the rate coefficients in the databases in order to evaluate the chemical models [16]. It is the purpose of the database KInetic Database for Astrochemistry (KIDA) [3] to provide all the above necessary information.

Only a fraction of the important reactions are characterized in the laboratory as will be explained below. And for many of those reactions the temperature dependence has not been measured. The temperature dependence of the rate coefficient is usually parameterized in the Arrhenius–Kooij formula

$$k(T) = \alpha(T/300\,\mathrm{K})^{\beta}\exp^{\left(\frac{-\gamma}{T}\right)} \tag{3.3}$$

where α, β, and γ are three parameters that describe the overall size of the rate coefficient (α) and its temperature dependence (β and γ). For reactions with barriers or endothermic reactions, γ is the typical Arrhenius value (E_a/k_B) expressed in Kelvin and β describes a temperature dependence which is characteristic of the type of interaction forces as will be explained below in this chapter. Some reactions have a much more complicated temperature dependence since the reaction mechanism changes in different temperature regimes. For those reactions, the values for α, β, and γ are given in the respective temperature ranges.

Figure 3.2 shows the temperature dependence of a couple of representative rate coefficients. Some reactions, such as the initial reaction $H_2^+ + H_2 \rightarrow H_3^+ + H$ forming the important H_3^+ molecule, show no temperature dependence. The value of this reaction ($\sim 10^{-9}\mathrm{cm}^3\mathrm{s}^{-1}$) is determined by the collision rate of the two reaction partners, which is governed by the long-range attractive ion–induced dipole forces as will be explained below. This interaction is different for collisions of ions

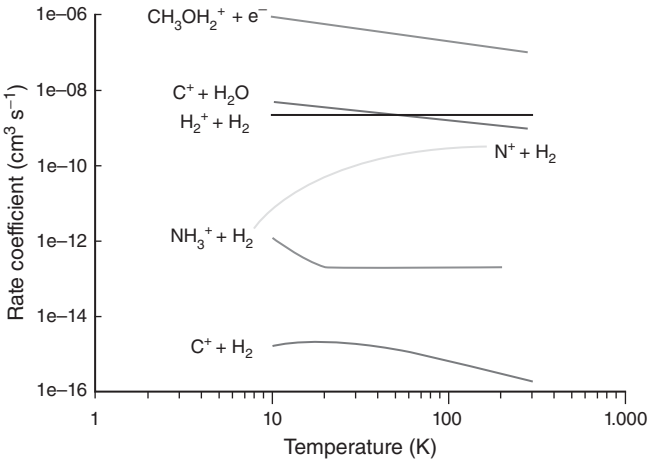

Figure 3.2 Typical temperature dependence of the rate coefficients for ion–induced dipole, ion–dipole, and ion–electron collisions as taken from the KIDA catalog [3].

with molecules with a permanent dipole moment as in the reaction $C^+ + H_2O$ and leads to a reverse temperature dependence, meaning that the rate coefficient increases at lower temperatures. For reactions with barriers, such as $OH + H_2$ discussed above, the rate coefficient is small at low temperatures as expected and increases exponentially as expressed in Eq. (3.3).

Radiative association is a slow process, as depicted for $C^+ + H_2 \rightarrow CH_2^+ + h\nu$. Here, the CII atomic ion cannot undergo a chemical reaction to form $CH^+ + H$ because this pathway is endothermic by several thousand kelvins. At low temperatures, C^+ and H_2 form a collision complex, instead. The lifetime of this complex strongly depends on the temperature and increases up to microseconds in cold molecular clouds. If during this lifetime the complex emits a photon ($h\nu$), it can stabilize the complex and form CH_2^+. The radiative lifetime τ_{rad} of the newly forming molecule is on the order of milliseconds. Based on the competition between these two processes, the chances to form CH_2^+ are rather small and the corresponding rate coefficient is small, too. Despite these circumstances, this reaction is a dominant pathway in the chemical networks to form carbonaceous species as shown in Figure 3.1.

In fact, slow association processes can play a significant role in a number of environments. The association of H^- and H turned out to be a rather fast process, which appears to be the dominant route to form H_2 in the early universe where molecular hydrogen cannot be formed on grain surfaces since dust can only form from heavier elements, which are not yet present. In order to evaluate the efficiency of hydrogen formation in these early phases of star formation, cross sections for the associative detachment process $H^- + H \rightarrow (H_2^-)^* \rightarrow H_2 + e^-$ have been worked out. The measurements and their analysis for use in early universe astrochemistry is described in Section 3.5.

The reaction $NH_3^+ + H_2 \rightarrow NH_4^+ + H$ shows a rather complex temperature dependence with an Arrhenius behavior at elevated temperatures, a minimum around 80 K, and an increase toward lower temperatures. As it turned out, this reaction is subject to an activation barrier of about 91 meV, which can be overcome by thermal activation (high temperatures) or by tunneling (see Ref. [17] and references therein). The latter process becomes probable only when the two collision partners stay together for a long enough time, which is the case at low temperatures as discussed for the previous example. The result is the small rate coefficient, which increases at low and high temperatures. This slow reaction is thus a rate-limiting step in the formation of interstellar ammonia, which is a key probe molecule for the astrophysical environment as discussed extensively in Ref. [18].

Another very important process in interstellar chemistry is DR, in which an ion recombines with an electron to form the neutral species that are detected in space. The relevance of this process is shown in Figure 3.1, where inside the dashed box chemistry is dominated by ion–molecule collisions and all the C-, N-, and O-containing larger neutral molecules are thought to be formed by DR. This hypothesis is challenged by alternative formation routes via gas–grain chemistry, as will be discussed below for the case of interstellar methanol (CH_3OH). Also, the DR reaction shows a reverse temperature dependence. Till recently, the rate coefficients for these reactions could be predicted reasonably well only for specific systems. In particular, measurements of DR of H_3^+ varied over many orders of magnitude, and theoretical predictions did not yield reliable quantitative values. This deficiency was lifted by recent measurements and the development of an appropriate theoretical approach which is described in detail in Section 3.2.

Neutral–neutral reactions are substantially slower than barrierless exothermic ion–molecule reactions because of the barriers that arise when nuclei have to be removed from their minimum energy configuration to undergo the necessary rearrangement to initiate the chemical reaction. However, reaction rates between radicals and between radicals and unsaturated molecules, such as $O(^3P) + C_4H_8$, can show much larger values. In Ref. [7], the low-temperature behavior for these kind of reactions is discussed in detail and compared with a microcanonical version of transition-state theory. It turns out that at the low temperatures of the ISM (10 K), the rate coefficients reach limiting values derived from simple collision theory, which can be comparable to those of ion–molecule reactions. Much less experimental data is available for such neutral–neutral reactions. However, it is gratifying that some general rules could be drawn from these recent experiments using the (Cinétique de Réaction en Ecoulement Supersonique Uniforme, engl. Reaction Kinetics in Uniform Supersonic Flow) CRESU technique, guiding the understanding of whole classes of chemical reactions.

In summary, rate coefficients for the gas-phase reactions and inelastic processes are needed in great detail to model the chemistry of molecular clouds and other environments in order to predict their chemical composition and physical properties. Laboratory measurements have to cover a large range of collision energies and temperatures to provide cross sections and rate coefficients, either for direct use in the models or to derive the rate coefficients based on appropriate

models describing the reactive and nonreactive collisions of molecules. Some of the physicochemical ideas linking the collision process to cross sections and rate coefficients are given in the subsequent section, followed by some typical experiments from which the relevant quantities are inferred. Following this introduction, recent progress in laboratory and theoretical work is demonstrated on selected examples already mentioned in part above.

3.1.1 Cross Sections and Rate Coefficients for Binary Collisions

The scattering process in all detail is described by the propagation of the center-of-mass collision system formed by the two collision partners on the interaction potential energy surface (PES). Strictly speaking, the time-dependent Schrödinger equation for the scattering problem has to be solved for a theoretical treatment of the problem. The adequacy of approximations for a theoretical description of the problem will be discussed below. In any case, the outcome of the scattering event will depend on the internal states of the collision partners, on the translational or collision energy in the center-of-mass frame ($E = E_t = E_{CM}$), as well as on the angular momentum, $L = l\hbar$ with $l = 0, 1, 2, ...$, which is related to the classical impact parameter parameter b by $L = \mu v b$. Classically, the deflection function $\vartheta(b, E)$ describes the result of the scattering process. Figure 3.4 shows a deflection function for an atom–atom collision where no internal degrees of freedom, that is, no internal states $|i\rangle$ or $|f\rangle$ of reactants or products, have to be taken into account. In fact, the deflection function can be derived analytically for a given potential $V(r)$, where r is the distance between the two collision partners, as the interaction does not depend on the relative orientation of the collision partners. Figure 3.3 shows a number of classical trajectories for the atom–atom collision system with a Lenard–Jones type potential with a van der Waals attraction ($\sim -r^{-6}$) and a repulsion ($\sim r^{-12}$). The potential well is indicated in this figure by the gray shaded area around the white circle, where the incoming atom is subject to strong repulsion. The situation is drawn for a fixed collision energy $E = 2.5\epsilon$, where ϵ is the well depth of the potential. As mentioned above, the collision system has been transferred into the single-particle system of reduced mass $\mu = m_1 \cdot m_2/m_1 + m_2$. As the impact parameter b is lowered, the particle starts to be deflected toward negative angles as a result of the attractive interaction. Figure 3.4 shows the respective deflection function for the depicted scattering process. At a particular impact parameter, the deflection angle becomes maximum (rainbow angle), then it decreases again, changes sign as the repulsive forces become dominant, and reaches π (backward scattering) for a head-on collision as expected. The deflection function is plotted for various values of the reduced collision energy E/ϵ.

Irrespective of whether the scattering is treated classically or quantum mechanically, the differential cross section

$$\frac{d\sigma}{d\omega}(\vartheta, E) \tag{3.4}$$

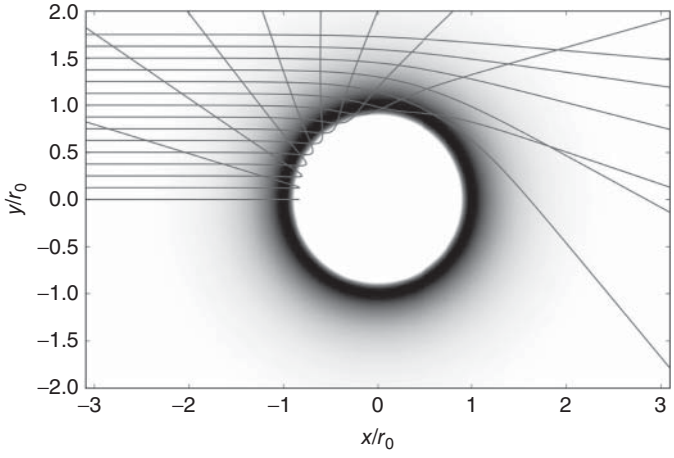

Figure 3.3 Trajectories of a diatomic collision with fixed collision energy E and varying impact parameter b in a Lenard–Jones potential.

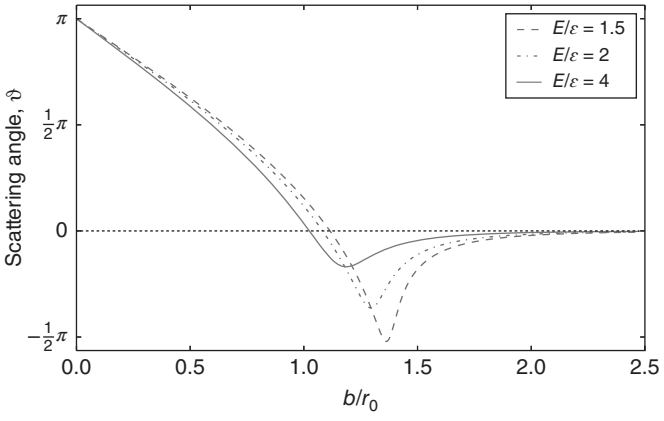

Figure 3.4 Example deflection functions $\vartheta(b, E)$ as a function of the impact parameter b with the reduced collision energy E/ϵ as parameter and ϵ the well depth of the potential.

describes the outcome of the scattering process, relating the flux of the products to the flux of the incoming particles, colliding at an energy E, as a function of the scattering angle ϑ. The classical and quantum mechanical (QM) problem for the one-dimensional potential $V(r)$ is well described in a number of textbooks (see, e.g., Ref. [19]). More complicated situations are described, for example, in the *Handbook of Atomic, Molecular, and Optical Physics* [20]. The reader is referred to these references for detailed derivations. The aim here is to connect the physical picture of the collision process with some of the key physical quantities and to supply a few useful relations and a coarse idea of the scale of rate coefficients that enter the astrochemical modeling. For that purpose, the one dimensional atom–atom collision system is used as an example.

In the classical derivation of the above problem, the cross section is related to the impact parameter b and the deflection angle ϑ by

$$\frac{d\sigma}{d\omega}(\vartheta, E) = \left|\frac{b}{\sin(\vartheta)}\right| \cdot \left|\frac{db}{d\vartheta}\right|. \tag{3.5}$$

Here, $db/d\vartheta$ is the inverse of the slope of the deflection function. Thus the differential cross section is large when the slope is small, meaning that many impact parameters b lead to the same scattering angle ϑ. For the simple atom–atom case, it is quite obvious that details of the potential influence the deflection function and thus also the differential cross section. In fact, the problem can be inverted, that is, the potential can be directly inferred from the differential cross section. Therefore, one can conclude that the most detailed information of the scattering process is contained in the differential cross section. It also becomes clear that single collision conditions must prevail in such experiments to relate the scattering angle to the underlying potential. For more complicated scattering problems, like an atom–molecule collision, the internal states can change and thus there exists one differential cross section $d\sigma/d\omega\,(\vartheta, E, i \to f)$ for each transition $i \to f$. In addition, the outcome of the collision process will depend on the relative orientation, and thus the differential cross sections are orientation averages. It is discussed in Section 3.3 how the details of the atom–molecule PES can be inferred from a comparison of the experimental individual differential cross sections with theoretical predictions. A wide variety of methods is used to create theoretical predictions, starting from the simple physical pictures we use in this chapter to give estimates for the physical quantities. Analyzing the outcome of classical trajectories takes into account details of the PES and can give quantitative and often rather realistic results. In cases where quantum effects play an important role, quantum scattering calculations are necessary but possible only for systems of restricted size.

One astrophysically important system that has been studied in great detail is the $H^+ + H_2$ system. Very recently, an extensive set of experimental measurements on the dynamics of the $H^+ + D_2$ and $D^+ + H_2$ isotopic variants of this prototypical ion–molecule reaction has been compared with the results of QM, quasiclassical trajectory (QCT), and statistical quasiclassical trajectory (SQCT) calculations [21]. From experimental side, the kinetic energy spectra (KES) of the ionic reaction products are available for which the simulations using the state-resolved differential cross sections (calculated with the QCT-GB (Gaussian binning) method) seem to account for most of the observed features. State-specific measurements for the $H^+ + H_2(J = 1) \to H^+ + H_2(J = 0)$ collision and thus detailed information on the transition of nuclear spin states (ortho–para conversion) have been available since 1981 [22]. Only recently were these experiments compared with detailed calculations. The role of state-specific rate coefficients is discussed in Section 3.4 for more complex systems which involve, for example, the most prominent molecular ion in dense clouds, H_3^+.

From the fundamental quantity of the differential cross section, the integral cross section $\sigma(E, i \to f)$ can be derived by integration over all scattering angles ϑ,

that is, over the full scattering sphere.

$$\sigma(E, i \to f) = \int_0^{4\pi} \frac{d\sigma}{d\omega}(\vartheta, E, i \to f)\, d\omega = 2\pi \int_0^{\pi} \frac{d\sigma}{d\omega}(\vartheta, E, i \to f) \sin(\vartheta) d\vartheta. \quad (3.6)$$

Summing over all possible internal states (where applicable) leads to the total integral cross section $\sigma(E) = \sum_{i,f} \sigma(E, i \to f)$.

Using relation (3.5) for the classical description of the problem leads to the relation

$$\sigma(E, i \to f) = 2\pi \int_0^{\infty} b\, d\, b. \quad (3.7)$$

In this simple approach, the scattering cross section is not limited. However, as seen from the trajectories in Figure 3.3, for large impact parameters, the deflection angle is zero. Thus the integration boundary is limited to an upper value, b_0. This leads to the simple formula

$$\sigma(E, i \to f) = \pi\, b_0^2 \quad (3.8)$$

where the cross section is the area of a circle with radius b_0. A practical value for b_0 can be read from Figure 3.3 as $\sim 2 \cdot r_0$, where r_0 is the position of the well depth. The relationship becomes even more obvious for a hard sphere model where b_0 is the sum of the hard sphere radii much like the collision between two billiard balls. Another interesting case concerns the ion–induced dipole interaction, which will be discussed below. The typical interaction radii are given by the sum of the ionic radii of the atoms and molecules, which are on the Angstrom scale. As a result, a considerable cross section would be squared Angstrom. The concept of a cross section, which is obvious for the simple cases discussed, is also transferred to chemical reactions.

If a chemical reaction is hindered for some reason (barrier, endothermicity, or steric effects), the probability for that reaction and thus the cross section is reduced. Based on the model used, theoretical cross sections can be compared with experimental cross sections. Below we will give examples of apparatuses and collision systems for determining integral cross sections. In Sections 3.2 and 3.5, two such experiments are described in detail and the results are discussed in the astrophysical context.

While differential and integral cross sections are measured under single collision conditions, the rate of change of the concentration of a species in an experiment or in space is proportional to the cross section of this event but also to the relative velocity v of the collision partners. Thus the two-body rate coefficient at a given energy E is then given by the product $k(E) = v\sigma(E)$ with $v \sim \sqrt{E}$, since E is the kinetic energy of the collision in the center-of-mass frame. In a thermal environment, the relative velocity v of the collision partners is given by its thermal distribution

$$f(v)dv = 4\pi \left(\frac{\mu}{2\pi kT}\right)^{\frac{3}{2}} v^2 e^{-\frac{\mu v^2}{2kT}} dv \quad (3.9)$$

and thus the thermal rate coefficient of an experiment is the thermal average of the energy specific rate coefficient $k(T) = \langle k(E) \rangle$,

$$k(T) = \int_0^\infty v\sigma(E) \cdot f(v)\, dv \tag{3.10}$$

as discussed above. In order to arrive at some practical values for $k(T)$, let us again assume the atom–atom collision from above. The average relative velocity $\langle v(E) \rangle$ is on the order of some hundred meters per second under ordinary laboratory conditions, that is, $T = 300$ K and somewhat more elevated for the light He–He collision system. By estimating $k(T)$ as $\langle \sigma(E) \rangle \cdot \langle v(E) \rangle$ with $\langle \sigma(E) \rangle \sim 10 \cdot 10^{-16}$ cm^2 as discussed above for the cross section and $\langle v(E) \rangle \sim 10^4$ cm s^{-1}, we arrive at a value of $k \approx 10^{-11}$ cm^3 s^{-1}.

We have seen in Figure 3.2 that the rate coefficients vary with temperature and that their magnitude varies over many orders depending on the process considered. The estimated value of 10^{-11} cm^3 s^{-1} is much smaller than the rate coefficients of fast ion–molecule reactions and it is substantially faster than the rate coefficients for radiative processes. It turns out that it is indeed in a range found for neutral –neutral reactions. However, no reaction but only the elastic collision of an atom–atom encounter has been considered for the estimate, instead. The reason that the value is still matching the order of magnitude for neutral–neutral reaction stems from the following picture. In order for a reaction to occur, the two collision partners have to approach each other. This is well described by the long range-forces, which in our system led to the deflection described above and to the simple expression (3.8) for the integral cross section.

The outcome of this interaction is temperature dependent and approximated in the Arrhenius–Kooij formula in the $(T/300\,\mathrm{K})^\beta$ part, where β depends on the kind of interaction as discussed in the following. In cases where reactivity is hindered by a barrier or endothermicity, the Arrhenius behavior governs the $\exp^{-\gamma/T}$ part. The pre-exponential factor α depends on the kind of interaction and can vary a lot as mentioned above.

In order to better understand the temperature dependence originating from the long-range part of the potential, we consider the ion–induced dipole interaction which appears in the most frequent ion collisions with molecular hydrogen as depicted in Figure 3.1 and leads to the well-known Langevin model [23]. When a charge polarizes an atom or a molecule, it creates a dipole moment. The attractive potential between the charge (ion) and the induced dipole gives rise to the effective potential

$$V_{\mathrm{eff}}(r) = -\frac{1}{8\pi\epsilon_0}\frac{q^2 \cdot \alpha_{\mathrm{n}}}{r^4} + E \cdot \left(\frac{b}{r}\right)^2 \tag{3.11}$$

where q is the charge of the ion and α_{n} is the polarizability of the neutral collision partner. The second term is the centrifugal potential which arises from the angular momentum when $b \neq 0$. This effective potential is plotted in Figure 3.5 for a single charge and a hydrogen molecule with a polarizability of $\alpha_{\mathrm{n}} = 0.8$ Å^3 and various angular momenta $L = l \cdot \hbar$. It becomes apparent from this graph that the

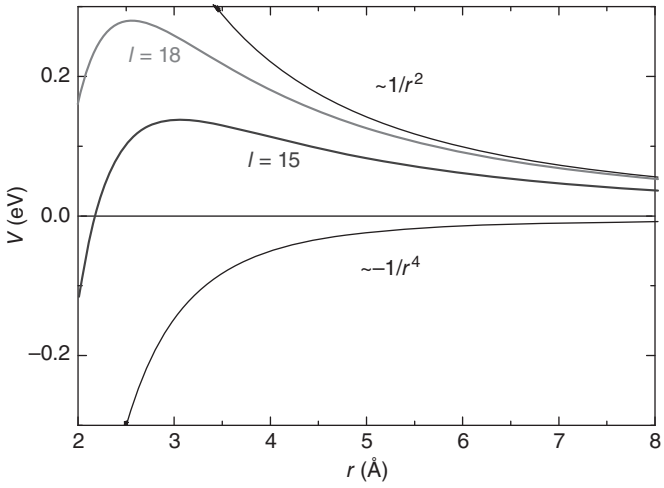

Figure 3.5 Effective potential for an ion–molecule collision. The reduced mass for this system is $\mu = 2$ as for a collision of a heavy ion with molecular hydrogen and the polarizability of hydrogen is $\alpha_n = 0.8$ Å^3.

centrifugal barrier can be overcome only for $E \geq V_{\text{eff}}^{\max}$. Thus, for a given collision energy E, one finds a maximum critical impact parameter

$$b_c^2 = \sqrt{\frac{q^2 \cdot \alpha_n}{2\pi\epsilon_0 E}} \tag{3.12}$$

for which the barrier can be surmounted. For larger impact parameters, the two collision partners do not come close enough to undergo a chemical rearrangement. Using the critical impact parameter for the integral cross section leads to

$$\sigma(E) = \pi b_c^2 \propto E^{-\frac{1}{2}}. \tag{3.13}$$

Since $v \propto E^{1/2}$, the thermal rate coefficient $k(T)$ becomes temperature-independent in this simple model first described by Gioumousis and Stevenson [23] with the so-called Langevin value

$$k_L = q\sqrt{\frac{\pi\alpha_n}{\epsilon_0\mu}}. \tag{3.14}$$

It can be seen from Figure 3.2 that some ion–molecule reactions follow this basic formula. In most cases, this simple model is describing an upper limit for the rate coefficient of reactions which are not hindered by any restrictions (barrier, endothermicity, or steric hindrance). For some cases such as the $H^- + H$ collision discussed in Section 3.5, the chemical attraction can be stronger than predicted by the long-range forces and thus the rate coefficient can even exceed the Langevin value. Still, this boundary value provides a good guidance to distinguish fast from slow reactions. The capture model described here has been expanded for different interactions, that is, the $-r^{-4}$ attraction of the ion–induced dipole is changed to

a different leading term $-r^{-m}$ in the attractive part. In addition, these potentials are nonspherical, that is, they depend on the relative orientation of the collision partners. As a result, a rigorous analytical expression no longer can be derived. Still, under specific assumptions, an approximate expression for the thermal rate coefficient can be obtained. Expanding the capture idea to these systems, the critical impact parameter has a different energy dependence and thus the thermal rate coefficient has a temperature dependence, too. This is seen very well for the example of an ion–permanent dipole system ($C^+ + H_2O$) (Figure 3.2), where the rate coefficient increases at lower temperatures as $T^{-1/2}$ as derived by Chesnavich *et al.* [24] and Su and Bowers [25] for an ion–dipole capture. A $T^{-1/2}$ temperature dependence is also found by estimating DR, and for negative ion formation $A + e^- \rightarrow A^{-*} \rightarrow A^- + h\nu$.

With today's computing capabilities, more realistic theoretical approaches are possible as already mentioned above. However, the simple treatment helps us to guide the way in the large variety of reactions used in the chemical networks to distinguish fast from slow reactions and to identify unusual temperature behaviors as seen for the reaction $NH_3^+ + H_2 \rightarrow NH_4^+ + H$. Details of the assumptions leading to these estimated rate coefficients are discussed by Herbst and Millar [5]. In the following, we will start to discuss some key experiments in which differential and integral cross sections as well as rate coefficients are determined. More detailed examples relating to recent progress are given in the respective subsections.

3.1.2
Differential Scattering and Crossed Beam Experiments

As explained above, the differential cross section $d\sigma/d\omega(\vartheta, E, i \rightarrow f)$ is the most detailed experimental quantity one can obtain for a scattering process. It can be determined in crossed beam experiments, where two well-collimated beams of atoms or molecules propagate in high vacuum ensuring that no collisions with other molecules in the experiment take place except for the *one* collision in the experimental scattering volume (single-collision conditions). Figure 3.6 shows a cross-sectional view of such an experiment with two such beams intersecting at right angles. If possible, supersonic molecular beam sources are used because rather intense and directed beams can be formed. A set of apertures and differential pumping are used to collimate the molecular beams, to define the scattering angle, and to maintain *single* collision conditions at the scattering center. Based on the expansion of the high-pressure gas entering the vacuum chamber, the thermal energy of the gas in the two reservoirs is converted into kinetic energy, leaving the molecules internally rather cold and with a narrow and directed velocity distribution [26]. As a result, the collision energy E is usually very well defined. Products of the scattering process are detected at a particular scattering angle ϑ_{LAB}, which is defined with respect to the scattering center by another set of apertures on the way to the detector. Velocity map imaging is a method developed by Parker, which allows the mapping of all scattering angles simultaneously. Details of the method and recent results will be presented in Section 3.3.

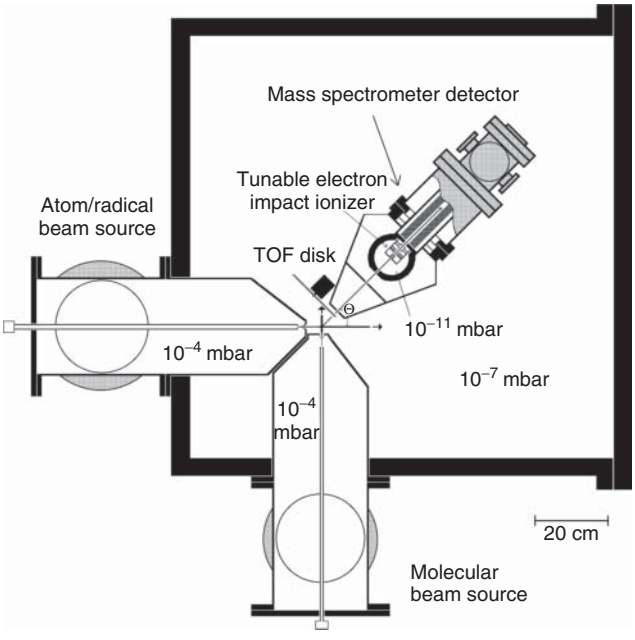

Figure 3.6 Typical crossed beam experiment consisting of two perpendicular supersonic beam sources and a rotatable mass spectrometer detector. The laboratory scattering angle $\Theta = \vartheta_{LAB}$ is given by the angle between one primary beam and the beam of detected products. (Reproduced from [27], copyright 2006 © permission from Taylor & Francis.)

Crossed beam experiments for neutral–neutral collisions have been developed by a number of groups worldwide [28–33]. Lee and collaborators [34] were the first to use it to study reactive collisions such as $F + H_2 \rightarrow HF + H$ in great detail. Flux distributions as a function of the laboratory scattering angle $F(\vartheta_{LAB})$ and velocity distributions in the laboratory frame $f(\vartheta_{LAB}, v)$ have been measured. From these quantities, flux maps in the center-of-mass frame have been derived corresponding to the differential cross section, which can be compared with theoretical predictions, leading to a detailed picture of inelastic and reactive scattering events. In favorable cases, the velocity resolution is high enough to obtain information on a state-to-state level. This has been achieved in recent years by the group of Yang, for example, for the $F + H_2$ reaction. Figure 3.7 shows a 3D diagram of the H-product flux for the $F(^2P_{3/2}) + H_2(v = 0, J = 0)$ reaction at a collision energy of $E = 0.94$ kcal mol^{-1} [35]. The reactants are predominantly prepared in just one quantum state $|i\rangle$, fluorine in the ground state fine-structure level $^2P_{3/2}$ and H_2 in the vibrational and rotational ground state (using *para*-H_2). At the given collision energy, the H atom is produced in the electronic ground state, so only the HF product can carry internal energy with vibrational quantum numbers $v = 0, 1, 2, 3$, of which the $v = 3$ state is best captured by the rotatable detector. In Figure 3.7, products with the highest velocity corresponding to HF ($v = 3, J = 0$) lie on the outer

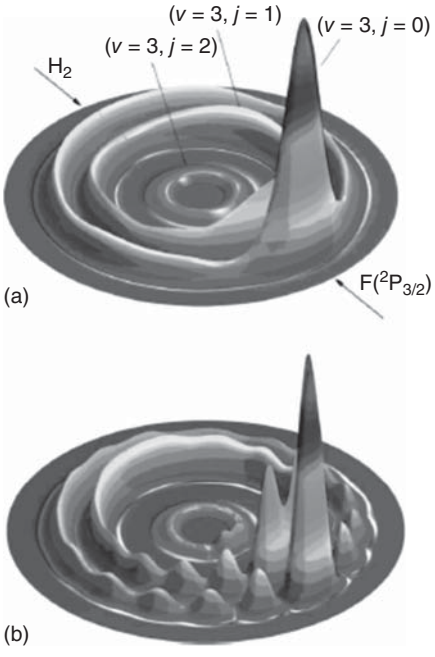

Figure 3.7 Experimental (a) and theoretical (b) differential cross section contour plots in the center-of-mass system for the $F(^2P_{3/2}) + H_2(J = 0) \rightarrow HF(v = 3,J) + H$ reaction at the collision energy 0.94 kcal mol^{-1}. The contours show the flux of H atoms as a function of the velocity of the outgoing H atom. (Copyright (2008) National Academy of Sciences, U.S.A. Ref [35].)

circle of the velocity map. Rotationally excited products HF ($v = 3, J \neq 0$) leave less energy in translation and are thus located on the inner circles of the diagram.

The angular distribution shows a strong peak in forward direction, that is, the direction in which the H_2 molecule started, and significant contributions of sideways and backward scattering. In a simple classical picture, the F atom forms a bond with one of the H atoms of the H_2 and leaves behind the other H atom. This situation is depicted in Figure 3.8, which shows the $F + H_2$ PES for the collision system for a fixed $F + H_2$ orientation ($\alpha = 61°$) which corresponds to the minimum energy path. In this "frozen picture," the reaction starts at the lower right corner where F approaches H_2, decreasing the H–F distance, R_{F-H}, almost without a barrier. After the formation of the HF product, the two H atoms are separated, thus proceeding on the PES on a trajectory with increasing H–H distance, R_{H-H}. From this PES picture, it becomes clear that the theoretical description is more involved than the atom–atom collision described above, as the PES of the internal motion is multidimensional ($3N - 6 = 3$, two distances and one angle in this case). Trajectory calculations or full quantum calculations are possible on such a PES in order to predict the differential cross section and compare it with the experiment.

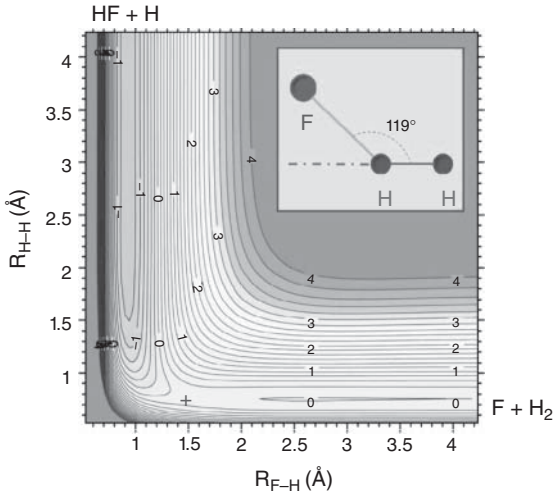

Figure 3.8 Contour plot of the PES for the $F + H_2$ reaction as a function of the H–H and H–F internuclear distances. The F–H–H bending angle has been fixed at 119° (see the inset in the figure), which is the angle of the transition state (TS). The bottom-right part of the plot corresponds to the $F + H_2$ reactant's arrangement channel, while the top-left part of the PES corresponds to the HF + H product's arrangement channel. The global TS is indicated in the figure by a + sign. (Figure courtesy of Aoiz, data from Ref. [36].)

Naively, one would expect the most efficient collision to be head on, such that the F atom is exciting the H_2 vibration, "helping" to break the H_2 bond. In such a scenario, the H-atom product would be scattered back into the direction where the H_2 reactant came from. It has been found in many experiments that this backscattering is indeed the most likely outcome. However, at specific collision energies, a strong forward scattering, as in the case presented here, is found in the experiment and from theory alike. The forward scattering under these conditions has been discussed to hint at Feshbach or dynamical resonances which are an expression of the quantum nature of the scattering process. A comparison with theoretical calculations based on a new PES [35] led, however, to the conclusion that the unexpected forward scattering is associated with a slow-down mechanism over the centrifugal barrier in the exit channel of the reaction. $F + H_2$ is one of the best studied systems, in which state-specific forward scattering has also been found earlier by QM calculations of Manolopoulos and coworkers [37] and in quasi-classical calculations (QCT) by Aoiz *et al.* [38]. The comparison in Figure 3.7 shows how well experiment and theory agree on a quantitative level, indicating that the underlying PES is known very accurately and the collision dynamics can be described adequately in such a relatively simple case of an atom–diatom reactive collision.

It turns out that the $F + H_2$ reaction system is of importance in astrophysics based on the recent detection of HF with HIFI onboard Herschel in diffuse clouds [39, 40]. The special role of fluorine is mentioned by the authors as "F being the only atom in the periodic table that can react exothermically with H_2

to form a hydride," and it was concluded that HF should be an ubiquitous tracer of molecular gas in this environment. The experiment shown here demonstrates that very detailed information is available for this system from the laboratory, from calculations of the PES, and new theoretical scattering simulations.

Today, several groups around the world are using crossed beam experiments to investigate reactive collisions relevant for astrophysics. Reactions of atoms $N(^2D)$, $C(^3P,^1D)$, $O(^3P)$, $S(^1D)$, $F(^2P)$, and $Cl(^2P)$ as well as small radicals such as C_2, OH, and CN with closed-shell molecules were studied for the first time to understand initial steps in the chemical networks present in the large variety of interstellar environments such as the cold ISM on one hand and planetary atmospheres on the other. More recently, also radical– radical collisions have become feasible in experiments because of the effective production of the radicals in molecular beam sources. As was discussed above, these reactions often can reach a reaction rate equal to those for ion– molecule reactions.

One general drawback of the crossed beam approach is that the collision energies are rather high, because they are based on atoms and molecules from sources operated at thermal energies ($E = kT = 25$ meV for $T = 300$ K). However, in cold interstellar clouds, the kinetic temperature can be as low as $T \sim 10$ K. This limitation can be partly overcome by changing the angle at which the two molecular beams intersect [41–43]. More importantly, even at higher collision energies, the full PES of interest is probed in the collision process. Therefore, if a good PES is found by comparison of experimental and scattering calculation results, the PES can be used to predict differential cross sections as well as integral cross sections over a wide range of energies and, finally, the thermal rate coefficients as a function of temperature. Thus crossed beam experiments are very valuable for understanding the dynamics of specific bimolecular collisions and serve as benchmark tests for calculations of PES and proper treatment of scattering collisions alike.

Crossed beam experiments are used to study reactive as well as inelastic collisions. In fact, inelastic collisions are easier to study in principle because molecules can be supplied in much larger abundance than atoms such as F or radicals such as C_2. As a result, the product intensities are considerably larger in inelastic experiments. Fewer product channels in inelastic collisions enhance this effect. Thus systems such as rare gas atoms–diatomic molecules were studied in great detail in a similar fashion like the $F + H_2$ reaction already in the 1980s. Understanding the efficiency of excitation of molecular levels in collisions with the most abundant molecule in space, H_2, is of great importance for the interpretation of emission spectra of astrophysically relevant molecules, such as water, H_2O, since the population of the quantum levels of the molecule is directly related to this mechanism. A detailed description of a dedicated experiment for a state-to-state inelastic $H_2 + H_2O(|i\rangle) \rightarrow H_2 + H_2O(|f\rangle)$ process is given in Section 3.3. Advanced laser techniques are used to address a specific product state $|f\rangle$, to ionize products in this state, and to switch electric fields to extract those ions at right angles to the scattering plane. Based on the different product velocities, an image of the flux of scattered products is imaged onto a two-dimensional detector, which reveals a map resembling the differential cross section, now obtained in a direct fashion

and not from a deconvolution of individual velocity distributions in the laboratory frame, $f(\vartheta_{\mathrm{LAB}}, v)$. The elegance and benefit of this technique and the results for water are discussed in Section 3.3. The diatomic–triatomic ($N = 5$ nuclei) collision system illustrates the rapid growth of complexity when trying to understand the dynamics on a state-to-state level as the PES needed is nine dimensional ($3N - 6 = 9$). This is about the level of complexity at which a PES can be calculated to an accuracy needed to compare scattering results to crossed beam experiments. For more complex systems, approximations have to be used.

Crossed beam experiments are also used to study ion–molecule collisions in great detail. Again, inelastic [44–46] as well as reactive scattering events [47] have been investigated. Ions can be detected with near-unity efficiency in contrast to neutral species which are usually ionized with a low efficiency prior to detection. This and larger cross sections make experiments with ions easier, and therefore such crossed beam experiments have been carried out already even earlier. However, it is not easy to guide ions at low energies, and therefore it is even more difficult to study ion–molecule collisions at energies simulating astrophysical situations except for high-energy encounters relevant, for example, in shocks and outflows. After all, it is at low collision energies that subtle details of the PES can lead to strong effects, that is, whether or not a molecule is formed in space, or which out of the many products will be formed (branching ratio).

3.1.3 Low-Energy Collisions in Merged Beams and Integral Cross Sections

The collision energy can be chosen much smaller in a merged-beams configuration where both beams co-propagate and might eventually travel at the same speed leading to a collision energy of $E = E_{\mathrm{t}} = E_{\mathrm{col}} \sim 0$. For neutral–neutral collision experiments, this is not really possible except if the species travel in the same beam right from the start. This will be discussed below. Since charged particles can be deflected by electric fields, it is possible to arrange a merged-beams configuration for ions or electrons in collision with another reactant species originating from a beam of atoms or molecules. One such instrument has been built in the group of Gerlich [48] to study ion–molecule reactions at very low collision energies. A detailed description of the setup and fundamental considerations on the actual collision energy when merging a molecular beam and a beam of slow ions in a guiding radio-frequency field is given in Ref. [49] along with a very detailed description of low-energy collision experiments in guided ion beam and trap experiments. Like in the crossed beam experiments, products are scattered out of their original direction. Thus, in the experiment the scattered flux is compared to the incoming flux of reactants. However, for intensity reasons, no differential cross sections are recorded but simply the attenuation of the reactant ions or the increase in product ions. The fractional attenuation or increase is a measure of the total integral cross section $\sigma(E)$.

The merged-beams apparatus described in Ref. [49] has been used to study, for example, the reaction $N^+ + H_2 \rightarrow NH^+ + H$, which is considered the first step in

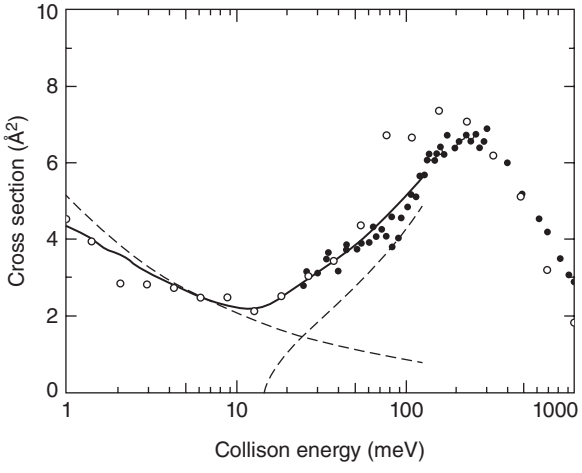

Figure 3.9 Integral cross section for the reaction $N^+ + D_2 \rightarrow ND^+ + D$ as a function of collision energy using an 80 K D_2 target. The solid circles have been measured with a crossed beam apparatus, the open ones with a merged-beams setup. (Reproduced from [50], copyright 1994 © permission from AIP Publishing.)

the formation of interstellar ammonia (NH_3) [50]. Figure 3.9 shows the integral cross section for the isotopic $N^+ + D_2$ variant of this reaction as a function of the collision energy. Solid points are from a crossed beam arrangement used in Trento for higher energies, while the open circles from the merged-beams experiment in Freiburg also extend to lower collision energies. The integral reaction cross section $\sigma(E)$ shows an increase from 10 meV to a maximum at around 150 meV. Such a behavior is typical for a reaction that is either slightly endoergic or subject to an activation barrier along the reaction path. For both scenarios, the energy needed to proceed from reactants to products is available only at elevated collision energies. Corroborative findings from trap experiments and uniform flow experiments point at an endoergicity of about 29 meV for the deuterated version and only 11 meV for the $N^+ + H_2$ reaction. This difference is mainly associated with the difference in zero-point energy of H_2 and D_2 on the reactant side with that of the NH^+ and ND^+ products. The difference in zero-point energy amounts to about 29.5 meV and is larger than the 18 meV difference in endoergicities from the experiment. Therefore it was thought to be indicative for the presence of an activation barrier.

Interestingly, $\sigma(E)$ shows an increase toward lower energies ($E \leq 10$ meV) as seen from the results of the merged-beams experiment. The temperature dependence of this contribution is indicated by a dashed line, which points to an exothermic process. It is thought to originate from collisions of rotationally excited D_2 which can react even at $E = 0$ meV based on the additional internal energy. This example shows that even small energy differences in the reactants can lead to quite different behaviors. In fact, the reactants in this experiment are prepared in a few quantum states only. N^+ occupies different fine-structure levels, $^3P_2$,$^3P_1$, and $^3P_0$.

Special care has been taken to cool down these fine-structure states prior to the collision process using buffer gas cooling of the N^+ parent ions in 20 K cold helium in a trap. There are no conclusive hints at the efficiency of spin–orbit relaxation under these conditions. However, the agreement between the solid points, where N^+ has been produced in a room-temperature ion source with an assumed statistical population of the fine-structure states $^3P_2, ^3P_1, ^3P_0 = 5 : 3 : 1$, with the data from the precooled N^+ indicated that fine-structure excitation has no influence, in contrast to the molecular rotation of the D_2 reactant and the difference in zero-point energy of reactants and products. Therefore, reactivity is not a question of only the total energy available. However, even for the seemingly simple atom–diatom reaction $N^+ + H_2 \rightarrow NH^+ + H$, the various internal states (fine-structure, rotation, and vibration) associated with energy differences on the same scale can govern the outcome of chemical reactions in a rather detailed way. Therefore state-specific experiments are needed to unfold these details. This aspect of gas-phase chemistry will be further detailed when discussing kinetic experiments in radio frequency traps.

In summary, merged-beams experiments are well adapted to determine $\sigma(E)$ over a wide range of energies, in particular at low energies. For higher energies, guided ion beam (GIB) setups have been used very extensively to determine the integral cross section $\sigma(E)$. It is discussed in Ref. [49] how the GIB technique can be used to also infer differential cross sections. Figure 3.10 shows the Trento GIB apparatus. Reactant ions are produced in an ion source. A beam of these

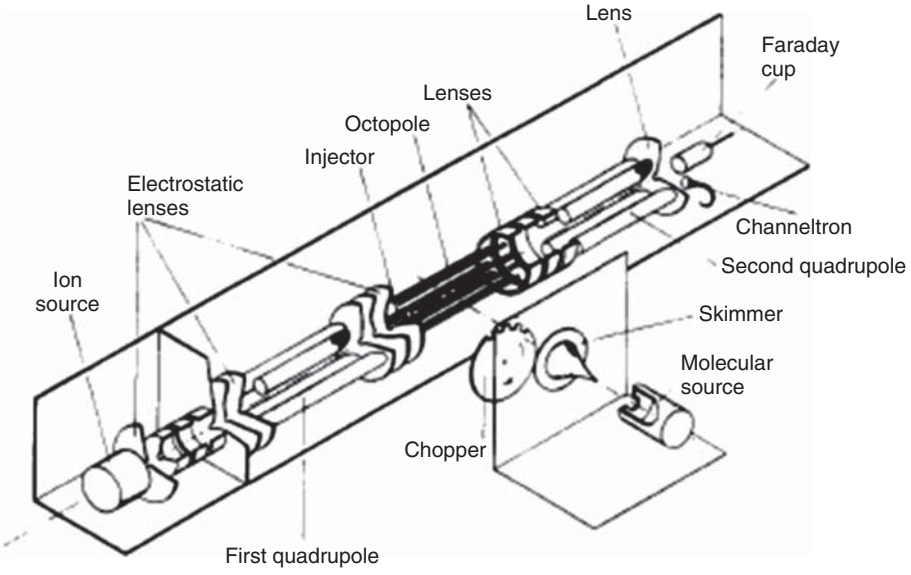

Figure 3.10 Schematic view of a guided ion beam (GIB) apparatus. It consists of a guided-ion-beam tandem mass spectrometer coupled with a supersonic molecular beam. The two beams cross at 90° at the octopole. (Reproduced from [51], copyright 1992 © permission from American Chemical Society.)

ions emerging from this source is mass-selected in a first quadrupole filter. These ions enter the field of an octopole ion guide at a fixed energy (laboratory frame). An octopole electrode configuration is chosen for guiding the ions because the radio frequency fields used for guiding change only negligibly the collision energy of the ions. Instead, the field acts as a mirror in the radial direction guiding all ions through the scattering cell. Therefore, this instrument is very well suited for determining integral cross sections where all products irrespective of their scattering direction will be recorded. In the scattering cell, the ions collide with a stationary target gas which is filled into the guide at a known number density [BC] (following the generic reaction of Eq. (3.1)). Part of the ion current I_A of species A is reacting due to the collisions with BC and thus AB products are formed. Comparing the currents I_{AB} and I_A, the rate equation (3.2) can be rewritten as $I_{AB} = \sigma(E) \cdot [BC] \cdot l \cdot I_A$, with l being the length of the scattering cell, leading to the determination of the cross section

$$\sigma(E) = \frac{I_{AB}}{[BC] \cdot l \cdot I_A}. \tag{3.15}$$

Alternatively, in the same apparatus, the ion beam can be crossed with a target from a molecular beam, see Figure 3.10. The collision energy in this arrangement is better defined because ions and neutrals travel at a given speed. Thus $\sigma(E)$ is not averaged over the thermal Maxwell–Boltzmann energy distribution of the gas in the room-temperature gas cell ($T_{MB} = 300$ K) but over a floating Maxwellian distribution ($T_{MB} = a$ few Kelvins). Still, due to the finite angular spread of the neutral beam, the energy resolution is diminished and some averaging effects have to be considered. In a merged-beams approach, the beam of ions is bend by a magnetic field to overlap the ion beam and the neutral beam. Details of kinematic averaging effects present in all these arrangements are discussed in Ref. [52].

Like in the crossed beam arrangement discussed above, in all these cases care has to be taken to ensure single collision conditions. The integral cross sections derived from these studies are suited to analyze threshold behaviors due to barriers or endothermicities as seen for the $N^+ + D_2$ reaction. Those behaviors can be compared to classical trajectory calculations or quantum scattering, from which barrier heights and endothermicities can be derived. The absolute value of the cross section is another key to the understanding of the dynamics of the scattering process. Simple models yield a coarse value for $\sigma(E)$ as was discussed above. Measured values well below these expectations indicate that the collision needs either substantial activation or the reaction has to pass a bottleneck of some sort on the PES or simply decay back to the entrance channel.

The merged-beams technique is also used to study the recombination of electrons and ions, one of the most important processes in interstellar chemistry. To simulate these collisions in the laboratory, ions are accelerated to rather high kinetic energies and injected into a storage ring where they cycle for many seconds. On a straight section of the storage ring, a beam of electrons is merged with the ion beam over a well-defined distance. The relative velocity of the collision partners is adjusted by tuning the electron kinetic energy. Upon recombination,

the products of this reaction are neutral species which no longer are held in the ring but move straight into a detector. Based on this signal, the integral cross sections $\sigma(E)$ are determined according to Eq. (3.15). Dielectronic recombination of electrons and atomic ions can be investigated, as well as the DR of electrons with molecular ions. It is the latter process that determines to a great extent which neutral atoms and molecules make up the inventory in space environments. Till recently, there was a big discrepancy on the absolute value of the rate coefficient for DR of the ubiquitous H_3^+ molecule when comparing different experimental techniques. Also, theoretical calculations were unable to predict the measured values. How this problem has been solved by a concerted effort of experiments and a big advancement in the theoretical description of the DR process is described in Section 3.2. This is another example how astrochemical modeling can be based on fundamental experiments in determining the integral cross section $\sigma(E)$.

Yet another example of laboratory work using a form of merged-beams collisions is concerned with the process of radiative detachment. As will be explained in Section 3.5, molecular hydrogen is formed in the early universe in two steps. First, an electron is attached to atomic hydrogen to build H^-. The rate-determining process lies in a subsequent radiative detachment collision with atomic hydrogen, where the two atoms attach to each other releasing the electron to form H_2. In order to study the collision process in detail, H^- is formed in a plasma source and accelerated to some 10 keV. A high-power laser is used to detach the electrons of a fraction of the fast-moving H^- to form H atoms. A slight acceleration of the ions determines the relative energy E at which the two partners collide. The formation of molecular hydrogen is then detected with a sophisticated setup by counting the fast-moving neutral species. Putting the number of products (I_{AB}) in relation to the number of reactant species (I_A) determines the integral cross section for radiative detachment in the merged-beams experiment colliding H^- and H atoms.

3.1.4
Low-Temperature Collisions in Beams and Traps, Thermal Rate Coefficients

Astrophysical environments evolve over a long period of time ($10^7 \text{a} > t > 10^4$ a). Under interstellar conditions with a hydrogen number density in dense interstellar clouds of 10^4 cm^{-3}, gas-phase collisions occur typically once every few days, and in other environments even less frequently. For obvious reasons, the timescale for laboratory experiments has to be chosen much shorter. In the experiments described so far, beams of atoms and molecules have been considered where a single collision takes place during the flight through the interaction region where the collision partners will meet. For an interaction region of 0.1 m length for a tabletop apparatus and a relative velocity of $\approx$100 m s^{-1}, for example, in beams or static gas at 300 K, the interaction time would be shorter than a millisecond. Because of these short interaction times, only processes with considerable reaction cross sections and systems providing exceptional detection efficiency can be studied in such detailed single-collision experiments aiming at integral cross sections or even differential cross sections.

Multiple collisions have to be allowed for, and longer interaction times have to be provided for less likely processes or if a larger variety of collision systems or conditions have to be considered. The collision rate K (in per second) for a collision between reaction partners A and BC is given by the collision rate coefficient k_c times the number density n =[BC] of the collision partner BC:

$$K_c = k_c \cdot n. \tag{3.16}$$

Thus the average time between collisions is $t_c = 1/K_c$. In general, only a fraction of these collisions, as discussed above, leads to reaction, i.e., $k < k_c$. As a result, the relative change of concentration of reactant A or product AB, $-\Delta[A]/[A] = \Delta[AB]/[A]$, detected in an experiment over a time period Δt is given as $k \cdot n \cdot \Delta t$. Thus the ability to determine the thermal rate coefficient k is given by

$$k = \frac{\Delta[AB]}{[A]} \frac{1}{n \cdot \Delta t} \quad . \tag{3.17}$$

Therefore, for small values of k, a larger density n or longer measuring time Δt are needed for a given fractional change of A or AB, $\Delta[AB]/[A]$.

Selecting the pressure and temperature conditions in the experiments enables one to vary the density and thus the time between collisions over a wide range, allowing measurements to be conducted before collisions with the vessel wall take place. However, the possible density range is limited by the fact that at higher pressures a collision with a second molecule can occur while the first two partners are still in interaction. Such ternary processes can play an important role in the chemistry of dense atmospheres such as those of planets; however, in order to determine the rate coefficient for a binary process, ternary collisions have to be avoided. For that, the interaction time τ has to be shorter than the collision time, $t_c > \tau$, that is, the time between two collisions. A characteristic interaction time is given by the range of interaction, typically several Å= 10^{-10}m and the corresponding relative velocity of the collision partners. A flyby event under thermal conditions with $v \approx 100$ m s^{-1} thus takes τ =10 ps or less. Instead of a transit, the collision partners can form a long-lived complex, where, for example, excess energy is redistributed among the different internal degrees of freedom before the complex decays back into the reactants. For an estimation of the necessary number density, an interaction time of τ <0.1 ms is more realistic. In conclusion, binary collisions dominate over ternary collision up to n<$1/k_c\tau$. For a typical collision rate coefficient of $k_c = 10^{-9}$cm^3 s^{-1} for ion–molecule encounters as discussed exemplarily above, the number density should be smaller than 10^{13}cm^{-3}, which corresponds to a pressure of about 10^{-3} mbar at room temperature. The validity of this rough estimate will be discussed at the end of this introduction for the $C^+ + H_2$ association.

The other quantity entering Eq. (3.17), namely the measuring time Δt for the experiments, is limited by the ability to maintain the reactants within the experimental conditions. Ideally, the reactants could be stored over long times. While this is possible for charged particles as will be discussed below, trapping is a technique which only in recent years has become an option for neutral reaction partners because of the extremely high electrical fields necessary [53–56]. In cell

experiments, jets, and beams, various kinds of atoms and molecules can be provided over periods of typically $\Delta t \sim$ milliseconds. For such times Δt, a detectable relative change $\Delta[AB]/[A] = 0.01$, and a number density of 10^{13}cm^{-3} as estimated above, the smallest measurable rate coefficients would be $k > 10^{-12}$cm^3 s^{-1}. Correspondingly, even smaller rate coefficients become measurable if measurement times exceeding milliseconds are possible. This is clearly the case for experiments in radio frequency (RF) traps where the storage times are limited by parasitic reactions or practical aspects to 100 s (five orders of magnitude longer than in cells and jets). In summary, when allowing more than one collision in an experiment, the rate coefficients in the range discussed in Figure 3.2 can be determined in cells, flow systems, jets, and traps.

Another challenge for conducting kinetic experiments is the thermal environment that needs to be established in order to derive the thermal rate coefficients $k(T)$. In high-pressure environments, thermalization can be reached as a result of the large number of nonreactive, thermalizing collisions before and after the reactions. Studying processes at high (>600 K) temperatures is a technical challenge because outgassing of impurities from the heated experimental environment might take place and lead to parasitic reactions. Additionally, molecules may start to decompose at elevated temperatures. At low temperatures (~10 K), on the other hand, condensation of the precursor or reactant molecules may hinder the determination of the target number density needed to determine the rate coefficient using Eq. (3.17). Therefore it is desirable to compare values from different experimental techniques, some of which are detailed in the following.

3.1.4.1 Selected Ion Flow Tubes

A common method to study ion–molecule chemistry is the selected ion flow tube (SIFT). One system, also used for astrochemical studies, is shown in Figure 3.11. Here, the ions, denoted as A^+ in Figure 3.11, with concentration $[A^+]$ following our previous labeling of the reactants are entrained into a considerable flow of a buffer gas (pressure ~ millibar, flow rate ~100 atm cm^3 s^{-1}). The flow rate of the gas, the pumping speed, and the diameter of the cell set the timescale (Δt) of the experiment. The ions are mass-selected under high vacuum conditions prior to injection into the gas flow [57]. The loss of reactants ($-\Delta[A]/[A]$) or the formation of products ($\Delta[AB]/[A]$) is recorded downstream, where a fraction of the flow enters a second mass spectrometer. The rate coefficient is determined from Eq. (3.17) by varying the concentration (number density) of the target gas $n = [BC]$ which is let into the flow at some point downstream of the injection of the ions. Loss of the reactant due to diffusion in the flow has to be taken into account to derive proper rate coefficients from these measurements. The flow tube can be heated or cooled to simulate the various astrophysical environments. Adams and Smith pioneered the field by studying many ion reactions with molecular hydrogen at room and liquid nitrogen temperature (77 K). More recent advancements concern reactions with atoms (H, N, and O) and in particular reactions of hydrocarbon cations ($C_mH_n^+$) with atomic hydrogen. From these studies, it turns out that hydrogen abstraction $C_mH_n^+ + H \rightarrow C_mH_{n-1}^+ + H_2$ prevails. The only other

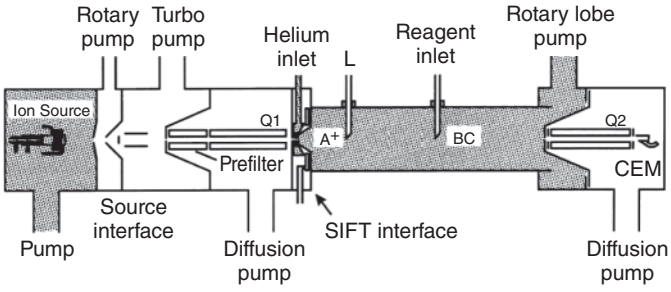

Figure 3.11 Schematic diagram of a selected-ion flow tube (SIFT) tandem mass spectrometer. Ions from the ion source are selected with a quadrupole mass filter (Q1) before injection into the flow tube. Reactants are introduced downstream in the flow tube. A second quadrupole mass filter (Q2) is used downstream to separate the reactant and product ions in the sampled reaction mixture. (Figure courtesy of Bohme.)

channel is the association of the hydrogen atom $C_mH_n^+ + H \rightarrow C_mH_{n+1}^+ + h\nu$. The reverse reaction $C_mH_{n-1}^+ + H_2 \rightarrow C_mH_n^+ + H$ has been studied as well in detail. As a result, the degree of hydrogen saturation for $C_mH_n^+$ in interstellar environments can be modeled reliably [58].

The role of negative ions and their chemistry was not clear even though they had been postulated some 30 years ago. The negative ions C_4H^-, C_6H^-, C_8H^-, and CN^- were detected in the ISM recently [59–61]. It has been found in SIFT experiments that C_n^- anions react rapidly with atomic hydrogen either by associative detachment $C_n^- + H \rightarrow C_nH + e^-$, which leaves the neutral species behind, or by association for larger chains (for $n \geq 7$). It also turns out that hydrogenated carbon chains react exclusively by associative detachment and none of these anions reacts with molecular hydrogen. Thus reactions of anions with H atoms are a main route for their destruction. At present, two processes are discussed as the main routes for formation: (i) radiative attachment

$$A + e^- \rightleftharpoons (A^-)\dagger \rightarrow A^- + h\nu \tag{3.18}$$

and (ii) dissociative attachment

$$AB + e^- \rightarrow A^- + B. \tag{3.19}$$

The latter process proceeds only exothermically, though, when the electron affinity of A exceeds the AB bond energy. Radiative attachment will be successful when the complex $(A^-)\dagger$ lives long, that is, for large molecules with many degrees of freedom. In conclusion, SIFT experiments are one of the key experiments providing rate coefficients for whole sets of reactions. Most of our knowledge on gas-phase anion chemistry stems from SIFT experiments. But this knowledge is still rather meager because there are no experiments on the anion formation processes. Experiments with low-energy electrons are rather difficult, and at present no standard technique supplies thermal rate coefficients for the above-mentioned processes. Instead, astrochemical modeling relies on the quality of

theoretical predictions that are mostly based on phase-space calculations, which will be explained in some detail below for radiative association, a related process.

3.1.4.2 Laval Nozzle Expansions

Flow tube experiments can also be used for neutral–neutral reactions. As mentioned above, especially reactions of one or two radicals (atoms and molecules) can have similar reaction rates as ion–molecule reactions and are therefore relevant to astrochemistry. The radicals of interest can be formed by microwave discharge, pyrolysis, photo-induced processes, or by secondary reactions prior to the injection into the main flow tube. Again, because of the constant flow rate, the concentration of reactants and products at a given point downstream can be related to the reaction time. For a given concentration of the co-reagents, the reaction rate coefficient can be calculated using Eq. (3.17). As for the SIFT experiments, the flow tubes can be cooled to cryogenic temperatures. But because of their considerable length and low-temperature condensation problems, cooling is limited to ~200 K. A real breakthrough in that respect is the CRESU method, pioneered by Rowe and coworkers [62] and further developed by Sims, Smith, and Canosa. The heart of this flow reactor is a Laval nozzle. Figure 3.12 shows the outline of such a nozzle. Gas is supplied in a stagnation region of known temperature (T_0), pressure (p_0), mass density (ρ_0), and related number density (n_0). Because of the proper design of the nozzle shape, a supersonic flow (flow velocity $u \gg 0$, mach number $M > 1$) exits after the throat as a uniform flow (u = constant) in its isentropic core part with constant temperature ($T < T_0$) and number density ($n < n_0$) downstream of the nozzle exit. This uniform flow enters into a background gas of equivalent pressure p, and extends over several tens of centimeters. Probing the concentration of the reactants and products at various points downstream by mass spectrometric or optical techniques enables deriving the desired rate coefficients. Owing to the supersonic flow into a vacuum vessel, reactions proceed without any wall interaction. As a result of the adiabatic expansion, low temperatures (15 K without precooling of the stagnation region) relevant for astrochemistry can be reached in continuous expansions. Large flow rates have to be handled in those experiments, requiring large and expensive pump equipment. Therefore, several groups use pulsed Laval nozzle expansions, which need much lower pumping capacities and still reach temperatures as low as some 50 K. For each temperature T and pressure p, a new nozzle has to be designed, which is customized

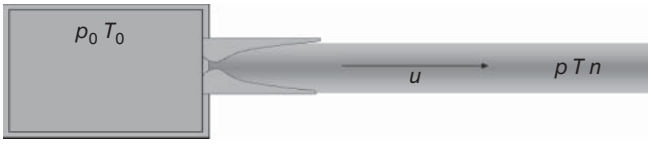

Figure 3.12 Laval nozzle. A longitudinal uniform flow is generated by the gas exiting from the nozzle. Because of viscosity, a boundary layer develops radially close to the walls of the nozzle, generating a radial gradient from the isentropic core to the walls. (Figure courtesy of Canosa.)

for the buffer gas used as a carrier of the reagents. The relatively high pressure (∼ millibar) ensures thermalization of the reagents and products, thus forming a truly thermal environment. Many types of collisions can be studied in this environment: neutral–neutral reactions, ion–neutral reactions, electron–neutral collisions, and inelastic collisions (electronic, spin–orbit, vibration, rotation).

Again, radical precursors or ions can be created inside the expansion or after exiting the nozzle throat as a starting point of the reaction process (e.g., via pulsed photolysis or by an electron beam). The biggest success of these uniform flow experiments is obtaining the rate coefficients for low-temperature neutral–neutral reactions which could not be determined experimentally otherwise. Reactions of radicals with unsaturated molecules as well as reactions between two radicals often lead to a negative temperature dependence, that is, they become faster at low temperatures. This has significant consequences on the predictions of chemical networks and thus on our understanding of astrochemistry as a whole. A rather detailed description of the method and a discussion of the rate coefficients derived have been provided recently [7, 63]. As an example, the collisions of $O(^3P)$ with a number of alkenes are presented [64]. The room-temperature rate coefficient for those reactions is $\approx 10^{-11}$ cm^3 s^{-1} and increases at lower temperatures, exceeding 10^{-10} cm^3 s^{-1} for butene (C_4H_8). Earlier, Smith [65] proposed two criteria for reactions that are expected to have rate coefficients larger than 10^{-10} cm^3 s^{-1} at 10 K. If the ionization energy (IE) of the neutral is not too much higher than the electron affinity (EA) of the radical [(IE–EA) < 8.75 eV], then the energy barrier for rearrangement of the nuclei in the reaction is assumed to vanish. As a result, the reaction can proceed at low temperatures with a model which is governed by the long-range interaction forces and by the capture idea discussed above for simple ion–molecule (induced dipole) reactions. In fact, calculations of long-range transition-state theory by Georgievsky and Klippenstein [66] compare very favorably with trajectory calculations and, more importantly, with experiments.

Another example of the success of the CRESU technique concerns reactions of the $C_2(X\,^1\Sigma_g^+)$ radical with a number of hydrocarbons [67]. The C_2 concentration has been created by 193 nm photolysis of C_2Cl_4. The concentration of the singlet $C_2(X\,^1\Sigma_g^+)$ has been detected by laser-induced fluorescence (LIF) by exciting the Mulliken bands of C_2 ($D\,^1\Sigma_u^- \leftarrow X\,^1\Sigma_g^+$) (0,0) and recording the fluorescence in resonance at around 228 nm. The photolysis and the LIF excitation are directed along the beam axis. The fluorescence is detected at a given distance downstream at right angle. Thus, from the time-dependent LIF signal, first-order rate coefficients have been derived. In another step, the concentration of the hydrocarbon reactants have been varied. From the resulting kinetic plots, the second-order rate coefficients $k(T)$ have been obtained.

Reactions with saturated (CH_4, C_2H_6, and C_3H_8) as well as unsaturated (C_2H_2 and C_2H_4) hydrocarbons proceed very rapidly ($\geq 10^{-10}$ cm^3 s^{-1}) in the temperature range 24–300 K with the exception of methane. The temperature dependence of those reactions can be well reproduced by the Arrhenius–Kooij formula, Eq. (3.3). Figure 3.13 shows the temperature dependence of the reaction of C_2 with propane. It is clearly visible that this reaction exceeds 10^{-10} cm^3 s^{-1}

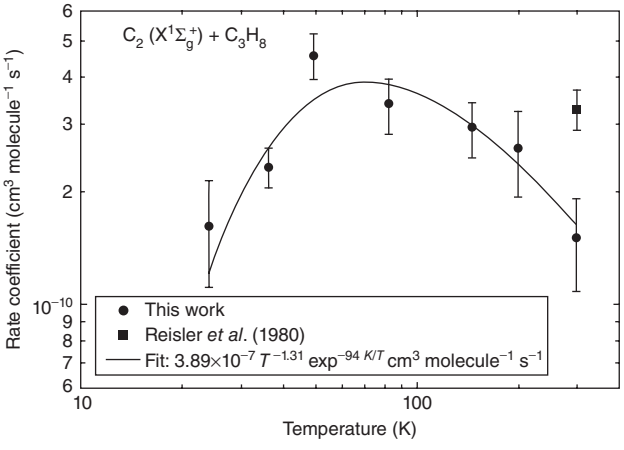

Figure 3.13 Rate coefficients for the reaction of C_2 with C_3H_8 as a function of temperature, displayed on a log–log scale. The filled circles show the results obtained in a CRESU apparatus, and the solid line is a fit. (Reproduced from [67], copyright 2007 © permission from Elsevier.)

over the full temperature range. Like for the other hydrocarbons, the exponent β is of the order of -1 and the Arrhenius parameter γ is $\approx$100 K. This leads to the maximum of the rate coefficient of around 80 K. Unlike in the case of the $O(^3P)$ reactions with the alkenes, the rate coefficient does not increase monotonically toward low temperatures. Therefore, the physical picture for C_2 collisions with hydrocarbons is different and not fully understood. However, because of the high efficiency of these reactions even at low temperatures, they have to be included in the modeling of the atmospheres of planets where hydrocarbons can lead to the destruction of C_2 ($X\ ^1\Sigma_g^+$) and thus alter the photophysics of these environments. As an example, the influence of the laboratory results on the photochemistry of Titan, a moon of Saturn, is described in Ref. [67]. The authors compare the destruction of C_2 by methane with that of the other hydrocarbons. It is found for Titan and the giant planets that the $C_2 + CH_4$ data should be revised in the models but there are several altitudes in the atmospheres of these planetary objects where other reactions compete significantly with $C_2 + CH_4$. In summary, the modeling of planetary atmospheres has to be updated by the CRESU experimental data to account for the proper destruction rates.

Over the last 20 years, reactions with many atomic (C, Al, Si, B, and O) and molecular (CH, CN, OH, NH, C_2H, C_2, and C_4H) radicals have been studied in a wide range of temperatures thanks to the CRESU technique. This method has helped in further developing some of the physical pictures for reaction mechanisms as discussed for the reactions of $O(^3P)$ with the alkenes as prototypes for barrierless reactions. Experimental data are used to compare to the results of theoretical calculations on a quantitative level (e.g., Ref. [66]) and to compare with analytical expressions useful to parameterize astrochemical modeling as described for the reactions of C_2 with hydrocarbons. A very recent success story of CRESU

concerns the fundamental F + H_2 reaction [68], which has been studied at very low temperatures for the first time. In this example as well as in the investigations on the OH + methanol reaction [69], it has been found that tunneling perhaps plays a more important role in astrochemistry than previously thought. Another interesting aspect of chemistry concerns the branching ratios in reactions, which have also been studied in CRESU-type experiments recently [70].

As for all experiments, the CRESU technique has limitations. In the Laval nozzle expansions, the number density of the carrier gas exceeds $10^{16}\,\mathrm{cm}^{-3}$. For a collision rate coefficient of $10^{-10}\,\mathrm{cm}^3\ \mathrm{s}^{-1}$, this corresponds to one collision per microsecond. At low temperatures where complex lifetimes become comparable, three-body collisions can no longer be neglected but might dominate instead. As a consequence, it can be difficult to determine small binary rate coefficients with the CRESU technique as discussed already above using Eq. (3.17). On the contrary, termolecular collisions

$$\mathrm{A} + \mathrm{B} + \mathrm{M} \rightarrow \mathrm{AB} + \mathrm{M} \tag{3.20}$$

have been studied in CRESU experiments. We will describe below how the ternary rate coefficients k_3 for these reactions are derived and how complex lifetimes can eventually be inferred from these quantities.

3.1.4.3 Trap Experiments

In trapping experiments, the number density of the reagents can be varied over many orders of magnitude (in ion traps from around $10^8\,\mathrm{cm}^{-3}$ to above $10^{16}\,\mathrm{cm}^{-3}$). Here, the reagents are available for rather long times (milliseconds to hundreds of seconds) in a finite volume. From Eq. (3.17), one can see that using the longest trapping times and the highest number densities (avoiding three-body collisions), the experimental ability to detect a small fractional change of AB, Δ[AB]/[A], determines the minimum measurable rate coefficient k. As a result, trapping experiments are extremely sensitive while determining not only small rate coefficients but also large ones in the same setup.

Figure 3.14 shows a 22-pole ion trap as the heart of a tandem mass spectrometer guided-ion-beam apparatus. In this setup, primary ions are created inside a storage ion source by electron bombardment. Since the ion source is itself a trap, chemical reactions can be used to create secondary ions as a starting point of the experiment. For example, ionized H_2 reacts with the neutral H_2 precursor gas to create H_3^+. As a result, a large variety of secondary ions can be created efficiently. Ions are extracted from the source periodically in short pulses. In a first quadrupole (Quad I), the ion of interest is mass-selected and enters the 22-pole trap at kinetic energies of about 100 meV or less. Trapping is achieved by a radio frequency (~20 MHz) voltage alternately applied to the 22 rods. This leads to an effective trapping potential in radial direction. Storage along the trap axis is achieved by appropriate DC potentials of the entrance and exit electrodes with respect to the DC potential of the 22 poles. Higher order multipoles are characterized by a large field-free region in the trap where ions can be cooled to the ambient temperature by collisions with He buffer gas. In the trap shown, the buffer

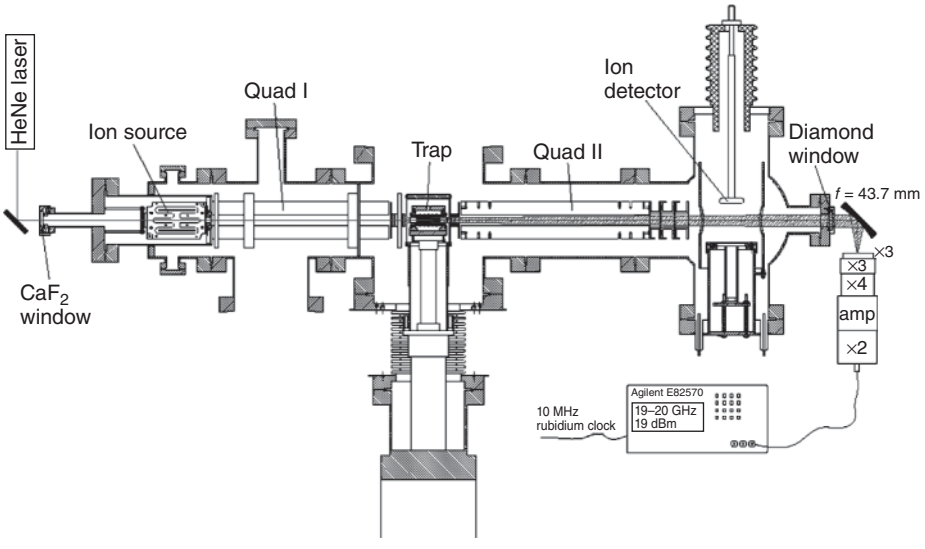

Figure 3.14 Setup of a 22-pole trapping apparatus. (Modified figure from Ref. [71].) The ions are generated and collected in the storage ion source, mass-selected in a quadrupole mass filter (Quad I), and then stored in the 22-pole ion trap. This trap consists of 22 small rods which confine the ions in the radial direction when suitable rf voltages are applied. Control of the injection and extraction of the ion cloud is achieved by small electrodes. On entry, the ions are cooled down to the ambient cryogenic temperature by a short, intense helium pulse. During the storage period of up to several seconds, the ions can collide with the admitted precooled reactant gas. The result of this interaction is detected by extracting the stored ion cloud into a second mass filter (Quad II) and counting the number of product ions in the detector. This instrument is suitable for terahertz spectroscopy of molecular ions, as discussed in Ref. [72].

gas is admitted as a short, intense pulse through a valve. This gas pulse is cooled to the ambient temperature by collisions with the wall prior to collisions with the injected ions. Besides the He pulses, precooled reaction gas is admitted constantly to the trap volume.

Reactant and product ions are extracted from the trap after a variable time Δt. They are mass-analyzed in the second quadrupole mass filter (Quad II) and detected in a Daly-type detector which is optimized for near-unity, mass-independent detection efficiency. By varying Δt and the transmitted mass in the second quadrupole, the time evolution of the ionic reactant and all ionic products can be recorded. Figure 3.15 shows the reaction of initially stored H_2^+ reacting with H_2 at a nominal temperature of 13 K to form H_3^+ as described above for the source. H_2^+ decays mono-exponentially (see linear behavior in the semilogarithmic plot) as expected for the kinetics described by Eq. (3.2). From the slope $(1/\tau)$, the rate coefficient k is inferred at a known number density of the target gas, $n = [BC]$. It can easily be verified that the measurement is not affected by three-body collisions by checking that k does not depend on the value of n. The trap temperature can be varied from room temperature (300 K) to the

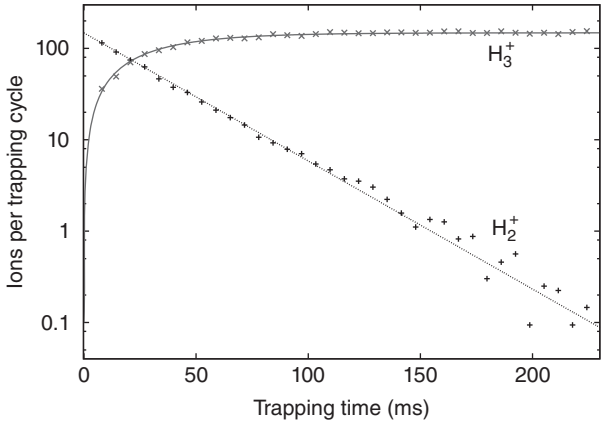

Figure 3.15 Temporal evolution of H_2^+ ions stored in hydrogen gas with number density $[H_2] = n = 1.55 \times 10^{10}$ cm^{-3} at a nominal trap temperature of 13 K. The solid lines are the result of a simple numerical simulation, yielding the rate coefficient $k = 2.1 \times 10^{-9}$ cm^3 s^{-1} for the formation of H_3^+.

lowest temperature reached by the cold head ($T \geq 10$ K). Thus, bimolecular rate coefficients for the coldest molecular clouds and other environments can be simulated in traps.

Figure 3.16 shows the effective bimolecular rate coefficient k^* for the reaction of C^+ with H_2 as a function of the H_2 number density. For densities larger than 10^{13} cm^{-3}, the rate coefficient depends linearly on the number density, indicating a three-body process

$$C^+ + H_2 + H_2 \rightarrow CH_2^+ + H_2 \tag{3.21}$$

as described before in Eq. (3.20) for $B = M = H_2$. k^* (dashed line) follows the relation $k^* = k_3 \cdot n$ and k_3 is determined to be $k_3 = 1.1 \cdot 10^{-28}$ cm^6 s^{-1}. For smaller number densities, the rate coefficient levels off to a constant value, which corresponds to the two-body process of radiative association $C^+ + H_2 \rightarrow CH_2^+ + h\nu$ with rate coefficient $k_{\mathrm{rad}} = 6.7 \cdot 10^{-16}$ cm^3 s^{-1}. This value is more than six orders of magnitude smaller than the Langevin limiting value of the order of $k_{\mathrm{L}} = 10^{-9}$ cm^3 s^{-1}, demonstrating the sensitivity of the trapping method, as discussed above. Conceptually, the process of radiative association is related to radiative attachment, which is also described as a two-step mechanism

$$C^+ + H_2 \rightleftharpoons (CH_2^+)\dagger \rightarrow CH_2^+ + h\nu. \tag{3.22}$$

Here, C^+ and H_2 form a collision complex $(CH_2^+)\dagger$ in every collision (rate coefficient: k_{L}, $\rightharpoonup$ in Eq. (3.22)). Most likely, this complex decays back into the reactants because of the total energy being above the dissociation limit (dissociation rate: $K_{\mathrm{dis}} = 1/\tau_{\mathrm{dis}}$, $\leftharpoondown$ in Eq. (3.22)) determined by the lifetime with respect to dissociation, τ_{dis}. Alternatively, the complex can undergo an electronic or a vibrational transition by emission of a photon (radiative rate: $K_{\mathrm{rad}} = 1/\tau_{\mathrm{rad}}$, $\rightarrow$ in Eq. (3.22)). This rate corresponds to the sum of all Einstein A coefficients of the individual

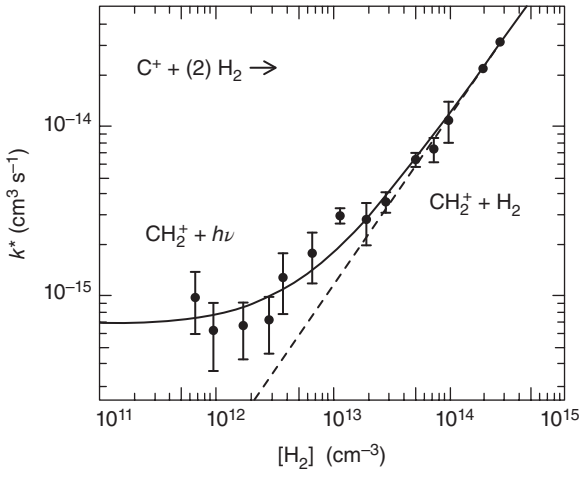

Figure 3.16 Effective binary rate coefficient k^* for the reaction of C^+ with n-H_2 at a nominal temperature of 10 K. The dashed line denotes the contribution from the ternary collision processes $k_3 \cdot [H_2]$, which prevails for $[H_2] > 10^{13}$ cm^{-3}. (Reproduced from [73], copyright 1993 © permission from AIP Publishing.)

transitions. An approximate relation has been derived for the vibrational energy E_{vib} of s coupled oscillators with an Einstein A_i coefficient for the fundamental transition of the ith mode (see chapter 37 of Ref. [20]):

$$K_{\mathrm{rad}} = \frac{1}{\tau_{\mathrm{rad}}} = \left(\frac{E_{\mathrm{vib}}}{s}\right) \sum_{i=1}^{s} \frac{\mathrm{A}_i}{h\nu_i}. \tag{3.23}$$

For vibrational transitions, these lifetimes are typically milliseconds to seconds. In contrast, the lifetime of the collision complex is of the order of nanoseconds to microseconds. It can be calculated from the density of states, which is strongly related to the size of the complex and to the bond energy, using statistical theories. This statistical approach in combination with the approximate relation for the radiative decay (3.23) and the capture rate coefficient (k_{L}) lead to very good approximate values for the rate coefficient for radiative association. Thus, our understanding of the processes that are dominated by phase-space considerations leads to quantitative estimates when experiments are missing as in the case of radiative attachment.

The experiments described in this chapter have been used to introduce differential cross sections, integral cross sections, and rate coefficients for astrophysically relevant collision systems and to relate these quantities to observables from experiment as well as to their theoretical counterparts. We derived some estimate values for the physical quantities in order to equip the reader with some useful physical pictures which are able to describe the respective gas-phase collision systems in a quantitative manner. For the modeling of gas-phase processes in space, a canonical ensemble is assumed where the probability of finding the system in a particular microscopic state i with energy level E_i is given by the Boltzmann distribution

($\exp^{-E_i/kT}$) and therefore the rate coefficient is a function of temperature $k(T)$, which is parameterized as given above. Especially, at low temperatures where only a few quantum states are populated, those states might not be in a thermodynamic equilibrium and thus the Arrhenius–Kooij formula (3.3) is no longer a proper description for astrochemical modeling. Instead, a whole set of state-specific rate coefficients k($i \rightarrow f$,T) are needed. This limitation points at the role of individual quantum states in reaction systems, which will be described in detail in Section 3.4 later in this gas-phase chapter.

Acknowledgement

The author wishes to thank Diethard Bohme for supplying information on the SIFT technique and its astrophysical applications. He acknowledges the suggestions and the supply of a figure from Javier Aoiz and Paolo Tosi. Careful reading and suggestions from Oskar Asvany, Dieter Gerlich, André Canosa, and Eric Herbst are gratefully acknowledged.

3.2
Dissociative Recombination

Wolf Geppert, Andreas Wolf, and Juraj Glosik

3.2.1
Principle and Main Occurrence

Natural and man-made plasmas such as those present in interstellar clouds, star-forming regions, planetary ionospheres, CSEs, cometary comae, as well as combustion engines and nuclear fusion reactors contain a multitude of molecular and atomic cations. Since such plasmas are electroneutral, a corresponding negative charge to compensate for these positive ions must exist either in the form of electrons or anions. Even though there have been some ongoing debates about the carriers of negative charges in the ISM, which have been fueled by the recent detection of anions found in several astronomical objects, it is still widely believed that electrons largely take up this role in the above-mentioned environments. Therefore, reactions between electrons and ions are of paramount importance in astrophysical plasmas. When an electron recombines with an ion, a highly excited intermediate is formed, which can dissipate its energy in different ways. Accordingly, the following types of reactions are possible when an electron meets an ion: AB^+:

- Elastic, inelastic, and superelastic collisions, $AB^+(v) + e^- \rightarrow AB^+(v') + e^-$;
- Radiative or dielectronic recombination, $AB^+ + e^- \rightarrow AB + h\nu$;
- Ion-pair formation, $AB^+ + e^- \rightarrow A^+ + B^-$;
- Dissociative excitation, $AB^+ + e^- \rightarrow A^+ + B + e^-$;
- Dissociative ionization, $AB^+ + e^- \rightarrow A^+ + B^+ + 2e^-$; and

– Dissociative recombination, $AB^+ + e^- \rightarrow A + B$.

Of these reactions, dissociative recombination (DR) [74] is arguably the most important process when molecular ions interact with electrons at low temperature. Elastic ($\nu' = \nu$), superelastic ($\nu' < \nu$), and inelastic ($\nu' > \nu$) collisions do not imply a chemical reaction (and are therefore of only minor astrochemical interest), although they play a decisive role in the thermal balance of natural and man-made plasmas. Ion-pair formation, dissociative ionization, and excitation tend to be too endoergic to be relevant for the interstellar medium. Radiative recombination and the related process of dielectronic recombination are important reactions of atomic ions in astronomical environments. However, in the hitherto investigated molecular ions their rate constants are usually well below those for DR. There might be some exceptions in the case of very large polyaromatic hydrocarbon ions, where radiative association might be favored because of the increased possibility of these species to undergo intramolecular vibrational relaxation. A further special case is also HF^+, for which the rate constant of the ion-pair formation was found to be only one order of magnitude below that for DR [75]. Nevertheless, DR is widely regarded as the dominating reaction of molecular ions and electrons in space.

DR is also a barrierless reaction, which makes it feasible even in very cold environments like dark cores and Bok globuli. Surprisingly, it was long regarded as too slow a process to be a major player in the degradation of molecular ions, and was first discussed by Bates and Massey [76] in as early as 1947 as a possible sink for ions in Earth's ionosphere. During the last decades, numerous research efforts have been undertaken to investigate DR processes of a large number of interstellar and other ions. In this chapter, the mechanism and relevance of DR and the possibilities and challenges of its experimental and theoretical investigations will be discussed.

3.2.1.1 Mechanisms of Dissociative Recombination

A possible mechanism of DR was first proposed by Bates [77], which involved a two-step process in which the electron first is captured by the molecular ion into an empty orbital under simultaneous excitation of one of the bound electrons. A neutral molecule is thus formed in a doubly excited and usually strongly repulsive state located above the first ionization potential. In the second step, the molecule dissociates rapidly along the repulsive potential energy curve. Bates estimated that DR would proceed at rate of about 10^{-7} cm^3 s^{-1}. Interestingly, many molecular ions have DR rate constants an order of magnitude below this value; only very complex ions tend to show faster DR reactions. Feasibility of this so-called direct process at zero relative kinetic energy strongly depends on the availability of dissociative potential surfaces crossing one of the ion ground states. Nevertheless, DR is not restricted to molecular ions where this is the case. In addition to this mechanism, an indirect process was proposed by Bardsley [78] and almost simultaneously by Chen and Mittelman [79], in which the electron is captured into a Rydberg state belonging to a series converging to

a vibrationally excited state of the ion core. If this Rydberg state is crossed by an electronically doubly excited repulsive state, it can predissociate into fragments. In this scenario, the availability of suitable Rydberg states into which the electron can be captured is vital for the feasibility of DR. If a certain relative kinetic energy of the reactant matches the energy difference between the ion state and a Rydberg state the electron can be captured in, maxima in the cross sections (resonances) can appear at this energy. Such resonances have, for example, been observed in the DR of HD^+ [80] and H_2^+ [81]. For these ions also, another interesting phenomenon has been observed: Since the repulsive H_2 $^1\Sigma_g^+$ state crosses the potential curve of the $^2\Sigma_g^+$ ground state of the ion above the $\nu = 2$ vibrational level of the ion, the direct process is hindered for the vibrational ground state of the ion. For the ground state, this leads to a DR rate constant which is about an order of magnitude below the ones for the excited vibrational states in the DR of H_2^+ and D_2^+ [82] and a similar ratio in HD^+ DR [83, 84]. Thus, this very simple molecular ion illustrates the importance of both the direct and the indirect mechanism of DR. Schematics of these different processes are depicted in Figure 3.17.

The high exoergicities of DR reactions often imply that a multitude of energetically possible (exoergic) reaction channels exist, whose relative importance is not straightforward to predict. In an earlier theoretical study, Bates and Massey [76] argued that the preferred pathway in such processes should be the one involving the least rearrangement of valence bonds. However, DR reactions do not tend to follow this prediction, and three-body breakups (which should be extremely unlikely following Bates's prediction) have been found for many ions. As a typical example, one can consider the DR of H_3O^+, which is the final step in the gas-phase synthesis of interstellar water. This process should, according to Bates, preferably form H_2O and H. However, the following energetically feasible pathways exist for

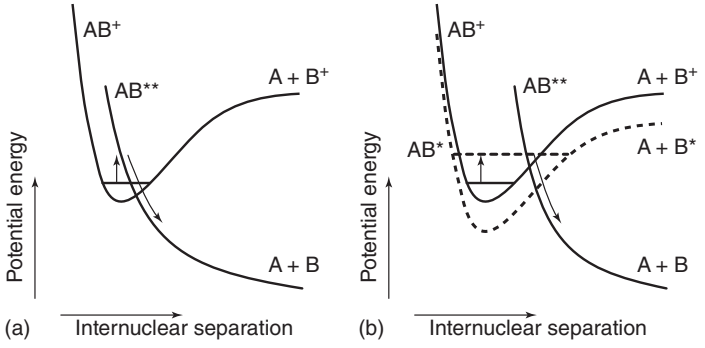

Figure 3.17 Schematic potential curves for cases where the direct (a) and the indirect mechanisms (b) give the dominant contribution to DR. Often, both effects occur at similar strengths, and quantum mechanically interfere with each other, which reflects in the energy dependence of the DR cross section.

this reaction:

$$H_3O^+ + e^- \rightarrow \begin{cases} H_2O + H \\ OH + 2H \\ H_2 + OH \\ O + H_2 + H \end{cases}$$

In this process, the DR channel leading to OH + 2H is by far the most important one (with a branching fraction of 60%), whereas H_2O and H are only produced in 25% of all DR events [85]. These results were somewhat different from the values used in previous models [86]. Owing to the unpredictability of the product branching ratios of DR reactions, experimental studies are necessary to secure reliable input data for astrochemical models.

In many cases, the temperature dependence of the DR rate constants follows a simple power-law behavior, as one would expect for a barrierless reaction. However, exceptions do exist. Opening of additional autoionization channels at higher collision energies might induce a steeper rate dependence on the temperature. Also, at higher collisional energies, slightly endoergic product channels might become viable. Vibrationally excited states might have much higher rates as a result of intersections with dissociative potential energy surfaces which do not exist for the ground state, as mentioned for H_2^+ and its isotopologs [81–84]. Last, but not least, resonances driving indirect processes can result in higher DR rates at elevated temperatures, as seen in the case of HeH^+ [87]. In the DR of the H_2^+ ion, even the nuclear spin plays a considerable role [81], and many resonances observed in *para*-H_2^+ are not found in the *ortho* form, and vice versa. Since the temperatures of astronomical objects span a wide range, such effects might substantially affect the ion chemistry in these environments.

3.2.1.2 Dissociative Recombination in Astronomical Environments

The large rate constants for molecular ion recombination render DR the dominant neutralizing process in a plasma where the gas temperature is a few thousand degrees or less and the electron temperature is lower than a few electronvolts. These conditions prevail in the interstellar medium and in planetary ionospheres. DR not only destroys molecular ions but also leads to the formation of neutral molecules. The importance of DR reactions is due to two facts: First, the process is barrierless, and second, like many reactions without an activation energy, its rate constant tends to increase with decreasing relative translational energy of the reactants. Roughly, the rate constants α of many DR reactions (especially those for larger ions) follow the expression (A and β being constants)

$$\alpha = A(300\,\mathrm{K}/T)^{\beta} \tag{3.24}$$

in which β usually lies between 0.5 and 1 and A (the rate coefficient at $T = 300$ K) is usually in the range between 5×10^{-8} and 4×10^{-6} cm^3 s^{-1}. Resonances at higher energies can occur, but usually are of lesser importance for interstellar chemistry.

In chemical networks constructed by ion–molecule reactions, DR is frequently the terminating step in a particular branch. Very often, the protonated form of the molecule is built up by consecutive ion–neutral reactions, and DR leads to the

final molecule under ejection of a hydrogen atom. In some environments, DR is the only process that can destroy stable cations; an example, such is the case with the cyclic $C_3H_3^+$ ion in Titan's atmosphere [88].

Especially in dark interstellar clouds, ion reactions are very relevant. In the outer more diffuse regions of dark clouds, UV photons are responsible for the production of ions, whereas in the more opaque inner regions (with opacity $A_v \geq 6$) of dark clouds, which are impenetrable to visible and UV light, cosmic rays can ionize molecules. In the vicinity of embedded low-mass stars, also X-ray photons cause ionization. The ionization of H_2 (the major constituent of dark clouds) rapidly leads to H_3^+ via the reaction sequence

$$H_2 + \text{c.r.} \rightarrow H_2^+ + e^-$$
$$H_2^+ + H_2 \rightarrow H_3^+ + H$$

(where c.r. indicates a cosmic ray particle) which, in turn, can form many important interstellar ions (HCO^+, N_2H^+, etc.) through proton transfer to the respective neutral molecules. The degree of ionization is crucial for the dynamics of dark clouds, since it governs the interaction between the magnetic field and the molecular gas and thus influences the timescale of gravitational collapse and star formation. Ion fractionation is usually determined by assessing the electron abundance, assuming that (i) molecular clouds are electroneutral and (ii) the negative charge is exclusively located in electrons. The latter statement might be questioned through the possible presence of negative charges on grains and the recent detection of carbon-chain anions in the dark cloud TMC-1 [89]. More severely, only indirect methods exist for the determination of the electron abundance and are often based on the prediction that DR is the only efficient process in reducing the total ion number density [90]. Measurements of rates of DR reactions are crucial to verify this assumption. They also yield information on to what extent DR is able to compete with other destruction pathways of ions, such as charge transfer, proton transfer, and depletion onto interstellar grains, which are regarded as negatively charged and thus can neutralize impinging cations [91].

In dark clouds, temperatures of gas-phase molecules and ions mostly lie in the range 7–20 K [92]. Consequently, DR should be the most important ion–electron reaction if the electrons are in thermal equilibrium with the other components of the cloud. Although electrons produced by cosmic radiation (which can penetrate into dark clouds further than to an opacity of ~6) have a mean energy of 30 eV [93], they are cooled very efficiently by interaction with H_2 (at higher energies through ionizations and electronic excitations, at lower energies by rotational excitations) [94]. Therefore, it is fair to assume that electrons are in thermal equilibrium with the ubiquitous and cold H_2 molecules in dark clouds. Since dark clouds are very cold and DR processes are more efficient at low collision energies, DR reactions are of pivotal importance for the ion chemistry at the equilibrium temperatures encountered there.

DR also plays an important role in the synthesis of many common interstellar molecules. It constitutes the final step of their formation pathway when (as mentioned above for the case of H_2O) the protonated form of the molecules is

subjected to this process under ejection of a hydrogen atom, leading to the desired species.

Thinner molecular clouds that, in contrast to dark clouds, do not block the visible light from the stars behind (traditionally called *diffuse clouds*) and translucent clouds (which occupy an intermediate place between dense and diffuse molecular clouds) also exhibit a versatile ion chemistry. Diffuse molecular clouds show a visible opacity of >0.2, a particle density of $n = 100–500\ \mathrm{cm^{-3}}$, and a temperature of 30–100 K, whereas for translucent clouds the respective figures are $A_v \sim 1–2$, $T = 15–30$ K, and $n \sim 500–1000\ \mathrm{cm^{-3}}$ [95].

Owing to the high UV density in diffuse clouds, hydrogen atoms and molecules can be effectively ionized. This can lead to considerable abundances of H_3^+, which has actually been detected in a diffuse cloud [96]. Consequently, also the abundance of electrons is enhanced by several orders of magnitude ($[e^-]/[H] \sim 10^{-4}$) in diffuse clouds compared to dark ones. Fast DR reactions can then play a major role as a destruction mechanism of ions, which may even impede the synthesis of more complex ions in diffuse clouds if most carbon atoms are ionized and electrons are, therefore, very abundant [95]. Regarding the production of ions in diffuse clouds, it should be mentioned that the cosmic ionization rate in these objects was very controversially debated and its determination relies heavily on the accurate determination of the H_3^+ DR rate. Experimental measurements of the rate constant differed by orders of magnitude, and earlier models used very low DR rates for this species. Only recently, the results from storage ring and afterglow measurements could be reconciled (see Section 3.2.3.1) [97, 98].

DR is also involved in the transformation of C^+ into CO, a very crucial process in translucent clouds according to the reaction sequence

$$C^+ + OH \rightarrow CO^+ + H$$
$$CO^+ + H_2 \rightarrow HCO^+ + H$$
$$HCO^+ + e^- \rightarrow CO + H$$

Interestingly, also the OH radical necessary for the first step is produced by DR, namely from H_3O^+. Thus, DR reactions are pivotal in the condensation of diffuse to dark clouds (see above) in which most carbon is present in the form of CO.

Also during star formation, chemistry plays a decisive role, especially in hot cores. These hot cores are regions in dense clouds that are warmed by an associated protostar to a temperature of about 100 K. They are important intermediate stages in star formation and an ongoing subject of intense discussion. The versatile chemistry in hot cores, which is triggered by the evaporation of molecules from icy grain mantles during the warm-up phase, also involves DR. At later stages of hot cores when the protostar has been formed, methanol and formaldehyde, among other compounds, are released into the gas phase. The latter compound can be protonated (by, e.g., H_3^+) to $CH_3OH_2^+$ and undergo methyl transfer:

$$CH_3OH + CH_3OH_2^+ \rightarrow CH_3O(H)CH_3^+ + H_2O$$

The resulting $CH_3O(H)CH_3^+$ (which can also be formed by radiative association from CH_3 and $CH_3OH_2^+$) can then undergo DR to dimethyl ether, which has been

detected in the star-forming regions:

$$CH_3O(H)CH_3^+ + e^- \rightarrow CH_3OCH_3 + H$$

Since many other products of the DR of $CH_3O(H)CH_3^+$ are energetically possible, the branching ratio this process is crucial to determine whether the invoked gas-phase synthesis is feasible or whether alternative pathways like the association reaction of CH_3O and CH_3 [99] have to be held responsible for dimethyl ether formation in star-forming regions.

Model reactions by Garrod and Herbst [100] have shown that even a branching ratio of 0.01 for the formation of dimethyl ether in the DR of $CH_3O(H)CH_3^+$ would allow the production of the abundances observed in, for example, the Orion Hot Core [101]. In a recent storage ring experiment, a branching fraction of maximum 0.07 was measured for this pathway of the DR reaction of protonated dimethyl ether [102], making the gas-phase process a possible mechanism for the formation of dimethyl ether. This example should illustrate the importance of DR in the synthesis of complex molecules in space.

DR is also crucial for planetary ionospheres. The atmospheres of the outer giant gas planets consist mostly of hydrogen and helium, as well as smaller amounts of methane and ammonia. Therefore, not surprisingly, H_3^+ is the most abundant ion in higher layers of their ionospheres. In lower regions, this ion undergoes proton transfer to methane or ethylene, forming the comparatively stable CH_5^+ and $C_2H_5^+$ ions:

$$H_3^+ + CH_4 \rightarrow CH_5^+ + H_2$$
$$H_3^+ + C_2H_4 \rightarrow C_2H_5^+ + H_2$$

DR functions as the main destruction mechanism for these ions, and considerable research efforts have been devoted to investigate its rate constants and the product distributions. This was not only because of their significance to the chemistry of planetary atmospheres but also mainly because of the role DR plays in combustion processes, where such ions are present. In the Jovian atmosphere, DR might be involved in the formation of water in the planet's ionosphere [103]. In this environment, O^+ is thought to be transformed into H_3O^+ by successive reactions with H_2, which then forms water through DR (as mentioned above).

DR is not only involved in the formation and (through protonation and subsequent breakup of the protonated ion through DR) destruction of substances in planetary atmospheres but possibly also for their removal from the planetary gravitation field. In the uppermost layers of the atmospheres of Mars and Venus, it is pivotal for the nonthermal escape of oxygen. Very exoergic DR pathways of O_2^+ molecules present in these environments produce fast oxygen atoms which are able to escape the gravitational field of lighter bodies such as Mars. Even in cases where their kinetic energy is insufficient to leave (e.g., in atmospheres of heavier bodies such as Earth and Venus), they can spend some time at high altitudes before falling down, forming a hot-atom corona [104], which has been detected on Venus [105] but not on Mars. According to model calculations, DR should be fundamental for both the carbon and oxygen atom escape (and thus the water loss)

on the Red Planet. The DR rate constant of O_2^+, which is the predominant ion in the lower ionosphere of Mars and readily produced from O^+ ions and CO_2 by the reaction [106]

$$O^+ + CO_2 \rightarrow CO + O_2^+$$

has been found to be strongly dependent on the vibrational state of the ion [107]. This can also have fundamental consequences for the ionosphere of Venus, where 60% of the O_2^+ ions are produced by the above-mentioned reaction in vibrationally excited states [108].

The reaction of CO_2^+ with electrons possesses two exoergic DR channels:

$$CO_2^+ + e^- \rightarrow CO + O$$

and

$$CO_2^+ + e^- \rightarrow C + O_2$$

Earlier storage ring experiments have yielded that in 9% of the reactive encounters between CO_2^+ ions and electrons, the reaction involves a radiative association of the electron forming C and O_2 [109], and model calculations identified this process as a major source for atomic carbon in the Martian atmosphere [110]. However, the models did not predict the formation of a sufficient amount of high-energy carbon atoms to allow for carbon escape. Moreover, another storage ring investigation cast doubts on the presence of a radiative recombination pathway in the reaction of CO_2^+ with electrons [111].

In addition, the escape of hot nitrogen atoms produced by the DR of N_2^+ is considered to play a major role for the nitrogen loss in the Martian atmosphere, where it is also a possible reason for the high isotope fractionation of N_2 (75% enrichment of ^{15}N compared to the terrestrial isotope ratio) measured in the Viking1 mission [112], since the lighter hot ^{14}N atoms are more prone to nonthermal escape [113].

Because of its exoergicity, DR is a feasible formation process of highly excited states of atoms and molecules. Radiative deactivation of these states leads to characteristic emissions found in light phenomena such as auroras and airglows. In the terrestrial and Martian atmosphere, DR of O_2^+ accounts for night glow emission of $O(^1D)$ [114]. Airglows are not exclusively due to excited atoms formed through DR; also excited states of molecules can be responsible for these phenomena. An interesting example is the Cameron ($a^3\Pi \rightarrow X^1\Sigma$) and Fourth Positive ($a^1\Pi \rightarrow X^1\Sigma$) bands of CO observed in the airglow of Mars and Venus, which are due to the electronically excited states of this molecule produced in the DR of CO_2^+ [115]. By producing fast molecules and atoms, DR may influence the temperature in planetary thermospheres. Collisional energy transfer from these particles to other species results in heating of the thermosphere [116], whereas radiative deactivation of excited species produced by DR can imply cooling of this environment [117].

Ion chemistry is not only happening on planets but also plays a pivotal role in satellites like Titan. Titan's atmosphere is one of the most peculiar of the solar system. It consists mostly of nitrogen, methane, and other hydrocarbons and is thus suspected to somewhat resemble the early Earth. Consequently, chemical

processes involving hydrocarbon ions are fundamental in Titan's ionosphere. The role of DR reactions in the nitrogen chemistry of this satellite is discussed later in this chapter.

Finally, it should be reported here that the importance of DR could even extend to extrasolar planets. Models of the atmospheres of these bodies include DR as a step in the destruction pathway for water [118], which might have repercussions on their habitability.

3.2.2 Methods of Laboratory Study

For the experimental study of DR, two principal methods have been developed, namely multicollisional swarm methods and single collision beam methods. We will first discuss the principles of both techniques and then present their recent implementations and typical results.

3.2.2.1 Multicollisional Swarm Methods

In multicollisional swarm methods, the interaction between a swarm of electrons and a swarm of ions is analyzed by monitoring how the densities of electrons (n_e) and of a certain ion species (schematically denoted as $[A^+]$) decrease by their mutual recombination in a given thermal ensemble at temperature T. The environment of this type best suitable for DR studies is a quasineutral afterglow plasma in which recombination is the dominant loss process. If the species of interest is the dominant ion in the plasma, the quasineutrality implies that $n_e = [A^+]$. Under these conditions, the electron density in a plasma test volume then varies as

$$\frac{dn_e}{dt} = -\alpha(T)\,[A^+]n_e = -\alpha(T)\,n_e^2 \tag{3.25}$$

where $\alpha(T)$ is the plasma recombination rate coefficient at the temperature T. This plasma recombination rate coefficient is related to the recombination cross section $\sigma(\vec{v}_c)$ at a given collision velocity $\vec{v}_c$ by averaging $v_c\sigma(\vec{v}_c)$ over the thermal velocity distribution $f_{th}(\vec{v}_c; T)$, yielding

$$\alpha(T) = \int v_c\sigma(\vec{v}_c)f_{th}(\vec{v}_c; T)d^3v_c \tag{3.26}$$

A modification of Eq. (3.25) must be used if several ionic species coexist.

In this analysis, $\alpha(T)$ represents the total binary recombination rate coefficient of the species A^+. If A^+ is a molecular ion, this represents the process of DR as the most efficient reaction. However, it has to be ensured that the density is low enough to avoid collision-assisted processes, and that ions and electrons are in thermal equilibrium. Among the swarm methods, stationary afterglow methods have been applied for more than 60 years [119], while flowing afterglow methods are used for about 45 years [120, 121]. Microwaves and Langmuir probes are the usual tools to monitor the electron density, and mass spectrometers are employed to identify the recombining ions. In afterglow experiments, absorption

spectroscopy was used to measure ion densities [122] and final states [123]. Similar spectroscopic methods were further developed recently to determine the rate coefficients of H_3^+ ions in specific nuclear spin states (*para-* and *ortho*-H_3^+) [124].

In the stationary afterglow plasma, the desired ions are formed in a pulsed discharge (usually a microwave discharge) and, when the discharge is switched off, the electron (or ion) density is monitored. This technique [119, 124–127] has produced many results on recombination of ions including astrophysically relevant species. Its disadvantage is that only ions that can be produced by ignition of a discharge in a gas (eventually a mixture of gasses) can be studied. This has been overcome by producing a streaming plasma and adding specific neutral reactants locally and then following their conversion to ionic species and their effect on the electron density in the host plasma.

The flowing afterglow technique realizing this approach represents a modification of the flow reactor used to study chemical reactions. It was introduced in 1965 by Ferguson, Fehsenfeld, and Schmeltekopf [120, 121] for the study of ion–molecule reactions and recombination of ionospheric ions. In 1971, Hasted *et al.* [128] modified this technique and equipped the flowing afterglow with a Langmuir probe to measure the electron density evolution along the flow tube. Smith and Adams at Birmingham University [129] further developed the new technique, which is now named FALP (flowing afterglow with Langmuir probe) .

In FALP (see Figure 3.18), a buffer gas (usually He at a pressure of 100–1000 Pa) flows with a high velocity of 10–100 m s^{-1} along the flow tube. Typically, the plasma is formed in a discharge at the beginning of the flow tube and carried downstream by the flow of He. When the plasma flows out from the discharge region, it is thermalized such that electron and ion temperatures approach the buffer gas temperature. To this plasma, Ar is added in order to remove He metastables (by Penning ionization). Further downstream, into the already thermalized plasma, neutral reactants are added, and in a sequence of ion–molecule reactions the desired ions are formed. This setup allows precise control of the plasma parameters.

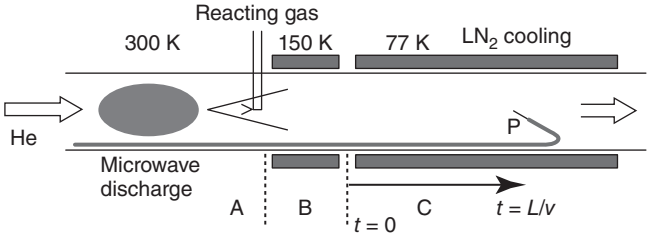

Figure 3.18 Schematic of the cryogenic FALP experiment, where He gas flows through a glass discharge tube and the plasma is carried into a cooled stainless-steel flow tube (thermal zones A–C). Reactant gases are added to the plasma through inlet ports. The electron density decay in the plasma is measured as a function of the time t along the flow, as indicated, using an axially movable Langmuir probe P.

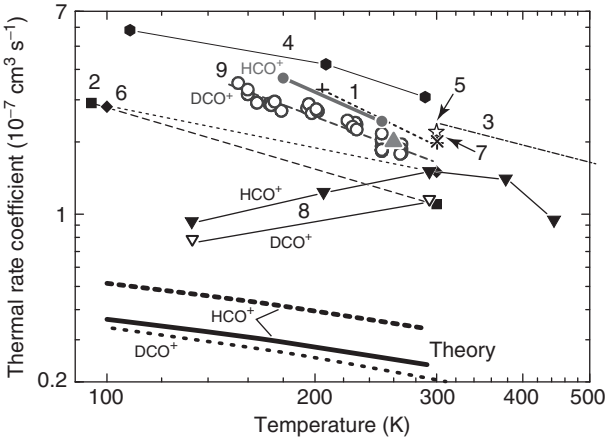

Figure 3.19 Results for the thermal DR rate coefficient of HCO^+ for a range of plasma temperatures obtained using multicollisional swarm methods. 1: Leu *et al.* [130]; 2: Adams *et al.* [131]; 3: Ganguli *et al.* [132]; 4: Amano [122]; 5: Rowe *et al.* [133]; 6: Smith and Spanel [134]; 7: Laubé *et al.* [135]; 8: Poterya *et al.* [136] (HCO^+ and DCO^+ as labeled); 9: Korolov *et al.* [137] from FALP (filled circles and strong line for HCO^+, open circles circles for DCO^+) and from stationary afterglow (large triangle for HCO^+). The typical given experimental errors are ±30%. Theory: Douguet, *et al.* [138] for both HCO^+ and DCO^+ (full and dotted line, respectively) and including the increase by the molecular electric dipole moment for HCO^+ (dashed line) [139].

FALP setups have been built in several modifications [140–144]. Further details are also given in Ref. [74], pp. 59–68. The majority of the presently available thermal and near-thermal recombination rate coefficients were measured using the FALP technique. Under suitable conditions, in addition to binary recombination processes, also ternary processes can be studied, where the electron–ion recombination is assisted by nearby electrons or ions, involving three-body collisions. In addition, the FALP technique was used to study ion–molecule reactions, electron attachment to neutral species, and electron detachment from anions. Only very exceptionally, the recombination products or the radiation emitted by them were investigated in FALP experiments [145, 146].

To illustrate the results obtained from plasma-type experiments, Figure 3.19 shows the data from over three decades for the important ionic species HCO^+. Various arrangements yielded results that scatter much wider than the estimated errors (typically ±30%). In the most recent experiment [137], the dependence of the electron density decay on the partial pressures of the reacting gases (H_2, CO, and Ar) was studied over wide ranges and appropriate parameter intervals for them were determined. In the applied reaction models also, various ionic species (H_3^+, HOC^+, Ar^+, etc.) were included. Merged-beams experiments, discussed in the following section, so far have obtained only a few experimental results for the HCO^+ DR rate coefficient. Early results from this method lie considerably below most FALP data (rate coefficient near 0.7×10^{-7} cm^3 s^{-1} at 300 K as derived [138]

from the merged-beams cross section data of Ref. [147]), while recent results (see Table 3 of Ref. [148]) indicate similar values as from FALP. Theory (Figure 3.19) still gives considerably lower results than all measured ones for the HCO^+ DR rate coefficient.

3.2.2.2 Single-Collision Beam Methods

As the second method, interacting beam methods in the single-collision regime are applied. They are based on the direct detection of reaction products in crossed or merged particle beams. The high beam velocity makes it possible to register the individual reaction products on an electron multiplier or on a similar detector based on ionization. With these detector signals, representing several coincident neutral fragments from the molecular dissociation, events resulting from DR can be identified. In dedicated experiments, even the individual dissociation momenta of the DR events can be analyzed. The interacting ion A^+ can be specified by producing an ion beam with a well-defined charge-to-mass ratio. Moreover, the collision energy between electrons and ions can be set at a quasi-uniform, experimentally controlled value E_d. From the count rate R_{DR} of DR products arriving from the beam–beam interaction volume, a collisional rate coefficient $\alpha_c(E_d)$ at the quasi-uniform interaction energy E_d is obtained from

$$R_{DR} = \alpha_c(E_d)\, n_e\, N_{A^+} \tag{3.27}$$

where n_e denotes the electron density in the interaction volume and N_{A^+} the number of parent ions present there. The collisional rate coefficient is related to the DR cross section at a given collision velocity $\vec{v}_c$ through

$$\alpha_c(E_d) = \int v_c \sigma(\vec{v}_c) f_c(\vec{v}_c; E_d) d^3 v_c \tag{3.28}$$

where $f_c(\vec{v}_c; E_d)$ describes the distribution of collision velocities representing a narrow energy band near the experimentally controlled value E_d.

The use of counting detectors, which often are sensitive also to the impact positions and impact times of the DR fragments, makes the method suitable for detailed studies of the underlying DR process aiming at individual fragmentation channels and its energy balance, equivalent to initial-to-final state studies. Moreover, this method works in the single-collision regime with well-defined parent ion beams. Through the quasi-uniform collision energies, the DR cross section $\sigma(E) \equiv \sigma(|v_c|)$ can be obtained by varying E_d and making use of Eq. (3.27) for these E_d steps. With suitable knowledge of the distribution $f_c(\vec{v}_c; E_d)$, a deconvoluted experimental DR cross section $\sigma(E)$ can be derived. This experimental cross section can in turn be inserted into Eq. (3.26) in order to determine the thermal DR rate coefficient $\alpha(T)$. Absolute calibration is obtained by measurements of n_e and N_{A^+} from the beam intensities and geometries.

The colliding beam method has found various applications in experiments on atomic and molecular collision studies [149] since about 1965. With collinear overlapping and velocity-matched beams, the DR between electrons and molecular ions can be studied down to very low energies, limited only by the electron

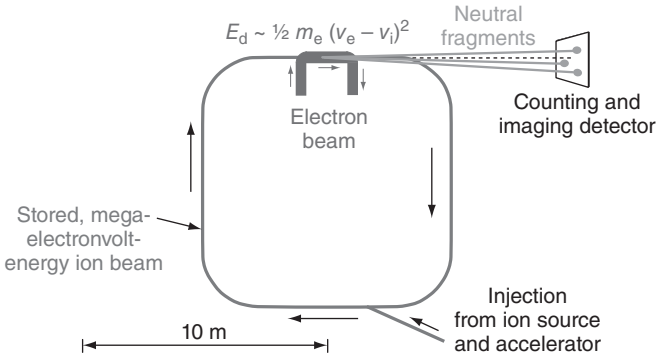

Figure 3.20 Schematic of the storage-ring technique to measure DR rate coefficients, fragment branching ratios, breakup geometries, and energy releases.

energy spread in the co-moving reference frame of the merged beams. Single-pass merged-beams studies [149] have been performed since 1977 on molecular DR [150] and later also on dielectronic and radiative recombination of atomic ions with electrons [151–153]. In these experiments, the reaction products resulting from DR in the fast moving interaction zone propagate in a narrow cone and are directly counted using particle detectors. A particular challenge are the low ion and electron densities and the usually much higher residual-gas densities, which cause similar reaction products from fragmentation or ionization reactions of the studied ions with the background gas. Moreover, in a single-pass colliding-beams experiment, the internal excitation of the molecular ions almost directly reflects the conditions at their production, which, especially for high-intensity sources, can cause very high rotational and also vibrational excitation.

Starting in the late 1980s, merged-beams arrangements were replaced by ion storage rings (see Figure 3.20), where the ion beam is continuously recirculated and largely improved in its quality by stored-beam cooling. Magnetic storage rings with ion beams of high laboratory energy up to several megaelectronvolts were used with velocity-matched electron beams of ∼100–1000 eV. The ultrahigh vacuum environment of these rings and the high beam velocity lead to storage lifetimes of many seconds and to a large reduction of background reactions in the merged-beams interaction zone. Thus, merged-beams studies of molecular DR could be tremendously improved using these devices (see the reviews in Refs [74, 154–156]). The long-time storage of the molecular ions was shown [83] to lead to their efficient vibrational relaxation for infrared active species; for lighter infrared active ions, also the rotational level populations relax [157] down to the storage ring's ambient temperature (300 K). In the first merged-beams experiments, the electron energy spread in the co-moving reference frame of the merged beams amounted to ∼100 meV (∼1300 K). Later, this limit was gradually reduced and recently reached ∼1 meV (see results reviewed in Refs [158, 159]), allowing the DR studies to be extended down to electron collision temperatures of ∼10 K. These

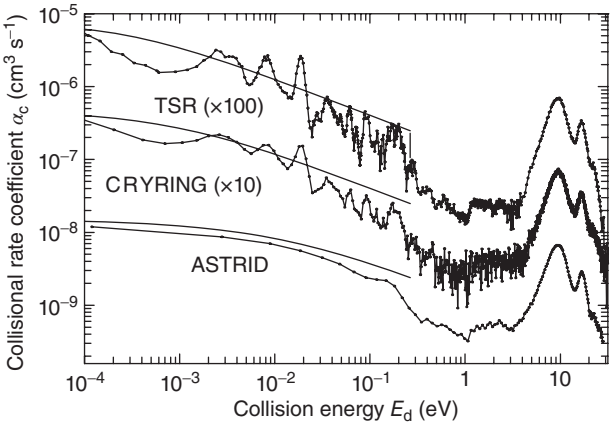

Figure 3.21 Results for the collisional rate coefficient as a function of the collision energy (tuning parameter E_d) for the DR of HD^+. The comparison of data from three ion storage ring facilities [80] is complemented by including the recent higher resolution data [161] from TSR (to the left of the vertical mark near 0.25 eV). The recommended rate coefficient derived from the three experiments [80] implies a simple E^{-1} power law of the DR cross section, averaging over the resonant structure; the collisional rate coefficients obtained from this power-law cross section for the respective electron temperatures of the three experiments are indicated by the full smooth lines. The absolute rate coefficients from the three facilities agree with each other at the 20% level.

values lie far below the ambient temperature of the presently realized merged-beams devices which have the dominant influence on the internal temperature of the stored molecular ions by the thermal equilibrium in their 300-K blackbody radiation field. The effect of superelastic collisions with the much colder electrons could be observed after several seconds of storage and lead to somewhat reduced equilibrium temperatures for infrared ions such as HD^+, where rotational temperatures down to ~125 K were found [160].

Detailed measurements on the magnitude as well as on the precise resonant structure of the DR cross section at low and intermediate electron energies were performed at the four ion storage ring facilities [162] applied in this field within about the first decade of their operation. The elementary infrared active species HD^+, stored at ro-vibrational temperatures near 300 K, became a test case, illustrated in Figure 3.21. Regarding both the size and the energy dependence of the measured collisional rate coefficient $\alpha_c(E_d)$, excellent agreement could be obtained and a recommended thermal rate coefficient $\alpha(T) = (9 \pm 2) \times 10^{-7}(300\,\mathrm{K}/T)^{1/2}$ cm^3 s^{-1} was derived. As seen in Figure 3.21, the resonant structures in $\alpha_c(E_d)$ at low collision energy for all three experiments oscillate around the curve obtained from folding the smooth power-law dependence corresponding to this $\alpha(T)$ with the respective electron energy distributions (see Eq. (3.28)). The most recent high-resolution measurement from TSR (upper curve in Figure 3.21) was compared with advanced theoretical calculations [161], yielding a good understanding of many of the observed structures. This work also reveals that a strong dependence

on the rotational level populations is expected for the DR at low temperature and that the detailed energy dependence of this process has not yet been studied experimentally with rotationally cold ions in the single-collision regime accessed by merged beams. A similar agreement, both with respect to the size of the rate coefficient and to the still imperfect control of rotational excitation below a level of ~200–300 K, has been found for H_3^+ (see Section 3.2.3.1).

Under the improved conditions realized at ion storage rings, also the fragments resulting from low-energy DR can be investigated in the single-collision regime for both diatomic and polyatomic ions. For diatomic ions, fast-beam fragment momentum spectroscopy revealed the internal excitation states of the atomic fragments [163, 164]. For polyatomic ions, the relative contributions (branching ratios) of the different molecular and atomic recombination channels become accessible by analyzing the fragment masses. In the merged-beams reaction geometry, these masses become observable by analyzing the laboratory kinetic energies of individual coincident fragments at the event detector. This principle was extensively used for the measurement of molecular product branching ratios [74, 165]. Recently, product mass identification was combined with fragment momentum spectroscopy for specific product channels [166], revealing also information on the internal states in which molecular products are produced by DR [167, 168]. Finally, the analysis of kinetic energy releases in low-energy DR reactions has been used as a tool to detect the internal excitation of the parent ions with a sensitivity limit lying in general at ~200 K through the achievable resolution of the fragment momentum measurement [169].

3.2.3
Recent Laboratory Results and their Impact on Molecular Astrophysics

3.2.3.1 DR of the Triatomic Hydrogen Ion H_3^+

In interstellar molecular clouds, the DR of H_3^+ is its prime destruction mechanism following its production through the ionization of H_2 and the rapid further reaction of H_2^+ to form H_3^+. Therefore, the H_3^+ DR rate coefficient decisively enters into chemical models of the interstellar matter at the very origin of the reaction network. A decades-long controversy about the order of magnitude of the DR rate coefficient was fought out until several years ago, as strongly contradictory results from experiments and theory caused a large uncertainty. First merged-beams experiments in the single-collision regime showed high DR rate coefficients, but also revealed strong internal excitation of the H_3^+ ion beams even after many seconds of recirculation in a storage ring [173]. Only measures to largely suppress any rotational excitation of H_3^+ ions prior to their injection into a storage ring led to consistent results on the H_3^+ DR rate coefficient from different experimental facilities (Figure 3.22a) [97, 169, 170, 174, 175]. The precise population conditions for the lowest rotational levels of H_3^+ (below ~300 K of excitation energy) are still not completely clarified for these experiments [169, 175], given the persisting lack of state-by-state measurements of parent-ion level populations and the limitation in fragment kinetic energy measurements discussed

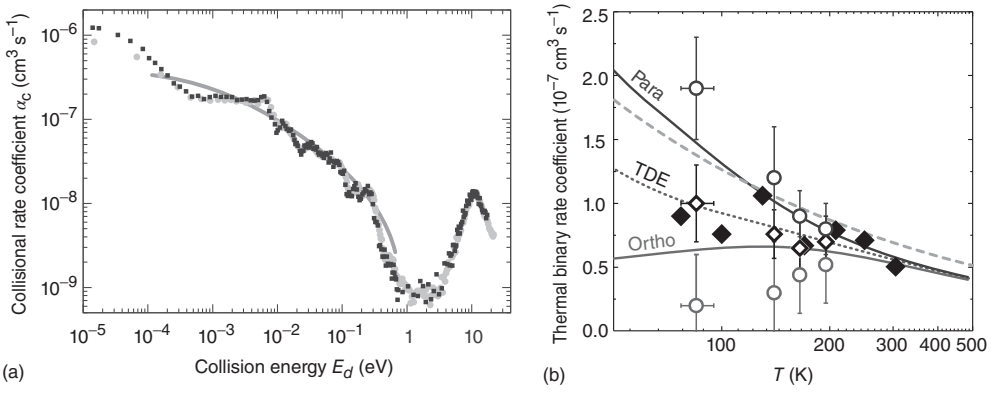

Figure 3.22 Results on the DR of H_3^+. (a) Collisional rate coefficient from ion storage ring measurements at CRYRING [97] (light symbols) and TSR [169] (dark symbols). Full line: collisional rate coefficients calculated from a DR cross section with the power-law collision-energy dependence yielding the recommended thermal DR rate coefficient of Ref. [170] (assuming 1 meV transverse electron temperature). (b) Thermal rate coefficient showing results of the cryo-FALP [98] (filled diamonds) and the recommended thermal rate coefficient [170] of the storage ring results (long-dashed line). Also shown are the results from CRDS in a stationary afterglow [124, 171] for *para*- and *ortho*-H_3^+ (upper and lower circles, respectively) and for the thermal-equilibrium mixture of both (open diamond). Theory [172] for *para*- and *ortho*-H_3^+ is shown by the full curves as labeled and by the dotted curve for the temperature-dependent thermal equilibrium (TDE) populations of both levels.

in Section 3.2.2.2. Nevertheless, the merged-beams results are widely considered a clear experimental proof of a large DR rate coefficient for H_3^+ ions in the cold interstellar medium. Also, theoretical calculations [176, 177] clearly identified the origin of a large low-energy DR rate coefficient for H_3^+ and gave detailed predictions of the resonant structures in the DR cross section [172]. These predictions and the merged-beams results on the energy dependence of the low-energy collisional rate coefficient show reasonable overall agreement with still considerable differences regarding the detailed structure [175].

In multicollisional swarm experiments, the understanding of the various ion-chemical reactions influencing the underlying electron density measurements has considerably developed over recent years. Detailed studies with a cryogenic FALP arrangement [143] and with an advanced integrated stationary afterglow (AISA) setup [178] have revealed a substantial dependence of the electron density decay in the mixed plasmas of He, H_2, and Ar applied in these measurements on the He buffer gas pressure and the partial pressure of H_2. In particular, it became clear that significant binary recombination rates in the H_3^+ dominated plasma occur only above a certain minimum H_2 partial pressure. Reactions of H_2 molecules are essential for H_3^+ formation, and collisions with H_2 may in addition be important for the H_3^+ ions to thermalize between their production and the recombination measurement. On the other hand, the pressure of the He buffer gas must be kept

low enough to avoid electron recombination in "ternary" processes where He leads to the collisional stabilization of autoionizing intermediate states formed by Rydberg electron capture on H_3^+. With a detailed study of these pressure dependences, the large scatter between previous FALP measurements of the H_3^+ recombination rate could be rationalized and a consistent dataset of temperature-dependent FALP and AISA results (Figure 3.22b) was provided [98]. As shown, these data lie slightly (by ∼10%) below the power-law rate coefficient $\alpha(T)$ extracted from the single-collision storage ring measurements. In the multicollisional measurements, thermalization of the H_3^+ rovibrational temperature is likely to be ensured down to the cryogenic range, while present single-collision measurement may still be limited to slightly higher rotational temperature [169, 175]. This may explain the differences in the rate coefficients at 100 K and below seen in Figure 3.22b.

Recent studies both by multicollisional measurements and by the storage ring technique also addressed the low-energy DR rate coefficient of H_3^+ in the two nuclear spin states *ortho* (total nuclear spin of 3/2) and *para* (total nuclear spin of 1/2). Storage ring experiments [169, 174, 179] found the collisional rate coefficient α_c of *para*-H_3^+ at energies in the range around 3 meV to be higher than that of *ortho*-H_3^+ by a factor of up to ∼3 [169]. The ratio of the rate coefficients was also measured by the plasma technique, using a stationary afterglow setup suitable for probing the *para*- and *ortho*-H_3^+ level populations by cavity ringdown spectroscopy (CRDS). Here, the thermal rate coefficient of *para*-H_3^+ at 77 K was found be higher than that of *ortho*- H_3^+ by a factor as large as 10 [124]. This even exceeds the theoretically predicted ratio of the rate coefficients (Figure 3.22b) at this temperature, where the low predicted value for *ortho*-H_3^+ is compatible with the measured value only within two standard deviations of the experimental result.

3.2.3.2 Branching Ratios and Internal Excitation for Molecular Fragments from DR

Both plasma-type measurements and merged-beams collision experiments have determined the branching ratios between the product channels with various atomic and molecular products that can occur in the DR of polyatomic molecular ions. In the plasma experiments, the fragments are identified by optical absorption spectroscopy or mass spectroscopy. In single-collision beam experiments, the masses of the fragments from individual reactions are analyzed by measuring the laboratory kinetic energies of the fragments, which are proportional to their mass. Experimental branching ratios were determined for many astrophysically important species (hydrogen, water, and hydrocarbon ions as well as nitrogen and sulfur containing ions) and are tabulated in Ref. [165]. Fragment mass identification by measuring their laboratory energies in fast-beam experiments was recently combined with momentum spectroscopy, using an energy-sensitive multiparticle imaging detector [166]. By this product-channel-specific momentum imaging, the kinetic energy release in well-defined molecular product channels could be obtained for the DR of polyatomic molecules. For the low-energy DR of protonated molecules abundantly occurring in cold

interstellar clouds, such as H_3O^+ and $HCNH^+$, the kinetic energy release was analyzed for the channel in which a hydrogen atom and the initial unprotonated species are left (H_2O and HCN or HNC, respectively, for the cases considered). Measurements were performed with deuterated species (D_3O^+ and $DCND^+$, respectively) for experimental reasons. Compared to the value expected when the product molecule would be created in its ro-vibrational ground state, much smaller kinetic energy releases were observed, which implies a vibrational excitation of the product molecules of several electronvolts. The product excitation revealed by these measurements can be expected to be mainly caused by the properties of the relevant electronic potential surfaces and hence to be present also for the undeuterated systems. Therefore, the measurement on D_3O^+ [167] showed that the water molecules produced in the low-energy DR of H_3O^+ are extremely hot, mostly being excited to high overtone vibrations all the way up to the dissociation threshold. Accordingly, most of the energy gained in the DR process will be released by infrared photons during the radiative relaxation of the H_2O product. Similarly, the measurement on $DCND^+$ [168] experimentally proved that low-energy DR of $HCNH^+$ produces both isomers of hydrogen cyanide, HCN and HNC. In fact, the product molecules of this DR process are similarly found to be mostly excited to very high vibrational levels not far below the dissociation threshold. The vibrational energy is much too high for the hydrogen atom in the HCN/HNC system to form a stable bond to either the C or the N atom. When the internal energy becomes smaller than the isomerization barrier between HCN and HNC during the gradual radiative cooling of the product molecule, both isomers will form with about equal probability [168, 180].

Mass-sensitive fragment imaging in fast beam experiments has also been used to obtain the branching ratios of polyatomic DR reactions as a function of the collision energy. Thus, for the DR of D_3O^+, only small variations of the branching ratios were found at collision energies below ~1 eV, while substantial changes occur at higher energy [181]. For D_2H^+, the branching ratios into partly and fully deuterated fragments ($D_2 + H$ and $HD + D$) as well as for the three-body fragment channel were mapped along increasing collision energies [166]. For the DR of DCO^+ [182], a strong increase of the branching ratio into $DC + O$ is found already below 1 eV, rapidly becoming almost as strong as that into the $D + CO$ channel which dominates at the lowest energy.

3.2.3.3 DR and Formation of Interstellar Methanol

Methanol has been detected in a multitude of astronomical objects. Abundance profiles of this compound can be used as evolution indicator for star formation [183], and methanol maser emission serves as a secure tracer for star-forming regions. In these environments, the abundance of methanol is greatly enhanced because of the evaporation from grain surfaces. Since this molecule is a slightly asymmetric rotor, ratios between several of its spectral lines are sensitive to both

kinetic temperature and spatial density. Thus, multiline observation on methanol can be used to determine these two parameters in an interstellar cloud with a single molecular species, avoiding the problems arising from possibly unlike spatial distributions when different tracers are used to assess these quantities [184].

The formation pathway of interstellar methanol, however, has been a subject of intense discussion. Previously, a gas-phase process consisting of radiative association of CH_3^+ and water followed by DR of the emerging protonated methanol was held responsible for the production of interstellar methanol:

$$CH_3^+ + H_2O \rightarrow CH_3OH_2^+ + h\nu$$

$$CH_3OH_2^+ + e^- \rightarrow CH_3OH + H$$

However, the rate constant of the radiative association of CH_3^+ and H_2O of a maximum of 2×10^{-12} cm^3 s^{-1}, which was determined in a cold ion trap experiment, clearly falls short of the rate constants (between 8×10^{-12} and 8×10^{-8} cm^3 s^{-1}) required to form methanol in the observed abundances under the assumption that the DR of protonated methanol entirely leads to the unprotonated species [185]. In a storage ring experiment [186], it was found that this is the case in only 3% of DR events and the predominant pathway (51% of DR incidents) is the three-body breakup into CH_3, OH, and H. An analogous pattern in the branching ratios has been observed in the DR of the related H_3O^+ ion [85]. Inclusion of the new branching ratio in a model calculation for TMC-1 using the UMIST code reduces the predicted steady-state abundance of methanol by more than an order of magnitude. If also the new rate constant for the radiative association of CH_3^+ and H_2O is accounted for, the agreement further deteriorates substantially [186].

Therefore, successive hydrogenation of carbon monoxide (CO → HCO → H_2CO → H_3CO, H_2COH → CH_3OH) on icy grain surfaces was invoked to be responsible for interstellar methanol production. However, there are two grave problems with this sequence in dark clouds: First, the hydrogenation reactions of CO and H_2CO have small but significant thresholds (26.4 and 73.6 meV, respectively) and, second, it is doubtful if the formed methanol can evaporate from the surfaces in sufficient quantities. Recently, experiments conducted by Watanabe and coworkers [187] and Fuchs *et al.* [188] have shown that the formation of methanol by hydrogenation of CO proceeds efficiently at 10 K on both pure CO and mixed CO/H_2O ices.

The presence of a grain surface mechanism to produce interstellar methanol is also corroborated by the high degree of correlation between CO and methanol abundances in star-forming regions [189]. Also, the low $^{12}CH_3OH/^{13}CH_3OH$ ratio detected in these objects points to a formation from CO, which is enriched in ^{13}C in cold environments. Furthermore, the observed deuterium fractionation in methanol indicates a grain surface process for its production [190].

The overall reaction rate constant of the DR of $CH_3OH_2^+$ has been measured as $(8.9 \pm 0.9) \times 10^{-7}(300\,\mathrm{K}/T)^{0.59\pm0.02}$ cm^3 s^{-1} [186]. Also this number

has some astrophysical implication. Since DR can be regarded as the dominating degradation pathway of this ion in the inner coma of Comet Halley, the $CH_3OH_2^+/H_3O^+$ ratio was used to determine the electron temperature there [191]. The rate coefficient used for the DR of $CH_3OH_2^+$ was a value rounded down from the one determined by Adams and Smith [192], namely $8 \times 10^{-7}(300\,\mathrm{K}/T)^{0.50}$ $\mathrm{cm^3\ s^{-1}}$. Although the DR rate coefficient appears as a squared term in the expression for the electron temperature, a dramatic change of the latter emerging from the slightly higher DR rate coefficient found in our experiment is unlikely.

3.2.3.4 DR of Protonated Nitriles in Titan's Ionosphere

One class of ions in Titan's ionosphere that re-emerged in the focus of interest comprises protonated nitriles, which were detected in surprisingly high abundance by the ion neutral mass spectrometer (INMS) on board the Cassini spacecraft. Densities of ions with masses corresponding to these ions (e.g., protonated acetonitrile, protonated acrylonitrile) were in some cases several orders of magnitude higher than predicted by pre-Cassini models [88]. Owing to the high proton affinity of nitriles, they are unlikely compared to other species in Titan's atmosphere and DR is probably their most important degradation mechanism. If that process leads to cleavage of the N–H bond, the nitrile lost through protonation will be recycled. DR competes with other reactions of protonated nitriles such as the association with neutral molecules to form larger protonated nitriles, which can decay to the unprotonated species upon DR. Thus, larger cyano compounds can be formed in Titan's atmosphere [193]. Experimental investigations on protonated acetonitrile [194] and cyanoacetylene [195] have shown that the DR of protonated nitriles only partly leads to the unprotonated species, although complete branching ratios for all pathways could not be established. DR might be also involved in the formation of nitriles. In the case of $HCNH^+$ (one of the most abundant ions in Titan's ionosphere), it can produce HNC, which can react with methyl radicals to form acetonitrile [196]:

$$CH_3 + HNC \rightarrow CH_3CN + H$$

Since the new data from the Cassini–Huygens mission suggests a much more versatile nitrogen chemistry than previously assumed, it is fundamental to establish rates and branching fractions of reactions involving nitrogen-containing neutrals and ions. Such information is, for the time being, only available to a very limited extent.

The above-mentioned DR reactions should serve as examples for the importance of this process in space. However, it would be beyond the scope of this article to discuss the subject of DR in the interstellar medium and planetary atmospheres in detail. For further information, the interested reader is referred to the recent review by Geppert and Larsson [197].

3.3
Inelastic Processes

David Parker and Laurent Wiesenfeld

3.3.1
Introduction

Because most molecules in interstellar space are observed via rotational transitions in emission, it is important to understand the details of gas-phase inelastic collisions that lead to population of the upper rotational state of the emitting molecule. This section describes the combination of crossed beam scattering experiments carried out in Nijmegen and theoretical analysis carried out in Grenoble which test our understanding of the inelastic scattering of H_2O with H_2 and He, the primary collision partners of astrophysical interest. Other systems under study in our group are mentioned at the end of this section.

The ultimate goal of scattering experiments is to determine the state-to-state differential cross section (DCS) $d\sigma/d\omega(\theta, E; i \rightarrow f)$, Eq. (1.3), which captures the variation of the scattering cross section for changing the initial state i to the final state f as a function of the center-of-mass scattering angle θ for a specified collision energy E. Equation (1.3) is expressed visually in the form of the surface distribution of particles on an expanding velocity sphere, the so-called Newton sphere. In our work, we measure these Newton spheres experimentally as product density spheres, convert them to the desired product flux spheres, extract from the flux sphere the desired state-to-state DCSs, and compare these DCSs with those predicted from calculations carried out on highly accurate potential energy surfaces (PESs), the same surfaces used to derive rate constants for astrochemical models. From the state-to-state DCSs that we measure, the integral state-to-state cross section $\sigma(E; i \rightarrow f)$ can be derived by integration over all scattering angles, Eq. (1.4), such state-to-state integral cross sections are then used to calculate thermal rate constants via Eqs (1.5) and (1.6).

Our experiment employs the velocity map imaging (VMI) technique [198] to determine state-to-state DCSs for water–He and water–H_2 collisions. In previous work, Bickes *et al.* have reported the final-state integrated total elastic (where $f = i$) plus inelastic (where $f \neq i$) DCSs ($\sum_f d\sigma/d\omega(\theta, E; i \rightarrow f)$ for water–He and water–H_2 [199], and Buck and coworkers [200] have reported partially final state resolved DCSs for water–He. Nesbitt and coworkers [201] have reported absolute integral state-to-state cross sections $\sigma(E; i \rightarrow f)$ for the related water–Ar collision system. Cappelletti and coworkers [202–204] have reported absolute total (elastic plus inelastic) scattering cross sections as a function of collision energy $\sigma(E)$, for the water–rare gas and water–hydrogen systems. We describe here our recently published measurements and analysis of DCSs for initial state-selected and fully resolved water final states for water–He and water–H_2 collisions [205–207].

With molecular hydrogen as scattering partner, it is not yet possible in our apparatus to produce a beam of H_2 only in its lowest ($J = 0$) rotational state. Instead, experiments using several different (known) population distributions of the H_2 $J = 0, 1$, and 2 rotational states are compared. A change in rotational state of H_2 due to collision with water is also possible, but at the collision energy we study this is not predicted by theory, or observed experimentally. For inelastic collisions of water with hydrogen, the rotational state changes (We use here the notation $J_{K_aK_c}$ for the rotational states of H_2O with total angular momentum J; the pseudo-quantum numbers K_a and K_c are the values for the projection of J on the *a* and *c* rotation axes of water.)

$$\begin{aligned} &ortho\text{–}H_2O\,(1_{01}) + H_2(J = 0, 1, 2) \rightarrow ortho\text{–}H_2O\,(J''_{K_a''K_c''}) + H_2(J'' = J) \\ &\qquad\qquad\qquad\qquad \text{or} \\ &para\text{–}H_2O\,(0_{00}) + H_2(J = 0, 1, 2) \rightarrow para\text{–}H_2O\,(J''_{K_a''K_c''}) + H_2(J'' = J) \end{aligned} \tag{3.29}$$

are studied. In our notation, unprimed quantum states of H_2O or hydrogen denotes levels before collision, and the double prime symbol ($''$) indicates nascent final states (H_2O or hydrogen) after collision. Single prime notation is used later in the text to denote intermediate resonant rotational levels of H_2O in the resonance enhanced multiphoton ionization (REMPI) process used to detect these final-state molecules. A scheme of the H_2O rotational energy level structure in its ground vibronic state ($v = 0, \tilde{X}$) is presented in Figure 3.23 along with the most probable collision-induced transitions to excited rotational final states. Figure 3.23 shows the rotational energy levels of *ortho*- and *para*-H_2O separately, plotting the K_a ladder.

The presence of two identical H atoms in H_2O results in two nuclear spin states: ortho ($K_a + K_c$ = odd), and para ($K_a + K_c$ = even). In addition to the conservation of total energy and momentum during the collisions, the rotational level transitions in H_2O conserve nuclear spin, that is, ortho-to-para transitions for our collision conditions are forbidden [201]. For the H_2 molecule, the coupling of nuclear spins of the two H atoms results similarly in *ortho*-H_2 and *para*-H_2, where in the electronic ground state J = even levels are para and J = odd levels are ortho. The ortho : para ratios are 3 : 1 for thermodynamic equilibrium values at the high-temperature limit for both H_2O and H_2.

3.3.2
Molecular Beam Measurements of Inelastic Scattering in Water

Molecular beams are used to define and control, as well as possible, the variables that determine the outcome of elementary single collision events in chemistry. The most important variables include the collision energy and the reactants' initial state (rotation, vibrational, electronic). By forming and crossing two well-collimated mono-velocity molecular beams, it is possible to measure the angular distribution for product-state- specific scattering in the center-of-mass frame.

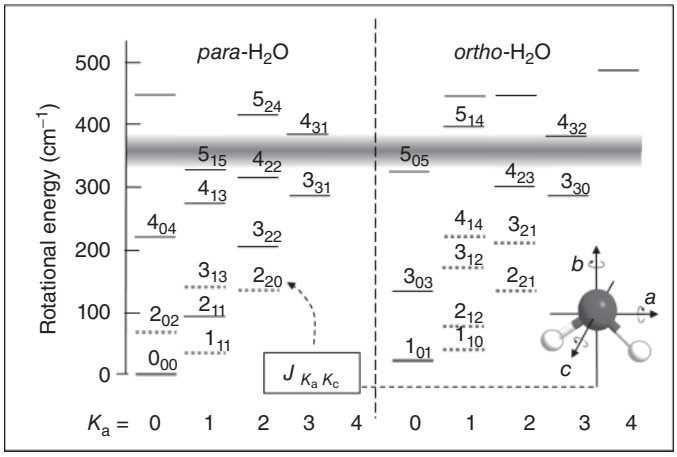

Figure 3.23 The rotational energy levels of *ortho*- and *para*-H_2O, plotted separately by the K_a ladder. The shaded region shows the collision energy when using the H_2 beam with a 200 K nozzle (collision energy 361 cm^{-1}). Ground state levels are indicated by a thick solid line, while the excited state levels populated by the collision and probed in this study are indicated by a thick dashed line. Principal rotational axes a, b, c are labeled in the inset ball-and- stick model.

During a bimolecular inelastic collision, a generic $A + B \rightarrow A'' + B''$ system (using the notation defined above) can be thought of passing through a "half-collision" transition state, AB^*, to the final products $A'' + B''$, where the velocity of the final products is governed by the conservation laws for momentum and energy (Newton's Laws). The energy of AB^* is determined from the velocity and crossing angle of the two molecular beams, which have been produced by supersonic expansion such that all molecules are populated in their lowest internal energy (rotation, vibration, and electronic) states.

As shown schematically in Figure 3.24, a pair of well-defined Newton spheres then exist for each final product channel ($A_{internal} + B_{internal}$). State-selective detection of one of the final product A'' internal states requires that the velocity of each internal state of the other product is confined to lie on the surface of nestled expanding Newton spheres. When B'' is a He atom, state-selective detection of A'' reveals only one velocity component (thus, one Newton sphere), while detection of B'' reveals nestled spheres for all possible A-copartners. By measuring the same process many times under the same conditions, we can build up the full Newton sphere.

In a crossed molecular beam scattering experiment, the product Newton sphere expands at its fixed recoil velocity, while the full ensemble of products moves at the center-of-mass velocity, as illustrated in Figure 3.25a. Most previous measurements, Figure 3.25b, of crossed-beam scattering used a neutral particle time-of-flight (TOF) detector with electron impact (or, more recently, tunable vacuum ultraviolet (VUV) photoionization). The detector is rotated around the scattering plane and intercepts small patches (front and back) of the product Newton

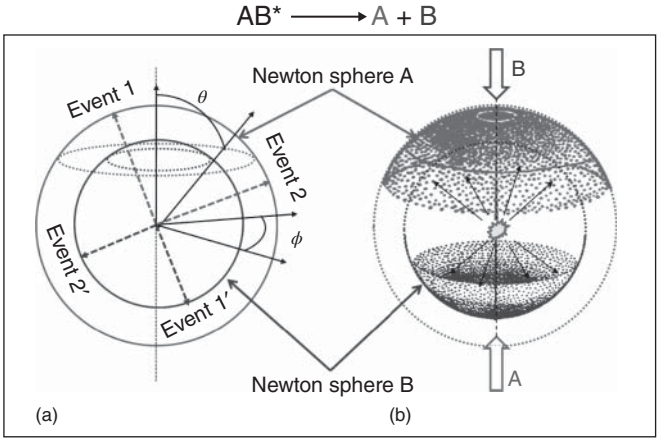

Figure 3.24 Newton spheres in the center-of-mass frame for inelastic scattering in the forward direction. By defining the energy of the transition state AB*, conservation of energy and momentum determines the velocity of the final products A and B (mass B > mass A), which recoil in opposite directions. In the center-of-mass frame, there is cylindrical symmetry about the azimuthal angle ϕ (defined in a). Two events are shown; by repeating the experiment, a sphere of products emerges (b) where the surface pattern on the sphere reveals the dynamics of the scattering process.

sphere. Measurements are made for each laboratory detection angle, and a lab to center-of-mass frame transformation is necessary in order to construct the Newton sphere. Owing to azimuthal symmetry around the collision line of center, a measurement only in the plane of scattering is sufficient to determine the DCS.

With the ion imaging method, Figure 3.25c, specific internal states of neutral scattering products are converted to ions by means of REMPI, and the ions are projected by an electric field *E* and mass- selected at the detector by their time of arrival. VMI is a high-resolution variant of ion imaging, where a special electrostatic immersion lens is used to project product velocity independent of the initial position of formation of the ion. The full Newton sphere is collected for each pulse of the REMPI laser, and crushed onto a two-dimensional charged particle detector, where it is recorded on a multi-anode collector or a phosphor screen monitored by a camera system. The advantage of VMI is the possibility to detect any product using REMPI, with 100% collection efficiency. From comparison of the two methods, it should be apparent that product ion imaging is much more efficient than universal TOF detection for systems where state-selective laser ionization is possible.

In order to illustrate the inelastic scattering imaging experiment with actual data, we show in Figure3.26 a raw image of H_2O^+ ions formed by state-selective photoionization of the $H_2O(110)$ rotational state. This state is present at low concentrations in the cold parent molecular water beam, and VMI maps the molecular velocity to a point at the lower right part of the image. A very small amount

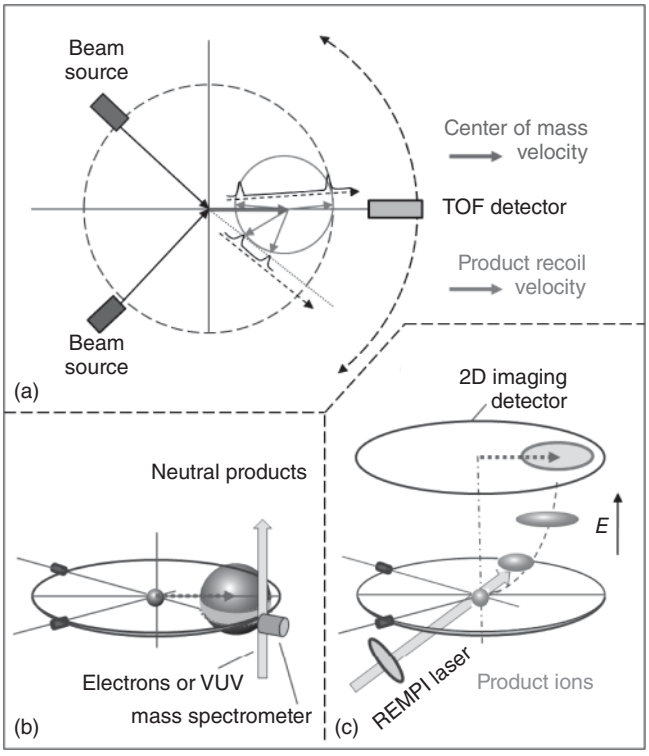

Figure 3.25 (a) Schematic picture of an equatorial slice through a Newton sphere (grey stripe) produced in the laboratory frame by crossed molecular beam scattering. A TOF detector measures the vector sum of the product recoil velocity (center-of-mass frame) and the center-of-mass velocity in the scattering plane of the two molecular beams. (b) Conventional detection of neutral scattering products (and the non-scattered parent molecular beams) takes place by electron impact or VUV photoionization in a mass spectrometer at the moment when the neutral Newton sphere reaches the detector. (c) Velocity map imaging uses laser ionization (REMPI) to convert the entire neutral Newton sphere to an ionic Newton sphere at the crossing point. The ion sphere is then projected by a special electrostatic (*E*) field onto a two-dimensional imaging detector. By adapting the *E* field, it is also possible to detect only the center slice of the product Newton sphere.

of this state is also present as an impurity in the beam of the scattering partner (He in this case); these molecules are mapped to a point at the upper left part of the image corresponding to the He beam velocity. Velocity information for molecules produced by inelastic scattering appears in the form of a single Newton sphere for the state-to-state process $H_2O(1_{01}) + He \rightarrow H_2O(1_{10}) + He$. In this process [206], only a small part of the $475\,cm^{-1}$ collision energy is transferred into rotational excitation of water from the lowest rotational state of *ortho*-water to the second lowest rotational state ($\Delta E_{rot} = 28 cm^{-1}$). Rainbow scattering, where a range of impact parameters produce the same final angle (for large-angle scattering), yields a maximum in intensity on the Newton sphere, in this case

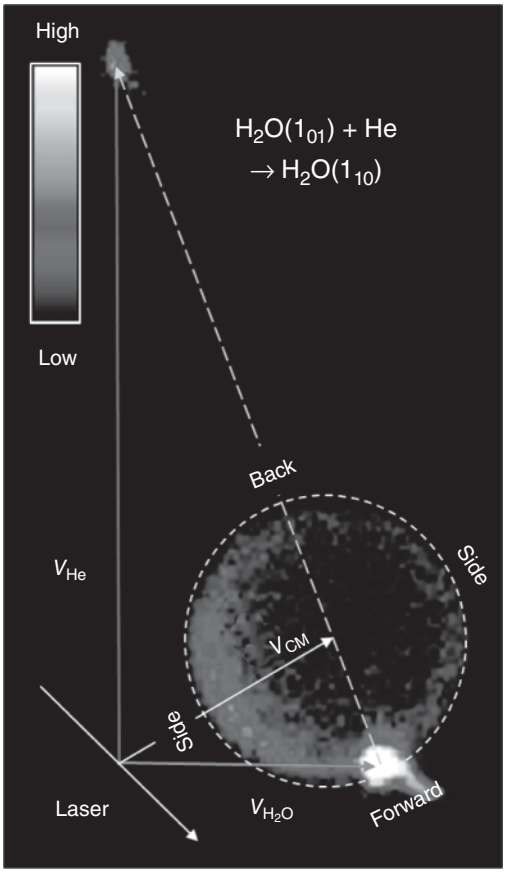

Figure 3.26 Newton diagram and raw image for inelastic scattering of *ortho*-water in the ground (1_{01}) rotational state to the first excited (1_{10}) state (energy levels are shown in Figure 3.23). The dark gray arrows show the laboratory velocity vectors for the H_2O and He molecular beams, and the light gray dashed arrows show the relative velocity vectors in the center-of-mass frame, along with V_{CM}, the center-of-mass velocity. Image intensity is coded by the gray scale bar, where the most intense dot corresponds to forward scattering with respect to the detected water molecules. See text for more details.

in the sideways scattering direction. The sensitivity and selectivity of the water REMPI process makes it possible to obtain this fully state-to-state data as shown in Figure 3.26.

3.3.3 Laser Ionization of Molecular Hydrogen and Nascent Water

The first step in the scattering experiment is to determine the initial state distribution of the parent molecules (water) and molecular hydrogen using REMPI

Table 3.2 Water REMPI levels quantum numbers.

Upper state $\tilde{C}(v = 0)$			Lower state $\tilde{X}(v = 0)$		
J'	K'_a	K'_c	J''	K''_a	K''_c
1	1	1	1	1	0
2	1	1	2	1	2
2	0	2	2	2	1
2	0	2	3	2	1
1	1	0	1	1	1
3	0	3	2	0	2
1	0	1	2	2	0

spectroscopy. We study both normal-H_2 or *para*-H_2, which is H_2 produced primarily in its para states ($J = 0, 2, 4, \ldots$) by condensation of normal-H_2 at low temperatures on a catalytic surface. An REMPI spectrum of our normal- and *para*-H_2 parent molecular beams is shown in Figure 3.27a. Analysis of these spectra yields J-state population distributions which we use as initial state inputs for the scattering process (Table 3.2).

Sensitive and state-selective detection of water (Figure 3.25b) as a scattering product, yielding an image such as that shown in Figure 3.26, requires a suitable intense, narrow-bandwidth, and isolated REMPI scheme. The interactions of the resonant electronically excited state used in the REMPI scheme with nearby excited electronic states are important because these interactions determine the predissociation rates and thus lifetime of the resonant state and thereby the spectral line widths and line strengths. We have analyzed the $\tilde{C}^1B_1(v = 0)$ - $^1A_1(v = 0)$ transition of the three water isotopomers H_2O, HOD, and D_2O [207] and identified the optimal $\tilde{C}$ - $\tilde{X}$ transitions using REMPI detection that are most appropriate for identifying the rotational states of $^1A_1(v = 0)$ water before and after collisions.

The $< J'^2_a >$ value or K'_a number of the resonant level in the $\tilde{C}$ state mainly determines the spectral line width of the REMPI transition [207]. A simple predissociation model for this systems shows that the line width $\Delta\omega$ is small for low values of $< J'^2_a >$ (or K'_a).

3.3.4 Experimental Details

3.3.4.1 Density to Flux Correction and Relative Collision Cross Sections

Owing to the azimuthal symmetry around the relative velocity vector (shown as a dashed yellow arrow in Figure 3.26), the two sections of the image labeled "side" in Figure 3.26 should be identical. The strong difference in intensity seen in the

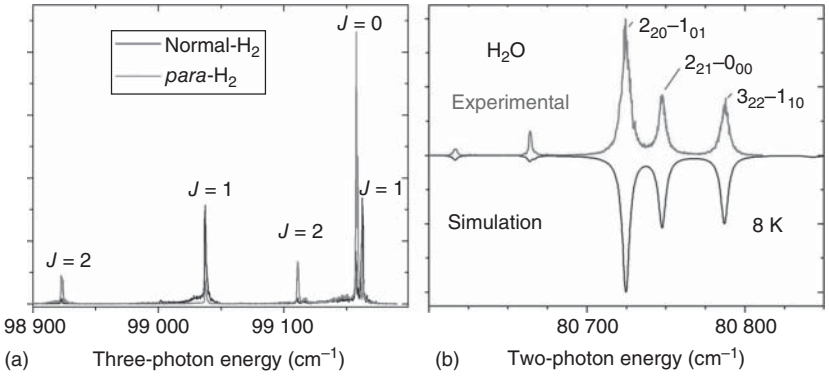

Figure 3.27 (a) (3 + 1) REMPI spectrum of normal- and *para*-H_2 molecular beams. (b) (2 + 1) REMPI spectrum of water beam with a simulation indicating 8 K beam temperature.

image for these sections is due to the fact that our pulsed (REMPI) laser detects product density instead of the desired product flux. While the pulse length of the REMPI laser is necessarily short (5 ns), the pulsed molecular beams overlap on the hundred microsecond timescales, which allows slow products to build up in the scattering center before the moment of detection. Molecules recoiling in the opposite direction to the center of mass (CM) velocity have the slowest lab velocity and are overdetected, as seen in Figure 3.26. After removing signals in the raw image from the parent beams and from thermal background, we correct for the resulting oversensitivity to slow products using the IMSIM program [208], which simulates the effect of all experimental parameters such as molecular beam pulse length, divergence, timing, and velocity spread on the probability for pulsed laser detection of products. The resulting flux images yield the desired state-to-state DCSs.

Our measured DCSs are relative cross sections, which means that the cross section for one final state can only be compared with those of other final states, providing all experimental conditions are kept constant during the measurements. We can also compare cross sections for the same final state at different collision energies, where the collision energy can be changed by varying the crossing angle between the two beams, or by varying the beam velocity at a fixed crossing angle by changing the pulsed nozzle temperature or the carrier gas composition. The accuracy of this comparison relies heavily on the quality of the density-to-flux conversion and on keeping the rotational population of the parent beams constant. Efforts are under way to obtain absolute cross sections by calibrating sensitivity with a known scattering process.

3.3.4.2 Temperature Control

The apparatus and experimental conditions used for measuring the inelastic scattering of water with molecular hydrogen are presented schematically in Figure 3.28. Normal H_2 is converted to *para*-H_2 on an iron oxide catalyst at 20 K

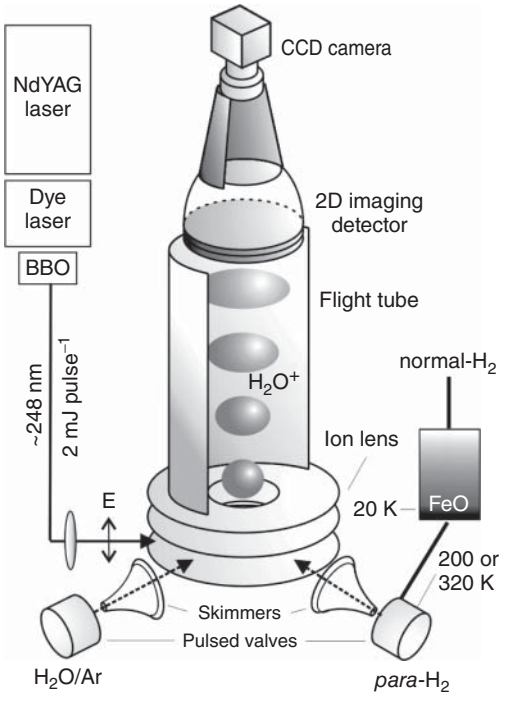

Figure 3.28 Scheme of the experiment.

and introduced into a pulsed valve held at 200 or at 320 K in order to vary the final rotational temperature after expansion through the valve. A pulsed dye laser focused tightly at the scattering center drives the REMPI detection process, and the nascent ions including their velocity patterns are mapped onto an imaging detector monitored by a charge coupled device (CCD) camera. The collision energy is determined by the beam velocities and the crossing angle. With a 90° crossing angle and argon as the carrier gas for H_2 (which provides the best rotational cooling), the collision energy is typically between 400 and 600 cm^{-1} for all scattering partners. For He, the collisional energy is 425 cm^{-1}.

3.3.5
Calculating Differential and Total Cross Sections

As described earlier in this chapter, one of the goals in studying the quenching of water by helium atoms and/or hydrogen molecules is to try and understand the excitation conditions of water in interstellar media (ISM). Since the interplay of photon emission/absorption and collisional excitation/quenching determines the population of the various rotational levels of water [209], one has to rely on computed or measured quenching rates. To the best of our knowledge, no quenching rates of water have been measured, at least in the low temperature

range ($T \leq 300\,\mathrm{K}$) that is of interest for star-forming regions [210]. Hence, we must rely on computational work, based on a water–collider PES on one hand, and on classical or quantum dynamical computations on the other.

Both tasks have been addressed for quite some time. Since collisions with helium are much easier to compute than collisions with molecular hydrogen, because of the supplementary degrees of freedom introduced by the rotation of molecular hydrogen, much work has been devoted to H_2O–He collisions, beginning with the pioneering work of Green *et al.* [211]. However, it became quickly apparent that for rotational quantum number $J(H_2) > 0$, the collisions with water (as with other polar molecules) become qualitatively different from those with helium [212, 213]. Indeed, the strong dipole of the target ($d(H_2O) = 1.856$ Debye $= 0.7303\, ea_0$) as well as the strong quadrupole of H_2($Q(H_2) = 0.48\, ea_0^2$ [214]) makes this dipole–quadrupole interaction the dominant one at large distances, for $J(H_2) > 0$. Also, the polarizability of the hydrogen molecule may not be neglected. Note that for the $J = 0$ states of H_2, both quadrupole and polarizability effects are averaged to zero, because of the random equiprobable ordination of the H_2 rod. As a result, while the very low temperature conditions with hydrogen mainly in the para $J = 0$ state is qualitatively well modeled by helium, this is not at all true as soon as the temperature increases or when the hydrogen gas is not in thermodynamic equilibrium between its para (J even) and ortho (J even) forms. It must be recalled here that this equilibrium is very slow to reach and proceeds via successive reactions $H_2 + H^+$ or $H_2 + H_3^+$, with an equilibrium time for ISM of the order of 10^6 years.

Observations on the deuterated analogs of water, both HDO and D_2O, give invaluable clues to the history of water [215, 216]. Especially for HDO, quenching coefficients are necessary to understand the observed spectra [217]. Anticipating the necessity of quenching coefficients, the Grenoble group undertook a vast program for the computation of all aspects of water–molecular hydrogen collisions: (i) computing a full, precise PES (Section 3.3.6), (ii) undertaking classical and quantum scattering computation (Section 3.3.7), and (iii) comparing as many experimental results to theory as possible (Section 3.3.8).

3.3.6
Water–Hydrogen Molecule PES

In order to assess the amount of computation needed for a given system, the number of degrees of freedom (dof) is the key number. Assuming a rigid water (the first vibrational frequency is the HOH bend, at 1595 cm^{-1}), the water–helium interaction needs three degrees of freedom: the spherical coordinates of He in the body frame of water. For water–H_2, both rigid bodies, five degrees of freedom are necessary (three for the CM of H_2, and two for the orientation of the H_2 rod). If, in addition, we allow for molecular vibrations, the full water–hydrogen PES requires nine degrees of freedom (five intermolecular coordinates plus four intramolecular vibrations).

Several water–helium (and other water–rare gas) PESs have appeared in the literature over the years. Green *et al.* ([211]) computed quenching rates based on a PES that was state of the art at that time. H_2O–He PESs were recalculated recently [218] and used independently of our work to compute quenching rates and DCSs [200].

Because of the larger number of degrees of freedom, fewer H_2O–H_2 high-precision PESs appeared in the literature. A PES was proposed by Green *et al.* in 1994 [219] and subsequently used by the same group to compute H_2O *ortho-* and *para*-H_2 quenching rates [212]. More recently, a similar 5-dof PES was computed by Hodges *et al.* [220]. Valiron *et al.* [221, 222] undertook the computation of the full, 9-dof water–molecular hydrogen PES, incorporating not only intermolecular but also intramolecular degrees of freedom, even though the latter ones are confined near equilibrium and cannot model reactions or exchanges between the various atoms. The PES is built by successive approximations. First a medium-precision CCSD(T) rigid-rotor calculation was performed for a very large set of *ab initio* points, at equilibrium geometry. This surface was corrected both by a small set of high-accuracy CCSD(T) points and by explicitly correlated methods. An accuracy better than $3\,\mathrm{cm}^{-1}$ was attained in the van der Waals minimum. Since intramolecular coordinates may vary by a certain amount around the equilibrium values, we could test or compute several effects and variances:

1) We examined the respective influence of the equilibrium versus average geometry of the molecules in interaction, and concluded that average geometries provide better PES than equilibrium ones [221] because of anharmonicities of the molecular vibrations. The main effect was found to be the lengthening of the H_2 molecule ($r_{\mathrm{eq}} = 1.400$ Å; $r_{\mathrm{av}}(v = 0) = 1.449$ Å) [222].
2) In order to compute a PES restricted to rigid molecules (5-dof PES) from the full 9-dof PES, two methods were found to be equivalent [223]:
   —Taking the average of the potential:

$$V(\text{5-dof}) = \left\langle v(\mathrm{H_2} = 0;\ v(\mathrm{H_2O}) = 0 \,|\, V(\text{9-dof}) \,|\, v(\mathrm{H_2} = 0;\ v(\mathrm{H_2O}) = 0 \right\rangle$$

   —Taking the $V(9 - \text{dof})$ at the average geometry r_{av}.
   These V(5-dof at average geometries) were subsequently used for all scattering properties (see below).
3) Since the PES does not depend on isotopic substitutions at the Born–Oppenheimer level, taking the $V(9\text{-dof})$ at the average geometry of the deuterium-substituted molecules yields a new $V'(5\text{-dof})$ of the same precision as the original $V(5\text{-dof})$ for the H_2O–H_2. In this manner, we computed the following substitutions: H_2O–D_2 (Scribano *et al.* unpublished results); HDO–H_2 [224]; and D_2O–H_2 [223].

All these potentials were used for computing quenching rates for astrophysics as well as for comparing experimental DCS and other experimental data to theoretical results, trying to assess the value of our original water–molecular hydrogen full potential.

3.3.7 Dynamical Calculations

3.3.7.1 Total Cross Sections and Rates

Dynamical calculations aim at calculating the quenching rates $k(T; i \to f)$, with $E_i > E_f$ (the opposite rates $f \to i$ are related to the direct ones by microreversibility relations). Quantum mechanically, over those rates are obtained by averaging the total cross sections $\sigma(E_{\text{coll}}; i \to f)$ or the Maxwellian distribution of incoming speeds $v_{\text{coll}} = \left(2\mu E_{\text{coll}}\right)^{1/2}$. Classically, it is possible to sample trajectories directly at a given temperature T instead of sampling at a given energy E_{coll} and averaging afterwards. E_{coll} is the kinetic energy of collision. A typical range of collision energy E_{coll} for getting rates at temperature T_0 is $E_{\text{coll}} \lesssim 5 \times kT_0$, in order to have the Maxwell average over collision velocities converge. For relatively low temperatures ($T \lesssim$ 300–500K), full quantum computations are feasible.

For quantum scattering, one usually resorts to the coupled-channels (CC) formalism in the lower end of the energy spectrum and to approximate quantum methods, like coupled-states (CS), as soon as the computations become too heavy [225]. For the computation to converge, at any given energy E_{coll}, it is necessary to include not only the energetically allowed rotational states of water and hydrogen but also some asymptotically closed channels because at short distances the attractive part of the PES may temporarily excite those transitions. Also, it is necessary to include both $J = 0$ and $J = 2$ in the rotational basis set of *para*-H_2 (or *ortho*-D_2), since the symmetry properties are different for $J = 0$: the $J = 0$ interaction is insensitive to any multipole of the hydrogen molecule, and hence to the large quadrupole–dipole interaction.

If the scattering energy becomes too high for quantum computation to remain practical, quasi-classical calculations may be used even though these are not always possible for the state-to-state quenching rates of asymmetric rotors, such as HDO [226]. A large set of high-temperature rates was proposed along those lines and is widely used in the astrophysical community [213, 213a]

3.3.7.2 Differential Cross Sections

The theoretical DCS used for comparison of H_2O, HDO, and D_2O colliding with H_2 and helium were all calculated by quantum CC methods. First, at the relevant collision energy, the Molscat scattering program [227] was used in conjuction with the relevant V(5 dof) to yield the state-to-state $\mathsf{S}(E)^j_{if}$-matrices. Here, i and f denote collectively the initial and final channel quantum states, that is, J_{K_a,K_b} for water and J for hydrogen, while $j = 0, \ldots, j_{\max}$ is the total angular momentum of the channel, a conserved quantum number. Then, the various observables are obtained by suitable summation over $\mathsf{S}(E)^j_{if}$ elements: total cross section, DCSs [205], and even, with some technical caveats, pressure broadening cross sections [228].

Special care was taken to ensure full convergence of the DCSs at all angles, including convergence of elastic DCSs. All relevant details of the Molscat parameters as well as the summation formulas are given in the original papers.

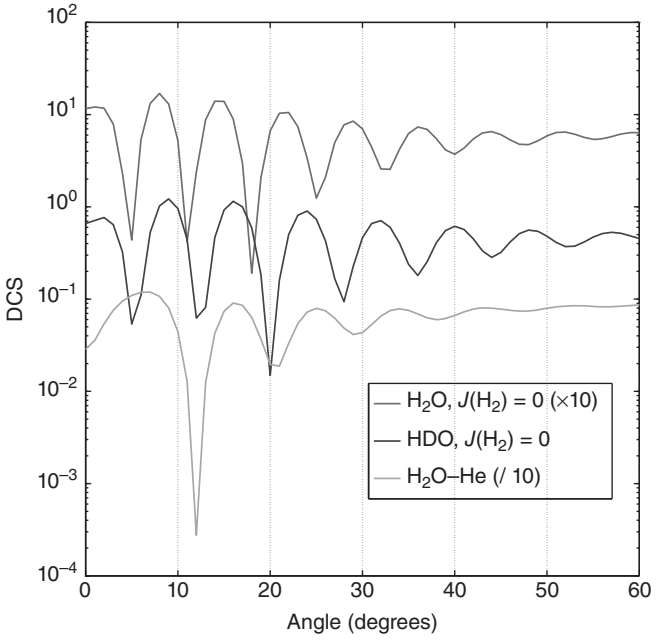

Figure 3.29 Comparison of H_2O–He and H_2O/HDO H_2, $J = 0$ DCS, for the $0_{00} \rightarrow 1_{11}$ transition, for $\theta \leq 60°$.

An example of theoretical computations is given in Figure 3.29. We see the presence of strong oscillations in the forward direction, resulting from rainbow interferences. We compare here between $H_2O + He$ scattering and $H_2O + H_2$, $J = 0$. Three parameters differentiate those two computations: (i) reduced mass, $\mu(H_2O–He) = 3.2746$a.m.u, $\mu(H_2O–H_2) = 1.8128$a.m.u; (ii) The PES of $rmH_2O + H_2$ is much more attractive than that of $rmH_2O + He$, with respective potential wells at -235.14 and $-34.9\,cm^{-1}$; (iii) While the initial and final states of H_2 is $J = 0$, thus similar to a He atom, the computation *includes* the $J = 2$, *para*-H_2 rotational state, which comes as a perturbation for short distances, since the potential well is deep enough to transitorily excite it ($E_{rot}(H_2) \simeq 360\,cm^{-1}$ with $J = 2$). The rainbow oscillations are very strong, and differ in their periods (because of the difference of reduced masses). However, the oscillations are so strong that they mask the more subtle differences, like the position of the rainbow.

3.3.8
Theory and Experiments Comparisons

3.3.8.1 Differential Cross Sections

Results for the relevant water excitation transitions are presented in Figures 3.29–3.31. Several test cases are presented here, with full comparisons shown in [205–207]. The set of comparisons presented Figure 3.30 shows the excellent

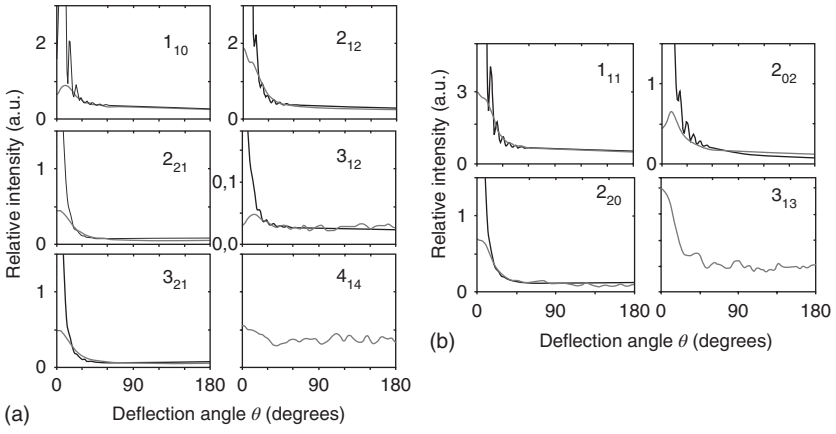

Figure 3.30 Overview of the theory versus experiment for H_2O colliding with normal H_2 (20% $J = 0$, 75% $J = 1$, 5% $J = 2$). (a) *ortho*-H_2O. (b) *para*-H_2O. All DCSs are normalized at the angle of $\theta = 60°$. (From Ref. [206].)

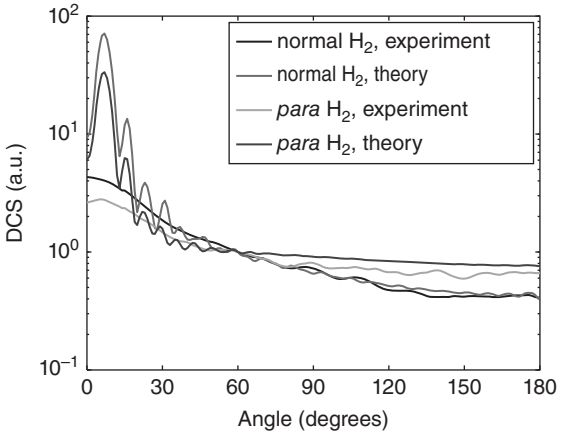

Figure 3.31 Comparison of theoretical and experimental HDO excitation DCSs, for the $0_{00} \rightarrow 1_{11}$ transition. The colliding H_2 beam has two different compositions, see text.

agreement between the experiments and the computations, for all the main transitions. It has to be remembered that these computations allow for only one free parameter, the normalization of the experimental DCS. The normalization was chosen to be the DCS at $\theta = 60°$, thereby bypassing the imprecise determination of the experimental DCS at low angles. Indeed, there is an overall difference between the experimental and theoretical DCS in the forward direction, originating probably from some imprecision of the density- to-flux correction for small deflection angles on one hand, and possibly some difficulty in the long-range PES. However, an excellent agreement is found for the total cross section between experiments and theory, since the definition of the total cross

section puts vanishing weight to the forward direction ($\sigma = \int_0^\pi d\sigma/d\theta \, \sin\theta \, d\theta$). The very strong forward DCS has been measured independently for the *elastic* scattering by Bickes *et al.* [199].

A comparison between *para*-H_2 or normal-H_2 is presented in Figure 3.31, for HDO–H_2 scattering, based on the HDO–H_2 PES of Ref. [224]. The measured compositions of the H_2 beams are as follows: *para*-H_2, 70% $J = 0$, 10% $J = 1$, 20% $J = 2$; normal H_2, 20% $J = 0$, 75% $J = 1$, 5% $J = 2$. One sees that the DCS difference is very well reproduced. Also, Figure 3.31 shows vividly the crucial importance of introducing the relevant beam composition for a proper analysis of an experimental scattering. It was crucial for many HDO and D_2O DCSs to introduce also the thermal population of the first rotational excited states of water, with an estimated $T_{rot} \sim 12$ K, thereby introducing a small percentage of *elastic* scattering in the simulations.

3.3.8.2 Total Cross Sections

The next meaningful comparison is the total cross section. While the experiments are unable to give absolute numbers for the cross sections, the ratios of the various cross sections are very well determined and may be compared with theoretical determination of the cross section. Figure 3.32 shows the comparison of the measured excitation cross section of *ortho*- and *para*-H_2O by a beam of *para*-H_2 with a measured composition of 60% $J = 0$, 10% $J = 1$, and 30% $J = 2$ rotational states. By making the appropriately weighted summation of the various theoretical values, the red crosses of Figure 3.32 are obtained. In particular, for the initial beam

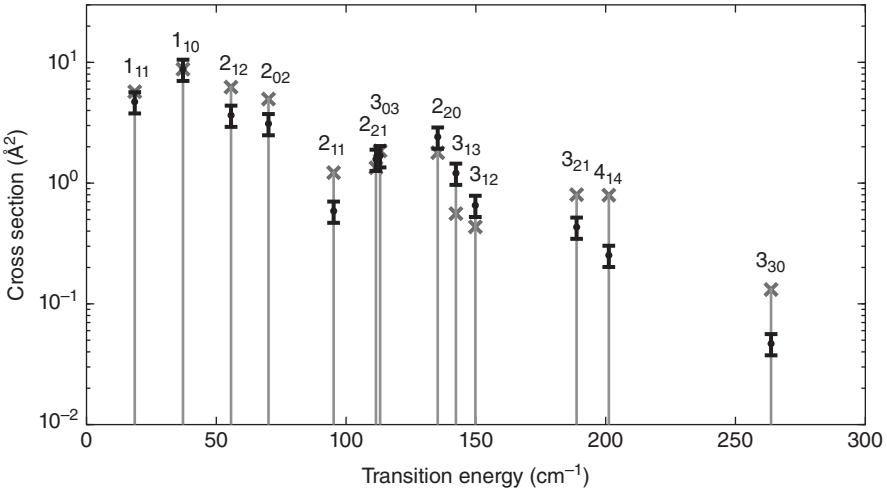

Figure 3.32 Comparison between experimental (black) and theoretical (red) total excitation cross sections. The upper level quantum numbers are shown above the transition. Transitions are shown with increasing energy change, *not* distinguishing between ortho or para levels for H_2O.

condition $J = 2$, the doubly inelastic transition

$$H_2O(J_{K_aK_c} = 0_{00} \text{ or } 1_{01}) + H_2(J = 2) \rightarrow H_2O(J''_{K''_aK''_c}) + H_2(J'' = 0)$$

may not be neglected, even though the opposite transition $J(H_2) = 0 \rightarrow J''(H_2) = 2$ is fully negligible.

Figure 3.32 shows the comparison. The relative errors on the experimental values are taken as constant at 20%. The normalization is performed by equating the theoretical and experimental values for the most intense transition, $1_{01} \rightarrow 1_{10}$. All values are given in angstrom squared.

One notes that the various trends are very satisfactorily reproduced, confirming the importance of forward scattering. The differences between theory and experiment tend to have no definite pattern. However, for higher transition energy and weaker sections, the agreement is less good, probably because of the less good convergence on the theoretical side and underestimations of the errors on the experimental side.

The very favorable comparison of theory and experiments for the inelastic DCS and total CS is a very stringent test on both experiment and theory. The sideways/backwards DCS (which contribute the most to the total CS) is sensitive to short-range anisotropy (the shape of the molecular wall opposed to the projectile) and is very well reproduced here for all scattering experiments. Also, the importance of selecting all the various relevant channels for a given experiment cannot be underestimated. Other parts of the PES are tested otherwise, as the next section shows.

3.3.8.3 Other Scattering Experiments

Pressure Broadening Several other types of experiments have been undertaken to test the water–helium and water–hydrogen interactions. One recent set is particularly relevant. Pearson, Drouin, and colleagues [229, 230] have measured pressure broadening cross section $\sigma^{pb}(T)$ (see Ref. [228] for a definition) of water transitions due to helium and molecular hydrogen under conditions relevant to ISM ($n < 10^6$ cm^{-3}; 20 K $< T <$ 300 K). Pressure broadening cross section [231] has been known for long to be tests of the overall interaction of two molecules, with an emphasis on elastic scattering at very low temperatures and inelastic scattering at higher temperatures [232]. Experiments rely on the translational cooling of diluted water in hydrogen and are very difficult to calibrate. The most recent experiments deal with several transitions of *ortho-* and *para*-water, cooled by nearly pure *para*-H_2 or by normal-H_2, with a undetermined ratio of *ortho-* to *para*-H_2. The theoretical $\sigma^{pb}(T)$ have recently been computed by us [228] in a manner quite similar to the DCS commutations, even though some technical details differ (see the original paper for all details).

Comparing theory and experiments, it was clear that the experiments above $T \sim 80$ K were in perfect agreement with theory, be it collisions with *para*-H_2 or with a mixture of *ortho-* and *para*-H_2. The agreement of $\sigma^{pb}(T)$ for *para*-H_2 collisions is all the more remarkable in that *no scaling* had to be applied to

compare theory and experiment, since both give absolute values, contrary to DCS measurements. While the situation remains not so clear below 80 K, very recent experiments tend to converge toward a perfect agreement between theory and experiments at all temperatures for *para*-H_2–H_2O and a ratio *ortho/para*-H_2 of ∼1 : 1 for normal H_2. The increase of $\sigma^{pb}(T)$ as T decreases seen in other systems [232] is not contradicted by experiments [232a, 232b]

The excellent agreement, including the low-T behavior, underlines the overall quality of the PES, both in its isotropic and anisotropic parts. Because of the large range of broadening temperatures, the various parts of the PES are here successfully tested in a manner very complementary to both total and differential state-to-state or integral sections.

Integral Cross Section Belpassi *et al.* [233] have recently measured the integral cross section D_2O–D_2 as a function of collisional speeds $Q(v)$. A very detailed modeling of the $Q(v)$ function shows that the inelastic events play minor roles and $Q(v)$ mostly arises from the elastic scattering driven by the rotationally averaged (isotropic) component of the interaction. The PES is thus tested in a totally different way. Once more, great confidence may be gained in the PES (see Figures 16 and 17 in the original paper).

3.4
Low Temperature Trapping Experiments

Oskar Asvany and Stephan Schlemmer

The coldest places in the universe are dark molecular clouds (T ∼ 10 K) where almost all gas-phase species are frozen onto dust grains and only He and the hydrogen species H_2 and H_3^+ and a few more molecules are left in the gas phase. These species are present in their lowest electronic state and the molecules are most likely in their vibrational ground state.

Fine-structure states, often separated by only a few millielectronvolts (E_i/k_B ∼ 10–100 K) have to be considered, for example, for the astrophysically relevant C, C^+, or N^+. Also, rotational states are separated by a few wavenumbers. Therefore, at low temperatures, only a few states might be populated by inelastic collisions. In addition, the zero-point vibrational energies (ZPVEs) of a chemical bond are typically of the order of several hundred wavenumbers. Therefore, in reactions where old bonds are broken and new bonds are forming, differences of ZPVEs are of the same order of magnitude as the different quantum levels discussed above. Thus differences of ZPVE, fine-structure states, and rotational states, as well as extremely low lying vibrational modes, for example torsions, can have a significant effect on the outcome of a reaction. If all these states are populated thermally, that is, assuming a canonical ensemble of temperature T, then the description of $k(T)$ in the Arrhenius–Kooij formula is appropriate. However, often thermalization is

not possible because transitions are forbidden due to selection rules or thermalization and reaction are competitive processes and therefore a thermal ensemble is insufficient to describe the physics and chemistry happening in space and the laboratory alike. In this chapter, we discuss a few illustrative and astrophysically relevant examples of gas-phase processes that have been studied in greater detail. These examples are not exhaustive but rather the tip of the iceberg spotted to date.

The situation becomes apparent considering the most abundant molecule in space, H_2. Owing to the Pauli exclusion principle, the total wave function has to be antisymmetric w.r.t. exchange of the two protons (fermionic nuclei). As a result, H_2 has two nuclear spin configurations. One is called *para*-H_2 (*p*-H_2) for which the nuclear spin state is the antisymmetric linear combination of the single spin functions $\alpha = |\uparrow\rangle$ for spin up and $\beta = |\downarrow\rangle$ for spin down,

$$\chi_{\mathrm{nuc}} = \frac{\sqrt{2}}{2}\{\alpha\beta - \beta\alpha\}. \tag{3.30}$$

This nuclear spin state occupies the even numbered rotational states ($J = 0, 2, 4,...$) whose wave functions are symmetric w.r.t. proton exchange. The other manifolds are the three symmetric linear combinations

$$\chi_{\mathrm{nuc}} = \alpha\alpha \tag{3.31}$$

$$\chi_{\mathrm{nuc}} = \frac{\sqrt{2}}{2}\{\alpha\beta + \beta\alpha\} \tag{3.32}$$

$$\chi_{\mathrm{nuc}} = \beta\beta \tag{3.33}$$

forming *ortho*-H_2 (*o*-H_2) with odd-numbered rotational states ($J = 1, 3, 5,...$) whose wave functions are antisymmetric w.r.t. proton exchange. Rotational transitions (radiative or collisional) occur only within the ortho or para species unless an external magnetic force leads to a nuclear spin flip. As a result, gas-phase collisional cooling (without spin flip) of an ensemble of H_2 finally leads to a population of the two lowest rotational states. Owing to the exclusion principle, the $J = 1$ rotational state, which is $E_{\mathrm{i}}/k_{\mathrm{B}} = 170.5$ K higher in energy than the ground state, cannot be cooled to its lowest state ($J = 0$).

As shown above, there are three ortho states for one para state, all of which are occupied with equal probability in a high-temperature thermal population. Therefore, hydrogen under normal conditions is found with an ortho to para (o/p) ratio of 3 : 1, called *normal hydrogen* (normal-H_2, n-H_2). As we will see, this ratio can be changed as a result of chemical reactions, leading to a different o/p ratio. Therefore, depending on the type of collision, the o/p ratio might be conserved or altered by spin-changing collisions. In the former case, the *ortho*- and *para*-hydrogen can be treated as different species and the rotational energy at low temperatures where, for example, only $J = 1$ is populated in *o*-H_2, would be locked in *o*-H_2 while in the latter case it can be redistributed among the collision partners. Since the energy difference between the lowest ortho and para states is several times larger than the kinetic temperature of a cloud (10 K), it becomes obvious from this simple example that ortho to para conversion can have dramatic effects on the outcome

of chemical reactions. In fact, in low temperature environments, it can dominate the result.

3.4.1
$N^+ + H_2$

In Section 3.1, the astrophysically relevant reaction $N^+ + H_2 \rightarrow NH^+ + H$ has been discussed already in some detail. Merged-beams and guided ion beam experiments showed that the reaction is slightly endoergic. Therefore, the reaction efficiency of ground state D_2 (and here H_2, $J = 0$) is much lower than that of rotationally excited D_2 (H_2, $J = 1$). This reaction has been studied with CRESU [234] and trap experiments [235, 236] as a function of temperature and as a function of the ortho to para composition of the H_2 ensemble in order to elucidate the question on the role of nuclear spin in chemical reactions.

In the laboratory, it is possible to produce very pure *n*-H_2 when cooling down n-H_2 to low temperatures in the presence of a paramagnetic catalyst (e.g., Fe(III)O) which promotes the ortho to para conversion of H_2. In such an environment, the o/p ratio is given by the thermodynamic equilibrium of both species at the temperature of the catalyst exit. Details of *para*-H_2 converter instrumentation can be found, for instance, in Refs [237, 238] and references therein. Figure 3.33 shows the temperature dependence of the rate coefficient $k(T)$ which varies drastically

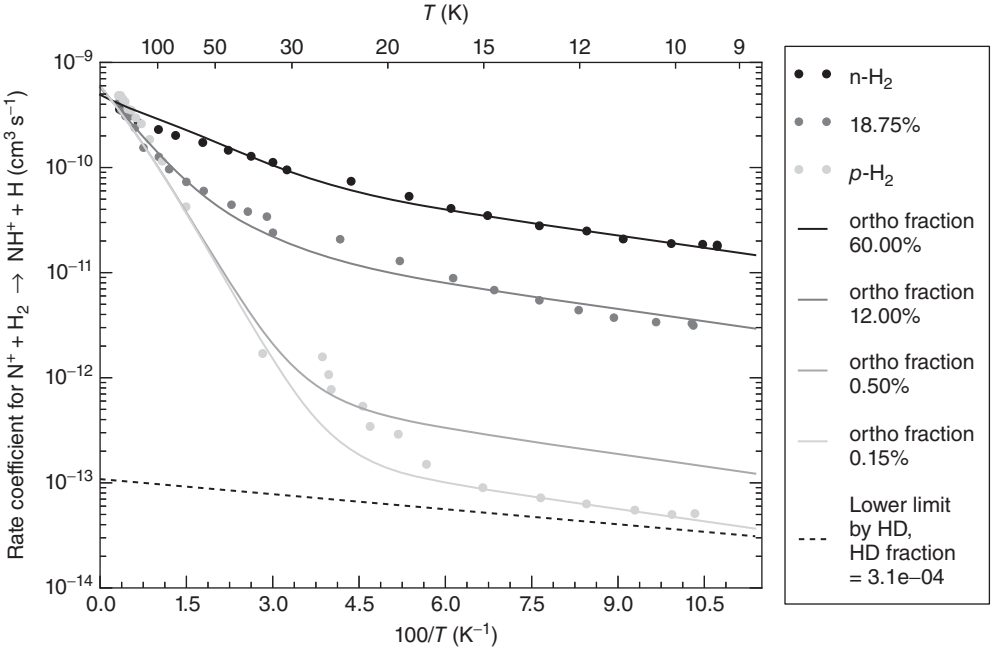

Figure 3.33 Dependence of the reaction $N^+ + H_2$ on temperature and on the *o*-H_2/H_2 fraction.

for a variety of o/p ratios of H_2 in the trap. At high temperatures, the rate coefficients are close to the Langevin limiting value of 10^{-9} cm^3 s^{-1}, irrespective of the nuclear spin configuration. At lower temperatures, the rate coefficients drop in a rather different manner depending on the *o*-H_2 content, given by the fraction $f = \mathrm{o} - \mathrm{H_2}/\mathrm{H_2}$.

One limiting experimental case is n-H_2, where three-fourths of the hydrogen is *o*-H_2, $f = 0.75$. Reaction with rotationally excited H_2 is considerable, and thus the rate coefficient follows an Arrhenius behavior with an activation energy ($E/k_B \sim 40$ K). The other limiting case is the measurement with *p*-H_2. Here, the rate coefficient drops much faster ($E/k_B \sim 230$ K) owing to the fact that at low temperatures only the $J = 0$ state is populated and the endoergicity appears larger for the *p*-H_2 species. In fact, at the temperature of cold clouds (10 K), the ortho/para difference would be even much larger if $k(T)$ would follow this Arrhenius behavior ($E/k_B \sim 230$ K). However, the experimental values depart from this behavior, and the slope of $k(T)$ follows pretty much that for the *o*-H_2 (see below). Note that the absolute values of the rate coefficients for *o*-H_2 and *p*-H_2 differ by more than two orders of magnitude at low temperature. Therefore, the rotational state of H_2 clearly has a pivotal role on the outcome of this reaction and at this point it becomes apparent that state-specific rate coefficients are needed for this and other similar reactions [236].

One interesting question associated with the results shown in Figure 3.33 is why the rate coefficient $k(T)$ for *p*-H_2 is departing from the Arrhenius behavior. One possible explanation is concerned with the purity of the *p*-H_2 produced in the laboratory. Even a small fraction of *o*-H_2 leads to a dominant contribution to the effective rate coefficient measured in the laboratory. As a result, the low-temperature slopes of $k(T)$ for both *o*-H_2 and *p*-H_2 would be very similar as found in the experiments. The lowest experimental $k(T)$ values taken in Cologne would be consistent with an ortho fraction of $f = 0.0015$. This value is significantly lower than previous values; however, the thermal fraction of *o*-H_2 is expected to be even lower, $f = 4.7 \times 10^{-4}$, in the para converter instrument operated at 17.3 K for these experiments. The purity of *p*-H_2 has been checked independently by Raman spectroscopic measurements of the o/p ratio of H_2, which led to a similar value of the ortho fraction with an upper limit of $f = 0.002$. Therefore, these results are all consistent with a tiny impurity *o*-H_2.

There are more subtle effects associated with the reaction of N^+ and hydrogen. Hydrogen contains a natural abundance of HD (which is different in the laboratory and in space), which can play an important role in chemical processes. In the reaction of $N^+ + HD$, the formation of $ND^+ + H$ is much more likely than $NH^+ + D$ since the difference in ZPVE favors this outcome. In fact, $N^+ + HD \rightarrow ND^+ + H$ is $\Delta E/k_B \sim 170$ K more exoergic than the $N^+ + \mathrm{p\text{-}H_2} \rightarrow NH^+ + H$ reaction. Accidentally, this is about the same energy difference as that between the two lowest rotational states of hydrogen. In effect, also $N^+ + HD \rightarrow ND^+ + H$ proceeds almost at collision rate. With a natural abundance of HD in H_2 of about 3×10^{-4} (on Earth), the effective rate coefficient of $N^+ + \mathrm{p\text{-}H_2}$ (with o/p = 0) and such an admixture of HD would lead to a similar experimental result. This indicates

that also the small HD content can have a very important influence on the outcome of low-temperature chemical reactions. More careful measurements of the $N^+ + HD \rightarrow ND^+ + H$ reaction have to be carried out to determine the rate coefficient at low temperatures.

Also, a closer inspection of the temperature dependence of $N^+ + n\text{-}H_2 \rightarrow NH^+ + H$ reveals that the rate coefficient $k(T)$ does not strictly follow the Arrhenius behavior. Instead of a straight line in the $\log(k(T))$ versus $1/T$ representation, the experimental values follow a curved line. Such a behavior could be due to different rate coefficients for the three different fine-structure states of N^+ ($^3P_2$, $^3P_1$, and $^3P_0$). Under the assumption of a thermal population of these three states in a trap experiment, state-specific rate coefficients can be inferred, as has been described in detail in Ref. [236]. A similar behavior can be reproduced when fitting $k(T)$ to a set of Arrhenius–Kooij expressions.

In summary, this seemingly simple atom–diatom reaction of N^+ and H_2 shows the importance of state-specific rate coefficients and the need for more detailed experiments unraveling the role of the different internal degrees of freedom: fine-structure states, nuclear-spin states, and states of different ZPVE. Owing to the correlation of the nuclear spin states to the rotational states, the influence of these states on the reactivity can be rationalized on the basis of energetics. To understand the influence of the fine-structure states on the reactivity, different spin–orbit potential energy surfaces have to be considered. Figure 3.34 shows the lowest energy curves for the $N^+ + H_2$ reaction. A closeup of the entrance channel shows the correlation of the three fine-structure states of N^+ with the repulsive and attractive states of NH_2^+. From this diagram, it becomes clear that, at the low collision energies considered, the $^3P_2$ state cannot react but is leaving the collision toward the reactants. This collision might change the fine-structure state and relax $^3P_2$ to $^3P_1$ as the two potential energy surfaces (PESs) are connected, that is, correlated. The $^3P_1$ state is correlated with the nonreactive and reactive PESs and

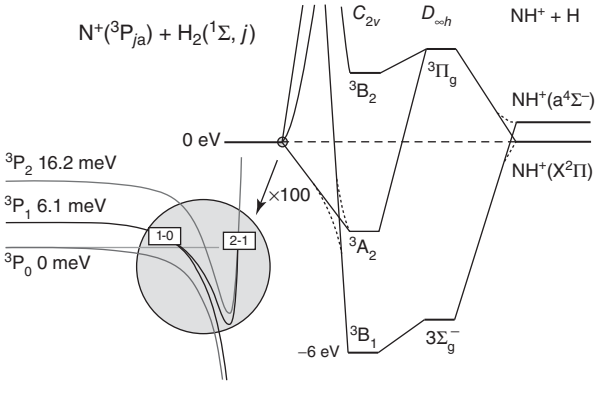

Figure 3.34 Correlation diagram of the NH_2^+ potential energy surface with special emphasis on the entrance channel. The figure is reproduced from Ref. [236] with permission from AAS, and is based on *ab initio* calculations cited therein.

can undergo inelastic fine-structure transitions connecting $^3P_1$ to the $^3P_2$ state. Finally, the $^3P_0$ state is correlated to the reactive PES. As a result, the outcome of an $N^+ + H_2$ collision is determined by the ratio of the probabilities for the reaction and inelastic processes. Current experiments indicate that reaction and inelastic processes are in competition in this collision system, which makes this an interesting test case for the advancement of theoretical modeling. At the same time, this reaction is the first step in the formation of interstellar ammonia. The outcome of the reaction and the influence of the internal states are related to the efficiency of ammonia formation.

3.4.2
$H_3^+ + H_2$

Following the reasoning of Section 3.1, the most frequent ion–molecule collisions are between the prominent H_3^+ ion and the most abundant neutral molecule, H_2. Both species have the two nuclear spin configurations, ortho and para, which are associated with specific rotational states as discussed before for H_2. In H_2, the nuclear spins of the two protons are combined to $I = 0$ (para) and $I = 1$ (ortho). In H_3^+, the three nuclear spins are combined to $I = 3/2$ (ortho) and $I = 1/2$ (para).

The lowest energy levels of H_3^+ and H_2 are presented in Figure 3.35 together with the lowest energy levels of H_2D^+ and HD. The latter species will be discussed in the subsequent section on deuterium fractionation. Owing to the Pauli exclusion principle, the 0_0 rotational state of H_3^+ is forbidden such that the lowest rotational state is the 1_1 state of p-H_3^+. The lowest ortho state is 1_0. The next higher rotational state is already considerably higher in energy because rotational level spacings are particularly large for molecules not containing any heavy nucleus. Thus effectively only two states of H_3^+ (one of ortho configuration (1_0) and one of

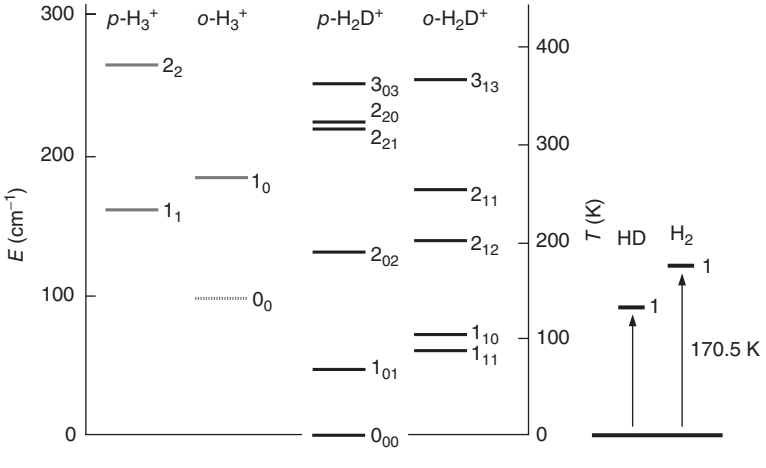

Figure 3.35 Lowest energy levels of H_3^+, H_2D^+, H_2, and HD. (Adapted from Figure 2 of Ref. [244].)

para configuration (1_1)) will be populated in a low-temperature environment. As discussed before, also only the two lowest states of H_2 (one of ortho configuration ($J = 1$) and one of para configuration ($J = 0$)) need to be considered.

In the collision $H_3^+ + H_2 \rightarrow H_3^+ + H_2$, the nuclear spin configurations of H_3^+ and H_2 are not altered in the so-called identity reaction, $H_3^+ + \tilde{H}_2 \rightarrow H_3^+ + \tilde{H}_2$. Here, $\tilde{H}$ indicates a proton which comes from the neutral H_2 reactant and in this particular case the protons stick to the same product entity as in the entrance channel. But the nuclear spin configurations of H_3^+ and H_2 may change as a simple consequence of a proton hop reaction, $H_3^+ + \tilde{H}_2 \rightarrow \tilde{H}_2H^+ + H_2$, or a so-called exchange reaction, $H_3^+ + \tilde{H}_2 \rightarrow H_2\tilde{H}^+ + H\tilde{H}$.

The outcome of these inelastic and reactive collisions determines the population of ortho and para states of H_3^+ and H_2. As a consequence, there is an effective ortho to para conversion in both H_3^+ and H_2 in which the four nuclear spin configurations cannot be treated as four independent species. It is necessary to use individual state-to-state rate coefficients to describe the evolution of an ensemble of H_3^+ and H_2 in the laboratory and in space. Such rate coefficients are not available from experiments to date. Also, from the theoretical side, only approximate values have been determined from phase-space calculations despite their fundamental importance in gas-phase chemistry.

Predicting the ortho/para ratio of the two molecules in space is a challenging task for experiment [239–241] and modeling [242, 243]. This is an active area of research because the result of these investigations influences the modeling of the o/p ratio of H_3^+ and H_2 and subsequently the outcome of many other reactions, as can be seen for the $N^+ + H_2$ reaction which depends so strongly on the o/p ratio of H_2. From these simple considerations, it is becoming clear that state-specific rate coefficients are not the exception in astrochemistry. Instead, they are ruling the initial chemical steps.

The complex dynamics hidden in the simple $H_3^+ + H_2 \rightarrow H_3^+ + H_2$ reaction is thoroughly discussed in the articles mentioned. However, experimental values of state-to-state rate coefficients for this system are missing despite their importance in gas-phase chemistry. Experimentally, this reaction system is challenging because it is not easy either to prepare an ensemble in a particular quantum state or to probe the outcome of the reaction state selectively. Nevertheless, at low temperatures only a limited number of states are involved and therefore the influence of the ortho to para conversion can be seen. Approaches along these lines are discussed at the end of this chapter. In the following, we will discuss the fundamental description of the collision of five identical fermions. Because of the mentioned difficulties, experimental and theoretical approaches have been followed to simulate the o/p ratio of H_3^+ and H_2 in the laboratory and space since this is an observable that can be accessed in both environments as will be described in the following.

It has been realized by Quack [245] and later refined by Oka and coworkers [239, 246] that selection rules for the nuclear spin modifications of both H_3^+ and H_2 play a role for the o/p ratio of H_3^+. In order to quantify this effect, the o/p abundance ratio of H_3^+ has been determined from the relative intensities of their

infrared spectral lines in a hydrogen plasma [239]. Here it is assumed that, after an initial generation of H_3^+ from the reaction $H_2^+ + H_2$ (see Figure 3.15), the plasma is dominated by the $H_3^+ + H_2$ collision. In these experiments, differences have been observed while comparing results using *p*-H_2 and n-H_2 as precursor molecules in the plasma discharge. The interpretation of the observations is rather difficult because of the complexity of the system. Also inelastic and spin-reactive collisions cannot be distinguished in such an experiment, as in both cases the products are made up from the same constituents.

Theoretically, the treatment is also rather demanding because it would be necessary to predict the evolution of the $H_3^+ + H_2$ on the complex PES of the H_5^+ system. This PES has $5! = 120$ equivalent minima [247] due to the equivalence of the five protons. The minima configurations are separated by small energy barriers associated with the extra energy necessary to rearrange the five protons. These barriers are small compared to the ZPVE of the lowest vibrational energy states associated with the different nuclear spin states of this system of five equivalent fermions. The situation becomes even more complicated by the fact that the PES is entered from the continuum via the $H_3^+ + H_2$ dissociative channel. At present, there are no dynamical calculations, neither quantum mechanical nor using classical trajectories, that yield differential cross sections or thermal rate coefficients as discussed in Section 3.1. Nevertheless, the outcome of this important $H_3^+ + H_2$ collision shall be envisioned as the result of wave packets evolving on this PES.

In view of these difficulties, Oka [246] introduced a model for the nuclear spin selection rules for this collision system and other reactions based on angular momentum algebra following the assumption that the total nuclear spin quantum number **I** given by the vector sum of the nuclear spins $\mathbf{I}_i$ of the equivalent identical nuclei is a *good* quantum number, that is, practically it is conserved and does not change in collisions. The result of this model can be considered as a limiting case where scrambling among the five identical fermions is only restricted by the fundamental laws of quantum mechanics. He introduced three elementary reaction mechanisms called *identity*, *proton hop*, and *hydrogen exchange* as discussed already above. On the basis of these mechanisms, he has derived probabilities for the o/p ratios of H_3^+ and H_2 as an outcome of the $H_3^+ + H_2$ collision without taking into account the dynamical effects of the PES.

The treatment is rather cumbersome and will not be repeated in this review. However, it is helpful to address the main assumptions that led to the models, which were also used in various publications thereafter. As discussed above, the ground state wave function and thus all wave functions describing the H_5^+ system are substantially extended over a large fraction of the full PES. Therefore, the full permutation inversion group of five equivalent protons has to be considered for a proper treatment. In practical terms, this implies the scrambling of all five protons in a $H_3^+ + H_2$ collision (full scrambling, [246]) provided the collision extends for long enough time that a wave packet can evolve over a substantial fraction of the PES. Under the assumption of full scrambling, $5!/3!2! = 10$ cases of proton partitions have to be considered when five equivalent particles are distributed to one particle with three and a second one with two identical particles. Of these, one

belongs to the identity operation, that is, the protons in the H_3^+ and H_2 products are the same as for the reactants (elastic and inelastic collisions). In three cases, a proton can be transferred from H_3^+ to H_2 (proton hop) and in the six remaining cases two protons are exchanged between H_3^+ and H_2 (hydrogen exchange). The true outcome of the collision is of course determined by the PES and thus also involves the kinetic energy of the collision, the angular momentum of the reactants (see impact parameter in Section 3.1), and their rotational states as shown in Figure 3.35. But, based on the assumption that all partitions are equally probable (statistical limit), branching ratios can be easily calculated on the basis of the angular momentum conservation mentioned above. It is often assumed that this result can be associated with the high-temperature limiting case. Such a high-temperature limit appears appropriate even at low collision energies since entering the PES from the $H_3^+ + H_2$ dissociation limit adds about 3000 K of potential energy with respect to the vibrational ground state of the H_5^+ complex.

In an attempt to account for the more complex dynamics of this system, the branching ratio between the fractions of proton hop events (S^H) versus proton exchange events (S^E) has been defined as the ratio

$$\alpha = \frac{S^H}{S^E} = \frac{k^H}{k^E}. \tag{3.34}$$

This ratio has been used as *one* free model parameter in order to describe the complex chemistry in the $H_3^+ + H_2$ collision system, for example, in the plasma cell experiments [239, 240] and in observations of the o/p ratio of H_3^+ in space [248, 249].

In the more recent laboratory experiments [240], the Cordonnier measurements [239] have been repeated for different temperatures and by varying the o/p ratio of H_2 in a hollow cathode discharge cell. The experiment was conducted in a pulsed manner in order to avoid changes of the p-H_2 fraction (para fraction: $p_2 = p\text{-}H_2/H_2$) as a result of the discharge process. After the steady state of the plasma is reached, the o/p ratio of H_3^+ is determined (para fraction: $p_3 = p\text{-}H_3^+/H_3^+$) by measuring the relative intensities of particular ro-vibrational levels of H_3^+.

These measurements of the para fraction p_3 are compared with a variety of kinetics models. In the high-temperature limit, a simple relation for p_3 can be derived with the p-H_2 fraction (p_2, fixed value given by precursor o/p ratio of H_2) and the hop to exchange branching ratio α as model parameters:

$$p_3 = \frac{\alpha + 2\alpha p_2 + 1}{3\alpha + 2}. \tag{3.35}$$

There is thus a linear relationship between p_3 and p_2. Interestingly for n-H_2 ($p_2 = 0.25$), the para fraction of H_3^+ is independent of α, $p_3 = 1/2$, producing 50 % o-H_3^+ and 50 % p-H_3^+. This corresponds to n-H_3^+. In n-H_3^+, eight (=2^3) nuclear spin states are generated from the three spin-1/2 nuclear spin states of each proton which have two possible relative orientations (up α or down β), four of which create symmetric nuclear spin wave functions of A_1 symmetry (multiplicity: 1) with a total nuclear spin $I = 3/2$ (o-H_3^+, degeneracy: 4), and two of which are

antisymmetric of the two-dimensional E-symmetry ($I = 1/2$, p-H_3^+, degeneracy: 2, multiplicity: 2) [250]. Therefore, the statistical ratio is $1 \times 4 : 2 \times 2 = 1 : 1$. The value $p_3 = 1/2$ is indeed found for an uncooled plasma for $p_2 = 0.25$. Changing the purity of p-H_2 led to a linear dependence on p_2 with a value of $\alpha = 1.6$, which is somewhat lower than the earlier results by Cordonnier *et al.* [239]. These findings support the simple high-temperature model, and the value for α indicates that the proton hop is considerably more likely than hydrogen exchange.

In the nitrogen-cooled plasma, p_3 shows a curved behavior, which could be described by a more sophisticated kinetics model using a micro-canonical statistical approach [242] that goes beyond the scope of this reviewing introduction to the subject.

A decreasing value for the hop to exchange ratio α with temperature has been inferred from those measurements, indicating that hydrogen exchange is more likely at lower temperatures than proton hop as expected from the pure statistical behavior ($S^I = 1/10$, $S^H = 3/10$, $S^E = 6/10$). These findings appear counterintuitive as α seems to approach the statistical value ($\alpha = S^H/S^E = 1/2$) at low temperatures whereas the high-temperature result points at a larger probability for proton hop. However, the reaction mechanism obviously changes as a function of temperature. At higher temperatures, that is, higher collision energies, the reaction might be envisioned as a more direct process where the details of the PES influence the outcome of the reaction and thus the effective parameter α. For low-temperature collisions, the two collision partners are thought to form a collision complex which can live substantially longer than the time for a molecular vibration. As a result, the wave packet explores a larger fraction of the PES and thus the complex decomposes according to the number of possible product channels, that is, in a statistical manner.

In another attempt to help astrophysical modeling of the hydrogen chemistry of the $H_3^+ + H_2$ reaction, the population of ortho and para states of H_3^+ as a function of the o/p ratio of H_2 has been investigated in a 22-pole ion trap in the temperature range 45–100 K [241]. The advantage of the trap experiment over the plasma investigations is that the experimental conditions can be controlled so that only H_3^+ ions are stored and H_2 is the only collision partner. Further limitations present in the relatively dense plasma experiments are discussed in detail in Ref. [240].

In the trap experiment, chemical probing has been used to distinguish between the ortho and para population of H_3^+. For that purpose, the lowest rotational states of H_3^+ have been probed by laser-induced reactions (LIRs) with Ar, which led to the selective formation of ArH^+. Originally, this method was developed for the spectroscopy of cold molecular ions [251, 252]. Here, the endothermic reaction of $H_3^+ + Ar \rightarrow ArH^+ + H_2$ has been promoted by state-selective ro-vibrational excitation of H_3^+. The number of ArH^+ products thus is a tracer of the number of H_3^+ in a particular rotational state. Figure 3.36 shows the result of a thorough investigation in which the fraction of p-H_3^+, p_3 as above, inferred from those measurements are plotted versus the fraction of p-H_2, p_2. The experimental results (solid pentagons with error bars) show that the measurement follows the predictions from the microcanonical statistical modeling [242] (solid line). The function

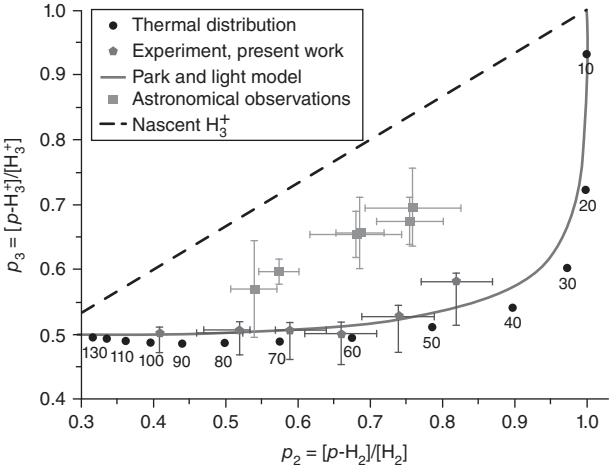

Figure 3.36 Experimental and astrophysically observed fraction $p_3 = p\text{-}H_3^+/H_3^+$ as a function of $p_2 = p\text{-}H_2/H_2$. In the trap experiment, the trap temperature was adjusted to the corresponding p_2 value. (Reproduced from [241], copyright 2012 © permission from AAS.)

$p_3 = f(p_2)$ is close to the result of a thermal distribution (solid dots without error bars but with indicated temperature values) as p_2 has been prepared close to its thermally equilibrated fraction.

Interestingly, these results deviate substantially from those derived from astronomical observations (shown in Figure 3.36 as full squares with error bars). Those values fall in between the thermal limit and the dashed curve $p_3 = 1/3 + 2/3p_2$, which describes the nascent p_3-distribution of the H_3^+ formed in the reaction $H_2^+ + H_2$. In space, the trajectory of evolution starts on the nascent curve at a given p_2 value depending on the o/p fraction of H_2 in the particular astrophysical environment and should develop from there toward the experimental (laboratory) value for a given parameter set (T, p_2). Apparently, the number of H_3^+–H_2 collisions in the sight lines of these observations are insufficient to establish the near-thermal distribution found in experiment.

Thus, the laboratory work aids the interpretation of the observations. In summary, our understanding for this utmost important $H_3^+ + H_2$ reaction is improved, but measurements of state-to-state rate coefficients are needed to be compared with the predictions of the microcanonical statistical model or more advanced models in the future.

It has been discussed above for the $N^+ + H_2$ reaction that small traces of deuterium in hydrogen (HD instead of H_2) can alter the outcome of chemical networks substantially. The presence of HD therefore has significant effects on the chemistry described for the $H_3^+ + H_2$ system and a few other reactions. This will be discussed in greater detail in the next section since it turns out that H_3^+ and its deuterated siblings are very important tracers of the chemical development of very cold astrophysical environments where eventually new stars are formed. The rotational levels of H_2D^+ (as one example of a deuterated sibling) also show an

ortho and a para fraction as displayed in Figure 3.35. The full energy diagram will be discussed in the following since it explains exemplarily the nature of deuterium enrichment in chemical reactions.

3.4.3 Deuterium Fractionation

As mentioned already the beginning of Section 3.4, the very early starting phases of a solar system are molecular clouds characterized by relatively high densities (up to $n(H_2) = 10^6$) and low temperatures, leading to heavy molecules such as CO or N_2 being frozen out onto small dust grains and thus being depleted, leaving mainly hydrogen, its heavy partner deuterium, and helium in the gas phase. As it turns out, very sensitive probes for the conditions in these environments are the molecules containing deuterium atoms. These can be easily distinguished from their hydrogen-containing counterparts by their different spectral fingerprints, and in laboratory experiments they can be distinguished by mass spectrometry. In the last four decades, many singly, some doubly (e.g., NHD_2, D_2CO, CHD_2OH, or c-C_3D_2), and even triply deuterated molecules (ND_3 [253], CD_3OH [254]) have been detected in cold interstellar clouds (see Table 3.3 for an overview). Surprisingly, the measured abundance ratios of the singly deuterated molecules to their undeuterated counterparts tend to be a factor of up to 10^4 greater than expected from the D/H elemental (cosmic) ratio of roughly 1.5×10^{-5} (measured by UV [255] or hyperfine transitions [256] of the atomic species). This enhancement strongly depends on the temperature and other subtle effects such as the o/p ratio of H_2 as will be discussed below.

It is now understood, mostly as a result of detailed low-temperature laboratory studies, that this deuterium enrichment in interstellar molecules is largely due to a chemical process, a phenomenon called *isotopic fractionation*. For simplicity, let us consider a diatomic molecule AH and its deuterated sibling AD. The frequency of the A–X (X = H, D) stretching vibration, $\omega = \sqrt{k/\mu}$, is related to the reduced mass μ of the A–X oscillator and the force constant k. In hydrogenated (AH) and deuterated (AD) molecules, the force constant is the same, as this is caused by the binding electrons, which are the same in both cases. But the reduced mass changes significantly. For $m(A) \gg m(H)$, $m(D)$, one obtains the simple relation $\mu(AH) \approx m(H)$ for AH and $\mu(AD) \approx m(D)$ for AD. As a result, this leads to lower ZPVEs (=$1/2\,\hbar\omega$) for deuterated molecules (AD) with respect to their hydrogenated siblings (AH). In the limiting case $m(A) \gg m(H)$, $m(D)$, this results in a difference in ZPVEs of

$$\Delta\mathrm{ZPVE} \approx \left(1 - \frac{1}{\sqrt{2}}\right) 1/2\hbar\omega \tag{3.36}$$

which is roughly a 30% reduction. For a typical vibrational energy of an A–H vibration ($\hbar\omega \approx 3000\,\mathrm{cm}^{-1}$), this amounts to a difference of several hundred wavenumbers.

In a bimolecular D/H exchange reaction, two reactants and two products are involved:

$$AH + BD \leftrightarrow AD + BH. \tag{3.37}$$

Only if the sum of ZPVEs of the products is less than the corresponding sum of the reactants, the deuterium enrichment AD versus AH is exothermic and thus can happen. Again, the total energy difference can be as large as a few hundred wavenumbers. Provided no barrier hinders the D/H exchange, this energy difference is also the exoergicity of the reaction. Taking the reverse reaction into account, the deuterium enrichment AD versus AH will thus depend exponentially on temperature, and therefore deuterium enrichment is unimportant for room-temperature chemistry but it can be significant at the low temperatures of cold molecular clouds. Owing to this critical dependence on temperature, observations of AD/AH ratios in space may be used as a very sensitive low-temperature thermometer.

Table 3.3 Deuterated molecules detected in interstellar environments (as of March 2014: only secure detections considered).

Mass	Name of parent	Detected D-isotopomer	Year of first detection
2	Molecular hydrogen	HD	1973
3	Protonated hydrogen	H_2D^+, HD_2^+	1999, 2004
15	Imidogen radical	ND	2010
17	Ammonia	NH_2D, NHD_2, ND_3	1978, 2000, 2002
17	Hydroxyl radical	OD	2012
18	Ammonium ion	NH_3D^+	2013
18	Water	HDO, D_2O	1975, 2007
25	Ethynyl radical	C_2D	1985
27	Hydrogen cyanide	DCN	1973
27	Hydrogen isocyanide	DNC	1977
29	Formyl ion	DCO^+	1976
29	Protonated nitrogen	N_2D^+	1977
30	Formaldehyde	HDCO, D_2CO	1979, 1990
32	Methanol	CH_3OD, CH_2DOH, CHD_2OH, CD_3OH	1988, 1993 2002, 2004
34	Hydrogen sulfide	HDS, D_2S	1996, 2003
38	Cyclopropenylidene	c-C_3HD, c-C_3D_2	1986, 2013
40	Methylacetylene	CH_2DCCH, CH_3CCD	1992, 2005
41	Methylcyanide	CH_2DCN	1992
46	Thioformaldehyde	HDCS, D_2CS	1997, 2005
49	Butadiynyl radical	C_4D	1989
51	Cyanoacetylene	DC_3N	1980
60	Methyl formate	$HCOOCH_2D$	2013
75	Cyanobutadiyne	DC_5N	1981

The species are ordered with increasing nominal mass of the undeuterated parent. Given is also the year of first detection (publication date). For up-to-date information, visit, for example, www.astro.uni-koeln.de/cdms.

This effect is especially pronounced for the hydrogen isotopic system, as the D/H mass ratio of 2 is much larger than the mass ratio of the C^{13}/C^{12} and N^{15}/N^{14} isotopes, leading to bigger differences in the ZPVEs. Nevertheless, also for these less pronounced cases determination of the isotopic ratios in interstellar molecules is used as a diagnostic tool for the chemical origin of these species [257]. Owing to its importance, only the D/H isotopic system will be considered in the following.

Two main chemical processes have been identified to mediate isotopic fractionation. On one side are the processes occurring on icy grain mantles (see Chapter 5): atoms can stick to grain mantles, wander around or tunnel the surface landscape, meet reactants to form new molecules, and finally escape the surface when heated, for example, by a cosmic ray particle or when a protostar forms and heats up the surrounding gas. One of the most prominent examples of molecules thought to be formed on icy grains is methanol (and its deuterated partners). On the other side, there are the gas-phase reactions, the focus of this chapter. As the deuterium in molecular clouds is mostly contained in the form of HD, it is assumed that gas-phase deuterium fractionation is initiated by ion–molecule exchange reactions involving HD as the neutral reactant. To date, only three of these primary deuteration reactions are known to be fast, namely the reactions of H_3^+, CH_3^+, and $C_2H_2^+$ with HD [258, 259]:

$$H_3^+ + HD \rightleftharpoons H_2D^+ + H_2 + 232\,K \tag{3.38}$$

$$CH_3^+ + HD \rightleftharpoons CH_2D^+ + H_2 + 375\,K \tag{3.39}$$

$$C_2H_2^+ + HD \rightleftharpoons C_2HD^+ + H_2 + 550\,K. \tag{3.40}$$

The significance of these (kind of) fractionation reactions was quickly realized [260] after the first observational data became available in the 1970s. All three reactions (3.38–3.40) are exothermic in the forward direction and endothermic in the reverse direction. In addition, the above reactions are not subject to a barrier on their respective reaction pathways, thus leading to, for example, an enhancement of H_2D^+ w.r.t. H_3^+. Owing to the exponential dependence of the rate coefficients on this energy difference, the H_2D^+ to H_3^+ ratio is a very sensitive probe of the temperature of the astrophysical environment as explained above.

The first of these reactions (3.38) is the main deuteration channel when hydrogen is the dominant species in the low-temperature environment. The lowest energy levels of the two reactants (H_3^+ and HD) and two products (H_2D^+ and H_2) participating in reaction (3.38) are depicted in Figure 3.35. The lowest energy state of the $H_2D^+ + H_2$ product channel is associated with the 0_{00} rotational state of p-H_2D^+ and the lowest rotational state of p-H_2 ($J = 0$). The lowest state of p-H_3^+ (1_1) is associated with the lowest energy state of HD ($J = 0$). The energy level of p-H_3^+ (1_1) is 232 K higher in energy than the lowest p-H_2D^+ product state, indicating the exoergicity of reaction (3.38). Since both neutral species are in the $J = 0$ state, the energetics of the colliding system can be depicted by the energy of the ions only. Further details of the energy scheme in Figure 3.35 will be discussed below.

Another challenge arises from the fact that H_2D^+ can be further deuterated in another D/H exchange in collisions with HD, forming D_2H^+ and H_2. Finally, in a last step, D_3^+ can be formed. All these reactions are exoergic, too. It is even discussed whether in very cold conditions practically all H_3^+ can end up in D_3^+. All of these H_3^+ isotopologs have similar nuclear spin configurations as discussed for H_3^+ and H_2D^+ and as depicted in Figure 3.35 with their respective rotational energy states. Like for the $H_3^+ + H_2$ system, also here state-to-state rate coefficients have to be considered as the nuclear-spin-changing collisions have to be taken into account. All this complicates the modeling of the $H_3^+ + H_2$ chemistry when deuteration is included.

It is the purpose of current experiments and calculations to simulate the H_2D^+ to H_3^+ ratio or other ratios such as the D_2H^+ to H_2D^+ or even the ortho to para ratio in H_2D^+. Like for the $H_3^+ + H_2$ collision system, experimental state-to-state rate coefficients are missing. A full set of state-to-state rate coefficients for all isotopologs has been calculated on the basis of a microcanonical system including nuclear restrictions as mentioned for the simpler $H_3^+ + H_2$ system above. Some details of this analysis will be discussed below.

Observationally, the importance of reaction (3.38) has been well established in the last 15 years. Direct detection of H_3^+ is difficult since it does not have a rotational spectrum [261]. In recent years, infrared absorption observations have become a standard technique to determine the H_3^+ abundance. Also, the detection of H_2D^+ is difficult since only one line of *o*-H_2D^+ ($1_{10} \rightarrow 1_{11}$) at 372 GHz is reachable by ground-based telescopes [262]. The lowest transition in *p*-H_2D^+ ($1_{01} \rightarrow 0_{00}$) lies at 1.37 THz and could not be observed until recently using the SOFIA airborne observatory. Because of these difficulties, other molecules such as N_2H^+ have been used as tracers for H_3^+.

While much less abundant than H_3^+, CH_3^+ and $C_2H_2^+$ are thought to be drivers for deuteration in molecular clouds with elevated temperatures (~50 K) [263]. The higher exothermicity of reactions (3.39 and 3.40) prevents the deuterated species CH_2D^+ and C_2HD^+ from being destroyed by the ambient warm H_2 gas. Still, while there is only tentative evidence for deuteration via CH_3^+ [264], a proof for deuteration via $C_2H_2^+$ is still missing (partly due to missing microwave laboratory data for C_2HD^+). The chemical situation is summarized in Figure 3.37, which displays the fractionation ratio of the deuterated species of the above reactions (3.38–3.40) in a semilogarithmic plot versus temperature. The fractionation ratio is defined as the enhancement factor, which is given by the AD^+/AH^+ ratio divided by the HD/H_2 ratio. For H_2D^+, enhancements of 10^4 and higher are predicted in this early model [265]. This factor drops down dramatically above 20 K. For CH_2D^+ and C_2HD^+, the enhancement reaches values of several thousand and several hundred, respectively, at temperatures of 40–50 K as rationalized above. The model underlying those predictions contains a few more boundary conditions which are relevant for understanding deuterium enrichment in cold cloud environments. In the simplest approach, the relative abundance of AD^+/AH^+ is governed by the exothermicity of the above reactions (3.38–3.40), which would lead to an exponential behavior as a

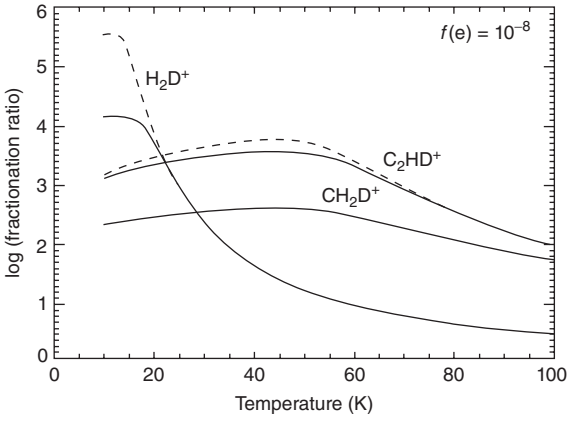

Figure 3.37 Enhancement factors for H_2D^+, CH_2D^+, and C_2HD^+ as a function of temperature for a fixed electron fraction of 10^{-8}. The dashed lines are calculations for heavily depleted molecular abundances. (Reproduced from [265], copyright 2003 © kind permission from Springer Science and Business Media.)

function of temperature as is approximately seen for the H_2D^+ enhancement factor. Both H_2D^+ and H_3^+ are destroyed primarily by electrons via dissociative recombination (see Section 3.2). This reaction becomes dominant at lower temperatures (see Figure 3.2) and therefore the H_2D^+ enhancement is limited at temperatures below 20 K. The electron fraction is assumed to be $[e^-]/[H_2] = 10^{-8}$ in this particular case. The enhancement ratios shown as solid lines in Figure 3.37 are modeled for a normal molecular abundance of $[M]/[H_2] = 10^{-4}$ and are compared with the situation where much of these molecules are depleted as a result of freeze out ($[M]/[H_2] = 10^{-6}$). The differences, taking into account the details of the cloud environment, are small for CH_2D^+ and C_2HD^+ compared to the dramatic enhancement in H_2D^+ as a function of temperature. Therefore, isotopic fractionation, especially in H_3^+, is a very strong effect and may be used for tracing cloud environments especially prior to star formation when low temperatures are reached.

Once the deuterium is enriched in H_3^+, CH_3^+, or $C_2H_2^+$ as mentioned above, it can be passed to other molecules in secondary ion–molecule reactions. Owing to the low proton affinity of H_2, H_3^+ donates a proton to most other molecules. The most abundant molecules after H_2 are carbon monoxide and nitrogen (as long as the mentioned gas-phase depletion is not too pronounced), and thus reactions of the type

$$H_2D^+ + CO \rightarrow HCO^+ + HD \tag{3.41}$$

$$\rightarrow DCO^+ + H_2 \tag{3.42}$$

produce secondary deuterated molecules. Actually, astronomical detections of DCO^+ or N_2D^+ are always a strong hint for deuteration processes in molecular clouds, and, as can be seen in Table 3.3, these species were among the earliest detections.

3.4.4
Trap Experiments on Deuterium Enrichment

Despite the simple deuterium exchange mechanism leading to deuterium enrichment, a more quantitative prediction of astrophysical quantities such as the H_2D^+ to H_3^+ ratio is difficult. Like in the $H_3^+ + H_2$ system, in $H_2D^+ + H_2$ collisions, inelastic processes and ortho–para conversion reactions (o/p-$H_2D^+ + o/p$-$H_2 \rightarrow o/p$-$H_2D^+ + o/p$-H_2) have to be considered, but also the backreaction ($H_2D^+ + H_2 \rightarrow H_3^+ + HD$) when trying to predict, for example, the H_2D^+ to H_3^+ ratio. Thus reaction (3.38) is even more complicated than the pure hydrogen system $H_3^+ + H_2$. However, the deuterated versions of the reaction can be followed with mass spectrometric methods and therefore have been the subject of a number of laboratory investigations. Several experimental methods have already been explained in Section 3.1, but details of studies of isotopic experiments are presented here before we describe the progress made in recent years based on trap experiments [243] and modeling based on a microcanonical statistical approach [243] similar to that of Park and Light [242] already discussed above for the $H_3^+ + H_2$ system.

The first low-temperature trapping experiments on the reaction $H_3^+ + HD$ were presented in 1993 [258, 266]. Figure 3.38a shows the temporal behavior of an ensemble of H_3^+ ions stored in an n-H_2 environment at a number density of 1.4×10^{14} cm^{-3}. According to the natural terrestrial abundance of HD in H_2 (3×10^{-4}), the number density of HD is 4.2×10^{10} cm^{-3}. The trap was cooled to the lowest possible temperature, 10 K. H_3^+ reacts with HD to form H_2D^+, which in reactions with H_2 undergoes the backreaction according to reaction (3.38). In fact, already after a few milliseconds, an equilibrium between H_3^+ and H_2D^+ is established. As a further channel, the three-body association (see Section 3.1) of H_3^+ with H_2 leads to an increasing fraction of H_5^+ clusters, which is the reason why the number of H_3^+ ions decreases very slowly. The same association happens to H_2D^+, creating a small fraction of H_4D^+ products. In this experiment, the H_2D^+/H_3^+ ratio is found to be 0.002. This value is larger than the terrestrial HD/H_2 ratio given above, indicating an enrichment of deuterium in H_3^+. But this enrichment is far from the high values predicted by the simple D/H exchange discussed so far and seen in Figure 3.37.

Figure 3.38b shows the same reaction but this time in collisions with p-H_2 ($J = 0$) instead. The number density is 10^{14} cm^{-3}. Again, an equilibrium between H_3^+ and H_2D^+ is reached after about 10 ms and also a fraction of the ions are subject to three-body association. The H_2D^+/H_3^+ ratio is about 0.2, that is, 100 times larger than with n-H_2 which contains three-fourths o-H_2 ($J = 1$). This is a very clear proof that the amount of $J = 1$, o-H_2, has a drastic influence on the H_2D^+/H_3^+ ratio in the laboratory and in space alike. However, it is rather difficult to quantify the influence of o-H_2 since it is not easy to determine the amount of o-H_2 impurities in p-H_2 as explained above.

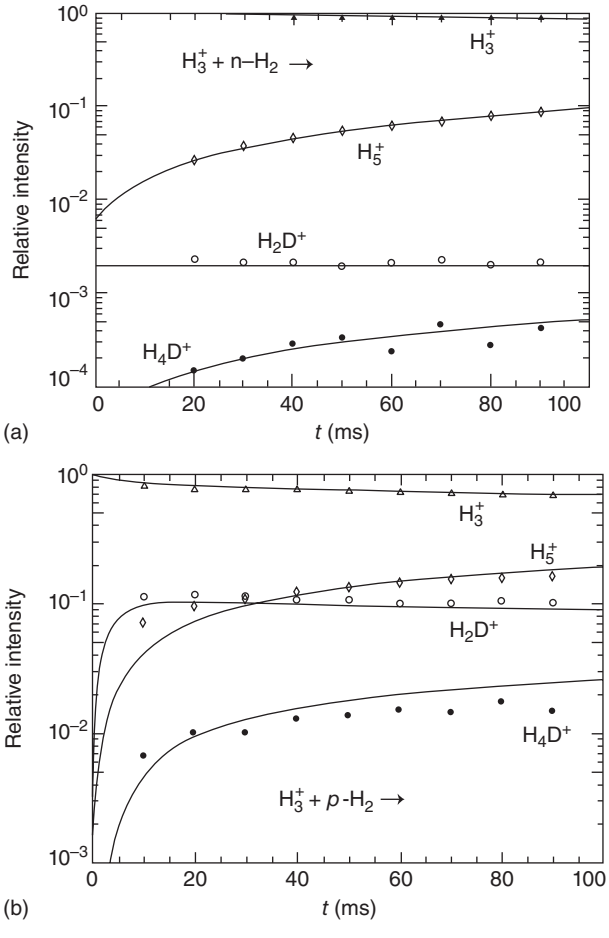

Figure 3.38 Temporal evolution of an H_3^+ ensemble injected and trapped in (a) n-H_2 and (b) p-H_2. (Reproduced from [258], copyright 2002 © permission from Elsevier.)

In Ref. [258], the fraction of o-H_2 was estimated to be about 1%. Thus the purity of p-H_2 is $p_2 = 0.99$. As discussed for the $N^+ + H_2$ reaction, this amount of o-H_2 appears to determine the outcome of the reaction. Thermodynamically, the reaction of H_2D^+ with p-H_2 should not lead to a substantial amount of H_3^+ products at a temperature of 10 K, reached in the laboratory and in space. Thus, the amount of H_3^+ products is governed by the fraction of rotationally excited H_2 and H_2D^+. As it is obvious that the rotationally excited o-H_2 carries an additional 170.5 K of rotational energy, a closer inspection of the energy diagram 3.35 shows that also the lowest level of o-H_2D^+ carries a substantial extra energy which influences the H_2D^+/H_3^+ ratio at low temperatures. It will be argued below that this particular quantum state of o-H_2D^+ (1_{11}) in fact governs the first step of deuterium fractionation.

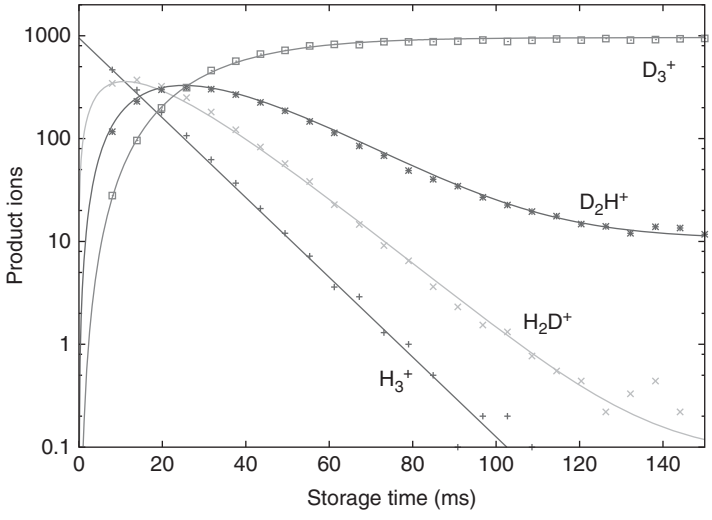

Figure 3.39 Sequential deuteration of H_3^+ in HD with a number density of $6.3{\times}10^{10}$ cm^{-3} at a nominal temperature of 13.5 K. Owing to the exothermicity of the reaction chain, a constant number density of about $6{\times}10^{12}$ cm^{-3} He has been applied to ensure full thermalization of all reactants. The lines are the solutions of a rate equation system fitted to the experimental data. (Copyright [2009], AIP Publishing LLC., Ref. [243].)

Owing to the impurities in *para*-hydrogen in those experiments, it is not possible to derive reliable rate coefficients for the reaction $H_2D^+ + p\text{-}H_2$. The situation is further complicated as inelastic collisions, nuclear-spin-changing collisions (ortho to para conversion), and reactions compete in these collisions. Therefore, it is very difficult to determine the state-to-state rate coefficients needed to model the deuterium chemistry. In contrast, the rate coefficient for the forward reaction has been determined independently in trap experiments of H_3^+ with HD. Figure 3.39 shows the temporal evolution of initially stored H_3^+ in collisions with HD ($n = 6.3 \times 10^{10}$ cm^{-3}) at a nominal trap temperature of $T = 13.5$ K. H_3^+ disappears, forming H_2D^+. It turns out that this reaction is relatively fast and therefore the ortho to para composition of H_3^+ apparently has a small influence which is neglected in further discussions. Still, in principle, individual state-to-state rate coefficients also for these reactions would be desirable. In consecutive collisions with HD, another deuterium atom is replaced in H_2D^+, leading to D_2H^+ products and, in a final step, to D_3^+ as discussed above. Back reactions with HD finally lead to a deviation from the sequential deuterium enrichment. As a result, the number of D_3^+, D_2H^+, and H_2D^+ reach a steady-state value as can be seen for longer times in Figure 3.39. The solid lines are simulations of the chemical network involving these reactions. While the rate coefficient for the first reaction of H_3^+ with HD could be inferred easily from the mono-exponential decay of H_3^+, the other rate coefficients are the result from a best fit of the experimental data.

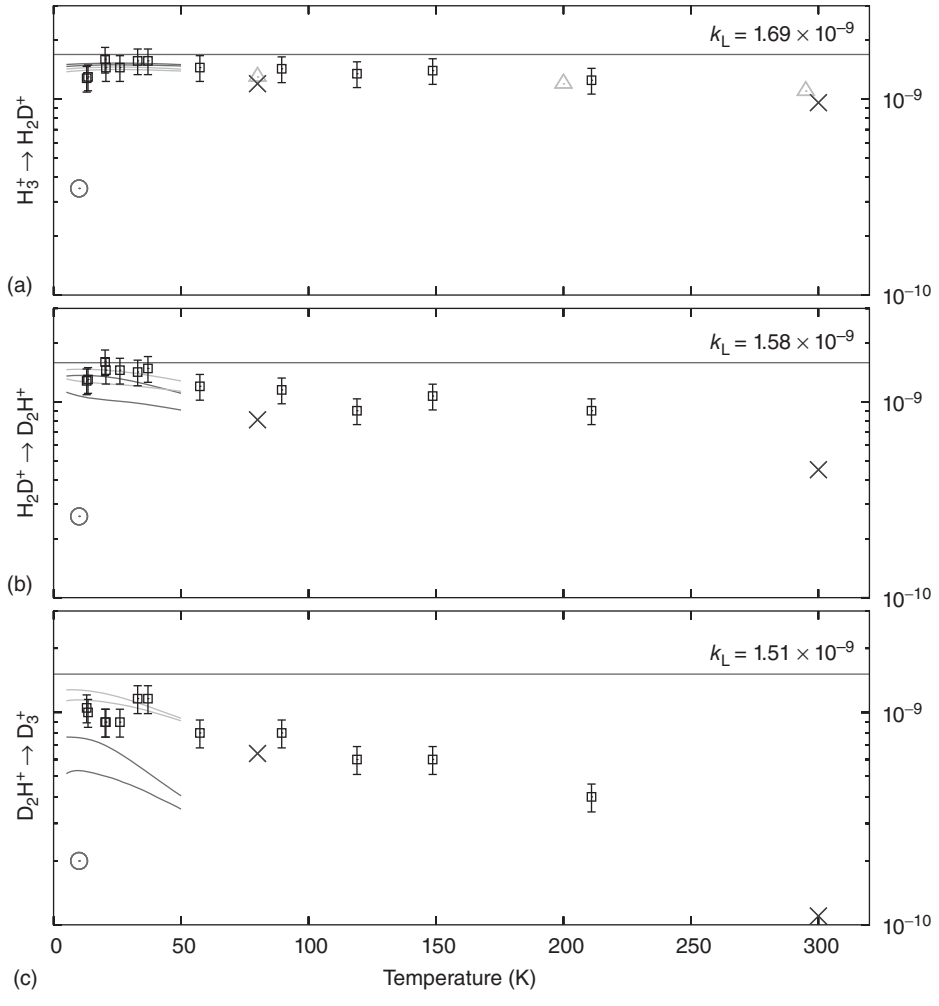

Figure 3.40 Temperature dependence of the rate coefficients for the reactions of (a) H_3^+ with HD, (b) H_2D^+ with HD, and (c) D_2H^+ with HD. The four lines are results from a microcanonical model representing different conditions and assumptions. (Reproduced from [243], copyright 2009 © permission from AIP Publishing.)

Figure 3.40 summarizes the rate coefficients derived from such measurements as a function of temperature for the individual deuteration steps. The rate coefficient for H_3^+ + HD at about 10 K has been found to be 3.5×10^{-10} cm^3 s^{-1} in the first trap experiment [258]. The later experiments, depicted exemplarily in Figure 3.39, conducted with the same apparatus but a different trap gave values much closer to the Langevin limit, as depicted in Figure 3.40 [243]. The reason for the discrepancy remains unclear; impurities of H_2 in the HD gas or incomplete

accommodation of the ion temperature to the nominal trap temperature being possible reasons. Therefore, even more thorough investigations and *in situ* measurements of the ion temperature are planned in the future. The faster reaction of the more recent measurements is more in line with the expectations for these barrierless exothermic reactions. In fact, all deuteration steps are rather fast at low temperatures and become slower at elevated temperatures. This result is in accordance with the physical picture that, in $H_3^+ + H_2$ collisions, an H_5^+ complex is formed at low temperatures and that the reaction proceeds more directly at higher collision energies, that is, higher temperatures. For longer lifetimes of the collision complex, the decomposition can be expected to take the most exoergic path as the number of product channels in this case is largest. For a direct reaction, the interaction time can become shorter than the time for a hydrogen exchange reaction, and thus the rate coefficient would decrease for increasing temperatures. This discussion is very much in line with the findings for the temperature dependence of the $H_3^+ + H_2$ collision system above.

It is interesting to see that, for the initial reaction $H_3^+ + HD$, this effect is rather small, that is, the rate coefficient is large at all temperatures. For the second deuteration step $H_2D^+ + HD$, the rate coefficient at room temperature is only about half the value compared to low temperature values. For the final deuteration step, the rate coefficient at 300 K drops by more than one order of magnitude. It is clear that the reaction of D_2H^+ and HD to form D_3^+ and H_2 must involve a hydrogen exchange since the H_2 product contains one proton from HD and one from D_2H^+. Instead, the proton transfer would lead to H_2D^+ or D_2H^+ and the identity pathway would leave D_2H^+ unchanged. Thus, apparently, hydrogen exchange can proceed efficiently only at low temperatures.

The solid lines in Figure 3.40 depict the results from the microcanonical model of Hugo *et al.* [243], which follow the experimental trend of a decreasing rate coefficient. These calculations were restricted to low temperatures ($T < 50$ K) due to a limited number of quantum states of the various reactants that were involved in this state-to-state treatment. The agreement between experiment and model description is taken as an indication that the microcanonical approach is an appropriate simulation even at lower temperatures where only a limited number of states is involved in the chemical reaction network.

These simulations are also used to predict the outcome of the trap experiments, for example, shown in Figure 3.38, for the dominant $H_3^+ + H_2$ collisions where HD is only a small contamination of hydrogen, leading to the formation of H_2D^+. In fact, the H_2D^+/H_3^+ ratio, which approaches a steady-state value in those experiments, can be predicted by the microcanonical model. Figure 3.41 shows the result of such calculations as a function of temperature. Each line has been calculated for a different o/p ratio of H_2 (p_2). These results are compared to experimental H_2D^+/H_3^+ ratios. It can clearly be seen that the H_2D^+/H_3^+ ratio strongly depends on temperature and very critically on the amount of o-H_2 in the experiment. This

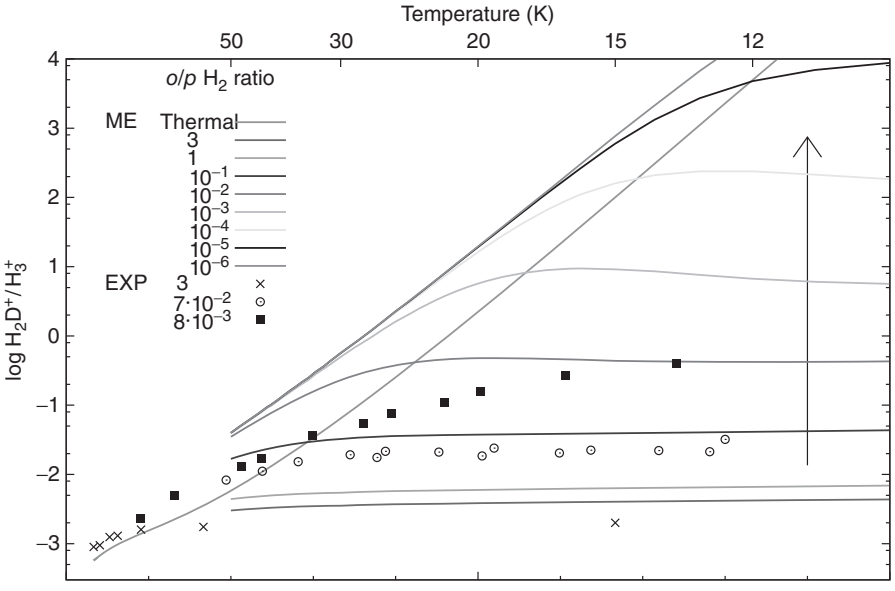

Figure 3.41 Experimental and modeled steady-state H_2D^+/H_3^+ ratio in a hydrogen environment with terrestrial abundance of HD. The data is shown as a function of temperature for a number of o/p ratios of H_2 (arrow indicates increasing p-H_2 purity). Reproduced from [243], copyright 2009 © permission from AIP Publishing.

trend is also predicted by the simulation. It also appears that the purity of p-H_2 was limited to values somewhat below 1% in these measurements. Experiments with higher purity p-H_2, as shown for our more recent $N^+ + H_2$ reaction, have to be carried out for a more critical test of the microcanonical model. However, it is gratifying that this rather simple statistical approach reproduces the experimental results on a near-quantitative level.

In this comparison between experiment and simulation, the coarse picture of understanding is hidden in the large number of states involved and in the even larger number of state-to-state rate coefficients which have to be considered. Thus, it is not clear which rate coefficients are dominating the deuterium chemistry of this simple set of reactions. As mentioned before, a closer inspection of Figure 3.35 helps in understanding the result of the experiments discussed in this section, namely that the o/p ratio of H_2 determines the speed of the back reaction and thus the H_2D^+/H_3^+ ratio.

Comparing the lowest energy state of p-$H_2D^+ + p$-H_2 with the one for p-$H_2D^+ + o$-H_2, it becomes clear that for the latter reaction the endothermicity is reduced by the rotational energy of o-H_2 ($J = 1$). Therefore, the activation energy is reduced from $\Delta E/k_B \sim 232$ to 57 K. Apparently, this leads to a great enhancement of the backreaction $H_2D^+ + H_2 \rightarrow H_3^+ + HD$. However, the situation is more complicated as nuclear-spin-changing reactions can lead to an enhancement of o-H_2D^+.

It is quite obvious that, for example, a deuteron transfer in the collision of p-H_2D^+ + o-H_2 can lead to o-H_2D^+ + p-H_2. This is a nuclear-spin-allowed and exoergic, that is, energetically favorable, process as can be seen from Figure 3.35. In contrast, the collision o-H_2D^+ + p-H_2 cannot form p-H_2D^+ + p-H_2. While this is energetically favorable, the reaction is forbidden by conservation of the total nuclear angular momentum as discussed above. As a result, collisions of low-temperature p-H_2D^+ with the ortho fraction of H_2 lead to an effective heating of the H_2D^+ sample by accumulating population in the lowest o-H_2D^+ state. From here, the reaction o-H_2D^+ + p-H_2 is about $\Delta E/k_B \sim 86$ K less endoergic than p-H_2D^+ + p-H_2.

In summary, these studies reveal that deuterium chemistry is governed by the o/p ratio of H_2 and the temperature. In fact, the population of a single quantum state of H_2D^+ (o-H_2D^+, 1_{11}) seems to determine the H_2D^+/H_3^+ ratio in the laboratory and in space. It is not easy to infer this ratio from observations since H_3^+ does not have a rotational spectrum. Similarly, the D_2H^+/H_2D^+ ratio can be taken as an indicator for the deuterium chemistry in cold clouds. Until recently, only the lowest transitions of o-H_2D^+ (372 GHz) and p-D_2H^+ (691 GHz) have been observed. Of course, also the ratio of these two species can be modeled and therefore compared with the observational results. Since state-to-state rate coefficients are missing, the models may suffer from the limitations of approximate methods that have been discussed in this section.

The picture of deuterium chemistry becomes more complete with the observation of the lowest transition of p-H_2D^+ (1370 GHz) and o-D_2H^+ (1477 GHz), as these intensities would allow us to account for both nuclear spin species of H_2D^+ and D_2H^+. Observation of these transitions in emission is difficult since the population of the corresponding upper states is rather low and thus the intensities of the emission lines are weak. Observation of the corresponding absorption requires a respective continuum source in the background, which limits the number of possible objects. This has recently been accomplished for the p-H_2D^+ transition toward IRAS16293-2422 A/B in ρ Ophiuchus.

In any case, knowing the D_2H^+/H_2D^+ ratio or the o/p ratio of H_2D^+ will reflect the physical conditions (temperature and density) as well as the o/p ratio of H_2 in these environments. The latter quantity is not a given value as a result of hydrogen formation on grains but it is subject to change due to spin-changing reactions such as H_3^+ + H_2 as discussed above. Another spin-changing collision is H^+ + H_2. Therefore, a detailed comparison of such ratios from observation and modeling results can reveal an evolutionary path of the cloud composition and help in determining the time elapsed in the process of deuterium fractionation in actual clouds. For a better comparison of the modeling with laboratory data, rate coefficients for state-to-state processes like the reactive and inelastic collision of o-H_2D^+ with p-H_2 are still missing. In the last part of this section, we will discuss how a single ion state can be prepared in the

laboratory, which is a prerequisite to determine the desired state-to-state rate coefficients.

3.4.5 Toward State-to-State Rate Coefficients

We have assumed in this chapter that only a few quantum states are populated in cold molecular clouds, and demonstrated low-temperature trap experiments in the laboratory. For simple heteroatomic molecules (CO, HD, etc.), only the lowest rotational state ($J = 0$) will be populated by inelastic collisions or radiation in very cold environments. Therefore, experiments in cold traps can be used to prepare reactants in well-defined states, a prerequisite to determine state-to-state rate coefficients. For the astrophysically very important H_3^+, however, at least two rotational states will be populated at low temperatures as a result of the Pauli exclusion principle. Therefore, it is not easy to determine state-to-state rate coefficients. In this section, reactions of H_3^+ with O_2 in a 22-pole ion trap are discussed, as they might serve in the future to prepare *o*-H_3^+ (1_0) in a low-temperature environment.

The proton transfer process

$$H_3^+ + O_2 \rightarrow O_2H^+ + H_2 \tag{3.43}$$

is near-thermoneutral, as the proton affinities of H_2 and O_2 are very similar. In this sense, this reaction is similar to

$$H_2 + N^+ \rightarrow H + NH^+. \tag{3.44}$$

For the latter reaction, it could be seen in previous sections that the reaction efficiency strongly depends on the rotational state of H_2. Similarly, the reaction efficiency for reaction (3.43) will depend on the rotational state of H_3^+, as the level spacing for both H_3^+ and H_2 are considerable compared to the exoergicity of the reaction. Therefore, it is interesting to study this reaction as a function of temperature as has been done for $N^+ + H_2$. Also, astrophysically, reaction (3.43) is interesting, as the product O_2H^+ might be a reservoir for the missing oxygen (O_2) in space, provided reaction (3.43) is exoergic. Actually, the first motivation to study this reaction was to determine the energetics of this reaction.

For that purpose, H_3^+ was prepared in a storage ion source from n-H_2. As seen in Figure 3.36, H_3^+ is thus prepared with a nascent distribution of 50% in the ortho configuration and 50% in the para configuration. These primary ions are introduced into the 22-pole ion trap and cooled down by a short pulse of He to the ambient trap temperature. At the same time, they are subject to collisions with O_2, which is admitted to the trap as a background gas. Figure 3.42 shows the temporal evolution of H_3^+ and O_2H^+ for the two temperatures 129 K (a) and 49 K (b). The experimental data points indicate that the loss of H_3^+ is no longer

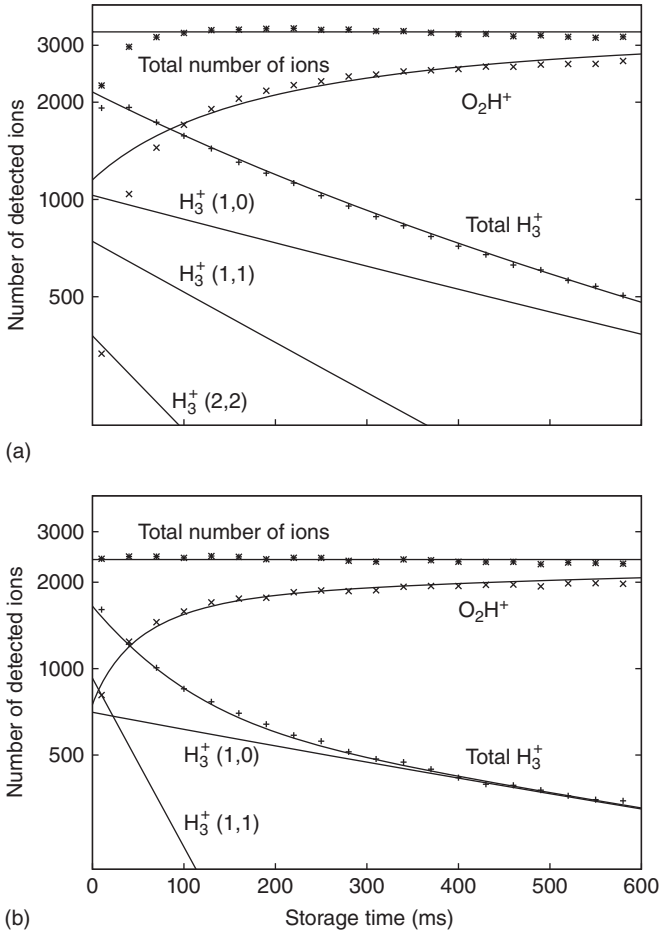

Figure 3.42 Temporal evolution of reaction (3.43) at two temperatures (a) 129 K and (b) 49 K.

a mono-exponential decay as expected for an exoergic reaction, but it is better described by a fast decay followed by a slow decay. This situation is reproduced by a simulation in which the individual rotational states of H_3^+ are treated individually. For the low-temperature data, the measurement is reproduced by a fast-reacting 1_1 para state of H_3^+ and a slow-reacting 1_0 ortho state of H_3^+. Thus, this experiment is another clear sign that state-to-state rate coefficients are needed.

For the $N^+ + H_2$ system, the additional rotational energy of the *o*-H_2 increased the reaction efficiency by several orders of magnitude at low temperatures. It has to be stressed here that actually the higher energetic *o*-H_3^+ (1_0) state reacts more slowly in this case. In order to understand this counterintuitive behavior, the energetics of the reactants H_3^+ and O_2 are depicted in Figure 3.43, together with the activation energy (E_A) for formation of $O_2H^+ + H_2$ in the lowest rotational states.

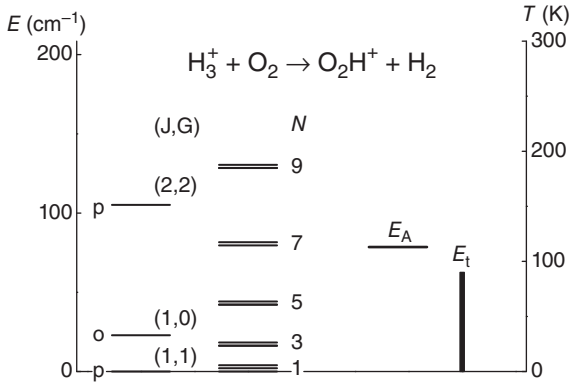

Figure 3.43 Energy diagram for reaction (3.43).

The rotational energy of both reactants helps in overcoming the activation energy. For p-H_3^+ (2_2), the reaction to O_2H^+ + p-H_2 is exoergic and will proceed rapidly. For the ground state of p-H_3^+ (1_1), the reaction is endothermic and proceeds with $k_{(1,1)} = 2.2 \times 10^{-10}$ cm^3 s^{-1} at 49 K. The lowest ortho state of H_3^+ (1_0) lies higher in energy; however, because of nuclear spin conservation, o-$H_3^+ + O_2$ can only form O_2H^+ + o-H_2, which is higher in energy by another 170.5 K. Thus this state is reacting more slowly at $k_{(1,0)} = 2.3 \times 10^{-11}$ cm^3 s^{-1} at 49 K.

This example demonstrates the impact of nuclear spin on the efficiency of chemical reactions. A closer look at Figure 3.42b shows that after some 200 ms only one rotational state (1_0) of H_3^+ survives in the trap. Thus a single quantum state has been prepared in these experiments since O_2 selectively destroys p-H_3^+ (1_1). In order to determine true state-to-state rate coefficients, also O_2 would have to be prepared in a single quantum state. This is possible in a molecular beam where all rotational states are practically cooled to the lowest state ($N = 1$ for O_2). When overlapping the ion cloud in the trap with a molecular beam, the energetics of this state-to-state experiment would be altered, as the beam carries an additional kinetic energy depicted as E_t in Figure 3.43.

Other interesting experiments become possible with this way of state preparation. Using a sequence of gas pulses, it will be possible to first cool down H_3^+ in collisions with He, and then prepare the 1_0 state of o-H_3^+. Admitting p-H_2 after this sequence will lead to a repopulation of both the ortho and para states of H_3^+. Probing the o/p population of H_3^+ can then be achieved either by LIR of H_3^+ as demonstrated before, or by chemical quenching when admitting O_2 a second time to the trap and conducting the same experiment as shown in Figure 3.42.

3.5
Negative Ion Chemistry in the Early Universe

Holger Kreckel and Daniel Wolf Savin

3.5.1
Introduction: Negative Ions in Space

Most naturally occurring elements can form stable atomic negative ions [268]. In addition, many molecules are known to form stable negative ions; even some multiply charged molecular anions have been observed [269]. The energy difference due to the addition of a free electron to a neutral atom or molecule is known as the *electron affinity* of said atom or molecule. Neutral counterparts of stable anions have positive electron affinities. The most common pathways for the formation of negative ions at low densities are radiative association (RA)

$$e^- + X \rightarrow X^- + \gamma \tag{3.45}$$

where γ represents the emission of a photon, and dissociative attachment

$$e^- + XY \rightarrow X^- + Y \tag{3.46}$$

At higher pressures, three-body capture processes and charge transfer become important [270].

In 1939, Wildt [271] drew attention to the fact that H^-, the simplest negative ion, serves as a very effective photon absorber in the photosphere of the Sun. Since then, it has been well established that hydrogen anions are the principal source of the opacity in the Sun [272]. Yet, despite the importance of H^- in stars and many other astrophysical environments, definitive detection still eludes astronomers [273].

In the cold and dilute interstellar medium of the present-day universe, atomic and molecular ions are important reaction agents, as ion–neutral reactions are often barrierless and proceed even at low temperatures. The role of negative ions in the formation of interstellar molecules was investigated first by Dalgarno and McCray in 1973 [274]. Although the detectability of interstellar anions had been considered by Sarre in 1980 [275] and Herbst in 1982 [276], it took another 25 years before the first molecular anion, C_6H^-, was identified in interstellar space [59]. At present, the negative ions (in order of identification) C_6H^- [59], C_4H^- [61], C_8H^- [60], C_3N^- [277], C_5N^- [278], and CN^- [279] have been detected in one or more instances in our galaxy.

This review focuses on the role of anions in the early universe and specifically on the critical role that H^- plays in the chemistry of the early universe and the formation of the first stars and protogalaxies. In the next section, we will give a brief overview of the chemistry of early universe. Sections 3.5.3–3.5.5 discuss fundamental processes involving H^- and their implications for primordial hydrogen chemistry. In Section 3.5.3, we will review the important $H^- + H \rightarrow H_2 + e^-$ associative detachment (AD) reaction in some detail. In Section 3.5.4, studies of

H^- photodetachment (PD) are discussed. Section 3.5.5 treats mutual neutralization (MN) of H^- and H^+. Section 3.5.6 gives a summary and outlook.

3.5.2 The Chemistry of the Early Universe

Standard Big Bang theory provides accurate predictions for the abundances and isotope ratios of the light elements ^{1}H, ^{2}H, ^{3}He, ^{4}He, and ^{7}Li which were created in the brief nucleosynthesis period in the first minutes after the Big Bang. Most heavier elements have been produced since then in stars or supernovae. The Big Bang Nucleosynthesis model has only one free parameter, the baryon–photon ratio, which is known from observation with high precision [280]. Furthermore, in the absence of external radiation sources and magnetic fields, the ingredients and conditions for chemistry of the early universe are well defined and exhibit only a fraction of the complexity of the present-day universe. The chemistry of the early universe was reviewed by Galli and Palla in 1998 [281], and a compilation of the relevant atomic and molecular processes was published by Lepp *et al.* in 2002 [282]. The most complete chemical network of early universe to date is that of Glover and Savin [283] with over 400 reactions reviewed and included. The most recent early universe chemistry review that we are aware of is that of Galli and Palla in 2013 [284].

Measurements of the cosmic microwave background allow us to take a glance back in time when the universe was ~380 000 years old (at a red shift of $z \sim 1090$). At this early stage, the universe was remarkably uniform and isotropic with density fluctuations on the order of 10^{-5}. How the universe evolved into the highly structured and hierarchical place that it is today is not fully understood. It is known, however, that in order for the initial density fluctuations to grow and eventually collapse to form stars and galaxies, cooling is required. Without cooling, a collapsing cloud of gas would end up in virial equilibrium and the collapse would stall. Cooling can be provided by transfer of kinetic energy to internal excitations in collisions of atoms and molecules and the subsequent spontaneous emission of photons. Photons leaving the cloud correspond to an energy loss, and the net effect is a reduction in temperature.

Much of our interest in early universe chemistry aims at an understanding of the formation of molecules under primordial conditions and the cooling they provided. Cooling by radiative transitions of atomic hydrogen becomes increasingly ineffective at temperatures below 8000 K, and at lower temperatures cooling through molecular transitions is the most effective mechanism, as the level spacings of rotational and vibrational states in molecules are much smaller than the electronic level spacings in atoms. It is commonly accepted that radiative cooling through ro-vibrational molecular transitions – of H_2 in particular – was crucial for the formation of the first stars and galaxies [285–287].

Initially, the high radiation temperatures after the Big Bang left all nuclei fully ionized. In the recombination era, when the universe was a few hundred thousand years old, electrons began to recombine with nuclei to form the first neutral atoms.

Helium was the first element to form neutrals because of its high first ionization potential of 24.6 eV. Small amounts of HeH^+ molecular ions were created via the reaction

$$He + H^+ \rightarrow HeH^+ + \gamma \tag{3.47}$$

and trace amounts of He_2^+ via

$$He + He^+ \rightarrow He_2^+ + \gamma \tag{3.48}$$

The universe was devoid of dust grains and only radiative processes contributed to the creation of the first molecular ions.

Molecular hydrogen was the first neutral molecule in the universe [282] and, because of the overwhelming abundance of hydrogen, H_2 remains the most abundant molecule by far to date. At the earliest times, trace amounts of H_2 formed in reactions with HeH^+

$$HeH^+ + H \rightarrow H_2^+ + He \tag{3.49}$$

followed by the charge-transfer reaction

$$H_2^+ + H \rightarrow H_2 + H^+ \tag{3.50}$$

However, most of the H_2 was immediately destroyed by the radiation field. At later stages (and lower temperatures), neutral hydrogen atoms became more abundant, and the first step was replaced by an RA reaction between protons and hydrogen atoms

$$H^+ + H \rightarrow H_2^+ + \gamma \tag{3.51}$$

followed by reaction (3.50). This pathway for H_2 formation reaction (3.51) followed by reaction (3.50) is referred to as the *H_2^+ channel*. At $z < 100$, another route for H_2 formation becomes more efficient. It proceeds through the RA formation of H^-

$$H + e^- \rightarrow H^- + \gamma \tag{3.52}$$

and the subsequent AD reaction

$$H^- + H \rightarrow H_2 + e^- \tag{3.53}$$

The above reaction sequence is called the *H^- channel*. This channel is effectively inhibited at $z > 100$ due to efficient PD of H^- by the surrounding radiation field.

The importance of H_2 cooling in primordial gas was first recognized by Saslaw and Zipoy in 1967 [288]. As it is known that RA of two H atoms in the gas phase is very ineffective [289], Saslaw and Zipoy considered all three "ionic" formation routes outlined above and came to the conclusion that the H_2^+ channel was the most important pathway. One year later, however, Peebles and Dicke [285] and, independently, Hirasawa *et al.* [290] correctly identified the H^- channel as the dominant source of primordial H_2. Molecular H_2 is known to be the most effective coolant for primordial gas at temperatures $T < 8000$ K. However, in some situations, radiative cooling through deuterated hydrogen molecules HD can become significant when temperatures $T < 200$ K are reached [283, 291]. While transitions between states with odd and even rotational J quantum number are strictly

forbidden in H_2, these transitions are allowed in HD. For example, the lowest lying rotational transition in HD is the $J = 1 \rightarrow 0$ dipole transition at 89.2 cm^{-1}, while the lowest transition in H_2 is the $J = 2 \rightarrow 0$ quadrupole transition at 354.2 cm^{-1}. The $1 \rightarrow 0$ transition probability for HD is three orders of magnitude larger than that for the $2 \rightarrow 0$ transition in H_2 [292]. The main pathway for HD formation is

$$H^+ + D \rightarrow H + D^+ \tag{3.54}$$

a reaction reviewed in Ref. [293], followed by the deuterium exchange reaction

$$H_2 + D^+ \rightarrow HD + H^+ \tag{3.55}$$

Besides H_2 and HD, the triatomic hydrogen ion H_3^+ can also be formed in primordial gas. The main formation mechanisms are the classical ion–neutral reaction

$$H_2 + H_2^+ \rightarrow H_3^+ + H \tag{3.56}$$

and the RA process

$$H_2 + H^+ \rightarrow H_3^+ + \gamma \tag{3.57}$$

this latter of which has recently been studied experimentally by Gerlich *et al.* [294]. The relevance of H_3^+ for the cooling of primordial gas has been studied in detail by Glover and Savin [283]. They found that, while the H_3^+ cooling rate per molecule exceeds that of H_2 by orders of magnitude, the H_3^+ abundance is never high enough to contribute more than a small percentage to the total cooling. Another molecule that has attracted significant attention because of its strong dipole moment of 5.9 D is LiH, which can be formed via RA

$$Li + H \rightarrow LiH + \gamma \tag{3.58}$$

However, recent simulations – using updated values for formation and destruction reactions – show that LiH never becomes a significant coolant [295]. Other primordial molecules that form in trace amounts are D_2^+, H_2D^+, D_2H^+, D_3^+, HeH^+, HeD^+, He_2^+, LiH^+, LiD^+, LiD, and LiH_2^+. The cooling provided by these molecular species has been considered for optimistic scenarios by Glover and Savin [283], who find that all of them remain less effective as coolants than H_2 by orders of magnitude.

3.5.3
H_2 Formation by Associative Detachment of H^- and H

The first step in H_2 formation via the H^- channel is RA between H and a free electron: reaction (3.52). The reverse process is the bound-free PD of H^- which has been investigated experimentally by Smith and Burch [296] and Popp and Kruse [297] and calculated by Wishart in 1979 [298]. Within the detailed-balance assumption, the RA rate coefficient can be derived from the PD rate coefficient. Both rate coefficients are believed to have relative uncertainties of only a small percentage [299].

The situation is much less clear-cut in the case of the AD reaction. Figure 3.44 shows a comparison of the experimental and theoretical results obtained

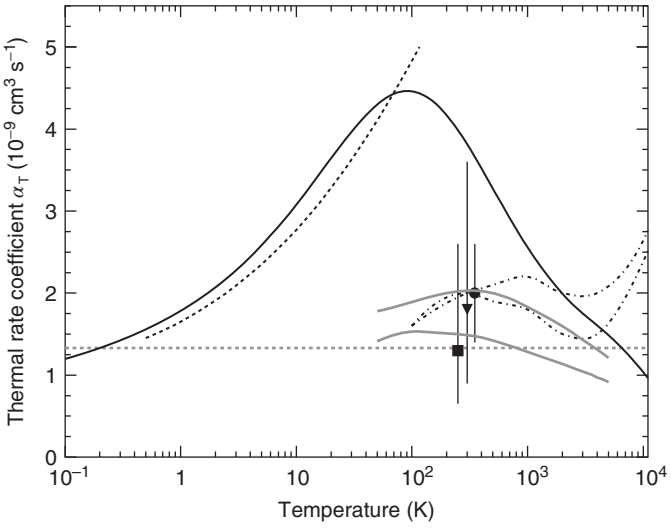

Figure 3.44 Comparison of experimental and theoretical results published before 2010 for the thermal rate coefficient of the AD reaction $H^- + H \rightarrow H_2 + e^-$. The filled square depicts the measurement of Schmeltekopf *et al.* [300], the filled triangle gives the measurement of Fehsenfeld *et al.* [303], and the filled circle shows the experimental result of Martinez *et al.* [304]. All three measurements were carried out in a flowing afterglow setup at room temperature. The results of Schmeltekopf *et al.* and Martinez *et al.* are offset by −50 and +50 K, respectively, for better visibility. The theoretical results of Browne and Dalgarno for two different H_2^- potentials are given by the dot-dashed black lines [309]. The calculations of Launay *et al.*, using two different potentials, are plotted by the solid gray lines. The calculation of Sakimoto and his extrapolation to 116 K is shown by a dashed black line [306]. The most recent calculation by Čížek *et al.* is shown by the solid black line [287, 310, 311]. The dashed gray line depicts the Langevin rate coefficient (see text).

prior to 2010. The first measurement of this process was performed in 1967 by Schmeltekopf *et al.* in a flowing afterglow setup at room temperature. The authors measured a rate coefficient of 1.3×10^{-9} cm^3 s^{-1} with an uncertainty of a factor of 2 [300]. This value is in good agreement with the classical Langevin rate coefficient if one considers the fact that the reactants can approach on two surfaces, the attractive $X^2\Sigma_u^+$ state or the repulsive $B^2\Sigma_g^+$ state. Effectively, this is accounted for by dividing the classical Langevin value by 2, yielding a value of 1.33×10^{-9} cm^3 s^{-1}. The AD reaction proceeds through the H_2^- collision complex

$$H^- + H \rightarrow (H_2^-)^* \rightarrow H_2 + e^-. \tag{3.59}$$

Taylor and Harris had shown in 1963 that the $X^2\Sigma_u^+$ H_2^- state is unstable for internuclear distances of $\lesssim 3\,a_0$ [301] and that autodetachment into H_2 and e^- will occur almost instantaneously. Hence, a rate coefficient in agreement with the Langevin collision rate coefficient was considered realistic. A semiclassical

calculation carried out by Dalgarno and Browne in 1967 [302] found a rate coefficient of 1.9×10^{-9} cm^3 s^{-1} at 300 K, in reasonable agreement with the previous experiment. Slightly revised calculations by the same authors were published in 1969 (shown in Figure 3.44). Another flowing afterglow study was published by Fehsenfeld *et al.* in 1973 [303], resulting in a rate coefficient of 1.8×10^{-9} cm^3 s^{-1}, also with an estimated factor of 2 uncertainty [304]. Lacking more accurate experimental data, and considering the simplicity of the theoretical calculations, the initial rate coefficient value of Schmeltekopf *et al.* was used in most model calculations of early universe chemistry, including the influential reviews of Abel *et al.* [299], Stancil *et al.* [305], Galli and Palla [281], and Lepp *et al.* [282].

More recent calculations, however, show a more diverse picture. Sakimoto calculated the H_2 AD rate coefficient in 1989, with special emphasis on accurate quantum mechanical description at very low energies (0.5–10 K) [306]. This treatment used the potential of Senekowitsch *et al.* [307], which is much more attractive than the pure polarization force, translating into a rate coefficient higher than the Langevin value. The extrapolation by Sakimoto to 0.01 eV resulted in a rate coefficient of 5×10^{-9} cm^3 s^{-1}, approximately three times larger than the experimentally measured values.

Two years later, Launay *et al.* [308] used resonant scattering theory to calculate state-specific rate coefficients for the population of individual rovibrational levels of the H_2 product. The absolute AD rate coefficient that the authors computed agreed well with previous measurements. Launay *et al.* used two different potentials for their calculation (see Figure 3.44). The use of the long-range H_2^- potential of Senekowitsch *et al.* – considered more accurate than previous potentials – lowered the room-temperature rate coefficient from 2.03×10^{-9} to 1.49×10^{-9} cm^3 s^{-1}. The latter value lies only 15% above the initial measurement of Schmeltekopf *et al.* The authors attribute the agreement to the quality of the new potential. Interestingly, the authors also note that the new potential of Senekowitsch *et al.* is considerably more attractive than the previous ones. This would lead one to expect a higher AD rate coefficient, yet it resulted in a much lower rate coefficient, a fact that the authors do not comment on.

This was followed in 1998 with a calculation of the AD rate coefficient by Čížek *et al.* [310]. Those authors used a nonlocal resonance model in which the short-lived H_2^- $X^2\Sigma_u^+$ collision complex interacted with the $H_2 X^1\Sigma_g + e^-$ continuum. While the same long-range potential was used as in the theory of Launay *et al.*, Čížek *et al.* predicted a much faster AD rate coefficient of 3.8×10^{-9} cm^3 s^{-1} at 300 K. The authors also assessed the thermal rate coefficient calculated by Launay *et al.* based on the potential of Senekowitsch *et al.* to be incorrect.

Subsequent flowing afterglow results were published in 2009 by Martinez *et al.* They [304] reported a room temperature rate coefficient of 2.0×10^{-9} cm^2 s^{-1} with an estimated uncertainty of only 30%. Martinez *et al.* noted that the corresponding results of Čížek *et al.* were nearly a factor of 2 higher. They concluded that "an accurate temperature variable experimental study would provide a valuable benchmark for theoretical assessments."

In summary, the more recent theoretical treatments of Sakimoto and Čížek *et al.* disagree with all of the afterglow results, all of the previously published calculations, and also the contemporaneous work of Launay *et al.* Since all three afterglow experiments were carried out at room temperature, they provide only limited guidance for theory, in particular when it comes to conflicting results on the energy dependence of the AD process. Given the significance of the AD reaction for our understanding of early universe chemistry and first star formation, an energy-resolved experimental study in the relevant energy range from ∼1 meV to 1 eV was called for.

In order to address these issues, a project aiming at energy-resolved experimental determination of the AD rate coefficient on an absolute scale was launched at Columbia University. The setup features a novel self-merged beams method, a detailed description of which can be found in Ref. [312]. An overview of the experiment is shown in Figure 3.45. Here, an H^- ion beam is extracted from a negatively biased duoplasmatron ion source and accelerated by a voltage of $V_b = -10$ kV, giving a kinetic energy of 10 keV. After being focused and guided with appropriate ion optics in the first leg of the apparatus, the beam is diverted by 90° and directed toward a PD section in the second leg of the setup. In this section, the ions are

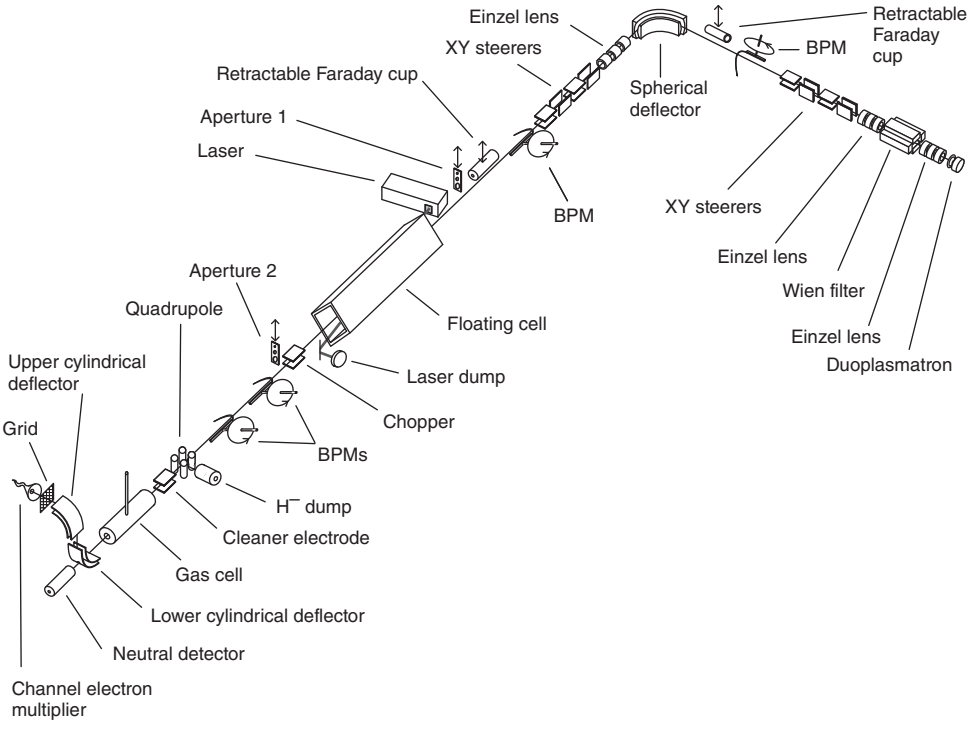

Figure 3.45 Overview of the Columbia merged beams setup. The first leg of the setup is ∼2 m in length, and the second leg is ∼7 m in length. Individual elements are not to scale. A detailed description can be found in Ref. [312].

superimposed with a continuous-wave infrared laser beam at 975 nm with 1.4 kW of power. At this wavelength, the PD process results in exclusively ground state H atoms. The laser field neutralizes ∼7.4% of the ions. From here on, H^- ions and neutral H atoms co-propagate. The PD takes place well inside a metal drift tube electrode that is supplied with a constant negative bias voltage V_d. The H^- beam is decelerated upon entering the drift tube. PD-generated neutral atoms are produced at the reduced energy $-e(V_b - V_d)$, where e is the unit charge. The energy of the neutral atoms is unaffected upon exiting the drift tube, whereas the anions are accelerated back to their initial energy. By varying the drift tube voltage, the relative collision energy between the H^- and H reactant beams can be adjusted. The AD reaction is studied in the interaction region where the overlap factor Ω and the individual profiles of the two co-propagating beams are determined by rotating wire beam profile monitors (BPMs). With H^- and H particle densities on the order of $\sim 10^5$ and $\sim 10^4$ cm^{-3}, respectively, about 100 H_2 molecules are formed per second. At the end of the interaction region, the H^- ions are diverted and the H^- current I_{H^-} is collected inside a Faraday cup, whereas both the neutral H atoms and the H_2 molecules resulting from AD fly on.

The detection of the H_2 reaction products is accomplished in two stages. First, the neutral H and H_2 particles enter a helium gas cell with a length of ∼80 cm. In the gas cell, ∼5% of the neutrals are electron-stripped at a helium pressure of $\sim 2 \times 10^{-4}$ Torr, creating H^+ and H_2^+ ions. In the second step, the ionized particles enter a two-stage electrostatic energy analyzer. As all particles have approximately the same velocity, the H_2^+ ions possess twice as much kinetic energy (∼20 keV) as the protons (∼10 keV) and can be selected in the energy analyzers and directed toward a channeltron detector which has a detection efficiency of unity at these energies. The signal rate S in the channeltron detector is recorded by a fast counter. The total neutral particle current I_H (measured in amperes) is determined at the end of the second leg by a calibrated neutral cup that utilizes secondary electron emission.

The H^- beam and the H beam are chopped out of phase from one another during the measurement, resulting in four different measurement phases. By recording the count rates of these phases separately, beam-related backgrounds can be eliminated effectively (see Ref. [312] for details). The measured merged beams rate coefficient is given by

$$\left\langle \sigma_{AD} v_r \right\rangle = \frac{S}{\sigma_{st} N_{He}} \frac{e^2}{I_{H^-} I_H} \frac{v_{H^-} v_H}{\Omega} \tag{3.60}$$

On the left-hand side, σ_{AD} is the AD cross section, v_r is the relative velocity between the two beams, and the angled brackets signify averaging over the velocity spread of the experiment. On the right-hand side, v_{H^-} and v_H denote the velocities of the H^- and H beams, respectively; σ_{st} stands for the stripping cross section; and N_{He} denotes the helium column density in the gas cell.

The experimentally determined merged-beams rate coefficient [287, 311, 313] is shown in Figure 3.46 as a function of the relative energy $\langle E_r \rangle$ between the two beams. Also shown are the updated calculations of Čížek *et al.* [310], as given in

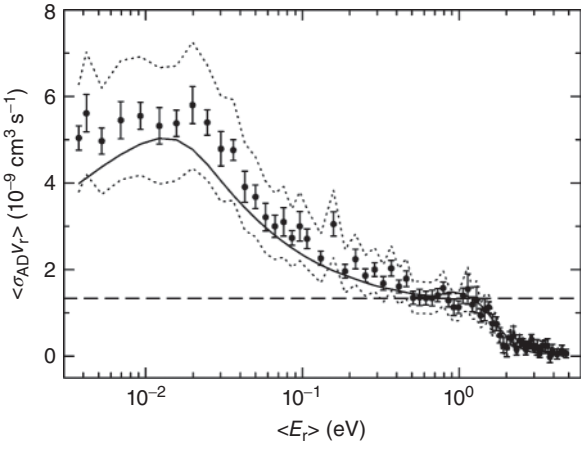

Figure 3.46 Merged-beams rate coefficient as a function of the relative collision energy for the AD reaction $H^- + H \rightarrow H_2 + e^-$. The filled circles show the experimental merged-beams results [287, 311, 313]; the error bars represent the 1σ statistical uncertainty. The short-dashed error bands represent the systematic uncertainty of ± 25 % (on a 1σ level). The solid line shows the updated cross section of Čížek *et al.* [310], as given in Miller *et al.* [311]. Multiplied by the relative velocity and convolved with the experimental velocity distribution. The dashed line shows the classical Langevin value (see text for specifics).

Miller *et al.* [311], and the classical Langevin collision rate. In order to compare the cross section of Čížek *et al.* with the measurement, it has been multiplied by the relative velocity and convolved with the experimental velocity distribution. As can be seen, the agreement between experiment and theory is excellent over the entire relevant collision energy range. The lowest collision energy sampled in this experiment is 3.7 meV. The lower end of the energy scale is limited by the divergence of the H^- and H beams which is restricted by circular 5 mm apertures before and after the PD section. The highest energy point of the initial measurements was around 1 eV [287, 313]. However, subsequent work has extended that to almost 5 eV [311] and has also studied the fully deuterated analog of reaction (3.59) [314].

Subsequent to the merged-beams work of Refs [287, 311, 313], Gerlich *et al.* [315] carried out ion trap measurements of the rate coefficient for reaction (3.59) over a temperature range 10–135 K. Within their estimated 40% systematic error bars, they could find good agreement both with the experimentally derived thermal rate coefficient from the merged-beams work and with the theoretical results of Sakimoto and of Čížek *et al.*

The convergence of two of the three most recent theoretical calculations with two different experimental approaches suggests that there may be an unknown systematic issue with the flowing afterglow results. It has been proposed that this may be due to a problem with the H atom density determination in the flow tube [313]. In the most recent afterglow measurements, the H density was calibrated

using the previously measured rate coefficient [316] for the reaction

$$H + Cl^- \rightarrow HCl + e^- \tag{3.61}$$

However, this rate coefficient is a factor of ∼1.5 lower than predicted by theory [317]. If the theoretical results are correct, then the afterglow rate coefficient would have to be scaled up by a factor of 1.5, and that would bring it into agreement with the recent merged-beams results and the calculations of Čížek *et al.* A new independent determination of the rate coefficient for reaction (3.61) might shed light on the cause of this discrepancy.

The excellent agreement between the energy-resolved merged-beams data and the latest theoretical effort is a strong support for both. To facilitate the integration of the new rate coefficient into cosmological models, a thermal rate coefficient has been derived based on the original calculations of Čížek *et al.* [310] that have been extended to lower and higher energies for this purpose. The corresponding thermal rate coefficient in the temperature range from 0.1 to 10^4 K is shown as the solid black line in Figure 3.44. An analytic fit function for the rate coefficient is provided in the online supporting material of Ref. [287].

In order to explore the implications that this experimentally confirmed rate coefficient has for cosmological models of first star and protogalaxy formation, a set of high-resolution simulations were carried out by S.C.O. Glover (see Ref. [287] and the associated supporting online material for details). The simulations represent a low-mass primordial protogalaxy forming inside an initially fully ionized protogalactic halo. In Figure 3.47, the outcome of the simulation is shown for five different runs, using different values for the AD rate coefficient. The simulation is aimed at a better understanding of the characteristic mass and the conditions for the formation of the first stars (the so-called Population III stars) and the first protogalaxies. In the upper panel, the temperature dependence in the gas cloud is shown as a function of the number density. The extreme cases (black dots) used the previous upper and lower limits of the AD rate coefficient. The open squares represent the new recommended value [287], and the gray dots depict simulation runs using rate coefficients that are 25% greater and smaller than the recommended value (representing the remaining experimental uncertainty for the absolute scale of the AD rate coefficient). It is generally assumed that the Jeans mass at the temperature minimum has an immediate impact on the characteristic mass of the Population III stars that form [318]. The Jeans mass derived from the two extreme cases in the simulation differs by more than a factor of 20. This implies that the previous uncertainty in the AD rate coefficient severely limited our ability to make predictions of the mass of the first stars and galaxies. The new merged-beams rate coefficient improves this situation significantly. Within the 25% uncertainty margin, the Jeans mass differs only by a factor of 2, corresponding to an improvement by an order of magnitude.

The lower panel of Figure 3.47 shows the HD abundance as a function of the number density. The different simulation runs show qualitatively different outcomes. While in the simulation using the previous upper limit for the AD rate

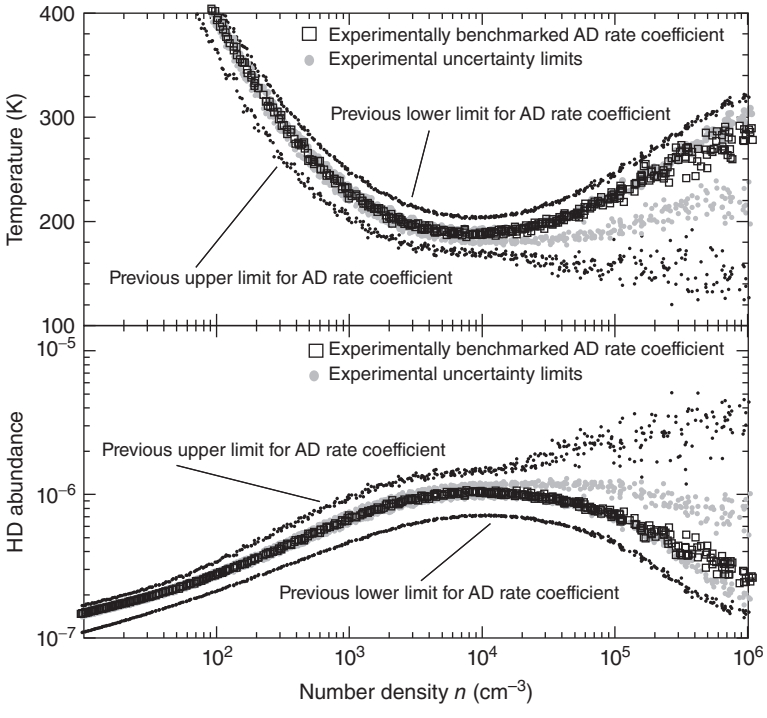

Figure 3.47 Simulations of a primordial gas cloud using different values for the AD rate coefficient. The upper panel shows the temperature as a function of the number density; the lower panel shows the fractional HD abundance. The plotted points correspond to concentric spherical shells of matter centered around the cloud center. The black points show the simulations using the previous upper and lower limits for the AD rate coefficient. The open squares represent a simulation run using the new recommended merged-beams AD rate coefficient, and the gray circles show simulations using a rate coefficient 25% larger or smaller than the recommended value. For details on the cosmological simulation, see Ref. [287] and the associated supporting online material.

coefficient (upper black dots) the HD abundance continues to rise at densities $n > 10^4$ cm^{-3} (and temperatures < 200 K are reached), all other runs, including the one using the recommended rate coefficient, show a distinct maximum in the HD density around $n \sim 10^4$ cm^{-3}. In these runs, HD cooling never really becomes significant. Further studies determining the implications of the new AD rate coefficient for HD cooling under different primordial environments and the impact on cloud collapse time scales are under way.

3.5.4
H^- Photodetachment

As described above, H_2 formation during the epoch of protogalaxy and first star formation requires the presence of H^- anions in order to go forward. However,

feedback from the first radiation sources can lead to H^- PD

$$H^- + \gamma \rightarrow H + e^- \tag{3.62}$$

which limits H_2 formation. This, in turn, can inhibit primordial star formation and delay reionization of the universe (see, e.g., Refs [319, 320]). Thus, it is important that models for structure formation in the early universe include PD in their chemical network.

H^- has only two discrete levels: a $1s^2\ ^1S^e$ ground state; and a metastable, doubly excited $2p^2\ ^3P^e$ level [321, 322]. Transition between these levels is spin-forbidden. As a result, the anion has no discrete spectrum. In the PD continuum region, however, the anion possesses a series of autodetaching resonances for photon energies above ~11 eV [323, 324].

Nonresonant PD of H^- has been extensively studied theoretically (for reviews, see Refs [325, 326]), and the calculation by Wishart [298, 327] is believed to be accurate to better than 1%. Experimentally, it has been measured on both a relative scale to better than 2% accuracy by Smith and Burch [296] and on an absolute scale by Popp and Kruse [297] with a mean error of 8%. These uncertainties pale in comparison to those for other atomic and molecular reactions important in the early universe (e.g., Refs [283, 328–330]). So, further experimental studies of the nonresonant portion of the PD cross section are not required at this time.

Extensive theoretical studies have also been performed of the autodetaching resonances in the PD cross section (see Refs [323, 324] and references therein). These resonances have been observed experimentally near the thresholds for forming H(n) with a principal quantum number n ranging from 2 to 8 [331–338]. However, none of these cross section measurements were on an absolute scale. So while the theoretical resonance energies and shapes have been well benchmarked, the strength of the resonances remain unchecked experimentally.

The cosmological implications of the autodetaching resonances have recently been investigated by Miyake *et al.* [324]. They find that these resonances can significantly enhance PD of H^- for the ultraviolet (UV) background spectrum of the high red-shift intergalactic medium and for blackbody spectra with effective temperatures exceeding ~40 000 K. As these resonances are likely to have been important during the epoch of primordial galaxy formation and first star formation and during the early reionization epoch, absolute cross-section measurements are called for to benchmark the theory.

3.5.5
Mutual Neutralization of H^- and H^+

Another important H^- destruction mechanism during the epoch of protogalaxy and first star formation is the MN reaction

$$H^- + H^+ \rightarrow H + H \tag{3.63}$$

The published theoretical and experimental rate coefficients for this reaction were reviewed in 2006 by Glover *et al.* [328] and the values span an order of magnitude.

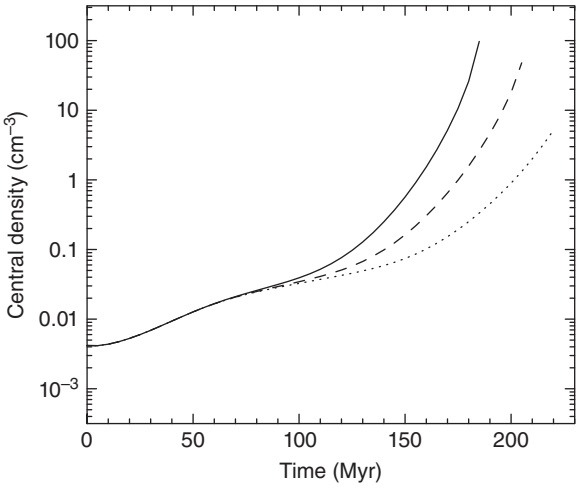

Figure 3.48 Evolution for the central density of an initially ionized primordial cloud as a function of time in the absence of a UV background. (Adapted from Ref. [328].) The MN rate coefficients used are from Refs [339] (solid curve), [340] (dashed curve), and [341, 342] (dotted curve), which span an order of magnitude [328]. For the first two cases, the cloud begins to collapse exponentially fast on a timescale sufficiently shorter than the mean collision time between halos and is thus likely to go on to form a protogalaxy. For the last case, the halo is more likely to be gravitationally disrupted in a collision with another halo, thereby halting the formation of a protogalaxy. See Ref. [328] for additional details.

Model calculations by Glover *et al.* indicate that this uncertainty limits our ability to determine whether a primordial halo of ionized gas, in the absence of a UV radiation field, will collapse and form a protogalaxy on a time scale sufficiently short that the cloud will not be gravitationally disrupted by a collision with another halo (see Figure 3.48). Here we briefly summarize and update the review of Glover *et al.* [328].

The temperatures relevant for this epoch (< 8000 K) correspond to collision energies of < 0.7 eV. The earliest MN calculations at these energies of which we are aware are the Landau-Zener (LZ) results of Bates and Lewis [343]. Additional LZ results were also performed by Olson *et al.* [344] and Eerden *et al.* [345]. The only published experimental results at these energies are those of Moseley *et al.* [341] who measured the MN cross section in the center-of-mass energy range from 0.15 to 300 eV. Peterson *et al.* [342] converted the cross section into a rate coefficient, yielding a value of $(3.9 \pm 2.1) \times 10^{-7}$ cm^3 s^{-1} at 300 K. This experimentally derived rate coefficient lies a factor of ~2–3 above the LZ results.

Quantum close-coupling calculations at the relevant energies have been carried out by Fussen and Kubach [346]. They were converted into a rate coefficient by Croft *et al.* [340]. These results are in excellent agreement with the LZ work of Bates and Lewis [343], about 30% lower than the LZ calculations by Eerden *et al.* [345], and discrepant with the experimental work. More recently, fully quantum

mechanical *ab initio* results using molecular close-coupling have been published by Stenrup *et al.* [347]. These results lie within 40% of the LZ work of Bates and Lewis [343], essentially on top of the LZ data from Eerden *et al.* [345], within 30% of the quantum close-coupling results from Fussen and Kubach [346], and a factor of ∼2–3 below the experimental work of Moseley *et al.* [341].

There are several other recommended MN rate coefficients in the literature for reaction (3.63) which we do not discuss here but which are reviewed by Glover *et al.* [328]. However, these seem essentially to be either guesses or potentially hampered by typographical errors (e.g., Refs [274, 339]).

At present, theory seems to have converged to within ∼40% for this reaction. However, experimental verification of this is still lacking. Experimental studies currently being performed by X. Urbain at the Université Catholique de Louvain in Louvain-la-Neuve, Belgium, are expected to finally resolve this matter in the near future.

3.5.6 Summary

Fundamental chemical reactions involving hydrogen atoms, molecules, and ions have a profound impact on the chemistry of the early universe. Molecular hydrogen has been identified as the dominant coolant for primordial gas at temperatures below 8000 K. The hydrogen anion H^- represents the major pathway for the formation of H_2 molecules in the early universe. Reaction rate coefficients for AD ($H^- + H \rightarrow H_2 + e^-$), for PD ($H^- + \gamma \rightarrow H + e^-$), and for MN ($H^- + H^+ \rightarrow H + H$) all influence the mass of the first stars and protogalaxies and the timescale for the collapse of primordial gas clouds.

In the case of AD, reaction (3.53), excellent agreement between theory and energy-resolved measurements has recently been achieved for the important collision energy range from 3 meV to 5 eV [287, 311, 313, 314]. These new merged-beams measurements significantly improve our ability to predict the mass of the first stars and protogalaxies.

Once the first radiation sources are formed, they can inflict negative feedback onto their surroundings in the form of UV radiation which destroys H^- by PD, Reaction (3.62), and thus slows down the H_2 production via the H^- channel. The nonresonant PD process is well understood. On the other hand, for H^- PD through resonant states lying in the continuum, no absolute measurements exist. Recent calculations indicate that this process may become important for radiation fields expected during this epoch, and therefore it should be taken into account in primordial simulations [324].

Another reaction that can have a negative impact on primordial H_2 formation, through destruction of H^-, is the MN process: reaction (3.63). At the time of writing, no consensus has been reached between experiment and theory for this process. More detailed experimental studies of this fundamental reaction are presently under way.

A lot of progress has been made in the past years for our understanding of primordial chemistry. However, despite the relative simplicity of the reaction systems, much more additional work will be needed in order to pin down all of the relevant rate coefficients to sufficient accuracy over the required temperature range.

Acknowledgments

The authors thank S.C.O. Glover and X. Urbain for stimulating discussions. HK was supported by the European Research Council under Grant Agreement No. StG 307163. DWS was supported in part by the NSF Division of Astronomical Sciences Astronomy and Astrophysics Grants Program.

References

1. McElroy, D., Walsh, C., Markwick, A.J. *et al.* (2013) *Astron. Astrophys.*, **550**, A36.
2. Eric Herbst, Ohio State University (OSU) network, *http://www.physics.ohio-state.edu/ eric/.*
3. Wakelam, V., Herbst, E., Loison, J.-C. *et al.* (2012) *Astrophys. J. Suppl. Ser.*, **199**, 21.
4. Smith, D. (1992) *Chem. Rev.*, **92**, 1473–1485.
5. Herbst, E. and Millar, T.J. (2008) in *Low Temperatures and Cold Molecules* (ed. I.W.M. Smith), Imperial College Press, pp. 1–54.
6. Herbst, E. and van Dishoeck, E.F. (2009) *Ann. Rev. Astron. Astrophys.*, **47** (1), 427–480.
7. Smith, I.W.M. (2011) *Annu. Rev. Astron. Astrophys.*, **49** (1), 29–66.
8. Herbst, E. and Klemperer, W. (1973) *Astrophys. J.*, **185**, 505–534.
9. Belloche, A., Menten, K.M., Comito, C. *et al.* (2008) *Astron. Astrophys.*, **482** (1), 179–196.
10. Wyrowski, F., van der Tak, F., Herpin, F. *et al.* (2010) *Astron. Astrophys.*, **521**, L34.
11. Bennett, C.J., Morales, S.B., Le Picard, S.D. *et al.* (2010) *Phys. Chem. Chem. Phys.*, **12**, 8737.
12. Bergin, E.A. and van Dishoeck, E.F. (2012) *Philos. Trans. R. Soc. London, Ser. A*, **370**, 2778–2802.
13. Chavarría, L., Herpin, F., Jacq, T. *et al.* (2010) *Astron. Astrophys.*, **521**, L37.
14. Caselli, P., Keto, E., Pagani, L. *et al.* (2010) *Astron. Astrophys.*, **521**, L29.
15. Hogerheijde, M.R., Bergin, E.A., Brinch, C. *et al.* (2011) *Science*, **334**, 338–340.
16. Wakelam, V., Herbst, E., and Selsis, F. (2006) *Astron. Astrophys.*, **451**, 551–562.
17. Herbst, E., DeFrees, D.J., Talbi, D. *et al.* (1991) *J. Chem. Phys.*, **94** (12), 7842–7849.
18. Ho, P.T.P. and Townes, C.H. (1983) *Annu. Rev. Astron. Astrophys.*, **21**, 239–270.
19. Child, M. (1996) *Molecular Collision Theory*, Dover Publications, New York.
20. Drake, G. (ed.) (2006) *Springer Handbook of Atomic, Molecular, and Optical Physics*, Springer, New York.
21. Jambrina, P.G., Alvarino, J.M., Gerlich, D. *et al.* (2012) *Phys. Chem. Chem. Phys.*, **14**, 3346–3359.
22. Gerlich, D. and Bohli, H.J. (1981) in *European Conference On Atomic Physics* (eds J. Kowalski, G. zu Putlitz, and H.G. Weber), Heidelberg, pp. 930–931.
23. Gioumousis, G. and Stevenson, D.P. (1958) *J. Chem. Phys.*, **29**, 294.
24. Chesnavich, W.J., Su, T., and Bowers, M.T. (1980) *J. Chem. Phys.*, **72** (4), 2641–2655.
25. Bowers, M.T. and Su, T. (1975) in *Interaction Between Ions and Molecules*, Vol. 6 (ed. P.J. Ausloos)

Proceedings of the NATO Advanced Study Institute, p. 163.
26. Scoles, G. (ed.) (1988) *Atomic and Molecular Beam Methods*, Oxford University Press, Inc..
27. Balucani, N., Capozza, G., Leonori, F., Segoloni, E., and Casavecchia, P. (2006) *Int. Rev. Phys. Chem.*, **25** (1-2), 109–163.
28. Lee Festschrift, Y.T. (2006) *J. Chem. Phys*, **125**, 13.
29. Casavecchia, P., Leonori, F., Balucani, N. *et al.* (2009) *Phys. Chem. Chem. Phys.*, **11**, 46–65.
30. Costes, M., Daugey, N., Naulin, C. *et al.* (2006) *Faraday Discuss.*, **133**, 157–176.
31. Fu, B., Han, Y.-C., Bowman, J.M. *et al.* (2012) *Proc. Natl. Acad. Sci. U.S.A.*, **109** (25), 9733–9738.
32. Balucani, N., Asvany, O., Huang, L.C.L. *et al.* (2000) *Astrophys. J.*, **545**, 892–906.
33. Kaiser, R.I., Chiong, C.C., Asvany, O. *et al.* (2001) *J. Chem. Phys.*, **114** (8), 3488–3496.
34. Neumark, D.M., Wodtke, A.M., Robinson, G.N., Hayden, C.C., and Lee, Y.T. (1985) *J. Chem. Phys.*, **82** (7), 3045–3066.
35. Wang, X., Dong, W., Qiu, M. *et al.* (2008) *Proc. Natl. Acad. Sci. U.S.A.*, **105** (17), 6227–6231.
36. Stark, K. and Werner, H.J. (1996) *J. Chem. Phys.*, 104, 6515.
37. Castillo, J.F., Manolopoulos, D.E., Stark, K., and Werner, H.-J. (1996) *J. Chem. Phys.*, **104**, 6531.
38. Aoiz, F.J., Bañares, L., Herrero, V.J. *et al.* (1994) *Chem. Phys. Lett.*, **223**, 215–226.
39. Neufeld, D.A., Sonnentrucker, P., Phillips, T.G. *et al.* (2010) *Astron. Astrophys.*, **518**, L108.
40. Sonnentrucker, P., Neufeld, D.A., Phillips, T.G. *et al.* (2010) *Astron. Astrophys.*, **521**, L12.
41. Chefdeville, S., Stoecklin, T., Bergeat, A. *et al.* (2012) *Phys. Rev. Lett.*, **109**, 023201.
42. Lara, M., Chefdeville, S., Hickson, K.M. *et al.* (2012) *Phys. Rev. Lett.*, **109**, 133201.
43. Chefdeville, S., Kalugina, Y., van de Meerakker, S.Y.T. *et al.* (2013) *Science*, **341** (6150), 1094–1096.
44. Faubel, M. and Toennies, J.P. (1979) *J. Chem. Phys.*, **71**, 3770–3785.
45. Niedner, G., Noll, M., and Toennies, J.P. (1987) *J. Chem. Phys.*, **87**, 2067–2083.
46. Maring, W., Toennies, J.P., Wang, R.G., and Levene, H.B. (1991) *Chem. Phys. Lett.*, **184**, 262–266.
47. Herman, Z., Pacák, V., Yencha, A.J., and Futrell, J. (1976) *Chem. Phys. Lett.*, **37**, 329–334.
48. Gerlich, D. (1989) in *XII International Symposium on Molecular Beams* (ed. V. Aquilanti), p. 37.
49. Gerlich, D. (2008) in *Low Temperatures and Cold Molecules*, Chapter 3 (ed. I.W.M. Smith), Imperial College Press, Distributor: World Scientific Publishing Co. Pte. Ltd., Singapore, pp. 121–174.
50. Tosi, P., Dmitriev, O., Bassi, D., Wick, O., and Gerlich, D. (1994) *J. Chem. Phys.*, **100** (6), 4300–4307.
51. Tosi, P. (1992) *Chem. Rev.*, **92** (7), 1667–1684.
52. Gerlich, D. (1989) *J. Chem. Phys.*, **90** (1), 127–139.
53. van Veldhoven, J., Bethlem, H.L., and Meijer, G. (2005) *Phys. Rev. Lett.*, **94**, 083001.
54. van de Meerakker, S.Y.T., Vanhaecke, N., and Meijer, G. (2006) *Annu. Rev. Phys. Chem.*, **57** (1), 159–190.
55. Bethlem, H.L., Veldhoven, J., Schnell, M., and Meijer, G. (2006) *Phys. Rev. A*, **74**, 063403.
56. Gilijamse, J.J., Hoekstra, S., Vanhaecke, N., van de Meerakker, S.Y.T., and Meijer, G. (2010) *Eur. Phys. J. D*, **57**, 33–41.
57. Adams, N.G. and Smith, D. (1976) *Int. J. Mass Spectrom. Ion Phys.*, **21** (3-4), 349–359.
58. McEwan, M.J., Scott, G.B.I., Adams, N.G. *et al.* (1999) *Astrophys. J.*, **513**, 287–293.
59. McCarthy, M.C., Gottlieb, C.A., Gupta, H., and Thaddeus, P. (2006) *Astrophys. J.*, **652**, L141–L144.

60. Brünken, S., Gupta, H., Gottlieb, C.A., McCarthy, M.C., and Thaddeus, P. (2007) *Astrophys. J.*, **664**, L43–L46.
61. Cernicharo, J., Guélin, M., Agündez, M. *et al.* (2007) *Astron. Astrophys.*, **467**, L37–L40.
62. Dupeyrat, G., Marquette, J.B., and Rowe, B.R. (1985) *Phys. Fluids*, **28** (5), 1273–1279.
63. Ian, W.M., Smith, and Barnes, P.W. (2013) *Annu. Rep. Prog. Chem. Sect. C: Phys. Chem.*, **109**, 140–166.
64. Sabbah, H., Biennier, L., Sims, I.R. *et al.* (2007) *Science*, **317** (5834), 102–105.
65. Smith, I.W.M. (2006) *Angew. Chem. Int. Ed.*, **45** (18), 2842–2861.
66. Georgievskii, Y. and Klippenstein, S.J. (2005) *J. Chem. Phys.*, **122** (19), 194103.
67. Canosa, A., Páramo, A., Le Picard, S.D., and Sims, I.R. (2007) *Icarus*, **187** (2), 558–568.
68. Tizniti, M., Le Picard, S.D., Lique, F. *et al.* (2014) *Nat. Chem.*, **6**, 141–145.
69. Shannon, R.J., Blitz, M.A., Goddard, A., and Heard, D.E. (2013) *Nat. Chem.*, **5**, 745–749.
70. Bouwman, J., Goulay, F., Leone, S.R., and Wilson, K.R. (2012) *J. Phys. Chem. A*, **116** (15), 3907–3917.
71. Sorgenfrei, A. (1994) Ion-Molekül-Reaktionen kleiner Kohlenwasserstoffe in einem gekühlten Ionen-Speicher. PhD thesis, University of Freiburg, Germany.
72. Asvany, O., Ricken, O., Müller, H.S.P. *et al.* (2008) *Phys. Rev. Lett.*, **100**, 233004.
73. Gerlich, D. (1993) in *XVIII International Conference on Physics of Electronic and Atomic Collisions* (eds T. Andersen, B. Fastrup, F. Folkmann, and H. Knudsen), AIP Press, New York, pp. 607–622.
74. Larsson, M. and Orel, A.E. (2008) *Dissociative Recombination of Molecular Ions*, Cambridge University Press, Cambridge.
75. Djuric, N., Dunn, G.H., *et al.* (2001) *Phys. Rev. A*, **64**, 02273.
76. Bates, D.R. and Massey, H.S.W. (1947) *Proc. R. Soc. London, Ser. A*, **192**, 1.
77. Bates, D.R. (1950) *Phys. Rev.*, **78**, 492.
78. Bardsley, J.N. (1967) *5th International Conference on the Physics of Electronic and Atomic Collisions (ICPEAC V)*, Abstracts of Papers, Leningrad, Nauka, p. 338.
79. Chen, J.C.Y. and Mittelman, M.H. (1967) *5th International Conference on the Physics of Electronic and Atomic Collisions (ICPEAC V), Abstracts of Papers*, Leningrad, Nauka, p. 329.
80. Al-Khalili, A., Rosén, S., Danared, H. *et al.* (2003) *Phys. Rev. A*, **68**, 042702.
81. Zhaunerchyk, V., Al-Khalili, A., Thomas, R.D. *et al.* (2007) *Phys. Rev. Lett.*, **99**, 013201.
82. Krohn, S., Kreckel, H., Lammich, L. *et al.* (2003) in *Dissociative Recombination of Molecular Ions with Electrons* (ed. S.L. Guberman), Kluwer, New York, pp. 127–138.
83. Amitay, Z., Baer, A., Dahan, M. *et al.* (1998) *Science*, **281** (5373), 75–78.
84. Amitay, Z., Baer, A., Dahan, M. *et al.* (1999) *Phys. Rev. A*, **60**, 3769–3785.
85. Jensen, M.J., Bilodeau, R.C., Safvan, C.P. *et al.* (2000) *Astrophys. J.*, **543**, 764.
86. Smith, D. (1992) *Chem. Rev.*, **92**, 1473.
87. Al-Khalili, A., Danared, H., Larsson, M. *et al.* (1998) *Hyperfine Interact.*, **114**, 281.
88. Keller, C.N., Anicich, V.G., and Cravens, T.E. (1998) *Planet. Space Sci.*, **46**, 1157.
89. Brünken, S., Gupta, H.C., Gottlieb, A., McCarthy, M.C., and Thaddeus, P. (2007) *Astrophys. J.*, **664**, 43.
90. McKee, C.F. (1989) *Astrophys. J.*, **345**, 782.
91. Weingartner, J.C. and Draine, B.T. (2001) *Astrophys. J. Suppl. Ser.*, **134**, 263.
92. Galli, D., Walmsley, M., and Goncalves, J. (2002) *Astron. Astrophys.*, **394**, 275.
93. Cravens, T.E. and Dalgarno, A. (1978) *Astrophys. J.*, **219**, 750.
94. Field, D., Balog, R., Feketeova, L. *et al.* (2007) *Molecules in Space and Laboratory* (eds J.L. Lemaire and F. Combes), S. Diana, Paris, p. 44.
95. Snow, T. and McCall, B.J. (2006) *Annu. Rev. Astron. Astrophys.*, **44**, 367.

96. Neufeld, D.A., Wolfire, M.G., and Schilke, P. (2005) *Astrophys. J.*, **628**, 260.
97. McCall, B.J., Huneycutt, A.J., Saykally, R.J. *et al.* (2003) *Nature*, **422**, 500.
98. Glosík, J., Plašil, R., Korolov, I. *et al.* (2009) *Phys. Rev. A*, **79**, 052707.
99. Allen, M. and Robinson, G.W. (1977) *Astrophys. J.*, **212**, 396.
100. Garrod, R.T. and Herbst, E. (2006) *Astron. Astrophys.*, **457**, 927.
101. Sutton, E.C., Peng, R.D., Danchi, W.C. *et al.* (1995) *Astrophys. J. Suppl. Ser.*, **97**, 455.
102. Hamberg, M., "Osterdahl, F., Thomas, R.D. *et al.* (2010) *Astron. Astrophys.*, **514**, A83.
103. Cravens, T.E. and Eisenhower, G.M. (1992) *Icarus*, **100**, 260.
104. Hodges, R.R. (2000) *J. Geophys. Res.*, **105**, 6971.
105. Nagy, A.F., Cravens, T.E., Yee, J.H., and Stewart, A.I.F. (1981) *Geophys. Res. Lett.*, **8**, 629.
106. Kaneda, K., Terada, N., and Machida, S. (2007) *Geophys. Res. Lett.*, **34**, 20201.
107. Petrignani, A., Hellberg, F., Thomas, R.D. *et al.* (2005) *J. Phys. Conf. Ser.*, **4**, 182.
108. Cosby, P.C., Peterson, J.R., Huestis, D.L. *et al.* (2003) *Bull. Am. Astron. Soc.*, **35**, 918.
109. Seiersen, K., Al-Khalili, A., Jensen, M.J. *et al.* (2003) *Phys. Rev. A*, **68**, 022708.
110. Fox, J.L. (2004) *J. Geophys. Res.*, **109**, A08306.
111. Viggiano, A.A., Ehlerding, A., Hellberg, F.T. *et al.* (2005) *J. Chem. Phys.*, **122**, 226101.
112. Fox, J.L. (1993) *J. Geophys. Res.*, **98** (E2), 3297.
113. Fox, J.L. and Hac, A. (1997) *J. Geophys. Res. E*, **102**, 9191.
114. Seth, S.P., Haider, S.A., and Oyama, K.I. (2002) *J. Geophys. Res. A*, **107**, 19.
115. Fox, J.L. (1997) *Venus and Mars: Atmospheres, Ionospheres and Solar Wind Interaction*, Geophysical Monograph 66, AGU Press.
116. Roble, R.G., Ridley, E.C., and Dickinson, R.E. (1987) *J. Geophys. Res. A*, **92**, 8745.
117. Fox, J.L. (2005) *J. Phys. Conf. Ser.*, **4**, 32.
118. Friedson, A.J., Wilson, E.H., and Moses, J.L. (2005) *Bull. Am. Astron. Soc.*, **37**, 683.
119. Biondi, M.A. and Brown, S.C. (1949) *Phys. Rev.*, **76**, 1697–1700.
120. Fehsenfeld, F.C., Schmeltekopf, A.L., Goldan, P.D., Schiff, H.I., and Ferguson, E.E. (1965) *J. Chem. Phys.*, **44**, 4087–4094.
121. Ferguson, E.E., Fehsenfeld, F.C., and Schmeltekopf, A.L. (1965) *Phys. Rev.*, **138**, A381–A385.
122. Amano, T. (1990) *J. Chem. Phys.*, **92**, 6492.
123. Rosati, R.E., Skrzypkowski, M.P., Johnsen, R., and Golde, M.F. (2007) *J. Chem. Phys.*, **126** (15), 154302.
124. Varju, J., Hejduk, M., Dohnal, P. *et al.* (2011) *Phys. Rev. Lett.*, **106**, 203201.
125. Johnsen, R. (1987) *Int. J. Mass Spectrom.*, **81**, 67–84.
126. Johnsen, R. (1986) *Rev. Sci. Instrum.*, **57**, 428–432.
127. Poterya, V., Glosík, J., Plašil, R. *et al.* (2002) *Phys. Rev. Lett.*, **88**, 044802.
128. Mahdavi, M.R., Hasted, J.B., and Nakshbandi, M.M. (1971) *J. Phys. B: At. Mol. Phys.*, **4**, 1726.
129. Smith, D., Adams, N.G., Dean, A.G., and Church, M.J. (1975) *J. Phys. D: Appl. Phys.*, **8**, 141.
130. Leu, M.T., Biondi, M.A., and Johnsen, R. (1973) *Phys. Rev. A*, **8**, 420.
131. Adams, N.G., Smith, D., and Alge, E. (1984) *J. Chem. Phys.*, **81**, 1778.
132. Ganguli, B., Biondi, M.A., Johnsen, R., and Dulaney, J.L. (1988) *Phys. Rev. A*, **37**, 2543.
133. Rowe, B.R., Gomet, J.C., Canosa, A., Rebrion, C., and Mitchell, J. (1992) *J. Chem. Phys.*, **96**, 1105.
134. Smith, D. and Spanel, P. (1993) *Int. J. Mass Spectrom. Ion Proc.*, **129**, 163.
135. Laubé, S., Le Padellec, A., Sidko, O. *et al.* (1998) *J. Phys. B: At. Mol. Opt. Phys.*, **31**, 2111.
136. Poterya, V., McLain, J.L., Adams, N.G., and Babcovo, L.M. (2005) *J. Phys. Chem.*, **109**, 7181.
137. Korolov, I., Plasil, R., Kotrik, T., Dohnal, P., and Glosik, J. (2009) *Int. J. Mass Spectrom.*, **280**, 144–148.

138. Douguet, N., Kokoouline, V., and Greene, C.H. (2008) *Phys. Rev. A*, **77**, 064703.
139. Douguet, N., Kokoouline, V., and Greene, C.H. (2009) *Phys. Rev. A*, **80**, 062712.
140. Alge, E., Adams, N.G., and Smith, D. (1983) *J. Phys. B: At. Mol. Phys.*, **16**, 1433–1444.
141. Gougousi, T., Johnsen, R., and Golde, M.F. (1995) *Int. J. Mass Spectrom. Ion Proc.*, **149-150**, 131–151.
142. Novotny, O., Sivaraman, B., and Rebrion-Rowe, C. (2005) *Chem. Phys.*, **123**, 104303.
143. Novotny, O., Plasil, R., Pysanenko, A., Korolov, I., and Glosik, J. (2006) *J. Phys. B: At. Mol. Opt. Phys.*, **39**, 2561–2569.
144. Tsuji, M., Nakamura, M., Nishimura, Y., and Obase, H. (1995) *J. Chem. Phys.*, **103**, 1413–1421.
145. Adams, N.G., Poterya, V., and Babcock, L.M. (2006) *Mass Spectrom. Rev.*, **25**, 798–828.
146. Rosati, R.E., Pappas, D., Johnsen, R., and Golde, M.E. (2007) *J. Chem. Phys.*, **126**, 154303.
147. Le Padellec, A., Sheehan, C., Talbi, D., and Mitchell, J.B.A. (1997) *J. Phys. B: At. Mol. Opt. Phys.*, **30**, 319.
148. Geppert, W.D., Thomas, R.D., Ehlerding, A. *et al.* (2005) *J. Phys. Conf. Ser.*, **4** (1), 26–31.
149. Phaneuf, R.A., Havener, C.C., Dunn, G.H., and Müller, A. (1999) *Rep. Prog. Phys.*, **62** (7), 1143–1180.
150. Auerbach, D., Cacak, R., Caudano, R. *et al.* (1977) *J. Phys. B: At. Mol. Opt. Phys.*, **10** (18), 3797–3820.
151. Dittner, P.F., Datz, S., Miller, P.D. *et al.* (1983) *Phys. Rev. Lett.*, **51**, 31–34.
152. Andersen, L.H., Bolko, J., and Kvistgaard, P. (1990) *Phys. Rev. A*, **41**, 1293–1302.
153. Andersen, L.H. and Bolko, J. (1990) *Phys. Rev. A*, **42**, 1184–1191.
154. Larsson, M. (1997) *Annu. Rev. Phys. Chem.*, **48**, 151–179.
155. Thomas, R.D. (2008) *Mass Spectrom. Rev.*, **27** (5), 485–530.
156. Wolf, A., Buhr, H., and Novotný, O. (2011) *J. Phys. Conf. Ser.*, **300** (1), 012008.
157. Hechtfischer, U., Amitay, Z., Forck, P. *et al.* (1998) *Phys. Rev. Lett.*, **80** (13), 2809–2812.
158. Wolf, A., Buhr, H., Grieser, M. *et al.* (2006) *Hyperfine Interact.*, **172**, 111–124.
159. Wolf, A., Orlov, D.A., Krantz, C. *et al.* (2009) *J. Phys. Conf. Ser.*, **194** (1), 012024.
160. Shafir, D., Novotny, S., Buhr, H. *et al.* (2009) *Phys. Rev. Lett.*, **102** (22), 223202.
161. Waffeu Tamo, F.O., Buhr, H., Motapon, O. *et al.* (2011) *Phys. Rev. A*, **84**, 022710.
162. Wolf, A. (1999) in *Atomic Physics with Heavy Ions* (eds H.F. Beyer and V.P. Shevelvo), Springer, Berlin, pp. 1–20.
163. Zajfman, D., Amitay, Z., Broude, C. *et al.* (1995) *Phys. Rev. Lett.*, **75**, 814–817.
164. Zajfman, D., Amitay, Z., Lange, M. *et al.* (1997) *Phys. Rev. Lett.*, **79** (10), 1829–1832.
165. Florescu-Mitchell, A.I. and Mitchell, J.B.A. (2006) *Phys. Rep.*, **430** (5-6), 277–374.
166. Buhr, H., Mendes, M.B., Novotný, O. *et al.* (2010) *Phys. Rev. A*, **81** (6), 062702.
167. Buhr, H., Stützel, J., Mendes, M.B. *et al.* (2010) *Phys. Rev. Lett.*, **105** (10), 103202.
168. Mendes, M.B., Buhr, H., Berg, M.H. *et al.* (2012) *Astrophys. J. Lett.*, **746** (1), L8.
169. Kreckel, H., Novotný, O., Crabtree, K.N. *et al.* (2010) *Phys. Rev. A*, **82** (4), 042715. and references therein.
170. McCall, B.J., Huneycutt, A.J., Saykally, R.J. *et al.* (2004) *Phys. Rev. A*, **70**, 052716.
171. Dohnal, P., Hejduk, M., Varju, J. *et al.* (2012) *J. Chem. Phys.*, **136** (24), 244304.
172. dos Santos, S.F., Kokoouline, V., Greene, C.H. (2007) *J. Chem. Phys.*, **127**, 124309.
173. Kreckel, H., Krohn, S., Lammich, L. *et al.* (2002) *Phys. Rev. A*, **66**, 052509.
174. Kreckel, H., Motsch, M., Mikosch, J., *et al.* (2005) *Phys. Rev. Lett.*, **95**, 263201.

175. Petrignani, A., Altevogt, S., Berg, M.H. *et al.* (2011) *Phys. Rev. A*, **83**, 032711.
176. Kokoouline, V., Greene, C.H., and Esry, B.D. (2001) *Nature*, **412**, 891–94.
177. Kokoouline, V. and Greene, C.H. (2003) *Phys. Rev. A*, **68**, 012703.
178. Plasil, R., Glosík, J., Poterya, V. *et al.* (2002) *Int. J. Mass Spectrom.*, **218** (2), 105–130.
179. Tom, B.A., Zhaunerchyk, V., Wiczer, M.B. *et al.* (2009) *J. Chem. Phys.*, **130** (3), 031101.
180. Herbst, E., Terzieva, R., and Talbi, D. (2000) *Mon. Not. R. Astron. Soc.*, **311** (4), 869–876.
181. Novotný, O., Buhr, H., Stützel, J. *et al.* (2010) *J. Phys. Chem. A*, **114** (14), 4870–4874. PMID: 20073483.
182. Nordhorn, C., Bing, D., Buhr, H. *et al.* (2011) *J. Phys. Conf. Ser.*, **300** (1), 012004.
183. van der Tak, F.F.S., van Dishoeck, E.F., and Caselli, P. (2000) *Astron. Astrophys.*, **361**, 327.
184. Leurini, S., Schilke, P., Menten, M.R., Pottage, J.T., and Xu, L.H. (2004) *Astron. Astrophys.*, **422**, 573.
185. Gerlich, D. and Smith, M. (2006) *Phys. Scr.*, **73**, C25.
186. Geppert, W.D., Hamberg, M., Thomas, R.D. *et al.* (2006) *Faraday Discuss.*, **133**, 177.
187. Hidaka, H., Watanabe, N., Shiraki, T., Nagaoka, A., and Kouchi, A. (2004) *Astrophys. J.*, **614**, 1124.
188. Fuchs, G.W., Cuppen, H.M., Ioppolo, S. *et al.* (2009) *Astron. Astrophys.*, **505**, 629.
189. Bisschop, S.E. (2005) Complex molecules in the laboratory and star forming regions. PhD thesis, University of Leiden.
190. Parise, B., Castets, A., Herbst, E. *et al.* (2004) *Astron. Astrophys.*, **416**, 159.
191. Eberhardt, P. and Krankowsky, D. (1995) *Astron. Astrophys.*, **295**, 795.
192. Adams, N.G. and Smith, D. (1988) *Chem. Phys. Lett.*, **144**, 11.
193. Molina-Cuberos, G.J., Schwingenschuh, K., López-Moreno, J.J. *et al.* (2002) *J. Geophys. Res.*, **107** (E11), 5099.
194. Vigren, E., Kamińska, M., Hamberg, M. *et al.* (2008) *Phys. Chem. Chem. Phys.*, **10**, 401.
195. Geppert, W.D., Ehlerding, A., Hellberg, F. *et al.* (2004) *Astrophys. J.*, **613**, 1302.
196. Petrie, S. (2001) *Icarus*, **151**, 196.
197. Geppert, W.D. and Larsson, M. (2008) *Mol. Phys.*, **106**, 2199.
198. Eppink, A.T.J.B. and Parker, D.H. (1997) *Rev. Sci. Instrum.*, **68** (9), 3477–3484.
199. Bickes, R.W., Duquette, G., Vandenmeijdenberg, C.J. *et al.* (1975) *J. Phys. B: At. Mol. Opt. Phys.*, **8** (18), 3034–3043.
200. Brudermann, J., Steinbach, C., Buck, U., Patkowski, K., and Moszynski, R. (2002) *J. Chem. Phys.*, **117**, 11166–11174.
201. Chapman, W.B., Kulcke, A., Blackmon, B.W., and Nesbitt, D.J. (1999) *J. Chem. Phys.*, **110** (17), 8543–8554.
202. Cappelletti, D., Aquilanti, V., Cornicchi, E., Teixidor, M.M., and Pirani, F. (2005) *J. Chem. Phys.*, **123** (2), 024302.
203. Belpassi, L., Tarantelli, F., Pirani, F., Candori, P., and Cappelletti, D. (2009) *Phys. Chem. Chem. Phys.*, **11** (43), 9970–9975.
204. Aquilanti, V., Cornicchi, E., Teixidor, M.M. *et al.* (2005) *Angew. Chem. Int. Ed.*, **44** (16), 2356–2360.
205. Yang, C.-H., Sarma, G., ter Meulen, J.J. *et al.* (2010) *J. Phys. Chem. A*, **114** (36), 9886–9892.
206. Yang, C.-H., Sarma, G., Parker, D.H., ter Meulen, J.J., and Wiesenfeld, L. (2011) *J. Chem. Phys.*, **134** (20), 204308.
207. Yang, C.-H., Sarma, G., Ter Meulen, J.J. *et al.* (2010) *J. Chem. Phys.*, **133** (13), 131103.
208. Lorenz, K.T., Chandler, D.W., McBane, G.C., Westley, M.S., and Houston, P.L. (1999) *Abstr. Pap. Am. Chem. Soc.*, **218** (2), U309.
209. Elitzur, M. (1992) *Annu. Rev. Astron. Astrophys.*, **30**, 75–112.
210. van Dishoeck, E.F., Kristensen, L.E., Benz, A.O. *et al.* (2011) *Pub. Astron. Soc. Pac.*, **123**, 138–170.
211. Green, S., Maluendes, S., and McLean, A.D. (1993) *Astrophys. J. Suppl.*, **85**, 181–185.

212. Phillips, T.R., Maluendes, S., and Green, S. (1996) *Astrophys. J. Suppl.*, **107**, 467.
213. Faure, A., Crimier, N., Ceccarelli, C. *et al.* (2007) *Astron. Astrophys.*, **472** (2), 1029–1035.
214. Karl, G. and Poll, J.D. (1967) *J. Chem. Phys.*, **46** (8), 2944–2950.
215. Meier, R., Owen, T.C., Matthews, H.E. *et al.* (1998) *Science*, **279**, 842.
216. Parise, B., Caux, E., Castets, A. *et al.* (2005) *Astron. Astrophys.*, **431**, 547–554.
217. Coutens, A., Vastel, C., Caux, E., Ceccarelli, C., and Herschel Chess Team (2011) IAU Symposium, Vol. 280, p. 139.
218. Hodges, M.P., Wheatley, R.J., and Harvey, A.H. (2002) *J. Chem. Phys.*, **116**, 1397–1405.
219. Phillips, T.R., Maluendes, S., McLean, A.D., and Green, S. (1994) *J. Chem. Phys.*, **101**, 5824–5830.
220. Hodges, M.P., Wheatley, R.J., Schenter, G.K., and Harvey, A.H. (2004) *J. Chem. Phys.*, **120** (2), 710–720.
221. Valiron, P., Wernli, M., Faure, A. *et al.* (2008) *J. Chem. Phys.*, **129** (13), 134306.
222. Faure, A., Valiron, P., Wernli, M. *et al.* (2005) *J. Chem. Phys.*, **122** (22), 221102.
223. Scribano, Y., Faure, A., and Wiesenfeld, L. (2010) *J. Chem. Phys.*, **133** (23), 231105.
224. Wiesenfeld, L., Scribano, Y., and Faure, A. (2011) *Phys. Chem. Chem. Phys.*, **13**, 8230–8235.
225. Wiesenfeld, L., Scifoni, E., Faure, A., and Roueff, E. (2011) *Mon. Not. R. Astron. Soc.*, **413** (1), 509–513.
226. Faure, A. and Wiesenfeld, L. (2004) *J. Chem. Phys.*, **121** (14), 6771–6775.
227. Hutson, J.M. and Green, S. (1994) *MOLSCAT computer code, version 14, distributed by Collaborative Computational Project No. 6 of the Engineering and Physical Sciences Research Council UK).*
228. Wiesenfeld, L. and Faure, A. (2010) *Phys. Rev. A*, **82** (4), 040702.
229. Dick, M.J., Drouin, B.J., and Pearson, J.C. (2009) *J. Quant. Spectrosc. Radiat. Transfer*, **110**, 619–627.
230. Dick, M.J., Drouin, B.J., and Pearson, J.C. (2010) *Phys. Rev. A*, **81** (2), 022706.
231. Hartmann, J.M., Boulet, C., and Robert, D. (2008) *Collisional Effects on Molecular Spectra*, Elsevier.
232. Thibault, F., Mantz, A.W., Claveau, C. *et al.* (2007) *J. Mol. Spectrosc.*, **246**, 118–125.
233. Belpassi, L., Reca, M.L., Tarantelli, F. *et al.* (2010) *J. Am. Chem. Soc.*, **132** (37), 13046–13058.
234. Marquette, J.B., Rebrion, C., and Rowe, B.R. (1988) *J. Chem. Phys.*, **89** (4), 2041–2047.
235. Gerlich, D. (1993) *J. Chem. Soc., Faraday Trans.*, **89**, 2199–2208.
236. Zymak, I., Hejduk, M., Mulin, D. *et al.* (2013) *Astrophys. J.*, **768**, 86.
237. Juarez, A.M., Cubric, D., and King, G.C. (2002) *Meas. Sci. Technol.*, **13** (5), N52.
238. Tom, B.A., Bhasker, S., Miyamoto, Y., Momose, T., and McCall, B.J. (2009) *Rev. Sci. Instrum.*, **80** (1), 016108.
239. Cordonnier, M., Uy, D., Dickson, R.M. *et al.* (2000) *J. Chem. Phys.*, **113**, 3181–3193.
240. Crabtree, K.N., Kauffman, C.A., Tom, B.A. *et al.* (2011) *J. Chem. Phys.*, **134** (19), 194311.
241. Grussie, F., Berg, M.H., Crabtree, K.N. *et al.* (2012) *Astrophys. J.*, **759** (1), 21.
242. Park, K. and Light, J.C. (2007) *J. Chem. Phys.*, **126**, 044305.
243. Hugo, E., Asvany, O., and Schlemmer, S. (2009) *J. Chem. Phys.*, **130**, 164302.
244. Gerlich, D., Windisch, F., Hlavenka, P., Plašil, R., and Glosik, J. (2006) *Philos. Trans. R. Soc. London, Ser. A*, **364** (1848), 3007–3034.
245. Quack, M. (1977) *Mol. Phys.*, **34**, 477–504.
246. Oka, T. (2004) *J. Mol. Spectrosc.*, **228**, 635–639.
247. Xie, Z., Braams, B.J., and Bowman, J.M. (2005) *J. Chem. Phys.*, **122**, 224307.
248. Crabtree, K.N., Indriolo, N., Kreckel, H., Tom, B.A., and McCall, B.J. (2011) *Astrophys. J.*, **729**, 15.
249. Indriolo, N. and McCall, B.J. (2012) *Astrophys. J.*, **745**, 91.

250. Crabtree, K.N. and McCall, B.J. (2013) *J. Phys. Chem. A*, **117**, 9950–9958.

251. Schlemmer, S., Kuhn, T., Lescop, E., and Gerlich, D. (1999) *Int. J. Mass Spectrom.*, **185**, 589–602.

252. Schlemmer, S., Lescop, E., Richthofen, J., and Gerlich, D. (2002) *J. Chem. Phys.*, **117**, 2068–2075.

253. Lis, D.C., Roueff, E., Gerin, M. *et al.* (2002) *Astrophys. J.*, **571**, L55–L58.

254. Parise, B., Castets, A., Herbst, E. *et al.* (2004) *Astron. Astrophys.*, **416**, 159–163.

255. Linsky, J.L., Draine, B.T., Moos, H.W. *et al.* (2006) *Astrophys. J.*, **647** (2), 1106.

256. Rogers, A.E.E., Dudevoir, K.A., and Bania, T.M. (2007) *Astron. J.*, **133**, 1625–1632.

257. Charnley, S.B., Ehrenfreund, P., Millar, T.J. *et al.* (2004) *Mon. Not. R. Astron. Soc.*, **347** (1), 157–162.

258. Gerlich, D., Herbst, E., and Roueff, E. (2002) *Planet. Space Sci.*, **50**, 1275–1285.

259. Gerlich, D. and Schlemmer, S. (2002) *Planet. Space Sci.*, **50**, 1287–1297.

260. Solomon, P.M. and Woolf, N.J. (1973) *Astrophys. J. Lett.*, **180**, L89–L92.

261. Geballe, T.R. and Oka, T. (1996) *Nature*, **384**, 334–335.

262. Stark, R., van der Tak, F.F.S., and van Dishoeck, E.F. (1999) *Astrophys. J.*, **521**, L67–L70.

263. Roueff, E., Parise, B., and Herbst, E. (2007) *Astron. Astrophys.*, **464**, 245–252.

264. Roueff, E., Gerin, M., Lis, D.C. *et al.* (2013) *J. Phys. Chem. A*, **117** (39), 9959–9967.

265. Millar, T.J. (2003) *Space Sci. Rev.*, **106**, 73–86.

266. Gerlich, D. (1993) *J. Chem. Soc., Faraday Trans.*, **89**, 2167–2168.

267. Kluge, L., Gärtner, S., Brünken, S. *et al.* (2012) *Philos. Trans. R. Soc. London, Ser. A*, **370**, 5041–5054.

268. Andersen, T., Haugen, H.K., and Hotop, H. (1999) *J. Phys. Chem. Ref. Data*, **28**, 1511–1533.

269. Rienstra-Kiracofe, J.C., Tschumper, G.S., Schaefer, H.F., Nandi, S., and Ellison, G.B. (2002) *Chem. Rev.*, **102**, 231–282.

270. Pegg, D.J. (2004) *Rep. Progr. Phys.*, **67**, 857–905.

271. Wildt, R. (1939) *Astrophys. J.*, **89**, 295–301.

272. Chalonge, D. (1946) *Physica*, **12**, 721–732.

273. Ross, T., Baker, E.J., Snow, T.P. *et al.* (2008) *Astrophys. J.*, **684**, 358–363.

274. Dalgarno, A. and McCray, R.A. (1973) *Astrophys. J.*, **181**, 95–100.

275. Sarre, P.J. (1980) *J. Chim. Phys. Phys.-Chim. Biol.*, **77**, 769–771.

276. Herbst, E. (1981) *Nature*, **289**, 656–657.

277. Thaddeus, P., Gottlieb, C.A., Gupta, H. *et al.* (2008) *Astrophys. J.*, **677**, 1132–1139.

278. Cernicharo, J., Guélin, M., Agündez, M., McCarthy, M.C., and Thaddeus, P. (2008) *Astrophys. J.*, **688**, L83–L86.

279. Agúndez, M., Cernicharo, J., Guélin, M. *et al.* (2010) *Astron. Astrophys.*, **517**, L2.

280. Spergel, D.N., Verde, L., Peiris, H.V. *et al.* (2003) *Astrophys. J. Suppl. Ser.*, **148**, 175–194.

281. Galli, D. and Palla, F. (1998) *Astron. Astrophys.*, **335**, 403–420.

282. Lepp, S., Stancil, P.C., and Dalgarno, A. (2002) *J. Phys. B*, **35**, R57–R80.

283. Glover, S.C.O. and Savin, D.W. (2009) *Mon. Not. R. Astron. Soc.*, **393**, 911–948.

284. Galli, D. and Palla, F. (2013) *Annu. Rev. Astron. Astrophys.*, **51**, 163–206.

285. Peebles, P.J.E. and Dicke, R.H. (1968) *Astrophys. J.*, **154**, 891–908.

286. Bromm, V., Yoshida, N., Hernquist, L., and McKee, C.F. (2009) *Nature*, **459**, 49–54.

287. Kreckel, H., Bruhns, H., Čížek, M. *et al.* (2010) *Science*, **329**, 69–71.

288. Saslaw, W.C. and Zipoy, D. (1967) *Nature*, **216**, 976–978.

289. Gould, R.J. and Salpeter, E.E. (1963) *Astrophys. J.*, **138**, 393–407.

290. Hirasawa, T., Aizu, K., and Taketani, M. (1969) *Prog. Theor. Phys.*, **41**, 835–838.

291. Ripamonti, E. (2007) *Mon. Not. R. Astron. Soc.*, **376**, 709–718.

292. Dalgarno, A. and Wright, E.L. (1972) *Astrophys. J.*, **174**, L49–L51.

293. Savin, D.W. (2002) *Astrophys. J.*, **566**, 599–603.
294. Gerlich, D., Plašil, R., Zymak, I. *et al.* (2013) *J. Phys. Chem. A*, **117**, 10068–10075.
295. Mizusawa, H., Omukai, K., and Nishi, R. (2005) *Publ. Astron. Soc. Jpn.*, **57**, 951–967.
296. Smith, S.J. and Burch, D.S. (1959) *Phys. Rev.*, **116**, 1125–1131.
297. Popp, H.P. and Kruse, S. (1976) *J. Quant. Spectrosc. Radiat. Transfer*, **16**, 683–688.
298. Wishart, A.W. (1979) *Mon. Not. R. Astron. Soc.*, **187**, 59P–60P.
299. Abel, T., Anninos, P., Zhang, Y., and Norman, M.L. (1997) *New Astron.*, **2**, 181–207.
300. Schmeltekopf, A.L., Fehsenfeld, F.C., and Ferguson, E.E. (1967) *Astrophys. J.*, **148**, L155–L156.
301. Taylor, H.S. and Harris, F.E. (1963) *J. Chem. Phys.*, **39**, 1012–1016.
302. Dalgarno, A. and Browne, J.C. (1967) *Astrophys. J.*, **149**, 231–232.
303. Fehsenfeld, F.C., Howard, C.J., and Ferguson, E.E. (1973) *J. Chem. Phys.*, **58**, 5841–5842.
304. Martinez, O. Jr., Yang, Z., Betts, N.B., Snow, T.P., and Bierbaum, V.M. (2009) *Astrophys. J.*, **705**, L172–L175.
305. Stancil, P.C., Lepp, S., and Dalgarno, A. (1998) *Astrophys. J.*, **509**, 1–10.
306. Sakimoto, K. (1989) *Chem. Phys. Lett.*, **164**, 294–298.
307. Senekowitsch, J., Rosmus, P., Domcke, W., and Werner, H.-J. (1984) *Chem. Phys. Lett.*, **111**, 211–214.
308. Launay, J.M., Le Dourneuf, M., and Zeippen, C.J. (1991) *Astron. Astrophys.*, **252**, 842–852.
309. Browne, J.C. and Dalgarno, A. (1969) *J. Phys. B*, **2**, 885–889.
310. Čížek, M., Horácek, J., and Domcke, W. (1998) *J. Phys. B*, **31**, 2571–2583.
311. Miller, K.A., Bruhns, H., Eliášek, J. *et al.* (2011) *Phys. Rev. A*, **84** (5), 052709.
312. Bruhns, H., Kreckel, H., Miller, K. *et al.* (2010) *Rev. Sci. Instrum.*, **81**, 013112.
313. Bruhns, H., Kreckel, H., Miller, K.A., Urbain, X., and Savin, D.W. (2010) *Phys. Rev. A*, **82**, 042708.
314. Miller, K.A., Bruhns, H., Čížek, M. *et al.* (2012) *Phys. Rev. A*, **86** (3), 032714.
315. Gerlich, D., Jusko, P., Roučka, v.S. *et al.* (2012) *Astrophys. J.*, **749**, 22.
316. Howard, C.J., Fehsenfeld, F.C., and McFarland, M. (1974) *J. Chem. Phys.*, **60**, 5086–5089.
317. Houfek, K., Čížek, M., and Horáček, J. (2002) *Phys. Rev. A*, **66**, 062702.
318. Bromm, V., Coppi, P.S., and Larson, R.B. (2002) *Astrophys. J.*, **564**, 23–51.
319. Glover, S.C.O. (2007) *Mon. Not. R. Astron. Soc.*, **379**, 1352–1358.
320. Chuzhoy, L., Kuhlen, M., and Shapiro, P.R. (2007) *Astrophys. J.*, **665**, L85–L88.
321. Bylicki, M. and Bednarz, E. (2003) *Phys. Rev. A*, **67**, 022503.
322. Kar, S. and Ho, Y.K. (2009) *J. Phys. B*, **42**, 185005.
323. Sadeghpour, H.R., Greene, C.H., and Cavagnero, M. (1992) *Phys. Rev. A*, **45**, 1587–1595.
324. Miyake, S., Stancil, P.C., Sadeghpour, H.R. *et al.* (2010) *Astrophys. J.*, **709**, L168–L171.
325. Bates, D.R. (1978) *Phys. Rep.*, **35**, 305–372.
326. Stancil, P.C., Miyake, S., Sadeghpour, H.R., McLaughlin, B.M., and Forrey, R.C. (2010) in *Contribution to Atomic, Molecular, and Optical Physics, Astrophysics and Atmospheric Physics: Proceedings the Dalgarno Celebratory Symposium* (ed. J.F. Babb, K. Kirby, and H. Sadeghpou), Imperial College Press, London, pp. 102–116.
327. Wishart, A.W. (1979) *J. Phys. B*, **12**, 3511–3519.
328. Glover, S.C., Savin, D.W., and Jappsen, A.-K. (2006) *Astrophys. J.*, **640**, 553–568.
329. Glover, S.C.O. and Abel, T. (2008) *Mon. Not. R. Astron. Soc.*, **388**, 1627–1651.
330. Turk, M.J., Clark, P., Glover, S.C.O. *et al.* (2011) *Astrophys. J.*, **726**, 55.
331. Bryant, H.C., Dieterle, B.D., Donahue, J. *et al.* (1977) *Phys. Rev. Lett.*, **38**, 228–230.
332. MacArthur, D.W., Butterfield, K.B., Clark, D.A. *et al.* (1985) *Phys. Rev. A*, **32**, 1921–1923.

333. Harris, P.G., Bryant, H.C., Mohagheghi, A.H. *et al.* (1990) *Phys. Rev. Lett.*, **65**, 309–312.

334. Harris, P.G., Bryant, H.C., Mohagheghi, A.H. *et al.* (1990) *Phys. Rev. A*, **42**, 6443–6465.

335. Halka, M., Bryant, H.C., Mackerrow, E.P. *et al.* (1991) *Phys. Rev. A*, **44**, 6127–6129.

336. Halka, M., Bryant, H.C., Johnstone, C. *et al.* (1992) *Phys. Rev. A*, **46**, 6942–6948.

337. Andersen, H.H., Balling, P., Kristensen, P. *et al.* (1997) *Phys. Rev. Lett.*, **79**, 4770–4773.

338. Balling, P., Andersen, H.H., Brodie, C.A. *et al.* (2000) *Phys. Rev. A*, **61**, 022702.

339. Dalgarno, A. and Lepp, S. (1987) in *Astrochemistry, IAU Symposium*, Vol. 120 (eds M.S. Vardya and S.P. Tarafdar), D. Reidel Publ. Co., Dordrecht, Holland, pp. 109–118.

340. Croft, H., Dickinson, A.S., and Gadea, F.X. (1999) *Mon. Not. R. Astron. Soc.*, **304**, 327–329.

341. Moseley, J., Aberth, W., and Peterson, J.R. (1970) *Phys. Rev. Lett.*, **24**, 435–439.

342. Peterson, J.R., Aberth, W.H., Moseley, J.T., and Sheridan, J.R. (1971) *Phys. Rev. A*, **3**, 1651–1657.

343. Bates, D.R. and Lewis, J.T. (1955) *Proc. Phys. Soc. London, Sect. A*, **68**, 173–180.

344. Olson, R.E., Peterson, J.R., and Moseley, J. (1970) *J. Chem. Phys.*, **53**, 3391–3397.

345. Eerden, M.J.J., van de Sanden, M.C.M., Otorbaev, D.K., and Schram, D.C. (1995) *Phys. Rev. A*, **51**, 3362–3365.

346. Fussen, D. and Kubach, C. (1986) *J. Phys. B*, **19**, L31–L34.

347. Stenrup, M., Larson, A.A., and Elander, N. (2009) *Phys. Rev. A*, **79**, 012713.

4
Molecular Photodissociation

Ewine F. van Dishoeck and Ruud Visser

4.1
Introduction

Photodissociation is the dominant process by which molecules are removed in any region exposed to intense ultraviolet (UV) radiation. Such clouds of gas and dust are indicated by astronomers with the generic title "photon-dominated region", or PDR. Originally, the term *PDR* referred mostly to dense molecular clouds close to bright young stars such as found in the Orion nebula. There are many other regions in space, however, in which photodissociation plays a crucial role in the chemistry: this includes diffuse and translucent interstellar clouds, high-velocity shocks, the surface layers of protoplanetary disks, and cometary and exoplanetary atmospheres.

In the simplest case, a molecule ABC absorbs a UV photon, which promotes it into an excited electronic state, and subsequently dissociates to AB + C. In reality, the situation is much more complex because there are many electronic states that can be excited, with only a fraction of the absorptions leading to dissociation. Also, there are many possible photodissociation products, each of which can be produced in different electronic, vibrational, and rotational states depending on the wavelength of the incident photons. The rate of photodissociation depends not only on the cross sections for all these processes but also on the intensity and shape of the radiation field at each position in the cloud. Thus, an accurate determination of the photodissociation rate of even a simple molecule like water involves many detailed considerations, ranging from its electronic structure to its dissociation dynamics and to the specifics of the radiation field to which the molecule is exposed.

In this chapter, each of these steps in determining photodissociation rates is systematically discussed. Section 4.2 reviews the basic processes through which small and large molecules can dissociate following UV absorption. Techniques for determining absorption and photodissociation cross sections through theoretical calculations and laboratory experiments are summarized in Section 4.3. This section also mentions new experimental developments that determine branching ratios of the different products. Various interstellar and circumstellar radiation

Laboratory Astrochemistry: From Molecules through Nanoparticles to Grains, First Edition.
Edited by Stephan Schlemmer, Thomas Giesen, Harald Mutschke and Cornelia Jäger.

fields are summarized in Section 4.4, including their attenuation due to dust and self-shielding deeper inside the cloud. The formulas for computing photodissociation rates are contained in Section 4.5, together with references to recent compilations of cross sections and rates. As a detailed example, recent developments in our understanding of the photodissociation of CO and its isotopologs are presented in Section 4.6. The chapter ends with a brief review of the photostability of polycyclic aromatic hydrocarbons (PAHs). Much of this chapter follows earlier reviews by van Dishoeck *et al.* [1, 2].

4.2
Photodissociation Processes

4.2.1
Small Molecules

The processes by which photodissociation of simple molecules can occur have been outlined by Kirby, van Dishoeck, and Schinke [3, 4]. A summary is presented in Figure 4.1 for the case of diatomic molecules. Similar processes can occur for small polyatomic molecules, especially if the potential surface is dissociative along one of the coordinates in the multidimensional space.

The simplest process is *direct photodissociation*, in which a molecule absorbs a photon into an excited electronic state that is repulsive with respect to the nuclear coordinate. Since spontaneous emission back to the ground state is comparatively slow (typical Einstein-A coefficients of 10^9 s^{-1} compared with dissociation times of 10^{13} s^{-1}), virtually all absorptions lead to dissociation of the molecule. The resulting photodissociation cross section is a continuous function of photon energy, and peaks close to the vertical excitation energy according to the Franck–Condon principle. The width is determined by the steepness of the repulsive potential: the steeper the curve, the broader the cross section. Its shape reflects that of the vibrational wave function of the ground state out of which the absorption occurs. Note that the cross section is usually very small at the threshold energy corresponding to the dissociation energy D_e of the molecule; thus, taking D_e as a proxy for the wavelength range at which dissociation occurs gives incorrect results.

In the process of *predissociation*, the initial absorption occurs into a bound excited electronic state, which subsequently interacts nonradiatively with a nearby repulsive electronic state. An example of such a type of interaction is spin–orbit coupling between states of different spin multiplicity. Another example is the nonadiabatic coupling between two states of the same symmetry. The strength of the interaction depends sensitively on the type of coupling and on the energy levels involved, but predissociation rates are typically comparable to or larger than the rates for spontaneous emission. The effective photodissociation cross section consists in this case of a series of discrete peaks, which reflect the product of the oscillator strength of the initial absorption and the dissociation

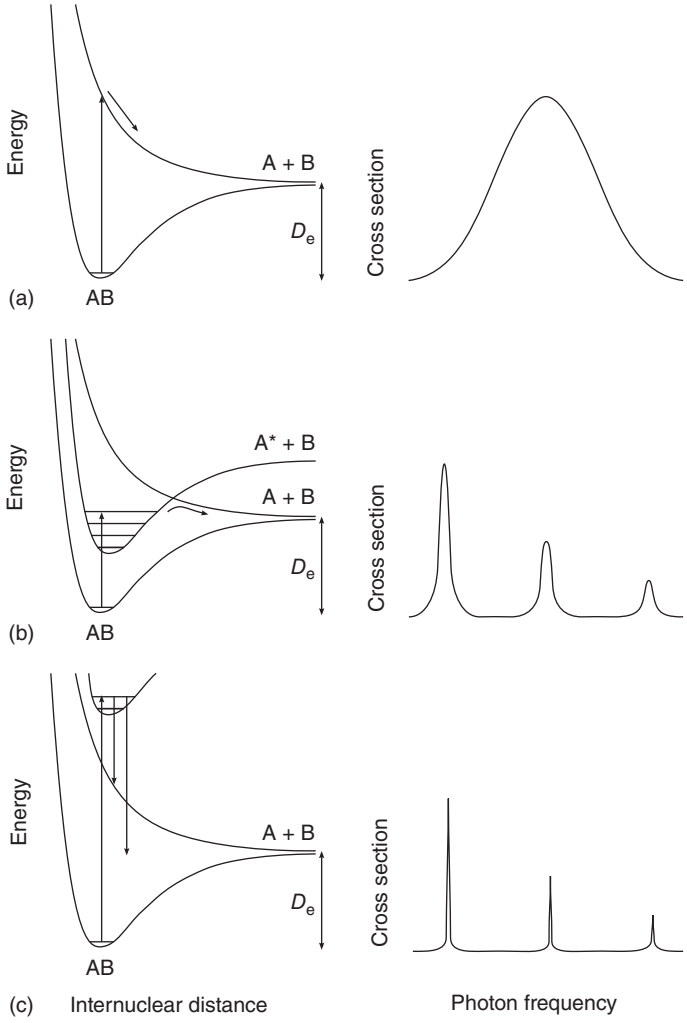

Figure 4.1 Photodissociation processes of diatomic molecules and corresponding cross sections. (a) Direct photodissociation, (b) predissociation, and (c) spontaneous radiative dissociation. (Based on Ref. [1].)

efficiency of the level involved. The width is controlled by the sum of the radiative and predissociation rates and is generally large (10^{12} s^{-1}, corresponding to 15 km s^{-1} or more in velocity units).

If the excited bound states are not predissociated, *spontaneous radiative dissociation* can still be effective through emission of photons into the continuum of a lower lying repulsive state or the vibrational continuum of the ground electronic state. The efficiency of this process is determined by the competition with spontaneous emission into lower lying bound states. The photodissociation cross section

again consists of a series of discrete peaks, but the peaks are not broadened and have widths determined by the total radiative lifetime (typically <0.1 km s^{-1}).

Because a molecule has many excited electronic states which can be populated by the ambient radiation field, in general all of these processes will occur. As an example, Figure 4.2 shows the potential energy curves of the lowest 16 electronic states of the OH radical: predissociation occurs through the lowest excited $A^2\Sigma^+$ electronic state, whereas direct dissociation can take place through the $1\,^2\Sigma^-$, $1\,^2\Delta$, and coupled 2 and $3\,^2\Pi$ electronic states. However, usually only one or two of these processes dominate the photodissociation of a molecule in interstellar clouds. In the case of OH, these are the direct $1\,^2\Sigma^-$ and $1\,^2\Delta$ channels. However, predissociation through the lower lying A state is important in cometary atmospheres and disks around cool stars, where the radiation field lacks high-energy photons.

The photodissociation of many simple hydrides such as H_2^+, OH, H_2O, CH, CH^+, and NH proceeds mostly through the direct process. On the other hand, the photodissociation of CO is controlled by predissociation processes, whereas that of H_2 occurs exclusively by spontaneous radiative dissociation for photon energies

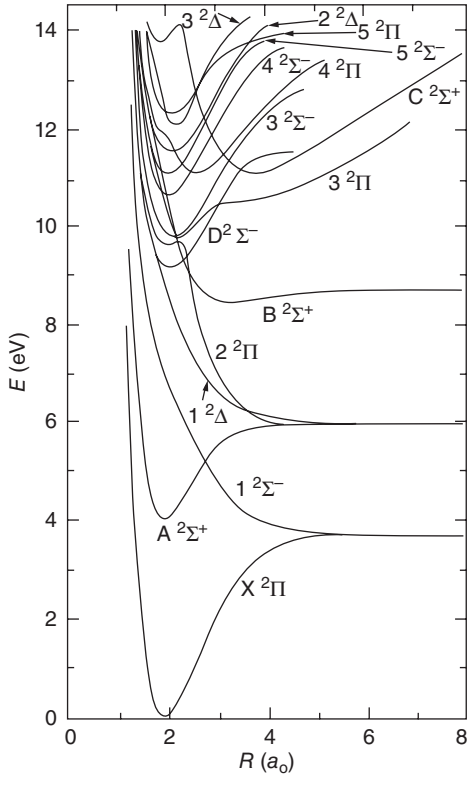

Figure 4.2 Potential energy curves of the OH molecule. (Reproduced from [5], with permission from Univ. of Chicago Press, copyright AAS.)

below 13.6 eV. Whether the photodissociation is dominated by continuous or line processes has important consequences for the radiative transfer through the cloud (see Section 4.4.6).

4.2.2 Large Molecules

For large molecules, the same processes as illustrated in Figure 4.1 can occur, but they become less and less likely as the size of the molecule increases. This is because the number of vibrational degrees of freedom of a nonlinear molecule, $3N - 6$, increases rapidly with the number of atoms N. Each of these modes has many associated vibrational levels, with quantum numbers v increasing up to the dissociation energy of the potential. For sufficiently large N, the density of vibrational levels becomes so large that they form a quasi-continuum with which the excited states can couple nonradiatively (Figure 4.3). Through this so-called process of internal conversion, the molecule ends up in a highly excited vibrational level of a lower lying electronic state. The probability is small that the molecule will find its way across the multidimensional surface to a specific dissociative mode, so the most likely outcome is that the molecule ends up in an excited bound level and subsequently relaxes by emission of infrared photons. Alternatively, the excited molecule can fluoresce down to the ground state in a dipole-allowed electronic transition, or it can undergo the so-called intersystem crossing to an electronic state with a different spin multiplicity from which it can phosphoresce down in a spin-forbidden transition.

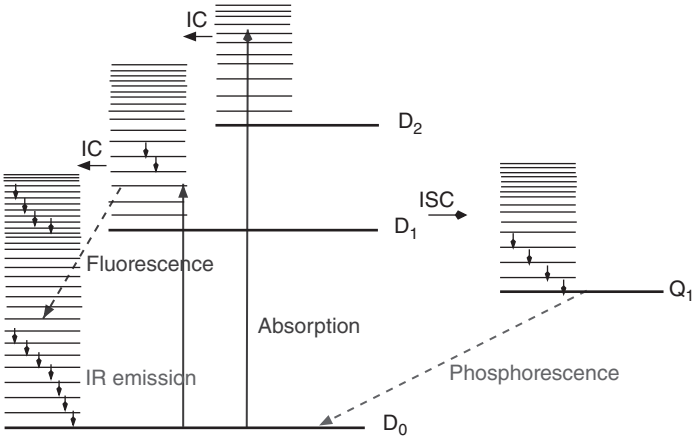

Figure 4.3 Radiative and radiationless decay of large molecules, illustrating the processes of internal conversion (IC), intersystem crossing (ISC), fluorescence, phosphorescence, and infrared emission. This example is for a large ion such as PAH^+ with a ground state with one unpaired electron (doublet spin symmetry) denoted as D_0, and doublet and quartet excited electronic states. Various vibrational levels within the electronic states are indicated.

Statistical arguments using the (modified) Rice–Ramsperger–Kassel–Marcus (RRKM) theory suggest that N-atom molecules with $N \gtrsim 25$ are stable with respect to photodissociation, although this number depends on the structure and types of modes of the molecule involved [6]. Thus, long carbon chains may have a different photostability than ring molecules. PAHs are a specific class of large molecules highly relevant for astrochemistry, and are discussed further in Section 4.7. Very few gas-phase experiments exist on such large molecules to test these theories.

Ashfold *et al.* [7] have recently pointed out that many intermediate-sized molecules with $N \approx 10$, including complex organic molecules such as alcohols, ethers, phenols, amines, and N-containing heterocycles, have dissociative excited states that greatly resemble those found in smaller molecules such as H_2O and NH_3. Experiments show that H loss definitely occurs in these larger systems.

The ionization potentials of large molecules lie typically around 7–8 eV. Most of the absorptions of UV photons with higher energies are expected to lead to ionization, but a small fraction can also result in dissociation through highly excited neutral states lying above the ionization threshold or through low-lying dissociative states of the ion itself. These branching ratios are not well determined experimentally.

4.3 Photodissociation Cross Sections

Quantitative information on photodissociation cross sections comes from theory and experiments. Theory is well suited for small molecules, in particular radicals and ions that are not readily produced in the gas phase. Laboratory measurements of absorption spectra over a wide photon range exist primarily for chemically stable molecules, both small and large. In the following, we first review the theoretical methods of computing potential energy surfaces and cross sections, and then discuss the experimental data.

4.3.1 Theory

All information about a molecule can be contained in a wave function Ψ, which is the solution of the time-independent Schrödinger equation

$$\mathcal{H}\Psi(x, R) = E\Psi(x, R) \tag{4.1}$$

Here x stands for the spatial and spin coordinates of the n electrons in the molecule, and R denotes the positions of all N nuclei in the molecule. The total Hamiltonian $\mathcal{H}$ consists of the sum of the kinetic energy operators of the nuclei α and the electrons and of their potential energies due to mutual interactions. Equation (4.1) is a $(3n + 3N)$-dimensional second-order partial differential equation that cannot be readily solved, even for small molecules.

4.3.1.1 Born–Oppenheimer approximation

Because the mass of the nuclei is much larger than that of the electrons, the nuclei move slowly compared to the electrons. Most molecular dynamics studies therefore invoke the Born–Oppenheimer approximation for separating the nuclear and electronic coordinates:

$$\Psi(x, R) = \Psi^{\mathrm{el}}(x; R)\Psi^{\mathrm{nuc}}(x, R) \tag{4.2}$$

where the electronic energies $E^{\mathrm{el}}(R)$ (also called *the potential energy curves* or *surfaces*) are determined by solving the electronic eigenvalue equation, with the nuclei held fixed:

$$\mathcal{H}^{\mathrm{el}}\Psi^{\mathrm{el}}(x; R) = E^{\mathrm{el}}(R)\Psi^{\mathrm{el}}(x; R) \tag{4.3}$$

Note that Ψ^{el} now only depends parametrically on the nuclear positions R. Substituting Eq. (4.2) into Eq. (4.1) and using Eq. (4.3) gives

$$\left[-\sum_{\alpha}\left(\frac{1}{2}M_{\alpha}\right)\nabla_{\alpha}^{2} + E^{\mathrm{el}}(R) - E\right]\Psi^{\mathrm{nuc}}(R) = 0 \tag{4.4}$$

where the sum is over nuclei α with mass M_{α}. In this equation, we use the assumption $\nabla_{\alpha}^{2}\Psi^{\mathrm{el}}\Psi^{\mathrm{nuc}} = \Psi^{\mathrm{el}}\nabla_{\alpha}^{2}\Psi^{\mathrm{nuc}}$, which is inherent in the Born–Oppenheimer approximation. The coupling terms involving $\nabla_{\alpha}\Psi^{\mathrm{el}}$ are called *nonadiabatic terms* and their neglect is usually justified. Atomic units (a.u., not to be confused with astronomical units or arbitrary units) have been adopted, which have $\hbar = m_{\mathrm{e}} = e = 1$. The unit of distance is then 1 a.u. = 0.52918 Å (also called the Bohr radius or a_0) and the unit of energy is 1 a.u. = 27.21 eV (or Hartree).

Consider, for simplicity, a diatomic molecule with internuclear distance R. The probability of an electronic transition from state i to state f is governed by the magnitude of the electronic transition dipole moment $D(R)$, which can be computed from

$$D(R) = < \Psi_{f}^{\mathrm{el}}(x; R)|d|\Psi_{i}^{\mathrm{el}}(r; R) > \tag{4.5}$$

where the integration is performed over the electron coordinate space and d is the electric dipole moment operator in atomic units.

The photodissociation cross section (in square centimeters) following absorption from a bound vibrational level v'' of the ground electronic state into the vibrational continuum k' of an upper state at a transition energy ΔE is then given by

$$\sigma_{v''}(\Delta E) = 2.69 \times 10^{-18} g \Delta E| < \Psi_{k'}^{\mathrm{nuc}}(R)|D(R)|\Psi_{v''}^{\mathrm{nuc}}(R) > |^{2} \tag{4.6}$$

where the integration is over the nuclear coordinate R. Here, g is a degeneracy factor (equal to 2 for $\Pi \leftarrow \Sigma$ transitions, 1 otherwise) and all quantities are in atomic units. Similarly, the absorption oscillator strength between two bound states is

$$f_{v'v''} = \frac{2}{3} g \Delta E_{v'v''}| < \Psi_{v'}^{\mathrm{nuc}}(R)|D(R)|\Psi_{v''}^{\mathrm{nuc}}(R) > |^{2} \tag{4.7}$$

Theoretical calculations of photodissociation cross sections thus consist of two steps: (1) calculation of the electronic potential curve or surfaces and (2) solution of the nuclear motion under the influence of the potentials.

4.3.1.2 Electronic Energies: Method of Configuration Interaction

Step 1 is the calculation of the electronic potential energy surfaces $E(R)$ and transition dipole moments $D(R)$ connecting the excited states with the ground state as functions of the nuclear coordinate R. It is important to realize that most aspects of chemistry deal with small energy differences between large numbers. For example, the binding energy of a molecule or the excitation energy to the first excited state is typically only 0.5% of the total energy of the molecule. Thus, the difficulty in quantum chemistry is not only in dealing with a $3n + 3N$ many-body problem but also in reaching sufficient accuracy in the results. For example, the Hartree–Fock method, in which all electrons are treated as independent particles by expanding the molecular wave function in Eq. (4.2) in a product of n one-electron wave functions, fails because it neglects the "correlation energy" between the electrons: when two electrons come close together, they repel each other. This correlation energy is again on the order of a fraction of a percent of the total energy.

Over the last decades, different quantum chemical techniques have been developed that treat these correlations, and there are several publicly available programs. Most of the standard packages, however, such as the popular GAUSSIAN package or packages based on density functional theory [8, 9], are only suitable and well-tested for the ground electronic state and for closed-shell electronic structures. More sophisticated techniques based on the CASSCF (complete active space self-consistent field) or coupled cluster methods work well for the lowest few excited electronic states of a molecule, but these states often still lie below the dissociation energy and do not contribute to photodissociation. Accurate calculation of the higher lying potentials through which photodissociation can proceed requires multi-reference configuration interaction (MR-CI) techniques [10, 11], for which only a few packages exist (e.g., MOLPRO [12]).

In the CI method, the wave function is expanded into an orthonormal set of M symmetry-restricted configuration state functions (CSFs):

$$\Psi^{\mathrm{el}}(x_1, ..., x_n) = \sum_{1}^{M} c_s \Phi_s(x_1, ..., x_n) \tag{4.8}$$

The CSFs or "configurations" are generally linear combinations of Slater determinants, each combination having the symmetry and multiplicity of the state under consideration. The Slater determinants are constructed from an orthonormal set of one-electron molecular orbitals (MOs; obtained from an SCF solution to the Hartree–Fock equations), which in turn are expanded in an elementary set of atomic orbitals (AOs; called *the basis set*) centered on the atomic nuclei. The larger the value of M, the more accurate the results.

In the MR technique, a set of configurations is chosen to provide the reference space. For example, the $X\ ^2\Pi$ ground state of OH has the main configuration $1\sigma^2 2\sigma^2 3\sigma^2 1\pi^3$, where σ and π are the MOs. The reference space could be chosen to consist of all possible configurations of the same overall symmetry that have a coefficient c_s greater than some threshold in the final CI wave function. For the OH example, this includes configurations such as $1\sigma^2 2\sigma^2 3\sigma^1 4\sigma^1 1\pi^3$ in which one electron is excited from the highest occupied molecular orbital (HOMO) to the

lowest unoccupied molecular orbital (LUMO). Alternatively, an "active space" of orbitals can be designated, for example, the $2\sigma-4\sigma$ and $1\pi-2\pi$ MOs in the case of OH, within which all configurations of a particular symmetry are considered. The CI method then generates all single and double (and sometimes even higher) excitations with respect to this set of reference configurations, several hundreds of thousands of configurations in total, and diagonalizes the corresponding matrix. The resulting eigenvalues are the different electronic states of the molecule, with the lowest energy root corresponding to the ground state.

The quality of an MR-CI calculation is ultimately determined by the choice of the AO basis set, the choice of the reference space of configurations, and the number of configurations included in the final CI. The basis set needs to be at least of "triple-ζ" quality (i.e., each occupied AO 1s, 2p, etc., is represented by three functions with optimized exponents ζ). Also, polarization and Rydberg functions (i.e., functions that have higher quantum numbers than the occupied orbitals, e.g., 2p for H, 3d and 4s for C) need to be added. The number of AOs chosen in the basis set determines the number of MOs, which in turn determines the number of configurations. For a typical high-quality AO basis set, the latter number is so large, of order 10^8, that some selection of configurations needs to be made in order to handle them with a computer. For example, all configurations that lower the energy by more than a threshold value (in an eigenvalue equation with the reference set) can be chosen to be included in the final CI matrix.

Once the electronic wave functions Ψ^{el} for the ground and excited electronic states have been obtained, the expectation values of other operators, such as the electric dipole moment or the spin–orbit coupling, can be readily calculated.

4.3.1.3 Nuclear Dynamics: Oscillator Strengths and Cross Sections

Step 2 in calculating photodissociation cross sections consists of solving Eq. (4.4) to determine the nuclear wave functions using the electronic potential curves from Step 1. Often, the nuclear wave function is first separated into a radial and an angular part. If the angular part is treated as a rigid rotor, the radial part can be solved exactly by one-dimensional numerical integration for a diatomic molecule so that no further uncertainties are introduced. Once the wave functions for ground and excited states are obtained, the cross sections can be computed according to Eq. (4.6).

For indirect photodissociation processes, the oscillator strengths into the discrete upper levels are computed according to Eq. (4.7) for each vibrational level v'. If the coupling between the upper bound level with the final dissociative continuum (as computed in Step 1) is weak, first-order perturbation theory can be used to calculate the predissociation rates k^{pr} in S^{-1}. The predissociation probability η_u of upper level u is then obtained by comparing k^{pr} with the inverse radiative lifetime of the molecule A^{rad}: $\eta_u = k^{\mathrm{pr}}/(k^{\mathrm{pr}} + A^{\mathrm{rad}})$. In our example of OH, this approximation works well for the calculation of the predissociation of the $A^2\Sigma^+$ state for $v' \geq 2$. If the coupling is strong, as is the case for the OH 2 and 3 $^2\Pi$ states, the coupled equations for the excited states (i.e., going beyond the

Born–Oppenheimer approximation) have to be solved in order to compute the cross sections.

For (light) triatomic molecules, the calculation of the full 3D potential surfaces and the subsequent dynamics on those surfaces is still feasible, albeit with significantly more effort involved [4, 13, 14]. For multidimensional potential surfaces, often time-dependent wave packet propagation methods are preferred to solve the dynamics rather than the time-independent approach. Besides accurate overall cross sections, such studies give detailed insight into the photodissociation dynamics. For example, the structure seen in the photodissociation of H_2O through the first excited $\tilde{A}$ state is found to be due to the symmetric stretch of the excited molecule just prior to dissociation.

For larger polyatomic molecules, such fully flexible calculations are no longer possible, and one or more nuclear coordinates need to be frozen. In practice, often the entire nuclear dynamics calculations are skipped and only electronic energies and oscillator strengths at the ground state equilibrium geometry are computed. Assuming that all absorptions into excited states with vertical excitation energies larger than D_e lead to dissociation (i.e., $\eta_u = 1$), this method provides a rough estimate (upper limit) on the dissociation rate [15]. This method works because of the Franck–Condon principle, which states that the highest cross sections occur when the excitation energies are vertical, that is, nuclear coordinates do not change between lower and upper states (Figure 4.1). Because only a single nuclear geometry has to be considered, the amount of work is orders of magnitude less than that of a full electronic and nuclear calculation.

The overall accuracy of the cross sections and oscillator strengths is typically 20–30% for small molecules in which the number of active electrons is at most ∼30. On the order of 5–10 electronic states per molecular symmetry can be computed with reasonable accuracy. Transition energies to the lowest excited states are accurate to ∼0.1 eV, and those to higher states to 0.2–0.3 eV. Thus, quantum chemistry cannot predict whether a molecule has an electronic state whose excitation energy matches exactly that of, say, Lyman α at 10.2 eV. However, if it has an electronic state with a vertical energy close to 10 eV, and absorption into the state is continuous, theory can firmly state that there is a significant cross section at Lyman α. An example is the $1\,^2\Delta$ state of OH: even with ±30 Å uncertainty in position, the cross section at 1215.6 Å is found to lie between 1 and 2×10^{-18} cm^2.

Virtually all molecules have more electronic states below 13.6 eV than can be computed accurately with quantum chemistry. Take our OH example: there is an infinite number of Rydberg states converging to the ionization potential at 13.0 eV. However, because the intensity of the radiation field usually decreases at shorter wavelengths, these higher states do not significantly affect the overall photodissociation rates. Their combined effect can often be taken into account through a single state with an oscillator strength of 0.1 lying around the ionization potential.

4.3.2 Experiments

Laboratory measurements of absorption cross sections have been performed for many chemically stable species, including astrophysically relevant molecules such

as H_2O, CO_2, NH_3, and CH_4. Most of these experiments have been performed at rather low spectral resolution, where the individual ro-vibrational lines are not resolved. Figure 4.4 shows an example of measurements for H_2O. A broad absorption continuum is observed between 1900 and 1200 Å, with discrete features superposed at shorter wavelengths. Note that the electronic states responsible for the absorptions at the shortest wavelengths have often not yet been identified spectroscopically.

The absorption of a photon can result in re-emission of another photon, dissociation, or ionization of the molecule, and most experiments do not distinguish between these processes. If the photon energy is below the first ionization potential and if the absorption is continuous, photodissociation is likely to be the dominant process. If not, additional information is needed to infer the dissociation probabilities η_u. For the H_2O example, the broad continuum at 1900–1400 Å corresponds to absorption into the $\tilde{A}\,^1B_1$ state, which is fully dissociative. However, this is not necessarily true for the higher lying discrete absorptions. An example is provided by the case of NO for which fluorescence cross sections have been measured directly and found to vary significantly from band to band, with η_u significantly less than unity for some bands [17].

Experiments typically quote error bars of about 20% in their cross sections if the absorption is continuous. For discrete absorptions, high spectral resolution and low pressures are essential to obtain reliable cross sections or oscillator strengths, since saturation effects can easily cause orders of magnitude errors.

Most broad-band absorption spectra date from the 1950s to 1980s and have been summarized in various papers and books [17–19]. An electronic compilation is provided through the MPI-Mainz UV–vis spectral atlas. Since about 1990, emphasis has shifted to experiments at single, well-defined wavelengths using

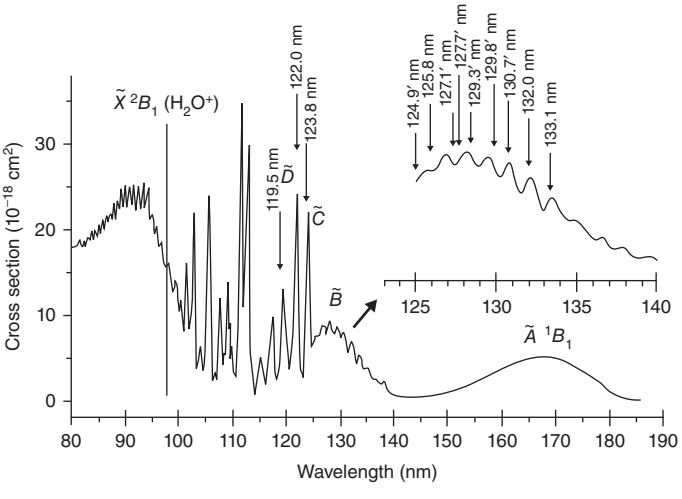

Figure 4.4 Absorption spectrum of gaseous H_2O illustrating the different electronic states through which photodissociation can occur. (Reproduced from [16], copyright 2001 © permission from Univ. of Chicago press.)

lasers, in particular at 1930 and 1570 Å. The aim of these experiments is usually to study the dynamics of the photodissociation process at that wavelength, rather than obtaining cross sections. Such studies typically target the lower excited electronic states because lasers or light sources at wavelengths <1200 Å are not commonly available except in specialized laboratories [20]. While these sophisticated experiments have provided much basic insight into photodissociation dynamics, the restriction to only one or two wavelengths and lack of cross-sectional data makes them of limited value for interstellar applications.

With the recent advent of powerful synchrotron light sources providing continuous radiation over a large wavelength range, the pendulum is swinging back to more astrophysically relevant results. For example, photodissociation cross sections of molecules such as CH_3OH are being measured in the X-ray regime up to 100 eV [21]. High-resolution data in the far-ultraviolet (FUV) regime up to 13.6 eV are eagerly awaited.

4.3.3 Photodissociation Products

Inclusion of photodissociation reactions in chemical networks requires knowledge not only of the rate of removal of species ABC but also of the branching ratios to the various products, AB + C, A + BC, or AC + B. Each of these species can be produced with different amounts of electronic, vibrational, and/or rotational energy, with the absolute and relative amounts depending on wavelength. None of this detail is captured in the standard tabulations, which, at best, give branching ratios between products integrated over all wavelengths or at a single wavelength, and neglect any vibrational or rotational excitation.

A great number of very elegant modern experiments are now available to explore the fragments, based on a range of photofragment translational spectroscopy and time-resolved photon–electron spectroscopy methods [7]. Product imaging techniques date back to the 1980s and characterize the velocities, internal energies, and angular distributions of the photodissociation products [22].

Velocity map imaging is a recent example of such a technique well suited for probing photodissociation (Figure 4.5) [23, 24]. In this method, a molecular beam containing the molecule of interest is created by a pulsed supersonic expansion, which ensures internal state cooling. After passing through a skimmer and a small hole in the repeller plate lens of an ion lens assembly, the beam is crossed by a dissociation laser beam to form neutral fragments, which are immediately state-selectively ionized by a probe laser beam using resonance enhanced multiphoton ionization (REMPI). The ions retain the velocity information of the nascent photofragments. Velocity map imaging uses a special configuration of an electrostatic immersion ion lens (combination of repeller, extractor, and ground electrodes) to ensure mapping of the ion velocity independent of its position of formation. After acceleration through the ion lens, the particles are mass-selected by time of flight upon reaching the surface of a two-dimensional imaging detector, which converts ion impacts to light flashes recorded by a charge-coupled device

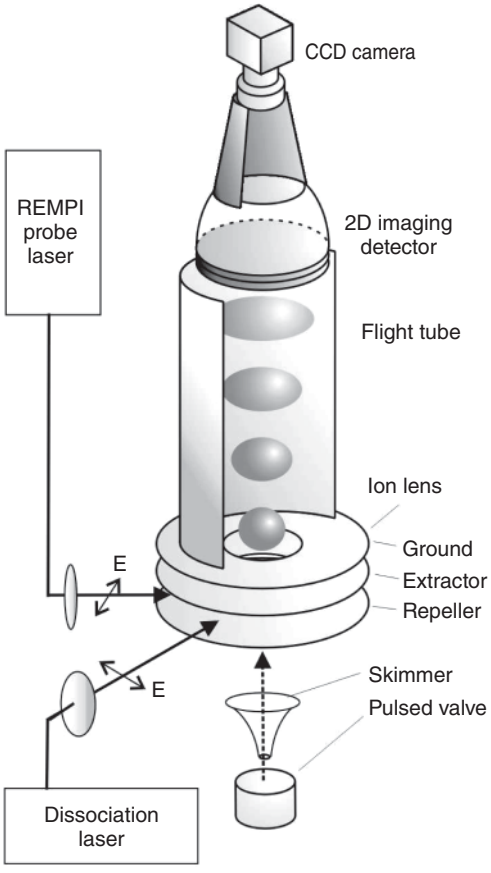

Figure 4.5 Experimental setup for velocity map imaging of photodissociation products. (Based on Ref. [23].)

(CCD) camera. The two-dimensional image can then be converted to its desired 3D counterpart by using an inverse Abel transformation. The lens effectively reduces the "blurring" of the images.

Another variant of this technique is Rydberg H-atom time-of-flight spectroscopy. Here, the nascent H atoms produced by photodissociation in the ground $n = 1$ state are excited into the $n = 2$ state using a Lyman α laser at 1216 Å and subsequently to a high Rydberg state with $n = 30–80$ using longer wavelength (e.g., 3650 Å) radiation. The neutral Rydberg H atoms then reach a microchannel plate where they are field-ionized and detected.

A completely different set of experiments has been applied to study the branching ratios of large carbon chain molecules. Here, high velocity collisions combined with an inverse kinematics scheme have shown that the most favorable channels are H production from C_nH and C_3 production from C_n [25]. Otherwise, the fragmentation behavior is largely statistical.

An example of the complexity of the situation is provided by the OH and H_2O cases. For OH, the potential curves in Figure 4.2 show that absorption into the $1\ ^2\Sigma^-$ state results in ground-state $O(^3P)$ + H, but absorption into the higher lying $^2\Delta$, $^2\Pi$, and $^2\Sigma^+$ states in excited $O(^1D)$ and $O(^1S)$. The cross sections into these states are such that about equal amounts of $O(^3P)$ and $O(^1D)$ are produced in the general interstellar radiation field (ISRF), but only 5% of $O(^1S)$ [5]. An astrophysical confirmation of this prediction is the detection of the red line of atomic O ($^1D \rightarrow {}^3P$) at 6300 Å from protoplanetary disks [26, 27]. On the other hand, for radiation fields dominated by lower photon energies such as in comets exposed to solar radiation, the main product is ground-state $O(^3P)$.

H_2O is one of the few polyatomic molecules for which the product distribution has been well characterized as a function of energy. Both theory and experiment have shown that absorption at 6–8 eV into the first $\tilde{A}$ electronic state produces OH in the ground electronic $^2\Pi$ state with some vibrational excitation but little rotational excitation. In contrast, absorption at 9–11 eV into the second $\tilde{B}$ electronic state produces OH in highly excited rotational levels of the $A^2\Sigma^+$ excited electronic state, but with low vibrational excitation. Absorption into even higher excited states results in O + H_2 or O + H + H products, rather than OH + H. For other polyatomic molecules, experimental information is spotty at best. Early experiments were often performed at high pressures, where the observed products could result from subsequent chemical reactions in the gas that would not occur at the low densities in space [19].

Some guess of the most likely products can be made on the basis of product energies (when does a product channel open up?) and correlation diagrams [7], but these techniques are usually limited to the lowest lying channels which may not dominate the overall dissociation. Often, the astrochemical databases simply assume a statistical distribution over the various products averaged over all photon energies. Note that the information on the product distribution of species such as CH_3OH is relevant not only for gas-phase chemistry but even more so for ice chemistry [28].

4.4 Astrophysical Radiation Fields

4.4.1 General Interstellar Radiation Field

Determinations of the average intensity of the ISRF fall into two main categories (see Refs [29, 30] for critical reviews). The first method is to estimate the number and distribution of hot stars (O, B, A, etc., type) in the Galaxy, use a model for the dust distribution and properties to determine the absorption and scattering of the stellar radiation, and then sum their fluxes to determine the energy density at a typical interstellar location. This method dates back to Refs. [31, 32], and has most recently been revisited by Parravano *et al.* [33]. The stellar fluxes used in these

models are a combination of observed fluxes of early type stars and extrapolations to shorter wavelengths using model atmospheres.

The second method is to use direct measurements of the UV radiation from the sky at specific wavelengths [34]. Also in this method, model stellar atmospheres are used to provide information at wavelengths not directly observed. In both methods, direct starlight from early B stars is found to dominate the measured interstellar flux. Specifically, most of the flux at a given point in space comes from the sum of discrete sources within 500 pc distance from that point.

The various estimates of the local ISRF in the solar neighborhood agree remarkably well, within a factor of 2. The median value found by Parravano *et al.* [33] is within 10% of the mean energy density of $U = 8 \times 10^{-17}$ erg cm^{-3} Å^{-1} of Ref. [32], averaged over the 912–2070 Å FUV band (Δ_{FUV}). The strength of the one-dimensional ISRF is often indicated by a scaling factor G_0 with respect to the flux F in the Habing field ($F_{\mathrm{FUV}} = cU_{\mathrm{FUV}}\Delta_{\mathrm{FUV}}$) of 1.6×10^{-3} erg cm^{-2} s^{-1}, which is a factor of 1.7 below that of Ref. [32]. Thus, the standard Draine field implies $G_0 = 1.7$. Care should be taken that photodissociation rates used in astrochemical models refer to the same radiation field.

If a cloud is located close to a young, hot star, the intensity incident on the cloud boundary may be enhanced by orders of magnitude compared with the average ISRF. A well-known example is the Orion Bar, where the intensity is enhanced by a factor of 4.4×10^4 with respect to the Draine field. In contrast, at high latitudes where few early type stars are located, the intensity may be factors of 5–10 lower in the FUV band than that of the standard ISRF field. Throughout the galactic plane and over time scales of a few billion years, variations in the local energy density by factors of 2–3 are expected as a result of the birth and demise of associations containing high-mass O and B stars within about 30 Myr. Moreover, the ratio of the highest energy photons capable of dissociating H_2 and CO and those in the more general FUV range may vary by a factor of 2 in time and place [33].

4.4.2 Stellar Radiation Fields

The surface layers of disks around young stars are another example of gas in which the chemistry is controlled by photodissociation. The illuminating stars range from late B- and early A-type stars (the so-called Herbig Ae/Be stars) to K- and M-type stars (the T Tauri stars). For the latter, if the stellar atmosphere dominates the flux, orders of magnitude fewer high-energy photons are available to dissociate the molecules than in the ISRF scaled to the same integrated intensity (Figure 4.6). In particular, the number of photons capable of dissociating H_2 and CO and ionizing carbon is greatly reduced [2, 35]. However, if accretion onto the star is still taking place, the hot gas in the accreting column produces high-energy photons, including Lyman α, which can dominate the FUV flux [36].

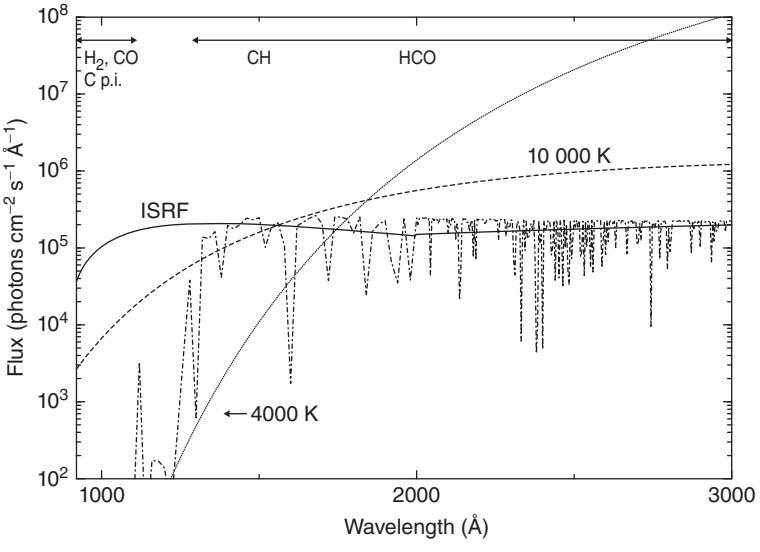

Figure 4.6 Comparison of the general interstellar radiation field of Draine [32] (extended for $\lambda > 2000$ Å using the representation of [37]) with various stellar radiation fields scaled to have the same integrated intensity from 912 to 2070 Å. The scaled NEXTGEN model radiation field of a B9.5 star [38] is included as well (dash-dotted). The wavelength ranges where the photodissociation of some important interstellar molecules occurs are indicated. (Adapted from Ref. [2] C. Joblin – Private Communication.)

4.4.3
Lyman α Radiation

Fast shocks (velocities >50 km s^{-1}) produce intense Lyman α radiation as a result of collisional excitation of atomic hydrogen in the hot gas or recombination of ionized hydrogen [39, 40]. Another prominent line in shocks is the C III resonance line at 977 Å. Fast shocks can be caused by supernovae expanding into the interstellar medium, or by fast jets from protostars interacting with the surrounding cloud. Accretion shocks onto the young star mentioned above are another example, as are exoplanetary atmospheres. Some molecules, in particular H_2, CO, and N_2, cannot be dissociated by Lyman α. Other simple molecules such as OH, H_2O, and HCN can. A recent summary of cross sections at Lyman α is given by van Dishoeck *et al.* [2].

4.4.4
Cosmic-Ray-Induced Photons

A dilute flux of UV photons can be maintained deep inside dense clouds through the interaction of cosmic rays with hydrogen in the following process:

$$\mathrm{H\ or\ H_2 + CR \rightarrow H^+\ or\ H_2^+ + e^*} \tag{4.9}$$

$$e^* + H_2 \rightarrow H_2^* + e$$

$$H_2^* \rightarrow H_2 + h\nu$$

The energetic electrons e^* produced by the cosmic rays excite H_2 into the $B\,^1\Sigma_u^+$ and $C\,^1\Pi_u$ electronic states, so that the FUV emission is dominated by Lyman- and Werner-band UV photons. Higher lying electronic states contribute at the shortest wavelengths. As a result, the UV spectrum produced inside dense clouds resembles strongly that of a standard hydrogen lamp in the laboratory. Figure 4.7 shows the UV spectrum computed following [41, 42] for e^* at 30 eV and either all H_2 in $J = 0$ or distributed over $J = 1$ and $J = 0$ in a 3 : 1 ratio. Note that the precise spectrum does depend on the H_2 level populations and the ortho/para ratio. Because of the highly structured FUV field and the lack of high-resolution cross sections for most species, the resulting photodissociation rates may be quite uncertain. On the other hand, the large number of lines has a mitigating effect.

4.4.5
Dust Attenuation

The depth to which UV photons can penetrate in the cloud and affect the chemistry depends on (i) the amount of photons at the boundary of the cloud; (ii) the scattering properties of the grains as functions of wavelength; (iii) the competition between the atoms and molecules with the grains for the available photons, which, in turn, depends on the density of the cloud; and (iv) possible self-shielding of the molecules.

The absorption and scattering parameters of the grains determine the penetration depths of photons. The UV extinction curve shows substantial variations from place to place, especially at the shortest wavelengths in the 912–1100 Å region, which can greatly affect the CO and CN photodissociation rates [43, 44]. Similar

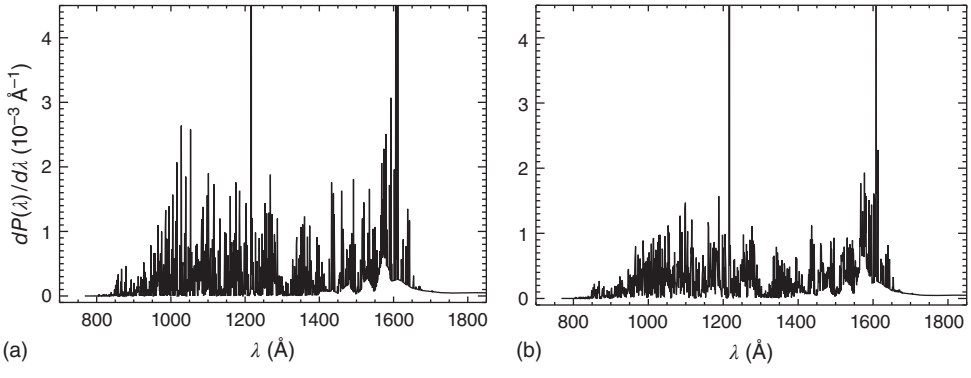

Figure 4.7 Cosmic-ray-induced spectrum of H_2 assuming that all H_2 is in $J = 0$ (a) or distributed over $J = 1$ and $J = 0$ in a 3 : 1 ratio (b). The spectrum shows the number of photons per 1 Å bin for initial 30 eV electrons and are normalized to the total number of ionizations. (Figure by Gredel, updated from Ref. [41, 42].)

variations are expected to occur for the albedo ϖ and the asymmetry parameter g as functions of wavelength, but little is still known about these parameters at the shortest wavelengths [45].

There is considerable observational evidence that dust grains in the surface layers of protoplanetary disks have grown from the typical interstellar size of 0.1 μm to at least a few micrometers in size or more. These large grains extinguish the UV radiation much less, allowing photodissociation to penetrate deeper into the disk [2, 46].

4.4.6 Self-Shielding

Because the physical and chemical structure of cloud edges is controlled by the photodissociation of H_2 and CO and photoionization of C, it is important to pay particular attention to the details for these molecules. CO is discussed in Section 4.6. The photodissociation of H_2 occurs by absorptions into the Lyman and Werner bands at 912–1100 Å followed by spontaneous emission back to the vibrational continuum of the ground state [47], see also Figure 4.1. The absorption lines have typical oscillator strengths $f \approx 0.0001$–0.03, and on average about 10% of the absorptions lead to dissociation. The strongest lines become optically thick at H_2 column densities of 10^{14}–10^{15} cm^{-2} for a Doppler broadening parameter b of 3 km s^{-1}, implying that molecules lying deeper within the cloud are shielded from dissociating radiation because all relevant photons have been absorbed at the cloud edge ("self-shielding"). The photodissociation rate of H_2 is about 4.5×10^{-11} s^{-1} in the unattenuated interstellar radiation field, corresponding to a lifetime of about 700 years. Inside the cloud, the lifetime becomes longer by several orders of magnitude because of the self-shielding process. The remaining 90% of the absorptions are followed by UV fluorescence back into the bound vibrational levels of the H_2 ground state.

Photoionization of atomic carbon has a continuous cross section of about 10^{-17} cm^2 over the 912–1100 Å region. Thus, for column densities $N(\mathrm{C}) > 10^{17}$ cm^{-2}, carbon starts to self-shield [48]. Moreover, the saturated absorption bands of H and H_2 over the same wavelength range remove a considerable fraction of the ionizing radiation ("mutual shielding").

4.5 Photodissociation Rates

The photodissociation rate k_{pd} of a molecule by continuous absorption is given by

$$k_{\mathrm{pd}}^{\mathrm{cont}} = \int \sigma(\lambda) I(\lambda) d\lambda \ \ \mathrm{s}^{-1} \tag{4.10}$$

where σ is the cross section for photodissociation in square centimeters and I is the mean intensity of the radiation in photons per square centimeters per second

per angstrom as a function of wavelength λ in angstrom (Figure 4.6). For the indirect processes of predissociation and spontaneous radiative dissociation, the rate of dissociation by absorption into a specific level of a bound upper state u from lower level ℓ is

$$k_{\mathrm{pd}}^{\mathrm{line}} = \frac{\pi e^2}{mc^2} \lambda_{u\ell}^2 f_{u\ell} \eta_u x_\ell I(\lambda_{u\ell}) \ \mathrm{s}^{-1} \tag{4.11}$$

where $f_{u\ell}$ is the oscillator strength, η_u is the dissociation efficiency of the upper level (between 0 and 1), and x_ℓ is the fractional population in level ℓ.

The determination of the cross sections and oscillator strengths from theory and experiments has been discussed in Section 4.3. Cross section databases, including references to the original data, are available from Ref. [2] at www.strw.leidenuniv.nl/~ewine/photo, and from Ref. [49] at amop.space.swri.edu for cometary species. For more complex species also of atmospheric interest, a large compilation is available through the MPI-Mainz UV–vis spectral atlas at www.atmosphere.mpg.de/enid/2295 and www.science-softcon.de/spectra.

Photodissociation rates as functions of depth into a cloud using the standard ISRF [32] have been presented for a variety of molecules [1, 45], and most recently by van Dishoeck *et al.* [2]. The latter paper and associated Web site also summarize rates in cooler radiation fields such as appropriate for late-type stars. The depth dependence due to continuum extinction can be represented by a simple exponential function, with exponents that vary with grain scattering properties and depend parametrically on cloud thickness. A list of cosmic-ray-induced rates for use in dense cloud models has been given by Gredel *et al.* [42].

4.6
Photodissociation of CO and its Isotopologs

CO is the most commonly observed molecule in interstellar space and used as a tracer of molecular gas throughout the universe, from local diffuse clouds to dense gas at the highest redshifts. Additional impetus for a good understanding of its photodissociation processes comes from recent interpretations of oxygen isotope fractionation in primitive meteorites, which are thought to originate from isotope-selective photodissociation of CO in the upper layers of the disk out of which our solar system formed [50]. To model these processes, information on the electronic structure of all the CO isotopologs, including those with ^{17}O, is needed.

CO is an extremely stable molecule with a dissociation energy of 11.09 eV, corresponding to a threshold of 1118 Å. It took until the late 1980s to establish that no continuum absorption occurs longward of 912 Å, but that CO photodissociation is dominated by line absorptions, most of which are strongly predissociated [51, 52]. These early laboratory data were used to build a detailed model of the CO photodissociation rate in an interstellar cloud [53, 54]. The depth dependence of the CO photodissociation is affected not only by self-shielding but also by mutual shielding by H and H_2 because these species absorb in the same wavelength region.

^{12}CO, in turn, can shield the less abundant ^{13}CO, C^{18}O, and C^{17}O species, with the amount of shielding depending on the wavelength shifts in the absorption spectrum. Thus, a complete numerical simulation of the entire spectrum of ^{12}CO, its isotopologs, H_2, and H is required to correctly compute the attenuation at each depth into a cloud [55, 56].

In the 20 years since these first models, a steady stream of new laboratory data has become available on this key process. In the late 1980s, many of the bands recorded in the laboratory were for ^{12}CO only and had no electronic or vibrational designations, so that simulation of the isotopolog spectra involved much guesswork. In particular, the magnitude of the isotopolog shifts depends sensitively on whether v' in the upper state is zero or not. Moreover, predissociation rates were generally not known and were simply assumed to be unity. High-resolution spectra for many important bands of ^{12}CO, ^{13}CO, C^{18}O, and ^{13}C^{18}O were subsequently measured with synchrotron light sources [52, 57–59]. The fact that the experimental oscillator strengths have now been reconciled with values inferred from astronomical measurements leaves little doubt about their accuracy [60]. Ultrahigh-resolution spectra of selected states have been obtained with vacuum-ultraviolet (VUV) lasers [20]. These exquisite data not only provide positions down to 0.003 cm^{-1} accuracy but also measure directly the line widths and thus the predissociation probabilities. This is especially important for the $C\,^1\Sigma^+$ and $E\,^1\Pi$ states responsible for most of the isotope-selective effects [61–64].

Visser *et al.* [65] used the recent laboratory data to develop a new model for the CO isotope-selective photodissociation including the ^{17}O isotopologs, and applied it to interstellar clouds and disks around young stars. They also computed shielding functions for a much larger range of CO excitation temperatures and Doppler broadenings. Although the overall rate has changed by only 30%, from 2.0 to 2.6×10^{-10} s^{-1} for the standard ISRF [32], the modeled depth dependence differs significantly from earlier work. In particular, the isotope-selective effects are diminished by a factor of 3 or more at temperatures above 100 K. Note, however, that even this new study [65] still had to make many assumptions on line positions, oscillator strengths, and predissociation rates for the minor isotopologs, since high-resolution spectra of these minor species have not yet been measured or published. Unexpected differences of up to an order of magnitude have been found between oscillator strengths of ^{12}CO and ^{13}CO for the same bands, complicating extrapolations from the main isotopologs. These differences likely arise from mixing between various electronic states that depend sensitively on the relative location of the energy levels and may thus differ for a specific ro-vibronic v', J' level of a particular isotopolog, as found for the case of N_2 [66].

Another set of experiments on the CO isotopolog photodissociation has been carried out using the Berkeley synchrotron source [67]. In contrast to the Paris and Amsterdam results, these data are at comparatively low spectral resolution and were analyzed much more indirectly by following a set of subsequently occurring chemical reactions. The data were interpreted to imply different predissociation probabilities for individual levels of isotopologs caused by near-resonance

accidental predissociation processes. In this interpretation, the isotope-selective effects found in meteorites would not require self- or mutual shielding processes. While accidental predissociation is not excluded, these experiments and their conclusions have been challenged on many grounds and are not supported by the higher resolution data cited above [65, 68–70]. This episode demonstrates that there is no substitute for high-quality molecular physics data in which individual unsaturated lines are recorded, in order to draw astrophysical conclusions.

Another very stable molecule for which the photodissociation occurs primarily by line absorptions is N_2. Thanks to decades of laboratory experiments, the line oscillator strengths and predissociation probabilities of the excited ro-vibrational states are now known with very high accuracy. The N_2 and $^{14}N^{15}N$ data have recently been summarized and applied to interstellar chemistry [71, 72].

4.7 Photostability of PAHs

PAHs constitute a class of large molecules that are very stable against photodissociation in the general interstellar medium, explaining their ubiquitous presence in galaxies [73]. However, in clouds exposed to very intense radiation, such as the inner regions of protoplanetary disks and the immediate environments of active galactic nuclei, the smaller PAHs can be destroyed within the lifetime of the source. As discussed in Section 4.2.2, the dissociation process of a large molecule involves a multistep process, in which the molecule first absorbs a photon and is promoted to an excited electronic state, then decays nonradiatively to high vibrational levels of the ground state, and finally finds a path to dissociation. The rate of this process thus depends not only on the initial absorption rate but also on the competition with other processes during these steps. In the first step, the absorption of the photon can also lead to emission of an electron through ionization or photodetachment with probability $\eta_{\rm em}$. In the final step, there is competition between dissociation and cooling by infrared emission. The PAH photodissociation rate thus becomes [74–78]

$$k_{\rm pd} = \int (1 - \eta_{\rm em}) \eta_{\rm diss} \sigma_{\rm abs} I_\lambda d\lambda$$

where $\eta_{\rm diss}$ is the yield of a single dissociation process given by

$$\eta_{\rm diss} = \frac{\sum_X k_{{\rm diss},X}}{(k_{\rm diss} + k_{\rm IR})}.$$

Here, $k_{{\rm diss},X}$ is the rate for a particular loss channel X (e.g., H removal), $k_{\rm diss}$ is the sum over all such channels, and $k_{\rm IR}$ is the infrared emission rate. Possible loss channels are H, H_2, C, C_2, and C_3 [74], with the rates determined by the RRKM quasi-equilibrium theory according to

$$k_{\rm diss,} X = A_X \frac{\rho(E_{\rm int} - E_{0,X})}{\rho(E_{\rm int})}$$

where A_X is the pre-exponential Arrhenius factor for channel X and $\rho(E)$ is the density of vibrational states at energy E. Dissociation occurs only if the internal energy of the molecule $E_{\rm int}$ exceeds the critical energy E_0 for a particular loss channel. Values for $E_{0,X}$ are summarized by Visser *et al.* [78]. The above formulation needs to be modified for clouds exposed to very intense radiation fields ($G_0 > 10^4$) when multiphoton events start to become significant, that is, the PAH molecule absorbs another UV photon before it has cooled down completely. This can significantly increase the dissociation rate.

To compute the dissociation rates, values of $\sigma_{\rm abs}$ as a function of wavelength are essential. The data used in astrophysical models largely come from models developed by Li and Draine [79], based on experiments by Joblin *et al.* [80]. There is also limited experimental information on the loss channels, as summarized by Le Page *et al.* [76]. For example, Jochims *et al.* [81, 82] have measured the photostability of small PAHs of various sizes and shapes against H loss. Figure 4.8 compares the H-loss channel quantitatively with that of other loss channels and illustrates the competition with ionization.

In a novel experiment, called *PIRENEA*, the spectroscopy and photodissociation of PAHs into various fragments could be studied [83–85]. Specifically, gas-phase PAH cations are produced by laser irradiation of a solid target and then guided into an ion cyclotron resonance cell, where they are trapped in a combined magnetic and electric field. The stored ions are irradiated by a xenon lamp (2000–8000 Å), and the products are analyzed by Fourier-transform mass spectrometry. The ions of interest can be selected and isolated by selective ejection of other species. Initial results show that irradiation leads predominantly to atomic hydrogen atom loss,

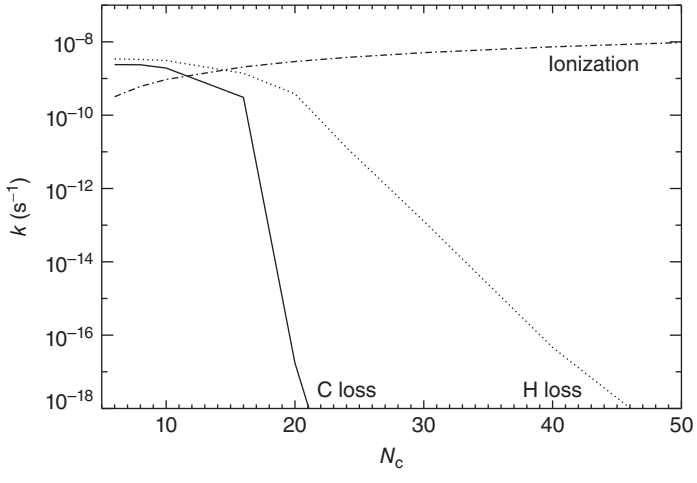

Figure 4.8 Photodissociation and photoionization rates of PAHs as functions of number of carbon atoms for the general interstellar radiation field. Solid: loss of C; dotted: loss of H; dash-dotted: ionization. Note the stability of the larger PAHs against dissociation. (Figure made using data from Ref. [78] following Ref. [75].)

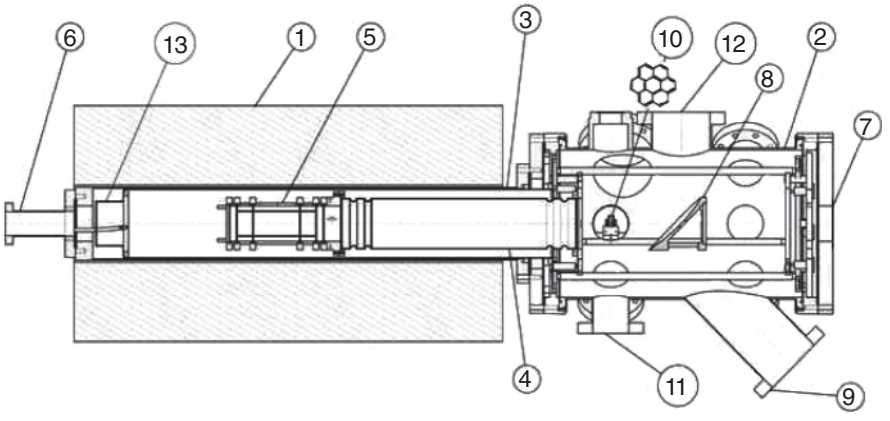

-1 Superconducting magnet (5 T)
-2 Ultra vacuum vessel
-3 External cryogenic shield
-4 Inner cryogenic shield
-5 Ion trap (ICR cell)
-6 Chemical interface and OPO laser entrance window
-7 Secondary laser entrance window
-8 Elliptical mirror
-9 Turbomolecular pump
-10 Target, laser ablation at 266 nm (perpendicular to this plane)
-11 Electronic interface
-12 Lamp irradiation interface
-13 Baffle

Figure 4.9 Overview of the PIRENEA experiment to study the photostability and fragmentation pattern of PAHs exposed to UV radiation [83].

consistent with the work of Jochims *et al.* [81], but loss of C_2H_2 and perhaps even C_4H_2 is also seen from dehydrogenated PAHs [86] (Figure 4.9).

4.8 Summary

This chapter has summarized our understanding of basic photodissociation processes and the theoretical and experimental approaches to determine cross sections, product branching ratios, and rates for astrophysically relevant species. The demand for accurate photorates is likely to increase in the coming years as new infrared and submillimeter facilities widen the study of molecules in the surfaces of protoplanetary disks and exoplanetary atmospheres. Critical evaluation of the photodissociation data for these different environments are needed, since rates or cross sections determined for interstellar clouds cannot be simply transposed to other regions.

Acknowledgments

The authors are grateful to Marc van Hemert and Geert-Jan Kroes for many fruitful collaborations on theoretical studies of photodissociation processes, and to Roland Gredel, Christine Joblin, and Dave Parker for providing figures. Support

from a Spinoza grant and grant 648.000.002 by the Netherlands Organization of Scientific Research (NWO) and from the Netherlands Research School for Astronomy (NOVA) is gratefully acknowledged.

References

1. van Dishoeck, E.F. (1988) *Photodissociation and Photoionization Processes*, in Rate Coefficients in Astrochemistry, eds. T.J. Millar & D.A. Williams, Kluwer Academic publisher, Dordrecht, Vol. 146, Springer, Berlin, pp. 49–72.
2. van Dishoeck, E.F., Jonkheid, B., and van Hemert, M.C. (2006) *Faraday Discuss.*, **133**, 231.
3. Kirby, K.P. and Van Dishoeck, E.F. (1989) *Adv. At. Mol. Phys.*, **25**, 437–476.
4. Schinke, R. (1993) *Photodissociation Dynamics*, Cambridge University Press, Cambridge.
5. van Dishoeck, E.F. and Dalgarno, A. (1984) *Astrophys. J.*, **277**, 576.
6. Chowdary, P.D. and Gruebele, M. (2008) *Phys. Rev. Lett.*, **101**, 250603.
7. Ashfold, M.N.R., King, G.A., Murdock, D. *et al.* (2010) *Phys. Chem. Chem. Phys.*, **12**, 1218–1238.
8. te Velde, G., Bickelhaupt, F.M., van Gisbergen, S.J.A. *et al.* (2001) *J. Comput. Chem.*, **22**, 931–967, *www.scm.com*.
9. Shao, Y., Molnar, L.F., Jung, Y. *et al.* (2006) *Phys. Chem. Chem. Phys.*, **8**, 3172.
10. Buenker, R.J. and Peyerimhoff, S.D. (1974) *Theor. Chim. Acta*, **39**, 217.
11. Buenker, R.J., Peyerimhoff, S.D., and Butscher, W. (1978) *Mol. Phys.*, **35**, 771–791.
12. Werner, H.-J. *et al.* (2010) *MOLPRO, version 2010.1, 1:0*, *www.molpro.net.*
13. Kroes, G.J., van Dishoeck, E.F., Beärda, R., and van Hemert, M.C. (1993) *J. Chem. Phys.*, **99**, 228–236.
14. Beärda, R.A., van Hemert, M.C., and van Dishoeck, E.F. (1995) *J. Chem. Phys.*, **102**, 8930–8941.
15. van Hemert, M.C. and van Dishoeck, E.F. (2008) *Chem. Phys.*, **343**, 292–302.
16. Fillion, J.H., van Harrevelt, R., Ruiz, J. *et al.* (2001) *J. Phys. Chem. A*, **105** (51), 11414–11424.
17. Lee, L.C. (1984) *Astrophys. J.*, **282**, 172–177.
18. Hudson, R.D. (1971) *Rev. Geophys. Space Phys.*, **9**, 305–406.
19. Okabe, H. (1978) *Photochemistry of Small Molecules*, John Wiley & Sons, Inc., New York.
20. Ubachs, W., Eikema, K.S.E., and Levelt, P.F. (1994) *Astrophys. J.*, **728**, L55–L58.
21. Pilling, S., Neves, R., Santos, A.C.F., and Boechat-Roberty, H.M. (2007) *Astron. Astrophys.*, **464**, 393–398.
22. Chandler, D.W. and Houston, P.L. (1987) *J. Chem. Phys.*, **87**, 1445–1447.
23. Eppink, A.T.J.B. and Parker, D.H. (1997) *Rev. Sci. Instrum.*, **68** (9), 3477.
24. Ashfold, M.N.R., Nahler, N.H., Orr-Ewing, A.J. *et al.* (2006) *Phys. Chem. Chem. Phys. (Incorporating Faraday Trans.)*, **8**, 26.
25. Chabot, M., Tuna, T., Béroff, K. *et al.* (2010) *Astronomy & Astrophysics*, **524**, A39.
26. Störzer, H. and Hollenbach, D. (1998) *The Astrophysical Journal, Letters*, **502**, L71.
27. Acke, B. and van den Ancker, M.E. (2006) *Astronomy & Astrophysics*, **449**, 267–279.
28. Öberg, K.I., Garrod, R.T., van Dishoeck, E.F., and Linnartz, H. (2009) *Astronomy & Astrophysics*, **504**, 891–913.
29. Black, J.H. (1994) *ASP Conf. Ser.*, **58**, 355.
30. van Dishoeck, E.F. (1994) *ASP Conf. Ser.*, **59**, 276–319.
31. Habing, H.J. (1968) *Bulletin of the Astronomical Institutes of the Netherlands*, **19**, 421.
32. Draine, B.T. (1978) *The Astrophysical Journal, Supplement*, **36**, 595–619.

33. Parravano, A., Hollenbach, D.J., and McKee, C.F. (2003) *The Astrophysical Journal*, **584**, 797–817.
34. Henry, R.C., Anderson, R.C., and Fastie, W.G. (1980) *Astrophys. J.*, **239**, 859–866.
35. Kamp, I. and van Zadelhoff, G.-J. (2001) *Astronomy & Astrophysics*, **373**, 641–656.
36. Bergin, E.A., Kaufman, M.J., Melnick, G.J., Snell, R.L., and Howe, J.E. (2003) *The Astrophysical Journal*, **582**, 830–845.
37. van Dishoeck, E.F. and Black, J.H. (1982) *The Astrophysical Journal*, **258**, 533–547.
38. Hauschildt, P.H., Allard, F., Ferguson, J., Baron, E., and Alexander, D.R. (1999) *The Astrophysical Journal*, **525**, 871–880.
39. Hollenbach, D. and McKee, C.F. (1979) *The Astrophysical Journal, Supplement*, **41**, 555–592.
40. Neufeld, D.A. and Dalgarno, A. (1989) *The Astrophysical Journal*, **340**, 869–893.
41. Gredel, R. (1987) *Fluorescent and collisional excitation in diatomic molecules*. Dissertation, Naturwiss.-Math. Gesamtfak., Ruprecht-Karls-University, Heidelberg.
42. Gredel, R., Lepp, S., Dalgarno, A., and Herbst, E. (1989) *The Astrophysical Journal*, **347**, 289–293.
43. Cardelli, J.A. and Savage, B.D. (1988) *The Astrophysical Journal*, **325**, 864–879.
44. van Dishoeck, E.F. and Black, J.H. (1989) *The Astrophysical Journal*, **340**, 273–297.
45. Roberge, W.G., Jones, D., Lepp, S., and Dalgarno, A. (1991) *The Astrophysical Journal, Supplement*, **77**, 287–297.
46. Vasyunin, A.I., Wiebe, D.S., Birnstiel, T. *et al.* (2011) *The Astrophysical Journal*, **727**, 76.
47. Dalgarno, A. and Stephens, T.L. (1970) *The Astrophysical Journal, Letters*, **160**, L107.
48. Werner, M.W. (1970) *Astrophysics Letters*, **6**, 81.
49. Huebner, W.F., Keady, J.J., and Lyon, S.P. (1992) *Astrophys. Space Sci.*, **195**, 1-294.
50. Lyons, J.R. and Young, E.D. (2005) *Nature*, **435**, 317–320.
51. Letzelter, C., Eidelsberg, M., Rostas, F., Breton, J., and Thieblemont, B. (1987) *Chem. Phys.*, **114**, 273–288.
52. Stark, G., Yoshino, K., Smith, P.L., Ito, K., and Parkinson, W.H. (1991) *The Astrophysical Journal*, **369**, 574–580.
53. Viala, Y.P., Letzelter, C., Eidelsberg, M., and Rostas, F. (1988) *Astronomy & Astrophysics*, **193**, 265–272.
54. van Dishoeck, E.F. and Black, J.H. (1988) *The Astrophysical Journal*, **334**, 771–802.
55. Lee, H.-H., Herbst, E., Pineau des Forêts, G., Roueff, E., and Le Bourlot, J. (1996) *Astronomy & Astrophysics*, **311**, 690–707.
56. Le Petit, F., Nehmé, C., Le Bourlot, J., and Roueff, E. (2006) *The Astrophysical Journal, Supplement*, **164**, 506–529.
57. Eidelsberg, M., Benayoun, J.J., Viala, Y. *et al.* (1992) *Astron. Astrophys.*, **265**, 839–842.
58. Eidelsberg, M., Launay, F., Ito, K. *et al.* (2004) *J. Chem. Phys.*, **121**, 292–308.
59. Eidelsberg, M., Sheffer, Y., Federman, S.R. *et al.* (2006) *The Astrophysical Journal*, **647**, 1543–1548.
60. Sheffer, Y., Federman, S.R., and Andersson, B.-G. (2003) *The Astrophysical Journal, Letters*, **597**, L29–L32.
61. Cacciani, P., Hogervorst, W., and Ubachs, W. (1995) *J. Chem. Phys.*, **102**, 8308–8320.
62. Cacciani, P., Brandi, F., Velchev, I. *et al.* (2001) *Eur. Phys. J. D*, **15**, 47–56.
63. Ubachs, W., Velchev, I., and Cacciani, P. (2000) *J. Chem. Phys.*, **113** (2), 547–560.
64. Cacciani, P. and Ubachs, W. (2004) *J. Mol. Spectrosc.*, **225**, 62–65.
65. Visser, R., van Dishoeck, E.F., Doty, S.D., and Dullemond, C.P. (2009) *Astronomy & Astrophysics*, **495**, 881–897.
66. Stark, G., Lewis, B.R., Heays, A.N. *et al.* (2008) *J. Chem. Phys.*, **128** (11), 114302.
67. Chakraborty, S., Ahmed, M., Jackson, T.L., and Thiemens, M.H. (2008) *Science*, **321**, 1328–1331.
68. Federman, S.R. and Young, E.D. (2009) *Science*, **324**, 1516.

69. Lyons, J.R., Bergin, E.A., Ciesla, F.J. *et al.* (2009) *Geochim. Cosmochim. Acta*, **73**, 4998–5017.
70. Yin, Q.-Z., Shi, X., Chang, C., and Ng, C.-Y. (2009) *Science*, **324** (5934), 1516.
71. Li, X., Heays, A.N., Visser, R. *et al.* (2013) *Astronomy & Astrophysics*, **555**, A14.
72. Heays, A.N., Visser, R., Gredel, R. *et al.* (2014) *Astronomy & Astrophysics*, **562**, A61.
73. Tielens, A.G.G.M. (2008) *Astronomy & Astrophysics*, **46**, 289–337.
74. Léger, A., D'Hendecourt, L., Boissel, P., and Désert, F.X. (1989) *Astronomy & Astrophysics*, **213**, 351–359.
75. Allain, T., Leach, S., and Sedlmayr, E. (1996) *Astronomy & Astrophysics*, **305**, 602.
76. Le Page, V., Snow, T.P., and Bierbaum, V.M. (2001) *The Astrophysical Journal, Supplement*, **132**, 233–251.
77. Habart, E., Natta, A., and Krügel, E. (2004) *Astronomy & Astrophysics*, **427**, 179–192.
78. Visser, R., Geers, V.C., Dullemond, C.P. *et al.* (2007) *Astronomy & Astrophysics*, **466**, 229–241.
79. Li, A. and Draine, B.T. (2001) *The Astrophysical Journal*, **554**, 778–802.
80. Joblin, C., Léger, A., and Martin, P. (1992) *The Astrophysical Journal, Letters*, **393**, L79–L82.
81. Jochims, H.W., Ruhl, E., Baumgärtel, H., Tobita, S., and Leach, S. (1994) *The Astrophysical Journal*, **420**, 307–317.
82. Jochims, H.W., Baumgärtel, H., and Leach, S. (1999) *The Astrophysical Journal*, **512**, 500–510.
83. Joblin, C., Pech, C., Armengaud, M., Frabel, P., and Boissel, P. (2002) *EAS Publications Series*, Vol. 4 (eds M. Giard, J.P. Bernard, A. Klotz, and I. Ristorcelli), Cambridge University Press pp. 73–77.
84. Joblin, C. and Tielens, A.G.G.M. (eds) (2011) *PAHs and the Universe: A Symposium to Celebrate the 25th Anniversary of the PAH Hypothesis*, EAS Publications Series, Cambridge University Press, Vol. 46.
85. Useli-Bacchitta, F., Bonnamy, A., Mulas, G. *et al.* (2010) *Chem. Phys.*, **371**, 16–23.
86. Useli Bacchitta, F. and Joblin, C. (2007) *Molecules in Space and Laboratory* S. Diana, Paris Observatory.

5
Surface Science

Liv Hornekær

Our insight into the influence of surface reactions on interstellar chemistry has been increasing rapidly over the last decades, as a result of increased computational and observational power and because of an increased number of dedicated laboratory astrophysical surface science experiments. It is now generally accepted that surface reactions are needed to understand the formation of a number of observed interstellar molecules, most notably the most abundant molecule in the interstellar medium, H_2, but also other important molecules such as water, carbon dioxide, and methanol [1]. Furthermore, surface or solid-state reactions are believed to be responsible for the formation of the observed more complex and biologically relevant molecules, such as the simple sugar glycolaldehyde [2]. Hence, an understanding of surface reaction under interstellar conditions is integral to understanding interstellar chemistry.

In this chapter, an introduction to surface astrochemistry is given, and examples of recent advances in our understanding of molecular hydrogen formation on carbonaceous surfaces, the influence of ice morphology on surface chemistry, and the formation of complex molecules on and in solids are presented. Furthermore, a description of the ongoing efforts to implement surface reactions in astrochemical network models is provided.

5.1
Introduction

The notion that surface reactions play a role in interstellar chemistry is by no means new. Even before molecular hydrogen was observed in interstellar clouds, van de Hulst [3] hypothesized its formation on interstellar dust grain surfaces. Gould and Salpeter [4] developed a model aimed at determining the equilibrium ratio of molecular to atomic hydrogen. They assumed that molecular hydrogen forms on dust grain surfaces from weakly bound physisorbed (van der Waals-bonded) atomic hydrogen via association and is destroyed via dissociation by UV radiation. Hollenbach and Salpeter [5] further refined the model for

Laboratory Astrochemistry: From Molecules through Nanoparticles to Grains, First Edition.
Edited by Stephan Schlemmer, Thomas Giesen, Harald Mutschke and Cornelia Jäger.

H_2 formation by including surface irregularities or defects implemented as a distribution of H-binding sites with different binding energy. They broke the H_2 formation process into two steps: (i) A hydrogen atom in the gas phase impinges on the dust grain surface and adsorbs on the surface with a probability S, called the *sticking coefficient*; (ii) the adsorbed H atom diffuses on the surfaces during a time interval determined by the (possibly site-specific) binding energy E_b of the atom to the surface and either meets a reaction partner and reacts within this time interval or desorbs (evaporates) back into the gas phase. Based on the model, they concluded that the molecular hydrogen formation probability for an atom hitting a dust grain should be within a factor of 3 of unity [5]. The first observations of molecular hydrogen in interstellar clouds [6] allowed Jura [7] to derive rates for molecular hydrogen formation in a number of diffuse clouds. He concluded that a uniform rate of $R \sim 3 \times 10^{-17} \mathrm{cm}^3\,\mathrm{s}^{-1}$ would be consistent with the observations [8].

The rationale behind this finding is that molecular hydrogen is continuously destroyed by UV radiation and cosmic rays under diffuse cloud conditions. Hence, to maintain the observed abundances of molecular hydrogen in these environments, a mechanism for continuous formation of H_2 from H atoms must exist. No sufficiently efficient gas-phase routes exist under present interstellar conditions, since H_2 formation via two-body collisions between H atoms is prohibited by energy and momentum conservation – H_2 is a homonuclear molecule and therefore has no dipole-allowed transitions which would otherwise have allowed for fast stabilization of the formed molecule by emission of radiation. Some H_2 is formed by gas-phase reactions involving the negative H ion, but this happens at a rate that is significantly smaller than the required rate derived by Jura [1]. If surface reactions are the only alternative H_2 formation pathway, Jura's derived rate implies that the surface formation of H_2 must be extremely efficient and that, once an H atom hits a grain surface, it must have almost unit probability of ending up as H_2. This agrees with the predictions of Hollenbach and Salpeter [5].

The potential for forming not only molecular hydrogen but also other molecular species on dust grain surfaces has likewise been discussed for many years [9]. In particular, the observed thickness of water ice layers on interstellar dust grain surfaces cannot be accounted for by condensation of water molecules from the gas phase. Hence, *in situ* mechanisms must exist for water formation from H and O atoms on the surface (Section 5.3). Efficient gas-phase routes for methanol formation were thought to exist, but recent storage ring experiments have disproved this [10]. Hence, methanol is now also thought to be formed on grain surfaces. Furthermore, because of the larger local concentration of reactive species on the dust grain surfaces, compared to in the gas phase, it is speculated that larger biologically relevant molecules, formed by numerous addition reactions, must also be formed on dust grain surfaces [2, 11].

In 1997, in a set of pioneering experiments, Vidali and coworkers [12] studied the formation of HD on an amorphous olivine surface under interstellar conditions. These experiments were the first attempt to realize the surface reactions leading to molecular hydrogen formation under interstellar conditions on

controlled surfaces, analogous to interstellar dust grain surfaces, in the laboratory. Their results showed that molecular hydrogen formation from atomic hydrogen impinging on a silicate surfaces is efficient for temperatures below 10 K. Since then, many new experimental setups dedicated to the study of astrophysically relevant surface reactions have appeared. Results of this intensified experimental effort are presented in the "Hot Topics Sections" below. Increased knowledge has revealed an astonishing complexity in the variation and detail of the surface reactions that play a role on the many different interstellar dust grain surface analogs under the wide range of physical conditions, which are of interstellar relevance.

5.1.1 Surface Reactions under Interstellar Conditions

The goal of astrophysical surface science is to study surface reactions and processes on astrophysically relevant surfaces under astrophysically relevant conditions. However, what are interstellar or astrophysically relevant surfaces and conditions?

Numerous different models have been proposed for the composition and size distribution of interstellar dust grains but some consensus does exist. It is generally agreed that the main dust components are silicates and carbonaceous dust grains and that, in cold, dense cloud environments, these grains will be covered by icy mantles consisting of H_2O, CO, CO_2, CH_3OH, and other atomic and molecular species. Furthermore, the models agree that the surface area of interstellar dust grains is dominated by small grains with diameters below 100 nm [1]. Polycyclic aromatic hydrocarbons are often viewed as the transition species between small dust grains and large molecules.

The chemical structure of interstellar dust grains is to some extent fixed by infrared (IR) observations of molecular vibrational transitions. These show that silicate surfaces are generally amorphous [1] and that icy mantles contain mainly water, but also various other species sometimes intermixed and other times in segregated layers [13]. Furthermore, they show the existence of aromatic C–H stretch and bend vibrations characteristic of polycyclic aromatic hydrocarbon structures. C–H stretch and bend vibrations characteristic of aliphatic chain-like carbon structures are also observed [1, 14, 15].

Little is known about the morphology – compactness or porosity – of interstellar dust grains. Dust samples from meteorites show the existence of both compact grains (e.g., graphitic onion-like particles) and amorphous grains [14]. Growth of carbonaceous grains by laser ablation and flame experiments show the formation of both porous and more compact structures depending on growth conditions [14, 15]. The question of the morphology of ice layers is just as complex. Water ice layers are known to be porous if formed by deposition of water molecules at very low fluxes, off-normal incidence, and low temperatures [16]. However, under interstellar conditions, water ice layers will be partly composed of water molecules formed *in situ* on the surface. Recent experiments indicate that this will lead to

decreased porosity of the resulting water ice [17]. Furthermore, subsequent processing of the ice films will take place by UV radiation, cosmic rays, and surface reactions. Experiments on water ice films show that these processes lead to compaction of the porous structures (see Section 5.3). The porosity of real interstellar ice layers will be further complicated by the mixing of various species with different condensation temperature and mobility on the surface (see Section 5.3).

Surface reactions are expected to play an important role under a wide range of interstellar conditions. These conditions range from dense cloud conditions where dust grains are predominantly ice covered and have surface temperatures of 10 – 15 K and where gas temperatures are 10 – 30 K and UV radiation levels are low; over diffuse cloud conditions with mainly bare grain surfaces at temperatures of 10 – 30 K and gas temperatures of 30 – 100 K and intermediate UV radiation fluxes; to hostile regions like photodissociation regions (PDRs) with grain surface temperatures of small dust grains reaching as high as 50 – 100 K due to stochastic heating by absorption of individual UV photons and gas temperatures of several hundred or even a thousand kelvin and high UV radiation fluxes [1, 18]; and to post-shock gasses with an even wider range of dust grain temperatures and comparably high gas temperatures [19]. Hence, conditions of interstellar relevance cover a wide range of surface and gas temperatures, UV fluxes, and surface conditions. However, in all of these environments, molecular hydrogen formation is expected to take place on the surface of dust grains. Observations even indicate that under hostile conditions, like those found in PDRs, H_2 formation rates should be even higher than under diffuse and dense cloud conditions [20, 21]. Hence, investigations of H_2 formation under interstellar conditions should not uncover one mechanism for H_2 formation, but rather a whole plethora of mechanisms the combination of which will result in efficient H_2 formation on surfaces of very different chemical and morphological character under the very different physical and chemical conditions found in the different interstellar environments.

How will atoms and molecules interact with and on astrophysically relevant surfaces under the wide range of astrophysically relevant conditions? As done in the early models, the formation of molecular hydrogen on grain surfaces can be broken down into several steps. Independent of the exact mechanism for H_2 formation, the first step is the sticking of one H atom on the surface. The H atom will then be adsorbed on the surface in either a weak physisorption state, where binding is provided by van der Waals forces, or in a strong chemisorption state, where real chemical binding occurs. On water ice surfaces, physisorption is generally observed, whereas on carbonaceous surfaces and on silicates both physisorption and chemisorption states are present. At the low surface temperatures encountered in dense and diffuse interstellar clouds, only physisorbed atoms and molecules will be mobile on the surface. In this case, the atoms and/or molecules can diffuse over the surface, meet each other, and react to form a molecule which will then either immediately desorb as a result of the energy release in the reaction or will be retained on the surface. Such a reaction pathway is referred to as a *Langmuir – Hinshelwood mechanism*. The formation of molecular hydrogen on water ice surfaces is a good example of such a reaction. Reactions

with chemisorbed atoms can also occur at low temperatures, either via reactions with mobile physisorbed species, or via different reaction mechanisms, namely by Eley–Rideal abstraction or hot atom reactions. Eley–Rideal abstraction refers to the situation where an incoming atom/molecule from the gas phase reacts with an atom or molecule on the surface and where the reaction product is then immediately released into the gas phase. Hot atom reactions refer to the case where an incoming atom adsorbs into a bound state on the surface but does not immediately thermalize to the surface. As a result, the atom has an initial increased mobility because of excess energy either from higher temperatures in the gas phase or from the energy released in the adsorption. This initial increased mobility will allow the atom to scan the surface and potentially react with other atoms or molecules adsorbed on the surface before thermalizing. Since the hot atom adsorption and diffusion takes place on a very short timescale, it is experimentally very challenging to distinguish between Eley–Rideal abstraction and hot atom reactions. Hence, in this chapter, these mechanisms will be treated as one. Eley–Rideal and hot atom mechanisms are expected to be the dominant pathways for H_2 formation on bare carbonaceous grain surfaces at higher temperatures and will coexist with Langmuir–Hinshelwood reactions at low temperatures. Once the surface temperatures increase above 10 K on silicate surfaces and 15 K on water ice and carbonaceous surfaces, the lifetime of atoms in physisorbed states becomes extremely short, making desorption into the gas phase rather than reaction the likely outcome. Chemisorbed species, on the other hand, will typically be stable up to temperatures of several hundred kelvin. However, these chemisorbed species will typically be so stable that diffusion will also be suppressed under the conditions found in dense and diffuse clouds and even PDRs. Hence, reactions from chemisorbed sites will generally occur via Eley–Rideal abstraction and hot atom reactions. On ice-covered grain surfaces, further reaction pathways in the ices are available. See Section 5.4 for a discussion of such "in-ice" reactions.

5.1.2 Experimental Methods

A wide range of different surface science techniques have been used to study surface reactions under interstellar conditions. These can be separated into methods aimed at detecting and characterizing atoms or molecules desorbing from the surfaces ("off-surface" methods), and methods aimed at detecting and characterizing atoms and molecules while these are adsorbed on the surface ("on-surface" methods). The methods in the last category can be further divided into local and global techniques. Global methods give average characteristics over a large surface area, while local techniques provide area-specific data on the nanometer or even subnanometer scale.

Examples of local techniques are scanning probe microscopy techniques such as scanning tunneling microscopy (STM) and atomic force microscopy (AFM), where sharp tips are brought very close to the surface and sample local properties.

In the case of STM, three-dimensional maps of the local electronic density of states (LDOS) are measured by sampling the position-dependent tunneling current between the tip and the sample. In the case of AFM, the local (van der Waals and chemical) forces are sampled. Both these techniques are capable of yielding atomic-scale resolution, including, in many cases, submolecular resolution of adsorbates. Hence, they are unique probes of local surface structure and adsorbate structures, but are chemically sensitive only to a limited degree. Detailed theoretical modeling using density functional theory (DFT) methods is generally needed to identify specific chemical species in STM images, and in some cases identification is not possible at all. On some well-defined systems, chemically sensitive data can, however, be obtained by inelastic tunneling spectroscopy (IETS). Hence, STM is often combined with other more chemically sensitive techniques such as temperature-programmed desorption (TPD) or X-ray photoelectron spectroscopy (XPS). Examples of the use of STM in surface astrochemistry is given in Section 5.2.

The global "on-surface" methods can be subdivided into structurally sensitive methods and chemically sensitive methods. The various diffraction techniques, namely X-ray diffraction, X-ray photoelectron diffraction, and low-energy electron diffraction (LEED), give information on the crystal structure of surfaces and surface adsorbates, while spectroscopic methods, such as infrared spectroscopy (IRS, FTIR), reflection–absorption infrared spectroscopy (RAIRS, FT-RAIRS), Raman spectroscopy, electron energy loss spectroscopy (EELS), and XPS, give information on the chemical composition of the upper layers of the sample. Especially, the various IRS techniques have been widely used in surface astrochemistry. These techniques are based on measurements of the frequency-dependent absorption of IR radiation in either thin films on IR-transparent substrates (transmission IRS) or in the surface layers on metal samples (RAIRS). At IR frequencies coinciding with vibrational transitions in the adsorbed molecules or in modes of the frustrated translation or rotation of the adsorbed molecule/atom on the surface, increased absorption is observed. The position and line width of the absorption lines are very much dependent on the local chemical environment, making IRS a very sensitive probe of surface chemistry. IRS techniques appear in all the experimental sections of this chapter.

All the "off-surface" techniques are global techniques and sample the average characteristics of adsorbates desorbing from a larger surface area. These techniques include thermal desorption spectroscopy (TDS), also referred to as temperature-programmed desorption (TPD), various time-of-flight (TOF) techniques, including laser-induced thermal desorption time-of-flight (LITD-TOF), and resonance-enhanced multiphoton ionization (REMPI). TPD methods have been used extensively in surface astrochemistry. In a typical TPD setup, atoms or molecules are deposited onto the sample, which is then placed in front of a quadrupole mass spectrometer (QMS) and heated linearly by either electron bombardment on the backside of the sample or by resistive heating. The QMS signal at the masses of interest is then monitored as a function of sample temperature (and thereby also time). Thermal desorption spectra yields several

types of information: (i) the masses of species desorbing from the surface is measured; (ii) the temperature at which the desorption rate reaches a maximum gives information on the desorption barrier or barriers (if different types of binding sites are populated) for the measured species; (iii) the behavior of the thermal desorption spectra with surface coverage gives information on the type of reaction occurring on the surface in the desorption event (i.e., for molecular desorption, it is in general possible to determine whether the molecules form on the surface in connection with the desorption event or whether they are formed on the surface well in advance of the desorption; (iv) thermal desorption spectra, also yields information on the surface structure (defects, step edges, different binding sites) and the morphology/porosity of the surface. TOF techniques have been used in a surface astrochemistry context mainly to measure the kinetic energy of molecules desorbing from the surface. In LITD-TOF, a temperature jump is induced in the surface by a nanosecond laser pulse. This results in an elevated surface temperature during a time interval of some tens of nanoseconds. If the temperature jump is sufficiently high to cause desorption of adsorbed species in this time window, their kinetic energy can be measured by measuring their TOF from the surface to the mass spectrometer (i.e., the time from the peak temperature in the thermal jump to the detection of the species in the mass spectrometer). The internal state distribution of the desorbing molecules can be measured by REMPI, where multiphoton laser ionization involving resonant excitation to an intermediate state provides state selectivity. REMPI techniques have also been used to detect H atoms desorbing from surfaces.

A more detailed discussion of a wide range of surface science techniques can be found in the book of, for example, Vickerman and Gilmore [22].

5.1.3 Introducing the Hot Topic Sections

Four different hot topics within surface astrochemistry are covered in the following sections.

Section 5.2 gives an overview of the extensive laboratory investigations of molecular hydrogen formation on carbonaceous surfaces ranging from graphite to mixtures of aliphatic or aromatic flame-deposited surfaces. These investigations have resulted in insights into often complex formation mechanisms operating in all these different systems. These investigations are steadily bringing us closer to the goal of achieving atomic-scale understanding of reactions on realistic interstellar grain surface analogs.

The influence of water ice morphology on desorption of surface species and on surface reactions, as well as the influence of surface reactions on the water ice morphology, is the subject of Section 5.3.

Moving beyond molecular hydrogen formation, Section 5.4 gives an overview of the current state of the art in laboratory studies of complex molecule formation on interstellar surface analogs.

To translate the experimental results into knowledge of chemical reactions in the interstellar medium and to relate this to observations astrochemical network, models are needed. An overview of the challenges and current state of the art for implementing grain surface reactions in astrochemical network models is given in Section 5.5.

5.1.4 Outlook

As we build up a larger knowledge base of surface reactions under interstellar conditions, it becomes possible to move closer and closer toward studies on realistic grain surface analogs characterized by complex surface structures exhibiting a wide variety of chemical and morphological structures, without losing the in-depth understanding of the processes occurring on these systems. This is further supported by increased knowledge of surface structure of samples produced under conditions emulating different interstellar environments (6 and 7) and by the advent of new observational facilities that will give increased information on the chemical and physical structure of interstellar dust grains and their coupling to the local gas-phase species. A common challenge for both theory and experiment is the handling of small interstellar dust grains. The challenges that this imposes for network models are discussed in Section 5.5. In all the experiments described in this chapter, macroscopic samples were used. Hence, an obvious avenue for future experiments is to investigate the influence of dust grain size by studying reactions on nanosized dust particles trapped in, for example, ion traps. As shown in Section 5.4, increased experimental effort is aimed at studying the formation of more complex molecules. This effort will continue and hopefully be able to provide information on the possibility of forming also more complex and biologically relevant molecules under interstellar conditions. Finally, to be able to relate the laboratory measurements to interstellar observations, the development of network models capable of handling large amounts of complex surface reactions will be necessary.

5.2 Molecular Hydrogen Formation on Carbonaceous Surfaces

Liv Hornekær and Stephen D. Price

A sizable fraction of interstellar dust grains in diffuse cloud environments and photodissociation regions (PDRs) are expected to have carbonaceous surfaces. Models of these surfaces vary from well-ordered graphite or graphene surfaces, where carbon atoms are arranged in planar sheets of aromatic rings, to amorphous, disordered carbon surfaces characterized by defects, a mixture of carbon atoms in aromatic chemical arrangements (polycyclic aromatic hydrocarbons (PAHs), graphene, graphite flakes, and graphitic onion-like particles), aliphatic chemical arrangements (carbon chains, CH_2, and CH_3 groups), and

possibly also porous morphologies [14, 23]. In this section, we give an overview of the experimental work done on the interaction of atomic hydrogen with these surfaces and the formation of molecular hydrogen on them.

5.2.1 Interaction of Atomic Hydrogen with Carbonaceous Surfaces

The interaction of hydrogen with carbonaceous surfaces involves both physisorption and chemisorption sites, depending on the surface structure, surface temperature, and energy of the incoming H atoms. Scattering experiments on graphite determine the binding energy of physisorbed H atoms to be 39.2 ± 0.5meV [24], while density functional theory (DFT) calculations find a binding energy for chemisorbed H atoms, on the graphite basal plane, of 0.7–0.8 eV [25–27] depending on calculation methods. Calculations also show an adsorption barrier of 0.15–0.2 eV for H atoms to adsorb into this chemisorbed state [25–27]. At defective or amorphous surfaces, binding energies can be even higher and adsorption barriers are typically lower or nonexistent; for example, calculations show that, at step edges on graphite, a single H atom can bind with an energy of 5 eV, while two H atoms can each bind with a coverage-dependent binding energy of $\sim 3.6 - 3.9$ eV [28].

The mobility of physisorbed hydrogen atoms on carbonaceous surfaces is expected to be high. Indeed, calculations show that the barrier to diffusion of physisorbed H atoms on graphite is only 4 meV [29], indicating that physisorbed H atoms move like free particles at all but the very lowest temperatures. For chemisorbed hydrogen, the diffusion barriers are much higher. Calculations show that diffusion of isolated chemisorbed H atoms on graphite has a barrier of 0.9–1.1 eV [30, 31], which is comparable to the desorption barrier. Hence, diffusion is limited for chemisorbed H atoms. For H atoms in hydrogen adsorbate clusters, lower diffusion barriers (typically a few tenths of an electronvolt) into energetically favorable cluster configurations can be found [32].

Chemisorption of H atoms on the graphite basal plane was studied by Hornekær and coworkers using combined scanning tunneling microscopy (STM) experiments and DFT calculations. The experiments were performed under ultrahigh vacuum (UHV) at surface temperatures from 210 to 300 K and H atom temperatures of 2000 K (sufficient to overcome the chemisorption barrier). In Figure 5.1a, an STM image of the graphite (1000) surface after a 1 min D atom dose at a flux of 10^{15} atoms cm^{-2} s^{-1} is displayed. The elongated bright protrusions are ascribed to H atom adsorbate structures on the surface. By comparison with DFT calculations of stable adsorbate structures, and derived simulated STM images, these elongated protrusions are identified as hydrogen dimers. Two different dimers were calculated to have the same binding energy, namely the para and ortho dimers [27] displayed in Figure 5.1(b) and (c). Both these dimer types are observed in experiments, with the para dimer being the most abundant (by a factor of 7) compared to the ortho dimer [27, 32]. The formation mechanism for the hydrogen dimers have

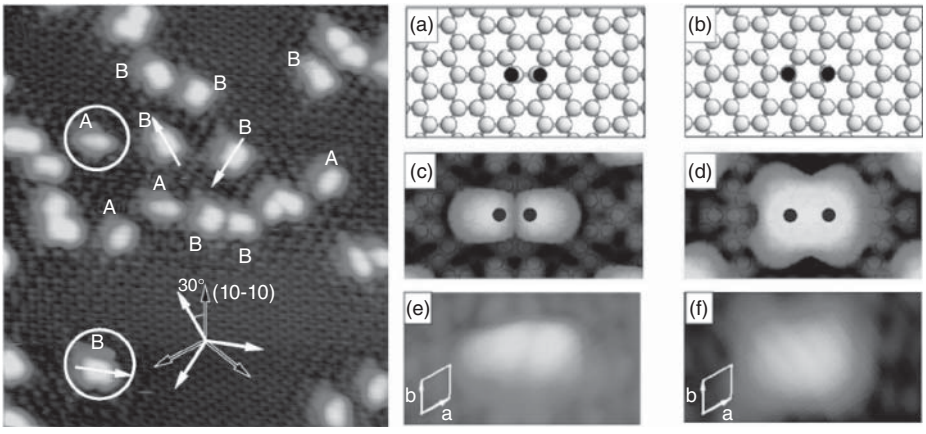

Figure 5.1 (a) STM image (103 Å × 114 Å) of dimer structures of hydrogen atoms on the graphite surface after 1 min deposition at a flux of 10^{15} atoms cm^{-2} s^{-1} on a room-temperature sample. Imaging parameters: V_t = 884 mV, I_t = 160 pA. Examples of dimer type A and B are marked. (b) Calculated structure for a hydrogen atoms adsorbed in an ortho-dimer configuration – one of the two most tightly bound dimer structures of hydrogen atoms on the graphite surface – identified as dimer A. (c) Calculated structure for a hydrogen atoms adsorbed in a para-dimer configuration – the second of the two most tightly bound dimer structures of hydrogen atoms on the graphite surface – identified as dimer B. (d) Simulated STM image of the dimer structure in (b). (e) Simulated STM image of the dimer structure in (c). The position of the hydrogen atoms is marked by black dots. (f) Experimental dimer A structure. (g) Experimental dimer B structure. The carbon unit cell is marked in white. (Reproduced from [27], copyright 2006 © permission from American Physical Society.)

been studied by DFT and kinetic Monte Carlo (KMC) calculations. DFT calculations show that the barrier to adsorption for an H atom into an ortho dimer configuration, alongside an H atom which is already adsorbed, is 0.1 eV, which is lower than the 0.15–0.2 eV barrier to adsorption for an isolated hydrogen monomer. Furthermore, the calculations show that there is no barrier to adsorption into a para dimer configuration [30, 33]. KMC calculations show that, when these reduced barriers are combined with the high initial mobility (hot atom) of incoming H atoms, then the formation of dimers is highly preferred, with the para dimer being the dominant structure [32]. At higher coverage, disordered hydrogen adsorbate clusters are observed [30, 34].

5.2.2
Formation of Molecular Hydrogen on Carbonaceous Surfaces

Depending on the physical conditions and the surface structure, different mechanisms are available for molecular hydrogen formation from reactions between atomic hydrogen on carbonaceous surfaces. At low temperatures, Langmuir–Hinshelwood, hot atom, and Eley–Rideal processes are all expected to play an active role in H_2 formation. At temperatures below 30 K, chemisorbed

H atoms in basal plane sites or defect sites are immobile and very stable. At high coverage, they react directly with gas-phase H atoms via Eley–Rideal abstraction processes, while at lower coverage, processes involving mobile H atoms adsorbed on the surface are expected to dominate. Adsorbed H atoms can be mobile either because they are in weakly bound physisorbed states or because they have not yet thermalized to the surface temperature and therefore have an excess kinetic energy. In the first case, the resulting reactions are Langmuir–Hinshelwood processes, while in the second case they are hot atom processes. Langmuir–Hinshelwood reactions between physisorbed H atoms and between physisorbed and chemisorbed H atoms are expected to be active even at very low temperatures because of the low diffusion barrier for physisorbed H atoms.

Vidali and coworkers [35] studied the formation of HD on an amorphous carbon surface under cold interstellar conditions. The experiments were performed, under UHV, at surface temperatures from 5 to 30 K utilizing 200 K H and D atomic beams. Hence, only physisorption sites and possibly some uncharacterized defect sites were probed in these experiments. Figure 5.2 displays the thermal desorption (thermal desorption spectroscopy (TDS)/temperature-programmed desorption (TPD)) spectra from an amorphous carbon surface after exposure to 24, 48, 96, and 192 s doses of H and D atoms at a flux of 10^{12} atoms cm^{-2} s^{-1}. A signal at mass 3, indicating HD formation from H and D reactions on the surface, is observed.

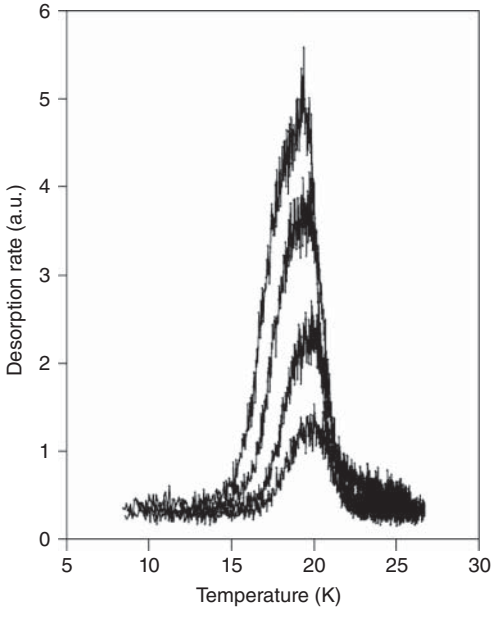

Figure 5.2 HD desorption rate versus surface temperature for an amorphous carbon sample during TPD runs following adsorption of H and D on amorphous carbon at 7 K for (bottom to top): 24, 48, 96, and 192 s. (Reproduced from [12], copyright 1997 © permission from IOP Publishing).

The desorption peak maxima occurs at ~ 20 K. The data indicates H_2 formation or desorption barriers of ~ 45 meV, depending on whether H_2 desorbs immediately upon formation or it is retained on the surface after formation. A weak HD signal was observed during H and D dosing, indicating some HD formation via Eley–Rideal abstraction or hot atom processes or via Langmuir–Hinshelwood processes with a very low activation barrier. Theoretical modeling based on the binding energies and barriers derived from these experiments indicate that H_2 formation from reactions between physisorbed H atoms on flat, nonporous, amorphous carbon surfaces is efficient at temperatures in the range of 10–20 K [36, 37]. At lower temperatures, H_2 might still be formed, but it will then be trapped at the surface.

Since astronomical observations show H_2 formation to be efficient also in higher temperature environments, the involvement of states with higher binding energy has to be invoked. Cazaux and Tielens [38] suggested the chemisorbed state of atomic hydrogen on the graphite basal plane as a possible candidate for these higher binding energy states. Alternatively, Cuppen and Herbst [37] showed that increased surface roughness can also increase the efficient temperature range for H_2 formation from physisorbed H atoms to 30 K or for extreme roughness to even 50 K.

Formation of H_2 from reactions between gas-phase H atoms and H atoms chemisorbed on the graphite surface via Eley–Rideal abstraction and hot atom processes was studied experimentally by Zecho and coworkers. In these experiments, 2000 K H/D atom beams were employed. Reaction cross sections were seen to decrease with H coverage on the surface and ranged from 17 $Å^2$ at low coverage to 4 $Å^2$ at high coverage. This behavior was successfully modeled by KMC calculations as a competition between dimer formation and a combination of different abstraction reactions with barriers of ~10 meV or lower [32]. Hence, the cross sections for Eley–Rideal abstraction of H/D chemisorbed on aromatic carbon structures, that is, on the graphite basal plane, are found to be at least two orders of magnitude higher than those found for H/D adsorbed into aliphatic $CH_{2,3}$ groups –as discussed below.

Formation of H_2 from reactions of H atoms chemisorbed on the graphite basal plane was studied by Zecho and coworkers using TDS/TPD methods. The TDS spectra exhibit a double-peak structure (Figure 5.3) with a main peak at 445 K (490 K) and a minor peak at 560 K (580 K). The TDS/TPD curves exhibit first-order kinetics [39], which would be expected for H atoms prepared into dimer configurations on the surface, as observed in STM [27]. Hornekær *et al.* studied the thermal stability of hydrogen adsorbate structures. STM images of a D covered surface after annealing at a temperature of 525 K (between the two D_2 desorption peaks) reveal that only ortho dimers are left on the surface at this temperature. The higher stability of ortho dimers compared to the more abundant para dimers can be explained by the kinetics of the H_2 formation process [27]. In Figure 5.4, diffusion and H_2 formation barriers for H_2 para, ortho, and meta dimers are displayed. The barrier to H_2 formation from the para dimer configurations is 1.4 eV, which is in good agreement with the first peak observed in the TDS spectra. Direct H_2

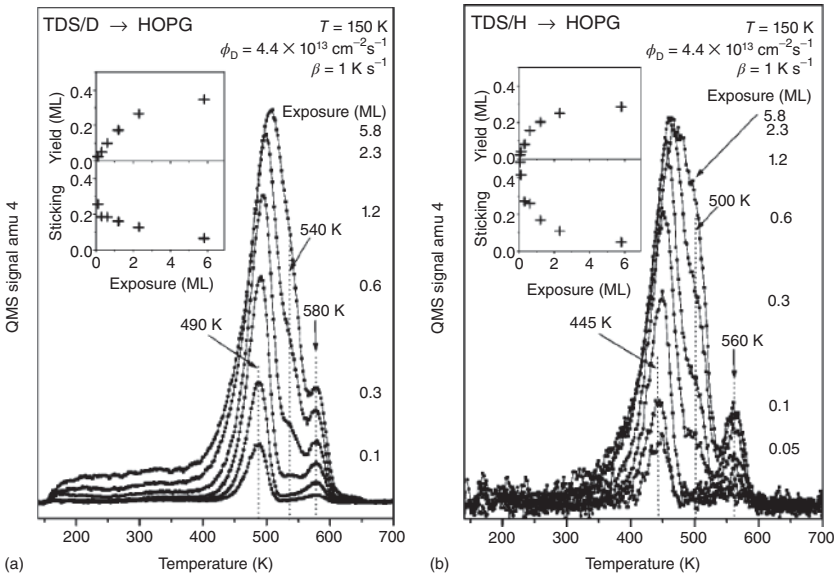

Figure 5.3 (a) Thermal desorption spectra measured after admitting D atoms to clean highly oriented pyrolytic graphite (HOPG) surfaces at 150 K. The atom exposures are given in units of graphite monolayers. The insets illustrate the D uptake and the sticking coefficient as a function of the D coverage. (b) Thermal desorption spectra measured after admitting H atoms to clean HOPG surfaces at 150 K. The insets illustrate the H uptake and the sticking coefficient as a function of the H coverage. (Reproduced from [39], copyright 2002 © permission from American Institute of Physics.)

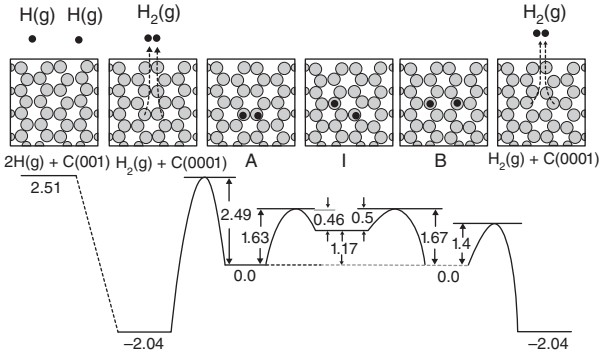

Figure 5.4 Energy barriers for atomic hydrogen diffusion and recombination from dimer A and B states on the graphite surface. The barrier to desorption of a single H atom out of structures A, I, and B are 2.08, 0.92, and 1.92 eV, respectively, and is hence energetically unfavorable in all three cases. (Reproduced from [27], copyright 2006 ©permission from American Physical Society.)

formation out of the ortho dimer configuration has a very high barrier of 2.5 eV. Hence, this process is prohibited and the hydrogen atoms will instead diffuse over the meta dimer configuration into the para dimer configuration and will recombine from here. The rate-limiting step for this process is the first diffusion step with a barrier of 1.6 eV, which is in good agreement with the barrier derived for the second peak in the TDS spectra.

At high coverages, H_2 formation from hydrogen adsorbate clusters on the graphite basal plane has been observed to be accompanied by desorption of atomic hydrogen [34]. Zecho and coworkers [40] also studied H_2 formation from defective graphite surfaces experimentally, and in that case found desorption barriers of 2.8–3.2 eV and observed the formation of carbohydrates, in good agreement with the high predicted binding energy for H atoms at defect sites.

The experiments on H_2 formation on graphite indicate that, in the interstellar medium, H_2 formation on graphitic surfaces with a low number of defects will only be efficient under dense and diffuse cloud conditions with grain temperatures below 20 K via reactions between physisorbed atoms, or under PDR conditions with high gas temperatures, where the chemisorbed state on the basal plane can be populated under the impact of H atoms with high kinetic energy. Under these last conditions, H_2 formation is expected to proceed via the Eley–Rideal and hot atom mechanisms, since even under PDR conditions the grain surface temperatures will rarely be high enough (400–450 K) for Langmuir–Hinshelwood processes to be activated.

Mennella characterized Eley–Rideal abstraction reactions on very rough porous amorphous carbon surfaces, namely surfaces dominated by carbon atoms in aliphatic chemical arrangements [41]. In these experiments, chainlike aggregates of carbon nanograins were first irradiated with H atoms, resulting in the formation of aliphatic CH_2 and CH_3 functional groups. The samples were subsequently exposed to 80–300 K beams of D atoms, and H/D exchange reactions were observed via infrared (IR) spectroscopy as a decrease in the sp^3 $CH_{2,3}$ stretching features accompanied by an increase in the sp^3 $CD_{2,3}$ stretching features. Furthermore, mass spectrometry measurements showed the simultaneous formation of HD molecules. Based on these measurements, cross sections for HD formation from Eley–Rideal abstraction of H in aliphatic $CH_{2,3}$ groups were determined. The reactions were best described by an initial high cross section of $3.0 \pm 0.4 \times 10^{-2}$ Å^2 and a low cross section of $2.7 \pm 0.3 \times 10^{-4}$ Å^2 at longer times (Figure 5.5). Similar results were found for HD formation from H abstraction of D atoms. The reaction cross sections were found to be independent of H (D) atom beam temperature, but were dependent on the temperature of the surface, with higher reaction rates and higher activation barriers ($T_a = 130$ K) at surface temperatures above 80 K, and lower reaction rates but negligible activation barrier at lower temperatures. Hence, even though the binding energy of H/D atoms in aliphatic $CH_{2,3}$ groups are of the order of several electronvolts, Eley–Rideal abstraction reactions were found to occur with very low or even negligible activation barriers. Furthermore, at low surface temperature, more

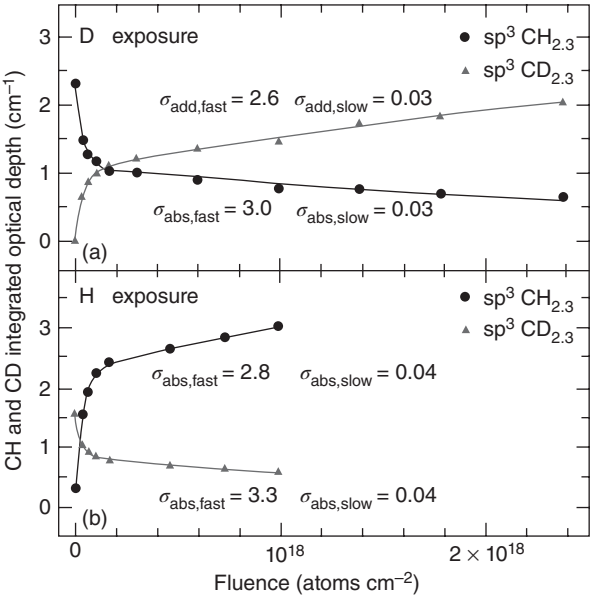

Figure 5.5 Evolution with atom fluence of the C–H and C–D integrated band optical depth during (a) D exposure of hydrogenated carbon grains and (b) H exposure of deuterated carbon grains. The estimated cross sections are expressed in units of 10 Å^2. (Reproduced from [41], copyright 2008 © permission from IOP Publishing.)

than 50% of the formed HD molecules were retained in the porous structure of the surface after formation. Hence, H_2 formation on these surfaces should be efficient for grain temperatures up to 300 K and over a very wide range of gas temperatures.

A further contribution to H_2 formation at intermediate temperatures could be H_2 formation catalyzed by PAHs [42] on grain surfaces or in the gas phase. Experimental investigations have shown that, when exposed to a beam of hydrogen atoms, the PAH molecule coronene can be driven into a fully superhydrogenated state with one excess hydrogen atom binding to each carbon atom [43]. Experiments also show that such superhydrogenated coronene molecules act as catalysts for molecular hydrogen formation via abstraction reactions [43, 44]. The derived cross sections could account for the increased molecular hydrogen formation rates observed in some PDR regions with abundant PAH emission features [20, 44].

5.2.3
Energy Partitioning in H_2 Formation

When an H_2 molecule is formed, ~4.5 eV of energy is released. How this energy is partitioned between external (kinetic energy) and internal (ro-vibrational excitation) molecular degrees of freedom and the surface on which the molecule formed

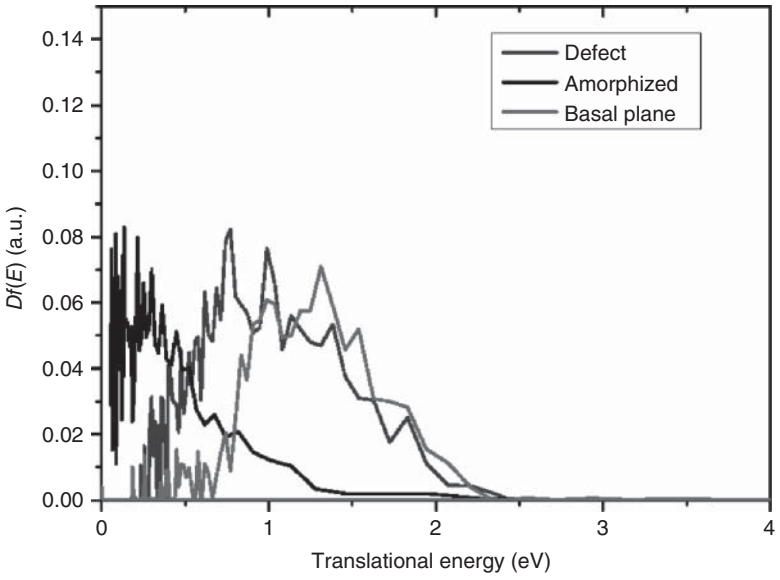

Figure 5.6 Translational energy distributions *Df*(*E*) from laser assisted associative desorption (LAAD) of D2 desorbing from the graphite basal plane, from defected graphite, and from an amorphized carbon surface.

has a major impact on the resulting energy input into the interstellar medium (ISM) [45]. Energy partitioned into kinetic energy of the molecule will lead to a heating of the surrounding molecular cloud, whereas energy partitioned into ro-vibrational excitation will most likely be lost as radiation. Energy partitioned into heating of the surface on which the molecule formed could catalyze further chemical reactions or desorption of atoms and molecules adsorbed on the surface, before being dissipated as IR radiation.

The translational energy of D_2 molecules formed on the graphite basal plane as well as on a defective and a flat, nonporous amorphized graphite surface was measured by Luntz and coworkers. The results are displayed in Figure 5.6. D_2 molecules formed on a defect-free graphite surface heated to 1000 K have an average kinetic energy of 1.3 eV and are hence strongly hyperthermal, indicating that roughly one-third of the energy released in H_2 formation is partitioned into the kinetic energy of the newly formed molecule. For a defective graphite surface, the average kinetic energy of the formed molecules is reduced, which is ascribed to the higher energy cost for H atoms reacting out of more strongly bound defect sites. On an amorphous surface, even lower kinetic energies are observed, indicating even stronger average binding for H atoms on this surface [46].

The energy partitioned into excitation of internal ro-vibrational states for H_2 formation on graphite was measured by Price and coworkers. In these experiments, atomic hydrogen and deuterium beams at 100–300 K impinged on a graphite surface (HOPG) held at a temperature of 15 K. Based on the low temperature of the incoming H and D beams, physisorbed H atoms are expected to

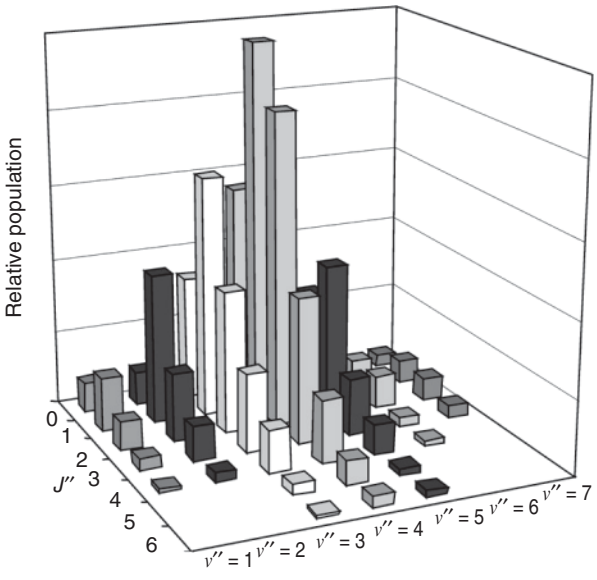

Figure 5.7 Derived relative ro-vibrational populations of HD formed on an HOPG surface at 15 K in the vibrational states v = 1-7. These ro-vibrational states are placed on a relative scale. (Reproduced from [49], copyright 2008 © permission from Elsevier.)

be the main contributor to these measurements. However, a further contribution from uncharacterized defect sites cannot be ruled out [47]. Resonance-enhanced multiphoton ionization was then used to detect HD molecules in specific ro-vibrational states. Using this method, a full mapping of the population of ro-vibrational states from $v = 1 - 7$ and $J = 1 - 6$ was achieved [47–49]. The compiled results are displayed in Figure 5.7. The measurements show high vibrational excitation (the $v = 4$ vibrational level has the highest population) and fairly low rotational excitation (only a very small population is observed in rotational levels with $J > 4$). The measured ro-vibrational excitation is low compared to that predicted by quantum dynamical calculations of H_2 formation on graphite via Langmuir–Hinshelwood processes [50] but is in good agreement with astronomical observations, indicating the formation and pumping of H_2 into vibrational levels $v = 4$ [51] and $v = 6$ [52]. These experimental measurements also yielded an upper limit on the energy partitioning into translational energy of approximately 1 eV [47, 48] for this system.

5.2.4
Summary and Outlook

Based on astronomical observations, molecular hydrogen formation on carbonaceous grains is expected to be efficient over a wide range of temperature: from dust grain temperatures of 15–30 K and gas temperatures of 30–100 K, as found in diffuse cloud environments, to grain temperatures of 100 K

and gas temperatures of several hundred to 1000 K, as found in PDRs. Vidali's experiments, combined with theoretical models, show that H_2 formation from physisorbed H atoms on flat carbonaceous surfaces is only efficient at temperatures below 20–30 K. At higher temperatures, more rough surfaces and chemisorbed states have to invoked to explain the observed interstellar H_2 formation efficiency. Experiments by Zecho and Hornekaer show that molecular hydrogen formation from chemisorbed H atoms on graphitic surfaces is efficient at the high gas temperatures relevant to PDRs. Mennellas's experiments show that H_2 formation from chemisorbed H atoms on very rough porous amorphous carbon surfaces dominated by carbon atoms in aliphatic chemical arrangements is fairly efficient over the entire temperature range from diffuse cloud conditions to PDRs, with estimated H_2 formation rates ranging from 19% to 50% of the rates derived for diffuse clouds and 8% to 40% of the rates for PDRs. A further contribution to H_2 formation via abstraction reactions from superhydrogenated PAHs can be expected in some interstellar environments [44].

Assuming that a realistic interstellar dust grain model is an amorphous disordered carbon surface with a mixture of carbon atoms in aromatic and aliphatic chemical arrangements [14, 23], then it appears that molecular hydrogen formation on carbonaceous surfaces will predominantly proceed via Eley–Rideal abstraction and hot atom reactions with chemisorbed H atoms over the full range of interstellar temperatures, with additional Langmuir–Hinshelwood and hot atom reactions between physisorbed H atoms at grain temperatures below 20–30 K. Whether these reactions occur with a sufficiently high efficiency to explain the observed interstellar H_2 formation rates must be probed by further modeling and experiments.

The question of energy partitioning in H_2 formation on carbonaceous surfaces has been answered in part for H_2 formation on graphite and defective/amorphized graphite [46, 49]. For reactions between physisorbed hydrogen atoms on graphite, high vibrational excitation was observed, and an upper limit on energy partitioning into translational energy of 1 eV was found. For reactions between chemisorbed H atoms on defect-free graphite, highly hyperthermal velocity distributions with an average energy of 1.3 eV were seen. As the number of defects increased, less and less energy was partitioned into translation. Energy partitioning in Eley–Rideal abstraction processes has so far not been measured. A further complication on these measurements is the possible porous morphology of interstellar carbonaceous dust grains. Mennella showed in his experiments that more than 50% of the H_2 molecules formed on very rough, porous amorphous carbon surfaces were retained on the surface upon formation. In such a case, the translational and possibly also internal energy of the formed molecules could well be dumped into the grain surface, as observed for H_2 molecules formed on porous amorphous solid water [53]. Hence, energy partitioning in interstellar H_2 formation will most likely be very sensitive to the dust grain morphology.

In short, experiments show that H_2 formation is possible on all the carbonaceous surfaces studied so far. However, the process by which H_2 is formed and the range of gas and grain temperatures over which H_2 formation is efficient depend

critically on the chemical structure of the carbon surface. Furthermore, energy partitioning in H_2 formation is observed to be dependent on the H_2 formation process (i.e., little energy partitioned into translation for reactions between physisorbed H atoms, while more than 1 eV is partitioned into translation for reactions between chemisorbed H atoms on defect-free graphite, and somewhat less for reactions between H atoms chemisorbed on a defected or amorphous graphite surface) and is expected to be highly dependent on the dust grain morphology.

5.3
The Influence of Ice Morphology on Interstellar Chemistry

Martin McCoustra, Mark Collings, Francois Dulieu, Jean-Hugues Fillion, and Maria Elisabetta Palumbo

Observations show that in dense interstellar clouds dust grains are covered by amorphous ice layers. These ice layers consist predominantly of H_2O, with other molecular species such as CH_3OH, CO_2, and CO mixed in. In this section, we discuss the structure of such amorphous ice surfaces, as well as the influence of this structure on the sticking, adsorption, diffusion, reactions, and desorption of atoms and molecules on them.

5.3.1
The Structure of Amorphous Solid Water (ASW)

Early studies of the structure of amorphous solid water (ASW) ice were performed by Jenniskens and Blake [54–56] who used transmission electron microscopy (TEM) to demonstrate the amorphous nature of icy films grown under conditions of temperature mimicking those in the dense interstellar medium and established the temperature evolution of such low-temperature ASW phases. In the first instance, their observation of diffraction rings as opposed to spots was indicative of the amorphous nature of water ice grown from the gas phase by deposition on a low-temperature solid. Conversion of the diffraction patterns to radial intensity distributions revealed the temperature dependence of the intermolecular distances, displaying the phase changes that the ASW film underwent during annealing.

It is rare that a single technique can provide a comprehensive picture of a complex system, and the behavior of ASW is no exception to this rule. Other techniques that provide direct information on bond length and arrangement, such as X-ray diffraction [57], neutron diffraction [58], and extended X-ray absorption fine structure (EXAFS) [59], have been applied to ASW. From such measurements, the local chemical density, referred to as the *true density*, of the water ice phases can be determined. Other techniques provide information about the porous structure of ASW. The simplest of these is interferometry [60, 61], whereby film thickness measurements in combination with the surface concentration of water molecules give the overall bulk density of the film. In association with

true density values, a measure of porosity can be obtained. Similarly, gas uptake experiments provide a measure of the surface area and pore volume of the ASW structure [62, 63].

Temperature-programmed desorption (TPD) has also provided much information on the structure of ASW films. In particular, the TPD studies of Kay and coworkers using nitrogen (N_2) and other probe species have revealed the temperature and angular dependence of the structure of ASW deposited from a molecular beam of water vapor and compared it with those of background deposition [16, 61, 64]. Their experiments showed that the structure of ASW depends on experimental conditions such as the temperature, deposition rate, and deposition angle. For low deposition rates (typically < 0.5 ML s^{-1}, where 1 ML $= 10^{15}$ molecules cm^{-2}), it is possible to form porous amorphous solid water (p-ASW) with varying degrees of porosity, compact amorphous solid water (c-ASW), or (poly)crystalline ice depending on the experimental deposition method and parameters [61]. c-ASW is formed during vapor deposition at high temperatures ($T = 120-140$ K) [65, 66], while p-ASW can be formed during deposition at low temperature ($T = 10-40$ K) [16, 61, 67]. The effective surface area of p-ASW films can be controlled by changing the temperature of the substrate during deposition and the deposition angle for low vapor deposition rates of water molecules. The effective surface area for p-ASW films can reach a few thousand square meters per gram [16, 62].

The local structure of ASW films can be characterized by infrared spectroscopy. Figure 5.8 shows the mid-infrared spectrum (in optical depth scale) of vapor-deposited ASW at 16 K. The absorption bands at 3300 cm^{-1} (3.03 μm; O–H symmetric and antisymmetric stretching modes), 2205 cm^{-1} (4.53 μm; combination mode), 1650 cm^{-1} (6.06 μm; overtone of the libration mode and H–O–H bending mode), 803 cm^{-1} (12.4 μm; libration mode) are present in the spectrum. In addition, a small feature is present, on the long wavenumber wing of the O–H stretching modes band, due to OH dangling bonds (dbs) in the micropores of the amorphous structure. This feature shows two peaks at 3720 and 3696 cm^{-1} due to two-coordinate and three-coordinate water molecules, respectively [65].

The shape, width, and peak position of the OH db feature depend on the morphology/porosity of the ice sample and on the presence of other molecular species mixed with water ice. In polycrystalline water ice, O–H dbs are present at the surface of large ice clusters [65] and the intensity of the related spectral features is too weak to be detected by infrared transmission spectroscopy of thin films [68]. Table 5.1 reports the position of the OH db feature in different H_2O:X mixtures. In a few instances, the two- and three-coordinate peaks merge into one broad feature.

Simple molecules, such as H_2, N_2, CO, CH_4, and Ar, absorbed in amorphous or crystalline water ice are often used as a probe to study the properties of the ice. This can be achieved by looking at both the profile of the OH db feature present in porous amorphous ice or on the surface of large crystalline ice clusters [65, 66, 72] and at the profile of the infrared bands of the absorbed species, as in the case of carbon monoxide [68, 73, 74].

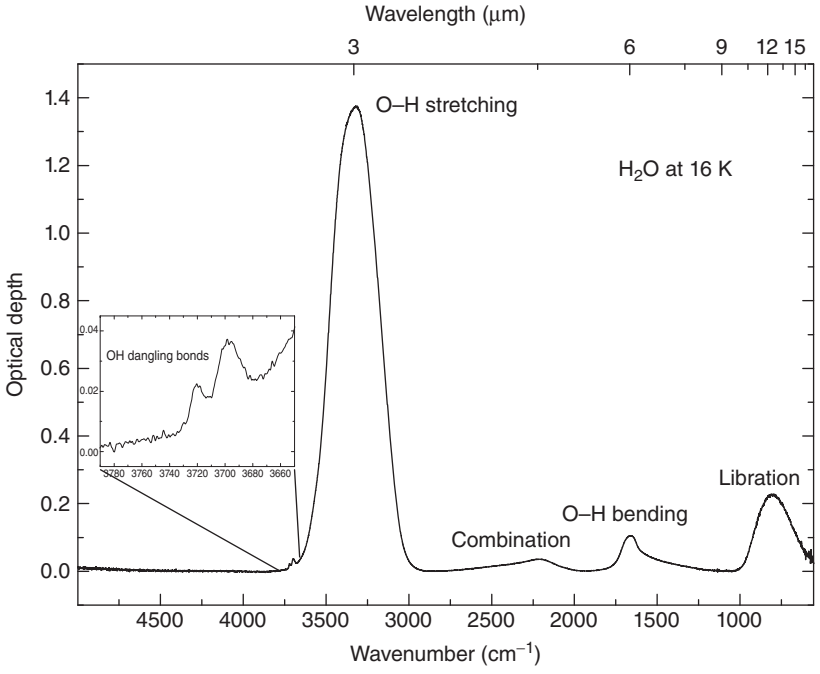

Figure 5.8 Mid-infrared spectrum of vapor-deposited porous amorphous solid water at 16 K.

Table 5.1 Peak position of the OH dangling bond features in different solid samples.

Sample	OH db peak positions (cm^{-1})	References
Pure H_2O	3695, 3720	[65, 69]
H_2O:N_2	3672, 3694	[65, 70]
H_2O:O_2	3669, 3694	[69]
H_2O:H_2O_2	3664	[69]
H_2O:CO_2	3657	[69]
H_2O:CO	3636	[69]
H_2O:CH_4	3669, 3684	[66, 69]
H_2O:SO_2	3606	[69]
H_2O:CH_3OH	3710	[71]

Together, such laboratory experiments demonstrate that water accreted under the conditions prevalent in dark clouds – temperatures of roughly 10 K, low adsorption rates, and random trajectories of adsorbate molecules – will form with a highly porous, amorphous structure with a high true density. When warmed, this p-ASW with a high true density and low bulk density undergoes an irreversible phase change to a more compact (less porous) amorphous structure

(c-ASW), with a lower true density and a higher bulk density over the temperature range 38–68 K. While the changes in intermolecular distance (the true density changes) are limited to this range, the information gleaned from a variety of techniques demonstrates that in fact the structural changes (bulk density changes) occur continuously and irreversibly up to a temperature of about 120 K.

ASW is a metastable phase; upon heating past the temperature of crystallization, about 135 K under ultrahigh vacuum (UHV) laboratory conditions, a cubic crystalline phase of water ice (c-Ice) is formed, and the amorphous phase does not re-form if the temperature falls back below the crystallization point. The cubic crystalline phase is also metastable, and is converted to the stable hexagonal crystalline ice phase (h-Ice) at ∼180–210 K. However, the hexagonal phase is not usually accessible under UHV conditions where desorption of ice occurs at around 160–180 K. The properties of water ice films in the temperature range around the transition from c-ASW to c-Ice have been extensively studied by a multitude of techniques [75]. This is in part due to the accessibility of this temperature range to conventional liquid nitrogen cooling. However, the properties of the supercooled liquid phase that exists above the glass transition at 136 K [76–79] and even the extent of crystallization within the c-Ice phase remain controversial.

5.3.2 Desorption of Molecular Hydrogen

c-ASW can be grown by background deposition on a sample holder held at 110 K < T < 130 K. c-Ice is obtained upon annealing of ASW or by direct growth in the 140–145 K temperature range. These two kinds of ice are commonly reproducible in the laboratory. In both cases, the surface area accessible to the gas phase is limited to the external layer of the film, which can be considered planar at the macroscopic scale. Consequently, the properties of these surfaces are not thickness-dependent.

The differences between these two samples are mainly seen is their distribution of adsorption sites.

As compared to that of c-Ice, the surface of c-ASW is more irregular and less homogeneous with few dangling bonds that appear as defects.

In contrast to the two previous cases, porous amorphous ice (p-ASW) is harder to control experimentally because of three main factors. Primarily, the properties of p-ASW with respect to gas-phase interaction are thickness-dependent because the surface area accessible to the gas phase is not limited to the external geometrical layer of the sample. Thus, thickness becomes an important parameter which has to be taken into account. Furthermore, a non-uniform deposition will complicate the interpretation by juxtaposing various thicknesses of ice. Second, the properties of the film are very sensitive to the deposition method, namely the surface temperature, the deposition rate, and the angular distribution of the water molecules with respect to the surface plane. All these parameters will affect the final degree of porosity. Third, the thermal history has a major impact because the porosity changes and reduces as soon as the ice is heated. Despite the fact that

the thickness and the degree of porosity can change from one sample to another, porous ice has three main properties: First, since it is constituted of a network of water molecules which are not fully coordinated (some are coordinated with only two or three neighbors, instead of four [80], the topology of the surface is highly disordered. At the molecular scale, this gives rise to a large number of dangling bonds and to a wide variety of adsorption sites. Second, at a larger scale, water ice forms cracks, holes, and even pores if the thickness is sufficient, and therefore the exchange with the gas phase is not homogeneous. Some adsorption sites can be directly accessible to the gas phase, but most of them can only be reached after diffusion or multiple desorption–adsorption events within the film. The ratio between the internal and external sites increases with the thickness of the ice. Third, the number of adsorption sites increases linearly with the ice thickness. Consequently, for a fixed dose of gas deposited on the substrate, the surface density (the fraction of occupied sites, also called the *coverage*) of the adsorbates is dependent on the thickness: the thicker the ice, the lower the surface density. Even though it is rarely done, the question of the homogeneity of the adsorbate over the entire sample should be considered each time.

TPD has been the most commonly used technique to investigate the interaction of hydrogen with water ice. Its simplicity of use is largely counterbalanced by the fact that it only gives direct information about desorption of molecules. Before studying the complex case of recombination of atomic hydrogen, the desorption of molecular hydrogen should be understood. It illustrates also perfectly the preponderance of the morphology of the surface.

Figure 5.9 shows the synthetic TPD spectra of H_2 desorption arising from different water ice substrates. These curves have been computed from the data and values given in Refs [81–83]. Compared to that of c-ASW, the desorption peak of 0.1 ML of H_2 from porous substrates is shifted toward higher temperature. There is a first shift when the substrate changes from c-ASW to 5 ML of p-ASW. This

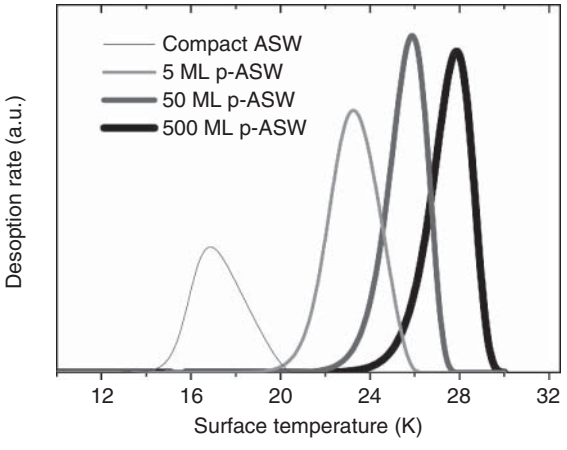

Figure 5.9 Simulated TPD profiles of H_2 desorbing from c-ASW and p-ASW (5, 50, 500 ML of thickness) at a heating rate of 10 K min^{-1}.

shift is even more pronounced for desorption curves obtained from 50 and 500 ML of p-ASW substrate.

Although the shift of the TPD curves appears to regularly move toward higher temperatures, there are in fact two different mechanisms contributing to the shifts.

On can distinguish two regimes depending on the thickness of the porous ice. In the "thin film regime", the energy distribution of adsorption sites is progressively changed from that of c-ASW to that of p-ASW.

Figure 5.9 gives snapshots of these modifications as p-ASW is grown over c-ASW. The main characteristic of this evolution is to add new (high-energy) binding sites. These new adsorption sites appear as soon as p-ASW is grown. Below 5 ML, the distribution of adsorption sites is intermediate between the two types of surfaces. After 5ML, the p-ASW energy distribution of the adsorption sites fully replaces that of c-ASW [83]. But with such thin layers, it is not obvious that the main property of porous materials, namely that most of the surface is not connected directly to the gas phase, as mentioned above, is present.

Basically, in thick samples, the molecules are spread within the film of p-ASW. The effective number of molecules present at the external part of the film is thus lowered as the thickness increases, which reduces the desorption rates; and a "delay to the desorption" [81] appears, as simulated in Figure 5.9. In the "thick film regime," the difference between the TPD curves arising from the three p-ASW ices is only due to ice thickness differences (governed by the ice thickness) and is not linked to a change in the energy distribution of the adsorption sites as shown previously in the "thin film regime." We can see here that TPD of molecular hydrogen is a powerful tool to investigate the morphology of the ice. The two regimes discussed here are also linked to two different scales for the interaction of the adsorbate with the surface. A molecular scale, which is ruled by the energy distribution of the binding sites, and a larger scale, where cracks, holes, and pores can trap and re-adsorb temporarily the adsorbed species, reduce the effective desorption rates as compared to a flat surface.

5.3.3
Influence of the Morphology of the Ice on the Sticking of Hydrogen

The first step of any gas–surface interaction is the sticking of the atoms or molecules from the gas phase. The sticking process is mostly governed by the ability of a species to decrease its initial kinetic energy and to be finally trapped (thermalized) on the surface. Hydrogen (in atomic or molecular form) has a low polarizability which induces a low binding energy. In addition, the light mass of hydrogen gives a low momentum transfer to the surface as a result of the mass mismatch between the two colliding partners. Finally, in contrast to most of the heavier species, hydrogen's (atomic or molecular) sticking coefficient (i.e., the probability for a particle from the gas phase to be thermalized with the surface) is not close to unity but varies between 0.1 and 1 depending on the temperature of the incident hydrogen.

There is some experimental work partly devoted to the sticking of atomic or molecular hydrogen [53, 84, 85]. The sticking of atoms is hard to measure experimentally because the atoms react together on the surface (see next section), but experimental results can be compared to calculations. Furthermore, the sticking coefficient depends on the temperature of the incident molecules. Recently, new experimental data was provided in Ref. [86], in which an analytic formula for the sticking of atoms and molecules on c-ASW was also derived. As expected, the sticking coefficient decreases with the temperature of the impinging gas.

The role of the surface morphology has not been explored in detail. Nevertheless, there are some estimates determined experimentally for D_2 [53] giving a sticking coefficient $S \sim 0.6$ on p-ASW and ~0.2 on c-ASW under the same experimental conditions (room temperature, normal-incidence molecular beam). These results are sufficient to emphasize two important points. First, as expected, the sticking coefficient is larger for p-ASW because the adsorption energy is higher on the surface and because the momentum transfer is enhanced by the roughness of the surface since multiple collisions are favored. Second, it gives a first insight into the differences in the recombination process because the recombination process starts by the sticking of the reactants.

5.3.4 Recombination Process

Because H is by far the most abundant atom in space, and as a consequence H_2 is the most abundant molecule, the equilibrium between the two forms of hydrogen (atomic/molecular) has been a central question since the beginning of astrochemistry. Solid water ice is observed in the dense and cold regions of the interstellar medium where most of the hydrogen is in molecular form. But the continuous formation of H_2 on the icy grain surfaces is still required to compensate for the destruction of H_2 induced by cosmic rays or by chemical pathways. In comparison to other interstellar regions where bare grains are present (silicate or carbonaceous particles without water mantles), the accretion rate of atoms on icy grains is rather low (2–3 orders of magnitude lower), but the recombination efficiency still has to be high (0.1–1) in order to compensate for the estimated destruction rate.

In contrast to silicates or carbonaceous grains, chemisorption seems to play no role in the reaction process. There are different pieces of experimental evidence for this claim. First, there is no detection of H_2 formation on ASW at temperatures higher than 20 K, which indicates that the binding energy ranges are related to physisorption (<70 meV). Second, if chemical binding has occurred, the irradiation of D atoms should lead to the production of OD bonds, which have never been observed [87, 88]. The recombination process of H on water appears to be purely governed by the physisorbed states of H and H_2.

The recombination of H on c-Ice or on c-ASW has been studied by four groups [53, 85, 89, 90]. For these two kinds of planar ice, the general result is that the reaction proceeds during the irradiation of the atoms on the substrate. The mobility of hydrogen is so high that the critical density of H atoms (required to induce H_2

formation by diffusion of H on the surface) is reached extremely rapidly. Several experimental techniques support this picture. (i) The simultaneous irradiation of D and H, or the successive irradiation of the two isotopes of c-Ice, gives rise to very different HD production rates [53]. If the two beams irradiate simultaneously, the yield is far higher than in the case of successive irradiations, indicating the kinetics occurring during atomic irradiation. (ii) The number of D_2 molecules has been estimated to be almost zero when TPD measurement is performed *after* irradiation with D atoms on c-ASW held at 10 K, whereas a formation yield depending on the surface temperature has been measured *during* the irradiation with D atoms [85]. In addition, molecules with a high degree of internal energy have been detected only during irradiation, showing again that the reaction takes place simultaneously with the irradiation of atoms. (iii) Finally, H-atom detection using laser techniques indicates that the desorption from c-Ice after irradiation with a very low flux of incoming atoms seems to be almost zero, indicating that they have reacted [90] and supporting totally the first two sets of experiments. The formation of H_2 on flat ice happens during irradiation of H atoms on the ice. This prompt reaction releases some excited molecules (see below).

The total reaction rate R (probability for an atom to be transformed into a molecule) has been measured in the case of c-ASW and is found to be dependent on the temperature of the surface. It is $R \sim 0.1$ at 10 K and almost zero above 13 K [85].

For the p-ASW, R has been measured for different types of porous ice (thickness, uniformity, annealing degree). At 10 K, R has been found to lie between 0.2 and 0.5 [53, 91]. It is also dependent on the temperature and, in the case of ice of well-controlled thickness, it exhibits a plateau from 8 to 14 K before decreasing to zero above 20 K [53, 92]. The recombination efficiency is always much higher than for the case of c-ASW ice. This is probably due to the difference in the sticking coefficients. This is supported by the fact that the ratio observed between the sticking coefficients relative to the two types of surfaces held at 10 K for the molecules ($S \sim 0.2/S \sim 0.6$) is about the same as the ratio of the recombination efficiency of the atoms for the two surfaces ($R \sim 0.1/R \sim 0.3$) held at the same temperature.

In contrast to c-ASW where the reactions take place during irradiation with the atoms, it is emphasized that the R mentioned above for p-ASW ice is obtained during TPD and therefore collected sequentially after the exposure step. Here appears clearly the limitation of this technique because it is not possible to know whether the reaction is thermally induced during the heating ramp or it occurs promptly during the exposure of the atoms as in the case of c-ASW or crystalline ice. The first alternative is supported and simulated in Ref. [93], but the value of the adsorption energy of the atoms is so high, and even more surprisingly greater than the values found for molecules, that the hypothesis of the model has to be questioned. The second alternative is supported by four experimental arguments. (i) When p-ASW samples are heated after H-atom irradiation, the kinetic temperature of the desorbing molecules is the same as the substrate temperature. (ii) There is no extra internal energy left in the nascent molecules. This is in strong contrast to the high internal energy observed in the case of c-ASW. (iii) When molecules are

formed on p-ASW, their interaction time with the surface is sufficiently long to reach an ortho/para ratio and rotational states in equilibrium with the substrate temperature. (iv) In Ref. [94], a set of experiments indicate, without the bias of any model, that H atoms are able to reach the entire surface of the p-ASW ice. O_2 molecules have been used as a probe, taking advantage of the fact that $O_2 + H$ is an efficient reaction able to compete with the H + H reaction. Even in the case of 200-ML-thick layers, O_2 molecules that have previously diffused in the pores during their exposure to the surface held at 25 K are destroyed by D irradiation of the surface held at 10 K. This set of experiments shows that the mean mobility of D is sufficient to induce H chemistry on p-ASW.

The above results can be understood considering that the interaction of H atoms with water is governed by a binding energy distribution which is highly sensitive to the coverage. As concluded by Watanabe and co-workers [90], based on their laser experiments detecting directly H atoms and also on calculations [95], the disordered structure of the ice provides a wide adsorption energy distribution induced by various sites of adsorption. A small number of sites <1% exist where the atoms can be trapped at 8 K during seconds, but most of the adsorption sites are spread following a distribution. This is also supported by the studies of such energy distributions in the case of adsorption of molecular hydrogen isotopes where both experiments and calculations match nicely [82].

If a distribution of adsorption energies exists, it is obvious that a distribution of diffusion barriers also exists. The average binding energy together with the average barrier to diffusion decreases with coverage. The average diffusion times thus decrease with coverage. Above a critical density on the substrate, a fast diffusion process can happen and reactions occur. This critical density, in principle, decreases with the temperature, but is extremely low ($<10^{12}$ atoms cm^{-2}) even at 10 K. It explains why diffusion of D in the pores of ASW has been observed [94] under their experimental conditions.

This finally also explains the plateau behavior experimentally observed in the recombination rate of D on p-ASW versus the temperature of the surface. The constant R is due to the fact that the critical density is reached whatever the surface temperature is and that the recombination occurs efficiently. The decrease of R at higher temperature is due to the evaporation of atoms, which competes with the diffusion. When evaporation is very efficient, no more molecules are formed.

5.3.5
Energetic Balance of the H_2 Reaction and its Consequences on the Morphology of Ice

As is very well explained in Ref. [53], the energy budget of formation of H_2 on grains plays a central role in the energetic balance of molecular clouds. Crudely, if the energy is kept by the grain, the gas phase is not heated by the nascent molecules, whereas if the molecules have a high kinetic energy, the chemical energy of H_2 formation is retained by the clouds and therefore the $H + H \longrightarrow H_2$ reaction does not act as a coolant of the medium. It has also been clearly shown that the presence of pores in the case of p-ASW keeps the

molecules on the surface and that, when they finally reach the gas phase, it is with a low kinetic energy [53] and a low internal energy [96].

In the case of c-ASW, the reaction is fast and produces excited molecules as already discussed above, but it happens only if the surface is free of adsorbed molecules.

More surprisingly, if some other H_2 molecules are previously adsorbed on the surface, the molecules formed by atomic recombination are released in the gas phase with low internal energy. Even though there has been no measurement of the kinetic energy yet, it seems to indicate that even for the c-ASW in the conditions of interstellar dense clouds, where other H_2 molecules should be adsorbed on the surface, the energy of the reaction is retained by the grains. Therefore, whatever is the structure of the ice, c-ASW or p-ASW, H_2 formation reactions acts as a cooling agent of the interstellar cloud.

It is well known that, if p-ASW is heated or exposed to radiations (UV or ionic bombardment, see next section), the porosity of the ice irreversibly decreases. The H_2 reaction can also be considered as an energetic processing of the ice sample, since it has been established that most of the energy is retained by the ice. It has been shown recently [97] that the formation of H_2 molecules on p-ASW ice reduces progressively the porosity of the ice. Under D irradiation of p-ASW, there is an exponential decrease of the porosity of the ice sample. This decrease is inversely proportional with the thickness of the ice and has a value of 2×10^{16} D atoms cm^{-2} per layer of H_2O. In such conditions, it is proposed, as for the other source of energy of the interstellar medium, that the ice, if formed as p-ASW from gas-phase accretion of H_2O at low temperature, should transform in a relatively short time into a more compact ice.

5.3.6
The Impact of Ice Morphology on Thermal Desorption Processes for Other Small Molecules

The interaction of astronomically relevant small molecules with water ice in the cold interstellar environment must be considered in the light of the morphological and phase changes detailed in Section 5.3.1. Observational evidence tells us that carbon monoxide (CO) is typically the second most abundant component after water in interstellar ices [13]. CO ice is detected in the infrared spectrum via its C–O stretch band at 4.67 μm. Two peaks are frequently co-evident in the CO stretch region – a broad, flat peak centered at 4.681 μm, and a sharper peak at 4.674 μm [98]. These two peaks are generally attributed to CO in polar (hydrogenated) and apolar (dehydrogenated) ice matrixes, respectively, which are thought to form an "onion-like" structure with an inner layer of a hydrogenated ice surrounded by an outer dehydrogenated layer [13]. Hydrogenated ices are dominated by water (H_2O), with lower concentrations of species such as methanol (CH_3OH), ammonia (NH_3), and methane (CH_4). Dehydrogenated molecules may also be present in low concentrations, with CO observed at up to 10%. Dehydrogenated ices are dominated by species such as CO, carbon dioxide (CO_2), N_2, and oxygen (O_2). While IR spectroscopic studies of CO in H_2O ice

abound (e.g., [99–101]) and have proved to be invaluable from the standpoint of interpreting and understanding astronomical observations, detailed investigations of the thermal behavior of these ices (e.g., Refs [102, 103]) were limited, and certainly detailed kinetic interpretation of the thermal desorption in this relatively simple system was absent until the work of McCoustra and coworkers [104, 105]. In their work, both TPD (Figure 5.10a) and reflection–absorption infrared spectra (RAIRS) (Figure 5.11) were measured for thin films of CO adsorbed on an ultrathin H_2O ice film ballistically deposited on a gold substrate at 8 K. The behavior of the CO on this p-ASW substrate that can be gleaned from these data is summarized in the cartoon in Figure 5.12. This succinct qualitative description of the behavior of CO in and on the pores of water ice reveals the unique role played by the H_2O ice morphology in complicating what had been considered a relatively simple ice system by astronomers. To understand the implications of this behavior on CO adsorption and desorption under astronomically relevant

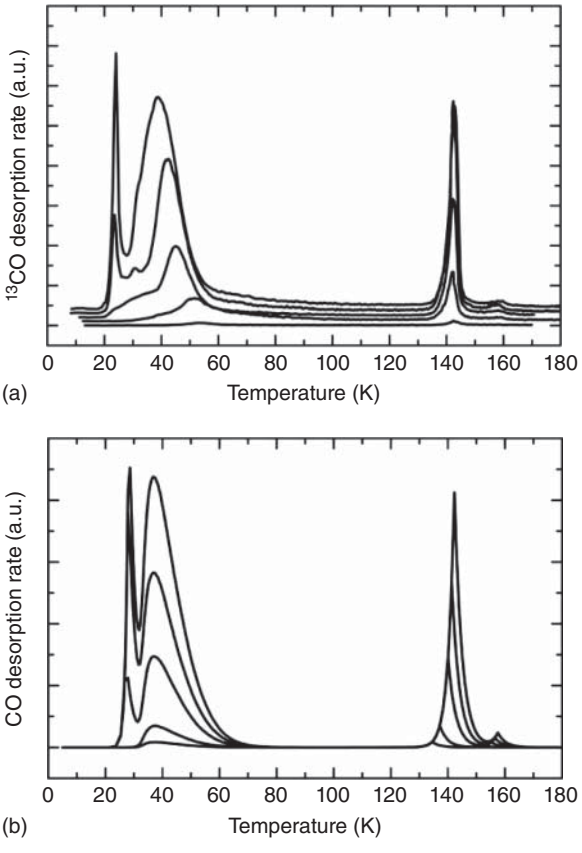

Figure 5.10 (a) Experimental TPD traces for varying coverages of ^{13}CO from p-ASW. (b) Theoretical TPD traces simulated using a 16-step kinetic model for CO under the same conditions. (Reproduced from [105], copyright 2003 © permission from Springer.)

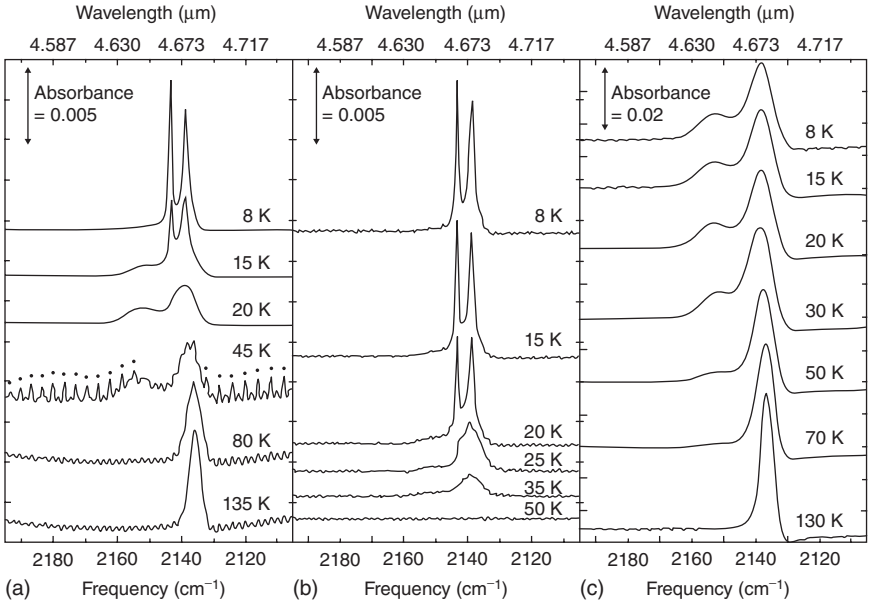

Figure 5.11 RAIR spectra of the ^{12}CO stretch region as a function of the annealing temperature for CO (a) adsorbed on p-ASW, (b) adsorbed on c-ASW, and (c) co-adsorbed with H_2O at 8 K. Features marked with an asterisk in the 45 K spectrum of (a) are due to gas-phase CO transitions, resulting from contamination of the dry air during purging of the IR optics. (Reproduced from [105], copyright 2003 © permission from Springer.)

conditions, the authors offered a detailed kinetic model of the TPD behavior in the CO–H_2O system (Figure 5.10b [105]. Most kinetic parameters in the model were fixed by independent experiments such that there were only three unknown rate parameters that required optimization to accurately reproduce the experimental data in Figure 5.10a. Formerly, astronomical desorption of CO was considered to occur as a single event at around 20 K under realistic heating rates. This new model, incorporating morphological behavior of the H_2O ice substrate, clearly indicates multiple desorption events. A significant fraction of the CO is trapped by the p-ASW to c-ASW transformation and remains in the ice matrix until the c-ASW to c-Ice phase transition.

Of course, in addressing astronomical ices, it is necessary to consider a wider range of potential species as being present in the solid state. While detailed TPD and IR studies on the quality of the CO/H_2O work reported above are desirable, a simpler interpretation suitable for simulations is required. Again, TPD experiments hinted at a relatively simple and concise global interpretation (Figure 5.13) [107, 108].

(i) Molecules that hydrogen-bond strongly to H_2O ice are retained on the ice surface until both species co-desorb at around 160 K (under laboratory conditions).

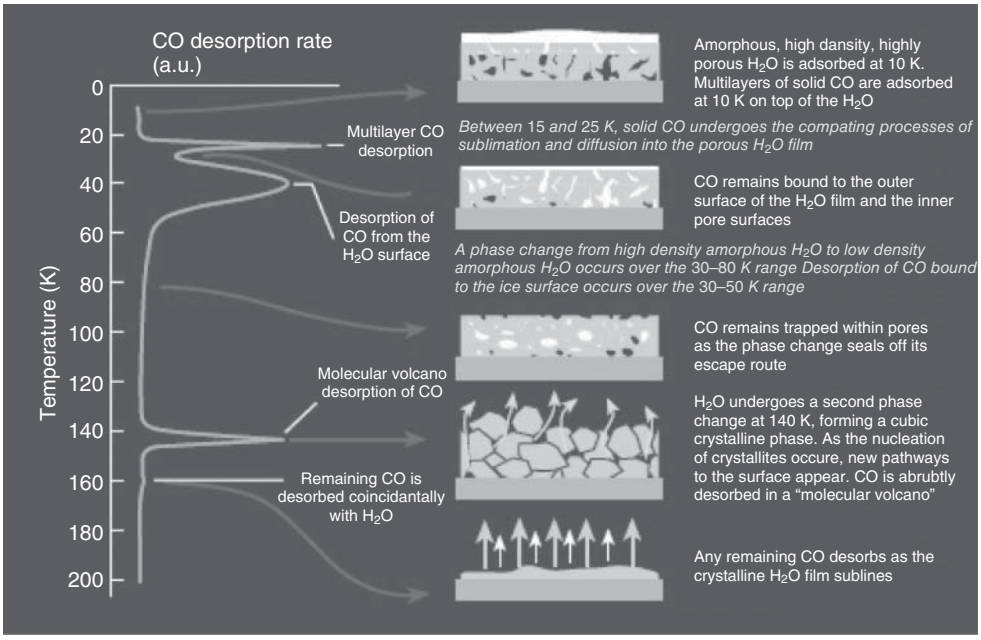

Figure 5.12 Cartoon depicting the adsorption, diffusion, and desorption behavior of CO on H_2O ice under laboratory "pseudo-interstellar" conditions. (Reproduced with permission from Fraser *et al.* [106].)

(ii) Molecules with low surface mobility will not penetrate the pores in p-ASW and, if co-deposited with a growing ice film, will desorb only when c-ASW crystallizes at 140 K and I_c desorbs at 160 K, or, if deposited on top of an ice film, will exhibit a simple molecular desorption reflecting the nature of the solid film produced.
(iii) Molecules with high surface mobility will exhibit CO-like behavior.
(iv) Refractory materials will tend to remain adsorbed on the grain until the grain itself is destroyed.

While not as quantitative as the studies of the $CO-H_2O$ system, this simple interpretation is open to wider implementation. Indeed, the second paper of this pair [108] has expertly illustrated the consequence of incorporating these ideas in to astronomical simulations. Of course, such a simplistic global TPD model of icy grain mantles is but a first step. There are today a number of groups engaged in high-quality TPD studies of model interstellar ices seeking to more fully understanding simple binary, ternary, and quaternary model of these complex icy grain systems.

Water ice morphology plays a crucial role in driving the thermal desorption behavior of water-based ice systems at astronomical temperatures. While a simple interpretation of that role is available, much remains to be done. In particular, the current generation of TPD experiments do not yet address the issue of the reactive

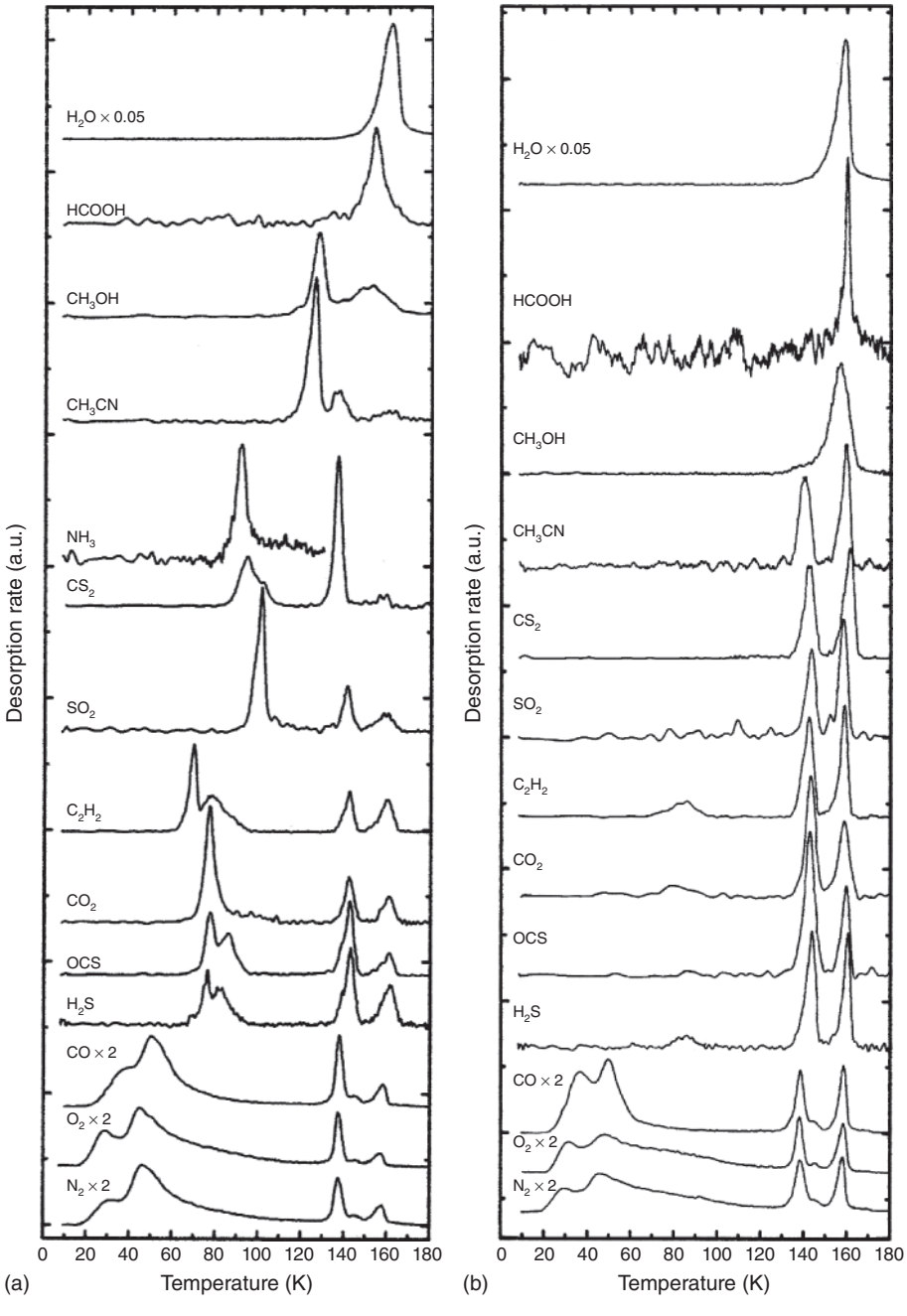

Figure 5.13 TPD profiles of various species (a) deposited on to a H_2O film preadsorbed at 8 K and (b) codeposited in a 5% mixture with H_2O at 8 K. (Reproduced with permission from Collings *et al.* [107].)

growth of the H_2O ice film. Do such films exhibit the same morphological behavior as ballistically deposited H_2O films? Simulations by Cuppen and coworkers [109] suggest that similar scale porosity may arise from reactive accretion of H_2O ice to that observed in ballistic deposition simulations. However, this observation awaits experimental verification.

5.3.7
ASW Morphology Changes due to Ion and UV Irradiation

It is generally accepted that icy grain mantles in quiescent molecular clouds and in star-forming regions are subjected to cosmic ion and UV photon irradiation (e.g., Refs [101, 110]).

Several experiments have been performed to study the effects of ion and UV photon irradiation on water ice films. Fast ions passing through a molecular solid release energy to the target material. As a consequence, many molecular bonds are broken along the ion track and, in a very short time (1 ps or less) the molecular fragments recombine, giving rise to a rearrangement of the chemical structure. In addition to the alteration of the chemical and lattice structure of the target material, new molecular species (not present before irradiation) are formed. In the case of UV photolysis, the energy is released to the target material through a single photodissociation or photoexcitation event. Also, in this case, new molecular species are formed.

In fact, hydrogen peroxide (H_2O_2) is formed after ion and UV irradiation of water ice at low temperature ($T = 10-80$ K), as is evidenced by the appearance of a new IR band at about 2850 cm^{-1} after irradiation [111–113].

The morphology of water ice also depends on the effects of ion and UV photon irradiation. On the basis of laboratory experiments, it has been shown that polycrystalline ice is converted to amorphous ice after irradiation [114–116]. This effect is clearly shown by a detailed study of the profile of the 3300 cm^{-1} water ice band which strongly depends on the structure of the ice sample. When amorphous ice is irradiated, a modification of the profile of the 3300 cm^{-1} band is also observed [116, 117]. However, based only on the 3300 cm^{-1} band, no definitive conclusions could be drawn on the morphology of amorphous water after irradiation. Ion irradiation also modifies the UV–vis reflectance spectrum of water ice, and this has been attributed to rearrangement processes that affect the physical microstructure of the sample [118].

Furthermore, molecular dynamics simulations, meant to reproduce the effects of cosmic ray bombardment of interstellar ices, have shown that a high-density phase of amorphous ice is obtained after irradiation [119].

Recently, laboratory experiments have been performed to study the morphology of porous water ice after ion and UV irradiation [69, 71, 120, 121]. Different studies have shown that porous ice evolves toward a compact ice after irradiation at low temperature ($T = 15-40$ K). Porous vapor-deposited ice films have been irradiated with different ions (such as H, He, Ar, Ne) with energy in the 80–400 keV range and with 10.2 eV Lyman-alpha photons. The porosity

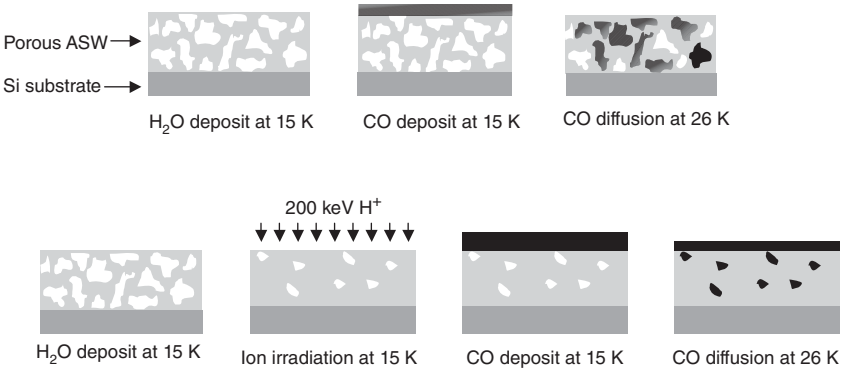

Figure 5.14 Schematic depiction of the experimental procedure followed for compaction studies.

has been characterized by the decrease of the intensity of the OH db infrared feature (discussed in Section 5.3.1), by adsorption of CO or CH_4, and by UV–vis spectroscopy [69, 71, 120, 121].

Figure 5.14 gives a schematic depiction of the experimental procedure followed to study the compaction of water ice by means of CO adsorption [69].

In the first experiment, porous amorphous water was deposited on a bare Si substrate at 15 K. Then, CO was deposited on top of the water ice at 15 K and then the sample was warmed up to 26 K. At this temperature, CO molecules diffuse into the porous ice underneath and an H_2O:CO mixture is obtained. Then the temperature of the sample was raised stepwise up to the water sublimation temperature. Transmission infrared spectra were recorded at each step of this procedure. In the irradiation experiments, the porous water ice sample was irradiated with 200 keV H^+ ions. After irradiation, CO was deposited on top of the irradiated ice at 15 K, and then the sample was warmed up to allow diffusion of CO in the ice underneath. Again, transmission infrared spectra were recorded at each step of this procedure.

This experimental procedure was repeated to test the diffusion of CO in water ice samples irradiated at different ion fluences. The experiments showed that the fraction of CO that diffuses into the water ice underneath decreases as the ion fluence increases. Other experiments have shown that the intensity of the OH db feature decreases as a function of irradiation fluence [69, 71, 120].

On the basis of these experimental results, it is possible to conclude that the porosity of water ice decreases after ion and UV irradiation. Laboratory experiments also show that the surface area of micropores decreases at a faster rate than the pore volume and that the absence of the dangling bond feature does not imply a fully compact ice. It has been suggested that three processes could take place along the ion track to explain these results: (i) coalescence of small pores which produces larger ones, (ii) preferential destruction of smaller pores, and (iii) smoothing of the roughness of the pore walls. All these process reduce the surface of micropores faster than the pore volume [120].

It is generally accepted that interstellar water ice forms because of surface reactions on grain mantles at low temperatures (about 10 K). Thus interstellar water ice is believed to be mainly amorphous [122]. However, we know very little about its morphology and, in particular, its porosity. It has been suggested [123] that the detection of the OH dangling bond feature in interstellar spectra would have given important information on the properties of water ice. This feature was predicted to have a detectable strength and should have been seen with the Infrared Space Observatory (ISO). However, so far, no clear detection of this feature has been reported [124]. In addition, a detailed study [74] of the profile of the interstellar solid CO band based on high signal-to-noise ratio observations toward low-mass star-forming clouds indicates that interstellar water ice is compact.

It has been estimated that the dense-cloud lifetime ranges between 3×10^7 and 5×10^8 years [125]. Assuming $n_0 \sim 10^4$ cm^{-3}, the gas takes $10^9/n_0 \simeq 10^5$ years to condense on grains [126]. Thus, icy grain mantles suffer cosmic ion irradiation for about $10^5 - 10^8$ years. The first estimate refers to the case of icy mantles that sublime as soon as they are formed (which could be the case for volatile species such as CO), while the second estimate refers to the limiting case of icy mantles that survive the whole cloud lifetime (which could be the case for less volatile species such as H_2O).

It is possible that after surface reactions only compact amorphous water ice forms on interstellar grains. Alternatively, it has been suggested that the compact structure of interstellar water ice is caused by cosmic ion irradiation of icy grain mantles [69, 121]. In fact, it has been estimated that porous icy grain mantles in dense molecular clouds are compacted by cosmic ions in $1 - 5 \times 10^7$ years. This time is comparable to or shorter than the estimated ice mantle lifetime [125].

5.4
Solid-State Pathways toward Molecular Complexity in Space

Sergio Ioppolo, Karin I. Öberg, and Harold Linnartz

Today, astrochemists explain the chemical complexity in space as the cumulative outcome of reactions in the gas phase and on icy dust grains. Gas-phase models explain the observed abundances of molecules such as the linear carbon chain radicals C_6H and $HC_{11}N$, but fail to explain the observed abundances of several stable species, for example, water, methanol, and acetonitrile (a closely related molecule for the simplest amino acid glycine) as well as larger compounds such as glycolaldehyde, dimethyl ether, and ethylene glycol. Evidence has been found that these and other complex organic compounds form on icy dust grains that act as catalytic sites for molecule formation. External triggers are provided upon (non)energetic processing, such as irradiation by vacuum UV (VUV) light, interaction with particles (atoms, electrons, and cosmic rays), or heating.

This chapter summarizes the state of the art in laboratory-based interstellar ice chemistry. The focus is on atom addition reactions and VUV-induced processes.

A quantitative characterization of such processes is possible only through dedicated laboratory studies that simulate the harsh conditions in space and explore the dependences on parameters such as temperature, atom or photon flux, and ice morphology. The resulting numbers (physical and chemical constants, e.g., barrier heights and reaction rates) provide information on the molecular processes at work and are needed as input for astrochemical models, in order to bridge the timescales typical for a laboratory setting and those needed to understand the evolutionary stages of the interstellar medium.

The following paragraphs deal with a general introduction to the much-used experimental techniques. The section starts with a general introduction on the used concepts. Two specific experiments – H-atom bombardment and VUV irradiation of interstellar ice analogs – are described in more detail. The experiments are explained within their astronomical settings. For the full picture summarizing all interstellar and circumstellar processes, the reader is referred to excellent text books and reviews, both on the physics and chemistry of the interstellar medium and ice in space (see e.g., Refs [1, 127–130] and references therein).

5.4.1 General Information on Experimental Techniques

Current state-of-the-art experiments on interstellar ice analogs are based on ultra-high vacuum (UHV) ($\approx 10^{-10}$ mbar or lower) surface techniques. Under such vacuum conditions, the buildup of ice contaminations from background gas is slow (<1 monolayer (ML) per hour). Consequently, the deposited ices are minimally contaminated, and this allows studying ices with ML precision. Ices are typically grown on a cryogenically cooled surface, with the substrate holder mounted on the tip of the cold head of a closed-cycle He cryostat. The minimum temperature depends on the employed cryostat as well as on the details of the substrate and substrate holder. Most contemporary experiments have a minimum temperature of ≈10 K, a value on the lower side for interstellar ice analogs, but sustained temperatures down to 4 K can be realized. The temperature is controlled through resistive heating, with access to values as high as several hundreds of kelvins.

In situ deposition of ices through condensation of volatiles admitted into the vacuum chamber at specific pressures and for a specific period of time enables control of ice thickness, ice mixing ratio, and porosity. Experiments have shown that the ice structure strongly depends on the deposition angle, with more compact ices forming from deposition along the surface angle and increasingly porous ices forming from depositions at smaller angles. A special case is diffusive deposition, where the molecular beam is directed away from the substrate to promote depositions at random angles. The final ice thickness and morphology can be estimated from the experimental conditions and checked in different ways; laser interference patterns and infrared (IR) spectroscopy of ice surface versus bulk modes, for example, the strength of the dangling OH feature in H_2O ice, offer *in situ* measurements, and mass spectrometry can be used as an indirect tool exploiting the

fact that trapping efficiencies of volatiles in less volatile ices increase with porosity. For a recent overview of laser interferometry techniques, see Bossa *et al.* [131]. The nature of the substrate varies between different research groups and experiments depending on the object of the study and the employed analysis methods. Silicate and graphite surfaces most closely resemble the expected composition of interstellar grains but have lower transmission and reflectance compared to many other materials, which limits the analysis methods. Such surfaces are usually employed to study ices in the (sub-)ML regime. Both surfaces are also chemically active, which complicates the analysis. Gold and other noble metals are chemically inert and highly reflective, enabling techniques based on reflection spectroscopy. Metal surfaces are often used to study processes that occur in the bulk of the ice. Any process that depends on the characteristics of the metal surface itself (e.g., the release of secondary electrons during UV irradiation) is obviously not relevant to interstellar environments. The surface normally matters only for very thin ices, as here the interaction between surface and ice is directly involved. For typical interstellar ices comprising tens of MLs, it is generally assumed that the influence of the substrate can be neglected. Glass windows constitute a third family of common substrates because of the possibility of transmission spectroscopy. There are, however, a limited set of windows that survive the rapid cooling and heating cycles needed for many ice experiments, and most windows experience some clouding when exposed to UV light for long periods.

The methods that are used to investigate reactions in interstellar ice analogs can be roughly divided in two groups, depending on analysis technique and thickness regime: (sub-)ML versus multilayer. In the first regime, the reactants and products can be probed mass spectrometrically. The surface is initially exposed to a small quantity of reactants, after which a temperature-programmed desorption (TPD) experiment is performed. In such an experiment, an ice sample is heated linearly, typically with a rate of $0.1-10\ \mathrm{K\,min^{-1}}$ [107, 132, 133]. The desorbing species are recorded as a function of temperature using a quadrupole mass spectrometer (QMS). Different initial exposures (with atoms, radicals, and molecules) and temperatures are probed to obtain information on, for instance, the reaction order. This technique is very sensitive and permits sub-ML exposure. Furthermore, it allows the study of reaction products that do not remain on the surface or form an ice, like the formation of H_2 from H atoms. The method, however, suffers from several disadvantages: the products cannot be probed *in situ*; additional reactions during the heat-up to desorption cannot be excluded; quantifying the desorbing species is not straightforward; some of the interesting species have equal, that is, undistinguishable masses; and a TPD experiment is possible only through evaporation, that is, destruction of the ice. The second method is to grow an ice of several MLs while recording transmission or reflection-absorption infrared spectra (RAIRS) e.g., upon irradiation or particle bombardment. For this, the IR beam is guided in the transmission/reflection mode through the ice. In this way, the reactants and products are probed *in situ* at the time and temperature of interest, which is the main advantage of this technique. Transmission

spectra are easier to interpret because absorption band strengths can be used directly, but RAIRS is more sensitive as the effective path length through the ice is longer. Quantifying the formed product, however, is straightforward only if the RAIRS is calibrated with an independent method. IR band intensities of ices can be calibrated using laser interference techniques to derive absorption coefficients which can subsequently be used together to derive ice thicknesses in a range of experiments. These absorption coefficients are tabulated for many common ices in the literature. A major complication is that many ice bands are sensitive to the local environment and an absorption coefficient derived for a pure crystalline ice is not *a priori* accurate for mixed ices or even amorphous and/or porous pure ices. When this technique is used to derive absolute ice abundances, great care must be taken to calibrate it for different kinds of ices. If well calibrated, spectroscopic techniques are very powerful tools, since they provide detailed information on the changes of ice composition and restructuring during processing and thus can be used to probe all kinds of ice processes as they occur, obtaining detailed kinetic information. The main disadvantages are that not all species can be detected in this way (e.g., when a species lacks a dipole moment) and that the sensitivity is inferior to that of the TPD technique. The RAIRS detection technique is therefore often complimented by TPD, as it is possible to perform both methods simultaneously. A good example of this approach is available from Ref. [134].

In the following sections, several examples of recent experiments using these methods are discussed. First, hydrogenation reactions in ice are discussed that take place in radiation-shielded regions in space, such as dark interstellar clouds [135]. Then UV photoprocessed ices are described that are important in different regions in space, at cloud edges, that is, in classical PDRs (photon-dominated regions) or in dense clouds where the interstellar radiation field is dominated by cosmic-ray-induced Lyman-α radiation and where the UV field is enhanced by orders of magnitude once a new star is born [ref. [136] – i.e. based on thesis Oberg]. The focus is on experimental details, and these are largely biased by recent and ongoing work in the Sackler Laboratory for Astrophysics in Leiden, the Netherlands (www.laboratory-astrophysics.eu).

5.4.2 Atom Bombardment

5.4.2.1 Introduction

Atom addition surface reactions are particularly important in those regions of the interstellar medium that are shielded from external radiation, that is, dark interstellar clouds that gravitationally collapse and in which new stars and planets are born. These are the densest and coldest regions in space, and consequently it is expected that here highly volatile species such as N_2, O_2, and CO freeze-out onto dust grains. In 1982, Tielens and Hagen [137] introduced an extended gas–grain model in which water ice – the dominant solid state species – is produced by sequential hydrogenation (i.e., H-atom addition)

of O-containing ices (O, O_2, and O_3). Since hydrogen is the most abundant component in the interstellar medium, this first stage of grain surface chemistry results in the formation of a polar (water-rich) ice. In the next phase, along the gravitational collapse, the density in the molecular cloud increases and CO freezes-out on top of the grains, forming an apolar (water-poor) ice layer on top of the polar one. Subsequent hydrogenation leads to the formation of formaldehyde and methanol. The proposed astrochemical surface reaction networks (see e.g., Wakelam *et al.* [138]) have been so far largely based on chemical intuition and gas-phase equivalent reaction paths. For about a decade now, highly specialized experimental techniques have become available to study these reactions under fully controlled laboratory conditions, boosting our knowledge of chemical processes taking place in ice. In this period, particularly four specific surface reaction schemes have been studied in much detail: (i) the formation of hydrogen peroxide and water upon hydrogenation (deuteration) of oxygen-containing ice, that is, O + H, O_2 + H, and O_3 + H [139–147]; (ii) the formation of formaldehyde and methanol upon sequential hydrogenation of CO ice [148–151]; (iii) the formation of carbon dioxide, mainly following CO + OH and CO + O [152–159]; and (iv) the formation of hydroxylamine NH_2OH upon NO hydrogenation [160, 161]. Other studies report the hydrogenation and oxidation/nitrogenation of other precursor species such as NO and NO_2 [162, 163] or resulting in the formation of ammonia (NH_3) [164–166], formic acid (HCOOH) [167], and ethanol (CH_3CH_2OH) [168]. As the focus in this book is specifically on laboratory techniques, only the ($O/O_2/O_3$ + H) channel will be described to illustrate the experimental concepts. This method follows a bottom-up approach which investigates selected surface reactions for astronomically relevant temperatures. Fundamental and molecule-specific parameters – reaction rates and diffusion barriers – are found that are needed as input for astrochemical models, pushing the experimental results beyond typical laboratory timescales. These laboratory data also provide the results against which theoretical calculations have to be tested in order to provide information on mechanisms at work such as diffusion, reaction, segregation, and desorption. A typical experiment needed to realize this work is described in the next section.

5.4.2.2 **Experimental Setup**

Several setups worldwide are capable of studying atom (and radical) addition reactions in interstellar ice analogs under UHV conditions. See also Ref. [169]. These setups typically comprise one or two atom beam lines suited to study hydrogenation, and simultaneous or sequential atom (H/D, O, OH, and N) addition reactions. The principal procedures used in these setups are rather similar and largely based on RAIRS and TPD, as discussed above. Here, SURFace REaction SImulation DEvice (SURFRESIDE^2) is described, a recently extended setup in Leiden (NL), which in many respects is representative for the methods and techniques used in other laboratories. Full details are available from Ioppolo *et al.* [158].

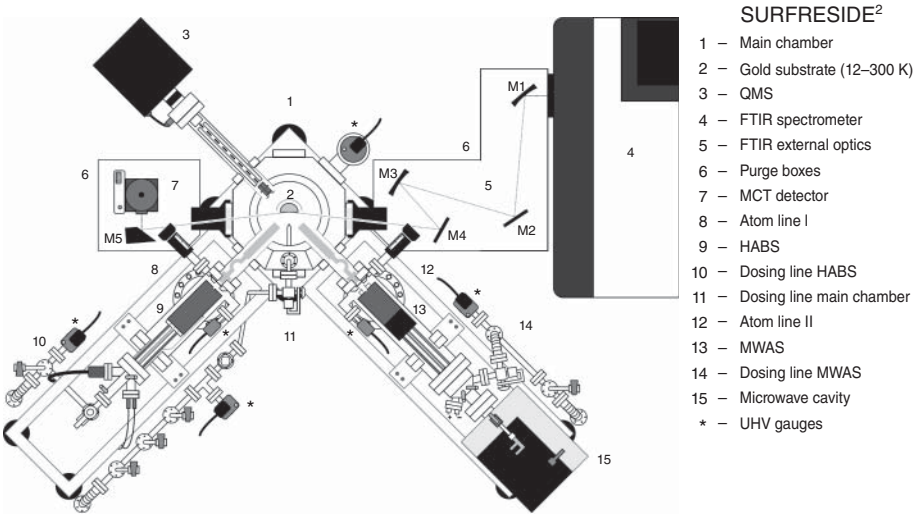

Figure 5.15 Schematic top view of SURFRESIDE^2. (Reproduced from [158], copyright 2013 © permission from American Institute of Physics.)

The central part of the SURFace Reaction Simulation Device (Figure 5.15) is a UHV chamber (10^{-11} mbar) on which two atom beam lines are mounted that aim at an optically flat, gold-coated cupper substrate (2.5 cm × 2.5 cm) placed at the center of the main chamber and mounted on the tip of a cold head with temperatures accessible between 12 and 300 K using resistive heating. Ices are grown using two all-metal, high-vacuum, stainless steel dosing lines, allowing different gasses to be deposited separately or simultaneously onto the gold substrate. This surface is not representative of an interstellar dust grain, but offers a chemically inert and effective heat conductor that is highly reflective in the IR region. Moreover, ice thicknesses in space and in the laboratory are typically tens of ML thick, which substantially reduces the role of the substrate on which the ice has been grown. Indeed, the use of other surfaces (such as highly oriented pyrolytic graphite (HOPG)) does not show different processes as long as these take place in the upper layers of the bulk ice. The deposition proceeds with a controllable flow which allows growing ices with ML precision.

The ices are monitored both spectroscopically by RAIRS using the light of a Fourier transform infrared (FTIR) spectrometer (4000 – 700 cm^{-1}, ≈ 0.5 – 4 cm^{-1} resolution) and mass spectrometrically by TPD using a QMS that is mounted behind the substrate and opposite to one of the two atom beam lines. The FTIR path is purged by dry air to minimize atmospheric pollution outside the vacuum system. Two different kinds of experiments can be performed with a system like SURFRESIDE^2. During *predeposition*, ices are first deposited and subsequently exposed to atoms or radicals produced by the atom beam lines. Newly formed stable species in the ice are monitored with respect to a reference spectrum of the

initially deposited ice using RAIR difference spectroscopy. During *co-deposition*, molecules and atoms/radicals are deposited simultaneously onto the substrate. By changing the molecule/atom ratio, different reaction stages in the selected chemical network can be simulated. In this case, RAIR difference spectra are obtained with respect to a bare gold substrate spectrum. After (co)deposition, a TPD can be performed by linearly heating the sample until the ice is fully desorbed. The thermal desorption is monitored indirectly by using RAIRS. Alternatively, when the sample is rotated to face the QMS, the latter can be used to monitor the evaporating species, and to constrain the RAIRS data. As discussed in the previous section, the integrated absorbance of the IR bands is commonly used to derive the column densities of selected species as long as the corresponding band strengths are known and applicable.

SURFRESIDE[2] uses two different and commercially available atom sources: a thermal cracking source (HABS – Hydrogen Atom Beam Source; [170]), and a microwave discharge atom source (MWAS – MicroWave Atom Source; [171]). The first one generates H and D atoms, while the second one can also produce N and O atoms and radicals such as OH. Before impacting on the ice, the atoms are first cooled to room temperature in a nose-shaped quartz pipe that is designed to quench excited species by collisions with the walls. In this way, "hot" species do not reach the ice. The relatively high remaining temperature of 300 K does not affect the reaction efficiency, as species are thermalized instantaneously upon impact on the ice surface, that is, before they can diffuse and react following a Langmuir–Hinshelwood mechanism. However, for instance, H collisions cause atoms to recombine to H_2, and as a consequence determining the impacting fluxes accurately is far from trivial. Calibration methods used so far are based on reaction dynamical constraints, involving the formation yield of final products in barrierless surface reactions, and have been described in detail by Fuchs *et al.* [151] and Ioppolo *et al.* [158]. Fluxes can be varied by changing the pressure and power settings. Typical fluxes amount to $10^{13}-10^{14}$ H atoms cm^{-2} s^{-1} (HABS) and $10^{10}-10^{12}$ N and O atoms cm^{-2} s^{-1} (MWAS). These absolute flux values have errors of the order of 30%. These uncertainties are large, but absolute flux values are only needed to interpret reaction rates quantitatively. The relative errors are generally much lower (≈10%), and this still allows comparison of branching ratios. It should be noted that two different types of experiments can be performed. In a predeposition experiment, an ice is prepared under fully controlled conditions (i.e., multilayered using different (isotopic) components that are subsequently bombarded). This generally limits the reactions to the surface layers depending on the penetration depths into the ice. In a co-deposition experiment, ice molecules and atoms or radicals are deposited simultaneously. This is generally closer to the processes taking place in space (although not exclusively), and this allows changing the mixing ratios during deposition to monitor reactions as a function of atom/molecule abundances [144].

5.4.3 $O/O_2/O_3 + H$

Water is the main constituent of interstellar and circumstellar ices. In dense, cold regions of the interstellar medium, gas-phase formation routes for H_2O and subsequent freeze-out mechanisms cannot explain the large ice abundances observed. It is therefore expected that water forms in the solid state. As stated before, this idea was first proposed by Tielens and Hagen in 1982, who suggested that water forms upon ongoing H-atom additions to atomic oxygen, molecular oxygen, and ozone on icy dust surfaces. It is only in the past few years, starting in 2008, that the first fully controlled laboratory experiments have been performed [139–141]. The O + H/O + D channel was extensively studied by Dulieu and coworkers [143] using amorphous water ice as a substrate. Water formation at low temperatures by surface O_2 hydrogenation has been studied in depth by the research groups of Watanabe (Hokkaido) and Linnartz (Leiden). Miyauchi *et al.* [139] presented results for O_2 + H for 10 K, and Ioppolo *et al.* [140] for temperatures covering 12–28 K. In both studies – bombardment of a predeposited O_2 ice with H (D)atoms – the formation of water ice via hydrogen peroxide was proved to be effective by RAIR techniques which permitted the derivation of reaction rates, also for the deuterated species. Moreover, Ioppolo *et al.* also showed that these rates were surprisingly independent of the studied temperatures.

In a follow-up study [144], it was confirmed that the H_2O_2 and H_2O formation rates are temperature and thickness independent, whereas the final total yield increases with increasing temperature and thickness. This can be explained by the competition between the reaction of H atoms with O_2 molecules (temperature independent) and hydrogen diffusion into the ice (temperature dependent): H atoms penetrate into the bulk of the ice with a penetration depth that is temperature dependent, and, once trapped in the ice, reaction is likely to occur. Consequently, the O_2 ice is mainly hydrogenated bottom-up.

Efficient deuterium diffusion and reaction in O_2 ice has also been indirectly observed mass spectrometrically by Matar *et al.* [141]. Ioppolo and coworkers [144] also concluded that the reaction scheme initially proposed by Tielens and Hagen [137] could not be fully complete, as clear evidence was found in the RAIR spectra for O_3 formation upon hydrogenation of pure O_2 ice. This observation was explained by Cuppen *et al.* [145], who performed co-deposition experiments in which the H/O_2 ratio was varied in order to trace each step of the reaction scheme, selectively. This experiment is illustrated in Figure 5.16.

The ratio between the deposited H atoms and O_2 molecules determines the hydrogenation grade. Four H atoms are needed to convert O_2 into two H_2O molecules. The four panels show decreasing H/O_2 ratios from top (100) to bottom (1). The top spectrum is clearly dominated by broad bands due to water and hydrogen peroxide, which are the final products of the reaction scheme as expected in a fully hydrogen-dominated regime. In the oxygen-dominated regime (bottom spectrum), that is, the domain where full hydrogenation cannot be reached anymore by a continuous supply of O_2, intermediate species – HO_2,

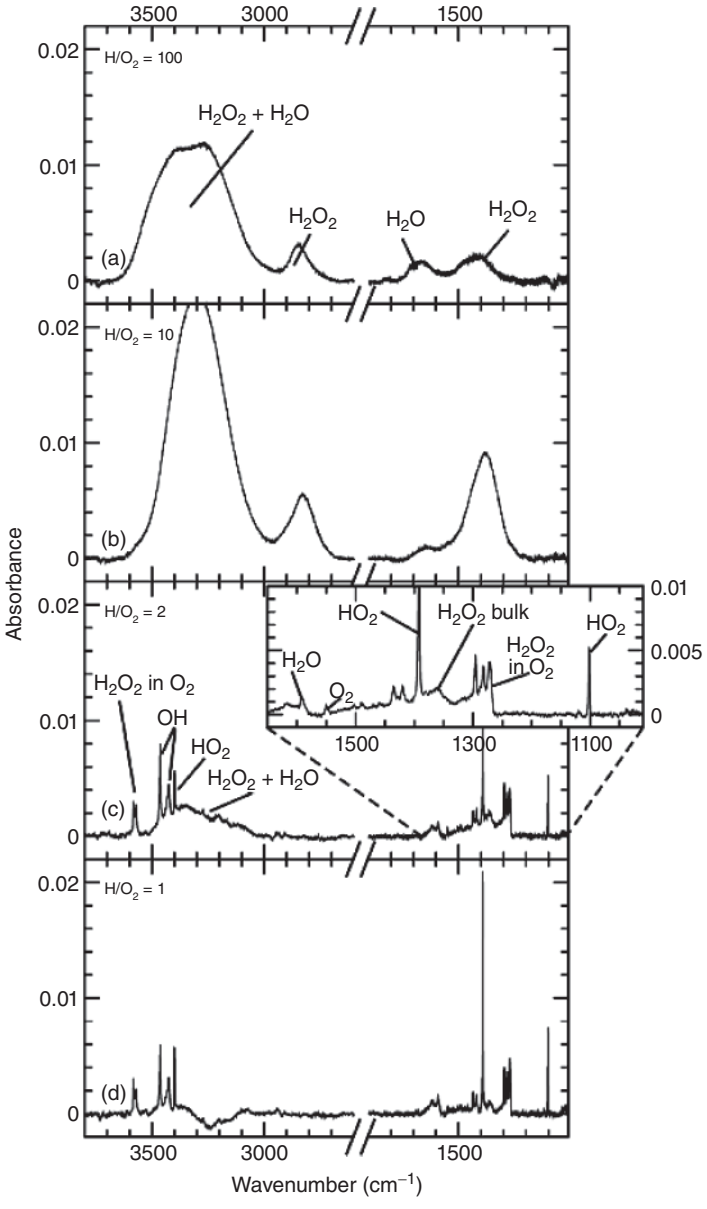

Figure 5.16 RAIR spectra of H and O_2 co-deposition experiments performed at 20 K and for different H/O_2 ratios of (a) 100, (b) 10, (c) 2, and (d) 1. The H-atom flux is 2.5×10^{13} atoms cm^{-2} s^{-1}, and is kept the same for all the experiments. (Reproduced from [145], copyright 2011 © permission from Royal Society of Chemistry.)

H_2O_2, and OH – become visible. The first intermediate (HO_2) is clearly visible in the $H/O_2 = 1$ experiment. Reducing the O_2 flow by a factor of 2 causes the HO_2 signal to decrease whereas H_2O_2 and OH signals appear to increase somewhat. A further reduction ($H/O_2 = 10$) results in broad bulk water bands, whereas the intermediate species are not visible anymore. A more complex and complete reaction scheme was derived by tracing the abundance of each single species involved in the reaction scheme versus the H-atom fluence for different temperatures and H/O_2 ratios. This way, Cuppen *et al.* [145] explained, for instance, the presence of ozone in the ice through the formation of atomic oxygen by the reactions $HO_2 + H \rightarrow H_2O + O$, which was not previously included in the scheme, and the subsequent reaction $O + O_2 \rightarrow O_3$.

The resulting reaction channels derived from all these experiments are indicated in the right part of Figure 5.17. It extends the diagram initially proposed by Tielens and Hagen [137] with a number of extra channels, including a cross channel between O_2 hydrogenation and O_3 formation, consistent with the earlier mentioned observation of ozone. Finally, also the hydrogenation of ozone ($O_3 + H$) was studied in Ref. [142, 146], showing H_2O and H_2O_2 formation (as well as their deuterated equivalents). It was found that this reaction channel interacts with the O and O_2 hydrogenation reaction scheme. Also this reaction

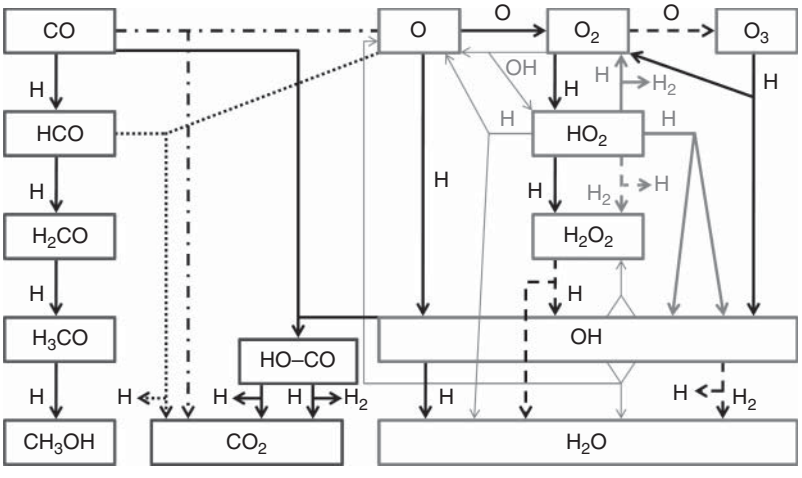

Figure 5.17 (Right) A schematic representation of the reaction network involving $O/O_2/O_3$ hydrogenation as discussed in the text and shown in Figure 5.16 for different co-deposition experiments. Other reactions, not discussed in the text and available from the listed references are shown as well. (Left) The hydrogenation of CO which results in the formation of formaldehyde (H_2CO) and methanol (CH_3OH). The latter species is shown in the next section to be an excellent starting point in the UV formation of more complex organic species. When bombarding a mixed ice, comprising both CO and O_2, also CO_2 is formed (middle panel) through de-hydrogenation of the HO-CO reactive intermediate. This shows that the processes at play in a binary mixture are already quite complex. (Reproduced from [144], copyright 2010 © permission from Royal Society of Chemistry.)

scheme is shown in Figure 5.17. In none of the experiments, the impact of H_2 was found to result in reaction products at a detectable level. However, Oba *et al.* [172] showed that the reaction OH + H_2 proceeds through quantum tunneling. In a recent study, Lamberts *et al.* [147] used continuous-time random-walk Monte Carlo simulations to disentangle the different processes that are shown in Figure 5.17. Simulations are here used to reproduce the experimental findings for two different temperatures – 15 and 25 K – and the two aforementioned different deposition methods. This study confirms that radical diffusion plays an important role in the full network and shows that the key pathways for the molecular oxygen channel are determined by the $O_2 + H, HO_2 + H$, OH + OH, $H_2O_2 + H$, and OH + H reactions. The relatively high hydrogen peroxide abundance observed in the experiments is explained by a slow destruction mechanism.

Meanwhile, also from an astronomical point of view, much progress has been made. The WISH (water in space with Hershel) key program of the space telescope Herschel has recently made observations of cold gas-phase water and species related to its chemistry in prestellar cores and young stellar objects at different evolutionary stages. Hot gas containing O(I), O_2, cold H_2O, HO_2, and H_2O_2, as well as OH, OH^+, H_2O^+, and H_3O^+, has been identified in the interstellar medium. The detection of these molecules is consistent with the solid-state network that has been derived in the laboratory experiments, but a further discussion falls outside the scope of this book. The interested reader is referred to van Dishoeck *et al.* [173].

5.4.4 UV Photoprocessing

5.4.4.1 Introduction

When an ice is exposed to UV irradiation, the UV photons can interact directly with the ice through excitations of electronic states, or indirectly through interactions with secondary electrons produced at the ice–substrate interface. The interaction of electrons with ices has been covered in detail by Arumainayagam *et al.* [174] and will not be further discussed here. Depending on whether the photon is absorbed into a non-dissociative, a pre-dissociative, or a dissociative state, it may be the starting point of ice reorganization, desorption, or chemistry. In the next subsection, we describe the experimental approaches that are used to measure the efficiency of these different processes under different ice and radiation conditions. Key experimental results on ice UV photodesorption and photochemistry are presented.

5.4.4.2 Radiation-Induced Dynamics and Chemistry in Ices

The interstellar radiation field results in a background UV field of roughly 10^8 photons cm^{-2} s^{-1}. The UV field is enhanced by orders of magnitude close to young stellar objects, increasing the rates of UV-induced ice processes. The external UV field is severely attenuated in dense cloud cores, in prestellar cores, in protostellar envelopes, and in disk mid-planes. In these regions, the primary source of

UV photons is hydrogen excited cosmic rays. Absorption of UV radiation can excite nondissociative and dissociative states in interstellar ices, depending on the photon energy and the ice composition. Excitation of nondissociative electronic states primarily affects the ice through the subsequent cascade into vibrationally, torsionally, and translationally excited states as the molecule de-excites into the electronic ground state. These excitations can cause rearrangements within the ice, which result in either changes in the ice structure or desorption of an ice surface molecule, depending on the location of the excited molecule within the ice. Absorptions into dissociative electronic states can have similar effects on the ice, but can also open up additional pathways because of the production of radicals which may be significantly excited or "hot." Depending on the ice characteristics and the ice location of the dissociation event, the produced radicals may desorb or diffuse, or become frozen into the ice. If diffusion is possible, the radicals can combine into new kinds of molecules, driving complex ice chemistry.

The ultimate goal of astrochemical experiments and theory on the VUV interaction with ices is to characterize each potential UV-induced ice process and to determine its probability when a particular ice is exposed to a specific radiation field. This is a massive undertaking because of the multitude of potential pathways in UV-irradiated, astrochemically relevant ice mixtures, including eventual dependence on UV frequency, flux and fluence, exact ice morphology, thickness, composition, and temperature. Several different strategies have been employed to approach this undertaking.

Early experiments, pioneered by Greenberg and Allamandola [175], typically focused on the exploration of the evolution of ice mixtures, reminiscent of the best models of interstellar ice mixtures, semiquantitatively. These experiments revealed that complex molecules can form in interstellar ice analogs exposed to UV, and this discovery has motivated many of the ice chemistry studies that were performed in the following decades, with two key papers published in 2002 [176, 177]. The relevance of some of the results to interstellar conditions has been questioned however, because of the large UV fluxes and ice thicknesses of these experiments and a lack of quantification of how these characteristics affect the results. The high fluxes and ice thicknesses were mandated by a combination of relatively poor vacuum (high-vacuum conditions instead of commonly employed UHV in modern setups) and a desire to produce sufficient amount of very complex material for extraction following completion of the experiment.

An orthogonal approach, applied in most contemporary experiments, is to focus on simpler ice systems and to pursue constraints on individual processes or families of processes at some detail. Such experiments are not intended to mimic interstellar conditions exactly but rather to derive conversion factors, rates, cross sections, and energy barriers that can be incorporated into astrochemical models. The following sections focus on such quantitative and/or mechanistic studies.

5.4.4.3 **Experiment**

Current UV ice experiments are generally carried out under UHV conditions. Typical pressures are 10^{-10} mbar or lower. As described in the previous section,

this prevents largely pollution with background gases and enables the study of thin (layered) ices (down to ML regime). This is clearly different from experiments in regular high-vacuum chambers, which are performed with ices thousands of MLs thick.

In typical astronomical UV photolysis experiments, the deposited ices are exposed to UV radiation from broadband UV lamps or from monochromatic sources such as atomic lamps, tunable lasers, and synchrotrons. The frequency specificity is therefore highly variable between different experiments, and in the case of broadband lamps (the most commonly used UV source) the exact UV profile is not always well constrained because it depends on the lamp conditions, in terms of gas pressure, plasma generation techniques, and power, as well as gas mixture ratios. This has been extensively described by Chen *et al.* [178] for microwave-driven H_2 lamps that have been used for decades by many groups to mimic the Lyman-α (121.6 nm/10.2 eV) emission in space. For experiments aimed at obtaining quantitative photolysis rates, the absolute lamp calibration as well as fluctuation levels are crucial. Absolute calibrations are typically obtained using photodiodes or different actiometry techniques, and relative calibrations can be obtained through continuous monitoring using the photoelectric effect in a thin metal wire placed in front of the lamp and thin enough not to deflect a significant amount of radiation.

Changes in ice composition, abundance, and structure, as well as the nature of desorbing ice fragments during UV irradiation, can be probed through a variety of techniques. RAIRS and TPD were already mentioned. Other techniques use regular IR transmission spectroscopy, Raman spectroscopy, time-of-flight (TOF) mass spectrometry, and quartz balance measurements. Of these, quartz balance measurements provide one of the most fundamental data points, that is, the overall change in ice mass. Mass spectrometry, in general, can be used to measure desorption efficiencies during irradiation of ices. As will be discussed later, a one-to-one conversion of a QMS signal to an absolute rate is far from trivial. Following completion of irradiation, TPD experiments can be carried out to obtain detailed final ice compositions. As stated earlier, in TPD experiments, the substrate is heated up linearly while measuring the desorption rate of different species. The peak desorption rate is directly related to the desorption energy, while the details of the TPD curve depend on the order of the desorption process. When the shape and peak of the TPD is combined with the *m/z* signal, this is a powerful technique to identify minor ice chemistry products.

In Figure 5.18, a schematic drawing of CRYOPAD is shown which is a setup fully devoted to the study of photo-induced solid state processes, namely photodesorption, photodissociation, and photochemistry. As in the case of SURFRESIDE^2, the ice is grown on a 10–15 K cold substrate in a UHV chamber, and the ice constituents are monitored using RAIRS. At other places, also transmission spectroscopy is applied. A standard microwave-driven H_2 discharge lamp is used to irradiate the ice with VUV light, centered around Lyman-α but also with a broad component in the 160 nm domain. Typical fluxes are $\approx 10^{14}$ photons cm^{-2} s^{-1}. This value comes with much uncertainty (see also

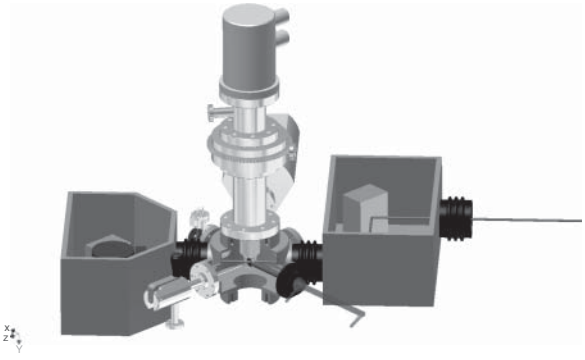

Figure 5.18 A systematic view of CRYOgenic Photoproduct Analysis Device (CRYOPAD). The ice is grown on a gold plate connected to the cold tip of a cryostat. IR light from an FTIR crosses the ice (either as RAIRS or in transmission). The ice sample is irradiated by a microwave-driven H_2 discharge lamp. On the backside of the setup, the QMS can be seen.

Chen *et al.* [178]). Moreover, the UV beam is generally not perfectly well defined, and it can therefore be challenging to calculate the amount of flux that the ice is exposed to at a certain distance from the radiation center, as the ice substrate is typically large compared to the UV beam size.

5.4.4.4 UV Photodesorption Experiments and Key Results

UV ice photodesorption is the process through which a molecular excitation event following the absorption of a UV photon results in desorption of a molecule or molecular fragment from the ice. This process can proceed directly, that is, desorption of the same molecule that absorbed the photon, or indirectly when a different molecule than the excited one is desorbed. Depending on the photon energy and ice species involved, the initial excitation step is dissociative or nondissociative, which will have a large impact on the photodesorption mechanism. UV-induced ice photodesorption has been investigated in detail in the laboratory for three ices of astrochemical interest, namely H_2O [179–181], CO_2 [182–185], and CO [178, 182, 185–189], and to a minor degree for another few species, for example, CH_3OH [134], N_2 [182, 190], and O_2 [190, 191]. Of these, CO has been extensively investigated using frequency-resolved UV radiation [188, 189] and thus is the ice with the strongest experimental constraints on both its efficiency and underlying molecular mechanism.

There are several strategies in the literature to measure photodesorption rates. Quartz balance measurements directly probe the loss of ice mass and offer an efficient tool to measure the total ice photodesorption rate. Such measurements do not provide any information about the nature of the desorbed species, and the technique is therefore frequently used in conjunction with mass spectrometry [192]. Another approach used by several groups is a combination of IR spectroscopy and mass spectrometry [188, 191]. When the absorption coefficients are well known, IR spectroscopy is a powerful tool to measure ice destruction

rates of different species. To separate ice destruction into ice dissociation and desorption is often challenging, however. Furthermore, absorption coefficients are generally known only for transmission spectroscopy, and several measurements were carried out using RAIRS, where the absorption coefficients were experiment- and ice-thickness-specific with uncertainties as large as a factor of 2. This should be noted when comparing results from different groups. Mass spectrometric signals are also difficult to convert into absolute desorption rates (see Zhen and Linnartz, [191]) and are therefore typically used to identify desorption products that are especially important for dissociative desorption and to measure relative photodesorption rates when the experimental conditions are varied.

Non-dissociative Photodesorption A few ices of astrochemical interest present nondissociative transitions in the VUV, including CO which is the most abundant molecule (after H_2) in most astrophysical environments and with a very low accretion temperature [132, 193]. Broadband UV CO ice photodesorption has been investigated by Öberg *et al.* [181, 186], and Munoz-Caro *et al.* [187] using H_2 discharge lamps as discussed above. The UV sources used in these experiments are expected to be dominated by Lyman-α radiation. Figure 5.19 illustrates the principle of a photodesorption rate experiment. A CO ice is prepared and irradiated, and the decrease in RAIR signal (a) is recorded as function of time, that is, fluence. As the signal strength can be converted into molecular density and the UV flux is known, this allows the determination of the number of CO molecules desorbed per incident UV photon, as illustrated in (b). Experiments can be performed in full dependence of other parameters, such as ice thickness and temperature, showing that CO desorption is a truly surface process dominated by the top few layers, ranging from two to five ML [178, 181, 187, 194, 195]. The observed inverse temperature dependence (not shown here) is probably due to a more strongly bound and compact CO ice at temperatures close to the CO crystallization threshold, which limits the effective surface. The overall rates yield values between 2×10^{-3} and 4×10^{-2} (at ≈ 15 K) in different experiments. The order of magnitude difference found here is most likely due to the different lamp profiles, though uncertainties in ice thickness measurements and lamp flux calibrations contribute as well.

The CO photodesorption mechanism following absorption of a Lyman-α photon was initially proposed to be due to excitation of vibrational and torsional states of the absorbing molecule causing its desorption if residing in the top ice layer. Recent experiments on CO photodesorption using frequency-resolved UV radiation from the DESIRS beamline at the SOLEIL synchrotron facility has improved the understanding of the involved desorption mechanism substantially (see Refs [188–190]) and also provided more accurate (wavelength-dependent) rates. Fillion [195] and coworkers found that the CO photodesorption profile follows one to one the previously measured absorption spectra for solid CO [194], conclusively demonstrating that CO photodesorption is induced by electronic transition (DIET, desorption induced by electronic transition) in the CO ice itself. The measurements also showed that around Lyman-α the resulting

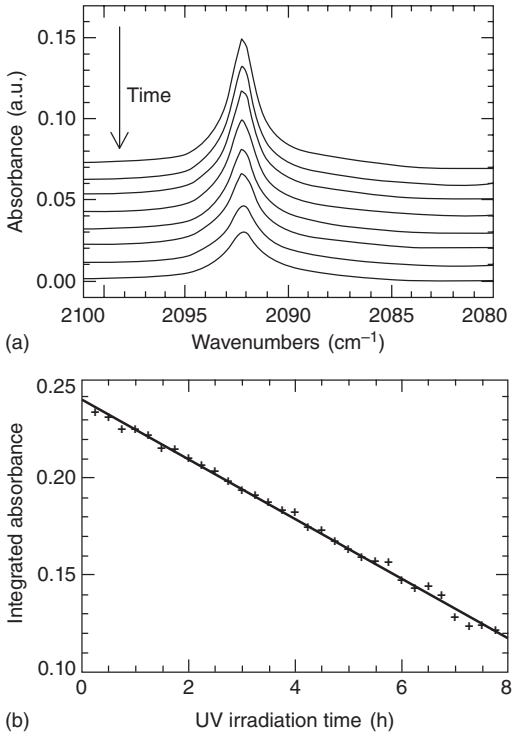

Figure 5.19 (a) Loss of CO ice RAIRS signal as a function of irradiation time (i.e., number of impacting VUV photons). The integrated signal in (b) shows that this ice loss is a zeroth-order process and thus due solely to surface desorption. (Reproduced from [186], copyright 2007 © permission from IOP Publishing.)

photodesorption rate is expected to be low, as CO here barely absorbs any VUV light; that is, for more resonant light, desorption rates increase substantially and therefore the emission pattern of the H_2 lamp needs to be accurately known. This observation is also important for the interstellar medium where different radiation fields are linked to different stages in star and planet formation. Additional measurements on isotopically labeled layered ices further revealed that the excited molecule is not necessarily the one typically desorbed. Rather, the desorption process begins with the excitation of a subsurface molecule, followed by the ejection of a surface molecule [189]. This process is efficiently quenched if the subsurface layer is changed from CO to H_2O. In contrast, it remains efficient if CO is deposited on top of N_2, and vice versa Fayolle *et al.* [190]. In the latter case, it was also found that nondissociative photodesorption can take place indirectly, that is, through excitation of another chemical component; excited CO can induce N_2 desorption, and N_2 excitation can induce CO desorption, typically for wavelengths for which these molecules separately would not desorb at all. This process may be astronomically relevant, as it provides a desorption mechanism for species that normally are expected to stay in the ice.

Dissociative Photodesorption Most molecules have dissociative transitions in the VUV (including CO and N_2, but at higher photon energies than can be reached with a H_2 discharge lamp, that is, that are normally at play in the interstellar medium). Of these, CO_2 and H_2O ice photodesorption have been studied in detail. CO_2 ice photodesorption induced by a H_2 discharge lamp has been investigated by Öberg *et al.* [181] for thin ices (<20 ML) and by Bahr *et al.* [183] for thick ices (300–600 ML). In Ref. [134], RAIRS was applied to quantify the total desorption, while Bahr and coworkers used a quartz balance. In both studies, a mass spectrometer was used to detect the desorption products, which in the case of Öberg *et al.* was CO and a less volatile species that was not picked up efficiently by the QMS. In the thicker ice experiments, CO completely dominated the desorbed species composition. Both sets of experiments showed that CO_2 photodesorption is mainly a dissociative process and that it is active over many ML down into the ice. The dissociative mechanism was further demonstrated by the observed ice chemistry using IR spectroscopy.

Both studies found an increasing rate with ice temperature. The fraction of the desorbed species that is due to CO also increases with temperature.

This can be explained by the thermal evaporation of CO above 25 K and is due to the fact that CO thermally evaporates above 25 K. Therefore, at least in thin ices, all CO produced through CO_2 dissociation will desorb at higher temperatures. Öberg *et al.* [182] also noticed an increasing rate with ice thickness (cf. CO ice photodesorption). At low temperatures ($T < 30$ K), this thickness dependence tapers off after a few MLs, but at high temperatures it does not as long as the investigated ices are on the order of tens of MLs. At all temperatures, there are clearly many more ice layers that are desorption-active for CO_2 compared to CO. At low temperatures ($T < 30$ K), a photodesorption yield of $\approx 2 \times 10^{-3}$ per incident photon was determined in Ref. [181], while Bahr and Baragiola [183] concluded a yield of $6 - 20 \times 10^{-3}$. Very recently, also wavelength-dependent VUV results for CO_2 ice photolysis were reported. The interesting finding here is an indirect DIET process mediated by photoproduced CO [185].

H_2O (D_2O) ice photodesorption has been studied by Öberg *et al.* and Westley *et al.* [179–181]. Both studies find that H_2O photodesorption has a yield between 10^{-3} and 10^{-2} molecules per incident UV photon with an increasing yield for higher ice temperatures. Both studies also find some mass spectrometric signals which suggest that dissociative desorption is important for H_2O. In contrast to Westley, Öberg *et al.* did not find evidence for a fluence delay before the onset of photodesorption. The reason for this discrepancy is unresolved, but may depend on the morphology of the grown ice; if the ice deposited is very compact, an initial dose of radiation may be required to make it more porous, increasing the effective ice surface area and thus the photodesorption yield. Similar to CO_2, a clear dependence on the ice thickness and ice temperature was found by Öberg *et al.*

The dissociative photodesorption process can occur through (i) direct or thermal desorption of the produced dissociation fragments (i.e., CO + O), (ii) desorption of the original molecule following recombination, or (iii) desorption

of a surface molecule that is kicked out by, for example, a non-thermal H atom released in the initial dissociation event. Depending on the ice temperature and structure, these processes can result in a desorption event beginning deep in the ice following the production of volatile dissociation fragments, which explains the different thickness dependence compared to the more surface-focused nondissociative desorption process. Furthermore, thermal evaporation of dissociation fragments, as well as diffusion, will be faster at higher temperatures, explaining the measured increase in photodesorption rates with temperature.

For completeness, it should be noted that H_2O and D_2O photodesorption mechanisms also have been studied theoretically in a number of papers using molecular dynamics and detailed quantum mechanical potentials (see, e.g., Refs [196, 197]). In all studies, they find that H_2O photodesorbs through several different channels, all of which begin with the dissociation of the molecule absorbing the UV photon. The relative importance of dissociation fragment desorption, desorption of recombined molecules, and the kick-out mechanism depends on the depth of ice and its isotopolog. In particular, D_2O photodesorption is a factor of two more efficient than H_2O photodesorption because of more efficient kickout by D than by H atoms.

Dissociative UV photodesorption is directly related to ice photochemistry, as will be discussed later. The dissociation of an existing molecule may result in a desorption event or provide the starting point to form a new ice constituent. This will depend on where in the ice the dissociation takes place and on the diffusion length scale of the formed fragments, that is, whether they can escape the ice before taking part in a chemical reaction or not.

Photodesorption Efficiencies All investigated species have VUV photodesorption yields per incident photon roughly in between 10^{-3} and 10^{-1}. These yields correspond to quantum efficiencies of close to unity for molecules in desorption-active layers. The results of these single experiments on pure ices cannot be directly applied to astrophysical environments. Rather, a series of detailed experiments are required to explore the dependence on ice morphology and specific physical conditions to derive empirical parameterizations. It should be noted, though, that these experimental values are orders of magnitudes higher than used for many years in astrochemical models. Actually, photodesorption was largely ignored for decades, and following the laboratory data that have become available over the last 10 years for non-thermal desorption processes as presented here, astrochemical models are now able to explain much better the relatively high gas-phase abundances of molecules for temperatures well below their accretion temperature. Moreover, recent work hints at a clear correlation between the position of snow lines in protoplanetary disks and photodesorption efficiencies in ice [198, 199]; the efficiency with which ices desorb may determine the efficiency of planet formation in a protoplanetary disk as function of the distance to the new-born star. Finally, photodesorption rates also offer a diagnostic tool to link astronomical observations to the strength of the interstellar radiation field.

5.4.4.5 Photochemistry Experiments

Ice photochemistry models rely on experimental and/or theoretical constraints; on the ice photodissociation efficiency, on the production branching ratio of different radicals following a dissociation event, and on the diffusion rate of the different radicals on the ice surface, in ice pores, and in the bulk of the ice (for ices where bulk diffusion occurs) and its dependence on the ice morphology and temperature. Optimally, this work should therefore result in ice-system-dependent dissociation cross sections, branching ratios, and diffusion barriers, with the ultimate goal of extrapolating the experimental results to astrophysical environments, where a range of ice compositions and morphologies as well as radiation and temperature profiles are present. This has yet to be realized, but recent experiments already provide valuable constraints on when and where ice photochemistry is important in interstellar environments. The major questions are: is ice photochemistry a plausible pathway to chemical complexity in space and what kinds of (families of) molecules can form in pure and mixed ice irradiation experiments? Is it possible, for example, to explain the observed abundances of complex molecules such as glycolaldehyde, dimethyl ether, and ethylene glycol in the interstellar medium, as stated in Section 5.1?

The idea was pioneered by Greenberg in Leiden in the 1970s and 1980s. In these early experiments, thick ice mixtures, representative of the existing constraints on interstellar ice compositions (mainly H_2O, CO, NH_3, and CH_4) were irradiated with very high UV doses, followed by warm-up to room temperatures to evaporate the remaining ice. What was left in these experiments was a residue – known in literature as *yellow stuff* – consisting of very complex molecules (m/z up to 500), which was inferred to contain both amino and carboxylic groups, demonstrating that UV irradiation of relatively simple ice mixtures can result in the production of very complex organic molecules with characteristics reminiscent of amino acids [175, 200].

This kind of experiments has continued to play an important role as detection thresholds, and schemes to identify the formed molecules have improved. As mentioned before, in 2002, two separate groups positively identified several amino acids in similar experiments using GC/MS [176, 177]. Both experiments made use of new estimates of realistic interstellar ice compositions, which included CH_3OH and CO_2. Because this type of experiments relies on the extraction of a residue – with many steps involved between ice processing and ice analysis – it is very difficult to deduce the formation kinetics of amino acids. The complexity of the product has also made it difficult to determine how the amino acid production depend on the initial ice composition quantitatively, and despite the increase in analysis precision, these experiments mainly address whether ice photochemistry offers a possible pathway to prebiotic complexity and not how efficient this process is, nor how to extrapolate mass conversion fractions estimated in the laboratory to astrophysical environments. In more recent experiments, the product identification was determined *in situ* [134].

Here the evolution of RAIR data was investigated as function of fluence upon UV irradiation of a pure methanol ice. It is found that, upon photodissociation,

different fragments form – CH_3, CH_3O, CH_2OH, OH – which can merge to form larger species such as ethanol from CH_3 and CH_2OH. Such reactions, possibly followed by desorption, have been proposed to explain the observations of gas-phase complex organic molecules in the warm inner regions of protostellar envelopes [201]. Indeed, in a series of dedicated RAIRS experiments, by monitoring the UV photoproducts as a function of fluence, the production of all commonly observed larger organic molecules has been realized. Identifications have been supported by complementary TPD experiments, since each product has a unique combination of mass signal and desorption temperature. The reaction scheme, summarizing how CH_3OH photolysis may trigger the formation of a substantial set of larger species, is shown in Figure 5.20. In this scheme, only dissociation and recombination of first-generation radicals from methanol dissociation are considered, with exception of the dissociation of H_2CO into HCO and CO and its reaction to CO_2 (see Ref. [134]). It is assumed that the vast majority of involved reactions consist of radical recombination without the breaking of bonds. The scheme shares many features with previous ones considered by, for example, Garrod and Herbst [202]. It starts with four possible photodissociation products of methanol that form from breaking one bond, that is, CH_2OH, OCH_3, CH_3, OH, and H. Recombination of radicals with other radicals or molecules can result in the formation of stable species, but this is only part of the story. The scheme shows that all complex molecules are formed in competition with several others which are formed from the same radicals; the recombination branching ratio of any one radical therefore depends both on the amount of other radicals and on their relative diffusion rates. Moreover, as the chemistry proceeds, the destruction of complex molecules becomes important and a more elaborate reaction scheme is required to analyze the outcome.

Despite this, from the experiment discussed here, it is already found that all observed molecules – in the laboratory – can be formed straightforwardly with a simple reaction scheme involving recombination of small radicals.

The formation of more complex species upon UV irradiation is interesting also from an astronomical point of view since solid methanol has been observed toward a range of young stellar objects, including solar-type protostars. A (V)UV-driven solid-state methanol chemistry – with methanol being efficiently formed upon CO hydrogenation – may thus offer a common pathway to chemical complexity in space.

5.4.4.6 Other Ice Photochemistry Studies

So far, most ice studies have been focusing on the formation of larger molecules starting from precursor species. An alternative approach to study molecular complexity in ice is to skip this formation process and to embed commercially available complex species – amino acids, polycyclic hydrocarbons, fullerenes, or other species – in solid water, using the ice as a matrix. The next step is to investigate how such species behave upon UV irradiation [203]. Such experiments have been performed, mainly in the IR and with a special focus on polycyclic aromatic hydrocarbons (PAHs). More recently, the use of optical ice spectroscopy ([204, 205]

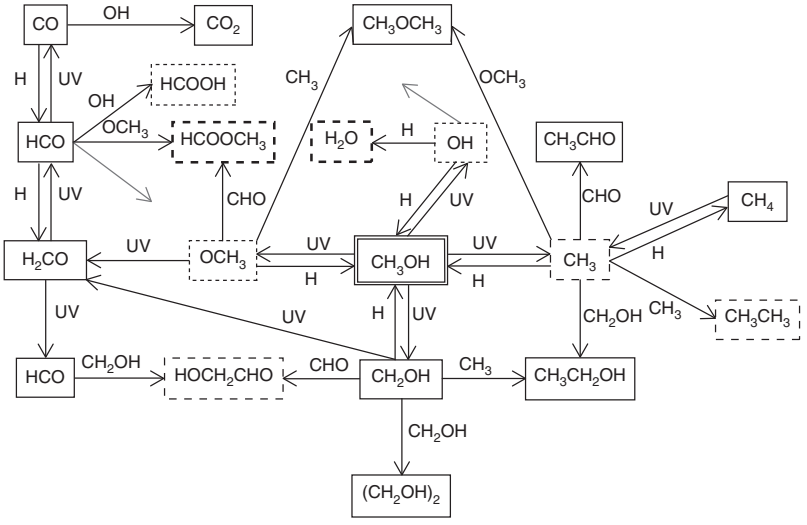

Figure 5.20 Systematic scheme showing how the UV photodissociation of methanol ice and the subsequent recombination of the resulting radicals can result in the formation of larger complex organic molecules, as observed in the interstellar and circumstellar medium. (Reproduced from [134], copyright 2010 © permission from EDP Sciences.)

and references therein) has boosted this research field, as optical spectra are more molecule-specific, matrix material generally does not absorb light, and detections become possible for much lower abundances as transition strengths are much larger. Such work also enters the field of astrobiology and is a research field in its own, beyond the context of this chapter.

Acknowledgments

This work is based on the hard work of many PhD students and postdoctoral fellows who have been working over the last years in the Sackler Laboratory for Astrophysics. We explicitly mention the persons who have been involved in the ice work in Leiden: Edith Fayolle, Junfeng Zhen, and Niels Ligterink on CRYOPAD, Guido Fuchs, Herma Cuppen, Claire Romanzin, Thanja Lamberts, and Gleb Fedoseev on SURFRESIDE, and Karoliina Isokoski, Daniel Paardekooper, Jean-Baptiste Bossa, Jordy Bouwman, Emily Tenenbaum, and Steven Cuylle on other ice setups.

5.5
New Calculational Strategies for Including Surface Reactions in Astrochemical Network Models

Eric Herbst

Although evidence has existed for many years that the study of interstellar chemistry is incomplete without the inclusion of surface processes, it is only

within the last 1–2 decades that chemical models of interstellar sources have included both gas-phase and grain-surface reactions [206]. There are several lines of evidence that point to the need for surface chemistry. The first is the formation of molecular hydrogen in interstellar clouds, both diffuse and dense, cold and warm: although H_2 can be synthesized in the gas under conditions of high temperature and density, as occurred in the early universe, its gas-phase formation under interstellar conditions in the present-day universe is very inefficient. Its formation on the surfaces of dust particles, on the other hand, is efficient over a wide range of temperatures on bare granular surfaces such as silicates and amorphous carbon, or complex ices [5]. The second line of evidence concerns the infrared detection of these assorted ices on grain mantles in the cold interstellar medium, mainly consisting of water, CO_2, methanol, and CO [207]. For the case of CO ice, it is possible that it is formed by accretion from the gas, but for water, methanol, and CO_2, the large abundances on grains cannot be produced by gas-phase chemistry followed by accretion. Instead, surface chemistry is required and, at least for the cases of water and methanol, reasonably well understood [109, 208]. The third line of evidence for grain-surface chemistry is based on the observation of partially and near-saturated "complex" organic species in the gas of the warm portions of the interstellar medium, In other words, there are two sources: (1) hot cores, and (2) regions subjected to shock waves [209]. Gas-phase chemistry, which is dominated by ion–neutral processes at low temperatures, tends to produce very unsaturated, so-called carbon-chain species, mainly because H_2 is not very reactive under these conditions. Moreover, gas-phase syntheses of the more saturated species involving two polyatomic reactants have been suggested in the past but appear to fail in some critical instances [210].

5.5.1 Rate Equations

Given the need for surface chemistry as well as gas-phase chemistry in simulations of interstellar sources, how can the rates and outcomes of the surface processes be computed? We are not yet at the stage where complex models of surface chemistry can be computed using the actual laws of molecular dynamics, in which, starting with a potential, one uses classical or quantum mechanics to follow the motions and reaction cross sections as a function of time. Although this reduction to basic physics is an ultimate goal [211], for the present we need to employ the simpler approaches of chemical kinetics. The simplest approach is to use the so-called deterministic rate equations for both the gas-phase and grain-surface processes, coupled by accretion onto grains and desorption from them. For the so-called standard grains with a radius 0.1 μm, the dust abundance is $\sim 3 \times 10^{-12}$ of the gas-phase abundance, and the timescale for accretion of a gas-phase species onto dust particles in a dense cloud is 10^{5-6} years. Although accretion onto grains is thus not a rapid process in a terrestrial sense, it is still a competitive one in the interstellar medium. The desorption from grains back into the gas can be thermal

in the warmer sources, but must be non-thermal for all but the most weakly bound species (H, He, H_2) in cold sources even if only physisorption is considered.

Consider that a species A that accretes onto a grain reacts with a species B via a diffusive (Langmuir–Hinshelwood) mechanism and desorbs thermally. The rate equation for A is then given by Hasegawa *et al.* and Caselli *et al.* [206, 212]

$$\frac{dN(\mathrm{A})}{dt} = k_{\mathrm{A,ads}}N(\mathrm{A}) - K_{\mathrm{A-B}}N(\mathrm{A})N(\mathrm{B}) - k_{\mathrm{A,des}N(\mathrm{A})} \tag{5.1}$$

where $N(\mathrm{X})$ is the average number of species X per grain. We do not utilize the symbols "$\langle\ \rangle$" for average because these symbols are typically reserved for stochastic treatments (see below). Alternative units for the amount of A and B often used are the areal concentration, the volume concentration (obtained by multiplication of the average number of species per grain by the volume concentration of grains), and the fractional abundance with respect to the volume concentration of total gaseous hydrogen nuclei. With the unit system used here, the rate coefficients are defined as follows:

$$k_{\mathrm{A,ads}} = s_{\mathrm{A}}\langle \nu_{\mathrm{A}}\rangle \sigma n(A) \tag{5.2}$$

$$K_{\mathrm{A-B}} = \frac{\kappa[k_{\mathrm{A,hop}} + k_{\mathrm{B,hop}}]}{N_{\mathrm{s}}} \tag{5.3}$$

and

$$k_{\mathrm{A,des}} = \nu \exp\left(\frac{-E_{\mathrm{D}}}{k_{\mathrm{B}}T}\right) \tag{5.4}$$

In these equations, $\langle \nu_{\mathrm{A}}\rangle$ is the average speed of A in the gas phase, $n(\mathrm{A})$ is its gas-phase concentration, s_{A} is its sticking coefficient, σ is the granular cross section, ν is the so-called attempt frequency of species A to leave a given binding site on the surface, E_{D} is the binding energy of A, N_{s} is the number of binding sites per grain, and k_{hop} is the hopping frequency to a nearest neighbor binding site. The hopping frequency can be written in a manner similar to the equation for $k_{\mathrm{A,des}}$, with the binding energy replaced by the barrier against hopping E_{b}, which is normally much smaller than the binding energy. It is typically assumed that the diffusive motion on interstellar grains involves hopping over rather than tunneling under barriers between neighboring binding sites, although for some surfaces in the laboratory, tunneling is known to occur. The expression for the rate coefficient $K_{\mathrm{A-B}}$ also contains a factor κ. With $\kappa = 1$, the rate coefficient is essentially the sum of the rates at which each reactant traverses a number of sites equal to the binding sites on the grain, although even in one dimension the existence of back diffusion means that the reactants will not see every site once. The rate law for diffusive reaction can be interpreted as the rate at which each species hops to a nearest neighbor multiplied by the probability of finding a reactant partner in this site. If there is a chemical activation energy for the reaction between A and B to occur, the factor κ will be less than unity, based on the probability of successful tunneling under or hopping over the chemical barrier, whichever is larger. Two expressions for κ in the presence of activation energy have been given in the literature: one is a simple factor for the probability of tunneling or

hopping, while the second incorporates the competition between reaction and leaving the reactant site via hopping and reacting. More details can be found in Ref. [213]. Most recently, Lohmar *et al.* [214] have developed an improved formulation of the rate coefficient for diffusive reactions based on random walk theory, which is typically significantly more accurate than the standard approximation used (see above). Actual sets of gas-phase and grain-surface equations for interstellar sources along with the software to integrate them can be found in http://www.mpia.de/homes/semenov/Chemistry_benchmark/home.html.

Although the Langmuir–Hinshelwood mechanism is by far the dominant one used in interstellar chemical simulations, there are instances where the Eley–Rideal mechanism has been incorporated [215]. For example, in older cold clouds, where ices have formed, the formation of CO_2 on a surface can occur by oxygen atoms striking sites where CO ice exists. To represent the rate of the O–CO reaction via the Eley–Rideal process on grains of finite size, the equation

$$\frac{dN(CO_2)}{dt} = k_{O-CO,ER} n(O) \tag{5.5}$$

can be used, with the rate coefficient given by the expression

$$k_{O-CO,ER} = \frac{\epsilon \langle v_O \rangle \sigma N(CO)}{N_s} \tag{5.6}$$

where the efficiency ϵ replaces the sticking coefficient in the adsorption rate coefficient, and also incorporates a Boltzmann factor for activation energy, if necessary. In case there is more than one monolayer of ice, the factor $N(CO)/N_s$ in the equation for the rate coefficient should pertain to the outermost layer.

In addition to thermal desorption, there are a number of nonthermal mechanisms that are critical at low temperatures (10–50 K), at which thermal desorption is very slow. The most important of these mechanisms is probably photodesorption, which has been studied in the laboratory mainly with pure ices, typically in the FUV portion of the spectrum [216, 217]. Such radiation exists even in dense clouds by virtue of cosmic ray bombardment, where the electrons formed in ionizing events excite molecular hydrogen, which then radiates UV photons. The photodesorption rates, though differing in mechanism, tend to have efficiencies of $\approx 10^{-3}$ per photon over the FUV range. This efficiency Y can easily be converted to a zeroth-order rate coefficient k_{pd} (s^{-1}) for a pure ice through the equation

$$k_{pd} = I_{CR-FUV} Y \sigma \tag{5.7}$$

where I is the radiation flux in the far-ultraviolet caused by cosmic ray bombardment, and σ is the granular cross section. If the ice is mixed, an additional factor for the mole fraction of the adsorbate of interest is needed throughout the number of monolayers that can be penetrated by the photons [218]. In diffuse clouds, and near the edge of dense clouds, a similar term for externally generated photons is necessary.

The rate equations for the Langmuir–Hinshelwood diffusive mechanism, though widely employed in astrochemistry, have several problems associated with them. Let us first consider a pure surface of either silicates or amorphous carbon, and let us ignore any irregularities. There is still one major problem, which is caused by the nature of the interstellar surface: it consists of small particles. On such particles, especially with the low fluxes in the interstellar medium, it is possible that the average number of reactive species on an individual grain at any given time can drop to below unity. Since the minimum number of reactants needed for a reaction on an individual grain is 2, a proper treatment of reaction rates then requires one to consider both the discrete aspects of the problem and fluctuations.

When the granular surfaces are irregular, which seems most likely in the interstellar medium, another problem ensues. Since sites associated with irregularities are likely to have different adsorbate binding energies and diffusive barriers from those of normal sites, the rate processes occurring on them have different rates from the norm. If one can group the irregular absorbates in these sites into a finite number of environments, it is possible to include irregularities in some average sense to a limited extent using rate equations by treating the species on irregular environments independently [93]. A more detailed approach requires the use of microscopic stochastic methods, to be discussed below.

Finally, there is the problem of ices. As ices build up in cold, dense clouds, reactions can take place not only on the surface, defined as the outermost monolayer, but also in pores within the ices. Moreover, the ices are certainly not pure, although water ice is the dominant one, and the structure of the porosity, if "structure" is the correct word, is rather complex. Although simplified rate approaches can be used to model the kinetics of reactions occurring within the ice, they likely do not represent the complexity of the interstellar problem [219]. Another possibility is to assume that the ices are not porous and that chemical reactions can occur only on the outermost monolayer. This type of approach can easily be done with rate equations, but may not be physically reasonable [220]. Whatever the likelihood that rate equations can be used in complex situations, they still fail on sufficiently small particles.

5.5.2 Stochastic Methods

Suitable approaches to these problems involve stochastic methods, which can be divided into two types: macroscopic and microscopic. Macroscopic methods are used to compute average abundances per grain without detailed knowledge of where the species lie on the surface or within ices. Microscopic methods compute rates of reaction as a function of position and can be used to determine exactly where the species are formed and destroyed. A more generally used term for the set of microscopic approaches is the *kinetic Monte Carlo method*. The general derivation of all stochastic treatments of kinetic equations stems from the so-called chemical master equation, which propagates probabilities instead of

concentrations. This set of differential equations can be integrated directly or simulated via a number of Monte Carlo algorithms, in which probabilities are treated in terms of random numbers. Macroscopic approaches based on both these methods have been utilized for interstellar problems [137, 221–224].

The two types of macroscopic approaches have their strengths and weaknesses. The direct master equation approach is much more easily coupled to gas-phase chemistry; both the rate equations normally used for the gas and the direct master equation approach used for the surface chemistry consist of coupled deterministic differential equations, which can be treated by a single integrating routine. The rate equation approach determines concentrations, whereas the master equation treatment obtains the probabilities of given numbers of particular species on an average grain. To get a sense of the master equation method, consider the relatively simple problem of molecular hydrogen formation from two hydrogen atoms [223]. In the rate equation approach to surface chemistry, the rate of destruction of atomic hydrogen on grains by reaction on the surface is given by the equation

$$\frac{dN(\mathrm{H})}{dt} = -K_{\mathrm{H-H}} N(\mathrm{H})\, N\,(\mathrm{H}) \tag{5.8}$$

along with terms for accretion, desorption, and reactions with other species, which are ignored. In the master equation approach, the above equation is replaced with a series of equations for the probabilities $P_n(\mathrm{H})$ of n hydrogen atoms on the grain:

$$\frac{dP_n(\mathrm{H})}{dt} = -K_{\mathrm{H-H}}[(n(n-1)P_n(\mathrm{H}) - (n+2)(n+1)P_{n+2}(\mathrm{H})] \tag{5.9}$$

Other probabilistic terms are added for adsorption, desorption, and, in more complex problems, for reactions with other species. Integration yields the various values of $P_n(\mathrm{H})$, which can be converted into the average number of hydrogen atoms per grain. Multiplying the equation by n and then summing over all n yields the equation

$$\frac{d\langle n\rangle}{dt} = -K_{\mathrm{H-H}}\langle n(n-1)\rangle \tag{5.10}$$

where the symbols $\langle\rangle$ refer to an average. This equation demonstrates that, for small $\langle n\rangle \equiv \langle N(\mathrm{H})\rangle$, the rate of reaction is smaller for the master equation approach, so that the use of rate equations for the reactive destruction of atomic hydrogen predicts too high a rate under these conditions.

In general, the use of the master equation method in gas–grain models is limited by two problems: (i) the equations are such that the probabilities for individual species are coupled, and (ii) there is no formal upper limit on the highest number of atoms/molecules per grain to be included, so that the number of equations is formally infinite. As an example of problem (i), suppose that H atoms are destroyed not only by reactions with themselves but also by reactions with O atoms [224]. Then the equations for $P_n(\mathrm{H})$ and $P_n(\mathrm{O})$ are coupled, and an equation for the joint probability $P_n(\mathrm{H})P_n(\mathrm{O})$ is needed. The result of the two problems is a large number of coupled equations to be solved.

Stantcheva and Herbst [225] developed an approximate method to solve the coupled gas–grain network in terms of rate equations for the gas and a mixed-rate equation master equation treatment for the surface chemistry, in which a number of atoms and radicals known to have low abundances on grains under all interstellar conditions are treated with a master equation, while the more abundant species, such as ices, are treated with rate equations [226]. In addition, the master equation is truncated at very low values of n so as to enable the equations for the coupled probabilities to be solved. With such a method, small networks of surface reactions coupled with complete gas-phase networks could be solved through 10^7 years. The results show differences from the rate equation treatments. It is to be noted that Stantcheva and Herbst [225] based their results on diffusive reaction rates that included tunneling under barriers, and so are much faster than most current values, which include only hopping. The higher rates of surface reactions lead to smaller surface abundances and larger stochastic effects than do current stochastic treatments, in which the macroscopic chemistry on standard grains at 10 K can often be treated adequately by rate equations.

An alternative approach to approximating the direct master equation technique is to use the master equation to obtain the time dependence of pure and mixed moments of the species. Consider once again the simple case of pure atomic hydrogen [227]. The mth moment can be written as

$$\langle N^m(\mathrm{H})\rangle = \sum_{n=1}^{\infty} n^m P_n(\mathrm{H}) \tag{5.11}$$

If one terminates the expansion at $n = j$ hydrogen atoms, one can solve for the $(j + 1)$th moment as a function of the first j moments. One can then use the results to obtain coupled differential equations for the $1 \leq m \leq j$ moments, which upon integration lead to surface populations as a function of time, as well as to higher moments. The extension to systems with more than one reactant leads to pure and mixed moments. A key question is to determine how many moments to keep in the solution. Results with termination after the second moment, in which the moment and direct master equation techniques are in good agreement, have been obtained for a variety of simple systems in the steady-state limit [228, 229]. Extension to systems not at steady state with a significant number of reactions appears to have numerical problems at the start of the calculation, during which negative abundances can be obtained. Research is currently being undertaken to eliminate this problem.

Recently, Vasyunin *et al.* [230] developed and utilized a pure Monte Carlo method in which both gas-phase and grain-surface chemistry are treated through a stochastic algorithm of Gillespie [231]. The approach considers an individual grain and the gas in a volume that contains exactly one grain. The calculations are quite computation-intensive, and so far have been solved only for grains of radius 0.1 μm. Results show little difference at 10 K with rate equation results as long as diffusion is limited to hopping, although somewhat larger effects are seen at higher temperatures. The inclusion of tunneling, which speeds up the diffusion rate, produces large deviations between the Monte Carlo and

rate equation treatments for some important species such as water, ammonia, and CO, just as occurred for Stantcheva and Herbst [225]. Unlike their work, the set of chemical reactions on grain surfaces is large. The combined Monte Carlo approach currently represents the gold standard for macroscopic surface chemistry, although to be used in a practical treatment algorithms will have to be found that lower the amount of computing time and allow the treatment of small grains on which stochastic effects are expected to be a maximum.

5.5.3 Modified Rate Equations

Given the amount of computer time involved in using even macroscopic stochastic methods for gas–grain chemical simulations of the interstellar medium, it has been suggested by several authors that the rate equations used for surface chemistry can be modified to incorporate some of the aspects of the stochastic approaches [212, 232–234]. The most recent attempts [232, 233] modify the form of the rate equations and not the actual rate coefficients. The modification depends on the average abundance of the reactants. For the case when each reactant has an average abundance $\langle N \rangle$ which is less than unity, presumably determined from a rate equation model, and the reactants are accreted from the gas, the modified rate for a fast reaction between reactants A and B is given by the equation

$$R_{\mathrm{mod}} = R_{\mathrm{acc}}(\mathrm{B})\langle N(\mathrm{A})\rangle + R_{\mathrm{acc}}(\mathrm{A})\langle N(\mathrm{B})\rangle \tag{5.12}$$

where the diffusion rates of both A and B are replaced in the rate law by the accretion rates (referred to earlier as *adsorption rate coefficients* – see Eq. (5.2)). In other words, the rate of reaction is determined by the rates of accretion, because diffusion is much faster than accretion. This limit, known as the *accretion limit*, was first studied by Tielens and Hagen [137]. More complex modifications are needed for other cases and for the transition when the accretion rate becomes larger than the diffusion rate at larger grain sizes. In the few tests run to date, the modified rate equation method is in much better agreement with the global Monte Carlo approach [230] than is the standard rate equation method for those conditions in which the methods diverge; for example, the conditions pertaining to a dense core at 30 K.

5.5.4 Microscopic Studies: A Kinetic Monte Carlo Approach

If one wishes more detailed information than the number of species on a granular mantle as a function of time, one can use a kinetic Monte Carlo approach, previously known as the *continuous-time random-walk approximation* [235]. One starts by approximating the initial grain surface as a two-dimensional lattice with periodic boundary conditions, each position on the lattice mimicking a binding site. For each lattice site and each adsorbate, there is an attempt frequency, a

binding energy, and a barrier to diffusion. These parameters can be the same for all lattice sites, in which case the lattice mimics a perfect crystal surface, or can represent the existence of irregularities, or even an amorphous structure, where a distribution of energy parameters is used. On the surface, species can adsorb from the gas, desorb into the gas, and diffuse on the surface via hopping motions between nearest neighbors, which leads to a random walk pattern. If two species diffuse onto the same binding site, there is a probability that the reaction will occur via the Langmuir–Hinshelwood mechanism. If there is no chemical barrier, reaction is assumed to occur, while if there is a chemical barrier, the competition between reaction and diffusion out of a lattice site can be simulated. If a gas-phase species lands atop a site with an adsorbate on it, there is the possibility of a reaction via the Eley–Rideal mechanism. Otherwise, especially at low temperatures, mantles of ices can build up. If the ices are porous, reactions can occur between two reactants found in the same pore.

To determine the rates of all these moves, one assumes individual motions to occur in a random Markovian manner. One starts a clock at $t = 0$, and determines the so-called waiting-time Poisson distribution for each independent process as well as an overall waiting time distribution. The individual Poisson distributions are based on the rates of each process, while the overall waiting time distribution contains the sum of all rates. Calling random numbers in the range (0, 1) determines the overall waiting time and the motion that occurs in that time. For example, if there are two processes with rates r_1 and r_2, the fraction $r_1/(r_1 + r_2)$ is compared with a random number at the waiting time. If the random number is less than the fraction, process 1 occurs. Otherwise, process 2 occurs. Once an overall waiting time is reached, a new waiting time is calculated [235].

The approach has been used mainly for studying grain processes without gas-phase chemistry. For example, it has been employed to study several details of surface H_2 formation, such as the roles of irregular and amorphous surfaces as well as cosmic ray bombardment [37, 235, 236]. It has also been used to study the development of water and methanol ice mantles in cold, dense clouds and how the growth of ices is affected by physical parameters [109, 237].

Creating a gas–grain model by coupling the kinetic Monte Carlo method to some approach for the gas-phase chemistry is very difficult and computation-intensive. At the time this manuscript was submitted," it had only been done once, with a rate equation approach to simulate the gas-phase chemistry, and that study is dominated by strong approximations [238]. In addition to the time-consuming nature of the kinetic Monte Carlo approach, one has to coordinate the time clocks for the stochastic surface processes and the deterministic gas-phase ones. The study was undertaken for a simple, homogeneous, cold cloud core, with a small number of surface rate equations leading to hydrogen, CO, O_2, CO_2, water, formaldehyde, and methanol. It was only possible to move the clock forward for the astronomically short time of 2×10^5 years, during which time many monolayers can be formed. Nevertheless, reasonable agreement with infrared

observations for the total abundances of ice components was obtained. More detailed information from the simulations concerns the composition and structure of each monolayer. Such information sounds too detailed for astronomical spectroscopic observations, but infrared line widths do give information on the environment of the absorbing species, and so can be compared with the results of detailed models [239]. Further development of the kinetic Monte Carlo method for gas–grain simulations, however, will require more efficient algorithms.

5.5.5 Summary

The standard kinetic treatment used in complex chemical simulations of interstellar sources is one in which deterministic rate equations are utilized for both the gas-phase and surface chemistries. These chemical processes are coupled through adsorption and desorption. Although the rate equations are an excellent approximation for the gas-phase chemistry, they suffer from a variety of problems for the case of surface chemistry. These problems include the difficulty of handling irregular and amorphous surfaces, the need to consider chemistry in the pores of porous ices, and, most importantly, the problems associated with small grains, especially in the limit where an average of less than one reactant atom or molecule per species exists on a grain. Most of these problems can be solved by stochastic methods, either macroscopic in nature, in which case only the average number of each species and its fluctuation is determined as a function of time on a grain, or microscopic in nature, in which case the detailed structure of the bare grain surface and of the ice forming atop it are taken into account. At the present time, the stochastic methods are not quite at the stage where they can be used over a wide range of physical conditions by nonexperts. Moreover, they also tend to be considerably more computation-intensive than the simple rate equation approach. The most advanced macroscopic approach is the global Monte Carlo procedure of Vasyunin *et al.* [230], in which both the gas-phase and grain-surface chemistries are treated via a Monte Carlo realization of the stochastic chemical master equation. Since this approach is exceedingly time consuming, new algorithms need to be found to make the procedure available to all those who are interested in the problem. Meanwhile, the use of the standard rate treatment is acceptable under a variety of physical conditions on all but the smaller grains, and the modified rate methods, in which the rate equations are altered to come closer to stochastic methods, extend this range of physical conditions. Ultimately, computational techniques should progress to the point where even a microscopic stochastic approach to the surface chemistry can be coupled to the gas-phase chemistry without severe approximation.

References

1. Tielens, A.G.G.M. (2005) *The Physics and Chemistry of the Interstellar Medium*, Cambridge University Press.
2. Hollis, J.M., Lovas, F.J., and Jewell, P.R. (2000) *Astrophys. J.*, **540** (2), L107–L110.
3. van de Hulst, H.C. (1949) *Rech. Astr. Obs. Utrecht*, **11** (part 2), 12.
4. Gould, R.J. and Salpeter, E.E. (1963) *Astrophys. J.*, **138**, 408–425.
5. Hollenbach, D.J. and Salpeter, E.E. (1971) *Astrophys. J.*, **163**, 155–164.
6. Spitzer, L., Drake, J.F., Jenkins, E.B. *et al.* (1973) *Astrophys. J.*, **184**, L114.
7. Jura, M. (1974) *Astrophys. J.*, **191**, 375–379.
8. Jura, M. (1975) *Astrophys. J.*, **197**, 575.
9. Stecher, T.P. and Williams, D.A. (1966) *Astrophys. J.*, **146**, 88–103.
10. Geppert, W.D., Hamberg, M., Thomas, R.D. *et al.* (2006) *Faraday Discuss.*, **133**, 177–190.
11. Sorrell, W.H. (2001) *Astrophys. J.*, **555** (2), L129–132.
12. Pirronello, V., Liu, C., Shen, L., and Vidali, G. (1997) *Astrophys. J.*, **475** (1), L69–L72.
13. Allamandola, L.J., Bernstein, M.P., Sandford, S.A., and Robert, R.L. (1999) *Space Sci. Rev.*, **90** (1/2), 219–232.
14. Henning, T. (1998) *Science*, **282** (5397), 2204–2210.
15. Dartois, E., Geballe, T.R., Pino, T. *et al.* (2007) *Astron. Astrophys*, **463**, 635–640.
16. Kimmel, G.A., Stevenson, K.P., Dohnálek, Z., Scott Smith, R., and Kay, B.D. (2001) *J. Chem. Phys.*, **114** (12), 5284–5294.
17. Accolla, M., Congiu, E., Manicò, G., Dulieu, F., Chaabouni, H., Lemaire, J.L., and Pirronello, V. (2013) *MNRAS*, **429** 3200–3206.
18. Li, A. and Draine, B.T. (2001) *Astrophys. J.*, **554** (2), 778–802.
19. Cuppen, H.M., Kristensen, L.E., and Gavardi, E. (2010) *Mon. Not. R. Astron. Soc*, **406**, L11–L15.
20. Habart, E., Boulanger, F., Verstraete, L. *et al.* (2003) *Astron. Astrophys*, **397**, 623–634.
21. Habart, E., Boulanger, F., Verstraete, L., Walmsley, C.M., and Pineau des Forêts, G. (2004) *Astron. Astrophys.*, **414** (2), 531–544.
22. Vickerman, J.S. and Gilmore I.S. (2009) *Surface Analysis – The Principal Techniques*, John Wiley and Sons, Ltd.
23. Pino, T., Dartois, E., Cao, A.-T. *et al.* (2008) Astronomy & Astrophysics, **490**, 665–672.
24. Ghio, E., Mattera, L., Salvo, C., Tommasini, F., and Valbusa, U. (1980) *J. Chem. Phys.*, **73** (1), 556–561.
25. Jeloaica, L. and Sidis, V. (1999) *Chem. Phys. Lett.*, **300** (1-2), 157–162.
26. Sha, X. and Jackson, B. (2002) *Surf. Sci.*, **496** (3), 318–330.
27. Hornekær, L., Šljivančanin, ., Xu, W. *et al.* (2006) *Phys. Rev. Lett.*, **96** (15), 156104.
28. Sha, X. and Jackson, B. (2004) *J. Am. Chem. Soc.*, **126** (40), 13095–13099.
29. Bonfanti, M., Martinazzo, R., Tantardini, G.F., and Ponti, A. (2007) *J. Phys. Chem. C*, **111** (16), 5825–5829.
30. Hornekær, L., Rauls, E., Xu, W. *et al.* (2006) *Phys. Rev. Lett.*, **97** (18), 186102.
31. Dumont, F., Picaud, F., Ramseyer, C. *et al.* (2008) *Phys. Rev. B*, **77** (23), 233401.
32. Cuppen, H.M. and Hornekær, L. (2008) *J. Chem. Phys.*, **128** (17), 174707.
33. Rougeau, N., Teillet-Billy, D., and Sidis, V. (2006) *Chem. Phys. Lett.*, **431** (1-3), 135–138.
34. Baouche, S., Hornekær, L., Baurichter, A. *et al.* (2009) *J. Chem. Phys.*, **131** (24), 244707.
35. Pirronello, V., Liu, C., Roser, J.E., and Vidali, G. (1999) *Astron. Astrophys.*, **344**, 681–686.
36. Katz, N., Furman, I., Biham, O., Pirronello, V., and Vidali, G. (1999) *Astrophys. J.*, **522**, 305–312.
37. Cuppen, H.M. and Herbst, E. (2005) *Mon. Not. R. Astron. Soc.*, **361** (2), 565–576.
38. Cazaux, S. and Tielens, A.G.G.M. (2004) *Astrophys. J.*, **604** (1), 222–237.

39. Zecho, T., Güttler, A., Sha, X., Jackson, B., and Küppers, J. (2002) *J. Chem. Phys.*, **117** (18), 8486–8492.
40. Zecho, T., Güttler, A., and Küppers, J. (2004) *Carbon*, **42** (3), 609–617.
41. Mennella, V. (2008) *Astrophys. J. Lett.*, **684**, L25–L28.
42. Rauls, E. and Hornekær, L. (2008) *Astrophys. J.*, **679** (1), 531–536.
43. Thrower, J.D., Jørgensen, B., Friis, E.E. *et al.* (2012) *Astrophys. J.*, **752** (1), 3.
44. Mennella, V., Hornekær, L., Thrower, J., and Accolla, M. (2011) *Astrophys. J.*, **745** (1), L2.
45. Flower, D.R. and Pineau-Des-Forêts, G. (1990) *Mon. Not. R. Astron. Soc.*, **247**, 500–505.
46. Baouche, S., Gamborg, G., Petrunin, V.V. *et al.* (2006) *J. Chem. Phys.*, **125** (8), 084712.
47. Islam, F., Latimer, E.R., and Price, S.D. (2007) *J. Chem. Phys.*, **127** (6), 064701.
48. Creighan, S.C., Perry, J.S.A., and Price, S.D. (2006) *J. Chem. Phys.*, **124** (11), 114701.
49. Latimer, E.R., Islam, F., and Price, S.D. (2008) *Chem. Phys. Lett.*, **455** (4-6), 174–177.
50. Morisset, S., Aguillon, F., Sizun, M., and Sidis, V. (2005) *J. Chem. Phys.*, **122** (19), 194702.
51. Burton, M.G., Bulmer, M., Moorhouse, A., Geballe, T.R., and Brand, P.W.J.L. (1992) *Mon. Not. R. Astron. Soc.*, **257**, 1P–6P.
52. Burton, M.G., Londish, D., and Brand, P.W.J.L. (2002) *Mon. Not. R. Astron. Soc.*, **333** (4), 721–729.
53. Hornekaer, L. (2003) *Science*, **302** (5652), 1943–1946.
54. Jenniskens, P. and Blake, D. (1994) *Science*, **265** (5173), 753–756.
55. Jenniskens, P., Blake, D.F., Wilson, M.A., and Pohorille, A. (1995) *Astrophys. J.*, **455**, 389.
56. Jenniskens, P. and Blake, D.F. (1996) *Astrophys. J.*, **473** (2), 1104–1113.
57. Narten, A.H. (1976) *J. Chem. Phys.*, **64** (3), 1106.
58. Wenzel, J., Linderstrom-Lang, C.U., and Rice, S.A. (1975) *Science*, **187** (4175), 428–430.
59. Zubavichus, Y., Yang, Y., Zharnikov, M. *et al.* (2004) *ChemPhysChem*, **5** (4), 509–514.
60. Westley, M.S., Baratta, G.A., and Baragiola, R.A. (1998) *J. Chem. Phys.*, **108** (8), 3321.
61. Dohnálek, Z., Kimmel, G.A., Ayotte, P., Scott Smith, R., and Kay, B.D. (2003) *J. Chem. Phys.*, **118** (1), 364.
62. Mayer, E. and Pletzer, R. (1986) *Nature*, **319** (6051), 298–301.
63. Manca, C., Martin, C., and Roubin, P. (2004) *Chem. Phys.*, **300** (1-3), 53–62.
64. Stevenson, K.P., Greg, A., Kimmel, Z., Dohnálek, R., Scott, S., and Bruce, D. Kay (1999) *Science*, **283**, (5407), 1505–1507
65. Rowland, B., Fisher, M., and Devlin, J.P. (1991) *J. Chem. Phys.*, **95** (2), 1378.
66. Raut, U., Famá, M., Teolis, B.D., and Baragiola, R.A. (2007) *J. Chem. Phys.*, **127** (20), 204713.
67. Kimmel, G.A., Dohnálek, Z., Stevenson, K.P., Smith, R.S., and Kay, B.D. (2001) *J. Chem. Phys.*, **114** (12), 5295.
68. Palumbo, M.E. (1997) *J. Phys. Chem. A*, **101** (23), 4298–4301.
69. Palumbo, M.E. (2006) *Astron Astrophys.*, **453** (3), 903–909.
70. Palumbo, M.E. and Strazzulla, G. (2003) *Can. J. Phys.*, **81** (1-2), 217–224.
71. Palumbo, M.E., Baratta, G.A., Leto, G., and Strazzulla, G. (2010) *J. Mol. Struct.*, **972** (1-3), 64–67.
72. Hixson, H.G., Wojcik, M.J., Devlin, M.S., Devlin, J.P., and Buch, V. (1992) *J. Chem. Phys.*, **97** (2), 753.
73. Devlin, J.P. (1992) *J. Phys. Chem.*, **96** (15), 6185–6188.
74. Fraser, H.J., Collings, M.P., Dever, J.W., and McCoustra, M.R.S. (2004) *Mon. Not. R. Astron. Soc.*, **353** (1), 59–68.
75. Angell, C.A. (2004) *Annu. Rev. Phys. Chem.*, **55** (1), 559–583.
76. Johari, G.P., Hallbrucker, A., and Mayer, E. (1987) *Nature*, **330** (6148), 552–553.
77. Kay, B.D. and Smith, R.S. (1999) *Nature*, **398** (6730), 788–791.
78. Yue, Y. and Angell, C.A. (2004) *Nature*, **427** (6976), 717–720.

79. Souda, R. (2005) *Chem. Phys. Lett.*, **415** (1-3), 146–149.
80. Buch, V. (1990) *J. Chem. Phys.*, **93**, 2631–2639.
81. Hornekær, L., Baurichter, A., Petrunin, V.V. *et al.* (2005) *J. Chem. Phys.*, **122** (12), 124701.
82. Amiaud, L., Fillion, J.H., Baouche, S. *et al.* (2006) *J. Chem. Phys.*, **124** (9), 094702.
83. Fillion, J.-H., Amiaud, L., Congiu, E. *et al.* (2009) *Phys. Chem. Chem. Phys. (Incorporating Faraday Transactions)*, **11**, 4396.
84. Govers, T.R., Mattera, L., and Scoles, G. (1980) *J. Chem. Phys.*, **72**, 5446–5455.
85. Amiaud, L., Dulieu, F., Fillion, J.-H., Momeni, A., and Lemaire, J.L. (2007) *J. Chem. Phys.*, **127** (14), 144709.
86. Matar, E., Bergeron, H., Dulieu, F. *et al.* (2010) *J. Chem. Phys.*, **133** (10), 104507.
87. Nagaoka, A., Watanabe, N., and Kouchi, A. (2005) *The Astronomical Journal, Letters*, **624**, L29–L32.
88. Mokrane, H., Chaabouni, H., Accolla, M. *et al.* (2009) *The Astronomical Journal, Letters*, **705**, L195–L198.
89. Govers, T. (2005) ArXiv Physics e-prints.
90. Watanabe, N., Kimura, Y., Kouchi, A. *et al.* (2010) *The Astronomical Journal, Letters*, **714**, L233–L237.
91. Roser, J.E., Manicò, G., Pirronello, V., and Vidali, G. (2002) *The Astronomical Journal*, **581**, 276–284.
92. Amiaud, L. (2006) Interaction d'atomes et de molécules d'hydrogène avec des glaces d'eau à très basse température: formation de H2 dans le milieu interstellaire. PhD thesis, Université de Cergy Pontoise.
93. Perets, H.B., Biham, O., Manicó, G. *et al.* (2005) *Astrophys. J.*, **627** (2), 850–860.
94. Matar, E., Congiu, E., Dulieu, F., Momeni, A., and Lemaire, J.L. (2008) *Astron. Astrophys.*, **492** (1), L17–L20.
95. Buch, V. and Czerminski, R. (1991) *J. Chem. Phys.*, **95**, 6026–6038.
96. Congiu, E., Matar, E., Kristensen, L.E., Dulieu, F., and Lemaire, J.L. (2009) *Mon. Not. R. Astron. Soc.*, **397** (1), L96–L100.
97. Accolla, M., Congiu, E., Dulieu, F. *et al.* (2011) *Phys. Chem. Chem. Phys. (Incorporating Faraday Transactions)*, **13**, 8037.
98. Pontoppidan, K.M., Fraser, H.J., Dartois, E. *et al.* (2003) *Astron. Astrophys.*, **408** (3), 981–1007.
99. Sandford, S.A., Allamandola, L.J., Tielens, A.G.G.M., and Valero, G.J. (1988) *Astrophys. J.*, **329**, 498.
100. Schmitt, B., Greenberg, J.M., and Grim, R.J.A. (1989) *Astrophys. J.*, **340**, L33.
101. Palumbo, M.E. and Strazzulla, G. (1993) *Astronomy & Astrophysics*, **269**, 568–580.
102. Bar-Nun, A., Herman, G., Laufer, D., and Rappaport, M.L. (1985) *Icarus*, **63** (3), 317–332.
103. Sandford, S.A. and Allamandola, L.J. (1988) *Icarus*, **76** (2), 201–224.
104. Collings, M.P., Dever, J.W., Fraser, H.J., McCoustra, M.R.S., and Williams, D.A. (2003) *Astrophys. J.*, **583** (2), 1058–1062.
105. Collings, M.P., Dever, J.W., Fraser, H.J., and McCoustra, M.R.S. (2003) *Astrophys. Space Sci.*, **285** (3/4), 633–659.
106. Fraser, H.J. *et al.* (2002) *Astron. Geophys.*, **43**, 2.10.
107. Collings, M.P., Anderson, M.A., Chen, R. *et al.* (2004) *Mon. Not. R. Astron. Soc.*, **354** (4), 1133–1140.
108. Viti, S., Collings, M.P., Dever, J.W., McCoustra, M.R.S., and Williams, D.A. (2004) *Mon. Not. R. Astron. Soc.*, **354** (4), 1141–1145.
109. Cuppen, H.M. and Herbst, E. (2007) *Astrophys. J.*, **668** (1), 294–309.
110. D'Hendecourt, L.B., Allamandola, L.J., Grim, R.J.A., and Greenberg, J.M. (1986) *Astronomy & Astrophysics*, **158**, 119–134.
111. Moore, M. (2000) *Icarus*, **145** (1), 282–288.
112. Gomis, O., Leto, G., and Strazzulla, G. (2004) *Astron. Astrophys.*, **420** (2), 405–410.
113. Gerakines, P.A., Schutte, W.A., and Ehrenfreund, P. (1996) *Astronomy & Astrophysics*, **312**, 289–305.

114. Baratta, G.A., Leto, G., Spinella, F., Strazzulla, G., and Foti, G. (1991) *Astronomy & Astrophysics*, **252**, 421–424.
115. Moore, M.H. and Hudson, R.L. (1992) *Astrophys. J.*, **401**, 353.
116. Leto, G. and Baratta, G.A. (2003) *Astron. Astrophys.*, **397** (1), 7–13.
117. Leto, G., Palumbo, M.E., and Strazzulla, G. (1996) *Nucl. Instrum. Methods Phys. Res., Sect. B*, **116** (1-4), 49–52.
118. Sack, N.J., Boring, J.W., Johnson, R.E., Baragiola, R.A., and Shi, M. (1991) *J. Geophys. Res.*, **96** (E2), 17535.
119. Guillot, B. and Guissani, Y. (2004) *J. Chem. Phys.*, **120** (9), 4366.
120. Raut, U., Teolis, B.D., Loeffler, M.J. *et al.* (2007) *J. Chem. Phys.*, **126** (24), 244511.
121. Raut, U., Famá, M., Loeffler, M.J., and Baragiola, R.A. (2008) *Astrophys. J.*, **687** (2), 1070–1074.
122. Fitz, D.E., Khare, V., and Kouri, D.J. (1981) *Chem. Phys.*, **56** (2), 267–276.
123. McCoustra, M. and Williams, D.A. (1996) *Mon. Not. R. Astron. Soc.*, **279** (3), L53–L56.
124. Keane, J.V., Boogert, A.C.A., Tielens, A.G.G.M., Ehrenfreund, P., and Schutte, W.A. (2001) *Astron. Astrophys.*, **375** (3), L43–L46.
125. Greenberg, J.M. (1982) in *Comets* (ed. L.L. Wilkening), The University of Arizona Press, Tucson, AZ, pp. 131–163.
126. Tielens, A.G.G.M. and Allamandola, L.J. (1987) in *NATO ASIC Proceedings vol 210: Physical Processes in Interstellar Clouds* (eds G.E. Morfill and M. Scholer), D. Reidel. Publ. Co. Dordrecht, Holland, pp. 333–376.
127. Herbst, E. and van Dishoeck, E.F. (2009) *Ann. Rev. Astron. Astrophys.*, **47**, 427–480.
128. Gibb, E.L., Whittet, D.C.B., Boogert, A.C.A., and Tielens, A.G.G.M. (2004) *Astrophys. J. Suppl.*, **151**, 35–73.
129. Boogert, A.C.A., Pontoppidan, K.M., Knez, C. *et al.* (2008) *Astrophys. J.*, **678**, 985–1004.
130. Öberg, K.I., Boogert, A.C.A., Pontoppidan, K.M. *et al.* (2010) *Astrophys. J.*, **740**, A109.
131. Bossa, J.B., Isokoski, K., Paardekooper, D.M. *et al.* (2014) *Astron. Astrophys.*, **561**, A136.
132. Acharyya, K., Fuchs, G.W., Fraser, H.J., van Dishoeck, E.F., and Linnartz, H. (2007) *Astron. Astrophys.*, **466** 1005.
133. Burke, D.J. and Brown, W.A. (2010) *Phys. Chem. Chem. Phys.*, **12**, 5947.
134. Öberg, K.I., Garrod, R.T., van Dishoeck, E.F., and Linnartz, H. (2009) *Astron. Astrophys.*, **504**, 891–913.
135. Partially based on PhD thesis Sergio Ioppolo (2010) Surface formation routes of interstellar molecules - a laboratory study. PhD thesis, Leiden University.
136. Partially based on PhD thesis Karin Öberg (2009) Complex processes in simple ices - Laboratory and observational studies of gas-grain interactions during star formation. PhD thesis, Leiden University.
137. Tielens, A.G.G.M. and Hagen, W. (1982) *Astron. Astrophys.*, **114** (2), 245–260.
138. Wakelam, V., Smith, I.W.M., Herbst, E. *et al.* (2010) *Space Sci. Rev.*, **156**, 13–72.
139. Miyauchi, N., Hidaka, H., Chigai, T. *et al.* (2008) *Chem. Phys. Lett.*, **456**, 27–30.
140. Ioppolo, S., Cuppen, H.M., Romanzin, C., van Dishoeck, E.F., and Linnartz, H. (2008) *Astrophys. J.*, **686**, 1474–1479.
141. Matar, E., Congiu, E., Dulieu, F., Momeni, A., and Lemaire, J.L. (2008) *Astron. Astrophys.*, **492**, L17–20.
142. Mokrane, H., Chaabouni, H., Accolla, M. *et al.* (2009) *Astrophys. J. Lett.*, **705**, L195–198.
143. Dulieu, F., Amiaud, L., Congiu, E. *et al.* (2010) *Astron. Astrophys.*, **512**, A30.
144. Ioppolo, S., Cuppen, H.M., Romanzin, C., van Dishoeck, E.F., and Linnartz, H. (2010) *Phys. Chem. Chem. Phys.*, **12**, 12065–12076.
145. Cuppen, H.M., Ioppolo, S., Romanzin, C., and Linnartz, H. (2010) *Phys. Chem. Chem. Phys.*, **12**, 12077–12088.
146. Romanzin, C., Ioppolo, S., Cuppen, H.M., van Dishoeck, E.F., and Linnartz, H. (2011) *J. Chem. Phys.*, **134**, 084504, 1–7.

147. Lamberts, T., Cuppen, H.M., Ioppolo, S., and Linnartz, H. (2013) *Phys. Chem. Chem. Phys.*, **15**, 8287–8302.
148. Charnley, S.B., Tielens, A.G.G.M., and Millar, T.J. (1992) *Astrophys. J.*, **399**, L71–74.
149. Hiraoka, K., Sato, T., Sato, S. *et al.* (2002) *Astrophys. J.*, **577**, 265–270.
150. Watanabe, N. and Kouchi, A. (2002) *Astrophys. J. Lett.*, **571**, L173–176.
151. Fuchs, G.W., Cuppen, H.M., Ioppolo, S. *et al.* (2009) *Astron. Astrophys.*, **505**, 629–639.
152. Roser, J.E., Vidali, G., Manrico, G., and Pirronello, V. (2001) *Astrophys. J.*, **555**, L61–L64.
153. Madzunkov, S., Shortt, B.J., Macaskill, J.A., Darrach, M.R., and Chutjian, A. (2006) *Phys. Rev. A*, **73**, 020901.
154. Raut, U. and Baragiola, R.A. (2011) *Astrophys. J. Lett.*, **737**, L14.
155. Oba, Y., Watanabe, N., Kouchi, A., Hama, T., and Pirronello, V. (2010) *Astrophys. J. Lett.*, **712**, L174–L178.
156. Ioppolo, S., Cuppen, H.M., van Dishoeck, E.F., and Linnartz, H. (2011) *Mon. Not. R. Astron. Soc.*, **413**, 2281–2287.
157. Noble, J.A., Dulieu, F., Congiu, E., and Fraser, H.J. (2011) *Astrophys. J.*, **735**, A121.
158. Ioppolo, S., Fedoseev, G., Lamberts, T., Romanzin, C., and Linnartz, H. (2013) *Rev. Sci. Instrum.*, **84**, A073112.
159. Ioppolo, S., Sangiorgio, I., Baratta, G.A., and Palumbo, M.E. (2013) *Astron. Astrophys.*, **554**, A34.
160. Congiu, E., Ioppolo, S., Dulieu, F. *et al.* (2012) *Astrophys. J. Lett.*, **750**, L12.
161. Fedoseev, G., Ioppolo, S., Lamberts, T., Zhen, H.M., Cuppen, J., and Linnartz, H. (2012) *J. Chem. Phys.*, **137**, 054714.
162. Minissale, M., Fedoseev, G., Congiu, E. *et al.* (2014) *Phys. Chem. Chem. Phys.*, **16**, 8257.
163. Ioppolo, S., Fedoseev, G., Minissale, M. *et al.* (2014) *Phys. Chem. Chem. Phys.*, **16**, 8270.
164. Hiraoka, K., Yamashita, A., Yachi, Y. *et al.* (1995) *Astrophys. J.*, **443**, 363–370.
165. Hidaka, H., Watanabe, M., Kouchi, A., and Watanabe, N. (2011) *Phys. Chem. Chem. Phys.*, **13**, 15798–15802.
166. Fedoseev, G., Ioppolo, S., Zhao, D., Lamberts, T., and Linnartz, H. (2014) in preparation.
167. Ioppolo, S., Cuppen, H.M., van Dishoeck, E.F., and Linnartz, H. (2011) *Mon. Not. R. Astron. Soc.*, **410**, 1089–1095.
168. Bisschop, S.E., Fuchs, G.W., van Dishoeck, E.F., and Linnartz, H. (2007) *Astron. Astrophys.*, **474**, 1061–1071.
169. Hama, T. and Watanabe, N. (2013) *Chem. Rev.*, **113**, 8783–8839.
170. Tschersich, K.G., Fleischhauer, J.P., and Schuler, H. (2008) *J. Appl. Phys.*, **104**, A034908.
171. Anton, R., Wiegner, T., Naumann, W. *et al.* (2000) *Rev. Sci. Instrum.*, **71**, 1177–1180.
172. Oba, Y., Watanabe, N., Hama, T. *et al.* (2012) *Astrophys. J.*, **749**, A67.
173. Van Dishoeck, E.F., Herbst, E., and Neufeld, D.A. (2013) *Chem. Rev.*, **113**, 9043–9085.
174. Arumainayagam, C.R., Lee, H.L., Nelson, R.B., Haines, D.R, and Gunawardane, R.P. (2010) *Surf. Sci. Rep.*, **65**, 1–44.
175. Hagen, W., Allamandola, L.J., and Greenberg, J.M. (1979) *Astrophys. Space Sci.*, **65**, 215–240.
176. Bernstein, M.P., Dworkin, J.P., Sandford, S.A., Cooper, G.W., and Allamandola, L.J. (2002) *Nature*, **416**, 401–403.
177. Munoz-Caro, G.M., Meierhenrich, U.J., Schutte, W.A. *et al.* (2002) *Nature*, **416**, 403–406.
178. Chen, Y.J., Chuang, K.J., Caro, G.M.M. *et al.* (2014) *Astrophys. J.*, **781**, A15.
179. Westley, M.S., Baragiola, R.A., Johnson, R.E., and Baratta, G.A. (1995) *Planet. Space Sci.*, **43**, 1311–1315.
180. Westley, M.S., Baragiola, R.A., Johnson, R.E., and Baratta, G.A. (1995) *Nature*, **373**, 405–407.
181. Öberg, K.I., Linnartz, H., Visser, R., and van Dishoeck, E.F. (2009) *Astrophys. J.*, **693**, 1209–1218.
182. Öberg, K.I., van Dishoeck, E.F., and Linnartz, H. (2009) *Astron. Astrophys.*, **496**, 281–293.
183. Bahr, D.A. and Baragiola, R.A. (2012) *Astrophys. J.*, **761**, A36.

184. Yuan, C.Q. and Yates, J.T. (2013) *J. Chem. Phys.*, **138**, A154303.
185. Fillion, J.-H., Fayolle, E.C., Michaut, X. *et al.* (2014) *Faraday Discuss.*, **168**, in press.
186. Öberg, K.I., Fuchs, G.W., Awad, Z. *et al.* (2007) *Astrophys. J. Lett.*, **662**, L23–L26.
187. Munoz-Caro, G.M., Jimenez-Escobar, A., Martin-Gago, C., Rogero, J.A. *et al.* (2010) *Astron. Astrophys.*, **522**, A108.
188. Fayolle, E.C., Bertin, M., Romanzin, C. *et al.* (2009) *Astrophys. J. Lett.*, **739**, L36.
189. Bertin, M., Fayolle, E.C., Romanzin, C. *et al.* (2012) *Phys. Chem. Chem. Phys.*, **14**, 9929–9935.
190. Fayolle, E.C., Bertin, M., Romanzin, C. *et al.* (2013) *Astron. Astrophys.*, **556**, A122.
191. Zhen, J.F. and Linnartz, H. (2014) *Mon. Not. R. Astron. Soc.*, **437**, 3190–3201.
192. Allodi, M.A., Baragiola, R.A., Baratta, G.A. *et al.* (2013) *Space Sci. Rev.*, **180**, 101–175.
193. Öberg, K.I., van Broekhuizen, F., Fraser, H.J. *et al.* (2005) *Astrophys. J.*, **621**, 33–36.
194. Lu, H.C., Chen, H.K., Cheng, B.M., Kuo, Y.P., and Ogilvie, J.F. (2005) *J. Phys. B.*, **38**, 3693–3704.
195. Fillion, J.-H., Fayolle, E.C., Michaut, X., *et al.* (2014) *Faraday Discussions*, **168**, 533–552.
196. Arasa, C., Andersson, S., Cuppen, H.M., van Dishoeck, E.F., and Kroes, G.J. (2010) *J. Chem. Phys.*, **132**, A184510.
197. Arasa, C., Andersson, S., Cuppen, H.M., van Dishoeck, E.F., and Kroes, G.J. (2011) *J. Chem. Phys.*, **134**, A164503.
198. Qi, C.H., Öberg, K.I., Wilner, D.J. *et al.* (2013) *Science*, **341**, 630–632.
199. Brinch, C. and Jorgensen, J.K. (2013) *Astron. Astrophys.*, **559**, A82.
200. Greenberg, J.M., vande Bult, C.E.P.M., and Allamandola, L.J. (1983) *J. Phys. Chem.*, **87**, 4243–4260.
201. Öberg, K.I., Bottinelli, S., Jorgens, J.K., and van Dishoeck, E.F. (2010) *Astrophys. J.*, **716**, 825–834.
202. Garrod, R.T. and Herbst, E. (2006) *Astron. Astrophys.*, **457**, 927–936.
203. Bernstein, M.P., Sandford, S.A., Allamandola, L.J. *et al.* (1999) *Science*, **283**, 1135–1138.
204. Bouwman, J. (2010) Spectroscopy and chemistry of interstellar ice analogues. PhD thesis, Leiden University.
205. Gudipati, M.S. and Allmandola, L.J. (2003) *Astrophys. J.*, **596**, L195–L198.
206. Hasegawa, T.I., Herbst, E., and Leung, C.M. (1992) *Astrophys. J. Suppl. Ser.*, **82** (1), 167–195.
207. Gibb, E.L., Whittet, D.C.B., Boogert, A.C.A., and Tielens, A.G.G.M. (2004) *Astrophys. J. Suppl. Ser.*, **151** (1), 35–73.
208. Watanabe, N. and Kouchi, A. (2002) *Astrophys. J.*, **571** (2), L173–L176.
209. Herbst, E. and van Dishoeck, E.F. (2009) *Ann. Rev. Astron. Astrophys.*, **47** (1), 427–480.
210. Horn, A., Mollendal, H., Sekiguchi, O. *et al.* (2004) *Astrophys. J.*, **611** (1), 605–614.
211. Arasa, C., Andersson, S., Cuppen, H.M., van Dishoeck, E.F., and Kroes, G.-J. (2010) *J. Chem. Phys.*, **132** (18), 184510.
212. Caselli, P., Hasegawa, T.I., and Herbst, E. (1998) *Astrophys. J.*, **495** (1), 309–316.
213. Herbst, E. and Millar, T.J. (2008) in *Low Temperatures and Cold Molecules*, Chapter 1 (ed. I.W.M. Smith), Imperial College Press, London, pp. 1–54.
214. Lohmar, I., Krug, J., and Biham, O. (2009) *Astronomy & Astrophysics*, **504**, L5–L8.
215. Hassel, G.E., Herbst, E., and Bergin, E.A. (2010) *Astronomy & Astrophysics*, **515**, A66.
216. Öberg, K.I., van Dishoeck, E.F., and Linnartz, H. (2009) *Astronomy & Astrophysics*, **496** (1), 281–293.
217. Öberg, K.I., Linnartz, H., Visser, R., and van Dishoeck, E.F. (2009) *Astrophys. J.*, **693** (2), 1209–1218.
218. Hassel, G.E. and Herbst, E. (2010) unpublished.
219. Perets, H.B. and Biham, O. (2006) *Mon. Not. R. Astron. Soc.*, **365** (3), 801–806.
220. Hasegawa, T.I. and Herbst, E. (1993) *Mon. Not. R. Astron. Soc.*, **263** (3), 589–606.

221. Charnley, S.B. (1998) *Astrophys. J.*, **509** (2), L121–L124.
222. Charnley, S.B. (2001) *Astrophys. J.*, **562** (1), L99–L102.
223. Biham, O., Furman, I., Pirronello, V., and Vidali, G. (2001) *Astrophys. J.*, **553** (2), 595–603.
224. Green, N.J.B., Toniazzo, T., Pilling, M.J. *et al.* (2001) *Astronomy & Astrophysics*, **375**, 1111–1119.
225. Stantcheva, T. and Herbst, E. (2004) *Astronomy & Astrophysics*, **423**, 241–251.
226. Stantcheva, T., Shematovich, V.I., and Herbst, E. (2002) *Astronomy & Astrophysics*, **391**, 1069–1080.
227. Lipshtat, A. and Biham, O. (2003) *Astronomy & Astrophysics*, **400**, 585–593.
228. Barzel, B. and Biham, O. (2007) *The Astronomical Journal, Letters*, **658** (1), L37–L40.
229. Le Petit, F., Barzel, B., Biham, O., Roueff, E., and Le Bourlot, J. (2009) *Astronomy & Astrophysics*, **505** (3), 1153–1165.
230. Vasyunin, A.I., Semenov, D.A., Wiebe, D.S., and Henning, Th. (2009) *Astrophys. J.*, **691** (2), 1459–1469.
231. Gillespie, D.T. (1976) *J. Comput. Phys.*, **22** (4), 403–434.
232. Garrod, R.T. (2008) *Astronomy & Astrophysics*, **491**, 239–251.
233. Garrod, R.T., Vasyunin, A.I., Semenov, D.A., Wiebe, D.S., and Henning, Th. (2009) *Astrophys. J.*, **700** (1), L43–L46.
234. Garrod, R. and Vasyunin, A. (2010) *Bull. Am. Astron. Soc. Meet. Abstr. #216*, **41**, 424.03.
235. Chang, Q., Cuppen, H.M., and Herbst, E. (2005) *Astronomy & Astrophysics*, **434** (2), 599–611.
236. Herbst, E. and Cuppen, H.M. (2006) *Proc. Natl. Acad. Sci. U.S.A.*, **103** (33), 12257–12262.
237. Cuppen, H.M., van Dishoeck, E.F., Herbst, E., and Tielens, A.G.G.M. (2009) *Astronomy & Astrophysics*, **508** (1), 275–287.
238. Chang, Q., Cuppen, H.M., and Herbst, E. (2007) *Astronomy & Astrophysics*, **469** (3), 973–983.
239. Tielens, A.G.G.M., Tokunaga, A.T., Geballe, T.R., and Baas, F. (1991) *The Astronomical Journal*, **381**, 181–199.

6
Dust and Nanoparticle Spectroscopy

Harald Mutschke

6.1
Introduction I: Spectroscopic Observations of Cosmic Dust

Thomas Henning

6.1.1
Dust in the Interstellar Medium

Cosmic dust particles are distributed throughout the cold phases of our and other galaxies. Their presence is easily recognized when they are blocking or reddening the light of background stars, an effect best seen by the appearance of "dark" clouds in the Milky Way. The analysis of extinction curves has led to the development of various models for interstellar dust with silicates and carbonaceous grains as the main components [1, 2]. Particle size distributions in these models are often assumed to be based on power laws with mean sizes in the submicrometer range in order to reproduce the optical and near-infrared (NIR) extinction [3, 4]. The extinction curves vary between the diffuse interstellar medium and denser molecular clouds. This variation can be quantified by a single parameter $R = A(V)/E(B-V)$, the ratio of visual extinction to reddening [5]. The diffuse interstellar medium has R values closer to 3.1 with molecular cloud values up to 5.3. This trend can be interpreted by a shift of the grain size distribution to larger particles in molecular clouds, leading to less extinction at shorter wavelengths. The stellar light absorbed by the dust grains at ultraviolet and optical wavelengths is re-emitted at IR and submillimeter wavelengths. The observed mid-IR emission requires a component of very small grains (VSGs), being heated to elevated temperatures by stochastic absorption of energetic photons [4, 6, 7] (Figure 6.1).

The only strong dust absorption feature at ultraviolet and visible wavelengths is the so-called UV bump at 217.5 nm. A remarkable property of this relatively strong UV resonance is the constancy of its position for different lines of sight and its relatively narrow width [8, 9]. The band properties have been successfully reproduced by nano-sized hydrogenated amorphous carbon grains [10] (Figure 6.2) or large polycyclic aromatic hydrocarbon (PAH) molecules [11].

Laboratory Astrochemistry: From Molecules through Nanoparticles to Grains, First Edition.
Edited by Stephan Schlemmer, Thomas Giesen, Harald Mutschke and Cornelia Jäger.

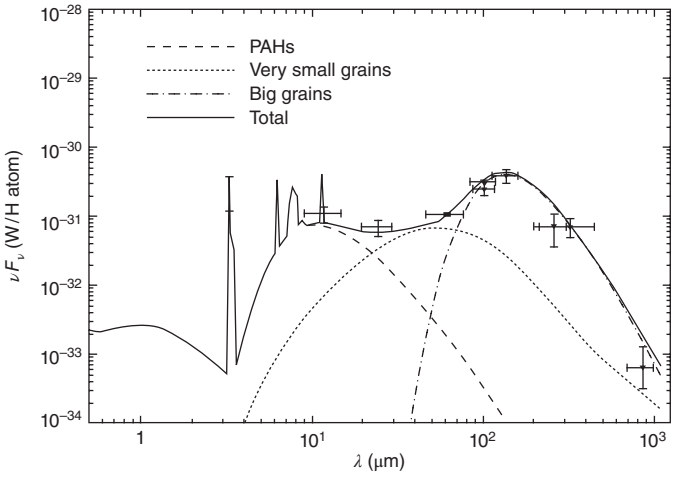

Figure 6.1 Dust emission spectrum. Observations (crosses) refer to the "cirrus" diffuse interstellar medium. The horizontal bars represent the filter widths. The model spectrum (solid line) is the combination of emission from PAHs, very small grains (VSGs), and big grains (BGs). (Reproduced from [6], copyright 1990 © permission from ESO.)

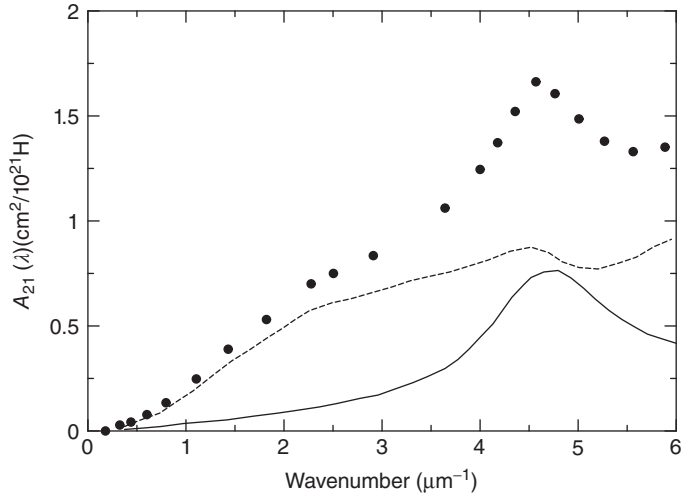

Figure 6.2 Mean interstellar extinction curve (filled circles) compared with the matrix-corrected spectrum of hydrogenated amorphous carbon nanoparticles (solid line), which is scaled in such a way that the Drude part of this spectrum completely accounts for the corresponding Drude part of the interstellar extinction curve. The difference between them (dashed line) represents the part of the extinction curve that can be attributed to other dust components (silicates). Reproduced from [10], copyright 1998 © permission from AAS.

The IR spectral region is often called the *fingerprint* region for cosmic dust because vibrational bands of oxides, carbonaceous solids, and molecular ices are located in this wavelength region. However, there are only very few pronounced bands in the spectra of IR background sources tracing the diffuse interstellar medium. These are the bands at 3.4 μm identified with aliphatic hydrocarbons and the absorption features at 9.7 and 18 μm caused by Si–O stretching and O—Si–O bending vibrations in amorphous silicates. Pendleton and Allamandola [12] concluded that the carbonaceous material, carrying the 3.4 μm feature, shares similarities with plasma-processed hydrocarbon laboratory dust analogs and is different from energetically processed molecular ices. Because of the unstructured and broad bands at 9.7 and 18 μm, a reliable identification of the band carrier with a specific amorphous silicate remains a difficult – if not impossible – challenge [13]. Cosmic abundance considerations and optical material properties have led to the frequently made proposal that amorphous silicates with olivine and pyroxene stoichiometry are responsible for the interstellar "silicate" absorption bands (see, e.g., Refs. [14–17]). The best analog material, possibly even actually interstellar, but a least circumstellar material from evolved stars, is the so-called GEMS particles (glasses with embedded metals and sulfides). These composite dust grains have been found in interplanetary dust particles; they share many of the properties assigned to amorphous silicates in the interstellar medium [18]. A potential contribution from crystalline silicates to the 9.7 μm feature must be <5% by mass [19]. In Figure 6.3, the observationally determined

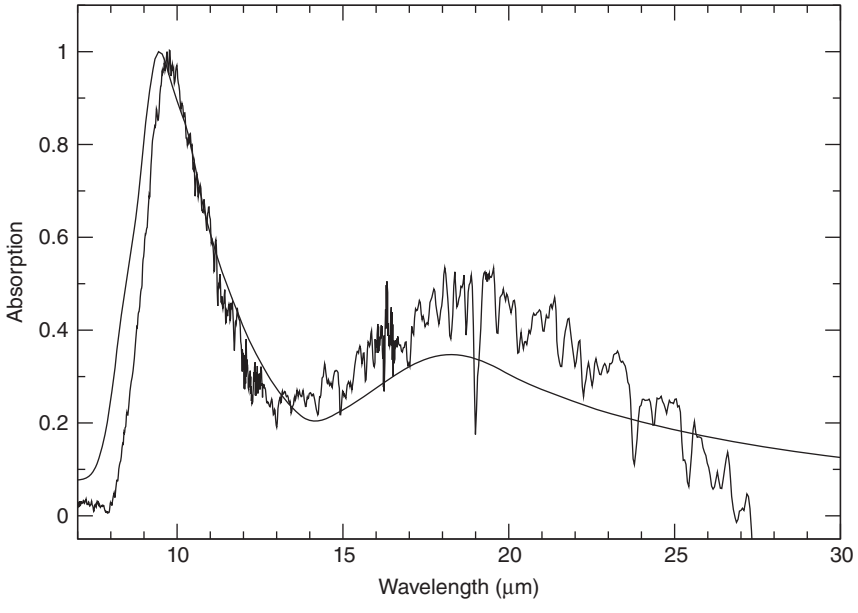

Figure 6.3 Interstellar dust absorption profile [15] compared to the extinction profile of "astronomical" silicates by Draine and Lee [1]. (Reproduced from [15], copyright 2006 © permission from AAS.)

silicate profiles are compared with the frequently used model for "astronomical" silicates by Draine and Lee [1].

Polarization measurements show very low values for the 3.4 μm feature, in remarkable contrast to the 9.7 μm silicate absorption band [20]. This observation supports the general view that the hydrocarbon material responsible for the 3.4 μm feature is not part of a mantle material around silicate particles, but forms a separate grain component. The relation of this carbonaceous dust material to the carrier of the strong UV bump remains one of the open questions of interstellar dust research.

In contrast to the diffuse interstellar medium, the spectra of IR sources embedded in molecular clouds show a very rich spectrum at near- and mid-IR wavelengths, mostly dominated by the silicate absorption bands and bands of molecular ices. The most abundant molecular ice is water ice. It was first discovered by Gillett and Forrest in 1973 [21] through its strong 3.08 μm stretching band and has abundances between 10^{-5} and 10^{-4} relative to hydrogen. Other water bands are located at 4.5 μm (combination mode), 6.0 μm (bending mode), 13.0 μm (libration mode), and 44 μm. Many of the molecular ice bands are not accessible from the ground. The Infrared Space Observatory (ISO), especially with its short-wavelength spectrometer (SWS) covering the wavelength range between 2.4 and 45 μm, provided the first complete inventory of molecular ice bands. The spectra with the best signal-to-noise ratios were obtained for bright IR objects embedded in molecular clouds. These sources are very young and massive stellar objects that are associated with local high-density molecular envelopes. The object W 33A is a prominent example for such sources. Its spectrum is characterized by a forest of molecular absorption bands [22] (Figure 6.4). ISO

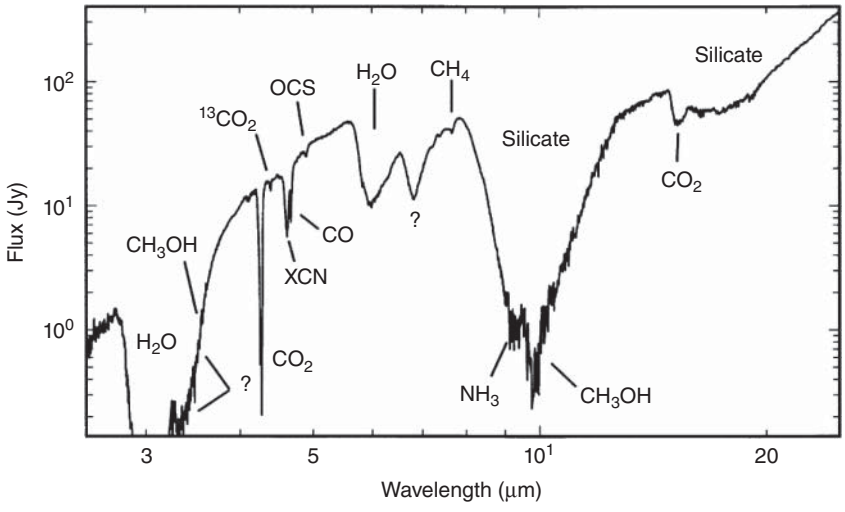

Figure 6.4 Complete 2.4–25 μm spectrum of W33 A obtained with the short-wavelength spectrometer of the ISO mission. (Reproduced from [22], copyright 2000 © permission from AAS.)

also provided a number of spectra of envelopes around intermediate-mass and even low-mass stars [23]. The spectra of all these objects trace molecular material that may have been modified by radiation and thermal processing caused by the embedded protostars. The median abundances of the various ices (CO, CO_2, CH_3OH, NH_3, CH_4, XCN[1]) relative to water are 100 : 29 : 29 : 3 : 5 : 5 : 0.3 and 100 : 13 : 13 : 4 : 5 : 2 : 0.6 for envelopes around low-mass and high-mass stars, respectively [24]. ISO and sensitive ground-based measurements, together with spectroscopy data provided by the Spitzer Space Telescope, also allowed obtaining spectra of background stars behind the Taurus, Serpens, ρ Oph, and IC 5146 molecular clouds and more isolated molecular cores [25–28]. These spectra trace the properties of molecular ices in more quiescent regions of molecular clouds and confirmed that the most abundant molecular ices are H_2O, CO_2, and CO, with CH_3OH and NH_3 being minor components; for a compilation of the abundances, we refer readers to the paper by Chiar *et al.* [27].

Multiple bands of H_2O, CO, CO_2, CH_3OH, and well-identified single bands of CH_4 (7.67 μm) and OCS (4.92 μm) have been observed with ISO [23, 29]. The CO_2 bending feature at 15.2 μm is the only non-water-ice band which has been discovered longward of the 9.7 μm silicate absorption band. Some of the bands are blended with other strong bands, which makes secure identifications more difficult. This is especially true for NH_3, H_2CO, and HCOOH. The exact shape, strength, and position of the various bands change from source to source, which can often be related to the environment of the molecule, especially the polar versus nonpolar phases of the ice. Water clearly dominates the polar phases and thus strongly influences the positions of some bands such as the CO bands at 4.67–4.68 μm [25, 26]. Such shifts in band positions can be used to reveal the thermal history of the ices [30]. Although the presence of OCN^- and NH_4^+ ions has been frequently discussed as evidence for energetic processing, both the identification of these ionic ices and their production by UV radiation or energetic particles remain a matter of considerable debate.

The molecular ices discovered thus far are all chemically simple. Their formation can be explained by the accretion of oxygen, carbon, and nitrogen atoms as well as carbon monoxide on grain surfaces and their subsequent hydrogenation and oxidation [31]. A picture of molecular ice evolution is presently emerging [24]: The first ice formation phase is driven by the hydrogenation of atoms, for example, $O + H \rightarrow OH$ and $OH + H \rightarrow H_2O$, and leads to water-dominated ices. Later, CO freezes out from the gas phase. Finally, the evolving protostars process the molecular ices thermally and through UV radiation. As a result, CO desorption and separation of the various individual ice components occur, and more complex organic molecules may form. The molecular mantles may also play an important role in the grain coagulation process in denser regions of molecular clouds. More complex molecular ices, although more difficult to detect, are much less abundant, if present at all, in quiescent regions of the molecular clouds, but may emerge in protostellar envelopes. Molecular oxygen and nitrogen would be important

1) XCN denotes the carrier molecules, such as OCN^-, of a C≡N stretching feature at 4.62 μm.

molecular ices to detect in order to constrain the oxygen and nitrogen budget, but they show no IR bands as pure systems because they lack dipole moments. Weak bands can be expected when these molecules are embedded in other molecular environments, but could not be detected so far.

6.1.2 Stardust

Evolved stars are a major source of cosmic dust in our and other galaxies [32]. These newly formed dust grains are often called *stardust*; components of this stardust could be directly identified by isotopic analysis of particles in meteorites [33]. In their late stages of evolution, low- to intermediate-mass stars are located on the so-called Asymptotic Giant Branch (AGB) of the Hertzsprung–Russell diagram. These AGB stars are characterized by vigorous mass loss, leading to the formation of large circumstellar envelopes. These envelopes are the sites where new dust grains form and get ejected into the general diffuse interstellar medium. The elemental and chemical composition of the envelopes mostly depends on the stage of evolution of the central stars and the associated radiation field. We can distinguish between oxygen-rich and carbon-rich envelopes, leading to a dichotomy of circumstellar envelopes with C/O ratios smaller or larger than 1. AGB stars start first as oxygen-rich stars, with C/O ratios close to 0.4, according to the cosmic abundance of these elements. In later stages of evolution, carbon will be dredged up from the stellar core region, resulting in C/O ratios larger than unity. The less abundant element is mostly consumed by the stable CO molecule, leading to oxygen-rich dust (silicates and other oxides) in oxygen-rich envelopes, and carbon-containing dust (carbonaceous material and carbides) in carbon-rich envelopes. In transition phases and under certain radiation conditions, both oxygen-rich and carbon-rich dust can occur in one and the same object.

AGB stars show a huge diversity of IR spectra, even among the class of oxygen-rich versus carbon-rich envelopes (for a classification based on ISO spectra, see, e.g., Ref. [34]). Some of these objects are among the brightest IR sources of our galaxy, and ISO could provide spectra with high signal-to-noise ratios (Figure 6.5). With the more sensitive Spitzer satellite, the spectroscopic studies of AGB stars have been extended to objects in the Magellanic Clouds [35]. A comprehensive overview on the results from the ISO and Spitzer missions has been provided by Molster *et al.* [36].

Oxygen-rich stars show the features of amorphous silicates at 10 and 18 μm. These silicate bands can occur in emission, absorption, and self-absorption, depending on the optical depth of the envelopes. The ISO mission led to the discovery of the spectral signatures of cold crystalline silicates in the spectra of AGB stars [38]. A forest of narrow features in the wavelength range between 20 and 70 μm could be attributed to pyroxenes and olivines [37–39]. (The structure of these species is discussed in Section 6.3.1.) Prominent olivine bands are located at 23.8 and 33.7 μm with pyroxene bands at 26.2, 32.9, 35.8, 40.5, and 43.1 μm. The analysis of the band positions, especially of the 69 μm olivine band and the

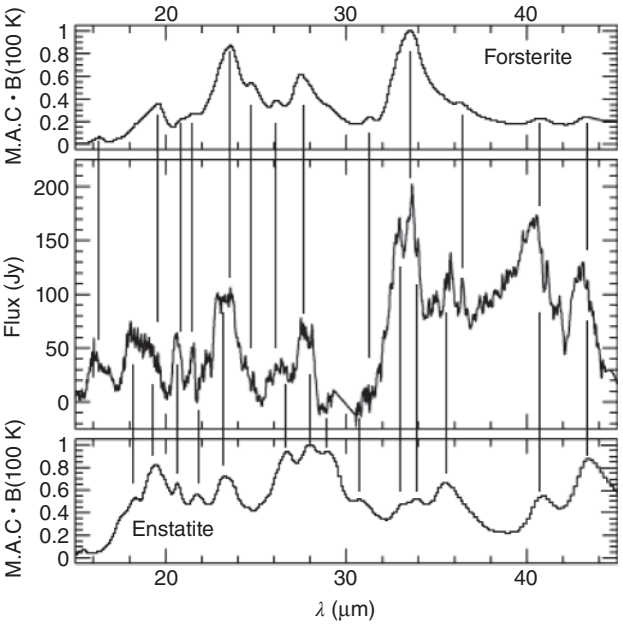

Figure 6.5 Comparison of the continuum-subtracted spectrum of the evolved stellar source AFGL 4106 with the normalized emission spectra of forsterite and clinoenstatite dust at a temperature of 100 K. (Reproduced from [37], copyright 1998 © permission from ESO.)

40.5 μm pyroxene bands, clearly indicated that the crystalline silicates are Mg-rich and Fe-poor in composition. The relative abundance of crystalline to amorphous silicates is, in general, quite modest, with typical values on the order of 10% and below. Other oxides in addition to silicates are present in oxygen-rich envelopes as well. The most prominent feature, detected in about 50% of oxygen-rich AGB stars, is located at about 13 μm. The carrier of the feature has been debated, and both corundum and spinel have been proposed with corundum as the more probable carrier (e.g., Refs. [40, 41]; for more details see Section 6.5.3).

Carbon-rich stars have envelopes that are characterized by very red dust continuum emission, which is, in general, attributed to hydrogenated amorphous carbon grains. A prominent feature located at about 11.3 μm is attributed to silicon carbide SiC (e.g., Refs. [42–44]; for experiments, see Section 6.6.3). Another feature, which is relatively common in carbon-rich AGB stars, post-AGB stars, and planetary nebulae, is located at 30 μm and has been convincingly attributed to magnesium sulfide (MgS) [45–47].

After an AGB star has passed through all its evolutionary stages, there is a relatively short-lived post-AGB phase. The mass-loss process comes to an end, and the star evolves to the planetary nebula phase. Some carbon-rich post-AGB stars show a "21 μm" feature [48], which is actually more closely located to 20.1 μm. The peak position and the band profiles of this feature are remarkably constant [49, 50]. The 21 μm feature could also be found in the spectra of carbon-rich post-AGB stars

in the Magellanic Clouds, but the features are generally weaker than in Galactic post-AGB stars [51]. Many materials have been proposed as potential carriers of this feature, but none has passed all the necessary tests. Two of these assignments are discussed in Sections 6.5.5 and 6.6.3.

Recently, the IR bands of fullerenes could be discovered in spectra of post-AGB stars and a planetary nebula [52, 53]. Although hypothesized for a long time, this discovery finally confirmed that fullerenes can form in astrophysical environments.

Binary post-AGB stars are often surrounded by stable dusty disks. Their IR emission is dominated by crystalline and amorphous silicates. With values of up to 60% [54], the fraction of crystalline silicates is the highest among all astronomical sources. This crystalline dust is mostly forsterite and enstatite. Some evidence for small amounts of amorphous silica has also been found in the spectra of this interesting class of objects.

6.1.3
Dust in Planetary and Protoplanetary Systems

Protoplanetary disks form another class of objects that show a rich variety of dust features in their IR spectra (for a review see, e.g., Ref. [55]). These features mostly occur in emission, tracing the optically thin surface layers of protoplanetary disks. Depending on the luminosity of the central objects and the wavelength position of the individual features, the emission comes from different radial zones in the disk. Optical depth effects have to be taken into account when analyzing the material distribution in the disks. The ISO mission provided spectra of high resolution over a broad wavelength region for the nearby IR-bright Herbig Ae/Be stars [56–58]. Herbig Ae/Be stars are young stars of intermediate mass often surrounded by protoplanetary disks. The nearby sample of these stars has been extensively studied from the X-ray region to the radio frequency region. Apart from the broad features produced by amorphous silicates, especially the 10 μm feature, evidence for the presence of crystalline silicates has been found in quite a number of Herbig Ae/Be disks. The spectrum of the bright IR source HD 100546 remains a classic example of disks with crystalline silicates. Strong bands at 10.2, 11.4, 16.5, 19.8., 23.8, 27.9, 33.7 μm and weaker bands at 10.5, 12.0, 21.7, 31.3, 36.3, and 69 μm have been found in the spectrum of HD 100546 [56]. They closely match in position and strength with those of crystalline forsterite as measured in the laboratory [59]. Forsterite is the dominating crystalline silicate dust component in these disks, although evidence for weaker enstatite features could be found. The HD 100546 spectrum also shows two broad bands at 23 and 60 μm, potentially originating from iron oxides and crystalline ice, respectively [56]. The analysis of the far-IR ISO spectrum of the young star HD 142527 indicated the presence of not only crystalline water ice but also hydrous silicates [60]. The latter are interesting because they are produced from other silicates by aqueous alteration. Since research on these minerals is not covered in this chapter, we refer the reader to the literature cited in Ref. [61].

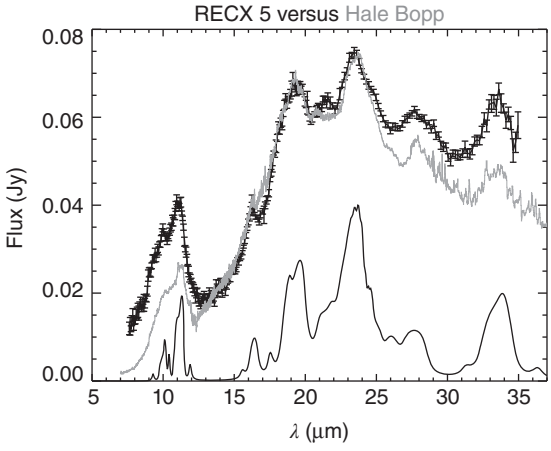

Figure 6.6 Comparison of the ISO spectrum of comet C/1995 01 (Hale-Bopp, gray curve) [69] with the spectrum of the disk around the young star RECX5, which has a spectral type of M4 (black bars [68]). The lower line is an emission spectrum for a distribution of hollow forsterite spheres (compact equivalent radius of 0.1 μm) at 200 K.

The Spitzer mission allowed extending these studies to objects of much lower brightness, including statistically relevant samples of disks around T Tauri stars [62–65] and brown dwarfs [66, 67]. The disks around brown dwarfs and T Tauri stars show a mineralogy similar to that of the disks around the higher mass Herbig Ae/Be stars. In general, these spectra are of lower quality and the mineralogy is less well constrained by them than for the brighter Herbig Ae/Be stars. The shape and the strength of the 10 μm feature indicate more processed dust for disks around very low mass stars and brown dwarfs [65, 67]. One of the best spectra of a low-mass object has been obtained for the M4 star RECX5 in the 8 Myr old η Chamaelontis star cluster [68] (Figure 6.6). Its spectrum and disk structure has many similarities with the much more massive object HD 100546.

A very comprehensive dataset of high-quality Spitzer spectra of Herbig Ae/Be stars with silicate features has been analyzed by Juhász *et al.* [70]. Spitzer's view of aromatic and aliphatic hydrocarbon emission in Herbig Ae stars has been summarized in an accompanying paper [71]. The study of silicate-containing Herbig Ae/Be disks demonstrated that, apart from amorphous silicates with olivine and pyroxene stoichiometry, forsterite and enstatite, and in some cases amorphous silicon dioxide, no other dust component with IR features is needed to represent the IR spectra. This does not preclude materials such as iron particles, pure carbonaceous particles, or larger iron sulfide grains that show no strong IR features from being dust components of protoplanetary disks. The analysis of the spectra also indicated that the enstatite grains are more concentrated toward the warm inner disk than the forsterite, in contrast to the predictions of equilibrium condensation models. Interferometric observations of the innermost disks showed high degrees of dust crystallinity and a dominance of olivine particles [72]. Crystalline silicon dioxide has been identified in the mid-IR Spitzer spectra of a number of T

Tauri stars [73]. In the lucky situation of a disk seen edge-on, Spitzer spectroscopy revealed strong features of molecular CO, CO_2, and H_2O bands and weaker bands of minor ice components [74].

The only young stellar object with a disk, where the far-IR band of forsterite at 69 μm could be detected with ISO spectroscopy, was the bright star HD 100546; despite the large IR fluxes of this source, the IR spectrum of this feature was relatively noisy [56]. The Herschel Space Observatory mission is now covering this wavelength region with the Photoconductor Array Camera and Spectrometer (PACS) instrument, of much increased sensitivity. One of the first results was the confirmation of the presence of the 69 μm feature in the spectrum of HD 100546 [75]. The analysis of the band position clearly demonstrated that the crystalline olivine grains are iron-poor. Meanwhile, the 69 μm forsterite feature has been discovered in a few more Herbig Ae/Be stars [76].

In contrast to the gas-rich and optically thick protoplanetary disks, debris disks contain only very little or no gas and are mostly optically thin. This means that the dust particles in debris disks are directly exposed to stellar radiation, implying that submicrometer-sized circumstellar dust grains would have very limited lifetimes on the order of 10 Myr. They also would have short lifetimes as a result of direct collisions. Therefore, the only viable explanation for the presence of such debris disks around relatively old stars is the continuous production of smaller boulders by the destructive collisions of larger bodies, followed by a collisional cascade which finally leads to small dust particles. This process explains the name "debris" disks for these circumstellar structures. The infrared excess emission of such a debris disk was observed for the first time from the infrared "standard" star Vega by the Infrared Astronomical Satellite (IRAS) [77]. This gave rise to the term *Vega-phenomenon* for this class of objects, which was frequently used in the past. The stars Vega, β Pictoris, Fomalhaut, and ϵ Eridani show particularly pronounced debris disks, which could all be spatially resolved at a variety of wavelengths. Therefore, they are often called the *big four* objects among the debris disks. Today, more than 1000 debris disks are known, and their spectral energy distributions have been extensively characterized by observations with ISO (e.g., Ref. [78]), the Spitzer space mission (e.g., Ref. [79]), and the Herschel Space Observatory (e.g., Ref. [80]).

Debris disks are considered to be related to mature planetary systems and, indeed, a planet in the β Pictoris system has been discovered [81, 82] and a planetary candidate has been identified in the Fomalhaut system [83]. Recently, quite a number of debris disks could be associated with planet host stars.

Most known debris disks contain relatively cold dust at larger distances from the star, resembling the Kuiper belt in the solar system [84]. A much smaller percentage of debris disks contains warmer dust closer to the star (<10 AU), similar to the dust in the asteroidal belt. A very interesting example of this class of objects is the K0V star HD 69830, which has a mid-infrared spectrum with a dust temperature of about 400 K, implying that the dust is concentrated in a relatively narrow ring around 1 AU from the star [85]. The infrared spectrum shows evidence for crystalline silicates, resembling the spectrum of the comet Hale-Bopp. HD 69830

was also found to host three Neptune-mass planets orbiting the central star on nearly circular orbits [86]. The first discovery of crystalline silicates in a debris disk was actually based on ground-based mid-infrared spectroscopy of β Pictoris [87]. From an analysis of the 69 μm feature observed with the Herschel PACS instrument in the β Pictoris spectrum, it was concluded that the grains contain 2–3% iron, in contrast to most of the observations of protoplanetary disks [88]. The main result of a comprehensive analysis of the silicate mineralogy of warm debris disks, based on Spitzer spectroscopy data, reveals the presence of Fe-rich olivine crystals [89]. The presence of these Fe-rich olivine grains and their general absence from protoplanetary disks, together with the overall differences in the mineralogy of these types of objects, suggest that the transient crystalline dust in warm debris disks is dust of a new generation. In the debris disk around the main-sequence star HD 165014, evidence for crystalline enstatite, but not forsterite, was found [90]. This is another surprising result of debris disk mineralogy and may imply that enstatite dust originates from differentiated parent bodies.

6.2
Introduction II: Techniques in Laboratory Dust Spectroscopy

Harald Mutschke and Akemi Tamanai

6.2.1
Calculated Versus Measured Comparison Spectra

In the previous section, we have shown how the properties of cosmic dust particles are derived from the interpretation of their absorption and emission spectra. The analysis of the spectral features is, of course, always based on spectroscopic data of their possible carrier dust species, which originate from laboratory work. The laboratory data may, for instance, be entered into a model of radiative transfer in the dusty cosmic environment aimed at reproducing the observed spectral energy distribution. Often, however, a first interpretation is attempted by looking for coincidences between observed astronomical features and the bands of a "comparison spectrum" such as, for example, shown in Figure 6.5, or by a simple fit with a linear combination of such comparison spectra.

Comparison spectra are obtained in two ways: either by direct measurement of absorption or emission spectra of laboratory "dust samples," or by calculating synthetic spectra from theoretical models of the emission or absorption of radiation by dust particles. Nowadays, calculated spectra are often preferred for the simple reason that parameters such as the grain size distribution, the grain geometry, and the composition of possibly inhomogeneous dust particles can be easily varied. It is not easy, however, to synthesize a spectrum that agrees well with a measured or observed dust spectrum. The reasons for that are a key to understanding small-particle spectra. Thus, in the beginning of this section, approaches to physically realistic models for the computation of such spectra will be discussed. On the other hand, laboratory-measured spectra of well-characterized dust particles are

not only essential for the model development but can also be equivalently used in many applications and are sometimes still easier to obtain than good simulated spectra. Measurements of such spectra will thus be subject of a second subsection. In addition, synthetic dust spectra depend on input data characterizing the optical properties of the solids constituting the dust particles. Measurements of these "optical constants" of relevant solids will be discussed in the third following section.

By "optical constants," we mean the wavelength-dependent complex refractive index $m = n + ik$ or the dielectric function $\varepsilon = m^2$ of a solid material. Dust particles can be considered to be characterized by these "bulk" optical constants if they consist of a sufficiently large number of atoms such that only a minority belongs to the "surface" with special electronic and vibrational states. A typical limiting particle diameter may thus be in the range of a few nanometers. Below this size limit, quantum size effects and thermal nonequilibrium (stochastic single-photon heating) may become important, which we, for the moment, exclude from consideration (but see Section 6.7). For most relevant solids, the optical constants are now available with sufficient wavelength coverage, and are tabulated in accessible databases. An important database in book form which should be mentioned here is the *Handbook of Optical Constants of Solids* edited by Palik [91], which comprises three volumes that appeared in 1985, 1991, and 1998. An important source of data and references is the Jena-St.Petersburg-Heidelberg internet database [92], which is specifically dedicated to cosmic dust applications. It is located at http://www.mpia-hd.mpg.de/HJPDOC. Data provided by the astrophysical laboratories in Jena and Osaka can be found at http://www.astro.uni-jena.de/Laboratory/OCDB and http://optik2.mtk.nao.ac.jp/~suto/Mineral/, respectively.

Calculating a dust absorption or emission spectrum from these optical constants means computing the wavelength-dependent cross sections $C(\lambda)$ of certain particles for these processes by means of a light-scattering model. Together with the areal density of particles in the line of sight, these cross sections will determine the amount of extinction (absorption and/or scattering) of light or, if multiplied with a Planck's function, the amount of emitted radiation. Sometimes, the cross sections are expressed in terms of efficiencies $Q(\lambda)$, which are given by the ratio of absorption (scattering) cross section to the geometrical particle cross section. According to Kirchhoff's law, the emission and absorption cross sections (efficiencies) of a particle in thermodynamic equilibrium are identical at each wavelength. Thus, when speaking of the absorption cross section, we will mean the emission cross section as well.

Many different models have been used to simulate dust absorption cross sections. These models can differ both in the grain geometry chosen and in the theoretical approach used to compute the electromagnetic fields scattered by the particles. Cosmic dust particles often cannot be considered to be homogeneous and spherically symmetric, which would have allowed the use of simpler approaches such as Mie theory [93]. Instead, they are often likely to be irregularly

shaped and/or aggregates of several grains. Since this determines the boundary conditions for the fields inside and outside the individual grains, it influences the spectra. This happens predominantly where the optical constants take high values, such as, for example, in infrared bands. The far-infrared emissivity is another important case that is sensitive to the particle morphology [94], especially if conducting materials such as carbon or metallic iron are involved. Consequently, in most cases, quite elaborate grain models are needed in order to predict spectra that match the observations (a possible exception to this will be discussed in Section 6.5).

In the first decade of the new century, the development of such models has made great progress, accompanied by a better understanding of the effects of grain morphology on infrared band profiles achieved by experimental studies. Although the most versatile and physically correct models, such as the discrete dipole approximation (DDA [95]), require quite large computational effort, in today's understanding it seems that the use of such models is unavoidable for a correct synthesis of dust spectra. In DDA, a particle is represented by a large number of electrical dipoles placed in a grid within the particle volume, and interacting through their dipole fields. The calculation of absorption and scattering by such a particle can be done only for one particle at a time, but for any particle geometry, even of relatively large size. Furthermore, complex particle geometries are now known to have spectra similar to those of particle ensembles with a distribution of geometries (see below). This reduces the required effort once such complex geometries have been identified. Figure 6.7 gives an example of size-dependent comparison spectra for a complex grain shape calculated with DDA (M. Min, personal communication).

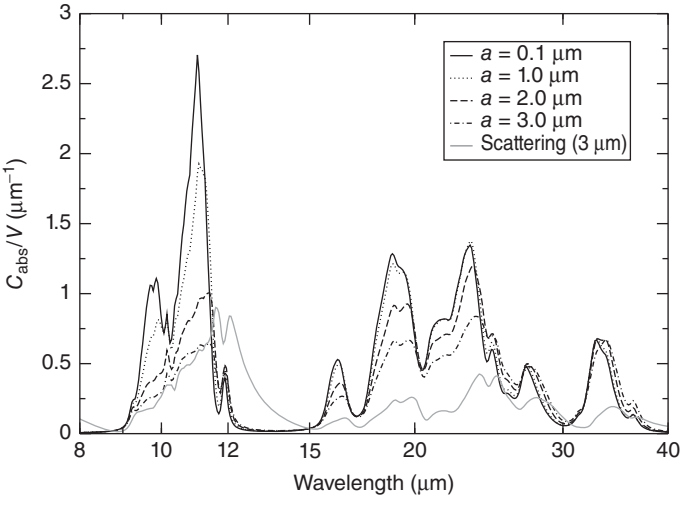

Figure 6.7 Infrared emission/absorption cross section spectra calculated for a statistical ensemble of porous irregular forsterite (Mg_2SiO_4) particles of different sizes (M. Min, personal communication).

When only *homogeneous* particles with sizes much smaller than the wavelength need to be modeled (i.e., in case of the so-called Rayleigh limit[2]), the spatial dipole distribution used to describe a particle in the DDA can be translated into a distribution of form factors (DFF),[3] as has been shown by Ref. [97]. The emission/absorption cross section of the particle can then be written as

$$C_{\mathrm{abs}} = V_{\mathrm{p}} \frac{2\pi}{\lambda} \int_0^1 \Im \left\{ \frac{P(L)}{1/(\varepsilon - 1) + L} \right\} dL \tag{6.1}$$

with V_{p} being the particle volume, λ the wavelength, and $P(L)$ the probability function of form factors L in the interval (0; 1). Note that for each L in this interval, a certain negative value of ε (with negligible imaginary part) will lead to a vanishing denominator in the integrand of Eq. (6.1), that is, each L will give a strong absorption "peak" at the spectral position of the corresponding ε value. An absorption band is then assembled by integrating these peaks with weights corresponding to $P(L)$. In (ideal) phonon resonances, the range of negative ε values roughly corresponds to the range between transverse optical (TO) ($\varepsilon = -\infty$) and longitudinal optical (LO) ($\varepsilon = 0$) phonon frequency, $P(L)$ for the small L values therefore determining the long-wavelength wing of a phonon band, $P(L)$ for the large L values the short-wavelength wing. Figure 6.8 demonstrates that a measured phonon spectrum can be nicely reproduced using the DFF model. Certain shape factor distributions have been shown to characterize some typical grain shapes of particulates [98].

Since a set of three form factors ($L_1 + L_2 + L_3 = 1$) also describes an ellipsoid of a certain geometry [96], the general validity of this approach means that the absorption and scattering properties of an arbitrary complex particle can be expressed by the average properties of an ensemble of ellipsoidal particles (and vice versa, see the discussion for the DDA above). The often-used "continuous distribution of ellipsoids" (CDE [96], $P(L) = 2(1 - L)$) is a special case of a DFF; strictly spherical particles would be represented by $P(L) = \delta(L - 1/3)$. Other statistical ensembles developed to describe complex particle morphologies such as the "distribution of hollow spheres" (DHS [99]), can be characterized by a certain DFF as well [97]. Consequently, it would seem that the statistical approach using, for example, the DFF model could simplify the spectra calculations compared to DDA computations if the particles can be assumed to be small and homogeneous.

However, it has recently been realized that statistical approaches, unfortunately, have some problems in handling the anisotropy of non-cubic crystalline materials. This anisotropy has to be treated by averaging the results of separate calculations for the optical constants corresponding to the crystal axes, which is exact for spherical grains in the Rayleigh limit. In other cases, the separation is an incorrect simplification and can lead to wrong results [98]. If the calculation aims at

2) This is the limit where a quasi-electrostatic treatment is possible; the condition is usually given as $2\pi a \ll \lambda$ and $2\pi a \mid m \mid \ll \lambda$, a being the particle radius. In this limit, the light scattering by the particles (Rayleigh scattering) is proportional to $(a/\lambda)^4$, but is still negligible compared to strong absorption.

3) The form factors are related to electrostatic depolarization factors, see Ref. [96].

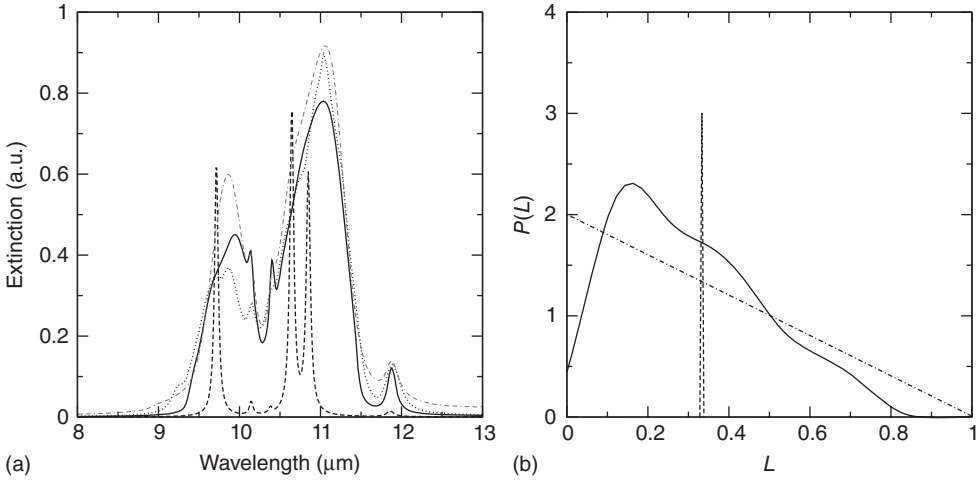

Figure 6.8 Fit of the measured Si–O stretching vibration band of small forsterite particles (a, double-dash-dotted line) by a distribution of form factors (DFF) model (solid lines in (a,b)). For comparison, we give the simulated band profiles for spherical grains (dashed lines) and for the porous irregular particles simulated with the DDA model from Figure 6.7. The DFF representation of spherical grains and of the CDE (b. dash-dotted line) are also shown.

precise band profiles, it is thus better to return to the DDA model, where dipoles of different polarizabilities can be handled simultaneously. For further information about the theoretical models, the reader is referred to the original papers and a number of monographs [96, 100, 101].

6.2.2 Measuring Dust Absorption Spectra

Direct measurements of the absorption spectra of solid particles or nanoparticles provide the second kind of comparison data for the analysis of cosmic-dust spectra. Unfortunately, there are some important limitations to this approach. The first major limitation is that, for particle sizes exceeding the Rayleigh limit, scattering losses become important even in comparison to strong absorption bands (see [2)] above). Therefore, measuring comparison spectra for larger dust grains observed in emission requires either measuring, indeed, emission spectra, or the separation of scattering and absorption losses when extinction is measured. Both are difficult (we will mention a method for the second option in Section 6.6.1, [15)]), so the direct measurement of comparison spectra is usually restricted to the size range within the Rayleigh limit. This is, of course, still a very important case, because small grains often dominate the spectroscopic signal. Other limitations concern sample preparation, which may include embedding the particles into a matrix or may introduce strong particle clustering. This may be untypical for the kind of cosmic dust considered but will often strongly influence the measured spectra.

Table 6.1 Ideal sample thicknesses d for transmission measurements in certain spectral ranges with typical k values.

Spectral range	Thickness	Areal mass density
UV electronic absorption (λ = 100 nm, $k \approx 1$)	10 nm	$\sim$2 μg cm^{-2}
Vis/NIR impurity absorption (λ = 1 μm, $k \approx 10^{-4}$)	1 mm	$\sim$200 mg cm^{-2}
IR phonon bands (λ = 10 μm, $k \approx 1$)	1 μm	$\sim$0.2 mg cm^{-2}
Submillimeter continuum absorption (λ = 100 μm, $k \approx 10^{-2}$)	1 mm	$\sim$200 mg cm^{-2}

Corresponding areal mass densities $d \times \rho$ assuming ρ = 2 g cm^{-2} for comparison with values in Section 6.2.2 are also given.

Thus, in general, laboratory-measured spectra should also be carefully evaluated before being used to help interpret astronomically observed spectra.

Most spectroscopic measurements of solids can be conducted with commercial spectrometers, that is, grating spectrometers for visible and ultraviolet wavelengths and Fourier transform spectrometers for the infrared range. The spectral resolution does not need to be very high. Spectral features of solids are relatively broad, so that a resolution $\lambda/\delta\lambda$ = 1000 is typically sufficient for the sharpest bands. For the shortest (<200 nm) and longest (>50 μm) "optical" wavelengths, spectrometers operating in vacuum are required. For temperature-dependent measurements (Sections 6.3.5, 6.4.2, and 6.5.8), commercial devices (cryostats, high-temperature cells) are available. At even shorter and longer wavelengths, synchrotron and microwave sources, respectively, can be used. Spectrometers for these wavelength ranges are often not routine instruments, although terahertz spectrometers have now reached a state of commercial availability. At high energies, electron energy loss spectroscopy can also provide spectroscopic data equivalent to optical ones and is often the major source of information on optical constants (Section 6.6.1).

The most widely used method of preparing a sample of particle material for absorption spectroscopy, in particular for infrared absorption measurements, is the pellet method. The vibrational excitations, which dominate the mid-infrared absorption by the solid particles (single-phonon excitation), produce absorption cross sections per unit particle volume[4] of up to 1 μm^{-1} (1 μm^2 per cubic micrometer). Thus, in the absorption peaks, a "compressed-sample thickness" of about 1 μm is sufficient to "block" the beam or, in other words, to produce an optical depth on the order of unity, which are the optimum conditions for the measurements (Table 6.1). A "compressed-sample thickness" of 1 μm corresponds to a sample volume of 0.1 mm^3 per square centimeter beam cross section. To evenly distribute these small amounts of material in the beam of the IR spectrometer, it is convenient to mix them with a transparent material such as potassium bromide, cesium iodide, or polyethylene powder (depending on the transparency in

4) For particles in the Rayleigh limit, this quantity is independent of the particle size, see Eq. (6.1). Since both C_{abs} and V are additive, it can also be considered the total cross section of an ensemble of identical particles.

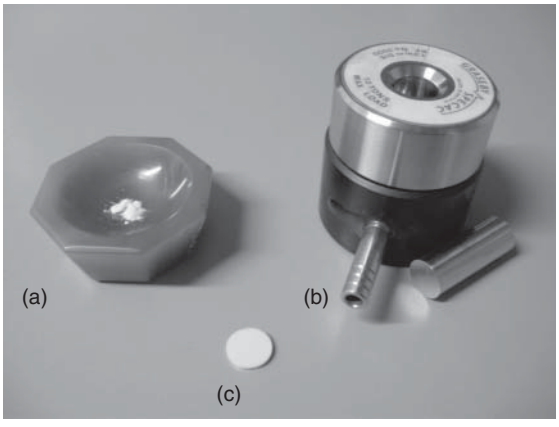

Figure 6.9 Illustration of pellet preparation. (a) Agate mortar for mixing sample and embedding material. (b) Pressing tool into which the mixture is placed and pressed for several minutes under 10 tons of load and concurrent vacuum pumping through the tube in front of it (for KBr and CsI pellets). (c) Resulting 13 mm pellet (200 mg polyethylene in this case).

the desired spectral range), which can be pressed into a pellet. Figure 6.9 shows the tools needed for mixing and pressing. Pellets of 13 mm diameter and 0.2 g mass are often used, with ≈0.1% of the mass corresponding to the sample.

Usually, the mass absorption coefficient κ, which is the sum of all particle absorption cross sections divided by the total sample mass,[5] is preferred as the measured quantity, because the sample mass (instead of the volume) is directly controlled in the preparation of the pellets. The transmission T through a pellet is then given by Beer's law in the form

$$T = (1 - R)^2 \cdot \mathrm{e}^{-\sigma \cdot \kappa} \tag{6.2}$$

where $\sigma = m_{\mathrm{sample}}/(\pi d^2_{\mathrm{pellet}}/4)$ is the areal mass density[6] of sample in the pellet. The reflection losses $(1 - R)^2$ at the pellet surfaces can be removed by normalizing to a reference measurement with a blank pellet.

If the absorption spectrum to be measured is characterized by lower κ values, such as often happens in the far-infrared spectral range, the areal mass density has to be increased. Pellets of up to $\sigma \approx 300\,\mathrm{mg\,cm^{-2}}$ have been produced for measurements of the continuum absorption in the submillimeter wavelength range (Section 6.3.5). In this case, the particles will no longer be separated by the embedding. This means that effects of particle clustering may influence the spectrum, which should be checked and, if possible, corrected by using theoretical models such as effective-medium theories [102, 103].

5) Thus, κ is equal to C_{abs}/V divided by the mass density.
6) In astronomy, the areal density is often called *column density*.

An important point in the sample preparation is the production of a sufficiently small-grained particulate satisfying the Rayleigh condition. Starting from an arbitrarily sized powder, milling with a ball mill is a suitable technique to decrease particle sizes. Care should be taken to use balls and containers of a material harder than the sample material in order to avoid contamination. Additionally, it should be noted that intense milling may introduce structural defects (Section 6.4.4). The remaining larger grains can be removed by sedimentation in a liquid such as ethanol or acetone. The sedimentation velocity for particle radius a can be estimated from Stokes' law

$$v_{\mathrm{p}} = \frac{2}{9} a^2 \cdot g(\rho_{\mathrm{p}} - \rho_{\mathrm{l}}) \cdot \eta^{-1} \tag{6.3}$$

where η and ρ_{l} are the dynamical viscosity and mass density of the liquid, respectively, ρ_{p} is the mass density of the particle, and g is the gravitational acceleration. After a few hours, in a several-centimeter- high column of liquid, only submicrometer sized particles, which fulfill the Rayleigh condition for infrared radiation, will remain, and can be recovered, for instance, by drying in an oven.

A particulate sample can also be split into rough size fractions by sequential sedimentation. Figure 6.10 gives an example of transmission spectra measured for such size fractions. The shoulder on the long-wavelength side of the absorption band, which is growing with the particle size, is due to a scattering contribution to the spectrum, similar to the one shown in Figure 6.7. Such scattering effects of larger grains, however, would be absent in emission. Thus, the measured transmission spectra of larger grains can only be used for comparison to dust extinction spectra.

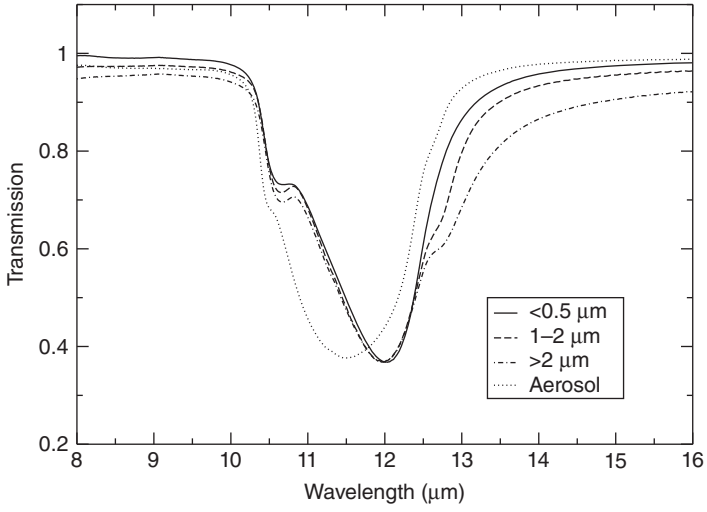

Figure 6.10 The lattice vibration band of silicon carbide particles in their infrared transmission spectrum measured for different size fractions embedded into the KBr pellet. The long-wavelength wing is caused by scattering losses [42]. The dotted line shows a spectrum of the smallest size fraction measured in aerosol (see text).

The advantages of the pellet technique are easy preparation, small sample consumption, and quantitative determination of the mass absorption coefficient from the measured spectral transmission of the pellet and the known areal mass density of the sample. The technique can also be used to measure variations of the absorption bands with temperature, at least toward low temperatures (Section 6.4.2). The drawback of the method is the possible influence of the polarization of the embedding medium on the spectra. It can be easily shown by calculations, for instance, using Eq. (6.1),[7] that such an influence exists. In the general case of nonspherical or even irregular particle shapes, however, it is difficult to correct for this influence, although it is possible if the optical constants of the particle's material are known [104, 105].

An interesting alternative to the pellet method is the so-called aerosol infrared spectroscopy, where the particles are dispersed in a gaseous environment which, of course, resembles much more the state in which cosmic particles actually exist than a pellet does. The sedimentation speed (Eq. (6.3)) of submicrometer-sized particles in a gas at normal pressure is slow enough to maintain the "aerosol" conditions for many minutes; thus a transmission spectrum of the "aerosol cloud" can be measured.

The aerosol spectroscopy technique was introduced to the measurement of astrophysically relevant dust spectra by Tamanai *et al.* [106]. The experimental setup used at the astrophysical laboratory at AIU Jena consists of a White-type multipath gas cell connected to a Bruker 113v FTIR spectrometer and using a deuterated triglycine sulfate (DTGS) pyroelectric detector with a CsI window. The aerosol is produced by a Palas RBG 1000 rotating-brush particle disperser and passes also an impactor-type grain-size discriminator to remove big clumps of particles before the aerosol reaches the gas cell. A sketch of the setup is shown in Figure 6.11.

This technique has proven suitable not only for avoiding the influence of a solid embedding medium but also for a detailed study of morphological effects on infrared spectra of dust particles [107]. The reason for this is that, in contrast to the pellet method, the aerosol particle morphology can be routinely inspected. To do this, after the spectroscopic measurement, a part of the particles is simply filtered from the aerosol and examined with a scanning electron microscope (SEM). Figure 6.11 gives an example of such an SEM image.

The drawback of this method is that the measured absorption spectra are not quantitative, because an independent measurement of the areal mass density (column density) in the spectrometer beam is not feasible with sufficient accuracy. However, by comparison with simulated spectra, the measured ones can be roughly normalized. Even without this procedure, the spectra measured with the aerosol method (an internet database is available at http://www.astro.uni-jena.de/Laboratory/Aerosol/index.php) have the advantage that the band profiles can be directly compared with astronomical spectra with no need to account for effects of an embedding medium, because the gaseous environment is sufficiently

7) To take an embedding medium into account, ε has to be divided by the dielectric constant of that medium, and λ by its refractive index.

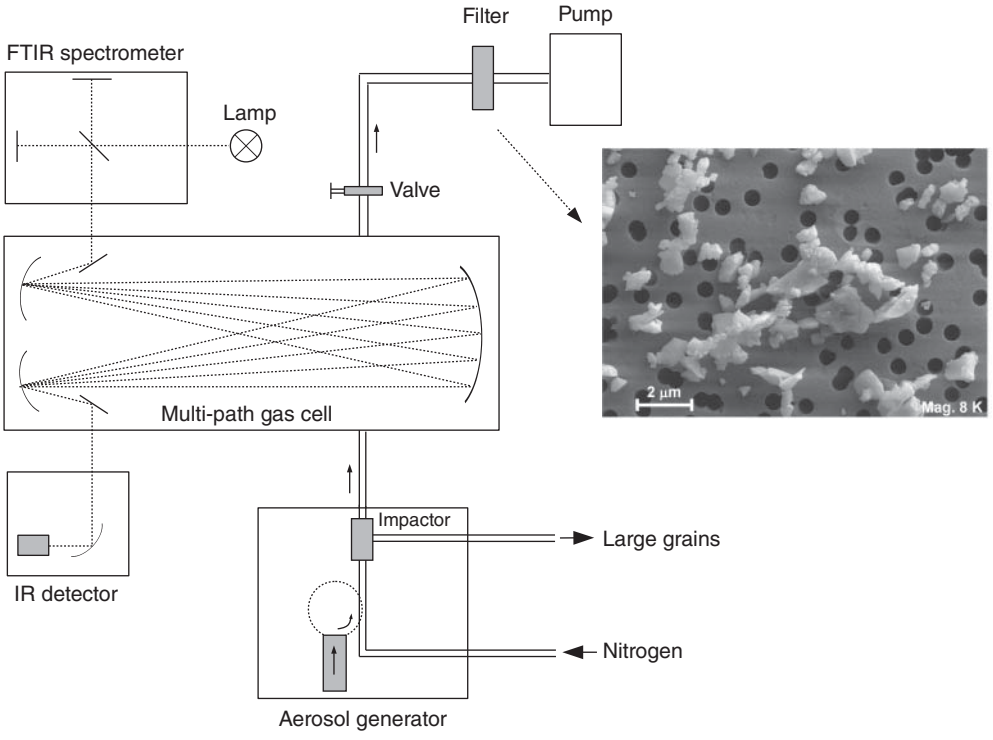

Figure 6.11 Schematic of the aerosol spectroscopy setup as used at AIU Jena. An SEM image of filtered aerosol particles is also shown.

dilute so as to be negligible. Figure 6.10 demonstrates how a gaseous environment changes the spectrum with respect to a solid matrix. More comparisons of aerosol and pellet spectra can be found in Refs. [108] and [109].

Quite often, dust particles are prepared by simple deposition onto the surface of an optical window. This is particularly the case in condensation experiments, where only small amounts of material are condensed and measurements within the vacuum apparatus are desired (Section 7.2). The deposited particles are often nanoparticles, that is, in the size range below 20 nm. In many cases, the amount of deposited material is at least approximately known, for instance, from the simultaneous deposition on a quartz microbalance. A problem with this method is that here the particles are heavily clustered, forming a highly porous film, which at least on the length scale of infrared wavelengths is more or less continuous. For infrared measurements, films with areal mass density similar to typical pellets are required, for measurements in the UV–vis wavelength ranges they need to be considerably thinner ("compressed-sample thickness," in the range of a few 10 nm, Table 6.1). In any case, the transformation of such a spectrum into that of an ensemble of isolated particles may be nontrivial, especially if strong absorption bands are present (remember that large optical constants tend to enhance morphological effects, Section 6.2.1).

A possibility to avoid this strong clustering of the deposited nanoparticles is through matrix-isolation spectroscopy, where the particles are frozen in an ice layer grown simultaneously as the particles are deposited. Noble gases such as Ar are well suited for this purpose but require an optical substrate cooled to temperatures of 30 K and below. Neon ice has a lower refractive index and thus less matrix influence, but has a very low condensation temperature and is difficult to grow with simultaneously impinging particles. Argon matrixes have been proven to allow rather good isolation of the particles both for UV–vis and infrared spectroscopy and are a valuable tool if clustering effects of particles need to be suppressed [10, 105].

Finally, special spectroscopic measurements of minerals are done with diamond anvil cells creating high pressures [110]. This technique has also been used for the spectroscopy of minerals of astrophysical interest. Usually, the high pressure will transform the dust particles into a continuous film. Although a thin-film spectrum is normally expected to differ from that of small particles (except for extremely flat particles oriented normal to the incident beam[8]), such measurements on, for example, SiC powders have yielded infrared data still showing the characteristics of small-particle spectra [111].

6.2.3
Determination of Optical Constants of Solids

In solid-state astrophysics, the term *optical constants* is mostly used synonymously with the complex refractive index $m = n + ik$ of a solid material. If magnetic material properties can be neglected, m is the square root of the (also complex) dielectric function $\varepsilon = m^2$, which governs the response of the atomic structure of a solid to an electromagnetic field. Whereas the refractive index, being a macroscopic quantity, entirely loses its meaning for small clusters and molecules, in the transition from macroscopic solids to molecules the introduction of size-dependent optical constants may be a reasonable way of including, for example, the confinement of charge carriers to a limited particle volume [112]. The term *optical constants* is a bit misleading because they are strongly frequency-dependent. The dispersion with frequency is determined by resonances of the electronic system and of the atomic lattice and, at very low frequencies, by relaxation of permanent dipoles. In the frequency regions of these resonances, k reaches high peak values while n can become close to zero. Figure 6.12 gives an example of optical constants of a solid in the frequency range of lattice vibration resonances.

Usually, optical constants are measured either on polished bulk surfaces or on thin slabs. The reason for this is that light propagation in planar geometries is much easier to describe than scattering and absorption by arbitrarily shaped particles, so that the data analysis becomes straightforward and independent of the effects of particle morphology. Of course, this requires the

8) Their spectrum can be described by Eq. (6.1) when $P(L) = \delta(L)$.

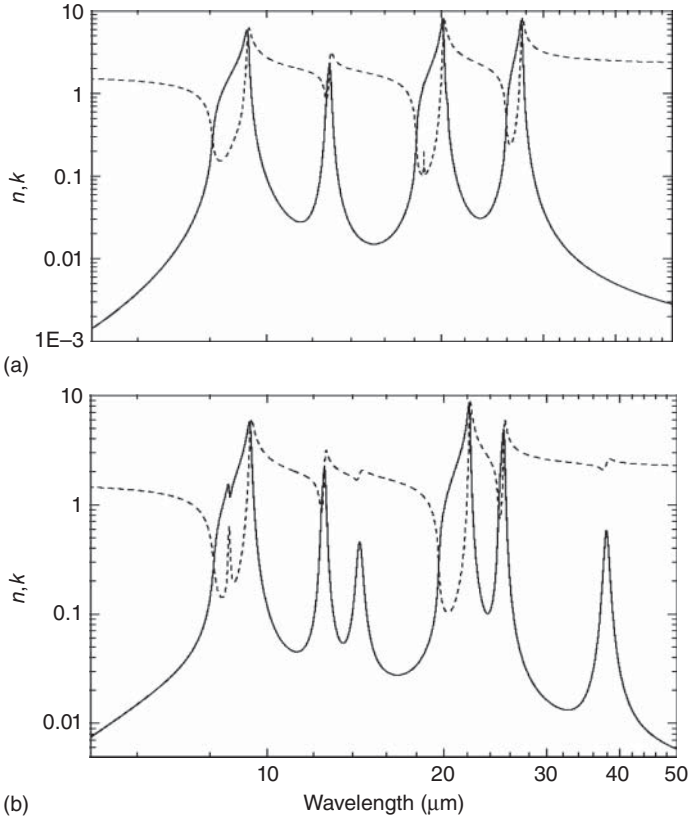

Figure 6.12 Measured n (dashed lines) and k (solid lines) of a quartz crystal (rock crystal) at polarization directions parallel (a) and perpendicular to the a-axis (b). The optical constants have been derived by fitting Lorentzian oscillator models with seven and eight oscillators, respectively, to measured reflectance spectra [113].

availability of sufficiently large pieces of bulk material or the possibility of preparing a homogeneous thin film. Furthermore, many crystalline solids show an anisotropy in their optical constants (Figure 6.12). In these cases, measurements with light polarized along the different axes of the crystal have to be carried out, which requires the preparation of oriented crystal faces (Sections 6.4 and 6.5).

Even in the case of ideal sample geometries, the derivation of the optical constants over a wide frequency or wavelength range is not a simple task. Since the material absorption in different spectral regions usually differs by many orders of magnitude, to determine k, either transmission measurements on samples of very different thicknesses (from millimeter down to nanometer scales, Table 6.1) or transmission and reflection measurements have to be combined.

Very thin samples for transmission measurements at wavelengths of strong absorption can be prepared by thin-film deposition techniques (see previous

subsection) or by ultramicrotomy (at least for the infrared). Since this is not always possible or desired, usually reflection measurements are applied in regions of strong absorption. In these spectral regions, n and k are of the same order of magnitude and both together determine the measured quantity (e.g., the reflectivity). Fortunately, n and k are not independent of each other and the Kramers–Kronig relations (see Ref. [96]) can be used to determine both of them. The parameterization of the dielectric function as a sum of Lorentzian oscillators is easier to handle:

$$\epsilon(\nu) = \epsilon_\infty + \sum_j \frac{\Omega_j^2}{\nu_j^2 - \nu^2 - i\gamma_j \nu} \tag{6.4}$$

the parameters of which (ϵ_∞, Ω_j, ν_j, γ_j) can be fitted to reproduce the measured spectrum. In certain cases such as titanium oxides, other oscillator models may be necessary to obtain satisfactory fits [114].

For most commercial spectrometers, accessories for reflection measurements at near-normal incidence are available. Using the formula for the reflectivity at normal incidence $R = [(n-1)^2 + k^2]/[(n+1)^2 + k^2]$, is usually unproblematic up to 10° deviation, and for unpolarized radiation perhaps even up to 20°. The reflectivity is the ratio of reflected to incident intensity, but it is usually obtained by comparison of the measured intensity with that for a reference sample of known reflectivity. In the mid-infrared wavelength range, a metal mirror (e.g., gold or aluminum film of sufficient thickness) possesses about 98% reflectivity, increasing toward longer wavelengths, and can be considered to be ideally reflecting. At visible wavelengths, however, this is not the case and the reference sample reflectivity needs to be calibrated.

In regions of weak absorption (small k), the reflectivity depends only on n, which then can be directly derived. For the determination of k, transmission measurements on plane-parallel slabs of material with different thicknesses are ideal. Slabs with thicknesses down to a few tens of micrometers can be prepared by polishing, but also millimeter-thick slabs may be needed to obtain a measurable absorption. According to Beer's law, the thickness is required to be on the order of $\lambda/(4\pi k)$ for optimum measurement conditions, which means that similar thicknesses can sometimes be used for far-infrared and visible wavelengths, although the k values are different (Table 6.1). Figure 6.13 gives an example of the imaginary part of the refractive index derived from combined transmission and reflection measurements on a ∼1 mm thick slab.

In some cases, also pellets pressed from powdered materials have been used to measure the absorption index in spectral regions of low absorption (Section 6.3.5). Contrary to high-absorption spectral regions, the measured absorptivity can be expected to be not much dependent on the grain morphology, so that a relatively simple model of these pellet samples can be used to correct for the porosity and the surface reflection losses. A suitable model is, for example, the Bruggeman theory (see, e.g., Ref. [117]), which allows one to calculate effective dielectric constants of the pellet from those of the constituents (e.g., sample plus vacuum) and the respective volume fractions [103].

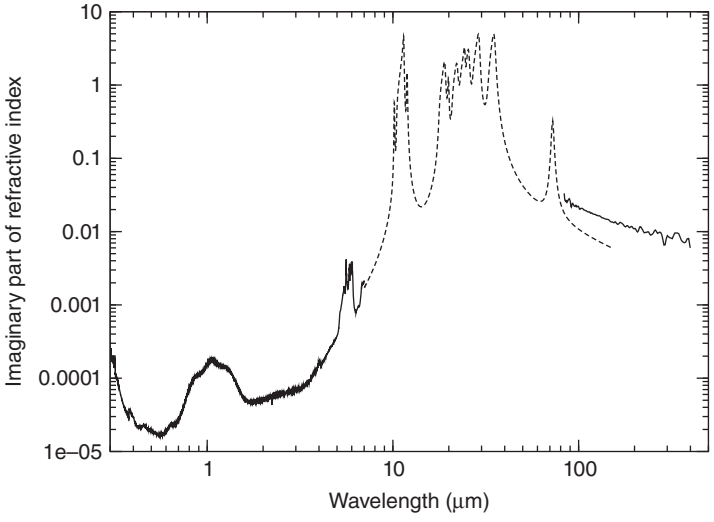

Figure 6.13 Imaginary part of the refractive index of olivine in the polarization direction parallel to the *y*-axis. The data were obtained from reflection measurements in the range of infrared bands (dashed line, [115]) and from transmission measurements of a ∼1 mm thick slab in the transparency ranges at the shorter and longer wavelengths (solid lines, [116]). Note that the different k values in the latter two datasets correspond to a similar linear absorption coefficient $4\pi k/\lambda$.

For further details, we refer the reader to the already mentioned original literature (as examples) and to the three volumes of the *Handbook of Optical Constants of Solids* [91], which also comprise detailed discussions of the source and errors of each dataset. Going back to the original literature is generally recommended because it should warn the user of uncritical application of optical-constants data.

6.3
The Bulk of Interstellar Dust: Amorphous Silicates

Harald Mutschke and Simon Zeidler

Silicates make up the majority of the dust mass in most cosmic environments. Fortunately, we can definitely prove this by spectroscopy as soon as the dust is emitting or absorbing radiation in the mid-infrared (IR) wavelength range. The spectrum of this radiation will then show a band caused by the Si–O stretching vibration of the silicate structure at about 10 μm wavelength (see Figure 6.4 in Section 6.1). Observations at this wavelength are possible from the ground. Therefore, this band has first been found and assigned already in the 1960s, for instance, in the interstellar extinction or the emission from Asymptotic Giant Branch (AGB) star outflows.

The reason for the dominance of silicate dust is, on one hand, the oxidizing chemical character of most cosmic environments and, on the other, the high abundance of the elements silicon, magnesium, and iron. It is known from the

mineralogy of terrestrial minerals that silicates can form an extremely wide variety of crystalline structures and, after rapid cooling, also glassy or amorphous compounds, for instance, volcanic or impact-produced glasses (tektites). Low temperatures dominate in space, and irradiation with cosmic rays destroys crystalline structures, so for a long time it was thought that cosmic silicates are exclusively amorphous. This also coincided with the results of the first spectroscopic observations. However, this view changed in the 1990s, and the mineralogy of cosmic silicate dust has become quite complex. However, for the *interstellar medium*, the original view has been proven to be correct. Interstellar dust, at least in the diffuse medium, is dominated by amorphous silicates.

This section will deal with the optical properties of such silicates and will discuss the state of the laboratory research and open problems.

6.3.1 Structure of Silicates

Detailed descriptions of the structure of amorphous and crystalline silicates can be found in mineralogical textbooks. Some important basics are presented here.

Silicon, together with carbon, is in the fourth main group of the periodic table of elements but, in contrast to carbon, silicon can form only single bonds because of the weaker overlap of its highest lying p orbitals with other atom's orbitals. Like in carbon, it is very easy to promote silicon atoms to an sp^3-hybridized state. Almost all the chemistry of silicon is based on its high affinity for oxygen. The Si–O single bond is highly stable because of the overlap of the oxygen nonbonding electron pairs with the empty d orbitals of silicon ($d_\pi p_\pi$-bonding). The bonding energy of the Si–O bond is 444 kJ mol^{-1}, which is more than that of the double bond in CO_2 (358 kJ mol^{-1}). Thus, very stable $[SiO_4]^{4-}$-tetrahedra form as the basic unit of all silicates. These tetrahedra can be linked to each other via the oxygen atoms in four spatial directions. For this reason, SiO_2 is a polymeric, hard solid with an unusually high melting point.

Metal ions such as iron and magnesium can be integrated within the $[SiO_4]^{4-}$ lattice, leading to its disruption and the formation of chains of tetrahedra, or even isolated single tetrahedra (Figure 6.14). The silicate formed can be seen as a compound of SiO_2 and the corresponding metal oxide. In the silicate lattice, aluminum has a special importance, on one hand, as a regular metal that interacts with the $[SiO_4]^{4-}$ lattice in the above mentioned way, and, on the other, as a substitute for the Si^{4+} ions leading to $[AlO_4]^{5-}$ tetrahedra in the silicate. In this process, the ratio of Si to Al cannot be lower than 1 since connections between two aluminum tetrahedra are forbidden. The charge balance in these alumosilicates is provided by metal ions integrated in the above-mentioned way.

Depending on the degree of polymerization, crystalline silicates can systematically be ordered in the following way:

Nesosilicates (island silicates) with independent, isolated $[SiO_4]^{4-}$-tetrahedra, which are only bond to each other via cations. For example, forsterite $Mg_2[SiO_4]$, olivine $(Mg,Fe)_2[SiO_4]$, zircon $Zr[SiO_4]$;

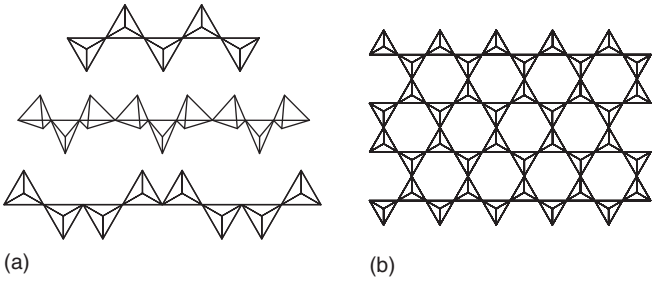

Figure 6.14 Examples of the arrangement of SiO_4 tetrahedra in (a) inosilicates (three types) and (b) phyllosilicates.

Sorosilicates (group silicates) with finite groups (mainly double tetrahedra) of the formula $[Si_2O_7]^{6-}$, for example, gehlenite (end member of the melilite series) $Ca_2Al[(Si,Al)_2O_7]$;

Cyclosilicates (ring silicates) with closed ring-like structures of tetrahedra (formulae $[Si_3O_9]^{6-}$, $[Si_4O_{12}]^{8-}$, or $[Si_6O_{18}]^{12-}$, for example, benitoite $BaTi[Si_3O_9]$, tourmaline $XY_3Al_6[(OH)_4/(BO_3)_3/(Si_6O_{18})]$);

Inosilicates (chain and double-chain silicates) with one-dimensional chains or double chains of tetrahedra; OH^- or F^- ions can be stored in the holes of the double chains. Most important representatives: pyroxene-group $[Si_2O_6]^{4-}_{\infty}$, for example, hypersthene $(Mg,Fe)_2[Si_2O_6]$

Phyllosilicates (plane silicates) with planes of tetrahedra; also here OH^- or F^- ions can fill the holes between the rings of tetrahedra. For example, talc $Mg_3[(OH)_2/Si_4O_{10}]$, pyrophyllite $Al_2[(OH)_2/Si_4O_{10}]$; (Figure 6.14b);

Tectosilicates (frame silicates) with all $[SiO_4]^{4-}$ tetrahedra bonded to others over their four corners. Metal ions are incorporated by parallel substitution of Si^{4+} with Al^{3+} in order to maintain charge balance. For example, alumosilicates such as feldspars albite $Na[AlSi_3O_8]$, orthoclase $K[AlSi_3O_8]$.

In contrast to crystals, amorphous solids have no periodically ordered structure expanding over the whole body (long-range order). The amorphous solid state can be seen as a kind of "snap-shot" of the atomic arrangements that might be found in a liquid. Therefore, amorphous solids have some short-range order only. Solids form amorphous states when the crystallization rate is smaller than the rate of solidification, for example, by rapid cooling of a liquid or by condensation from the gas phase. Also, the destruction of crystalline structures, for example, by ion bombardment, can lead to an amorphous state. In Figure 6.15, crystalline and amorphous silicate structures are compared.

Amorphous silicates are generally characterized by statistical methods since the absence of long-range order leads to a continuous variety of arrangements of $[SiO_4]^{4-}$ tetrahedra and metal ions. In X-ray diffractograms and in IR spectra, for instance, this leads to an extreme broadening of diffraction peaks and

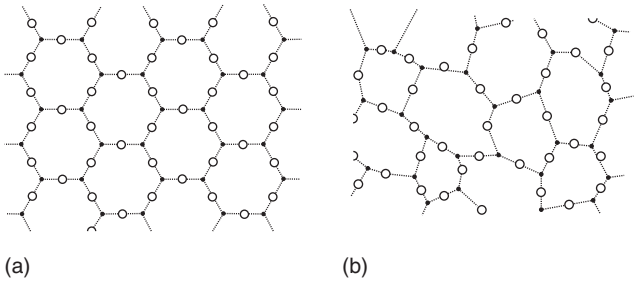

Figure 6.15 Two-dimensional representation of crystalline (a) and amorphous (b) silicate structures. Dots: silicon atoms; circles: oxygen atoms.

vibration absorption bands, which, in the end, only provide information about the short-range order. An example of IR spectra for a crystalline and an amorphous magnesium silicate is given in Figure 6.16. Three major differences arise between crystalline and amorphous solids:

Isotropy: the physical properties of amorphous solids are independent of the direction, while in crystals they are highly directional.

Melting point range: amorphous solids have very broad softening and melting ranges, whereas crystals have a distinct melting point. There are no well-defined phase transitions in amorphous solids; one can only look at thermal gradients of specific parameters.

Thermodynamical instability: the amorphous state has more internal energy than the crystalline state, therefore crystals represent a state of higher thermodynamic stability.

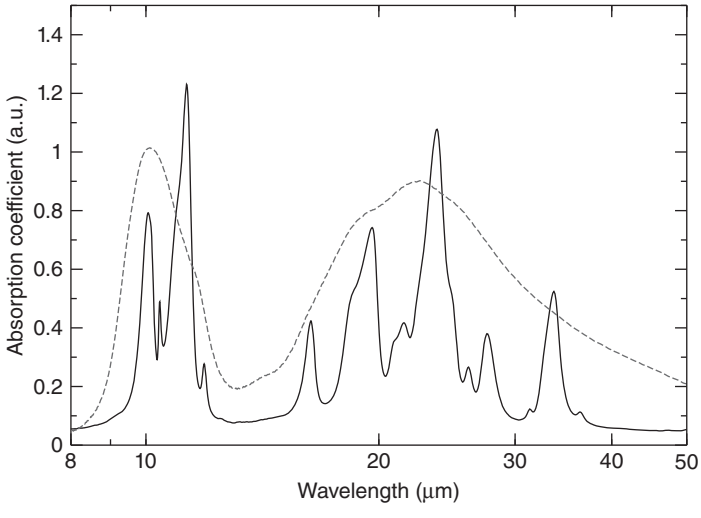

Figure 6.16 Infrared absorption spectra measured for a crystalline (solid line) and an amorphous (dashed line) silicate of the same composition (Mg_2SiO_4).

6.3.2 Production Techniques for Amorphous Silicates

The easiest way of making an amorphous silicate is by quenching a melt. For Fe–Mg silicates, such a melt can be obtained from a homogeneous mixture of iron(II) oxalate dihydrate ($Fe(C_2O_4) \cdot 2H_2O$), magnesium carbonate ($MgCO_3$), and SiO_2 powder filled into a platinum crucible and placed in a high-temperature oven. To warm up the mixture homogeneously, it is heated slowly (about 10 K min^{-1}). The iron(II) oxalate and $MgCO_3$ decompose to FeO (at 190°C) and MgO (at 350°C) forming CO and CO_2 which are important for maintaining the oxidation state of the metal ions. The melting range of the FeO–MgO–SiO_2 system is determined by the ternary phase diagram [118] and is very different from the melting points of each of the single components. The mixture 0.5MgO + 0.5FeO + SiO_2 has a melting temperature of 1410 °C; 0.8MgO + 0.2FeO + SiO_2 of ∼1510 °C; and 0.95MgO + 0.05FeO + SiO_2 of about 1550–1560 °C, whereas FeO melts already at 1369 °C, SiO_2 at 1723 °C, and MgO at 2800 °C. In order to allow MgO to dissolve, a 30-min heating step at 1400 °C has been proven to be efficient.

The melt has to be held above the melting temperature for at least 1 h before the quenching process can be started. Fast cooling on the order of $\approx 10^3$ K s^{-1} is important, especially for melts with a high iron content. In practice, very rapid cooling can be achieved by using rotating copper rollers. The melt is drawn through the rotating rollers and pressed to a thin ribbon with a thickness of a fraction of a millimeter (Figure 6.17).

Glassy Fe–Mg silicates of relatively wide compositional range have been produced [119]. When the Fe/Mg ratios are larger than 1, however, the melts tend to

Figure 6.17 Photograph of the of quenched silicate ribbon just coming out between the copper rollers. (Photo: FSU.)

phase-separate and crystallize. In this case, some parts of the melt produced can still be salvaged by looking for sections with a glossy black surface (under a magnifying glass). In olivine stoichiometry (Fe, Mg)/Si = 2, a high Mg content leads to melting temperatures higher than the melting point of a platinum crucible. To our knowledge, such silicates have been produced only by a sol–gel technique (see below). It should be also mentioned that preventing the oxidation of the iron(II) ions in the melt is difficult without a nonoxidizing ambient atmosphere.

An important advantage of this technique is that thin sheets of bulk material are produced. After polishing, they can be directly used for reflection and transmission measurements and, hence, for the determination of optical constants [119].

Although producing an amorphous solid by quenching a melt is straightforward, very high temperatures are needed. A "cold" method for creating an amorphous solid is the "sol/gel" method [120]. In a sol phase, colloidal particles of ~100–1000 Å size are dispersed in another medium by virtue of electrostatic interactions between each other and the medium. If the repulsive interactions can be reduced, the colloidal particles form a network enclosing the other medium, thus forming a gel.

To form silicates of astrophysical interest, first a metal alkoxide, for example, tetra-ethoxy silane $Si(C_2H_5O)_4$ (TEOS) [121], is hydrolyzed:

$$Si(OR)_4 + H_2O \rightarrow HOSi(OR)_3 + ROH \tag{6.5}$$

where R is the alkyl group. To this solution $Mg(C_2H_5O)_2$ is added, along with H_2O_2 as a catalyst. The degree of hydrolysis is dependent on the amount of water and catalyst. The hydrolyzed Mg and Si species then polymerize (Eq. (6.6)). Ideally, all of the alkyl groups leave as alcohols.

$$(OR)_3SiOH + HOSi(OR)_3 \rightarrow (OR)_3Si—O—Si(OR)_3 + H_2O \tag{6.6}$$

The last step is to remove the water and the alcohol from the gel. There are different ways of doing this. One is to warm up the gel at low pressure and to evaporate the liquid. This process has to be done very carefully and in several steps to avoid crystallization of the material or further chemical reactions, which could destroy the network. Vacuum- and also freeze-drying processes are other possibilities.

Subsequent tempering of the material under a pure oxygen atmosphere allows removal of the remaining liquid organic phase. Because this requires temperatures higher than 800 °C and crystallization sets in at about 600 °C, amorphous sol/gel materials often have organic groups incorporated into their network, which can be detected in IR spectra.

The methods described above are meant to produce analogs of cosmic materials in relatively large amounts and with well-defined (homogeneous) structure and properties, so that all kinds of analytical and spectroscopic methods can be applied. They certainly do not reproduce cosmic dust properties in all aspects, since real cosmic dust is formed and influenced by other processes.

Direct condensation of silicate dust particles from the gas phase in the laboratory will be presented in Chapter 7. However, we would like to note that such condensates do usually appear as thin layers of either nanometer-sized dust particles or compact material (films), deposited onto an optical substrate.

The thicknesses of these layers are usually in the submicrometer range, so absorption can be measured in a transmission experiment. If absorption is strong enough, such as for the mid-IR vibrational bands or the interband absorption in the UV, the spectral properties can be determined and compared with astronomical spectra. However, the amount of material is too small for measuring weak absorptions such as in the submillimeter wavelength range. Nevertheless, these condensed amorphous silicates are not only important for studies of actual formation processes in space, but also some optical constants of amorphous silicates could be measured on such materials [122].

Another method that should be mentioned is amorphization using energetic ions. This is again a process that can be assumed to be important in, at least, the interstellar space. It works best with heavy ions, where collision of nuclei is more important than heating via electronic excitation [123]. The penetration depth is quite low, so such samples will also have a submicrometer thickness, perhaps supported by the original crystalline silicate. Either transmission or reflection IR spectroscopy is an important tool to analyze amorphization effects. Both the condensation and irradiation of silicates are currently being intensively studied, and future results will certainly bring insight into the properties of cosmic dust particles.

6.3.3 The Infrared Spectra of Amorphous Silicates

Besides the already mentioned Si–O stretching vibration band at 10 μm wavelengths, silicates have a number of other IR absorption bands originating from deformation vibrations of the SiO_4 tetrahedra and from vibrations of the metal ions relative to their oxygen environment. These bands are found typically between 15 and 70–80 μm; layer-lattice silicates also have longer wavelength bands. With the wavelength coverage of IR space observatories and their spectrometers such as the Spitzer IRS or Herschel PACS (Photoconductor Array Camera and Spectrometer), it is, in principle, possible to use all of them for the diagnostics of dust composition.

In amorphous silicate networks, however, bond lengths, angles, force constants, and, therefore, vibrational frequencies are statistically distributed. This results in strong broadening and merging of the bands into only two almost structureless features. This is true in particular for the astrophysically most relevant magnesium–iron silicates, because the Mg–O and Fe–O stretching vibrations appear close to the Si–O deformation band and can easily merge with that. Under certain conditions, a third small band can be found between the two complexes, at about 12–13 μm. The question is whether, despite this lack of structure, such a spectrum can still reveal information on the silicate structure and composition.

For the Si–O stretching band, the answer to this question is well known. The frequency of the stretching vibrations depends primarily on the degree of polymerization of the SiO_4 tetrahedra in the network, that is, on the number of

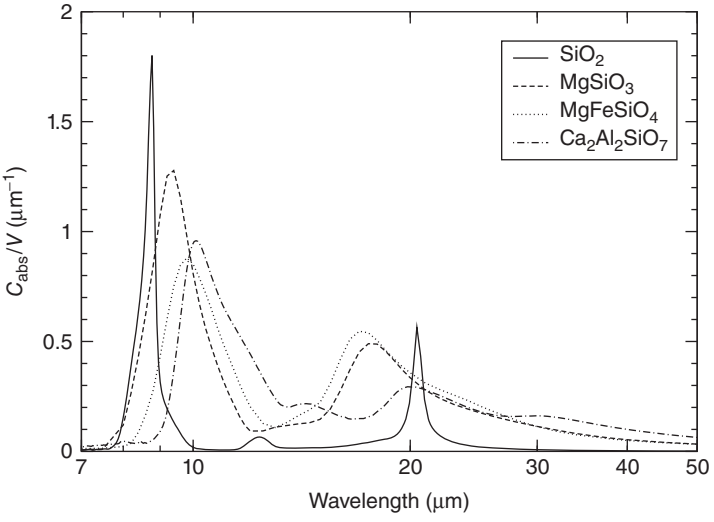

Figure 6.18 Absorption efficiencies of amorphous SiO_2 and of various amorphous silicates in the infrared spectral range. Note the systematic shift of the 10 μm band with increasing metal ion content.

Si–O–Si bonds connecting them. The higher the degree of polymerization, the higher the vibrational frequency, and, of course, the shorter the wavelength of the band. For the completely polymerized SiO_2, the peak wavelength is below 9 μm; for an almost unpolymerized Mg_2SiO_4 glass it is at about 9.8 μm [120]. Interestingly, this trend is opposite for the maximum of the deformation band complex: for Mg_2SiO_4 glass it peaks at about 17 μm, whereas for SiO_2 it shifts to about 21 μm (Figure 6.18). The reason for that could partly be the Mg–O vibrational band, which occurs around 17 μm [124] and blends with or, better, couples to, the Si–O deformation vibration.

Replacing some of the of magnesium with iron tends to broaden both the bands even more [119]. There is still discussion on whether the iron content of the silicates can be deduced from the IR bands [16]. If yes, this would enable us to determine whether iron becomes oxidized in space or preferentially remains metallic as predicted from equilibrium condensation theory (Section 7.1). In the latter case, glasses with embedded metals and sulfides (GEMS) probably can be really considered to be typical interstellar dust grains. Another point is that the presence of metallic constituents could influence the optical properties at far-IR wavelengths dramatically. The iron content problem will be addressed further in Section 6.4.6.

Other metal ions such as aluminum and calcium are much less abundant and less likely to influence the IR band profiles. Aluminum actually would cause absorption at 13–16 μm, that is, in the "trough" between the two Si–O bands [125], and calcium may cause absorption beyond the 20 μm band region (see Ref. [126] and Figure 6.18 for an extreme example).

6.3.4
Optical Constants at UV/Vis/NIR Wavelengths

The absorption cross section of cosmic dust particles in this wavelength range determines the amount of energy transferrable from starlight and, hence, their temperature. Unfortunately, this quantity is not easy to constrain. Pure magnesium silicates are transparent in the visible and near-IR, that is, the linear absorption coefficient $\alpha = 4\pi k/\lambda$ is <1 cm^{-1}. Incorporation of iron changes this and will give the silicate a greenish or brownish color, depending on whether the iron is ferrous (Fe^{2+}) or ferric (Fe^{3+}).

This coloring arises from electronic transitions, either involving the d-electron levels which are energetically split in the field of the surrounding oxygen ions (so-called crystal-field bands [127]), or by charge transfer between the iron and other metal or ligand ions. Whereas the former give rise to distinct absorption bands in the visible or near-IR, the latter will lead to a broad absorption increasing toward shorter wavelengths, that is, peaking in the ultraviolet, and merging there with the edge of the fundamental electronic interband transition.

Crystal-field transition bands are also seen in silicates containing other metal ions, and they always contribute to the absorption at visible and near-IR wavelengths for silicates (this will also be discussed for oxides in Section 6.5.7). However, they are relatively weak. The charge-transfer absorption is considerably stronger but it occurs only when ferric ions are present. Figure 6.19 shows the spectra of Mg/Fe silicate glasses prepared in air, in which the percentage of Fe^{3+} relative to the total iron content is relatively high, 30–50%. In contrast, terrestrial olivine crystals, with low Fe^{3+} content, show no charge-transfer absorption [116]. Whether cosmic silicates show this absorption behavior is currently not well known. Interstellar silicates absorb at visible wavelengths with $\alpha = 10^3$–10^4 cm^{-1}.

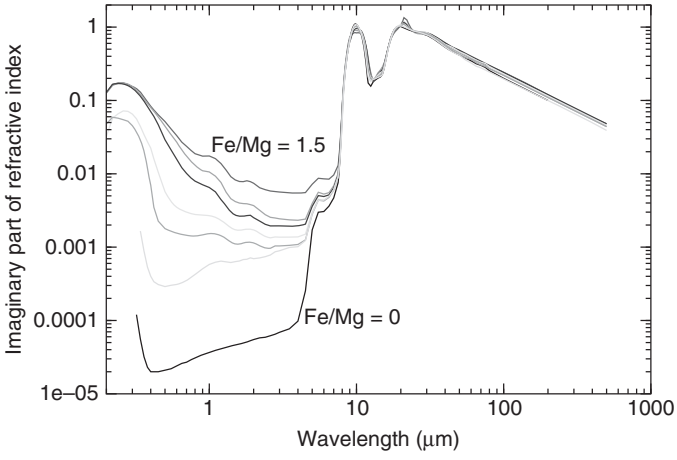

Figure 6.19 Absorption index *k* of glassy silicates with pyroxene-like stoichiometry $(Mg/Fe)SiO_3$ in a wide wavelength range. The near-infrared and visible absorption increases with growing iron content. (Reproduced from [119], copyright 1995 © permission from ESO.)

However, this could also occur when metallic or carbonaceous admixtures are present.

We should also mention that additional absorption in the near-IR can of course be caused by vibrational bands. The most important of these is certainly the O–H stretching vibration band at about 3 μm. O–H groups can be incorporated in the silicate network. However, it seems that in (interstellar) space the 3 μm absorption band originates from water ice. Whether such groups might exist in circumstellar silicates is not known, because they would be observable in emission spectra only at very high dust temperatures.

At ultraviolet wavelengths, very little data on silicates has been obtained thus far. The most well-known experiments are those by Huffmann and Stapp [128] based on reflectivity measurements of a natural olivine, and by Scott and Duley [122] based on transmission measurements of amorphous magnesium silicate films produced by laser ablation deposition. These data show the interband transition edge to be located at about 170 nm, the linear absorption coefficient rising to values of about $10^6\,\mathrm{cm}^{-1}$ as is typical for the fundamental electronic absorption at UV wavelengths. For crystalline olivine, the absorption shows more structure than for the amorphous silicates, but the general shape of the curves is roughly similar as expected. Although this situation may be a bit unsatisfying from the point of view of solid-state physics, from the astrophysical viewpoint these data might be sufficient to constrain the UV properties of silicate dust. Cosmic UV photons will be strongly absorbed by silicates in any case.

6.3.5
The Far-Infrared Emissivity of Cold Amorphous Silicates

The thermal dust emission in the far-IR ($\lambda \sim$50–1000 μm) up to the millimeter wavelength range is an important source of information on the spatial distribution of dust in cold circumstellar disks and in interstellar clouds. In this wavelength range, even massive dusty structures are usually optically thin, so that the dust column density can be determined from the emitted flux. This, of course, depends on knowing the emissivity of the dust particles. As already noted, this quantity is not easy to predict since cosmic dust particles are likely to have quite complex structures. Moreover, even the optical constants of the constituent materials may not be well known in this wavelength range and at the relevant low temperatures.

Silicates with disordered structural networks are capable of absorbing (and emitting) long-wavelength radiation more efficiently than crystalline silicates, as has been demonstrated by mechanical defect-generation and annealing experiments [130, 131], (see also Section 6.4.4). The increased absorption coefficient is partly related to the breakdown of the selection rules valid for crystals, which enables the excitation of normally IR-inactive phonons. This contribution to the opacity is roughly temperature-independent. It can be theoretically understood by introducing a statistical charge distribution with a certain degree of correlation [132, 133]. Within this theory, the spectral slope of the absorption coefficient is predicted to change from λ^{-2} to λ^{-4} at wavelengths exceeding $c \times l/\nu_\mathrm{t}$, with l the correlation length of the disorder, ν_t the sound speed, and c the speed of

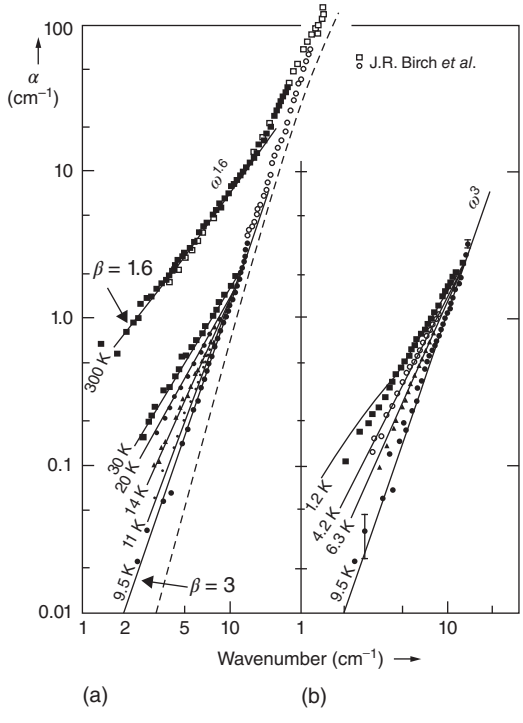

Figure 6.20 Temperature-dependent absorption coefficient of a soda lime–silica glass at submillimeter and millimeter wavelengths. The data are plotted versus the inverse wavelength, 10 cm^{-1} corresponding to λ = 1 mm. (a) Temperatures between 9.5 and 300 K; (b) temperatures <10 K. β values represent fitted power-law exponents. (Reproduced from [129], copyright 1978 © permission from American Physical Society.)

light (see the dashed line in Figure 6.20a). This feature likely corresponds to the "Boson peak" seen, for example, in Raman scattering measurements.

However, there is also a strongly temperature-dependent contribution to the opacity of amorphous silicates. This contribution, which was found in the 1970s in studies of acoustic and dielectric losses of glasses [129, 134], dominates the submillimeter and millimeter absorptivity at room temperature and decreases toward cryogenic temperatures. Below a certain minimum temperature of the order of 10 K, again an increase of the absorption is observed (Figure 6.20). The reason for this behavior is the fact that, in a disordered network, atoms or groups are able to flip between two or more adjacent sites, which are energetically only slightly different. At very low temperatures, these two-level systems can absorb low-energy photons from a broad wavelength range by resonant excitation. At higher temperatures, these resonant processes disappear because the two levels become equally populated. The increase of absorption that is then observed is based on the increasing similarity of photon frequency and structural relaxation frequencies, allowing fast energy dissipation [132]. This "relaxation absorption" leads to a flattening of the spectral slope – reaching power-law exponents (β-values) smaller than 2 at room temperature – and to a strong increase of the opacity.

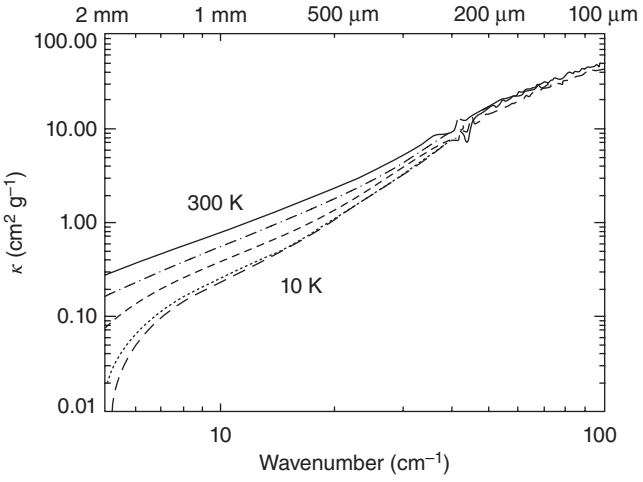

Figure 6.21 Temperature-dependent absorption coefficient of a $MgSiO_3$ glass at far-infrared and millimeter wavelengths. From top to bottom, the spectra correspond to temperatures of 300, 200, 100, 30, and 10 K. Top axis gives the wavelength. (Reproduced from [103], copyright 2005 © permission from AAS.)

In the end of the 1990s, the absorption coefficients at long wavelengths and low temperatures were measured for a number of astrophysically interesting solids and the relevance of low-energy absorption processes was confirmed. Agladze *et al.* [135] measured the absorption coefficients of sol–gel-produced amorphous magnesium silicates and their crystalline counterparts at very long wavelengths (0.7–2.9 mm) and at temperatures below 30 K, whereas Mennella *et al.* [102] measured the absorption of a pure iron silicate (Fe_2SiO_4) in both amorphous and crystalline states over a wider temperature and wavelength range.

Interest in submillimeter opacity data was renewed by the observational finding of a temperature versus opacity gradient anticorrelation for interstellar dust [136, 137]. The submillimeter emissivity of dust in the coldest interstellar regions has been demonstrated to have a very steep slope, corresponding to power-law coefficients up to $\beta = 4$, which seems to correspond to the predicted properties of certain amorphous materials [132]. New measurements of amorphous silicates in a wider wavelength and temperature range were carried out for amorphous $MgSiO_3$ and silica SiO_2 (Figure 6.21) [103]. Currently, these investigations are being continued in groups in Toulouse and Jena [138].

6.4
Crystalline Silicates
Chiyoe Koike

As for crystalline silicates, the spectra in the infrared (IR) band range and the far-IR continuum absorption have been thoroughly investigated in the past few years and have been made clear to be strongly influenced by chemical composition,

temperature, and grain morphology (size, shape, agglomeration, porosity, defects) [106, 131, 139–144]. Further, new optical constants of the most important pyroxene and olivine crystals have been derived, and the dependence of the optical constants on temperature has now been studied in great detail [37, 115, 145–147]. These data are very important, as observations can be discussed in comparison with both measured and calculated absorption data for crystalline pyroxene and olivine. We review the latest results on these points in the following section. The experimental data measured in our laboratory are available on the Web site (http://optik2.mtk.nao.ac.jp/~suto/Mineral/).

6.4.1 The Effect of Silicate Composition on Infrared Spectra

The IR spectra of crystalline silicates such as olivine and pyroxene are strongly dependent on their chemical compositions, and show many sharp peaks in contrast to the broad bands of amorphous silicates [37, 139, 140, 148]. These bands are stretching and bending vibrations of the SiO_4 tetrahedra in the mid-IR region, translational motions of the metal cations within the oxygen cage, and complex translations involving metal and Si atoms in the far-IR region (Section 6.3.1).

The chemical composition of olivine is $[Mg, Fe]_2SiO_4$, which can be considered as solid solution of Mg_2SiO_4 (forsterite) and Fe_2SiO_4 (fayalite); the mixture ratio can be expressed as $Fo_xFa_{(1-x)}$ (Fo, forsterite; Fa, fayalite) or shorter as Fo_X ($X = 100x$), and the ratio of Mg and Fe can vary continuously with X varying between 100 and 0. The olivines belong to the rhombic crystal system. Samples measured in our lab are both natural and synthetic.

The synthetic Mg–Fe olivines were produced in our laboratory from MgO, FeO, and SiO_2 powders mixed in appropriate mole ratios. This method requires controlling the oxidation state of the iron already at the stage of the production of the FeO powder. Under atmospheric conditions, iron is easily oxidized to three-valent iron, while in olivines the iron has to be two-valent, and higher oxidation would lead to phase separation. Consequently, both the FeO powder preparation (from ferric oxalate) and the reaction of the three precursors to a silicate had to be performed in a controlled H_2-CO_2 gas flow ensuring controlled O_2 fugacity. The products were carefully checked by a scanning electron microscope and an electron probe microanalyzer for homogeneity and chemical composition, respectively. The spectroscopic measurements were done using the pellet method (Section 6.2).

The spectra of these polycrystalline olivines are shown in Figure 6.22. The main effect of the increase of the Fe content (as X decreases from bottom to top) is that the peak positions are shifted to longer wavelengths. Especially, the main peak positions shift clearly. The 11 μm band is shifted from 11.24 to 11.40 μm, for forsterite and fayalite, and the peaks at 16.35 μm shifted to 17.7 μm, 19.65 to 20.9 μm, 23.75 to 27.7 μm, 27.51 to 31.9 μm, and 33.75 to 38.9 μm. As for the 49 and 69 μm bands of forsterite, the intensities decrease dramatically with increasing Fe content, and the peak positions also shift to longer wavelengths. The peak

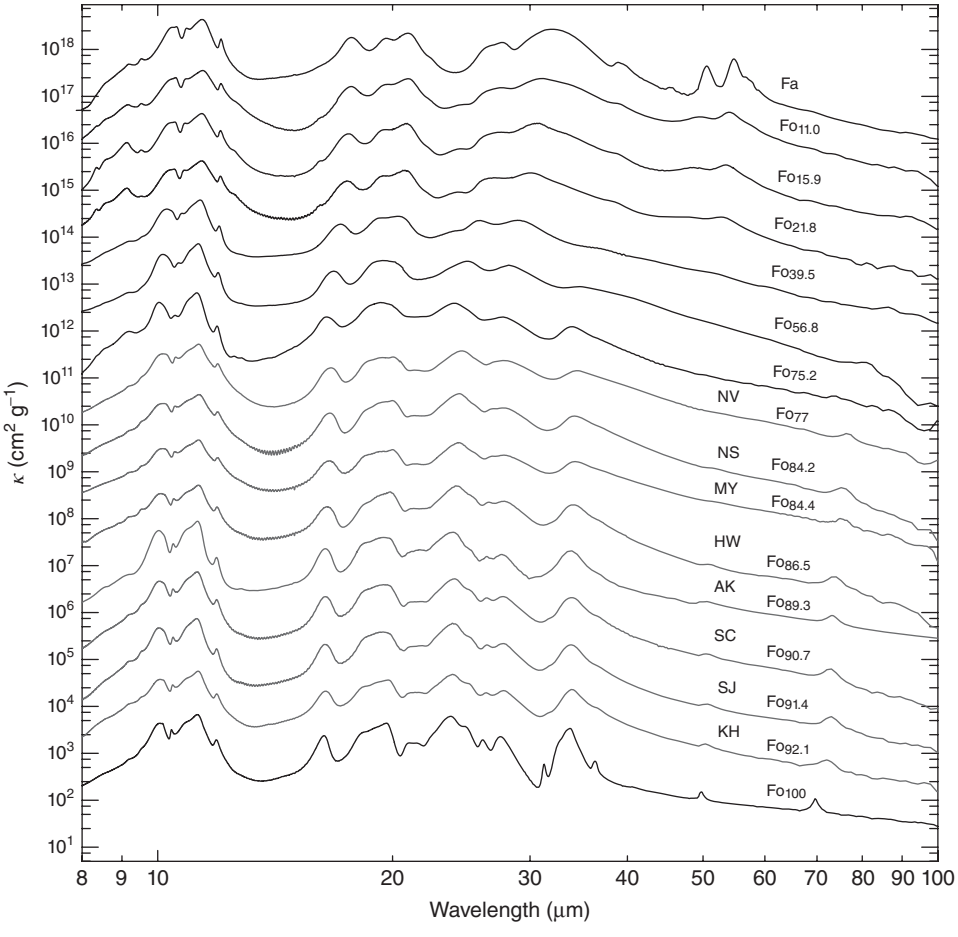

Figure 6.22 Spectra of synthetic and natural olivine. Each spectrum, indicated by the forsterite content in percent, is shifted upwards for clarity. For natural olivines, their place of origin is indicated (e.g., Kohistan (KH), Hawaii (HW), Nivitigala (NV), etc.). (Reproduced from [140], copyright 2003 © permission from ESO.)

positions of olivine grains are a good indicator of the composition of these dust grains.

In the case of pyroxene, the chemical composition is $[Mg, Fe]SiO_3$, which can be considered as solid solution of $MgSiO_3$ (enstatite, En) and $FeSiO_3$ (ferrosilite, Fs); the mixture ratio can analogously be expressed as $En_xFs_{(1-x)}$ or En_X ($X = 100x$). Pyroxenes can occur in two different main crystallographic systems, that is, clino-pyroxenes and ortho-pyroxenes. Most of the samples measured in our lab belong to the ortho-pyroxenes, except for one of the En_{100} and for the En_{90} materials. All samples have been produced synthetically (for details, see Koike *et al.* [148] and Chihara *et al.* [139]). Compared to the spectra of the olivines, those of pyroxenes (Figure 6.23) show a more complicated dependence on the Fe content, although

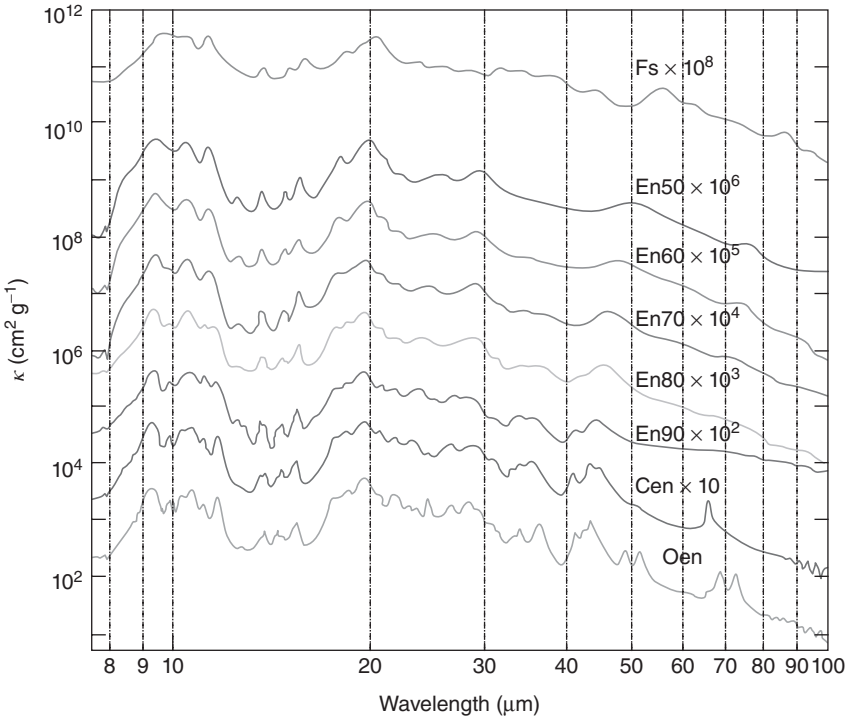

Figure 6.23 The spectra of pyroxene changing with composition. The Mg/(Mg + Fe) ratio decreases in 10% intervals from the bottom to top ($En_{100} - En_{50}$). Bottom two spectra are for the Mg end members, clino- and ortho-enstatite. Top spectrum is for ferrosilite. (Reproduced from [139], copyright 2002 © permission from ESO.)

most of the absorption bands are still systematically shifted to longer wavelengths with decreasing X.

The Mg end members of the pyroxene series, that is clino- and ortho-enstatite, show very sharp peaks at about 50 and 70 μm. In case of clino-enstatite (Cen), these peaks are single peaks at 51 and 65.9 μm, whereas for ortho-enstatite (Oen) they are double peaks at 49.2, 51.6 μm and 68.7, 72.5 μm, respectively [139, 148]. These results suggest that the far-IR features of pyroxenes are very sensitive to the chemical composition and crystal structure. In contrast to the far-IR band at 69 μm of forsterite, which was detected in some astronomical objects (Section 6.1), the band of clino- or ortho-enstatite at 70 μm was not detected in any objects. This is very mysterious, since in the mid-IR region Mg-rich crystalline silicates such as forsterite and enstatite were detected in many objects.

The spectra of diopside ($CaMgSi_2O_6$), a Ca-rich pyroxene, show a very strong band at 65 μm [148]. Infrared Space Observatory (ISO)-observed spectra of a planetary nebula in the 60 μm region show a strong and broad emission band, which is likely a blend of features of crystalline water ice (centered near 60 μm), diopside, and/or melilite materials. Melilite is a Ca–Al–Mg silicate belonging to

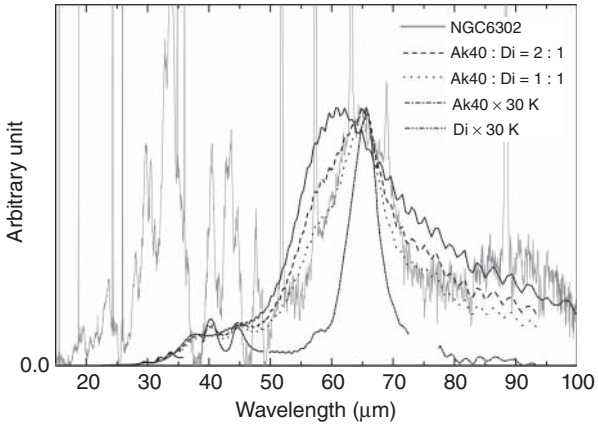

Figure 6.24 Fitting of the 65 μm region in the spectrum of NGC6302 by a combination of the laboratory-measured spectra of diopside (Di, narrow feature at about 66 μm) and melilite ($Åk_{40}$, broader feature at about 61 μm). The latter are multiplied by a blackbody curve at a temperature of 30 K. The best match is achieved with equal portions of Di and $Åk_{40}$. (Reproduced from [142], copyright 2007 © permission from ESO.)

the sorosilicate group. It is frequently found in meteorites (in the so-called calcium–aluminum-rich inclusions (CAIs)) as one of the first minerals condensing from the solar nebula gas.

The IR spectra of the melilite solid solution series ($Ca_2Al_{2(1-x)}Mg_xSi_{1+x}O_7$ ($0 \leq x \leq 1$)) have also been measured in our laboratory [142]. The melilite samples between the aluminum end member (gehlenite) and the magnesium end member (Åkermanite) were synthesized in about 10% intervals of the chemical composition ($Åk_X$ ($X = 100x$)). The spectra in the mid-IR region and the prominent 60 μm feature are again very sensitive to the chemical composition. In particular, the observed spectrum of the planetary nebula NGC 6302 is fitted well with two components: the 60 μm broad band of $Åk_{40}$ and the 65 μm band of diopside as shown in Figure 6.24.

6.4.2
Temperature Effects on Infrared Spectra of Olivine and Pyroxene Particles

As circumstellar and interstellar dust may exist at low temperatures, it is very important to investigate the temperature effects on the IR spectra. Chihara *et al.* [149] measured the IR spectra of pyroxene and olivine grains at liquid He temperature (4 K). As a result of the cooling, the absorption bands became sharper and stronger, peak positions shifted to shorter wavelengths, and the continuum absorption became steep. Similar measurements had been performed by Bowey *et al.* [150]. The spectra of olivine grains were also measured in detail from room temperature (RT) down to 10 K. These measurements were done independently in two laboratories in Kyoto and Jena [141]. The olivine particles used were forsterite, olivine, and fayalite. Forsterite and fayalite were synthesized by different methods in these two laboratories, whereas the olivine used was a natural mineral

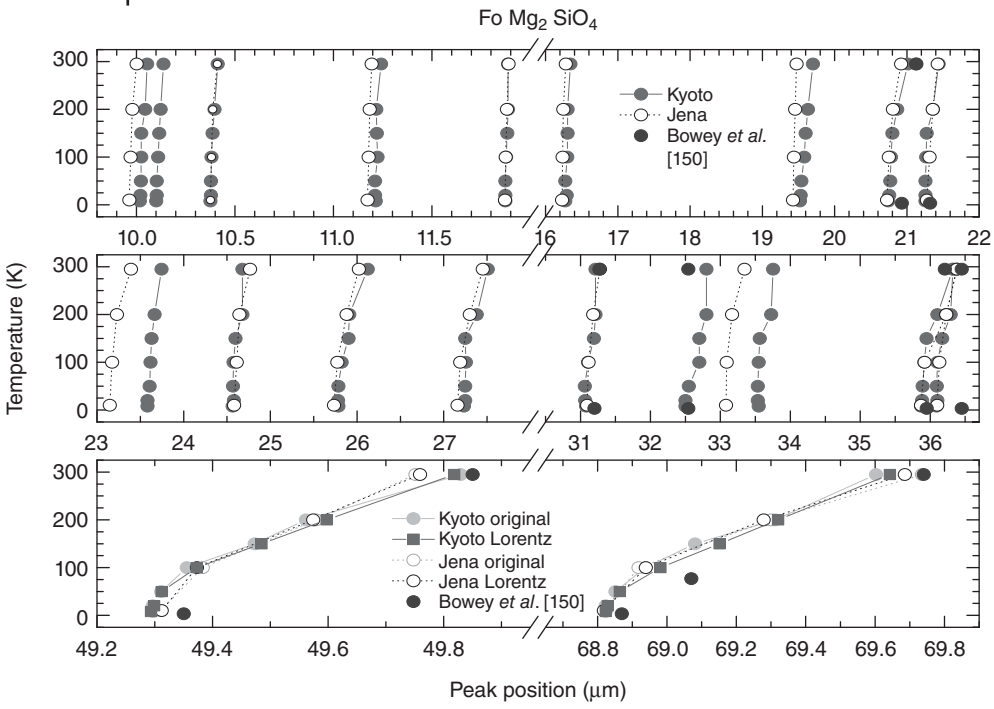

Figure 6.25 The peak positions in the infrared spectra of forsterite grains depending on temperature. Positions are partly determined by Lorentzian fitting of the bands, apart from simple reading from the original spectra. Shifts between the Jena and Kyoto data are likely due to grain shape effects. Values measured by Bowey *et al.* [150] are given for comparison. (Reproduced from [141], copyright 2006 © permission from ESO.)

from San Carlos, Arizona, in both labs. The measurements at low temperature in the two laboratories with different spectrometers and cryostats gave very similar results. The main peaks in the spectra shifted to shorter wavelengths at low temperature (Figure 6.25), and the intensities and widths of those peaks became larger and narrower, respectively.

In particular, the position of the 69 μm band shifted to shorter wavelength by about 1 μm from RT down to 10 K (Figure 6.25). Thus, the peak position of the 69 μm band may indeed become a thermometer for circumstellar dust if the observed peak position of this band is compared with laboratory data. However, as described in the previous section, the peak position is also dependent on the iron content of the olivine grains. Consequently, the dust composition needs to be independently constrained in order to exploit the temperature dependence.

6.4.3
Optical Constants of Olivine at Room Temperature and Low Temperature

As has been frequently pointed out in the previous sections, knowledge of the optical constants is necessary to understand the effects of particle size, grain

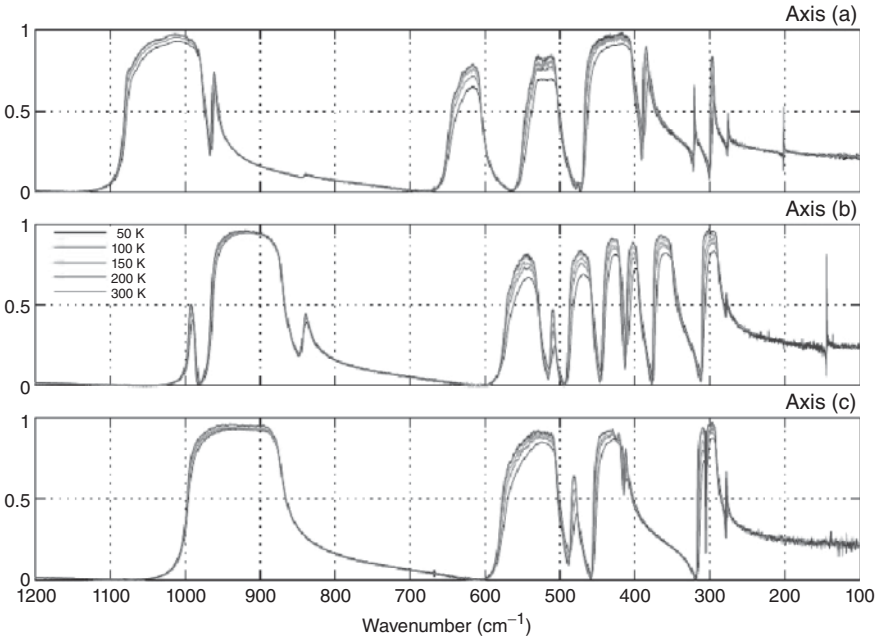

Figure 6.26 Reflectance of forsterite for polarization along the three crystallographic axes (*a*, *b*, and *c*) measured at RT as well as 200, 150, 100, and 50 K. Cooling the crystal leads to higher reflection peaks. (Reproduced from [147], copyright 2006 © permission from John Wiley & Sons.)

shape, coagulation, or embedding medium on the IR spectra of crystalline silicates and other minerals. As for enstatite, Jäger *et al.* [37] derived the optical constants for three axes of natural enstatite with $En_{0.96}Fs_{0.04}$.

As for forsterite, optical constants of a synthetic bulk forsterite had been measured by Servoin and Piriou [151]. These data were of a very low resolution and a low S/N ratio, especially in the far-IR region. Fabian *et al.* [115] supplied the lacking far-IR data from measurements of a synthetic forsterite powder. A few years later, Sogawa *et al.* [146] derived the optical constants for three axes from measured reflectances of a single-crystalline forsterite in the mid- and far-IR regions. This bulk sample was synthesized with the Czochralski (CZ) method. Furthermore, Suto *et al.* [147] measured the reflectances while cooling the bulk forsterite sample from RT to 50 K, and derived these optical constants at each temperature (Figure 6.26). In the far-IR region, each band became strong and sharp when the bulk sample was cooled to low temperature. As for the 69 μm band, the intensity of the band became remarkably strong at 50 K compared with that at RT.

As for fayalite and olivine, Fabian *et al.* [115] and Suto *et al.* [145] independently derived these optical constants after measuring reflectances for each of the samples. It is noticeable that the data of fayalite by Suto *et al.* and Fabian *et al.* are almost the same inspite of the different synthesis methods used, namely the floating zone method and the scull method, respectively.

Especially, the forsterite data have already proven to be useful for interpreting the spectra measured with the Spitzer space observatory and for the modeling of grain-shape effects in laboratory spectra (see Sections 6.1 and 6.2). The temperature dependence is especially important for understanding astronomical detections of the 69 μm band, since this is primarily observed with cold dust, for instance in protoplanetary disks.

6.4.4 Structural Defects of Silicates

Until now, we have only considered the solid state as being either totally amorphous or perfectly crystalline. However, for circumstellar/interstellar dust, we must certainly pay attention to the case of imperfect crystal structure. In circumstellar environments, it is likely that the temperatures experienced by amorphous silicate grains are not high enough to anneal them into perfect crystals and, also, violent impacts during radial mixing of circumstellar dust grains and planetesimals may create structural defects.

In our laboratory measurements [131, 144], intensively milled olivine and forsterite grains showed many crystal defects, and their spectra showed amorphous-like characteristics: the main peaks became broad and the continuum absorption increased. These defects disappeared after annealing at high temperature (700–1000 °C). After annealing at 1000 °C, the intensity of the 69 μm band of the milled forsterite grains recovered to nearly the same value as that of the original fine-ground bulk forsterite produced by the Czochralski method (Fo-fine) at RT. However, the strength of the 69 μm band did not increase as much as that of Fo-fine when both materials were cooled to low temperature.

We annealed the milled forsterite grains at a higher temperature of 1200 °C, and then measured the IR spectra. The intensity of the 69 μm band, which at RT was also nearly the same as that of Fo-fine, now increased to be the same as that of Fo-fine, when cooled to low temperature [152]. Thus, for cold forsterite dust particles, the intensity of the 69 μm band is very sensitive to the perfection of the crystal lattice. The detection of the 69 μm bands is limited to a few objects in the ISO spectra, and this may be connected to the imperfection of most grains.

It has been suggested that the amorphization of circumstellar dust might be explained by lattice defects caused by cosmic ray hits. However, Day [153] showed that bombardment with 1.5–2.0 MeV protons hardly has any influence on crystalline silicates, and Carrez *et al.* [154] demonstrated that irradiation with 300 keV electrons might even make grains more crystalline. In contrast, Jäger *et al.* [123] experimented with the bombardment of silicates with kiloelectronvolt ions and showed that small crystalline silicates are likely to be amorphized. Koike *et al.* [155, 156] also tried to amorphize silicates by irradiation of high-energy neutrons and electrons (28 MeV) at 4 and 77 K for a long time (several hours to 4 days). The high-energy neutron irradiation with total doses of about 2.5×10^{17} n cm^{-2} had hardly any influence on the IR spectra of the crystalline silicates, even though

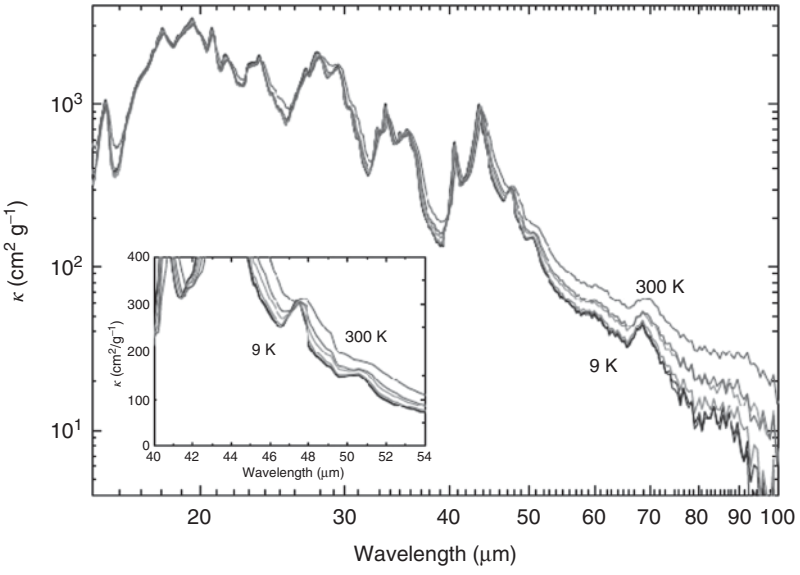

Figure 6.27 The infrared spectra of enstatite with stacking faults at low temperature. The spectra have been measured at 9, 50, 100, 150, and 200 K and at room temperature. The inset shows the sharpening of the 47 μm band with cooling. (Reproduced from [143], copyright 2009 © permission from AAS.)

many lattice defects were created, as revealed by electron spin resonance (ESR) and photoluminescence measurements. The IR spectra were measured in reflection and transmission for irradiated bulk samples and fine grains, respectively. In contrast, irradiation with high-energy electrons at 77 K with total doses of about 4.0×10^{18} e cm^{-2} did further amorphize fused quartz and created many lattice defects as was demonstrated by IR reflectances and ESR measurements [155, 156].

Murata *et al.* [143] synthesized structurally imperfect enstatite with many stacking faults by annealing amorphous silicate produced by the sol–gel method. They showed that the spectra of this enstatite matched the ISO observations well, while those of perfect crystalline enstatite were badly matched at the observed 19.6 and 26.6 μm bands. Further, the broad peak at about 70 μm of the imperfect enstatite differed remarkably from the sharp spectral features of perfect crystalline (clino- and ortho-) enstatites. Thus, the absence of sharp peaks at about 70 μm wavelength in the spectra of circumstellar disks may be due to the imperfection of enstatite crystals in these disks. Finally, an unidentified band at 47.7 μm can be attributed to enstatite with many stacking faults, as the band became pronounced when the samples were cooled down to about 50–100 K (Figure 6.27). The carrier material for this band has been debated for a long time, with, for example, FeSi being one candidate.

6.4.5
Shape Effects and Medium Effects on Infrared Spectra of Forsterite

Effects of grain shape on the measured spectra (for models, see Section 6.2.1) have been noted in laboratory work by, for example, Fabian *et al.* [115], Koike *et al.* [141], and Tamanai *et al.* [106]. For olivine, for example, roundish particles showed spectra with main peaks shifted to shorter wavelengths and with narrower band widths than those of irregularly shaped particles [131].

A systematic study has been performed by Koike *et al.* [144]. Forsterite particles of various grain shapes such as irregular, cauliflower, elliptical, and spherical have been prepared and the spectra of these particles were measured. The spectra changed drastically with the grain shape for the 11, 19, 23, and 33 μm bands. The positions of the main peaks shifted to shorter wavelengths as the shape changed from irregular to spherical, that is, 11.2 μm to 10.99 /11.06 (double peak) μm, 16.35 to 16.23 μm, 19.65 to 18.99 μm, 23.75 to 22.6 μm, and 33.8 to 33.0/33.8 (double peak) μm, respectively (Figure 6.28).

Almost all peaks in observed spectra that are assigned to forsterite grains are explained by an irregular grain shape, but some observed peaks appear at a wavelength shorter than usual. These peaks might be identified with the signatures of spherical or nearly spherical forsterite based on the discussed laboratory measurements. Especially for the 33 μm band, the unidentified peak at 32.8 or 32.5 μm may be due to spherical forsterite grains. If so, studying these peak shifts and the corresponding peak intensities and peak widths could provide evidence of the processing of silicate dust particles in circumstellar environments.

These data have been measured with the pellet method (KBr and polyethylene), so we must pay attention to medium effects; that is, peak positions and peak intensities may be different in a solid medium and vacuum. In aerosol measurements (see Section 6.2.2), the positions of the main peaks are shifted to shorter wavelengths compared to those measured for embedded particles [106].

6.4.6
The missing Iron Content Problem

The crystalline silicates detected in circumstellar (protoplanetary) disks have been shown to be in general Mg-rich, that is, forsterite and enstatite minerals. In stellar atmospheres, the abundance of Mg and Fe is nearly the same, but the composition of the crystalline silicate dust around these stars (at least in the protoplanetary phase) is strongly deficient in iron. Where could the missing iron be? This has been a puzzle for a long time.

Murata *et al.* [157] tried to clarify this question. Using the sol–gel method, they prepared amorphous silicates with solar abundance (Mg/Si ratio equal to the solar abundance ratio of 1.07). They assumed that all sulfur present in the solar-composition elemental mixture formed iron sulfide grains. Thus, a part of

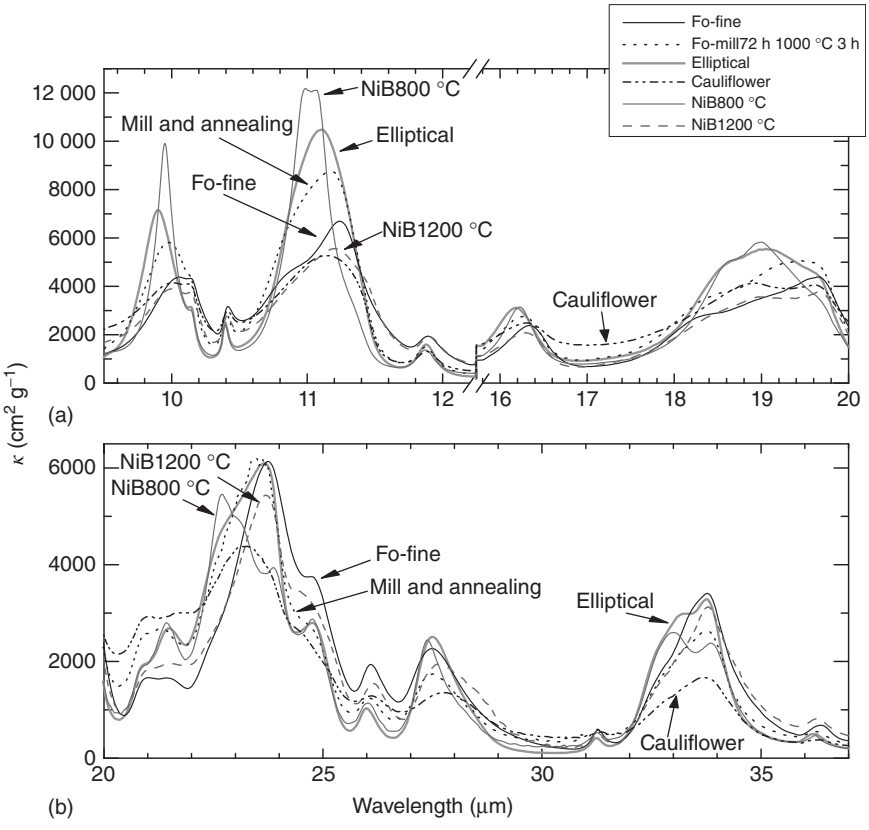

Figure 6.28 (a,b) Shape effects on the infrared spectra of forsterite grains. The grain shapes of Fo-fine and NiB1200 °C are irregular, while sample NiB800 °C has spherical grains. Grains of sample Fo-mill72h1000°C 3h are plate-like with no sharp edge, and grains of the sample cauliflower are porous-like. (Reproduced from [144], copyright 2010 © permission from AAS.)

the Fe is locked in FeS, and the Fe content of the amorphous silicate was thus reduced to an Fe/Si ratio of 0.39.

They annealed the amorphous silicates at 700 °C with annealing times between 10 min and 10 h. Then, the abundances of Mg, Fe, and Si in the produced crystalline silicate were estimated from X-ray diffraction data based on the lattice spacings. The degree of crystallinity was estimated from fitting the IR spectra with a combination of amorphous silicate and olivine spectra. The analysis showed that the crystallized material was rich in Mg, while the residual amorphous silicate was rich in Fe. Thus, the iron had somehow been removed from the forming lattice in the annealing process. The experiments demonstrate the possible coexistence of Mg-rich crystalline and Fe-bearing amorphous phases in circumstellar silicates. More results about structural changes by annealing and irradiation processes will be reported in Section 7.5.

6.5
Oxides as High-Temperature Condensates

Thomas Posch and Simon Zeidler

6.5.1
The Role of Oxide Dust in the Cosmic Matter Circuit

Oxides constitute, together with hydroxides, one of the 10 classes of minerals, that is, one of the 10 classes of natural crystalline solids.[9] Most of the abundant oxides in space are relatively simple with respect to their chemical composition; for example, they are binary compounds of metals with oxygen like MgO and FeO. Despite their chemical simplicity, metal oxides comprise <1% of the total dust mass in most cosmic environments. The bulk of cosmic and terrestrial minerals are silicates. However, among the oxides, there are materials that play a decisive role in *initiating* the dust formation process in oxygen-rich (as opposed to carbon-rich) environments. This is due to the existence of oxides with very high melting points, above 1200 K – the "refractory oxides." In a cooling gas with near-solar elemental abundances, oxides such as ZrO_2 (baddeleyite), α-Al_2O_3 (corundum), $CaTiO_3$ (perovskite), and $MgAl_2O_4$ (spinel) are able to form as small solid grains at higher temperatures than the majority of silicate minerals (such as diopside, forsterite, or enstatite).

Thus, oxides such as corundum, perovskite, and spinel are able to condense in the innermost region of a circumstellar shell – close to the stellar photosphere, where the density of the expanding gas is still high (about 10^7–10^{10} hydrogen atoms per cm^3). Those grains may therefore provide important seed nuclei for the formation of the much more abundant silicates, which will take place farther away from the respective stars. There is also observational evidence of refractory oxides, especially amorphous Al_2O_3, in the inner parts of circumstellar shells [159].

Whittet describes the evolutionary view on the formation of oxygen-rich dust species in the following way:

> The most abundant monomers that lead to the production of solids are expected to be Fe, Mg, SiO and H_2O. Initially, at $T > 1500$ K, these remain in the gas and only rare metals such as tungsten and refractory oxides such as corundum (α-Al_2O_3) and perovskite ($CaTiO_3$) are stable in the solid phase. Although contributing little in terms of mass, these high-temperature-condensates might facilitate the deposition of more abundant solids by providing nucleation centers […]. The major condensation phase occurs at temperatures 1200 → 800 K with the nucleation and growth of amorphous SiO clusters. These clusters chemisorb other monomers and subsequent annealing may result in the growth of linked SiO_3 chains with

9) Different ways of classifying the minerals can be found. We refer to the taxonomy of Strunz and Nickel [158] which introduces the following classes: (i) elements; (ii) sulfides and related compounds; (iii) halides; (iv) oxides and hydroxides; (v) carbonates and nitrates; (vi) borates; (vii) sulfates, selenates, chromates, tellurates, molybdates, and wolframates; (viii) phosphates, arsenates, and vanadates; (ix) silicates and germanates; and (x) organic compounds.

> attached Mg cations (enstatite, $MgSiO_3$) or individual SiO_4 tetrahedra joined by cations (forsterite, Mg_2SiO_4). […] As the temperature drops further, iron is increasingly oxidized to FeO until little or no pure metallic phase remains below ∼400 K. Finally, H_2O-ice may condense as the temperature drops below ∼200 K. ([160], p. 230–232).

As before, it becomes evident from these considerations that refractory oxides do not represent a large mass fraction of a circumstellar shell, but their significance lies in their role as growth centers for the bulk of the (silicate) dust. Furthermore, it should be noted that, at the low-temperature end of the condensation sequence, another oxide is to be found: solid H_2O, or water ice. Solid H_2O is by far the most abundant of all solid oxides in space. It will not be discussed in this section, since we will focus on the high-temperature oxides. The properties and the infrared (IR) spectrum of water ice have been discussed in Chapter 5. Another low-temperature oxide that is found in the cold cosmic environments is dry ice, CO_2.

The "pioneering" role of refractory oxide dust in the cycle of cosmic matter is supported by investigations on calcium–aluminum-rich inclusions (CAIs) and presolar grains (PSGs) from meteorites. CAIs represent the oldest minerals found in our solar system. Their age has been found to be 4567 million years.[10] Apart from Ca- and Al-rich silicates – especially melilite and diopside – which constitute the bulk of the CAI minerals, oxides such as spinel, hibonite, and – with lower abundance – corundum, grossite, and perovskite are major constituents of the CAIs [162, 163].

An extremely important source of information on oxide minerals in stardust grains is the study of presolar material conserved in primitive types of meteorites, especially carbonaceous chondrites, and interplanetary dust particles (IDPs). PSGs are extracted from those chondrites and from IDPs by chemical methods (acids are used to extract them from their respective matrixes). Their defining property is the isotopic abundances which strongly deviate from the mean values characteristic of solar system matter, where "strongly" means up to factors of up to 50 and even more (for an overview, see Nittler [164] and McSween and Huss [165], Chapter 5). Oxide minerals that have been found in PSGs include spinel, hibonite, Al_2O_3, TiO_2 [166], and wustite (FeO; [167]). For Al_2O_3 and the rare TiO_2 in PSGs, the polytype has not yet been determined, hence it remains unclear whether they occur as corundum and rutile or other polytypes, possibly including amorphous Al_2O_3.

6.5.2
A General Remark on the IR Bands of Refractory Oxides

Before we turn to the IR properties of individual refractory oxides, a distinctive feature that they share should be stressed: their capacity to be excited to strong dipole vibrations – corresponding to large strengths of their mid-infrared (MIR)

10) For example, the isotopic age of CAIs in the CV chondrite Efremovka has been determined to be 4567.2 ± 0.6 Myr [161].

bands. This is a long-known fact which John Salisbury, in the introduction to his atlas of *Infrared Spectra of Minerals*, expressed thus:

> An interesting aspect of these features [= the stretching vibration bands in metal oxides] is that, because of the intense dipole oscillations induced by the vibration of highly ionic oxides, their powder spectra are profoundly modified by the shape and size of the particles […]. ([168], p. xv)

This statement contains several terms and concepts that deserve further discussion: namely, *ionic oxides*, *intense dipole oscillations* and, finally, the *particle size* as well as *particle shape dependence* of IR powder spectra of oxides.

The term *ionic oxides* refers to oxide minerals where ionic bonds play at least a significant role (however, covalent bonds should be simultaneously considered). Among them are periclase (MgO), spinel ($MgAl_2O_4$), corundum (α-Al_2O_3), and perovskite ($CaTiO_3$). The IR resonances treated in the following are largely due to vibrations of the ions constituting the lattice of the respective material that is exposed to a stellar radiation field or to a light beam in a terrestrial laboratory. In fact, the strongest IR active modes in solids are related to dipole moments induced in a crystalline ion lattice by electromagnetic radiation. Crystalline ionic or partly ionic oxides can therefore have intense dipole oscillations. They may thus reach very large values of the IR optical constants n and k. This becomes evident from Figure 6.29 for the case of α-Al_2O_3, where k exceeds 10 in the 10–25 μm range (while this is not the case for amorphous Al_2O_3).

But how is this finally related to significant effects of grain shapes and sizes in powder spectra of these materials? The size and shape of particles always have an influence on their respective IR spectra – not only, of course, for highly ionic crystals. This has been demonstrated, for example, by Bohren and Huffman [96]. However, there are solids such as amorphous silicates for which the grain shapes have less dramatic effects on their IR spectra, while other minerals – metal oxides with ionic bonds, but also some crystalline silicates among them – show *very* strong influence of the particle size and shape on IR band positions and profiles. For crystalline silicates, these influences have already been demonstrated in Section 6.4.5. The larger the intrinsic strength of an IR active mode in a solid, the stronger is the potential "shift" of the corresponding observed band due to varying particle morphologies, for example, in differently produced powders that are used for spectroscopy.

This general consideration has some significant consequences:

- IR transmission spectra of powders do not yield sufficient information to identify IR bands of cosmic dust, in particular if the latter contains highly ionic crystals. Bands seen in transmission spectra (especially of large or strongly elongated grains) could be at positions totally different from their respective cosmic counterparts.
- The derivation of optical constants (instead of absorption efficiencies of powders) is of particular importance in the case of refractory oxides. In the MIR, the optical constants can be very well derived from reflectance spectroscopy of polished bulk surfaces.

– Once the optical constants n and k have been determined for a mineral or for an amorphous solid, it is – at least in principle – possible to calculate the absorption efficiencies of arbitrarily shaped (and arbitrarily sized) grains which are characterized by these optical constants. How to perform such calculations has been discussed in Section 6.2.

The remaining parts of this section are structured as follows:

In Sections 6.5.3–6.5.6, a selection of astrophysically relevant solid oxides is presented, mainly with respect to their IR properties. The order in which the individual minerals and amorphous solids are presented roughly follows their stability limits, starting with the most refractory materials and subsequently going "down" in the pT plane. An exception to this rule are the Ti oxides, which will be treated at the end despite their high stability limits, because their abundance in space is expected to be still much lower than that of the other metal oxides.

The final two subsections (6.5.7 and 6.5.8) highlight two problems that are common to most studies of oxygen-rich circumstellar dust analogs: the question of how to constrain the absorption behavior of those materials in the near-infrared (i.e., at 1 µm to a few micrometers) and the question of how optical properties depend on the dust temperature.

6.5.3
Al Oxides, Ca–Al Oxides, and Mg–Al Oxides

Al_2O_3 is one of those solid oxides of which several polytypes exist – that is, many crystallograhically distinct arrangements of oxygen anions and aluminum cations. Most authors admit the existence of seven well-defined structures: α-, γ-, χ-, δ-, ϑ-, η-, and κ-Al_2O_3 (e.g., Ref. [169]). These polytypes can be produced in the laboratory, are mostly metastable, and are studied also with respect to industrial applications. Additionally, Al_2O_3 occurs as an amorphous solid. Different degrees of amorphousness exist.

In the astronomical literature, the term *corundum* is often erroneously assigned to different kinds of solid Al_2O_3, or even to solid Al_2O_3 regardless of its crystal structure. However, only *one* of the crystalline Al_2O_3 deserves the name corundum: namely α-Al_2O_3, the trigonal modification, which has the highest stability of all polytypes and may occur in gem quality on Earth (known as *ruby* and *sapphire*). Amorphous Al_2O_3 should not at all be referred to as *corundum*. Its IR properties are extremely different from those of α-Al_2O_3 and the other crystalline polytypes. This is illustrated in Figure 6.29 by a comparison of $k(\lambda)$ for these two species of solid aluminum oxide. While α-Al_2O_3 has extremely sharp peaks and high maximum values of $n(\lambda)$ and $k(\lambda)$, this is not the case for amorphous aluminum oxide according to Begemann *et al.* [170].

It is not yet clear whether amorphous or crystalline aluminum oxide (most likely α-Al_2O_3, but γ-Al_2O_3 – cf. e.g., Ref. [172] – may also form) prevails in circumstellar shells (and maybe in supernova remnants), but we do have good evidence from PSGs that *some* kind of this material is indeed formed in a number of cosmic environments. The relevance of aluminum oxides in the context of astronomical

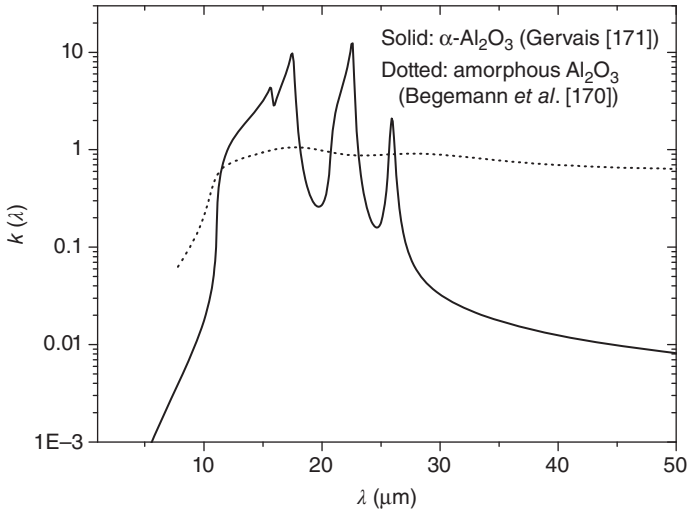

Figure 6.29 Absorption index $k(\lambda)$ of α-Al_2O_3 according to Gervais [171] and amorphous Al_2O_3 according to Begemann *et al.* [170]. For α-Al_2O_3, the k values refer to the case of orientation of the electric field vector perpendicular to the crystal's symmetry axis.

IR spectroscopy was first discussed by Onaka *et al.* [173]. They assigned a broad emission band, centered around 12 μm, which had been detected in the Infrared Astronomical Satellite (IRAS) spectra of M-type Mira variables by Vardya *et al.* [174], to Al_2O_3 grains. This assignment was not based on the optical constants of corundum but on those of partially amorphized γ-Al_2O_3.

In addition to this broad feature, a sharp band peaking at 13 μm was found in the 1990s, based on spectra of Asymptotic Giant Branch (AGB) stars taken by IRAS, the Kuiper Airborne Observatory, and Infrared Space Observatory (ISO) [170, 175–177]. This narrower feature, which is frequently seen "on top" of a broad structure peaking at 11–12 μm (Figure 6.30), was first assigned to corundum but later on to spinel ($MgAl_2O_4$). Almost certainly, it is due to an Al–O vibration. A clear assignment, either to (crystalline) α-Al_2O_3 or else to crystalline $MgAl_2O_4$ (see below), is difficult on the basis of the 13 μm band alone. It should be noted that the optical constants of corundum change significantly at high temperatures (Section 6.5.8), so that the assignment also depends on the dust temperature. Secondary bands of the potential carriers spinel and corundum (and their temperature-dependent optical constants) must be taken into account as well, meaning that their presence has to be verified in astronomical spectra. The broad structure peaking at 11–12 μm is assigned to an amorphous aluminum oxide, based on the data by Begemann *et al.* [170].

Hibonite ($CaAl_{12}O_{19}$) has a chemical composition close to that of Al_2O_3, since its ideal sum formula may also be written as $CaO + 6Al_2O_3$. Crystallographically, hibonite has hexagonal symmetry. In many meteorites, hibonite is a common component, but also other Ca–Al-oxides have been found there, namely $CaAl_4O_7$

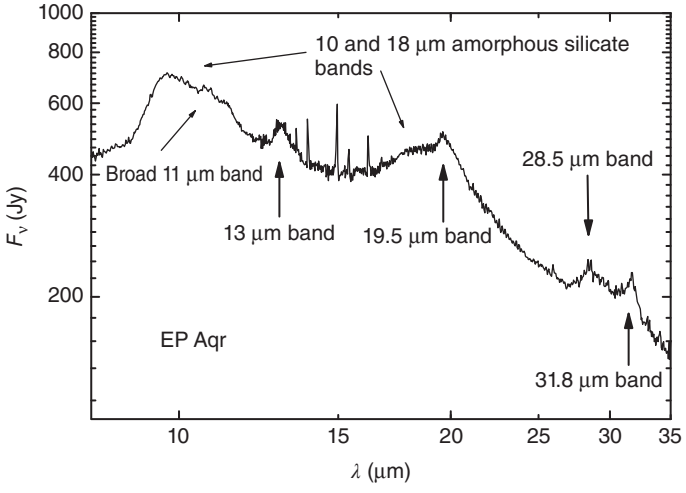

Figure 6.30 Mid-infrared (7–35 μm) spectrum of the semiregular variable star EP Aqr, taken with the short wavelength spectrograph of the Infrared Space Observatory (ISO). The dominant dust feature seen in this spectrum is the 10 μm amorphous silicate band, which is accompanied by a weaker band at 18 μm. At 11–12 μm, a broad band is detected, which may be due to amorphous alumina. The narrow band at 13 μm is assigned to an Al–O vibration in a crystalline Al-oxide or Mg–Al-oxide (corundum or spinel). The prominent band at 19.5 μm is probably due to crystalline oxides as well (Section 6.5.5).

(grossite), $CaAl_2O_4$, and $CaAl_{24}O_{37}$ [178]. We shall discuss only the IR properties of hibonite here. (For the MIR spectrum of grossite, see Mutschke *et al.* [179].)

Figure 6.31 demonstrates how strongly the mass absorption coefficient of hibonite depends on the grain shape – with respect to both the band positions and the band profiles. The strongest IR resonance of hibonite is located at 12.3–13.3 μm, depending on the grain shape. The peak position 12.3 μm refers to spherical grains, and in this case the maximum of the absorption efficiency is rather sharp, though not as sharp as in the case of corundum. The peak position of 13.3 μm refers to an ensemble of hibonite grains with different, partly strongly elongated shapes, which are typically present in a powder embedded in a pellet. Many more absorption maxima are present in the IR spectrum of $CaAl_{12}O_{19}$, reaching to far-infrared (FIR) wavelengths of about 80 μm; see Figure 6.31 (no such FIR peaks are found in the spectrum of corundum).

The strong 12.3 μm feature predicted for small hibonite spheres has been discussed as a potential carrier of a weak emission at this wavelength, detected in the spectra of some oxygen-rich circumstellar dust shells of pulsating red giant stars [179]. Hibonite is also found in PSGs originating from AGB stars and from supernovae [180–182].

As mentioned above, spinels are abundant in calcium–aluminum-rich inclusions and in PSGs – more abundant than corundum in PSGs and much more abundant than hibonite grains [180] – which indicates the high probability for this mineral species to form in a hot, but cooling gas of solar-like composition.

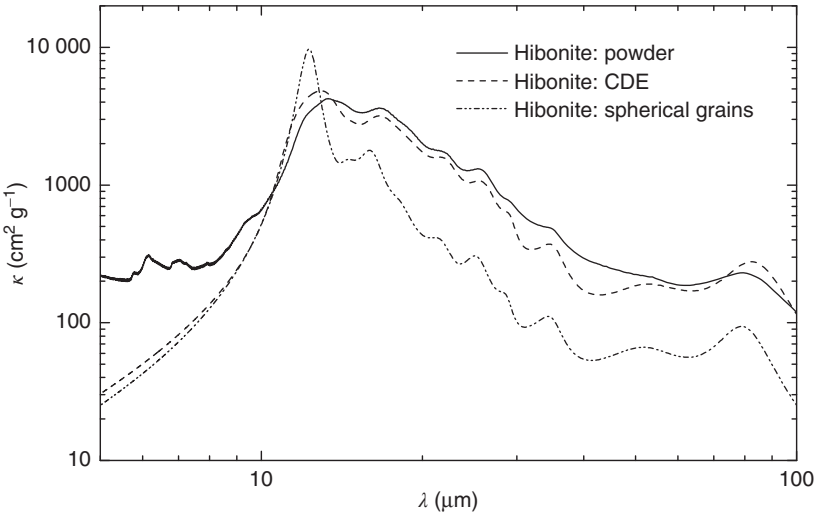

Figure 6.31 Small-particle absorption spectra of hibonite for different grain shapes: spherical grains (dotted line, derived from the optical constants after orientational averaging), continuous distribution of ellipsoids with equal probability of all axis ratios (dashed line), and mass absorption coefficient measured by the pellet method. (Data taken from Ref. [179].)

From terrestrial mineralogy, many more spinels besides $MgAl_2O_4$ are known. This is due to the fact that the Mg–Al spinel forms a three-dimensional structure which is suitable for a large variety of ions to fit in. For example, bivalent iron Fe^{2+} can fully substitute magnesium, thereby forming hercynite ($FeAl_2O_4$). Trivalent iron Fe^{3+} may substitute aluminum, thereby forming magnetite ($FeFe_2O_4$, or, which is the same, Fe_3O_4). These are just two examples for a large manifold of cubic oxides with spinel structure.

Only Mg–Al spinels are under consideration here. However, we do also consider spinels in which a partial exchange between aluminum and magnesium ions has taken place. Usually, Mg cations occupy the tetrahedrally coordinated interstices of the cubic oxygen anion lattice, while Al cations are located in the octahedrally coordinated interstices. Upon heating, Mg and Al ions can partially change places in the spinel lattice, which also effects the IR spectra of this mineral. Furthermore, the Mg/Al ratio may vary in spinels, which again influences the spectral features at MIR wavelengths. All these effects have been discussed by Fabian *et al.* [183]. Other temperature-induced changes of the IR spectra of spinels, as mentioned above, will be discussed in Section 6.5.8.

6.5.4
Silicon Oxides (SiO_2 and SiO)

SiO_2, like Al_2O_3, may form several crystalline polymorphs as well as an amorphous solid (which is very well known as *quartz glass*). The umbrella term for the various kinds of SiO_2 is "silica." We will focus here on two crystalline polytypes,

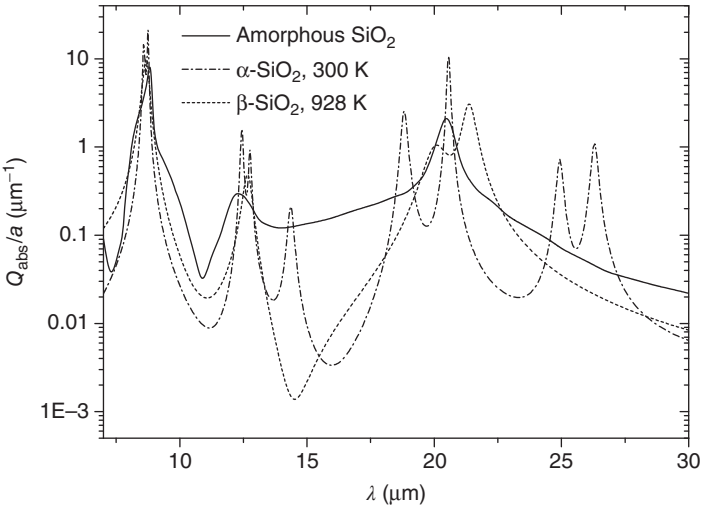

Figure 6.32 Comparison of the infrared spectra of amorphous SiO_2, α-quartz, and β-quartz. Q_{abs}/a, the absorption efficiency divided by the particle radius (this quantity is independent of the particle radius within the Rayleigh limit), has been calculated for spherical grains, which leads to very sharp peaks, in particular for the crystalline modifications. The optical constants are from Palik [91] and from Zeidler *et al.* [113], see Figure 6.12.

namely α- and β-quartz, plus amorphous SiO_2. Among the many forms of crystalline SiO_2, α-quartz is the most stable form of silica at room temperature (RT) (and at terrestrial atmospheric pressure). It has trigonal crystal symmetry. High-temperature and high-pressure polymorphs of silica include β-quartz (with hexagonal crystal structure), tridymite (rhombic), cristobalite (tetragonal), coesite (monoclinic, forming at very high pressures), and stishovite (tetragonal, also forming at very high pressures). The transition between the low-pressure phases α- and β-quartz takes place at 846–847 K under terrestrial conditions. α-Quartz, β-quartz, and amorphous SiO_2 differ strongly in their IR properties. This is shown in Figure 6.32.

The strongest resonance features of silica have been identified in Spitzer MIR spectra of five T Tauri stars [73]. The silica bands at 9, 12.5, and ≈20 μm seem to have counterparts in the spectrum of these Young Stellar Objects of Class II. The form of SiO_2 that provides the best fits of the astronomical dust spectra is amorphous silica which has been heated at 1220 K for 5 h [130], ending up as a mixture of (mainly) cristobalite and (partly) tridymite. Sargent *et al.* [73] point out that SiO_2 in the form of tridymite has also been found in cometary dust by the Stardust mission (which collected dust from Comet 81P/Wild 2). Furthermore, the spectra of other dusty environments show signs of SiO_2 features as well; for example, Juhász *et al.* [70] identified amorphous silica in the spectra of several Herbig Ae/Be stars.

Given the wide range of dust temperatures that can occur in the above-mentioned astronomical objects, it is desirable to provide laboratory data on the temperature dependence of the IR properties of silica (in its various forms). This is a fairly large task, which could only be partly accomplished so far. The changes in the IR bands of amorphous SiO_2 at low temperatures have been studied rather extensively: Henning and Mutschke [184] derived n and k for this material at 10, 100, 200, and 300 K for wavelengths ranging from 2 to 500 μm. Additionally, the IR spectra of α-quartz and β-quartz at high temperatures have been studied recently by Zeidler *et al.* [113]. They were able to demonstrate in detail how the number of IR active modes is greatly reduced (actually by a factor of 2) upon heating to temperatures above 847 K, in parallel to the above-mentioned transition from α- to β-quartz, in accordance with theoretical predictions. Figure 6.32 shows a crucial step in this transition.

Yet another oxide of silicon, namely amorphous SiO, is a potential component of stardust. Molecular SiO is known to be very common in many stellar environments. Solid amorphous SiO is a material that disintegrates into silicon and nanoclusters of SiO_2 upon annealing to about 900 K. Under terrestrial atmospheric conditions, SiO is oxidized to SiO_2. This reaction, however, may be inhibited under particular conditions in space.

Wetzel *et al.* [185] produced films of SiO and studied their IR properties, partly confirming earlier results on bulk SiO. According to Wetzel *et al.*, the main IR band of amorphous SiO is a broad peak centered at ∼10.2 μm (the exact value is sensitive to the temperature); this band corresponds to an Si–O stretching mode. This band is much broader and located at a longer wavelength than the strongest IR band of SiO_2, which is due to the existence of $Si–Si_y–O_{4-y}$ tetrahedra with $y > 0$ [186]. Weaker and still much broader bands of SiO are located at 14 μm (bending mode) and 26 μm (rocking mode; measured by Philipp [187]).

Amorphous solid SiO could be the carrier of the broad 10 μm band in those cases where the latter is *not* accompanied by any significant 18 μm band, for example, in the spectra of some S stars on the Asymptotic Giant Branch (AGB). In these stars, there is a lack of free oxygen compared to stars with solar elemental abundances and, therefore, molecular SiO may rather condense into solid SiO than into SiO_2 or silicates.

6.5.5
Iron Oxides and Mg–Fe Oxides

Partly because of the polyvalency of iron, several iron oxides occur as natural solids. Most widely known are α-Fe_2O_3 (hematite) and Fe_3O_4 (magnetite). Hematite is isostructural with corundum; hence, it also forms trigonal crystals. Magnetite is isostructural with spinel – whence its alternative name *ferrite spinel*.

On the other hand, the iron oxide FeO (wüstite) is rare as a mineral on Earth. In terrestrial wüstite, some of the crystallographic positions that should be occupied by iron are usually empty, such that its actual stoichiometry is $Fe_{0.84}O$ to $Fe_{0.95}O$ [188].

Since it has been suggested that a solid solution of FeO and MgO could be the carrier of a spectral feature seen in the AGB stars, we concentrate on the (FeO…MgO) series in the following.

While MgO (periclase) has a very high melting point (3125 K at atmospheric pressure), the iron oxides FeO, Fe_2O_3, and Fe_3O_4 have stability limits that are lower than all the other oxides discussed above.[11)]

Both MgO and FeO have only one strong vibrational band in the IR. The peak position of this band is at a much smaller wavelength for MgO (e.g., 16.6 μm for spherical grains) than for FeO (19.9 μm for the same grain shape) and intermediate between both for the solid solutions of (Mg,Fe)O composition. Periclase has a much sharper (narrower) IR band than wüstite and the Fe-rich solid solutions of MgO and FeO. The optical constants of MgO are well known and have been published in the second volume of Palik [91]; n and k values for (Mg,Fe)O were published by Henning *et al.* [124].

Grains composed of $Mg_{0.1}Fe_{0.9}O$ are a promising candidate carrier of a strong IR band observed in the dust shells of AGB stars with small mass loss rates like EP Aqr (Figure 6.30): both the peak position (19.5–19.6 μm) and the band width (Full width at half maximum (FWHM) = 3.3 μm) are in good agreement with astronomical data.

Another spectral feature with a band position close to 20 μm has been discussed by Posch *et al.* [189] with respect to its possible causal connection to FeO: the so-called "21" micrometer band detected in some spectra of protoplanetary nebulae. The carrier of this band – which actually has a position of 20.1 μm and a width (FWHM) larger than 2 μm – is, however, still a matter of a lively debate (e.g., Refs. [190, 191], see also Section 6.6.3).

6.5.6 Titanium Oxides

As mentioned above, titanium oxides cannot be a major component of any dust-forming environment because the (solar) elemental abundance of Ti is lower than that of Si by a factor of 400. Nevertheless, titanium oxides (as well as titanium carbides) may have the function of providing nucleation seeds in circumstellar shells because of their refractory nature and of reaction paths leading from molecular TiO, for example, to solid TiO_2 [192].

Several forms of solid TiO_2 as well as $CaTiO_3$ deserve attention as possible stardust components. $CaTiO_3$ is the thermodynamically most stable titanium oxide considered here. Its melting point is 2188 K at atmospheric pressure [193].

Posch *et al.* [114] have studied those Ti oxides with respect to their IR properties. The main results can be summarized as follows:

- Solid TiO_2 – in its various crystalline forms – and $CaTiO_3$ have very sharp peaks in their optical constants in the MIR. They may thus produce extremely strong IR bands (e.g., in their reflectance spectra).

11) Pure FeO has a melting point that is ~1500 K lower than that of MgO!

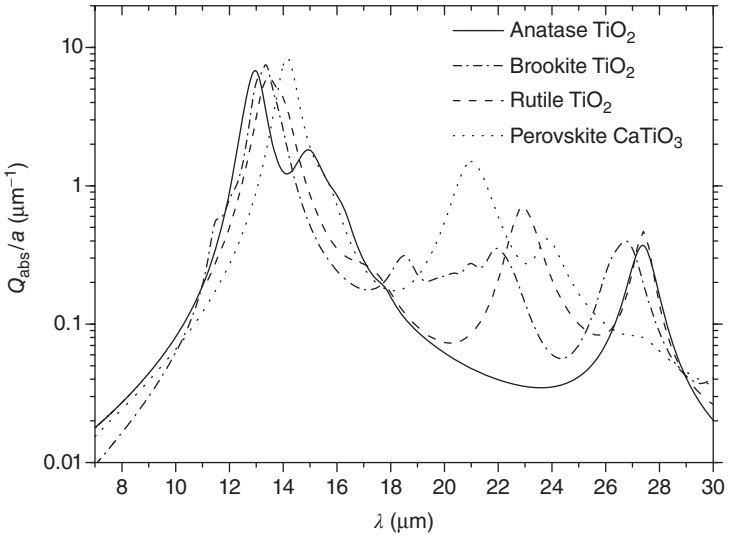

Figure 6.33 Calculated absorption efficiency factors Q_{abs}/a for small spherical grains of rutile, anatase, brookite, and perovskite. The strongest mid-infrared resonance of all these grains is located at 13–14 μm if their shapes are (near)spherical, but shifts to considerably longer wavelengths for nonspherical grains (not shown here). For clarity, the spectra are shown up to 30 μm only, but several of the plotted curves have peaks beyond this wavelength.

- The exact position of the peaks in their small-particle spectra again strongly depends on the grain shape, in accordance with the general statement in Section 6.5.2.
- For spherical grains, for example, the principal maximum of the absorption efficiency of three naturally occurring TiO_2 modifications (rutile, anatase, and brookite) and for $CaTiO_3$ (perovskite) is located between 13 and 14 μm. Many additional resonances occur at longer wavelengths (see Figure 6.33 for spectra until 30 μm).

The fact that several titanium oxides are able to produce strong IR bands in the ∼13 μm region could make them candidates for the carrier of the 13 μm band shown in Figure 6.30. More data on the IR bands of Ti oxides can be found in Tamanai *et al.* [108].

6.5.7
Constraining the Optical Constants in the NIR Region

The characteristic strong vibrational bands of silicates (both amorphous and crystalline ones) are located at wavelengths beyond 5 μm. Hence, many studies aiming at a characterization of stardust analogs – as well as many mineralogical papers – give figures/tables for the optical constants and/or mass absorption coefficients for $\lambda > 5\,\mu m$. In this wavelength region, not only do the most interesting and

most intense IR active modes of solids occur but also two standard measurement techniques are well applicable (Section 6.2.3): reflectance spectroscopy of polished samples at near-normal incidence, and powder transmission spectroscopy.[12] For $\lambda < 5$ μm, measurements especially of the *imaginary* part k of the complex index of refraction are difficult for transparent materials (e.g., Mg silicates, Mg–Al-oxides), and data are thus rare.[13]

But from an astrophysical point of view, it is crucial to have information on k (or, as an alternative, the mass absorption coefficient) also at NIR wavelengths, since k indicates how efficiently a material is able to absorb radiation in a region in which the stellar radiation field is most intense. (The spectral energy distributions of cool stars peak at about 1 μm!) So if a radiative transfer calculation is to be made, it is necessary to constrain n and k ideally from the UV to the far IR.

One possibility to constrain the absorption behavior of not strongly absorptive materials such as iron-poor oxides and silicates in the NIR is to perform transmittance spectroscopy of thin sections (compare Section 6.2.3). This has been shown in detail by Zeidler *et al.* [116]. It is demonstrated there that oxides that are entirely free of transition-metal ions (e.g., Fe or Cr) are supposed to have k values going down to $<10^{-10}$ in the NIR; but already 1% of Fe or Cr included into the crystal lattice leads to NIR k values of more than 10^{-4} (Figure 6.34). This has important consequences for the energy balance of dust grains with Fe (or comparable) impurities, since an increase in k in the NIR goes along with an increase in a grain's ability to absorb energy from the stellar radiation field, as indicated above.

6.5.8
Temperature Dependence of the Optical Constants

Optical constants of stardust (and of its laboratory analogs) may depend on the temperature in several ways. First of all, *heating* or formation at a high temperature may result in *irreversible* changes in a solid compared to its respective room-temperature structure. This is the case, for example, for $MgAl_2O_4$ (Mg–Al spinel), in which the Mg and the Al ions partly exchange their crystallographic positions at temperatures of ∼1200 K or more, which leads to a change of the MIR properties (concerning band positions, fine structure of the bands, and band strengths). For more details, see Ref. [183].

Second, heating may also result in *reversible* changes of the optical constants. To measure this is more difficult, since those changes are, by definition, no longer detectable after a sample has been cooled down to RT, so spectrometers equipped

12) In fact, reflectance spectroscopy of polished samples *is* also applicable at $\lambda < 5$ μm, but there $R(\lambda)$ often does not lead to constraints on the absorption index k, since it gets too small in the NIR. For powder transmission spectroscopy, additional problems come into play: the grain sizes of powders produced by grinding are usually so large compared to NIR wavelengths that scattering becomes a source of errors.

13) The situation is less problematic for the *real* part n of the complex index of refraction. In many cases, it does not change much in the NIR (while k may vary over several orders of magnitude), so that it may be extrapolated or interpolated without too large uncertainties.

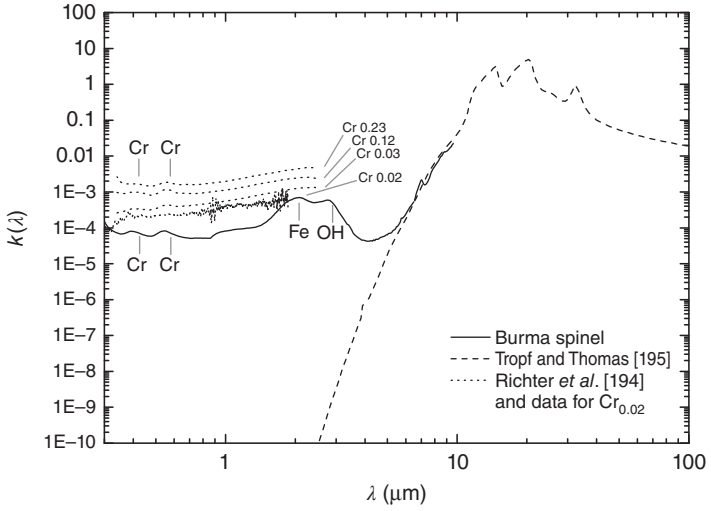

Figure 6.34 Measured vis/NIR absorption index of synthetic and natural spinels containing different amounts of chromium (and iron in the natural sample). The data are derived from transmission spectroscopy of thin sections [116, 194]. The mid-infrared data (dashed line) are from lattice-vibration models [195], which do not include impurity absorption. (Reproduced from [116], copyright 2011 © permission from ESO.)

with high-temperature cells are needed in order to measure the changes *in situ*. A classic example is the reversible changes of the absorption index of MgO measured by Jasperse *et al.* [196]. Measurements on the temperature dependence of n and k of other refractory oxides such as corundum and spinel were recently done at the Jena astrophysical laboratory. Figure 6.35 shows the temperature dependence of the absorption index k, as derived from reflection measurements with a high-temperature cell, for spinel [113].

Finally, very low temperatures also affect the dielectric properties of stardust (and of minerals in general). This is especially the case for the FIR properties. Since many dust-rich environments are indeed very cold and radiate substantially at FIR wavelengths, this is a significant effect and needs to be accounted for in laboratory measurements.

For silicates, low-temperature spectroscopic measurements of both the optical constants and of IR band positions and band widths have already been described in Section 6.4.2. Posch *et al.* [197] and Mutschke *et al.* [61] also presented detailed case studies on the low-temperature IR properties of carbonates and phyllosilicates. For oxides, we have to mention again the data on MgO by Jasperse *et al.* [196] and on FeO and amorphous SiO_2 by Henning and Mutschke [184].

Most of the mentioned measurements deal primarily with the temperature-dependent characteristics of the IR bands. However, the continuum value of the mass absorption coefficient in the FIR and at submillimeter wavelengths, that is, beyond the range of strong bands, also strongly changes at low temperatures. Compared to RT, it can decrease by orders of magnitude, the slope becoming

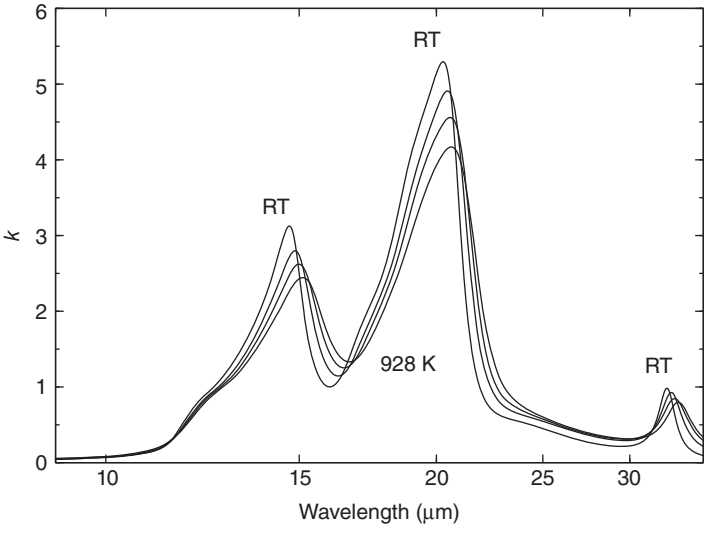

Figure 6.35 Variation of the absorption index k of synthetic spinel with the temperature [113]. As the temperature increases, the peaks in k shift to larger wavelengths and broaden. Spectra are shown for the temperatures 300 (RT), 551, 738, and 928 K.

much steeper with (increasing) wavelength for many stardust analogs upon cooling.

For amorphous materials, this has already been discussed in Section 6.3.5. For crystals, there are at least comparably strong effects (Figure 6.27 for enstatite), but based on different physical mechanisms. In the case of oxides, data are unfortunately rare. Measurements on Al_2O_3 at high temperatures can be found in Mitra *et al.* [198]. Magnetite has also been intensively studied because of a phase transition (metal–insulator transition) that influences the continuum absorption strongly [199]. With the current progress of the terahertz technology[14], further detailed studies are to be expected.

6.6
Spectroscopic Properties of Carbon Compounds

Harald Mutschke and Cornelia Jäger

The silicates and oxides discussed in the previous sections are not the only important solids in cosmic dust. Carbon is one of the most abundant elements in space, and only a part of it resides in the gas phase. From the C–H stretching vibration observed in the interstellar extinction, it is known that a form of hydrogenated amorphous carbon (HAC) particles must be present in interstellar space [12].

14) The terahertz frequency range corresponds to the FIR/submillimeter wavelength range and is becoming more and more accessible by modern laser and semiconductor techniques (e.g., photomixing, ultrashort pulses). Mostly, the intense radiation produced using this technology is applied to imaging purposes, but commercial spectrometers are also becoming available.

Most models of interstellar dust also predict a component of small graphite particles, which are needed to explain the strong interstellar UV extinction band at 217.5 nm [200]. Furthermore, meteorites contain micrometer-sized graphitic particles of extrasolar origin, as proven by isotope analysis, often with inclusions of small carbide grains (e.g., Ref. [201]). In the same meteorites, nanodiamonds of only a few nanometer size are present with high abundances, representing another interesting carbon species. Diamond has also been spectroscopically proven to be present in circumstellar disks around young stars [202]. Finally, infrared (IR) emission features have been found for fullerenes, C_{60}, in reflection nebulae [203, 204] and in planetary nebulae [52, 205].

In this section, we will describe the spectroscopic properties and the problems related to obtaining optical constants and emission/absorption cross sections of carbonaceous dust species. We will start with the pure carbon allotropes graphite, diamond, and fullerite, then review data on amorphous carbon forms, and, finally, close with a short consideration of carbides.

6.6.1
Graphite, Diamond, and Fullerite

Graphite and diamond are the two most important crystalline forms of pure carbon. While the former consists of graphene layers that are stacked to form a strongly anisotropic crystal of hexagonal symmetry, the latter is held together by three-dimensional covalent bonding and is of cubic symmetry; that is, it is isotropic. Besides these two well-known modifications, there are two additional carbon polymorphs (lonsdaleite and chaoite), which are found in meteorites and shocked rocks. Although there are Raman studies of lonsdaleite, we will not discuss the optical properties of these minerals here.

The striking differences in the optical, electrical, and mechanical properties of graphite and diamond are well known. The black color and the high conductivity of graphite in the plane of the graphene layers arise from the π-bonding within these layers formed by sp^2-hybridized carbon atoms. The π-electrons are free to move along the graphene layers, which gives rise to the high conductivity and to the possibility of collective excitation by electromagnetic fields. Consequently, when electromagnetic fields are directed along the graphene layers, graphite shows metallic behavior, with high reflectivity for photon energies lower than the plasma frequency of the free-electron gas, 0.44 eV [206]. Optical excitation of valence band π-electrons to the conduction band additionally contributes to the absorption coefficient. Owing to the lack of an energy gap between these bands, this interband contribution is strong down to photon energies of about 0.01 eV (wavelengths $\sim$100 μm). In the visible and UV spectral ranges, the interband transitions of the π- and σ-electrons produce further strong maxima in the optical constants, at about 270 nm for the former and at 90 nm for the latter (Figure 6.36).

For light with its electric field oriented perpendicular to the graphene layers, the behavior is different: in accordance with the lower electrical conductivity, metallic reflection sets in at longer wavelengths (>10 μm), and interband absorption is

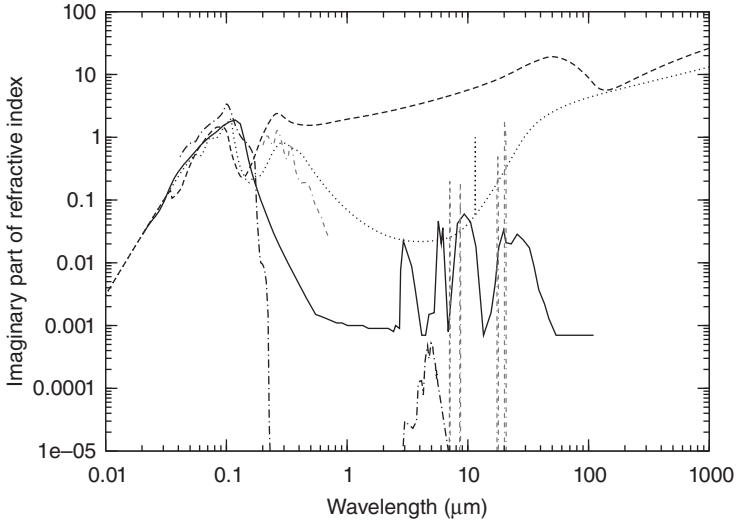

Figure 6.36 Imaginary part of the refractive index for small graphite particles at 20 K [1] (dashed and dotted curves for parallel and perpendicular polarization, respectively, see text), nitrogen-free bulk diamond [207] (dash-dotted), fullerite C_{60} [208] (grey double-dash-dotted), and meteoritic nanodiamonds [209] (solid line).

much weaker than for the parallel polarization in the whole range of π-electron transitions. Note that we define here the direction of polarization with respect to the graphene plane and not to the crystallographic *c*-axis. Optical measurements for perpendicular polarization (i.e., parallel to the *c*-axis) are nontrivial, because the preparation of high-quality polished samples cut perpendicular to the graphene layers is difficult. Data at higher energies are therefore partly based on electron spectroscopy. Draine and Lee [1] (see also Refs. [210, 211]) and Borghesi and Guizetti [212] have compiled the available data into, so far, the most complete tables of optical constants and discussed their limitations. For the optical to IR ranges, we are not aware of any new or more accurate measurements. Note that Borghesi and Guizetti [212] do not consider the free-electron absorption in the data for the perpendicular polarization. Draine and Lee [1] have also taken the influence of temperature and particle size on the charge-carrier densities and their scattering rates into account and have correspondingly modified the optical constants for the case of low temperature and small particle sizes. Note that, therefore, these optical data deviate from the bulk values at long wavelengths in the parallel polarization (perpendicular to the *c*-axis).

The optical properties of diamond have been investigated in great detail. Because the diamond structure is based on four tetrahedrally arranged bonds of sp^3-hybridized carbon atoms, there are no π electrons. Optical absorption occurs only in the ultraviolet wavelength range because of the interband transitions of the σ electrons and, with a relatively small absorption coefficient, at wavelengths between 2 and 7 μm (Figure 6.36). These IR absorption bands are overtones of

the fundamental lattice vibrations. The latter cannot be excited directly because of the lack of an associated dipole moment. The optical properties of diamond are often complicated by the presence of nitrogen or boron impurities, which produce, on one hand, visible absorption, that is, coloring of the diamonds and, on the other, IR absorption due to additional vibrational bands. Boron impurities also create charge carriers, which give rise to a continuous absorption increasing toward longer wavelengths.

An interesting question is whether diamonds may be identifiable in cosmic environments by these IR bands. The overtone (multiphonon) bands seem to be too weak for this, and it was also argued that they might be suppressed in very small particles [213]. The strongest nitrogen bands at 7.8, 8.6, and 8.8 μm are actually close to the bands of polyaromatic molecules, which are observed in many cosmic environments. So far, it has not been possible to separate the diamond bands from the latter, even in the environments where diamonds are evidently present. Braatz *et al.* [214] searched for these bands in laboratory spectra of meteoritic nanodiamonds, but could not definitely detect them, although the abundance of nitrogen could be estimated to be 1–10 atoms per nanodiamond of 2 nm size [213]. Hill *et al.* [215] found that nitrogen-rich diamonds produce an absorption band around 21 μm, which can be created by neutron irradiation of N-free diamonds as well. A strong band at this position is known from carbon-rich protoplanetary nebulae, but this identification is contradicted by the fact that the band is not detected in the two young stars in which diamonds have been definitely identified.

This actual spectroscopic identification of diamond is based on the IR bands of hydrogen atoms bound to diamond surfaces. If the diamond particles are large enough to possess well-ordered crystal surfaces, C–H stretching vibrations of surface hydrogen produce a well-recognizable pattern of bands with main peaks at 3.43 and 3.53 μm, which has been observed in the emission spectra of the inner disk regions of the mentioned young objects and in the emission of a carbon-rich post-AGB (Asymptotic Giant Branch) star [202]. Jones *et al.* [216] have experimentally investigated the dependence of these bands on the particle size by cleaning and re-hydrogenating the surfaces of diamonds with different sizes, among them synthetic diamond powder and nanodiamonds extracted from the Orgueil meteorite. The results confirm earlier findings that the astronomically detected diamonds are likely larger than about 50 nm and not in the size range of the meteoritic nanodiamonds, which would produce broader bands at somewhat shifted positions. Very interesting in this respect are also spectroscopic studies of diamondoid molecules (e.g., Ref. [217]), which support the assignment of the broad dense-cloud 3.47 μm absorption band to very small diamond-like structures [218].

In the case that nanodiamond surfaces in space would not be passivated by full hydrogenation and would instead undergo a restructuring of their surfaces, these could contain a large number of aromatic and olefinic bonds and could be considered to be similar to amorphous carbon structures [219, 220], such as discussed in the next subsection. Most of the nanodiamond samples extracted from meteorites by the standard techniques are likely to have such surfaces. Because of the quite big volume that can be assigned to surface atoms, this can not only

be proven by the presence of typical IR bands (e.g., Ref. [214]) but also by the spectroscopic properties in the range of electronic transitions. Bernatowicz and Gibbons [220] have demonstrated the presence of π-electron states in a nanodiamond sample extracted from the Murray carbonaceous chondrite by electron energy loss spectroscopy (EELS). Furthermore, they could reproduce the plasmon excitation spectrum by a mixture of diamond and amorphous carbon spectra.

EELS is a spectroscopic technique using electrons that are inelastically scattered while traversing through a very thin sample, for example, in a transmission electron microscope (TEM). Since this inelastic scattering excites electronic and vibrational transitions in the sample, the energy loss of the electrons is a measure of the resonance energies, and the energy-dependent so-called loss function (the number of scattered electrons vs the energy loss) is a measure of the probability of the transitions. It turns out that the loss function is proportional to the imaginary part of the negative inverse of the dielectric function. Thus, optical constants can be derived from such measurements, especially in the interband transition region (1–50 eV, "plasmon loss region"), where optical measurements are difficult to conduct. However, to warrant compatibility with an optical experiment, one has to ensure that the momentum transfer in the EELS experiment is comparably small, as for the absorption of photons, that is, electrons scattered into very small angles have to be selected by a proper aperture [221].

Mutschke *et al.* [209] have converted a plasmon loss spectrum measured for a nanodiamond sample from the Allende meteorite into a dielectric function valid for optical excitation. We used a Kramers–Kronig technique to derive both the real and imaginary parts of the optical constants from the loss function. Also, a normalization factor is generally necessary for the loss function, which was provided by the refractive index value of the nanodiamonds previously estimated by other authors [222]. By using an integrating-sphere detector,[15] we also succeeded in measuring the optical absorption of nanodiamond films deposited on a CaF_2 substrate and nanodiamond dispersed in a KBr pellet in the wavelength range 0.12–2 μm.

Combining the EELS, optical, and IR results allowed calculation of the optical constants of such a nanoparticle material over a wavelength range useful for radiative transfer modeling. The imaginary part of the refractive index is displayed in Figure 6.36, together with that of terrestrial diamond. Interestingly, these optical constants were applied in the modeling of dust extinction in active galactic nuclei [223].

Finally, we would like to discuss briefly another solid modification of pure carbon, the so-called fullerite. This material was introduced into the literature by Krätschmer *et al.* [208], who were the first to synthesize and isolate large amounts of fullerenes, that is, the ball-like carbon molecules C_{60} and its relatives.

15) An integrating-sphere detector is a diffusely reflecting sphere surrounding the sample, in which the level of scattered radiation is measured with respect to the incident radiation. Closing the ports for the transmitted and reflected beams also allows one to measure the total radiation coming from the sample, i.e., without that part which is absorbed. Both this "absorption mode" and the "scattering mode" (with open ports) are required for determining the absorption coefficient [209].

Krätschmer *et al.* showed that the C_{60} molecules condense into an at least partly crystalline structure of hexagonal symmetry. The spectroscopic properties of these solids are, of course, mainly determined by those of the fullerenes and can be easily measured by standard techniques. The optical properties in the UV and visible wavelength range are again determined by the transitions of π electrons, where, however, the hybridization state of the carbon atoms must be considered to be a mixed one (between sp^2 and sp^3) and the band structure is, therefore, different from that of graphite. The UV spectrum reveals three typical broad peaks at 216, 264, and 339 nm, plus weaker structures in the visible range (Figure 6.36). The range of absorption does not extend into the IR. The color of fullerite in transmitted light has been reported as being reddish, which is consistent with an optical gap energy of about 1.8 eV, as determined from EELS spectra [224].

In the IR, the absorption spectrum of C_{60} is characterized by another distinct pattern of only four bands at 7.0, 8.45, 17.3, and 18.9 μm wavelength [208]. These bands have been recently discovered in astronomical spectra of reflection nebulae and planetary nebulae, as already mentioned. Their positions are in between those of the gas-phase fullerene molecules and those of the solid fullerite. Cami *et al.* [52] derive from the excitation temperature that the emitters may be C_{60} molecules attached to larger carbon or silicate grains. Such attached C_{60} molecules have also been found in high-temperature soots (Section 7.4), so fullerenes may be generally present in interstellar carbonaceous dust. However, it is also proposed that they are produced in photodecomposition processes from HAC particles when they become exposed to intense UV radiation fields [225].

6.6.2
Hydrogenated Amorphous Carbon

Most of the carbonaceous dust in space is thought to be in the form of hydrogenated amorphous carbon (HAC) particles. The formation and the structural properties of HAC are reviewed in Chapter 7. Here, we will just discuss the optical constants derived for HAC particles, comparing them with those of the crystalline carbon modifications. These optical constants are important for the absorption and emission properties of carbonaceous dust and, therefore, for dust temperatures and opacities, of course, also in cases when complex dust aggregates contain a carbon component. We exclude details of the IR bands from this consideration (again, see Chapter 7), but will briefly discuss optical constants in the ultraviolet that could possibly reproduce the 217.5 nm band in the interstellar extinction (Section 6.1.1, Figure 6.2).

HAC can have a wide range of optical and mechanical properties, from soft hydrogen-rich material to one with a graphite-like or diamond-like habit. A derivation of appropriate optical constants of HAC is difficult, mainly because analog materials are often in the form of small-grained powders. This means that optical constants have to be deduced from absorption (or diffuse reflection) spectra, implying the necessity of modeling their morphology accurately. An alternative is HAC films such as the "quenched carbonaceous composite" [226], which, however, allow measurements only in spectral ranges of strong absorption.

There is little data that has been derived from bulk analog materials which allowed reflection measurements. Such a material is, for instance, glassy carbon, a hard material produced by the pyrolysis of organic polymers at high temperature and consisting of sp^2 carbon, but with a disordered structure. Optical constants of this material have been derived by Arakawa *et al.* [227] and by Edoh [228]. Another example achieved by a similar approach is the optical constants of pyrolyzed cellulose measured by Jäger *et al.* [229], which have been derived for different (lower) pyrolysis temperatures. If pyrolyzed at only 400 and 600°C, the material still behaves like an insulator or semiconductor, showing a low IR reflectivity. In contrast, if pyrolyzed at 800 and 1000°C, it becomes strongly reflecting in the IR, indicating electrical conductivity similar to that of graphite and glassy carbon.

Although these optical constants have the advantage of a straightforward and exact derivation and may serve as a rough model of HAC optical constants, it is, of course, desirable to obtain optical constants based on more realistic materials. Spectroscopic extinction data in a wide wavelength range of analog materials condensed from the gas phase have been available at least since 1987, when Bussoletti and coworkers [230] published "Tabulated extinction efficiencies for various types of submicron amorphous carbon grains in the wavelength range 1000 Å to 300 μm." The materials were produced from an arc discharge between graphite electrodes in argon (AC, later ACAR) and by burning hydrocarbons such as benzene (BE) in air. Similar data had already been published by Koike *et al.* [231] in graphical form.

Rouleau and Martin (1991) [232] constructed sets of optical constants from these extinction data by modeling the grain morphology by different approaches, such as the "continuous distribution of ellipsoids (CDE) model" and by effective-medium models simulating fractal cluster and homogeneous porous aggregate morphologies. They noted that, especially for the stronger IR-absorbing "BE" carbon, the morphological model is essential for obtaining physically reasonable and self-consistent optical constants. This analysis was later refined by Zubko *et al.* [233] based on new extinction data [234] and modified CDE models, which had become necessary because Rouleau and Martin's morphological models were no longer consistent with the newer data now available for a wider wavelength range. The new data also comprised a sample that had been produced by condensation in a hydrogen atmosphere (ACH2), which promised to be the method most similar to the condensation processes in space.

Several of the resulting data are shown in Figure 6.37. It can be seen that, apart from the weakly pyrolyzed cellulose, the data fall roughly in between the two graphite spectra taken perpendicular and parallel to the graphite planes. All these spectra rise toward the far-infrared (FIR), which indicates that the materials are at least semiconducting. The electronic gap energy, which for these amorphous semiconductors has to be taken as a statistical "optical gap" which can, for instance, be described by the "Tauc model" [235], is a major parameter that determines the absorption in the visible and IR ranges. Since the optical gap is determined by the π-electron states, it is mainly dependent on aromatic bonding in the amorphous carbon network. Since the pioneering work of Robertson [236], it is known that the aromatic bonding occurs in "basic structural units," the size of

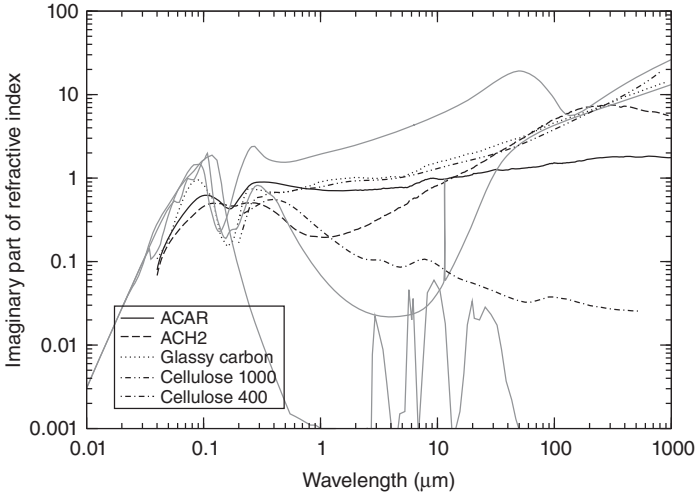

Figure 6.37 Imaginary part of the refractive index for different amorphous carbon materials. (Data for ACAR and ACH2 are from Zubko *et al.* [233], glassy carbon from Edoh [228], and cellulose from Jäger *et al.* [229].) Data of graphite and meteoritic nanodiamonds (from Figure 6.36) are shown as grey lines for comparison.

which is related to the gap energy. This has been verified by several experimental studies, which will not be discussed in detail here. For ACH2 soot, for example, the gap energy has been determined to be about 1.34 eV [237]. For glassy carbon, ACAR soot, and the cellulose pyrolyzed at 1000 °C, the gap is much smaller, resulting in an almost "graphitic" optical behavior, but not reaching the same high values of the optical constants as graphite.

Recently, an adaptable model for the optical constants of HAC has been developed by Jones [238], which provides synthetic optical constants for HAC with gap energies from −0.1 to 2.7 eV. The synthesis is based on simple log-normal absorption profiles for the interband transitions and on a power-law extrapolation in the visible and IR. The synthetic curves have been adapted to the Tauc/Urbach models for different gap energies, which originate from experimental data. Underlying structural models of HAC [239] allow relating in turn the gap energies to the hydrogen content – thus also permitting the addition of modeled IR bands – and the inclusion of restrictions imposed by small particle sizes [240]. This model is certainly a very promising step to overcome the lack of comprehensive sets of optical constants for various HAC structures, at least as long as more precise physical models of cosmic HACs cannot be derived with certainty.

An interesting question is whether the optical constants of HAC could produce a UV extinction feature similar to the 217.5 nm bump of the interstellar extinction curve (Section 6.1.1, Figure 6.2). The optical constants of graphite have been intensively discussed in this respect and various difficulties have been noted, such as the strong dependence of the band profile on particle size and shape, as well as the unknown mechanism of formation of graphite crystals. If HAC particles could

reproduce the UV bump, these problems would be largely solved and they could simultaneously contribute to carbon-related IR features, which would mitigate the problems of reproducing all features under the constraint of the quite tight cosmic carbon budget. Mennella *et al.* [241, 242] and recently Gadallah *et al.* [243] have demonstrated a way to produce suitable HACs by UV irradiation. Unfortunately, the structure of the irradiation products could not yet be clarified, but it seems that they still show aliphatic C–H bands at 3.4 μm [243].

It is obvious that such a HAC material needs to be dominated by aromatic structural units in order to produce a strong π–π^* feature, but for many sp^2-rich HACs, for instance, those processed by thermal annealing, the feature will appear at too long wavelengths. Schnaiter *et al.* [244] and Steglich *et al.* [11] measured the UV spectra of soots being rich in polycyclic aromatic hydrocarbon molecules and showed that these can cause a strong absorption band at about the right wavelength. A perfect spectroscopic match with the interstellar band was not achieved with these soots, possibly because of the still too small size of these polyaromatic molecules [11]. However, if correct, this proposal would open a link to the aromatic IR bands observed in emission in interstellar sources.

The size and the clustering of particles, of course, plays an important role in their UV properties. This has been investigated both theoretically [245] and experimentally (i) by the matrix-isolation technique (to avoid the clustering [10]) and (ii) by measurements of the scattering component of the extinction by means of an integrating-sphere detector (for particles of about $\geq$20 nm size [246]). When clustering could not be avoided, the previously mentioned CDE model allowed a rough account of these effects. By applying this model, Mennella *et al.* [242] derived a dielectric function for their UV-irradiated HAC. This dielectric function reproduced the interstellar UV bump if spherical particles were assumed for the interstellar case. The band strength resulting from this dielectric function ($C_{ext}/V \sim 1.8 \times 10^6$ cm^{-1} at the peak) is comparable to that of graphite particles.

The optical constants derived by Schnaiter *et al.* [10] for matrix-isolated HAC particles give a somewhat weaker feature (peak value $C_{\mathrm{ext}}/V \sim 6 \times 10^5$ cm^{-1}). Their approach relied on a spherical particle model because the clustering was negligible and also the particles appeared to be round-shaped in the TEM analysis. The UV band was indeed positioned at the right wavelength already in the measured spectra if the hydrogen content in the Ar/H_2 quenching gas during the condensation experiment was properly chosen ("H50"). The internal structure of such an HAC was later found to be dominated by bent structural subunits and a relatively low hydrogen content [247]. The band strength found by these authors is at the limit of explaining the interstellar feature with the available carbon abundance. It had been noted by Rouleau *et al.* [245] that negative values of the real part of the dielectric constant are required to produce a sufficiently strong resonance, which is also the reason for the importance of size and shape effects. The optical constants derived by Zubko *et al.* [233] and Jäger *et al.* [229], as well as the model optical constants given by Jones [238] in his Figure 7, do not fulfill this condition. A comparison of these different sets of optical constants can be found, for instance, in Schnaiter *et al.* [10] and in Quinten *et al.* [248]. Some

theoretical investigations on how a dielectric function fitting the interstellar band could be constructed from mixtures of graphitic and amorphous subunits in various arrangements have been published by Michel *et al.* [249].

6.6.3 Silicon Carbide and Other Carbides

Carbide dust was quite early predicted to be a major condensate in the outflows from carbon stars [250–253]. This is not only because of the elemental abundance of carbon but also because of the outstanding thermal (and mechanical) stability of carbide compounds, which makes them also very interesting materials for technical applications. Later, more detailed thermodynamic modeling of condensation sequences confirmed that silicon carbide as well as carbides of Zr, Ti, and other metals are indeed expected to condense in such carbon-rich outflows [254, 255]. First direct observational evidence for the presence of circumstellar carbide dust came in the 1970s from IR spectroscopy performed by Hackwell [256] and Treffers and Cohen [257], who observed a relatively broad emission feature at about 11.3 μm and interpreted it as being caused by the thermal emission of silicon carbide grains.

Using the IR satellites Infrared Astronomical Satellite (IRAS), Infrared Space Observatory (ISO), and Spitzer, but also ground-based telescopes, the spectra of a large number of carbon stars have been analyzed since then (e.g., Refs. [258–261]). These studies have revealed substantial variability in the profile and peak position of this band, which triggered spectroscopic laboratory studies with the purpose of understanding this variability [42, 44, 111, 262]. SiC forms a large number of cubic, hexagonal, or rhombohedral crystalline modifications (i.e., polytypes, see e.g., Ref. [42]) and determination of the polytype would enable conclusions about the thermal history of the grains. The cubic polytype is often referred to as β-*SiC*, whereas the other modifications are collectively referred to as α-*SiC*. However, it has turned out from laboratory studies that the observed band profile depends not only on the SiC polytype but also on grain shape, grain size, possible grain mantles, the temperature, and other factors, turning the determination of grain properties from the band profile into a complicated task (see below, compare also Section 6.5.2 for similar problems with oxides).

A direct proof for "stardust" with carbide composition came from the isotopic analysis of SiC grains in primitive meteorites [263–265]. These grains, which are found in a variety of meteorite classes with abundances of several parts per million, are isotopically anomalous, similar to the "presolar" oxide grains mentioned in Section 6.5. Since some of these grains have a size in the 10 μm range, they can be individually analyzed by mass spectrometric techniques (see, e.g., Refs. [166, 266, 267] for reviews). The $^{12}C/^{13}C$ ratios of most of the analyzed individual "presolar" SiC grains differ greatly from the solar values and are similar to that predicted for carbon stars [266]. The s-process isotopic signatures in the heavy elements identified in the majority of the SiC grains (so-called "mainstream" SiC grains) can be produced in the atmospheres of thermally pulsing low-mass AGB stars [268].

No spectroscopic evidence has been found for SiC grains in the diffuse interstellar medium. Their abundance must be smaller than 5% compared to silicates, based on the lack of a significant 11.3 μm band [269]. This is consistent with the low abundance in meteorites and implies a high rate of destruction for SiC grains in the interstellar medium.

Some of the presolar SiC (and especially graphite) grains have been found to carry small inclusions of metal carbides (Ti, Mo, and Zr carbides) that were identified by TEM [270, 271]. These crystals are between 5 and 200 nm in size and may have served as nuclei for subsequent carbon or SiC condensation. This result points to a radial condensation sequence in the stellar envelopes, which starts with metal carbides, proceeds with carbon, and finally with SiC. Thermodynamic condensation calculations for carbon-rich envelopes (elemental C/O ratio larger than 1) indeed suggest that ZrC and TiC always condense prior to carbon and SiC at any reasonable pressure and C/O ratio [255]. SiC formation would precede graphite formation only at high total pressures, which would imply a location too close to the star for any condensation to occur.

The detection of the metal carbides in presolar grains originating from carbon stars could be related to the presence of another spectroscopic feature at about 20.1 μm, observed in the spectra of carbon-rich post-AGB stars [48, 49, 272]. Based on laboratory data obtained with laser-induced thermal ionization spectroscopy, von Helden *et al.* [273] proposed titanium carbide clusters or nanocrystals as a very good candidate to carry this feature. Such small clusters of transition-metal carbides have attained strong interest in the physical literature, because they show formation of very stable cage-like structures, the prototype being Ti_8C_{12} [274]. Larger clusters, for example, $Ti_{14}C_{13}$, have been proposed to be cubic nanocrystals [275]. The presence of such stable cluster species could be an important aspect for the condensation of transition-metal carbides in carbon-rich stellar atmospheres [276], considering that titanium is not a very abundant element.[16] Although the spectroscopic match of the band profile presented by von Helden *et al.* is excellent, the low abundance of TiC makes it difficult to explain the strength of the 20.1 μm emission band. Thus, also other dust species are being discussed in this respect [189].

For the 11.3 μm band, there is general agreement that SiC grains are the carrier. As already mentioned, there have been attempts to derive the SiC polytype from the band profile. The Si–C lattice vibration frequencies depend slightly on the crystal symmetry and, for the noncubic polytypes, on the orientation of the crystal. These variations can be measured with Raman spectroscopy or in reflection spectra of large surfaces but are, unfortunately, hard to observe with the IR band observable for ensembles of small particles. Besides the dependence on the grain shape, which has been frequently discussed throughout this chapter, it has also been found that impurities such as nitrogen may influence the band profile strongly [42].

16) Even larger particles should show metallic properties. Lattice vibrations with resonance frequencies in the IR would then be screened by the free metal electrons and should, therefore, be difficult to observe [277].

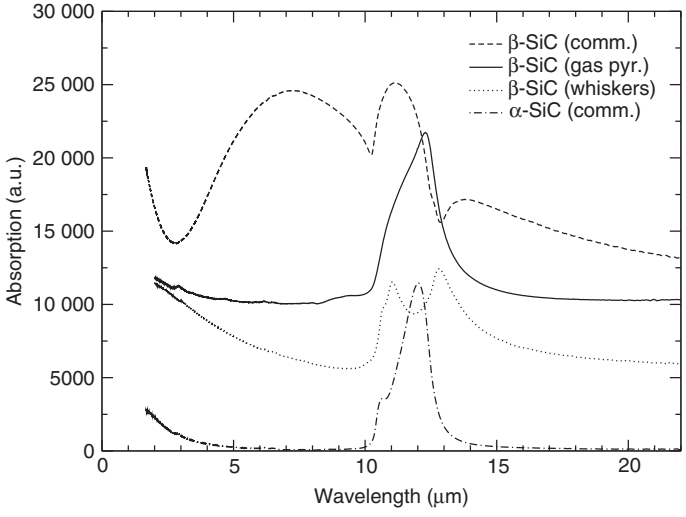

Figure 6.38 IR absorption spectra of different SiC particulates embedded in KBr: β-SiC from gas pyrolysis (solid line), commercial β-SiC (Alpha Johnson) (dashed line), β-SiC whiskers (dotted line), and commercial α-SiC (dash-dotted line). For clarity, the curves have been shifted vertically. (Reproduced from [277], copyright 2001 © permission from Elsevier.)

Figure 6.38 shows the IR absorption spectra of four SiC powders, three of them belonging to the β polytype. The completely different phonon band profiles produced by these are in one case due to the particle morphology (one powder consisting of needle-like "grains" producing a double-feature). The topmost spectrum with the peak at about 11 μm is produced by a material containing free charge carriers, probably introduced by nitrogen impurities. These free charge carriers enable the excitation of a surface plasmon (the broad absorption at shorter wavelengths) which interacts with the phonon and thereby shifts the maximum of the phonon band toward shorter wavelengths.

For the two other spectra, of which one is an α- and the other a β-SiC spectrum, the peak is longward of 12 μm. This would change for aerosol spectra (non-embedded particles, Section 6.2.2), where the peak shifts to shorter wavelengths (cf. Figure 6.10) producing a better match with the observed profiles. Clément *et al.* [105] had shown the same for β-SiC nanoparticles produced by CO_2-laser pyrolysis of SiH_4/C_2H_2 gas mixtures (see Ref. [278] and references therein), which they embedded into Ar ice matrixes instead of a KBr pellet. Using this matrix-isolation technique (see again Section 6.2.2), a similarly good match with carbon star spectra had been found.

The question for the polytype of SiC "stardust" could finally be settled by TEM of presolar grains from meteorites. Both β- and α-SiC grains, the latter of polytype 2H, were found, but no higher order polytypes [279]. This was interpreted as a condensation sequence, the cubic grains forming closer to the star. At first glance, this is in disagreement with the statement by Mutschke *et al.* [42] that β-SiC is the

typical structure for lower temperature condensates in technical processes. So the relative behavior of the SiC polytypes in condensation must still be clarified.

6.7
Photoluminescence Studies of Silicon-Based Nanoparticles

Friedrich Huisken, Olivier Guillois, Olivier Debieu, Karsten Potrick, and Torsten Schmidt

6.7.1
Effects of Nanoscale Particle Size

As already discussed in this chapter, evidence for silicon-based grains in various astronomical objects is provided by infrared (IR) absorption and emission spectra and by the analysis of interstellar grains and meteorites in the laboratory. While most of the silicon-based grains are made from amorphous or crystalline silicates, evidence for the existence of silicon dioxide (SiO_2) or silica grains [70, 73] has also been found. Another simpler oxide, SiO, has also been discussed as a component of stardust. If SiO grains are present, it is also conceivable that Si nanocrystals (Si NCs) surrounded by a layer of SiO_2, produced by phase separation in SiO grains at elevated temperature, could be present.

Since a substantial portion of interstellar dust particles were found to have diameters below 10 nm [4, 280], we can assume that silicon-based nanoparticles (NPs) of this size may play a major role in astrophysics. Aside from their IR absorption and emission characteristics already discussed in this chapter, Si-based grains may have the attractive property of showing rather strong photoluminescence (PL) in the visible to near-IR spectral range. The PL mechanism includes the absorption of a UV photon by the NP, the creation of an electronically excited state, and the relaxation of this excited state by the emission of a visible or IR photon. If such a process occurs in astrophysical environments, it should be possible to observe the PL arising from the NPs and to identify them by their characteristic emission. Of course, the identification is possible only if the PL properties of the respective NPs had been investigated before, in the laboratory.

Almost all calculations of the optical properties of interstellar grains rely on optical constants derived from bulk materials. This approximation, however, is not valid anymore if the diameter of the grains becomes smaller than ~10 nm. As a result of the reduced size, the electronic wave function becomes strongly localized and the optical properties will be governed by quantum effects, which are not considered in a classical treatment. For semiconductor nanocrystals (NCs), which are also called *quantum dots* (QDs), the effect of quantum confinement is rather spectacular as it may increase their absorption energy by more than 50%, when going from a diameter of 10 to 3 nm (for the case of Si NCs). Even more dramatic is the effect of quantum confinement on the ability to emit light, at least if we consider silicon, which is an indirect-bandgap semiconductor. While bulk Si has a PL quantum efficiency on the order of 10^{-6}, Si NCs with diameters between 3 and 4 nm achieve quantum efficiencies of 0.65 and more [281], resulting in a huge enhancement factor of 6.5×10^5.

Another effect associated with nanometer-sized grains is the increased importance of the surface compared to the volume. This becomes evident if one considers that, for example, for an NP with 3 nm diameter, about 45% of all atoms constituting the NP are on its surface. For a bulk body, the surface atoms can be neglected, but for a NP they may seriously affect its optical properties. Owing to their nonsaturated dangling bonds, surface atoms may be very reactive, so that the surface can be easily contaminated, thus altering its optical properties. Even more crucial is the role of dangling bonds as nonradiative defect centers quenching the PL, in particular, of long-lived excited states, as encountered in Si NCs. Finally, surfaces offer new possibilities for the creation of luminescent defect centers, thus yielding enhanced PL capabilities compared to the bulk material.

Silicon nanocrystals surrounded by a thin layer of SiO_2 have been discussed as carriers of the extended red emission (ERE), an astrophysical phenomenon observed in many stellar objects and clouds, and even in the interstellar medium [282, 283]. Our laboratory studies on oxygen-passivated Si NCs have shown that all ERE spectra known so far can be perfectly matched by laboratory spectra, suggesting that Si NCs could indeed be responsible for this PL phenomenon [284]. However, more recent classical model calculations revealed that free-flying oxygen-passivated Si NCs should give rise to an emission feature around 20 μm, which in fact is not observed in ERE regions [285]. A possibility to satisfy this constraint is to assume that the Si NCs are not individual free-flying NPs, but instead agglomerated to larger units or embedded in larger grains of some other material such as silica or silicate.

In the following, we summarize the results that we obtained when we studied the PL properties of size-selected Si NCs produced by gas-phase condensation of Si vapor via laser pyrolysis of SiH_4. The NCs were size-selected and deposited on a quartz window. When the samples are taken out of the vacuum apparatus, the Si NCs are subjected to a gentle natural oxidation. As a result, they are covered by a thin layer of SiO_2 but can be considered as an ensemble of *free* noninteracting NPs. To model the situation of Si NCs embedded in silica or silicate grains, we have also synthesized them in SiO_2 windows, using ion implantation into quartz and subsequent annealing. Finally, we have investigated how a complete oxidation of Si NCs to SiO_2 NPs affects the PL properties. It turns out that, depending on the local oxygen concentration, the PL band splits into two components, one in the blue and the other in the red, close to the PL band of the Si NCs from which the silica nanopowder was prepared.

6.7.2 PL Spectra of Free Si NCs

High-quality silicon nanocrystals (Si NCs) are synthesized via laser-induced pyrolysis using silane (SiH_4) as gaseous precursor [286, 287]. The dissociation of SiH_4 takes place in a gas flow reactor and is accomplished by the IR radiation of a pulsed CO_2 laser, which provides a steep temperature gradient ensuring that the reactions take place in a wall-less environment. The molecular flow emanating

from the gas inlet is crossed perpendicularly by the focused laser radiation, inducing the decomposition of the SiH_4 molecules. The high concentration of Si atoms thus generated results in a supersaturation, giving rise to nucleation and subsequent growth of the nuclei to clusters and NPs. The originally liquid species are cooled by collisions with the helium buffer gas, and free-flying crystalline silicon QDs are formed.

The flow reactor for gas-phase condensation is mounted into the source chamber of a cluster beam apparatus [286, 287]. A conical nozzle with a tiny aperture extracts the as-synthesized Si NCs from the reaction zone and supersonically expands them with helium as carrier gas into the evacuated source chamber. Employing a skimmer and differential pumping, a "molecular beam" of freely propagating Si NCs is formed. The mass and size of the NCs can be determined *in situ* by time-of-flight mass spectrometry. It is found that the size of the Si NCs correlates with their velocity in the cluster beam in such a way that the smallest NCs are faster by 20% than their heavier counterparts. As the laser is pulsed with a repetition rate of 20 Hz, we can take advantage of the correlation between size and velocity using a fast-spinning chopper wheel with two slits. The synchronization between the chopper and the CO_2 laser can be adjusted such that Si NCs with different sizes are transmitted by the chopper at different times, so that they are deposited at different positions on the quartz substrate, thus producing a sample with size-dispersed coverage. The typical size variation is from 2.5 to 7.5 nm (diameter).

After waiting for a few days to allow proper surface passivation via oxidation, we analyzed the samples. Electron microscopy analysis shows that our Si NCs consist of a perfectly crystalline core surrounded by a 1–2 nm thick shell of SiO_2. As a result of oxidation, the dangling bonds of the Si atoms residing at the surface of the crystalline core are passivated. It should be stressed that, without proper passivation, photoluminescence from recombining excitons, which are produced by the absorption of UV photons, cannot be observed.

It has been mentioned that the PL of Si NCs in the size regime below 10 nm in diameter is subjected to quantum confinement. As a result, the bandgap of Si NCs increases as $\sim d^{-1.39}$ if the diameter d is reduced [288]. Along with the bandgap, the PL energy increases (or the PL wavelength decreases) as the Si NC size is reduced. The quantum effect nicely manifests itself in the results shown in Figure 6.39. The upper panel shows a photo of the size-dispersed sample taken during UV illumination ($\lambda = 254$ nm). The millimeter scale gives an idea of the actual size. The diameter d of the Si NCs increases from left to right, giving rise to a change in color from yellow/orange through red to IR (brighter to darker in the greyscale image). The 27 crosses between 4 and 9 mm mark the positions where PL spectra were measured, using a proper spectrometer and 266 nm laser excitation from a quadrupled Nd:YAG laser. The normalized spectra are plotted in the main frame of the bottom panel. It is seen that the peak position varies from 650 nm (corresponding to the position of the left cross) to just below 900 nm (right cross). Altogether, luminescence is observed from 550 to 1000 nm. The inset shows the same set of PL spectra with intensities as measured (not normalized). Summing

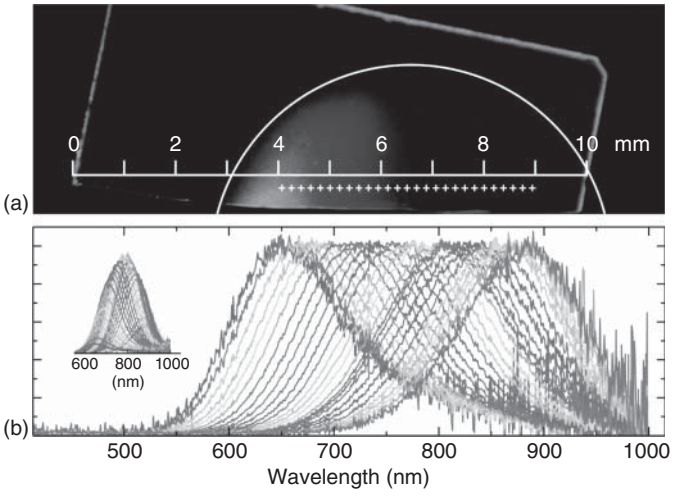

Figure 6.39 See the electronic version for a color image. (a) Sample of size-dispersed Si NCs deposited on a quartz window as seen under UV illumination. The crosses mark the positions where PL spectra were recorded. (b) PL spectra as measured (in the inset) and normalized to equal height (main frame). Going on the sample from left to right, the spectra continually shift to larger wavelengths.

up all PL spectra, we obtain a PL curve, which is very similar to the envelope of the entire dataset. Such a PL response would have been measured if the size selection technique were not applied.

The diameter of the Si NCs at the positions of the crosses varies from 2.74 nm (left) to 6.77 nm (right). Plotting the PL peak position (in energy) as a function of size, we obtain very good agreement with the theoretically predicted dependence, $E = E_0 + 3.73\, d^{-1.39}$ (E_0 = 1.12 eV = bandgap of bulk Si at 300 K; d, diameter in nanometers) [288]. This finding can be taken as a proof that the observed PL results from the radiative recombination of electron–hole pairs (excitons) in the quantum-confined system represented by the Si QD. Other mechanisms, such as defect PL, would not comply with the size dependence observed.

The extended red emission (ERE) observed in various astrophysical objects such as reflection nebulae, planetary nebulae, HII regions, halos of galaxies, and even in the interstellar medium (ISM) is characterized by broad PL bands peaking in the range between 600 and 850 nm [283], that is, just in the same range that is covered by the PL bands of Si NCs. To compare other parameters such as the overall shape and width, we have presented in Figure 6.40 a few representative astronomical observations with experimental PL spectra of Si NCs measured in our laboratory. Note that, from (a) to (d), the spectra are selected in the order of increasing peak wavelength. The truncation in some of the spectra is due to the limited observation range of the respective detector. It is seen that the agreement is rather good, indicating that Si NCs could be an attractive carrier candidate for the ERE, at least as far as the positions and shapes of the PL bands are concerned. The slightly varying peak positions and widths of the ERE bands can be explained

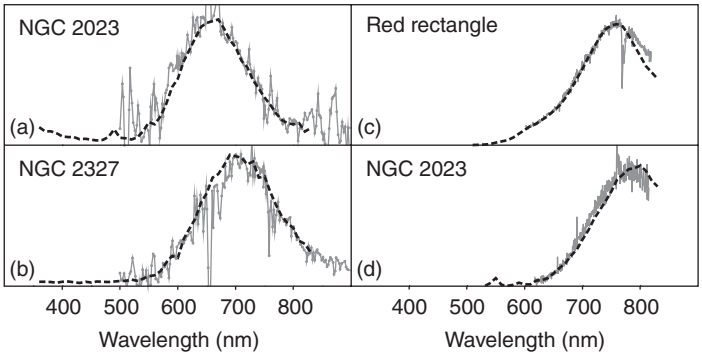

Figure 6.40 Comparison of ERE observations (gray curves) from various objects indicated in the figure with the best fitting laboratory spectra (dashed black curves).

by somewhat different size distributions of the Si NCs responsible for the PL, as is also the case for the laboratory spectra.

The detection of ERE photons generated in the diffuse ISM requires that the PL quantum efficiency, η, of the carrier must be larger than 10% [289]. By determining quantum yields with $\eta \geq 0.3$, we could show that this condition can be easily satisfied by Si NCs [290]. Recent measurements employing more sensitive methods such as laser-induced deflection revealed even higher η values of more than 0.65 at 766 nm [281]. Such high PL efficiencies could not be observed for carbon-based materials.

An attractive feature of Si NCs is the fact that intrinsic properties restrict the positions of the PL bands to a narrow wavelength range, which agrees perfectly with the ERE observations. The maximum PL wavelength ($\lambda = 1060$ nm) is given by the bandgap of silicon (1.17 eV at 0 K); but the PL quantum efficiency is extremely small at these long wavelengths (on the order of 10^{-6}), because of the indirect bandgap of silicon. Only for Si NCs with diameters smaller than 10 nm does the PL yield become large enough to comply with the ERE observations. On the other hand, on the high-energy (low-wavelength) side, the band gap of oxygen-passivated Si NCs cannot further increase because of the appearance of oxygen-related defect states within the bandgap, which restricts the maximum PL energies to values below 2.6 eV (corresponding to 475 nm) [291]. The quantum yield of this defect PL has not yet been measured.

The situation is visualized in Figure 6.41, where we have plotted our earlier measured PL quantum yields [290]. Here we have converted the Si NC diameters to their corresponding peak wavelengths using the formula of Delerue *et al.* [288]. This representation allows us to indicate by the dark-gray areas on either side the wavelength ranges that cannot be accessed. According to what has been said before, oxygen-passivated Si NCs are allowed to emit only in the wavelength range between 475 and 1060 nm; beyond 900 nm, the quantum yield is very small. It is interesting to note that the highest PL efficiency is found in the middle of the light-gray area, which represents the observed variation of ERE peak positions (600–850 nm).

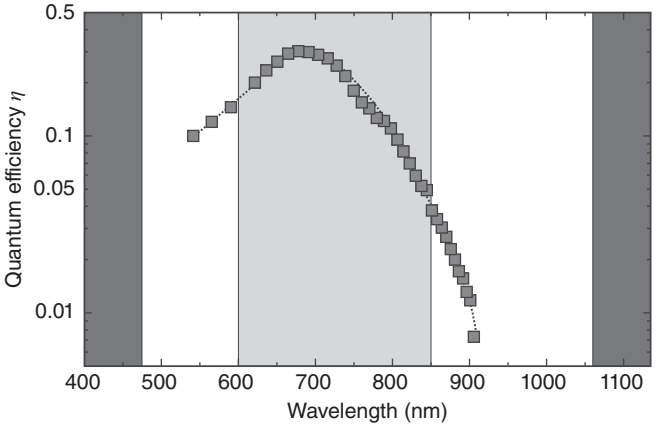

Figure 6.41 Measured quantum efficiency of oxidized Si NCs [290] as a function of the peak wavelength that can be associated with the NC diameter (2.4 nm $\leq d \leq$ 8.2 nm) via the formula of Delerue *et al.* [288].

6.7.3
PL Spectra of Matrix-Embedded Si NCs

Despite the close agreement between the PL properties of free Si NCs and the ERE characteristics, Li and Draine [285] expressed their concern about oxygen-passivated Si NCs, because, as a result of their small dimension, they should be heated to temperatures around 100 K (calculated for a Si NC with a diameter of 6 nm) and thus give rise to an oxide-related emission band at 20 μm, which is not observed. A possible explanation could be that the Si NCs were embedded in larger grains which would not be heated to such "high" temperature.

In order to model the situation of nanocrystalline silicon seeds in silica grains, we synthesized Si NCs embedded in an SiO_2 matrix and studied their optical properties. The samples were prepared by implanting Si ions (Si^+) with an energy of 100 keV into a fused quartz window for different exposure times (fluences). Subsequent annealing for 1 h at a temperature of 1100 °C resulted in the nucleation of the excess Si in the matrix and the formation of Si NCs which were concentrated in a thin layer 150 nm below the surface [292].

Figure 6.42 shows the PL response after excitation with 266 nm photons for four samples prepared with different Si ion fluences. It is observed that the maximum of the PL band shifts to larger wavelengths as the ion fluence is increased. This can be explained within the frame of quantum confinement if it is noted that larger ion fluences result in higher concentrations of excess Si after implantation and in larger NCs after annealing. For high fluences, the red shift associated with a further increase of the irradiation dose becomes less pronounced. This is consistent with the asymptotic Ostwald ripening growth model for Si NCs [293], where, for one annealing condition (duration and temperature), the size of the Si NCs does increase with an excess of Si but to a lesser extent.

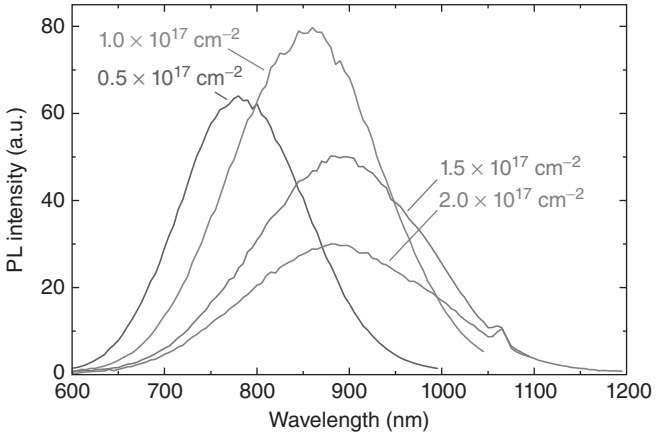

Figure 6.42 PL spectra of Si NCs embedded in a fused quartz window. The NCs were produced by ion implantation using the fluences given in the figure followed by an annealing at 1100 °C in N_2. The PL spectra can be nicely fitted by log-normal distributions [292].

At first glance, the results on the PL of Si NCs embedded in SiO_2 seem to agree with those obtained for free oxygen-passivated Si NCs. However, when we were able to determine the size distribution of the Si NCs in the quartz window by cross-sectional transmission electron microscopy (TEM), we found that the embedded Si NCs showing similar PL characteristics as their free counterparts were somewhat smaller. The situation is depicted in Figure 6.43, where we have plotted the energy of the PL peak as a function of the diameter of the nanocrystalline Si seeds.

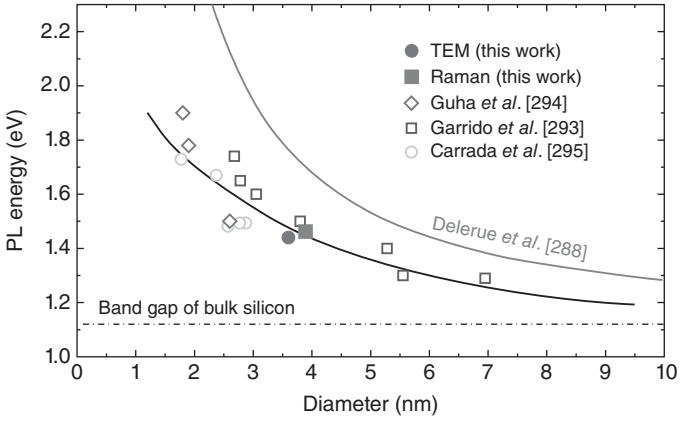

Figure 6.43 PL peak positions of Si NCs embedded in SiO_2 as a function of Si NC size. The filled symbols represent our results, while the open symbols are obtained by other authors [293–295] also employing ion implantation. The black curve through the data points is drawn to guide the eyes.

The filled symbols represent two samples of our laboratory where the size of the Si NCs could be determined by either Raman spectroscopy or TEM [292]. Results obtained by other authors also employing ion implantation are plotted as open symbols. It is seen that the data points follow the black curve, which has been drawn to guide the eyes. The curve designated "Delerue *et al.* [288]" is the result of a theoretical calculation describing very well the size dependence of *free* Si NCs discussed earlier. From this figure, it becomes evident that, for a given diameter, the Si NCs embedded in the SiO_2 matrix show PL that is red-shifted by 0.1–0.5 eV, depending on the size. This effect should be attributed to the stress exerted by the surrounding matrix on the lattice of the embedded Si NCs.

It can be anticipated that a similar situation will be encountered when the Si NCs are embedded in micrometer-sized SiO_2 grains. If free Si NCs with diameters between 2.8 and 6.3 nm produce PL compatible with ERE observations, it can be concluded that the size regime for Si NCs embedded in SiO_2 must be shifted to 1–4 nm in order to give rise to PL in the same wavelength range. Unfortunately, for various reasons, it was not possible to determine the PL quantum efficiency of Si NCs embedded in SiO_2. Therefore, we cannot provide quantitative information on the PL strength, which would be required for a conclusive discussion of matrix-embedded Si NCs as carrier candidates of the ERE.

6.7.4
PL Spectra of Silicon Dioxide NPs

Our studies on the oxidation of Si NCs under atmospheric conditions have shown that the oxidation is self-terminating. This means that the oxidation stops if the SiO_2 shell has reached a certain thickness. For NCs larger than 5 nm in diameter, it was found that the final thickness of the oxide shell amounts to 10% of the total NP diameter [296]. In an attempt to increase the oxidation rate and to accelerate the appearance of PL, we have carried out experiments with Si NCs that were dispersed in water. Within a few days, an originally brown solution turned into a colorless liquid, suggesting that the Si NCs were completely oxidized. In fact, using high-resolution transmission electron microscopy (HRTEM]), selected area electron diffraction (SAED), and electron energy loss spectroscopy (EELS), we could show that crystalline Si NPs were transformed into completely amorphous SiO_2 NPs with somewhat larger diameters [297].

An attractive feature of the as-prepared SiO_2 NPs is their strong PL in the red spectral region, which could be attributed to oxygen-related defect centers (nonbridging oxygen hole centers; NBOHCs; ≡Si–O·) [297]. Later studies showed that, depending on the oxidation conditions, the PL could also contain a blue contribution [298]. In Figure 6.44, we present, as a typical example, the PL spectrum of a sample of SiO_2 NPs obtained by complete oxidation of Si NCs in water. The entire spectrum can be fitted by two Gaussian distributions peaking at 475 and 660 nm (dashed curves). While the red PL band is attributed to NBOHCs, the blue channel can be assigned to oxygen-deficient centers (ODCs; ≡Si–Si≡). Both defect centers are associated with completely different excited

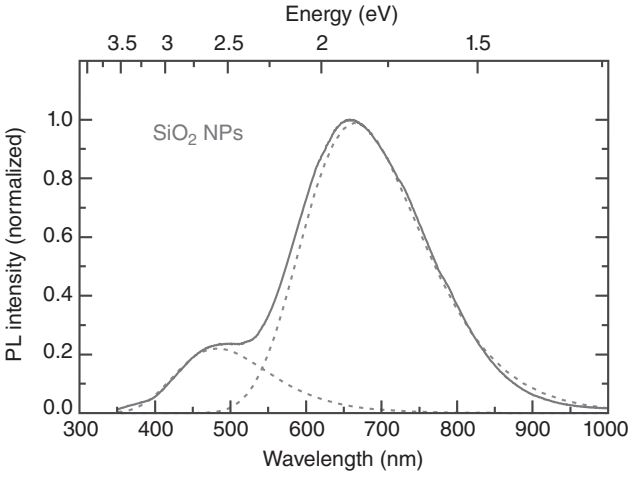

Figure 6.44 PL spectrum of an ensemble of SiO_2 NPs obtained by the oxidation of Si NCs in water. The blue and red PL bands (dashed lines) are associated with oxygen-related defect centers and should not be confused with the excitonic PL observed for Si NCs.

state lifetimes (70 ns for the blue and ~40 μs for the red channel) [298]. The coexistence of both defect centers (oxygen-rich and oxygen-deficient regions) points to a stoichiometrically very inhomogeneous material. It should be mentioned that, for pure SiO_2 NPs, the red PL band dominates over the blue PL feature but the intensity ratio of the two bands may depend on the details of the oxidation process.

Annealing experiments with Ge-doped SiO_2 NPs under exclusion of oxygen showed that, at 1000 °C, a new broad PL band appeared at 700 nm [298]. This PL band is interpreted to arise from the radiative recombination of excitons in Si NCs, which were formed by phase separation in Si-rich SiO_2. The formation of Si NCs could also be confirmed by HRTEM [298]. Thus, we found evidence for the same processes as described before when discussing the formation of Si NCs by ion implantation into SiO_2 and subsequent annealing. The detection of Si NCs after annealing revealed that the original oxide material was on the average sub-stoichiometric in oxygen.

To summarize the results on SiO_2 NPs obtained by oxidation of Si NCs, we can state that the NPs are characterized by oxygen-related defect centers. NBOHCs give rise to a strong fluorescence in the red, that is, in the same spectral range where ERE is observed. On the other hand, we could also observe the formation of luminescent Si NC seeds when the SiO_2 particles, which were sub-stoichiometric in oxygen, were subjected to a thermal processing up to 1000 °C. These results compare nicely with the findings of Kahler and Hofmeister [299] who used thermal evaporation of SiO and subsequent annealing to produce luminescent Si NCs in an SiO_2 matrix.

6.7.5 Consequences for the Interpretation of PL Observations

We have studied the optical properties of silicon nanocrystals (Si NCs) covered by a native oxide layer and embedded in a SiO_2 matrix as well as of intentionally oxidized Si NCs giving rise to amorphous SiO_2 NPs. Both kinds of nanosystems play an important role for applications in various fields of science ranging from photonics to biology and medicine. In this article, we examined whether and to what extent the same species may be made responsible for an astrophysical phenomenon called *extended red emission* (*ERE*).

It has been discussed that, if bulk crystalline silicon is reduced in size, so that its diameter becomes smaller than 10 nm, quantum effects start to govern the optical properties of the NPs. As far as Si NCs are concerned, the quantum confinement results in a considerably enhanced PL quantum efficiency and a shift of the PL from the near-IR to optical wavelengths. If the Si NCs are covered by a SiO_2 layer, however, the wavelength may not drop below 475 nm. This is due to the appearance of oxygen-related defect states within the widening bandgap [291]. Toward the large-wavelength side, the PL efficiency drops exponentially for wavelengths larger than 700 nm. Thus efficient luminescence for oxidized Si NCs can be expected only for a wavelength range between the theoretical limits of 475 and 1060 nm. This interval covers the entire range in which the ERE is observed. Besides the peak wavelengths, the bandwidth of ERE observations can be nicely reproduced by Si NC spectra, in which the width of the PL band is determined by the size distribution of the NCs giving rise to the observed PL. Thus, variations of ERE observations in wavelength and width can be explained by different size distributions of the Si NCs: smaller sizes can be associated with shorter wavelengths, and larger size distributions result in broader PL spectra.

Using the thermodynamic parameters and optical constants of silicon and silicon dioxide, Li and Draine [280] modeled the thermodynamic response of Si NCs upon excitation by the UV radiation field present in NGC 2023 as well as in the ISM and the following emission of 700 nm photons. If Si NCs were responsible for the ERE phenomenon, they should be heated up to temperatures around 100 K. It follows that these Si/SiO_2 core/shell NPs should give rise to an SiO_2-related emission band around 20 μm, which is actually not observed in the corresponding astronomical objects.

The conclusion of Li and Draine [280] is based on the assumption that the energy difference between excitation and emission is converted into heat, which results in the calculated temperature rise. We are somewhat skeptical that such classical treatment is adequate for nanosystems in the quantum confinement regime. QDs, such as the Si NCs considered here, have lost the continuous nature of their energy bands and are instead characterized by discrete energy levels. In this sense, Si QDs may be regarded as large molecules. The quantum nature of the core/shell system may also be an obstacle to an efficient energy transfer between the Si core that was originally excited and the outer SiO_2 shell, leading

to a mismatch in temperature between the core and the shell. Thus, the emission arising from the SiO_2 shell may be weaker than expected by the model.

Even if it were correct that, in a single Si NC, the shell would be heated to 100 K, there are other possibilities of explaining the failure of observing the 20 μm SiO_2 band. (i) The surface of the Si NCs could be passivated by hydrogen atoms. Because of the fourfold higher energy of the Si–H bond, the vibrational population is 11 orders of magnitude smaller than for the Si–O vibration, so that the associated Si–H emission feature at 4.5 μm should be much weaker than the 20 μm band. With hydrogen passivation, however, we would not have the natural lower limit of the emission wavelength imposed by oxygen-related defects. Therefore, one has to find arguments why Si NCs below a certain size, which would emit green light, are not encountered in ERE regions. Perhaps a solution could be that the small Si NCs are not stable in the radiation field. (ii) Another possibility for oxygen-passivated Si NCs would be that they are agglomerated to larger units so that they are not heated to such high temperature. The light emission characteristics would be the same as for free-flying Si NCs. (iii) Finally, we can propose that the Si NCs could be embedded in larger grains of, for example, silica or silicate. Depending on the size of the grains, the temperature rise could be rather small.

In order to study the effect of an SiO_2 matrix around individual Si NCs, we have performed measurements on fused quartz samples produced by Si ion implantation and subsequent annealing. We found that the PL response of matrix-embedded Si NCs is similar to the case of free oxygen-passivated Si NCs, except that the PL peak energy for a given nanocrystal size is shifted to smaller energy. It follows that the Si NC size distribution must be shifted to smaller sizes in order to be compatible with ERE observations.

During the course of our studies on Si NCs with SiO_2 shell, we found that the shell itself may give rise to rather strong PL near 700 nm. This PL originates from point defects at the interface between the crystalline Si core and the SiO_2 shell, or within the SiO_2 shell itself. Experiments on amorphous SiO_2 NPs produced by full oxidation of Si NCs reveal the same red PL. Although the excitation mechanism for the PL is not clear, it is suggested that the stoichiometrically inhomogeneous NPs contain tiny Si clusters acting as absorption centers. We observed that, upon annealing at temperatures around 1000 °C and above, these Si clusters may grow to larger Si NCs which give rise to a strong PL band with a maximum around 700 nm. It is conceivable that a similar process, resulting in light-emitting Si NCs embedded in larger SiO_2 grains, could also occur in astrophysical environments. Perhaps, also silicate grains could be subject to a similar process. In order to clarify this question, dedicated experimental studies should be carried out.

Analyzing the Hubble space telescope observations of NGC7023, Witt *et al.* [300] found that the precursor of the ERE carrier has been processed by far-UV photons with energies $E > 10.5$ eV. The carriers are then excited by near-UV/optical photons, giving rise to the PL observed. As possible candidates, the authors suggest doubly ionized PAHs (PAH dications). This proposition, however, is difficult to prove, as laboratory experiments involving PAH dications are extremely difficult. In this context, it should be mentioned that, although

PAHs leave their fingerprints as a global signature in IR emission spectra, no individual PAH molecule has been detected so far. Moreover, two-step mechanisms consisting of a process by far-UV photons and fluorescence induced by UV/optical photons could also be conceived for other nanosystems. For example, far-UV photons could generate defects in silica or silicate grains, which then give rise to fluorescence around 700 nm when excited by lower-energy UV photons.

It is interesting to note that Si NCs can be made responsible not only for the ERE but also for the blue luminescence first observed by Vijh *et al.* [301] in the Red Rectangle. Nayfeh *et al.* [302] suggested that, instead of the originally proposed small PAHs consisting of three to four aromatic rings, hydrogen-passivated ultrasmall Si NPs of 1 nm in diameter, such as the particularly stable $Si_{29}H_{24}$ cluster, could be potential carriers of the observed blue fluorescence feature.

To conclude this section, we would like to emphasize that, also in astrophysics, one should consider that classical methods may not be adequate to describe the optical properties of small dust grains. For diameters below 10 nm, the electronic wave function becomes strongly confined. Quantum effects must be taken into account to describe the optical properties correctly. Computational methods such as the linear combination of atomic orbitals (LCAOs) or the tight-binding technique offer the possibility of calculating energy levels and emission rates. However, laboratory measurements carried out under astrophysically relevant conditions are still indispensable for providing a meaningful comparison with astronomical observations.

Acknowledgments

C. Koike
I would like to thank my collaborators H. Chihara, H. Suto, H. Sogawa, K. Murata, and Y. Imai for many interesting discussions and for providing material for this review.

F. Huisken
This work was supported by the Deutsche Forschungsgemeinschaft (DFG). The authors are grateful to the Max Planck Institute for Astronomy for continuous support.

H. Mutschke, Th. Posch, A. Tamanai, S. Zeidler
We would like to thank G. Born for great help with the preparation and analysis of samples throughout all of our laboratory studies, and W. Teuschel for setting up and maintaining nice experiments. We thank M. Min for the fruitful collaboration and for providing material for this review. This work was supported by the Deutsche Forschungsgemeinschaft (DFG), during and after the "Forschergruppe Laborastrophysik."

References

1. Draine, B.T. and Lee, H.M. (1984) *Astrophys. J.*, **285**, 89–108.
2. Draine, B.T. (2003) *Annu. Rev. Astron. Astrophys.*, **41**, 241–289.
3. Mathis, J.S., Rumpl, W., and Nordsieck, K.H. (1977) *Astrophys. J.*, **217**, 425–433.
4. Weingartner, J.C. and Draine, B.T. (2001) *Astrophys. J.*, **548**, 296–309.
5. Cardelli, J.A., Clayton, G.C. and Mathis, J.S. (1989) *Astrophys. J.*, **345**, 245–256.
6. Desert, F.-X., Boulanger, F., and Puget, J.L. (1990) *Astron. Astrophys.*, **237**, 215–236.
7. Draine, B.T. and Li, A. (2007) *Astrophys. J.*, **657**, 810–837.
8. Fitzpatrick, E.L. and Massa, D. (1986) *Astrophys. J.*, **307**, 286–294.
9. Fitzpatrick, E.L. and Massa, D. (2005) *Astron. J.*, **130**, 1127–1140.
10. Schnaiter, M., Mutschke, H., Dorschner, J., Henning, T., and Salama, F. (1998) *Astrophys. J.*, **498**, 486.
11. Steglich, M., Jäger, C., Rouillé, G. *et al.* (2010) *Astrophys. J. Lett.*, **712**, L16–L20.
12. Pendleton, Y.J. and Allamandola, L.J. (2002) *Astrophys. J. Suppl. Ser.*, **138**, 75–98.
13. Henning, T. (2010) *Annu. Rev. Astron. Astrophys.*, **48**, 21–46.
14. Guertler, J. and Henning, T. (1986) *Astrophys. Space Sci.*, **128**, 163–175.
15. Chiar, J.E. and Tielens, A.G.G.M. (2006) *Astrophys. J.*, **637**, 774–785.
16. Min, M., Waters, L.B.F.M., de Koter, A. *et al.* (2007) *Astron. Astrophys.*, **462**, 667–676.
17. van Breemen, J.M., Min, M., Chiar, J.E. *et al.* (2011) *Astron. Astrophys.*, **526**, A152.
18. Bradley, J. (2010) in *Astromineralogy*, Lecture Notes in Physics, Vol. 815 (ed. T. Henning), Springer, Berlin, pp. 259–276.
19. Kemper, F., Vriend, W.J., and Tielens, A.G.G.M. (2004) *Astrophys. J.*, **609**, 826–837.
20. Chiar, J.E., Adamson, A.J., Whittet, D.C.B. *et al.* (2006) *Astrophys. J.*, **651**, 268–271.
21. Gillett, F.C. and Forrest, W.J. (1973) *Astrophys. J.*, **179**, 483–491.
22. Gibb, E.L., Whittet, D.C.B., Schutte, W.A. *et al.* (2000) *Astrophys. J.*, **536**, 347–356.
23. van Dishoeck, E.F. (2004) *Annu. Rev. Astron. Astrophys.*, **42**, 119–167.
24. Öberg, K.I., Boogert, A.C.A., Pontoppidan, K.M. *et al.* (2011) *Astrophys. J.*, **740**, 109.
25. Chiar, J.E., Adamson, A.J., Kerr, T.H., and Whittet, D.C.B. (1994) *Astrophys. J.*, **426**, 240–248.
26. Chiar, J.E., Adamson, A.J., Kerr, T.H., and Whittet, D.C.B. (1995) *Astrophys. J.*, **455**, 234.
27. Chiar, J.E., Pendleton, Y.J., Allamandola, L.J. *et al.* (2011) *Astrophys. J.*, **731**, 9.
28. Boogert, A.C.A., Huard, T.L., Cook, A.M. *et al.* (2011) *Astrophys. J.*, **729**, 92.
29. Gibb, E.L., Whittet, D.C.B., Boogert, A.C.A., and Tielens, A.G.G.M. (2004) *Astrophys. J. Suppl. Ser.*, **151**, 35–73.
30. Cook, A.M., Whittet, D.C.B., Shenoy, S.S. *et al.* (2011) *Astrophys. J.*, **730**, 124.
31. Tielens, A.G.G.M. and Hagen, W. (1982) *Astron. Astrophys.*, **114**, 245–260.
32. Zhukovska, S., Gail, H.-P., and Trieloff, M. (2008) *Astron. Astrophys.*, **479**, 453–480.
33. Ott, U. (2010) in *Astromineralogy*, Lecture Notes in Physics, Vol. 815 (ed. T. Henning), Springer, Berlin, pp. 277–311.
34. Kraemer, K.E., Sloan, G.C., Price, S.D., and Walker, H.J. (2002) *Astrophys. J. Suppl. Ser.*, **140**, 389–406.
35. Sloan, G.C., Kraemer, K.E., Wood, P.R. *et al.* (2008) *Astrophys. J.*, **686**, 1056–1081.
36. Molster, F.J., Waters, L.B.F.M., and Kemper, F. (2010) in *Astromineralogy*, Lecture Notes in Physics, Vol. 815 (ed. T. Henning), Springer, Berlin, pp. 143–201.
37. Jäger, C., Molster, F.J., Dorschner, J. *et al.* (1998) *Astron. Astrophys.*, **339**, 904–916.

38. Waters, L.B.F.M., Molster, F.J., de Jong, T. *et al.* (1996) *Astron. Astrophys.*, **315**, L361–L364.
39. Molster, F.J., Waters, L.B.F.M., Tielens, A.G.G.M., and Barlow, M.J. (2002) *Astron. Astrophys.*, **382**, 184–221.
40. DePew, K., Speck, A., and Dijkstra, C. (2006) *Astrophys. J.*, **640**, 971–981.
41. Sloan, G.C., Kraemer, K.E., Goebel, J.H., and Price, S.D. (2003) *Astrophys. J.*, **594**, 483–495.
42. Mutschke, H., Andersen, A.C., Clément, D., Henning, T., and Peiter, G. (1999) *Astron. Astrophys.*, **345**, 187–202.
43. Sloan, G.C., Little-Marenin, I.R., and Price, S.D. (1998) *Astron. J.*, **115**, 809.
44. Speck, A.K., Thompson, G.D., and Hofmeister, A.M. (2005) *Astrophys. J.*, **634**, 426–435.
45. Begemann, B., Dorschner, J., Henning, T., Mutschke, H., and Thamm, E. (1994) *Astrophys. J. Lett.*, **423**, L71–L74.
46. Hony, S., Waters, L.B.F.M., and Tielens, A.G.G.M. (2002) *Astron. Astrophys.*, **390**, 533–553.
47. Volk, K., Kwok, S., Hrivnak, B.J., and Szczerba, R. (2002) *Astrophys. J.*, **567**, 412–422.
48. Omont, A., Moseley, S.H., Cox, P. *et al.* (1995) *Astrophys. J.*, **454**, 819.
49. Volk, K., Kwok, S., and Hrivnak, B.J. (1999) *Astrophys. J. Lett.*, **516**, L99–L102.
50. Hony, S., Waters, L.B.F.M., and Tielens, A.G.G.M. (2001) *Astron. Astrophys.*, **378**, L41–L44.
51. Volk, K., Hrivnak, B.J., Matsuura, M. *et al.* (2011) *Astrophys. J.*, **735**, 127.
52. Cami, J., Bernard-Salas, J., Peeters, E., and Malek, S.E. (2010) *Science*, **329**, 1180–118.
53. Zhang, Y. and Kwok, S. (2011) *Astrophys. J.*, **730**, 126.
54. Gielen, C., Bouwman, J., van Winckel, H. *et al.* (2011) *Astron. Astrophys.*, **533**, A99.
55. Henning, T. and Meeus, G. (2011) in *Physical Processes in Circumstellar Disks around Young Stars* (ed. P.J.V. Garcia), University Of Chicago Press, pp. 114–148.
56. Malfait, K., Waelkens, C., Waters, L.B.F.M. *et al.* (1998) *Astron. Astrophys.*, **332**, L25–L28.
57. Meeus, G., Waters, L.B.F.M., Bouwman, J. *et al.* (2001) *Astron. Astrophys.*, **365**, 476–490.
58. Bouwman, J., Meeus, G., de Koter, A. *et al.* (2001) *Astron. Astrophys.*, **375**, 950–962.
59. Koike, C., Shibai, H., and Tuchiyama, A. (1993) *Mon. Not. R. Astron. Soc.*, **264**, 654.
60. Malfait, K., Waelkens, C., Bouwman, J., de Koter, A., and Waters, L.B.F.M. (1999) *Astron. Astrophys.*, **345**, 181–186.
61. Mutschke, H., Zeidler, S., Posch, T. *et al.* (2008) *Astron. Astrophys.*, **492**, 117–125.
62. Kessler-Silacci, J., Augereau, J.-C., Dullemond, C.P. *et al.* (2006) *Astrophys. J.*, **639**, 275–291.
63. Bouwman, J., Henning, T., Hillenbrand, L.A. *et al.* (2008) *Astrophys. J.*, **683**, 479–498.
64. Olofsson, J., Augereau, J.-C., van Dishoeck, E.F. *et al.* (2009) *Astron. Astrophys.*, **507**, 327–345.
65. Furlan, E., Luhman, K.L., Espaillat, C. *et al.* (2011) *Astrophys. J. Suppl. Ser.*, **195**, 3.
66. Apai, D., Pascucci, I., Bouwman, J. *et al.* (2005) *Science*, **310**, 834–836.
67. Pascucci, I., Apai, D., Luhman, K. *et al.* (2009) *Astrophys. J.*, **696**, 143–159.
68. Bouwman, J., Lawson, W.A., Juhász, A. *et al.* (2010) *Astrophys. J. Lett.*, **723**, L243–L247.
69. Crovisier, J., Leech, K., Bockelee-Morvan, D. *et al.* (1997) *Science*, **275**, 1904–1907.
70. Juhász, A., Bouwman, J., Henning, T. *et al.* (2010) *Astrophys. J.*, **721**, 431–455.
71. Acke, B., Bouwman, J., Juhász, A. *et al.* (2010) *Astrophys. J.*, **718**, 558–574.
72. van Boekel, R., Min, M., Leinert, C. *et al.* (2004) *Nature*, **432**, 479–482.
73. Sargent, B.A., Forrest, W.J., Tayrien, C. *et al.* (2009) *Astrophys. J.*, **690**, 1193–1207.
74. Pontoppidan, K.M., Dullemond, C.P., van Dishoeck, E.F. *et al.* (2005) *Astrophys. J.*, **622**, 463–481.

75. Sturm, B., Bouwman, J., Henning, T. *et al.* (2010) *Astron. Astrophys.*, **518**, L129.
76. Sturm, B., Bouwman, J., Henning, T. *et al.* (2013) *Astron. Astrophys.*, **553**, A5.
77. Aumann, H.H., Beichman, C.A., Gillett, F.C. *et al.* (1984) *Astrophys. J. Lett.*, **278**, L23–L27.
78. Habing, H.J., Dominik, C., Jourdain de Muizon, M. *et al.* (2001) *Astron. Astrophys.*, **365**, 545–561.
79. Rieke, G.H., Su, K.Y.L., Stansberry, J.A. *et al.* (2005) *Astrophys. J.*, **620**, 1010–1026.
80. Eiroa, C., Marshall, J.P., Mora, A. *et al.* (2011) *Astron. Astrophys.*, **536**, L4.
81. Lagrange, A.-M., Gratadour, D., Chauvin, G. *et al.* (2009) *Astron. Astrophys.*, **493**, L21–L25.
82. Chauvin, G., Lagrange, A.-M., Beust, H. *et al.* (2012) *Astron. Astrophys.*, **542**, A41.
83. Kalas, P., Graham, J.R., and Clampin, M. (2005) *Nature*, **435**, 1067–1070.
84. Carpenter, J.M., Bouwman, J., Mamajek, E.E. *et al.* (2009) *Astrophys. J. Suppl. Ser.*, **181**, 197–226.
85. Beichman, C.A., Bryden, G., Gautier, T.N. *et al.* (2005) *Astrophys. J.*, **626**, 1061–1069.
86. Lovis, C., Mayor, M., Pepe, F. *et al.* (2006) *Nature*, **441**, 305–309.
87. Knacke, R.F., Fajardo-Acosta, S.B., Telesco, C.M. *et al.* (1993) *Astrophys. J.*, **418**, 440.
88. de Vries, B.L., Acke, B., Vandenbussche, B. *et al.* (2011) in *The Molecular Universe*, Proceedings IAU Symposium No. 280 (eds J. Cernicharo and R. Bachiller), ASP, San Francisco, p. 148.
89. Olofsson, J., Juhász, A., Henning, T. *et al.* (2012) *Astron. Astrophys.*, **542**, A90.
90. Fujiwara, H., Onaka, T., Ishihara, D. *et al.* (2010) *Astrophys. J. Lett.*, **714**, L152–L156.
91. Palik, E.D. (1985–1998) *Handbook of Optical Constants of Solids*, Academic Press Handbook Series, Academic Press, San Diego, CA.
92. Henning, T., Il'In, V.B., Krivova, N.A., Michel, B., and Voshchinnikov, N.V. (1999) *Astron. Astrophys. Suppl.*, **136**, 405–406.
93. Mie, G. (1908) *Ann. Phys.*, **330**, 377–445.
94. Stognienko, R., Henning, T., and Ossenkopf, V. (1995) *Astron. Astrophys.*, **296**, 797.
95. Purcell, E.M. and Pennypacker, C.R. (1973) *Astrophys. J.*, **186**, 705–714.
96. Bohren, C.F. and Huffman, D.R. (1983) *Absorption and Scattering of Light by Small Particles*, John Wiley & Sons, Inc., New York.
97. Min, M., Hovenier, J.W., Dominik, C., de Koter, A., and Yurkin, M.A. (2006) *J. Quant. Spect. Radiat. Transfer*, **97**, 161–180.
98. Mutschke, H., Min, M., and Tamanai, A. (2009) *Astron. Astrophys.*, **504**, 875–882.
99. Min, M., Hovenier, J.W., and de Koter, A. (2003) *Astron. Astrophys.*, **404**, 35–46.
100. Mishchenko, M.I., Hovenier, J.W., and Travis, L.D. (2000) *Light Scattering by Nonspherical Particles: Theory, Measurements, and Applications*, Academic Press, San Diego, CA.
101. Mishchenko, M.I., Travis, L.D., and Lacis, A.A. (2002) *Scattering, Absorption, and Emission of Light by Small Particles*, Cambridge University Press.
102. Mennella, V., Brucato, J.R., Colangeli, L. *et al.* (1998) *Astrophys. J.*, **496**, 1058.
103. Boudet, N., Mutschke, H., Nayral, C. *et al.* (2005) *Astrophys. J.*, **633**, 272–281.
104. Papoular, R., Cauchetier, M., Begin, S., and Lecaer, G. (1998) *Astron. Astrophys.*, **329**, 1035–1044.
105. Clément, D., Mutschke, H., Klein, R., and Henning, T. (2003) *Astrophys. J.*, **594**, 642–650.
106. Tamanai, A., Mutschke, H., Blum, J., and Meeus, G. (2006) *Astrophys. J. Lett.*, **648**, L147–L150.
107. Tamanai, A., Mutschke, H., Blum, J., and Neuhäuser, R. (2006) *J. Quant. Spect. Radiat. Transfer*, **100**, 373–381.
108. Tamanai, A., Mutschke, H., Blum, J. *et al.* (2009) *Astron. Astrophys.*, **501**, 251–267.

109. Tamanai, A., Mutschke, H., and Blum, J. (2009b) in *Cosmic Dust - Near and Far*, Astronomical Society of the Pacific Conference Series, Vol. 414 (eds T. Henning, E. Grun, and J. Steinacker), ASP, San Francisco, p. 438.

110. Hofmeister, A.M. (1997) *Phys. Chem. Miner.*, **24**, 535–546.

111. Speck, A.K., Hofmeister, A.M., and Barlow, M.J. (1999) *Astrophys. J. Lett.*, **513**, L87–L90.

112. Kreibig, U. and Vollmer, M. (1995) *Optical Properties of Metal Clusters*, Springer, Berlin.

113. Zeidler, S., Posch, T., and Mutschke, H. (2013) *Astron. Astrophys.*, **553**, A81.

114. Posch, T., Kerschbaum, F., Fabian, D. *et al.* (2003) *Astrophys. J. Suppl. Ser.*, **149**, 437–445.

115. Fabian, D., Henning, T., Jäger, C. *et al.* (2001) *Astron. Astrophys.*, **378**, 228–238.

116. Zeidler, S., Posch, T., Mutschke, H., Richter, H., and Wehrhan, O. (2011) *Astron. Astrophys.*, **526**, A68.

117. Henning, T., Michel, B., and Stognienko, R. (1995) *Planet. Space Sci.*, **43**, 1333–1343.

118. Nafziger, R.H. and Muan, A. (1967) *Am. Mineral.*, **52**, 1364–1385.

119. Dorschner, J., Begemann, B., Henning, T., Jäger, C., and Mutschke, H. (1995) *Astron. Astrophys.*, **300**, 503.

120. Jäger, C., Dorschner, J., Mutschke, H., Posch, T., and Henning, T. (2003) *Astron. Astrophys.*, **408**, 193–204.

121. Brinker, C.J. and Scherer, G.W. (1990) *Sol-Gel Science*, Academic Press, San Diego, CA.

122. Scott, A. and Duley, W.W. (1996) *Astrophys. J. Suppl. Ser.*, **105**, 401.

123. Jäger, C., Fabian, D., Schrempel, F. *et al.* (2003) *Astron. Astrophys.*, **401**, 57–65.

124. Henning, T., Begemann, B., Mutschke, H., and Dorschner, J. (1995) *Astron. Astrophys. Suppl.*, **112**, 143.

125. Mutschke, H., Begemann, B., Dorschner, J. *et al.* (1998) *Astron. Astrophys.*, **333**, 188–198.

126. Gervais, F., Blin, A., Massiot, D. *et al.* (1987) *J. Non-Cryst. Solids*, **89**, 384–401.

127. Burns, R.G. (1993) *Mineralogical Applications of Crystal Field Theory*, Cambridge Topics in Mineral Physics and Chemistry, 2nd edn, Vol. 5, Cambridge University Press.

128. Huffman, D.R. and Stapp, J.L. (1973) in *Interstellar Dust and Related Topics*, Proceedings IAU Symposium No. 52 (eds J.M. Greenberg and H.C. van de Hulst), Reidel, Dordrecht, p. 297.

129. Bösch, M.A. (1978) *Phys. Rev. Lett.*, **40**, 879–882.

130. Fabian, D., Jäger, C., Henning, T., Dorschner, J., and Mutschke, H. (2000) *Astron. Astrophys.*, **364**, 282–292.

131. Imai, Y., Koike, C., Chihara, H. *et al.* (2009) *Astron. Astrophys.*, **507**, 277–281.

132. Meny, C., Gromov, V., Boudet, N. *et al.* (2007) *Astron. Astrophys.*, **468**, 171–188.

133. Schlömann, E. (1964) *Phys. Rev.*, **135**, 413–419.

134. Hunklinger, S. and von Schickfus, M. (1981) in *Amorphous Solids: Low-Temperature Properties. Series: Topics in Current Physics*, Vol. 24 (ed. W.A. Phillips), Springer, Berlin, pp. 81–105.

135. Agladze, N.I., Sievers, A.J., Jones, S.A., Burlitch, J.M., and Beckwith, S.V.W. (1996) *Astrophys. J.*, **462**, 1026.

136. Dupac, X., Bernard, J.-P., Boudet, N. *et al.* (2003) *Astron. Astrophys.*, **404**, L11–L15.

137. Désert, F.-X., Macías-Pérez, J.F., Mayet, F. *et al.* (2008) *Astron. Astrophys.*, **481**, 411–421.

138. Coupeaud, A., Demyk, K., Meny, C. *et al.* (2011) *Astron. Astrophys.*, **535**, A124.

139. Chihara, H., Koike, C., Tsuchiyama, A., Tachibana, S., and Sakamoto, D. (2002) *Astron. Astrophys.*, **391**, 267–273.

140. Koike, C., Chihara, H., Tsuchiyama, A. *et al.* (2003) *Astron. Astrophys.*, **399**, 1101–1107.

141. Koike, C., Mutschke, H., Suto, H. *et al.* (2006) *Astron. Astrophys.*, **449**, 583–596.

142. Chihara, H., Koike, C., and Tsuchiyama, A. (2007) *Astron. Astrophys.*, **464**, 229–234.
143. Murata, K., Chihara, H., Koike, C. *et al.* (2009) *Astrophys. J.*, **698**, 1903–1906.
144. Koike, C., Imai, Y., Chihara, H. *et al.* (2010) *Astrophys. J.*, **709**, 983–992.
145. Suto, H., Koike, C., Sogawa, H. *et al.* (2002) *Astron. Astrophys.*, **389**, 568–571.
146. Sogawa, H., Koike, C., Chihara, H. *et al.* (2006) *Astron. Astrophys.*, **451**, 357–361.
147. Suto, H., Sogawa, H., Tachibana, S. *et al.* (2006) *Mon. Not. R. Astron. Soc.*, **370**, 1599–1606.
148. Koike, C., Tsuchiyama, A., Shibai, H. *et al.* (2000) *Astron. Astrophys.*, **363**, 1115–1122.
149. Chihara, H., Koike, C., and Tsuchiyama, A. (2001) *Publ. Astron. Soc. Jpn.*, **53**, 243–250.
150. Bowey, J.E., Lee, C., Tucker, C. *et al.* (2001) *Mon. Not. R. Astron. Soc.*, **325**, 886–896.
151. Servoin, J.L. and Piriou, B. (1973) *Phys. Status Solidi B*, **55**, 677–686.
152. Koike, C., Imai, Y., Noguchi, R., *et al.* (2010), in 28th Grain Formation Workshop proceedings, (eds. T. Yamamoto, A. Inoue, H. Kimura), Center of Planetary Science, Kobe University.
153. Day, K.L. (1977) *Mon. Not. R. Astron. Soc.*, **178**, 49P–51P.
154. Carrez, P., Demyk, K., Leroux, H. *et al.* (2002) *Meteorit. Planet. Sci.*, **37**, 1615–1622.
155. Koike, K., Nakagawa, M., Koike, C. *et al.* (2003) *KURRI Prog. Rep.*, **VIII-II**, P54.
156. Koike, C., Chihara, H., Koike, K. *et al.* (2006) *KURRI Prog. Rep.*, **VIII-II**, PR4–P–8.
157. Murata, K., Takakura, T., Chihara, H., Koike, C., and Tsuchiyama, A. (2009) *Astrophys. J.*, **696**, 1612–1615.
158. Strunz, H. and Nickel, E.H. (2001) *Strunz Mineralogical Tables*, 9th edn, Schweizerbart Verlag, Stuttgart.
159. Karovicova, I., Wittkowski, M., Ohnaka, K. *et al.* (2013) *Astron. Astrophys.*, **560**, A75.
160. Whittet, D.C.B. (2003) *Dust in the Galactic Environment*, Series in Astronomy and Astrophysics, 2nd edn, Institute of Physics (IOP) Publishing, Bristol and Philadelphia, PA.
161. Amelin, Y., Krot, A.N., Hutcheon, I.D., and Ulyanov, A.A. (2002) *Science*, **297**, 1678–1683.
162. Brearley, A.J. and Jones, R.H. (1998) in *Planetary Materials*, *Reviews in Mineralogy and Geochemistry*, Vol. 36 (ed. J.J. Papike), Mineralogical Society of America, pp. 3.1–3.398.
163. MacPherson, G.J., Simon, S.B., Davis, A.M., Grossman, L., and Krot, A.N. (2005) in *Chondrites and the Protoplanetary Disk*, Astronomical Society of the Pacific Conference Series, Vol. 341 (eds A.N. Krot, E.R.D. Scott, and B. Reipurth), ASP, San Francisco, p. 225.
164. Nittler, L.R. (1997) in *Astrophysical Implications of the Laboratory Study of Presolar Materials*, American Institute of Physics Conference Proceedings, Vol. 402 (eds E.K. Zinner and T.J. Bernatowicz), AIP, College Park (MD), pp. 59–82.
165. McSween, H.Y. Jr. and Huss, G.R. (2010) *Cosmochemistry*, Cambridge University Press.
166. Hoppe, P. (2009) in *Cosmic Dust - Near and Far*, Astronomical Society of the Pacific Conference Series, Vol. 414 (eds T. Henning, E. Grun, and J. Steinacker), ASP, San Francisco, p. 148.
167. Floss, C., Stadermann, F.J., and Bose, M. (2008) *Astrophys. J.*, **672**, 1266–1271.
168. Salisbury, J.W., Walter, L.S., Vergo, N., and D'Aria, D.M. (1992) *Infrared (2.1–25μm) Spectra of Minerals*, The Johns Hopkins University Press, Baltimore, MD and London.
169. Pecharromán, C., González-Carre no, T., and Iglesias, J.E. (1996) *J. Mater. Res.*, **11**, 127–133.
170. Begemann, B., Dorschner, J., Henning, T. *et al.* (1997) *Astrophys. J.*, **476**, 199.
171. Gervais, F. (1991) in *Handbook of Optical Constants of Solids II* (ed. E.D. Palik), Academic Press, San Diego, CA, pp. 761–776.

172. Koike, C., Kaito, C., Yamamoto, T. *et al.* (1995) *Icarus*, **114**, 203–214.
173. Onaka, T., de Jong, T., and Willems, F.J. (1989) *Astron. Astrophys.*, **218**, 169–179.
174. Vardya, M.S., de Jong, T., and Willems, F.J. (1986) *Astrophys. J. Lett.*, **304**, L29–L32.
175. Glaccum, W. (1995) in *From Gas to Stars to Dust*, Astronomical Society of the Pacific Conference Series, Vol. 73 (eds M.R. Haas, J.A. Davidson, and E.F. Erickson), ASP, San Francisco, pp. 395–396.
176. Sloan, G.C., Levan, P.D., and Little-Marenin, I.R. (1996) *Astrophys. J.*, **463**, 310.
177. Posch, T., Kerschbaum, F., Mutschke, H. *et al.* (1999) *Astron. Astrophys.*, **352**, 609–618.
178. Ulyanov, A.A. (1998) in *Mineral Matter in Space*, Advanced Mineralogy, Vol. 3 (ed. A.S. Marfunin), Springer, Berlin, pp. 47–72.
179. Mutschke, H., Posch, T., Fabian, D., and Dorschner, J. (2002) *Astron. Astrophys.*, **392**, 1047–1052.
180. Clayton, D.D. and Nittler, L.R. (2004) *Annu. Rev. Astron. Astrophys.*, **42**, 39–78.
181. Stroud, R.M., Nittler, L.R., Alexander, C.M.O., Stadermann, F.J., and Zinner, E.K. (2005) *Meteorit. Planet. Sci. Suppl.*, **40**, 5171.
182. Stroud, R.M., Nittler, L.R., and Alexander, C.M.O. (2008) in *Lunar and Planetary Science Conference*, Vol. 39, LPI, Houston (TX), p. 1778.
183. Fabian, D., Posch, T., Mutschke, H., Kerschbaum, F., and Dorschner, J. (2001) *Astron. Astrophys.*, **373**, 1125–1138.
184. Henning, T. and Mutschke, H. (1997) *Astron. Astrophys.*, **327**, 743–754.
185. Wetzel, S., Klevenz, M., Gail, H.-P., Pucci, A., and Trieloff, M. (2013) *Astron. Astrophys.*, **553**, A92.
186. Wetzel, S., Klevenz, M., Pucci, A., and Gail, H.-P. (2012) *Appl. Spectrosc.*, **66**, 1061–1066.
187. Philipp, H. (1971) *J. Phys. Chem. Solids*, **32**, 1935–1945.
188. Holleman, A.F. and Wiberg, E. (1995) *Lehrbuch der Anorganischen Chemie*, de Gruyter, Berlin.
189. Posch, T., Mutschke, H., and Andersen, A. (2004) *Astrophys. J.*, **616**, 1167–1180.
190. Papoular, R. (2011) *Mon. Not. R. Astron. Soc.*, **415**, 494–502.
191. Li, A., Liu, J.M., and Jiang, B.W. (2013) *Astrophys. J.*, **777**, 111.
192. Jeong, K.S., Winters, J.M., and Sedlmayr, E. (1999) in *Asymptotic Giant Branch Stars*, IAU Symposium, Vol. 191 (eds T. Le Bertre, A. Lebre, and C. Waelkens), ASP, San Francisco, p. 233.
193. Nagahara, H. and Mysen, B.O. (1991) *LPI Contrib.*, **766**, 165.
194. Richter, H., Posch, T., Taran, M.N., and Mutschke, H. (2005) *Mineral. Petrol.*, **85**, 53–65.
195. Tropf, W.J. and Thomas, M.E. (1991) in *Handbook of Optical Constants of Solids II* (ed. E.D. Palik), Academic Press, San Diego, CA, pp. 883–898.
196. Jasperse, J.R., Kahan, A., Plendl, J.N., and Mitra, S.S. (1966) *Phys. Rev.*, **146**, 526–542.
197. Posch, T., Baier, A., Mutschke, H., and Henning, T. (2007) *Astrophys. J.*, **668**, 993–1000.
198. Mitra, S.S. (1985) in *Handbook of Optical Constants of Solids* (ed. E.D. Palik), Academic Press, Orlando, FL, pp. 213–270.
199. Degiorgi, L., Blatter-Mörke, I., and Wachter, P. (1987) *Phys. Rev. B*, **35**, 5421–5424.
200. Draine, B.T. and Malhotra, S. (1993) *Astrophys. J.*, **414**, 632–645.
201. Croat, T.K., Bernatowicz, T., Amari, S., Messenger, S., and Stadermann, F.J. (2003) *Geochim. Cosmochim. Acta*, **67**, 4705–4725.
202. Guillois, O., Ledoux, G., and Reynaud, C. (1999) *Astrophys. J. Lett.*, **521**, L133–L36.
203. Werner, M.W., Uchida, K.I., Sellgren, K. *et al.* (2004) *Astrophys. J. Suppl. Ser.*, **154**, 309–314.
204. Sellgren, K., Werner, M.W., Ingalls, J.G. *et al.* (2010) *Astrophys. J. Lett.*, **722**, L54–L57.

205. García-Hernández, D.A., Manchado, A., García-Lario, P. *et al.* (2010) *Astrophys. J. Lett.*, **724**, L39–L43.

206. Philipp, H.R. (1977) *Phys. Rev. B*, **16**, 2896–2900.

207. Edwards, D.F., Philipp, H.R., and Palik, E.D. (eds) (1985) in *Handbook of Optical Constants of Solids*, Academic Press, Orlando, FL, pp. 665–673.

208. Krätschmer, W., Lamb, L.D., Fostiropoulos, K., and Huffman, D.R. (1990) *Nature*, **347**, 354–358.

209. Mutschke, H., Andersen, A.C., Jäger, C., Henning, T., and Braatz, A. (2004) *Astron. Astrophys.*, **423**, 983–993.

210. Draine, B.T. (1985) *Astrophys. J. Suppl. Ser.*, **57**, 587–594.

211. Draine, B.T. (2003) *Astrophys. J.*, **598**, 1026–1037.

212. Borghesi, A. and Guizetti, G. (1991) in *Handbook of Optical Constants of Solids II* (ed. E.D. Palik), Academic Press, San Diego, CA, pp. 449–460.

213. Hill, H.G.M., D'Hendecourt, L.B., Perron, C., and Jones, A.P. (1997) *Meteorit. Planet. Sci.*, **32**, 713–718.

214. Braatz, A., Ott, U., Henning, T., Jäger, C., and Jeschke, G. (2000) *Meteorit. Planet. Sci.*, **35**, 75–84.

215. Hill, H.G.M., Jones, A.P., and D'Hendecourt, L.B. (1998) *Astron. Astrophys.*, **336**, L41–L44.

216. Jones, A.P., d'Hendecourt, L.B., Sheu, S.-Y. *et al.* (2004) *Astron. Astrophys.*, **416**, 235–241.

217. Pirali, O., Vervloet, M., Dahl, J.E. *et al.* (2007) *Astrophys. J.*, **661**, 919–925.

218. Allamandola, L.J., Sandford, S.A., Tielens, A.G.G.M., and Herbst, T.M. (1992) *Astrophys. J.*, **399**, 134–146.

219. Jones, A.P. and d'Hendecourt, L. (2000) *Astron. Astrophys.*, **355**, 1191–1200.

220. Bernatowicz, T.J., Gibbons, P.C., and Lewis, R.S. (1990) *Astrophys. J.*, **359**, 246–255.

221. Pflüger, J. and Fink, J. (1991) in *Handbook of Optical Constants of Solids II* (ed. E.D. Palik), Academic Press, San Diego, CA, pp. 293–311.

222. Lewis, R.S., Anders, E., and Draine, B.T. (1989) *Nature*, **339**, 117–121.

223. Binette, L., Magris C., G., Krongold, Y. *et al.* (2005) *Astrophys. J.*, **631**, 661–677.

224. Hansen, P.L., Fallon, P.J., and Krätschmer, W. (1991) *Chem. Phys. Lett.*, **181**, 367–372.

225. Micelotta, E.R., Jones, A.P., Cami, J. *et al.* (2012) *Astrophys. J.*, **761**, 35.

226. Sakata, A., Wada, S., Okutsu, Y., Shintani, H., and Nakada, Y. (1983) *Nature*, **301**, 493.

227. Arakawa, E.T., Williams, M.W., and Inagaki, T. (1977) *J. Appl. Phys.*, **48**, 3176–3177.

228. Edoh, O. (1983) *Optical properties of carbon from the far infrared to the far ultraviolet*. PhD thesis, University of Arizona.

229. Jäger, C., Mutschke, H., and Henning, T. (1998) *Astron. Astrophys.*, **332**, 291–299.

230. Bussoletti, E., Colangeli, L., Borghesi, A., and Orofino, V. (1987) *Astron. Astrophys. Suppl.*, **70**, 257–268.

231. Koike, C., Hasegawa, H., and Manabe, A. (1980) *Astrophys. Space Sci.*, **67**, 495–502.

232. Rouleau, F. and Martin, P.G. (1991) *Astrophys. J.*, **377**, 526–540.

233. Zubko, V.G., Mennella, V., Colangeli, L., and Bussoletti, E. (1996) *Mon. Not. R. Astron. Soc.*, **282**, 1321–1329.

234. Colangeli, L., Mennella, V., Palumbo, P., Rotundi, A., and Bussoletti, E. (1995) *Astron. Astrophys. Suppl.*, **113**, 561.

235. Tauc, J., Grigorovici, R., and Vancu, A. (1966) *Phys. Status Solidi B*, **15**, 627–637.

236. Robertson, J. and O'Reilly, E.P. (1987) *Phys. Rev. B*, **35**, 2946–2957.

237. Mennella, V., Colangeli, L., Bussoletti, E. *et al.* (1995) *Astrophys. J. Suppl. Ser.*, **100**, 149.

238. Jones, A.P. (2012) *Astron. Astrophys.*, **540**, A2.

239. Jones, A.P. (2012) *Astron. Astrophys.*, **540**, A1.

240. Jones, A.P. (2012) *Astron. Astrophys.*, **542**, A98.

241. Mennella, V., Colangeli, L., Palumbo, P. *et al.* (1996) *Astrophys. J. Lett.*, **464**, L191.

242. Mennella, V., Colangeli, L., Bussoletti, E., Palumbo, P., and Rotundi, A. (1998) *Astrophys. J. Lett.*, **507**, L177–L180.

243. Gadallah, K.A.K., Mutschke, H., and Jäger, C. (2011) *Astron. Astrophys.*, **528**, A56.
244. Schnaiter, M., Gimmler, M., Llamas, I. *et al.* (2006) *Atmos. Chem. Phys.*, **6**, 2981–2990.
245. Rouleau, F., Henning, T., Stognienko, R. (1997) *Astron. Astrophys.*, **322**, 633–645.
246. Llamas-Jansa, I., Jäger, C., Mutschke, H., and Henning, Th. (2007) *Carbon*, **45** (7), 1542–1557.
247. Jäger, C., Henning, Th., Schlögl, R., and Spilleke, O. (1999) *J. Non-Cryst. Solids*, **258**, 161–179.
248. Quinten, M., Kreibig, U., Henning, T., and Mutschke, H. (2002) *Appl. Opt.*, **41**, 7102–7113.
249. Michel, B., Henning, Th., Jäger, C., and Kreibig, U. (1999) *Carbon*, **37**, 391–400.
250. Wildt, R. (1933) *Z. Astrophys.*, **6**, 345.
251. Friedemann, C. (1969a) *Physica*, **41**, 139–143.
252. Friedemann, C. (1969b) *Astron. Nachr.*, **291**, 177.
253. Gilman, R.C. (1969) *Astrophys. J. Lett.*, **155**, L185.
254. Cherchneff, I. and Cau, P. (1999) in *Asymptotic Giant Branch Stars*, *IAU Symposium*, Vol. 191 (eds T. Le Bertre, A. Lebre, and C. Waelkens), ASP, San Francisco, p. 251.
255. Lodders, K. and Fegley, B. (1997) in *Astrophysical Implications of the Laboratory Study of Presolar Materials*, American Institute of Physics Conference Proceedings, Vol. 402 (eds E.K. Zinner and T.J. Bernatowicz), AIP, College Park (MD), pp. 391–423.
256. Hackwell, J.A. (1972) *Astron. Astrophys.*, **21**, 239–248.
257. Treffers, R. and Cohen, M. (1974) *Astrophys. J.*, **188**, 545–552.
258. Little-Marenin, I.R. (1986) *Astrophys. J. Lett.*, **307**, L15–L19.
259. Goebel, J.H., Cheeseman, P., and Gerbault, F. (1995) *Astrophys. J.*, **449**, 246.
260. Justtanont, K., Barlow, M.J., Skinner, C.J. *et al.* (1996) *Astron. Astrophys.*, **309**, 612–628.
261. Speck, A.K., Barlow, M.J., and Skinner, C.J. (1997) *Mon. Not. R. Astron. Soc.*, **288**, 431–456.
262. Pitman, K.M., Hofmeister, A.M., Corman, A.B., and Speck, A.K. (2008) *Astron. Astrophys.*, **483**, 661–672.
263. Bernatowicz, T., Fraundorf, G., Ming, T. *et al.* (1987) *Nature*, **330**, 728–730.
264. Zinner, E., Ming, T., and Anders, E. (1987) *Nature*, **330**, 730–732.
265. Ming, T., Anders, E., Hoppe, P., and Zinner, E. (1989) *Nature*, **339**, 351–354.
266. Hoppe, P. and Ott, U. (1997) in *Astrophysical Implications of the Laboratory Study of Presolar Materials*, American Institute of Physics Conference Proceedings, Vol. 402 (eds E.K. Zinner and T.J. Bernatowicz), AIP, College Park (MD), pp. 27–58.
267. Zinner, E. (1998) *Annu. Rev. Earth Planet. Sci.*, **26**, 147–188.
268. Gallino, R., Arlandini, C., Busso, M. *et al.* (1998) *Astrophys. J.*, **497**, 388.
269. Whittet, D.C.B., Duley, W.W., and Martin, P.G. (1990) *Mon. Not. R. Astron. Soc.*, **244**, 427–431.
270. Bernatowicz, T.J., Amari, S., Zinner, E.K., and Lewis, R.S. (1991) *Astrophys. J. Lett.*, **373**, L73–L76.
271. Bernatowicz, T.J., Cowsik, R., Gibbons, P.C. *et al.* (1996) *Astrophys. J.*, **472**, 760.
272. Kwok, S., Volk, K.M., and Hrivnak, B.J. (1989) *Astrophys. J. Lett.*, **345**, L51–L54.
273. von Helden, G., Tielens, A.G.G.M., van Heijnsbergen, D. *et al.* (2000) *Science*, **288**, 313–316.
274. Guo, B.C., Kerns, K.P., and Castleman, A.W. Jr. (1992) *Science*, **255**, 1411–1413.
275. Pilgrim, J.S. and Duncan, M.A. (1993) *J. Am. Chem. Soc.*, **115**, 9724–9727.
276. Patzer, A.B.C., Wendt, M., Chang, C., and Sülzle, D. (2011) in *Why Galaxies Care about AGB Stars II: Shining Examples and Common Inhabitants*, Astronomical Society of the Pacific Conference Series, Vol. 445 (eds F. Kerschbaum, T. Lebzelter, and R.F. Wing), ASP, San Francisco, p. 361.
277. Henning, T. and Mutschke, H. (2001) *Spectrochim. Acta*, **57A**, 815–824.

278. Huisken, F., Kohn, B., Alexandrescu, A. *et al.* (1999) *J. Nanopart. Res.*, **1**, 293–303.

279. Daulton, T.L., Bernatowicz, T.J., Lewis, R.S. *et al.* (2002) *Science*, **296**, 1852–1855.

280. Li, A. and Draine, B.T. (2001) *Astrophys. J.*, **550**, L213–L217.

281. Potrick, K., Schmidt, T., Bublitz, S. *et al.* (2011) *Appl. Phys. Lett.*, **98** (8), 083111.

282. Ledoux, G., Ehbrecht, M., Guillois, O. *et al.* (1998) *Astron. Astrophys.*, **333**, L39–L42.

283. Witt, A.N., Gordon, K.D., and Furton, D.G. (1998) *Astrophys. J. Lett.*, **501**, L111–L115.

284. Ledoux, G., Guillois, O., Huisken, F. *et al.* (2001) *Astron. Astrophys.*, **377**, 707–720.

285. Li, A. and Draine, B.T. (2002) *Astrophys. J.*, **564**, 803–812.

286. Ehbrecht, M. and Huisken, F. (1999) *Phys. Rev. B*, **59**, 2975–2985.

287. Ledoux, G., Guillois, O., Porterat,D. *et al.* (2000) *Phys. Rev. B*, **62**, 15942–15951.

288. Delerue, C., Allan, G., and Lannoo, M. (1993) *Phys. Rev. B*, **48**, 11024–11036.

289. Gordon, K.D., Witt, A.N., and Friedmann, B.C. (1998) *Astrophys. J.*, **498**, 522–540.

290. Ledoux, G., Gong, J., Huisken, F., Guillois, O., and Reynaud, C. (2002) *Appl. Phys. Lett.*, **80**, 4834–4836.

291. Wolkin, M.V., Jorne, J., Fauchet, P.M., Allan, G., and Delerue, C. (1999) *Phys. Rev. Lett.*, **82**, 197–200.

292. Debieu, O. (2007) *Silicon nanocrystals in matrices and their relation to the Extended Red Emission*. PhD thesis, Friedrich Schiller University, Jena, Germany.

293. Garrido, B., López, M., Pérez-Rodríguez, A. *et al.* (2004) *Nucl. Instrum. Methods B*, **216**, 213–221.

294. Guha, S., Qadri, S.B., Musket, R.G., Wall, M.A., and Shimizu-Iwayama, T. (2000) *J. Appl. Phys.*, **88**, 3954–3961.

295. Carrada, M., Wellner, A., Paillard, V. *et al.* (2005) *Appl. Phys. Lett.*, **87** (25), 251911.

296. Hofmeister, H., Huisken, F., and Kohn, B. (1999) *Eur. Phys. J. D*, **9**, 137–140.

297. Colder, A., Huisken, F., Trave, E. *et al.* (2004) *Nanotechnology*, **15**, L1–L4.

298. Ma, L.B., Schmidt, T., Jäger, C., and Huisken, F. (2010) *Phys. Rev. B*, **82** (16), 165411.

299. Kahler, U. and Hofmeister, H. (2001) *Opt. Mater.*, **17**, 83–86.

300. Witt, A.N., Gordon, K.D., Vijh, U.P. *et al.* (2006) *Astrophys. J.*, **636**, 303–315.

301. Vijh, U.P., Witt, A.N., and Gordon, K.D. (2005) *Astrophys. J.*, **633**, 262–271.

302. Nayfeh, M.H., Habbal, S.R., and Rao, S. (2005) *Astrophys. J. Lett.*, **621**, L121–L124.

7
Formation of Nanoparticles and Solids

Cornelia Jäger

7.1
Condensation of Cosmic Dust in Astrophysical Environments

Hans-Peter Gail

Dust forms in abundance during the final parts of stellar evolution. This has been found in various analyses, for example, by observations of infrared emission from warm dust with temperatures up to ≈1000 K from the environment of late-type stars, or from material ejected some time ago during stellar explosions. The details of the observations and the information obtained from remote sensing on the nature of the dust material, as well as on the properties of the dust-forming matter around the stars, were discussed in Chapter 5. In short, one observes dust formation at the end of life of all stars with initial stellar masses $M \gtrsim 0.8\,\mathrm{M}_{\odot}$, that is, stars with lives short enough so that one can observe their final evolutionary stages now.

An explanation of the observational findings requires the study of the physics of the outflows from stars, the chemistry operating in the cooling and expanding gas, including the formation and growth of dust particles, and the radiative transfer problem in the dusty shells surrounding the central stellar objects. This complex problem is not yet completely solved because of the strong nonlinear coupling of the different processes, each of which is difficult to solve by itself. Only separate treatments of the different major subproblems have had some success so far. In particular, the radiative transfer problem in dust shells can be treated for assumed dust abundances. In numerous studies, this has been used with much success to study the dust content of circumstellar dust shells by comparisons of theoretical models with observed spectra (cf. Chapter 5 and Ref. [1]) using laboratory-determined optical properties of candidate materials for circumstellar dust. Almost all our knowledge of dust production by stars is derived in this way.

In the following, we consider the problem of how dust may be formed in stellar environments, but we do not discuss details of the hydrodynamics and radiative transfer.

Laboratory Astrochemistry: From Molecules through Nanoparticles to Grains, First Edition.
Edited by Stephan Schlemmer, Thomas Giesen, Harald Mutschke and Cornelia Jäger.

7.1.1 Element Abundances in Dust-Forming Objects

The most important factor that determines the chemical composition and the quantities of dust that may be formed by a star is the element mixture in its surface material. At late evolutionary stages, element abundances in the stellar surface material frequently differ from the cosmic element mixture of the interstellar medium (ISM) from which stars form. Either material from the nuclear burning core region is transported to the surface by deeply extending convection zones or by large-scale circulation flows, or stellar winds peel the outer stellar layers until the material is exposed to the surface where formerly nuclear burning processes were active. In the following, we give a brief overview of the possible element mixtures at stellar surfaces.

7.1.1.1 Cosmic Standard Mixture

The element mixture of the ISM at the time and location of stellar birth determines the initial mix of chemical elements in a star. The ISM element mixture shows slight radial variations in the Milky Way's disk and varies in time by the chemical evolution of the Milky Way which results from element synthesis in stars and mass return by dying stars. The most notable evolutionary change of the element abundances is an increase of the abundances of elements heavier than He, the so-called metals, relative to H and He. Relative abundance variations between the metals are only moderate. Only their total abundance, the metallicity Z, increases over time. In our solar system and in the Sun, we find a snapshot of the ISM abundances at the solar birth place at an instant 4.57 Gyr ago. This element mixture of the solar system (e.g., Refs [2, 3]) is usually taken as the standard cosmic element mixture. For stars having metallicities Z other than the solar value of $Z_{\odot} = 0.0141$ [2, 3], one can scale the abundances according to the metallicity ratio. Though not exactly valid, for most purposes this is a sufficiently accurate approximation.

For the longer part of the stellar lifetime, this element mixture is found in the photosphere and in the material of the stellar wind. Even though stars become cool giant stars and start to form dust, this mixture is still preserved, except for some minor modifications (by first and second dredge-up) that are inconsequential for dust formation. At this stage of evolution, the stars are generally classified as being of spectral type M. Only at the very end of the stellar evolution does one observe substantial changes of the elemental composition of the surface layers, if products of nuclear burning processes are presented at the surface. This is accompanied by strong changes in the spectra of such stars. In the next sections, we will discuss the consequences of this, but for the moment we remain with the cosmic standard mixture.

From the 81 stable (H to Bi, without Tc, Pm) and two long-lived radioactive elements (Th, U), only those elements that form solid chemical compounds which are stable with respect to vaporization or decomposition up to rather high temperatures (at least > 1000 K) are of interest for the dust formation problem. Of these so-called refractory elements, the few that show the highest abundances will form

the dominating dust species. All other refractory elements with significantly lower abundances will at most be taken up as impurities by the main dust components into their lattice structure.

For the standard cosmic element mixture, the main dust-forming elements are the rock-forming elements Na, Mg, Al, Si, Ca, Ti, Fe, and Ni. With oxygen, they form a number of very stable oxides and mineral compounds, and they may also form an Fe/Ni alloy. Also some compounds with sulfur are very stable. Table 7.1 lists the most important species and some of their properties. There exist many more stable minerals; the table lists only compounds that either are observed to exist in circumstellar dust shells or could exist in theory.

The elements that do not participate in the formation of refractory condensed phases and preferentially stay in the gas phase are the so-called volatile elements. These are essentially the following ones: H, the noble gases, C, N, O, Cd, Hg, Tl, Pb, and Bi. Note that oxygen is grouped with the volatile elements even though it is an essential constituent of the crystal lattice of most refractory compounds. This is because only part of the oxygen is used in dust formation. The excess oxygen remains in the gas phase.

Some elements also form refractory compounds with C and N, but these are subject to rapid oxidation in an element mixture with an excess of oxygen. They

Table 7.1 Mineral compounds of the most abundant refractory elements, cosmic element mixture.

Mineral	Formula	T_m	T_b	T_v		cds	prae
—Pure substances—							
Forsterite	Mg_2SiO_4	2163		1055		√	√
Enstatite	$MgSiO_3$	1830 dec[a)]		1030		√	√
Corundum	Al_2O_3	2327	3250	1346		√	√
Hibonite	$CaAl_6O_{19}$	2181 dec[a)]		1340			√
Gehlenite	$Ca_2Al_2SiO_7$	1868		1184			
Spinel	$MgAl_2O_4$	2408		1104		√	√
Diopside	$MgCaSi_2O_6$	1664		1076			
Quartz	SiO_2	1978	2500	1030		√:	
—Solid solutions—							
Olivine	$Mg_{2x}Fe_{2(1-x)}SiO_4$	2180		1055	$x = 1$	√	√
		1776		950	$x = 0$		
Pyroxene	$Mg_xFe_{1-x}SiO_3$	1850		1030	$x = 1$	√	√
		1420			$x = 0$		
Wüstite	$Fe_xMg_{1-x}O$	1640		872	$x = 1$	√	
Nickel–iron	Fe_xNi_{1-x}	1808	3020	987	$x = 1$	√:	

[a)] Decomposes.

Temperatures T_m and T_b are the melting and boiling temperature, respectively, at laboratory conditions ($p \approx 1$ bar), and T_v is the evaporation temperature under circumstellar conditions ($p \approx 10^{-10}$ bar). It is indicated whether the species are detected in circumstellar dust shells (cds) by IR spectroscopy, or as presolar dust grain (prae); a colon indicates a tentative identification.

may be stable, however, in carbon-dominated environments that are encountered in part of the Asymptotic Giant Branch (AGB) stars and in Wolf–Rayet (WR) stars.

7.1.2 AGB Stars

Low- and intermediate-mass stars that have initial masses between $0.8\,M_\odot$ and $8\,M_\odot$ lose mass by stellar winds as they evolve upwards on one of the Giant Branches, first on the Red Giant Branch (RGB) and later on the AGB. On the upper part of the AGB, they start copious dust production in their outflows and develop optically thick circumstellar dust shells.

The post-main-sequence evolution of these single stars runs, in short, as follows: First they evolve to the RGB, where they burn H to He via the CN cycle in a shell source over a He core until He ignites in the core.

Stars with initial masses $M \lesssim 2\,M_\odot$ (low-mass stars) develop an electron-degenerated He core. They move up very high on the RGB and become cool M stars before they ignite He. At the tip of the RGB, they develop a strong stellar wind with substantial mass-loss rate (up to $10^{-6}\,M_\odot\,\mathrm{year}^{-1}$). The elemental composition of the stars corresponds to the cosmic standard mixture, except that most currently observed low-mass RGB stars ($\lesssim 1\,M_\odot$) are metal-poor ($Z \ll Z_\odot$) because of their long lifetimes. They formed many billion years ago when metallicity of the ISM was still low. Possibly, they do form dust on the tip of the RGB, but this has not yet been unequivocally demonstrated by observations of the characteristic infrared dust features of silicate dust, and theoretical reasons strongly argue against it [4].

Stars with initial masses $2\,M_\odot \lesssim M \lesssim 8\,M_\odot$ (intermediate-mass stars) do not evolve much upward on the RGB until they ignite He in a nondegenerate core. Since effective temperatures stay well above 3000 K and mass-loss rates remain low, such stars cannot form dust on the RGB.

After He ignition, there follows a phase of core He burning in which He is converted to C (and some O) by the 3α process. The stars are located to the left of the RGB, are too hot, and have much too low mass-loss rates to form dust. If the He core becomes exhausted of fuel, they evolve to the AGB where they burn He in a shell source over a degenerate carbon–oxygen core. The C–O core is covered by a thick He layer, and this in turn is enclosed by an enormously extended H-rich envelope. Hydrogen burns in a shell source at the interface between the He shell and the H-rich envelope. As the star evolves up the AGB, it becomes very cool and luminous and develops a massive stellar wind. Then conditions become favorable for dust formation. According to observations, all stars on the upper part of the AGB are enclosed by dust shells that become increasingly optically thick as the stars grow cooler and more luminous. Finally, the mass-loss rate increases to such a level ($> 10^{-5}\,M_\odot\,\mathrm{year}^{-1}$) that the whole H-rich envelope over the core is lost in a few thousand years and the exposed core region develops into a White Dwarf star. Figure 7.1a shows for stars of initial mass $2M_\odot$ and $3M_\odot$ and initial metallicity $Z = 0.008$ (typical for stars in the Large Magellanic Cloud) how the stellar mass

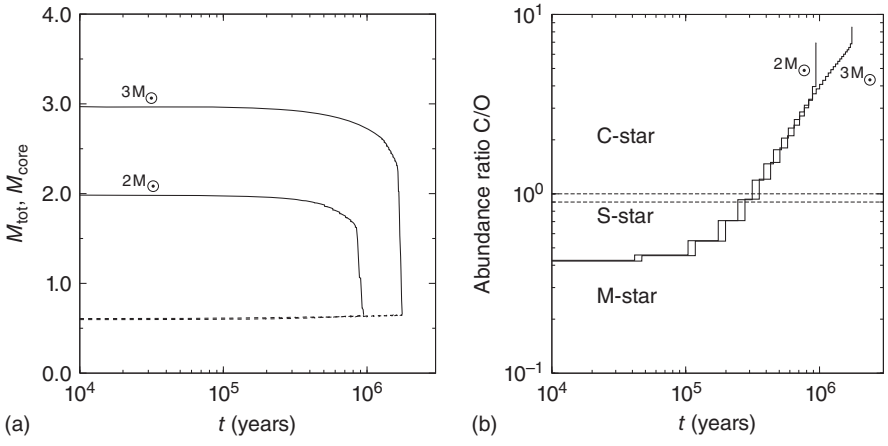

Figure 7.1 (a) Evolution of total mass (full line) and mass of the CO core (dashed line) of AGB stars with initial masses of $2\,M_\odot$ and $3\,M_\odot$ (synthetic AGB models, see Ref. [5]). The timescale refers to the time elapsed after the first thermal pulse. Most part of the envelope is lost in a very brief superwind phase with $\lesssim 10^5$ year duration. (b) Evolution of the carbon/oxygen abundance ratio at stellar surface for the same AGB models. For C/O ratios $\lesssim 0.9$, a star appears spectroscopically as an M star and for C/O ratios $\gtrsim 1$ as a C star. The in-between stars are of the rare transition type S.

evolves during the final million years of the star's life. It is thought that efficient dust formation is limited to the brief final superwind phase and that mass loss is driven in this evolutionary phase by radiation pressure on the dust.

7.1.2.1 Element Abundance Evolution on the AGB

During the initial evolution on the AGB, the elemental composition of the H-rich envelope corresponds essentially to the cosmic standard mixture and the stars appear spectroscopically as M stars.

If He burning at the interface between the He shell and the CO core has consumed almost the whole He layer, the star starts a sequence of thermal pulses where He and H burn intermittently, first He in a violent flash of a few hundred year's duration, followed by a long phase of H burning of several thousand years, thereby recovering the He layer for the next flash. During this phase, the star consists of an electron-degenerated CO core ($\approx 0.7 \ldots 1.1\,M_\odot$) with an overlying thin He layer ($\approx 0.02\,M_\odot$), enclosed in the extended, fully convective H-rich envelope. The He layer is highly carbon-rich because, during a flash, part of the C resulting from He burning at its bottom is mixed across the He shell. After a few such pulses, the convective zone of the envelope starts to penetrate briefly into the He layer after each thermal pulse and mixes some material from this zone with the envelope material. He and C as well as other nucleosynthetic products, for example, s-elements, are mixed in this way into the stellar envelope, the so-called third dredge-up. The C/O abundance ratio at the stellar surface then increases

stepwise after each thermal pulse (Figure 7.1b), and after a number of pulses the C/O ratio exceeds unity. From that moment on, the star is a carbon star.

The final value of the C/O ratio at the very end of the AGB evolution is small and can take values as high as ≈10, Figure 7.2. The observed values for the C/O ratio in stellar atmospheres are usually <1.2 because at higher values the stars are completely obscured by an optically thick dust shell and no stellar spectrum can be observed. Only if finally the naked degenerate core, the White Dwarf, is exposed and dust formation is shut off can one observe in the planetary nebula the final high (≳2) C/O ratios achieved during the superwind phase.

Not all AGB stars finally develop into C stars. First, as can be seen from Figure 7.1b, a number of thermal pulses are required to mix sufficient amounts of carbon into the envelope, so that the C abundance increases over the O abundance. Very low mass stars ($M \lesssim 1.5\,M_\odot$ for solar metallicity, the limit decreases with decreasing Z) suffer too few pulses before the envelope is completely lost. They always stay oxygen-rich. Second, stars from the higher end of the range of intermediate masses ($M \gtrsim 4\,M_\odot$, the limit decreases with decreasing Z) are sufficiently hot at the bottom of their envelope convection zone to convert the dredged-up carbon into nitrogen via $^{12}C(p,\gamma)^{13}N(\beta^+\nu)^{13}C(p,\gamma)^{14}N$ while the oxygen abundance remains essentially unchanged. These stars also do not become carbon stars. Figure 7.2 demonstrates that most, but not all, stars evolve into carbon stars. The fraction of carbon stars increases with decreasing metallicity; in the Small Magellanic Cloud with one-fourth of the solar metallicity, for example, O-rich giants are rare.

The transition from the oxygen-rich composition to the carbon-rich composition changes the whole chemistry in the stellar atmosphere and in the stellar outflow. For C/O ratios <1, the chemistry is dominated by O-bearing molecular

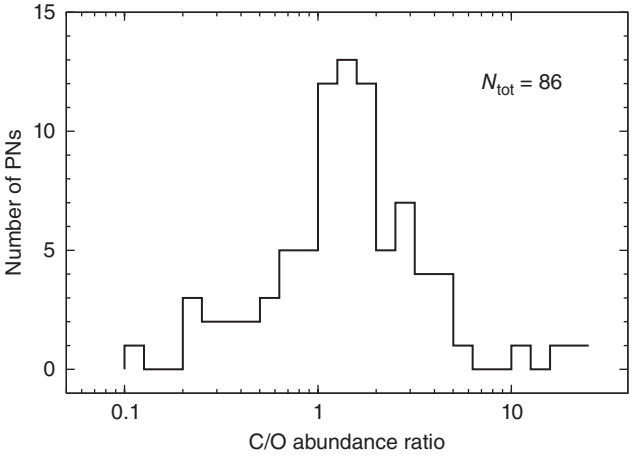

Figure 7.2 Carbon/oxygen abundance ratios observed in planetary nebula. (Data mainly from Ref. [6].). These are the descendants of the AGB stars and represent a transition stage on the way to the White Dwarfs sequence.

compounds and oxidic condensed phases, while C is completely locked in the CO molecule. The stars appear spectroscopically as M stars for which the optical spectrum is dominated by molecular bands of TiO. For C/O ratios > 1, the gas-phase chemistry is dominated by hydrocarbons, and the condensed phases are dominated by carbides, sulfides, and nitrides. In the C-rich case, the O is completely locked in the CO molecule. The stars appear spectroscopically as C stars,[1)] where the optical spectrum is dominated by molecular bands of CN and C_2. The strongly different kinds of chemistry encountered in M and C stars require treating these cases separately.

In the transition region, $C/O \approx 1$, the stars are of spectral type S, where molecular bands of some rare molecules with extremely high bond energies, such as VO and LaO, dominate the optical spectrum. The chemistry in this case is very peculiar and not yet adequately studied. Part of the S stars show lines of the unstable element Tc in their spectra, which is synthesized in the He shell by the s-process and dredged up into the atmosphere during thermal pulses. In S stars, we can directly observe the effect of the dredge-up processes. In thermally pulsing M and C stars, the Tc lines should also be present but are hard to detect for a number of reasons.

7.1.3 Massive Stars

Massive stars, from the mass range of $8\,M_\odot$ to about $40\,M_\odot$, finally evolve to the RGB and start massive dust production once they arrive on the upper part of the RGB. They finally explode as supernovae (SN) and, at least in some cases, also form dust in the mass shell ejected by the SN. The elemental composition of the envelope corresponds essentially to the cosmic standard mixture at their birth. On the RGB, the stars appear spectroscopically as M stars, the so-called supergiants.

Massive stars from the mass range $M \gtrsim 40\,M_\odot$, all seem to evolve through a stage where they are Luminous Blue Variables (LBVs) which suffer sporadic massive mass-ejection events accompanied by copious dust formation (like in the event observed around 1840 for η Car). Their mass loss is so strong that they fail to enter the RGB stage and lose most of their initial mass before they explode. During the course of this process, mass layers are exposed to the surface where formerly nuclear burning processes operated.

First, material is presented in which the CNO cycle operated. Hydrogen gradually disappears at the expense of He; the nuclei of C, N, and O approach their equilibrium abundances in the CNO cycle. The result is that the initial inventory of C, N, and O is almost completely converted into ^{14}N. The C and O abundance drops below the abundance of the refractory elements Si, Mg, Fe, and so on, but the element mixtures stays oxygen-rich, see Figure 7.3.

1) Occasionally, the older designation of spectral classes R and N are used, where N are the cooler ones.

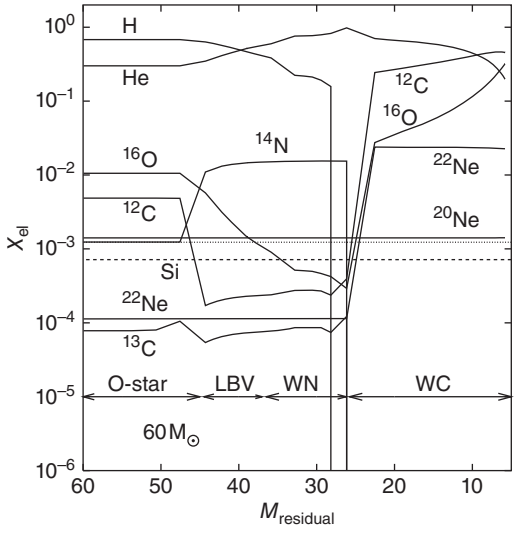

Figure 7.3 Evolution of surface mass fractions X_{el} of a number of elements for a non-rotating star with 60 $M_\odot$ initial mass and solar metallicity. (Model from Ref. [7].) The abscissa is the residual mass of the star left over after long-lasting strong stellar wind mass loss. The dashed line corresponds to the Si abundance and the dotted line to the minimum abundance of O required to form normal silicate dust.

Initially, such stars appear spectroscopically as normal O stars; finally they evolve into WN stars, characterized by a high N abundance in the stellar atmosphere. The stars are too hot for dust formation to be possible. At some intermediate stage during the evolution, at least part of the massive stars become the so-called LBVs that suffer strong outbursts where large amounts of mass (up to a few $M_\odot$) are ejected as an expanding shell. Copious dust formation is observed to occur in these shells, for example, in the 1840 outburst of η Car. The element mixture in this stage seems to correspond to the mixture indicated in Figure 7.3 as LBV, where the O abundance is strongly reduced. This differs from the element mixture in O-rich AGB stars since there is a scarcity of oxygen to convert all refractory elements into oxides if condensation becomes possible. Next, material appears at the surface where He burning operated (in the model shown in Figure 7.3, after 34 $M_\odot$ of the initial mass is lost). H is completely absent from the stellar envelope which essentially consists of He, ^{12}C, and some ^{16}O. The star appears from that point on spectroscopically as a WC star. This element mixture prevails until the star finally explodes (or collapses into a Black Hole).

WC stars are observed to form dust, at least some of them. The element composition of the WC stars differs from that of carbon stars on the AGB because of the lack of any hydrogen.

7.1.4 Condensation Sequences

The kind of dust formed by stars is different for different stellar types and may change during their evolution. Observationally, this is known from the different characteristics of the infrared emission from circumstellar dust shells (Chapter 5). It is evident that the composition of the dust mixture depends strongly on the element mixture in the ejected material, which may be significantly different for different stars and for different evolutionary phases, as we have just seen. One has to consider the different possible element mixtures separately.

From the theoretical side, strong hints on the mixture of dust species expected to be formed in a particular element mixture can be obtained by calculations of gas–solid chemical equilibria at the typical pressures encountered in the condensation zone of circumstellar dust shells and for the range of temperatures of interest. If a gas with a given chemical composition cools down, it becomes unstable with respect to formation of a condensed phase at a certain temperature. This occurs if the cooling trajectory of the gas in the pressure–temperature plane crosses the stability limit curve of the condensate given by (law of mass action)

$$1 = \prod_i p_i \, \exp\left(-\frac{\Delta G}{RT}\right) \tag{7.1}$$

with p_i being the partial pressures of the molecules (or atoms) of the gas phase from which the condensate can be formed and ΔG the difference between the free enthalpy of formation of the solid and the free enthalpies of formation of the molecules. From such calculations, one can find the species that exist at the highest temperatures in the given chemical environment, at least under chemical equilibrium conditions. In the past, such calculations helped greatly the interpretation of the first observational findings on circumstellar dust [8, 9] and on presolar dust grains [10, 11]. The theoretical background and the methods of such calculations are described in detail in Ref. [12]; special applications of the method to mineralogical problems that are also of relevance to cosmic dust are described, for example, in Refs [13–15].

Such calculations show that the basic characteristics of the chemistry are governed by the C/O abundance ratio. Because of the extraordinarily high bond energy of the CO molecule, the less abundant of the two elements O and C is completely consumed by CO formation and is essentially unavailable for the formation of other chemical compounds. In oxygen-rich element mixtures, therefore, it is possible to form from the refractory elements their oxides and related compounds, such as the typical rock minerals. In carbon-rich element mixtures, one may form, instead, carbides (including solid carbon, which in astrophysics is frequently denoted as graphite), nitrides, and sulfides of the refractory elements.

The two main oxygen-rich mixtures encountered in stars, element abundances of some characteristic elements, and the main condensed phases in chemical equilibrium are listed in Table 7.2. The H-dominated mixture is that which is typically

found in M stars on the AGB and in massive RGB stars (supergiants). The suite of condensed phases predicted from equilibrium calculations is also found in IR observations from circumstellar dust shells around M stars, and most of them also have been detected as presolar dust grains, see Table 7.1. The He-dominated phase is found in dust-forming LBVs which seem to form a somewhat different dust mixture (e.g., Refs [16, 17]).

For the three main carbon-rich mixtures encountered in stars, element abundances of characteristic elements and the main condensed phases in chemical equilibrium are listed in Table 7.3. The H-dominated mixture is found in carbon

Table 7.2 Main condensed phases in chemical equilibrium for stars with an oxygen-rich element mixture (see, e.g., Ref. [10]) and particle concentrations of some elements.

Element mixture	:	**H-dominated**	**He-dominated**
Stellar type	:	**M stars**	**WN stars, LBVs**
Element abundances			
H	:	0.93	0.0
He	:	0.065	0.996
C	:	0.00037	0.0012
N	:	0.00011	0.00037
O	:	0.00063	0.0021
Condensed phases			
		Mg_2SiO_4, $MgSiO_3$, Fe	FeSi, Fe, Mg_2SiO_4
		Al_2O_3, $CaAl_{12}O_{19}$, $MgAl_2O_4$	Al_2O_3, $MgAl_2O_4$
		$Ca_2Al_2SiO_7$, $CaMgSi_2O_6$	MgS
		$CaTiO_3$, TiO_2	TiC, TiN, $CaTiO_3$

The abundances of refractory elements correspond essentially to the cosmic standard mixture.

Table 7.3 Main condensed phases in carbon-rich stars in chemical equilibrium (see, e.g., Ref. [10]) and particle concentrations of some elements.

Element mixture	:	**H-dominated**	**He-dominated**	**C-dominated**
Stellar type	:	**C stars**	**post-AGB, R CrB stars**	**WC stars**
Element abundances				
H	:	0.93	0.0	0.0
He	:	0.065	0.994	0.0
C	:	0.00094	0.0032	0.65
N	:	0.00011	0.00037	0.0
O	:	0.00063	0.0021	0.32
Condensed phases				
		C, SiC, Fe	C, SiC, Fe_3C, Fe	C, SiC, Fe_3C, Fe
		AlN, Al_2O_3, $MgAl_2O_4$	AlN, Al_2O_3, $MgAl_2O_4$	Al_2O_3, $MgAl_2O_4$
		CaS, MgS	CaS, MgS	CaS, MgS
		TiC	TiC	TiC

The abundance of refractory elements corresponds essentially to cosmic standard mixture.

stars on the AGB. The two other mixtures are found in the rare R CrB and in WC stars. From the predicted condensed phases, only graphite, SiC, and MgS are detected in IR observations, and graphite and SiC as presolar dust grains. Titanium carbide is detected not as a separate dust species but as an inclusion in presolar carbon grains. The carbon-rich mixtures are further considered in Section 7.1.9.3.

Figure 7.4a shows the temperatures of appearance of condensed phases of the most abundant refractory elements Si, Mg, Fe, Al, Ca that exist in an oxygen-rich element mixture. "Temperature of appearance" means that the indicated mineral starts to form at this temperature in a cooling environment. In chemical equilibrium, one has a well-defined ordering of the different minerals that are expected to form, starting with aluminum and calcium compounds at high temperature, followed by the silicates and iron at lower temperatures. The silicates and iron are more abundant because Mg, Si, and Fe are more than 10 times more abundant than Al and Ca; that is, the dust mixture is strongly dominated by the silicates.

The mineral mixture shown in Figure 7.4a is calculated under the assumption that only pure substances condense from the gas phase. However, many minerals form solid solutions with a number of other minerals, in particular if they have similar lattice structures. If the solution components have mole fractions exceeding 5%, they are called *major components*. Between 5% and 0.1% abundance, they are called *minor solution components*, and for <0.1% abundance they are called *impurities*. Table 7.4 shows the important cosmic minerals that are known to form solid solutions. In particular, the dominating dust components of M stars, namely the silicates, form the following two solid solutions:

1) Olivine with the composition $Mg_{2x}Fe_{2(1-x)}SiO_4$. The end members of this solution series are forsterite (Mg_2SiO_4) and fayalite (Fe_2SiO_4). The mixing ratio x can take any value $0 \leq x \leq 1$.

Table 7.4 Composition of some solid solutions and how such grains are detected. In the last column, "rs" means that solid solutions are detected by the composition-dependent spectral features (remote sensing), and "prae" means the composite nature is found by laboratory analysis of presolar dust grains.

Solid solution	Major components	Detected
Olivine	Mg_2SiO_4, Fe_2SiO_4, Ni_2SiO_4	rs, prae
Ortho-pyroxene	$MgSiO_3$, $FeSiO_3$, $CaMgSi_2O_6$, Al_2O_3	rs, prae
Clino-pyroxene	$MgSiO_3$, $FeSiO_3$, $CaMgSi_2O_6$, Al_2O_3, $NaAlSiO_3$	rs, prae
Spinel	$MgAl_2O_4$, $FeAl_2O_4$	
Melilite	$Ca_2Al_2SiO_7$, $Ca_2MgSi_2O_7$	
Fe, Ni alloy	Fe, Ni, Si	prae (subgrains)
Silicon carbide	SiC, AlN	prae
Titanium carbide	TiC, MoC, VC	prae (subgrains)

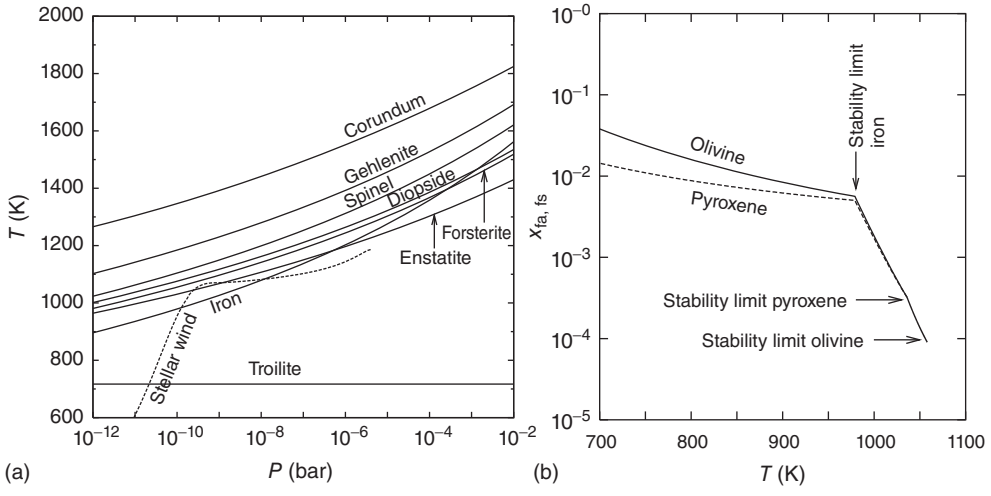

Figure 7.4 Temperatures of appearance or disappearance of condensed phases in chemical equilibrium (a) for a cosmic standard element mixture. The dotted line shows the temperatures and pressures along a stationary outflow from an AGB star. (b) The iron content of silicates in chemical equilibrium at a pressure of 10^{-10} bar.

2) Pyroxene with the composition $Mg_xFe_{1-x}SiO_3$. The end members of this solution series are enstatite ($MgSiO_3$) and ferrosilite ($FeSiO_3$). The mixing ratio x also can take any value $0 \leq x \leq 1$, at least in principle.[2)]

The pyroxene exists in two modifications (ortho-pyroxene and clino-pyroxene) with slightly different arrangements of the SiO_4 tetrahedrons (cf. Ref. [14]) which are the basic building block of all silicates. The pyroxenes also take up many other solution components, in particular, Al and Ca compounds. Their composition can be very complex for this reason. In principle, they can serve as the ash that takes up all refractory elements from the whole periodic table of elements as impurities. For olivine, this is possible only to a limited extent. For presolar silicates, laboratory analysis shows that they frequently contain, indeed, Al and Ca compounds as minor solution components [18–20].

At chemical equilibrium, the composition of the solid solutions is not arbitrary. The composition is uniquely determined at each pressure and temperature by the thermochemical equilibrium conditions between all components in the system, from which the composition can be calculated [13, 21]. In particular, the mole fractions x_{Fa} and x_{Fs} of the iron-bearing silicates fayalite and ferrosilite in olivine and pyroxene, respectively, have well-determined values. Figure 7.4b shows the equilibrium values of x_{Fa} and x_{Fs} at a typical pressure of 10^{-10} bar in the condensation zone of a stellar wind. The iron content at chemical equilibrium is low, at most a small percentage; this is in the range where it would be considered as an

2) The pure end member fayalite seems to decompose into FeO and SiO_2; it possibly exists only at elevated pressures.

impurity or at most as a minor component. Under equilibrium conditions, most of the Fe does not condense in silicates but exists as metallic iron grains.

This prediction from equilibrium chemistry is not in accordance with what one derives from IR observations for silicate dust in circumstellar shells (cf. Ref. [1] and Chapter 5) and with what is found by laboratory analysis of presolar silicate grains [18–20, 22]: The silicates are generally found to contain iron silicates as a major solution component. This shows that the conditions under which the condensation process occurs in circumstellar dust shells are far from chemical equilibrium. Since in silicates the Fe^{2+} and Mg^{2+} cations can be easily interchanged, it is possible that under nonequilibrium conditions all or most of the iron is taken up by olivine and pyroxene once the vaporization rate of the less stable Fe-bearing component drops below the growth rate during rapid cooling. Two other facts that point to nonequilibrium are as follows: (i) quartz and wüstite seem to be formed in stellar outflows (cf. Table 7.1, Section 5.5, and Ref. [1]), though these oxides would not form under chemical equilibrium conditions; (ii) melilite has not yet been found, but all other possible Ca/Al compounds have been. Hence, one has to accept the predictions from equilibrium calculations with some caution, but this does not make equilibrium calculations entirely useless.

7.1.5
Principles of the Dust Formation Process

From a microscopic point of view, the formation of mineral particulates in a stellar outflow is a complex sequence of chemical reactions which starts from simple atoms and molecules in the gas phase and proceeds toward forming more and more complex molecular aggregates, the so-called clusters, that may contain dozens or hundreds of atoms. At some point, there occurs a transition, during which the properties of the clusters change to those of solid particles, and further addition of material can be conceived as the growth of a tiny particulate by the precipitation of material from the gas phase. The dust formation process can therefore be considered as being essentially a two-step process: (i) the creation of surfaces, and (ii) the surface growth of particulates to macroscopic dust grains. The first part of the problem requires studying the reaction kinetics in the gas phase, and the second part the reaction kinetics at the surface of grains.

Let us consider the first step, that is, the formation of the first surfaces. As Figure 7.4a shows (cf. also Figure 7.8 for the carbon-rich case), usually more than one kind of condensed material can be formed in a gas of a given elemental composition. It is frequently assumed that (i) the first material formed is that for which the chemical system first becomes unstable with respect to the phase transition and (ii) condensation commences immediately after the stability limit is crossed. Laboratory experiments show, however, that frequently it is not the thermodynamically most stable condensate which is formed first and that condensation in a cooling gas usually occurs with a considerable delay if the gas has significantly cooled below the stability limit.

The requirement of strong supercooling results from the fact that the condensation process is basically a long chain of chemical reactions

$$A_1 \xrightarrow{+A_1} A_2 \xrightarrow{+A_1} A_3 \xrightarrow{+A_1} A_4 \xrightarrow{+A_1} \cdots \longrightarrow \text{solid}$$

where a certain "growth species" (A_1) is added stepwise to form clusters of increasing complexity. The onset of condensation requires that the whole sequence of reactions becomes possible and that all members of the reaction chain are formed in sufficient quantities so that association reactions to the next member on the chain proceed fast enough to pass through the whole sequence of reactions in a finite amount of time. If only one member of the chain is readily dissociated at the given temperature and pressure conditions, condensation does not occur under these conditions. Thus, the abundance of the least stable member on the reaction chain governs the possibility or impossibility of condensation. Usually, the small molecules on the initial part of the reaction chain are more loosely bound than the bulk material. They are formed in sufficient quantities only if the temperature is sufficiently reduced below the stability limit of the condensate.

The rate of formation J_* of condensation nuclei, hence, is given by

$$J_* = n_{\mathrm{gr}} v \sigma \alpha n_{\mathrm{cr}} \tag{7.2}$$

with n_{cr} being the particle density of the least abundant intermediate cluster on the reaction chain from molecules to dust — the critical cluster — which forms the bottleneck of the whole process. n_{gr} is the particle density of the growth species responsible for the transition from the critical cluster to the next more stable member of the reaction chain, v is the average thermal velocity of the growth species, σ is the collision cross section, and α is the reaction probability. For condensation under near-stationary conditions, it can be shown that n_{cr} can be calculated from the law of mass action:

$$\frac{p_{\mathrm{cr}}}{\prod_i p_i} = \exp\left(-\frac{\Delta G}{RT}\right) \tag{7.3}$$

where p_{cr} is the equilibrium partial pressure of the critical cluster and p_i are the partial pressures of the molecules from which the critical cluster is formed (e.g., Ref. [23]). The process of formation of the critical cluster, thus, depends on the chemical properties of the molecules and the small clusters on the initial part of the reaction chain. Their properties may be quite different from those of the final condensed phase.

If there exist several competing reaction chains, obviously the most efficient one with the highest nucleation rate J_* wins. It is not necessarily the most stable condensate (i.e., one that first becomes thermodynamically stable during cooling) that forms but the one for which the first efficient reaction chain starts to operate.

Thus, if we intend to find out the processes responsible for dust formation in circumstellar shells, we have to go through the following steps:

1) Determine the molecular composition of the gas. This determines the raw material from which the condensate forms.

2) Determine the possible condensates that might be formed from these molecules, Eq. (7.1).
3) Find out the possible reaction paths from molecules to large clusters and determine the corresponding critical cluster by means of Eq. (7.3).
   Then we have to determine from Eq. (7.2) the most efficient reaction chain operating at the highest temperature. This determines the dust formation process.
4) For this most efficient nucleation process, we have to determine the growth processes from large clusters to macroscopic grains. This determines the kind of dust material finally formed in the condensation process.

Up to now, it has not been possible to follow this program in complete generality. Only very preliminary results have been obtained so far. They are discussed in Sections 7.1.8 and 7.1.9.

Once the first surfaces are formed, they may serve as substrates for surface growth of other dust materials, except for materials with incompatible lattice structures.

7.1.6
Condensation Temperature

One important piece of evidence on the condensation process in stellar dust shells comes from the observed condensation temperatures.

Dust is formed in circumstellar environments of giant stars in an outflow from a stellar surface that is much too hot to allow condensation of solids in the stellar photosphere itself, much less in deeper layers. According to interferometric observations (e.g., Ref. [24]) and dust-shell modeling, condensation commences at distances of several ($\approx$5, … 15) stellar radii, R_*, above the photosphere. The temperature of the hottest grains that contribute to the observed infrared emission is taken to be the condensation temperature of dust. It usually refers to the dust components with high abundances. Minor components that contribute insignificantly to the observed spectra could have even higher temperatures.

Because of the different extinction behaviors of gas and dust with wavelength, the gas temperature at the location of the hottest observed grains may be different. The *gas temperature* governs the initiation of condensation from the gas phase if seed particles for particle growth do not yet exist and still have to be formed from the gas phase. The *dust temperature* determines the onset of condensation if the condensable material precipitates on already existing surfaces.

Figure 7.5 shows the temperature at the inner boundary of the dust shell for a rather homogeneous dataset for giants from the Large Magellanic Cloud, that is, for objects with known luminosity (because distance is accurately known), all analyzed with the same method and the same radiative transfer code [25]. The mass-loss rates are dust-loss rates converted to total mass loss with an assumed gas-to-dust ratio; these rates are only estimates. Much more data are available

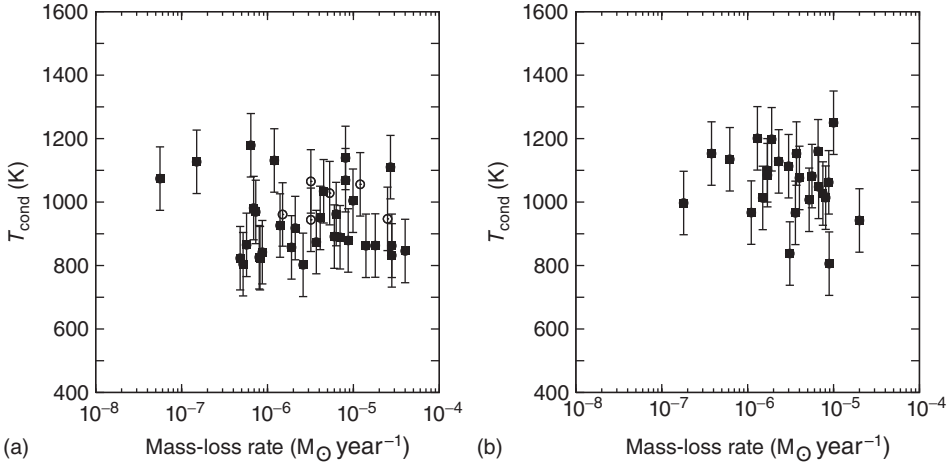

Figure 7.5 Condensation temperature of dust in (a) oxygen-rich objects and (b) carbon-rich objects with different mass-loss rates, derived by modeling the IR emission of a sample of stars from the Large Magellanic Cloud. (Data from Ref. [25].) Error bars correspond to an estimated uncertainty of the T_{cond} determination of about ±100 K. Open circles correspond to supergiants, and filled squares to AGB stars.

from the literature than those shown in Figure 7.5, but they are not easily comparable because of the different approaches used by the different authors in analyzing the spectra. The accuracy of condensation temperatures derived by this method is rather poor, perhaps on the order of ±100 K, and there is large scatter in the data. But it is clear that condensation temperatures are all on the order of 1000 K – for oxygen-rich objects on average even somewhat lower, and for carbon-rich objects on average perhaps slightly higher.

The gas temperature at the inner edge of the dust shell cannot be readily determined from observations. An estimate can be obtained as follows: In radiative equilibrium and for optically thin dust shells, one has, at the inner edge of the envelope, for the temperature of gas and dust $\varkappa_{d,g}(T_{g,d})T_{g,d}^4 = W\varkappa_{d,g}(T_*)T_*^4$, with $\varkappa_{d,g}$ being the Planck average of the dust or gas absorption coefficient and W the geometric dilution factor. The ratio of dust-to-gas temperature is then

$$\frac{T_d}{T_g} = \left[\frac{\left(\frac{\varkappa_g(T_g)}{\varkappa_g(T_*)}\right)}{\left(\frac{\varkappa_d(T_d)}{\varkappa_d(T_*)}\right)}\right]^{\frac{1}{4}} \tag{7.4}$$

The absorption coefficients $\varkappa_{d,g}(T_{g,d})$ correspond to that at about 1 μm for T_* and 3 μm for $T_{g,d}$. For the oxygen-rich mixture, the first ratio on the right-hand side is about 10 (cf. Ref. [26]), while the second is for dirty silicate dust on the order of 2 and for amorphous silicates on the order of 3. The temperature of the gas is significantly lower, by a factor of about 2, than the dust temperature. Inspection of Figure 7.4a indicates then that silicate dust condensation seems to commence

in most cases at a substantial degree of supercooling below the stability limit of the silicates (at ≈1100 K). This behavior is characteristic for a condensation process that starts with the formation of seed particles from the gas phase. Growth on pre-existing seed particles slightly below the stability limit does not seem to be the standard route to silicate dust formation. However, this route cannot be completely excluded since the data points in Figure 7.5a suggest that it might be followed in some cases.

In the case of carbon stars, the observed condensation temperatures are much lower than the stability limit of solid carbon (Figure 7.8). Carbon dust formation obviously occurs under extreme nonequilibrium conditions. This will be considered later.

7.1.7
Reaction Kinetics

The chemical composition of the gas phase determines the material that is available for dust formation. With very few exceptions, the composition of stellar outflows with dust condensation is calculated by assuming that the molecular composition of the gas phase is the same as in a chemical equilibrium state at the local pressure and temperature in the wind. However, if an outflowing gas element enters the dust condensation zone, the particle density is already rather low and the timescales of many chemical reactions become comparable to the characteristic timescales for changes of temperature and particle densities. Under such circumstances, the composition is determined by the kinetics of the chemical reactions and this is ruled more by the reaction cross sections than by the energy levels of the involved particles as in chemical equilibrium. Then, one has to solve the set of transport–reaction equations

$$\frac{\partial c_i}{\partial t} + v\frac{\partial c_i}{\partial r} = \sum_{j,l} k_{i,j,l}\, N_{\mathrm{H}}^2\, c_j c_l + \sum_{j,l,m} k_{i,j,l,m}\, N_{\mathrm{H}}\, c_j c_l c_m \tag{7.5}$$

for each species i and all possible binary and ternary reactions between them. Here, v is the velocity of the outflow, c_i is the concentration of species i relative to hydrogen nuclei, and N_{H} is the particle density of H nuclei. Only a few studies of the chemistry based on numerical solutions of this system of rate equations in the O-rich or C-rich case have been performed (e.g., Refs [27–30]).

The main problem with this approach is that one needs to know all rate coefficients $k_{i,j,l}$ and $k_{i,j,l,m}$ for all relevant binary and ternary reactions, respectively. Fortunately, for the special case of the gas-phase chemistry in outflows from late-type stars, the chemical reactions occur in an environment that is characterized by high, but not extremely high, temperatures, and low, but not extremely low, pressures. The inner dust-forming region of the outflow is shielded from the outer harsh interstellar UV radiation by the dust, such that the degree of ionization in the dust-forming zone is low and only reactions between neutral species are important. The conditions in outflows are then to some extent similar to those under which some technically important combustion systems operate, and one can take

advantage of the fact that the reaction kinetics of flames is frequently studied in the laboratory by means of low-pressure flames. Appropriate datasets have been determined and validated by experimental studies involving the important species that need to be considered and the rate coefficients of the important reactions. For astrophysical applications, two special kinds of combustion processes are of interest:

1) Silane combustion. The elemental composition in stellar outflows from oxygen-rich stars corresponds to a large extent to the elemental composition of the fuel gas mixtures used in studies of silane flames.
2) Combustion of hydrocarbons. The elemental composition in stellar outflows from carbon-rich stars corresponds to a large extent to the elemental composition of the fuel gas mixtures used in burners and engines.

The main difference between flames studied in the laboratory and stellar outflows is the huge excess of hydrogen over all other elements in stellar winds; but it is not to be expected that this strongly modifies the general reaction schemes since hydrogen is already abundant in the flames studied in the laboratory. Another major difference is that there is a certain degree of ionization due to chromospheric UV fields (e.g., Ref. [28]) and radioactivity (cf. Ref. [31]), but no systematic studies on the role of ionization for the chemistry in the innermost parts of the outflows from late-type stars presently exist.

7.1.8 Mineral Formation in M Stars

7.1.8.1 Gas-Phase Composition

For the problem of silicate dust in outflows from M stars, one has to study in particular the H–O–Si chemistry. The H–O–Si chemistry has been well studied for silane (SiH_4) combustion, and appropriate reaction networks for modeling this kind of chemistry are available [32, 33]. Figure 7.6a shows a result for modeling the Si chemistry in a cooling flow with hydrogen nuclei density of $N_H = 10^{12}\,cm^{-3}$ that cools with a rate of $dT/dt = 3\,K\ year^{-1}$. The reaction network includes the clusters $(SiO)_n$ and $(SiO_2)_n$ with n up to 10. This corresponds to conditions close to those in the star. It is seen (i) that Si is almost quantitatively converted to SiO already at the base of the outflow, and (ii) that below ≈1200 K the Si chemistry starts to freeze out because of low particle density. At a temperature of ≈600 K, efficient clustering of SiO into $(SiO)_n$ clusters commences and consumes all silicatic material from the gas phase. This clustering of SiO is shown in more detail in Figure 7.6b for a model with more rapid cooling at a rate of $30\,K\,year^{-1}$, which corresponds more closely to the conditions in the dust-formation zone.

7.1.8.2 Seed Particles

At first glance, the SiO molecule seems to be the most likely candidate for the nucleation of seed particles (see Refs [35–37]) because this species satisfies two of the most important conditions: it has a very high bond energy, and it has a very

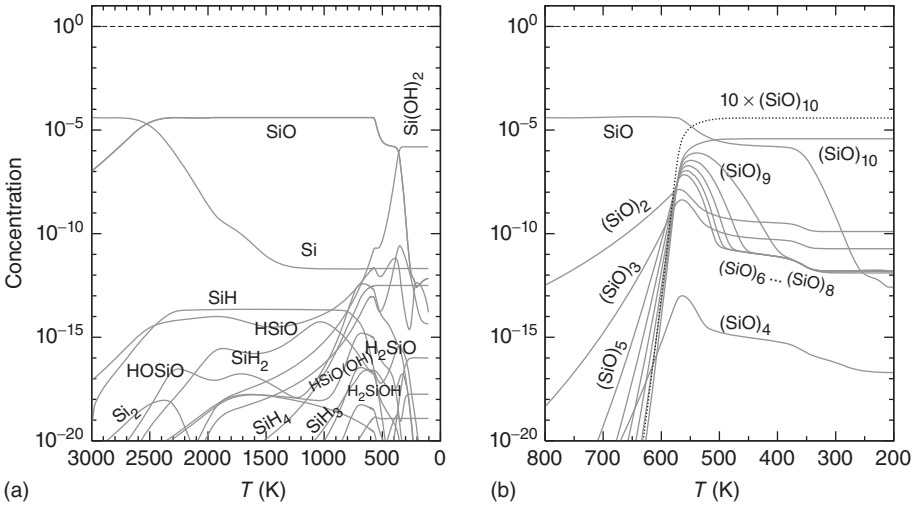

Figure 7.6 Temperature variation of abundances of (a) Si-bearing gas-phase species ($(SiO)_n$ clusters are not shown) and (b) of $(SiO)_n$ ($n = 1, \ldots, 10$) clusters in a cooling gas at a density of $N = 10^{10}\,\mathrm{cm}^{-3}$ hydrogen nuclei. Densities of $(SiO_2)_n$ clusters are negligibly small.

high abundance in the gas phase. In the past, it seemed not to satisfy, however, the requirement that the condensed phase has a high vaporization temperature. Based on published thermodynamic data, SiO seemed to have a much too low condensation temperature under circumstellar conditions to be the first condensed phase [37]. A recent redetermination of the vapor pressure of SiO [38, 39] indicates the older data to be considerably in error, and SiO has still to be considered as a candidate for the condensation of silicate dust [38, 40–42].

This is also strongly supported by models of silane combustion, where clustering of SiO molecules seems to be the initial step for the formation of silica dust particles [32, 33]. Figure 7.7a, shows the temperature variation of the cluster size spectrum of SiO_n ($n = 1 - 10$) calculated according to Eq. (7.3) with thermodynamic data for the clusters from [33]. Above $T \approx 650\,\mathrm{K}$, the size spectrum is strongly decreasing; there is no cluster with an equilibrium abundance that is lower than all the others'. No condensation occurs in this case. Below $T \approx 650\,\mathrm{K}$, the cluster with size $n = 4$ has lower abundance than all smaller and bigger clusters. This is the critical cluster that rules nucleation in this case. Figure 7.7b illustrates the structure of SiO_n clusters of lowest energy (including some isomers). Figure 7.6b shows a model calculation based on the H–O–Si reaction network of [32], which demonstrates that clustering of SiO is also kinetically possible under conditions of circumstellar outflows and operates at temperatures that may be compatible with observed condensation temperatures.

Hence, clustering of SiO remains a candidate for the nucleation mechanism of silicate dust in circumstellar shells. This remains to be demonstrated, however, by complete model calculations. It has also often been speculated that Al compounds condense first (because of the high stability of the solid compounds, cf. Figure 7.4)

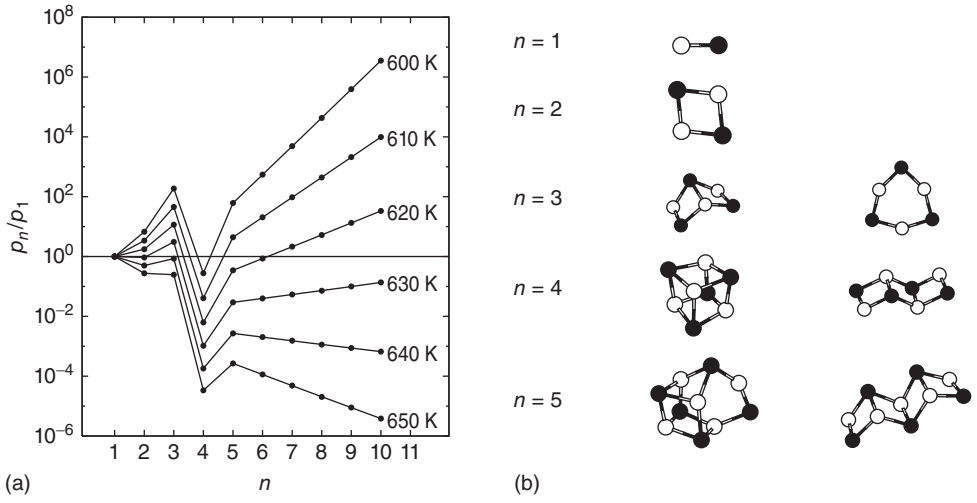

Figure 7.7 (a) Equilibrium abundance of $(SiO)_n$ clusters ($n \geq 2$) relative to the SiO molecule. (Thermochemical data from Ref. [33].) (b) Structure of clusters with mixed ionic and covalent bonding with $n = 1 - 5$ monomers [34].

and that silicates grow on this kind of seed particles. Figure 7.5a seems to suggest that this occurs in some cases. In such cases, one should find an Al-rich core in presolar silicate dust grains, but so few of them have been investigated so far that no information of this kind is presently available. Other possible candidates for nucleation in M stars that have been discussed are, for example, TiO clusters [43, 44]. The low abundance of Ti seems to preclude this for low mass-loss rates, but for higher mass-loss rates model calculations [45] were successful when based on this nucleation process.

7.1.9
Condensation of Carbonaceous Grains in C Stars

7.1.9.1 Carbon Stars on the AGB

Carbon stars form a dust material in their outflows which probably closely resembles soot as is known to form in flames of hydrocarbon fuels. This dust species is observed in space only by its continuous infrared emission. It does not show any characteristic spectral features. The two observed spectral features in the IR spectra of carbon stars have different origins: (i) a strong emission band around 11.2 μm is identified as resulting from β-SiC, and (ii) a rather broad feature extending between about 26 and 34 μm is attributed to solid MgS. No other solids formed in outflows from carbon stars have yet been detected, though additional dust species from carbon stars have been found as presolar dust grains (e.g., Si_3N_4, TiC). Their features are too weak compared to the strong emission from carbon dust to be clearly observable.

Observation shows that carbon dust is always the most abundant dust species in the dust shells around carbon stars [46]. This simply results from the fact that stars having evolved to carbon stars synthesize the carbon required for soot formation for themselves. Even if the initial metallicity of a star is very low, its carbon abundance finally becomes very high.

For the other two observed dust species in carbon stars, namely SiC and MgS, their formation requires, of course, the elements Si, Mg, and S, which, however, are not synthesized in these stars. The possibility of their formation depends on the metallicity of the ISM at the instant of stellar birth. This gradually increases from values of $Z < 10^{-5}$ (much too low to enable dust formation) at the onset of galactic disk formation up to the value of $Z \approx 0.02$ of the present ISM in the solar neighborhood. A dependence of the efficiency of SiC and MgS formation in carbon stars on metallicity is difficult to detect for carbon stars in the Milky Way because here stars of low metallicity are rather old (age > 10 Gyr), that is, of low initial mass ($M < 1\,M_\odot$). Such stars, however, suffer too few thermal pulses to become carbon stars. So, one has to rely on observations from dwarf galaxies where element synthesis proceeds more slowly such that low-metallicity stars of higher initial masses can be observed.

The best possibility for comparison is offered by the Magellanic Clouds because they are small enough to show low metallicity but sufficiently big to contain many observable AGB stars. Observation shows that, besides soot,

- SiC is usually, and MgS frequently, present in dust shells of carbon stars from the Milky Way,
- in the Large Magellanic Cloud, with its lower metallicity of $Z \approx 0.008$, the SiC is still frequently found to be formed along with soot, and also MgS in a number of cases [46], and
- in the Small Magellanic Cloud with $Z \approx 0.004$, SiC is only found in part of the dust shells of sooty carbon stars and MgS is mostly missing in them [46].

Here one observes a clear effect of galactic chemical evolution. Silicon, magnesium, and sulfur are not yet produced in sufficient abundance to form SiC and MgS at $Z = 0.004$ except for a few favorable cases, and at $Z = 0.008$ their abundances are still insufficient to form SiC and MgS at all instances. This observational finding indicates, further, that carbon dust formation is independent of the abundance of other refractory elements. They are not involved in the chemistry of soot formation, at least not in an essential way.

The matter from which soot and other dust species form in giant carbon stars on the AGB is dominated by hydrogen and He (but He is unimportant for the chemistry). The dust-forming elements C, Si, Mg, and O are only minor components. This means that in outflows from carbon stars the excess carbon (over O) forms hydrocarbons. The most abundant carbon-bearing molecule in outflows of carbon stars other than CO is C_2H_2. This can be shown by model calculations, as also found in observations of molecular emission lines from rotational transitions in the radio regime. This makes the chemistry of soot formation in carbon stars somewhat similar to that of soot formation in flames of aliphatic hydrocarbon

fuels where also C_2H_2 plays a key role. This kind of chemistry of soot formation will be discussed in Section 7.1.9.5.

An additional piece of information on the dust formation process acting in carbon stars on the AGB comes from the dust temperature at the inner edge of the dust shell. Figure 7.5b shows that the temperature of the hottest dust is generally found to be $T \lesssim 1100\,\mathrm{K}$. Though this method is of limited accuracy, the results exclude carbon formation at temperatures as high as $T \gtrsim 1500\,\mathrm{K}$ which would be found if condensation occurs under chemical equilibrium conditions (Figure 7.8).

7.1.9.2 Other Carbon-Rich Stars

There are some other rare cases of sooting stars where the general elemental composition is quite different from that of carbon stars on the AGB. While in the latter case one has material of standard cosmic element mixture blended with a small admixture of material from the He-burning zone, there are stars where one directly sees (almost) undiluted material from the He-burning zone at their surface or even the ashes of He burning, Figure 7.3. The chemistry of soot formation must be completely different in such objects from that of normal AGB stars because the envelope material is almost free of H and is dominated by He, C, and O (but C/O > 1). This is the mixture denoted as "He-dominated" in Table 7.3. It resembles somewhat that used for fabricating C_{60} by an electric arc between graphite electrodes in a He atmosphere. The dust material produced by such stars therefore may be closer to this fullerene-rich material produced in the laboratory than to the soot from hydrocarbon flames.

A very different element mixture exists in the atmospheres of WC stars, where the carbon core of a formerly very massive star is exposed to the surface because

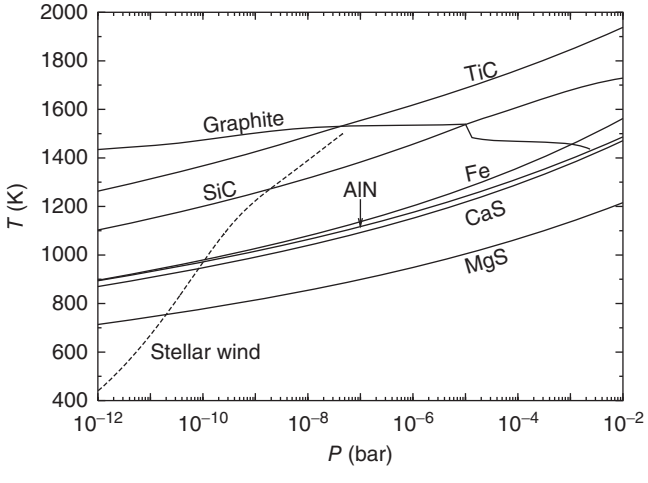

Figure 7.8 Stability limits of some solids that form in chemical equilibrium in the element mixture of a carbon star on the AGB. The dashed line shows the variation of pressure and temperature in a model for a stationary outflow with C/O = 1.2 and mass-loss rate $dM/dt = 10^{-5}\,\mathrm{M}_\odot$.

of complete loss of the overlying H and He layers by a massive stellar wind. The corresponding element mixture is denoted as "C-dominated" in Table 7.3. These stars are extremely hot and normally do not form dust. If they are members of a binary system, in some cases carbon dust is observed to form. This seems to happen in the sheet of matter that builds up between the colliding winds of the two stars [47]. In this layer, the density is probably high, and line-cooling is sufficiently strong to form favorable conditions for soot formation. To what extent H from the companion O star is mixed with the H-free matter from the WC star is not known. The kind of chemistry of dust formation acting in this case remains an open question.

7.1.9.3 Predictions from Equilibrium Calculations

Also for carbon-rich element mixtures, it is useful to perform calculations of gas–solid equilibria to determine which kind of solids are expected to form for a given set of chemical elements, as discussed in Section 7.1.4. For the carbon-rich stars, one has to consider essentially the three different mixtures just discussed:

1) the *hydrogen-dominated* mixture encountered in carbon-rich AGB stars,
2) the *helium-dominated* mixture encountered R Cor B stars and "born-again" AGB stars, and
3) the *carbon-dominated* mixture encountered in WC stars.

The differences between the mixtures can be best characterized by the abundances of the elements H, He, C, N, and O, see Table 7.3. For the heavier refractory elements, the abundances are essentially their initial abundances at stellar birth because temperatures in H and He burning are not high enough for significant abundance changes of these elements.

Figure 7.8 shows the stability limits for the most important condensed phases predicted by calculations of equilibrium compositions to exist at rather high temperatures, see also Table 7.3. These are almost the same for all three mixtures; that is, the absolute abundance of C and O is not important for the kind of solids that can be formed in a carbon-rich mixture, but what matters is only the fact that one has an abundance ratio of $C/O > 1$. The list of condensed phases given in Table 7.3 is not complete; there may exist additional minor condensed phases that are not important for the general dust formation problem.

Of the predicted condensed phases, carbon, SiC, and MgS are observed by their infrared emission to exist in circumstellar dust shells. Some compounds TiC, Fe, and Fe_3C are detected as inclusions in presolar carbon dust grains but are not found by spectroscopy. Of the Al compounds, AlN forms a solid solution with SiC and therefore is unlikely to exist as a separate dust component. In fact, most presolar SiC dust grains are found to contain several percent AlN [48]. For the other Al-bearing compounds, it is doubtful whether they really can be formed, because oxygen is used to form CO at much higher temperature than solids can be formed, and it seems unlikely that there exist kinetically allowed reactions to draw O from CO at lower temperatures to form other O-bearing compounds.

For the hydrogen-dominated element mixture of AGB stars, Figure 7.8 shows the upper stability limits of some of the important possible condensed phases in the pT plane. The observed condensation temperature of carbon dust ($T \lesssim 1100$ K) is significantly lower than the upper stability limit of graphite ($\approx$1550 K). Although for condensation to occur in a seed-particle-free environment it usually requires significant cooling of the gas below the theoretical upper stability limit, the extremely high supercooling of $\gtrsim$450 K observed for carbon condensation in stellar outflows is unusual. It is related to the difficulty of forming the first closed aromatic six rings from aliphatic precursor molecules.

There are some other condensed phases for the element mixture in AGB stars with upper stability limits above the observed condensation temperature of graphite, in particular TiC and SiC. If their formation does not require such extreme degrees of supercooling below their stability limit as carbon does, they may form first. In that case, they could

1) serve as seed particles for carbon growth, or
2) be found as inclusions in the later-formed graphite grains.

In fact, investigations of presolar graphite grains have clearly shown that part of the graphite grains grew around TiC cores that obviously served as growth centers [49, 50]. It was demonstrated also by a laboratory investigation of the condensation of tiny TiC crystals [51] that epitaxial growth of C on TiC is possible. For SiC grains, this does not seem to work, but in rare cases they are also found as inclusions in graphite grains [50].

Generally, not all condensed phases are suited for epitaxial carbon growth on their surface because of structural dissimilarity. If small particles of such dust species (e.g., kamacite, nickel silicide, SiC) collide with the growing graphite grains, they may stick to their surface and are then overgrown by later-formed carbon layers [52].

7.1.9.4 Molecular Composition of Outflowing Gas

The molecular composition of the outflowing gas in carbon stars is dominated by a few species with a small number of atoms and with particularly high bond energy. In the following, the evolution of the molecular abundances in a simple model system is shown, where at fixed mass density the temperature drops at a fixed rate. The real density–temperature evolution of a gas element in the outflow from a pulsating Mira star, involving shocks, is more complex, but the essentials can also be seen from the much simpler case. The HCO chemistry in the cooling gas is calculated by solving the system of rate equations (7.5) for the reaction kinetics of a chemical reaction system containing 54 species from the O–H system and the C–H system with compounds containing up to six carbon atoms. In total, 354 reactions are considered for this system, drawn from the model of formation of soot precursors of Marinov *et al.* [53]. The initial composition is assumed to be atomic H, C, and O with particle densities $n_{\mathrm{H}} = 10^{12}\,\mathrm{cm}^{-3}$ and $n_{\mathrm{O}} = 6 \times 10^{-4} n_{\mathrm{H}}$ and $n_{\mathrm{C}} = 8 \times 10^{-4} n_{\mathrm{H}}$. These are typical densities expected at the base of the outflow somewhat above the stellar surface.

Figure 7.9a shows the evolution of atomic and molecular abundances for the HCO system at high temperatures. It demonstrates that O is completely consumed to form CO already at temperatures found in the stellar atmosphere. The conversion of the excess carbon into C_2H_2 occurs in the cooling flow around 2000 K. It is, from that point on, the only really abundant carbon-bearing compound besides CO. Thus the composition in the outflow is essentially the same as in chemical equilibrium. Figure 7.9b shows the results for the abundances of C–H compounds that contain up to two carbon atoms. They represent the natural first step in the formation of complex molecules with many atoms. Deviations from chemical-equilibrium composition become visible if the H–H_2 equilibrium starts to freeze out below 1600 K because the three-body reactions

$$H + H + H_2 \longleftrightarrow H_2 + H_2$$

become inefficient because of too low densities. Radicals remain abundant in the outflow by means of H-abstraction reactions X-H + H → X• + H_2 and because of dissociation disequilibrium of hydrogen. This disequilibrium would certainly be enhanced by the presence of shocks, but no results are presently available for this case.

7.1.9.5 **Formation of PAHs in AGB Stars**

The basic problem of carbon dust formation is how one forms the first aromatically bound species, for example, C_6H_6, from the small linear chain molecules with less than six C atoms. The complex PAH molecules are rather rare at elevated temperatures and their formation is therefore difficult. Figure 7.10 shows the abundances of C–H compounds (summed over all compounds with the same number of C atoms) with up to 18 carbon atoms in chemical equilibrium. At temperatures above ≈1000 K, the abundance of compounds with eight or more C atoms is so

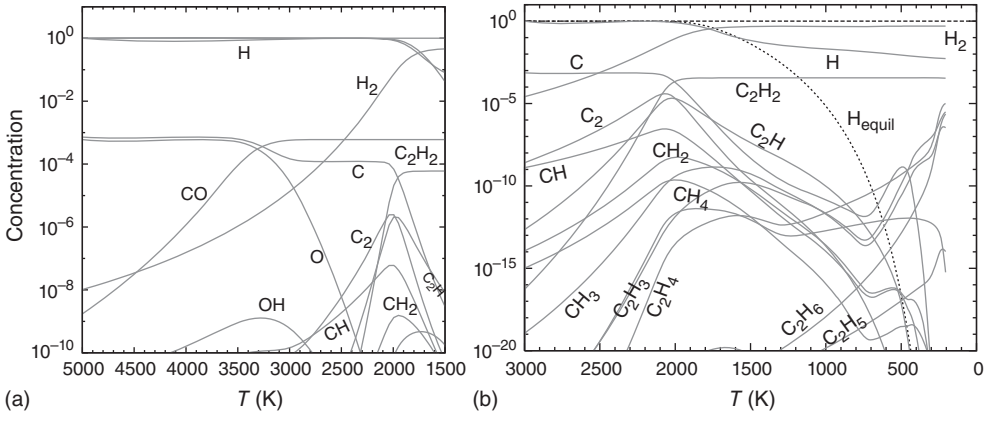

Figure 7.9 (a,b) Concentrations of CH compounds with up to two carbon atoms and H–H_2 kinetic equilibrium in a cooling gas with $N_H = 10^{12}$ cm^{-3}. The dotted line shows the abundance of H atoms in chemical equilibrium.

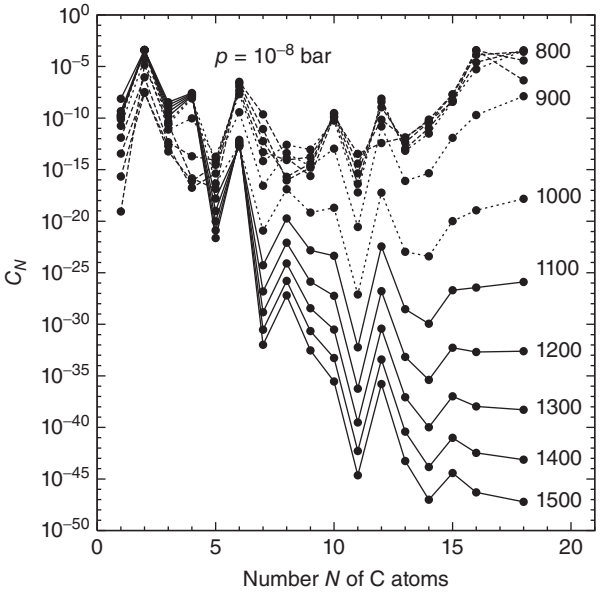

Figure 7.10 Variation of chemical equilibrium concentrations (with respect to H) of all C–H compounds with a fixed number N of the C atoms at different temperatures and the indicated pressure.

low that any chemical route from C_2H_2 to soot is effectively blocked. This compares favorably with the observation of the highest dust temperatures $T \lesssim 1200$ K in dust shells around C stars, cf. Figure 7.5b. The impossibility of forming members with $n > 8$ carbon atoms along the reaction chain from C_2H_2 to soot with non-negligible abundance prevents efficient dust formation in stellar outflows before the temperature drops below 1000 K.

If carbon dust formation should occur under quasi-stationary conditions, the bottleneck for soot formation would be naphthalene, $C_{10}H_8$, because it has the lowest abundance under all compounds with an even number of carbon atoms (only these can be easily formed by growth reactions with C_2H_2). However, if the reaction kinetics is similar to that known for combustion chemistry, then the most difficult reaction step will be the first ring closure. The first complete model computation of the reaction kinetics for the formation of soot precursors in carbon-rich stellar outflows was in [54]. It demonstrated that the formation of soot precursors, also in models based on combustion reactions, did not start before the temperature in the outflow dropped below about 1100 K. A model calculation for PAH formation in carbon-rich stellar outflows based on an improved version of the reaction mechanism in [54] which significantly improved modeling of the stellar wind properties was performed in [55, 56]. This model included the

Bockhorn–Fettig–Wenz cyclization step used in the model in Ref. [54]

$$\text{1-buten-3-ynyl}\,(C_4H_3) + \text{ethyne}\,(C_2H_2) \longrightarrow \text{benzyne}\,(C_6H_4)$$
$$\xrightarrow{+H} \text{phenyl}\,(C_6H_5)$$

(ethyne = acetylene), the Miller and Melius cyclization step

$$\text{propargyl}\,(C_3H_3) + \text{propargyl}\,(C_3H_3) \longrightarrow \text{phenyl}\,(C_6H_5) + H$$

and the Frenklach and Warnatz cyclization step

$$\text{1-buten-3-ynyl}\,(C_4H_3) + \text{ethyne}\,(C_2H_2) \longrightarrow \text{phenyl}\,(C_6H_5)$$

The first two of these are the most efficient reactions for cyclization in the model [56].

Once the first aromatic ring is formed, further growth is assumed to proceed via a series of H-abstraction and carbon-addition reactions (usually abbreviated as HACA, cf. Ref. [57]). Carbon addition here means acetylene addition, as shown in Figure 7.11.

A shortcoming of these models is that the production of PAHs is not efficient enough and limited to a temperature window between 1100 and 900 K. Figure 7.12 shows the PAH abundances calculated with an improved set of reactions from Ref. [53]. The formation of soot precursors commences in such models only after the gas has cooled below 1100 K, and freezes out below 900 K. The models cannot yet explain the efficient growth of soot. It seems unlikely that the chemistry is not correctly described by the model, but rather that the problem is an oversimplified treatment of the radiation hydrodynamics of the outflow.

7.1.10
Formation of Minerals in C Stars

For the mineral species SiC, MgS, and TiC formed in carbon stars, no details of the chemistry of their formation are presently known. In particular, for TiC this is a significant shortcoming because analysis of presolar graphite grains have shown that for part of them TiC nanoparticles served as seed particles for carbon

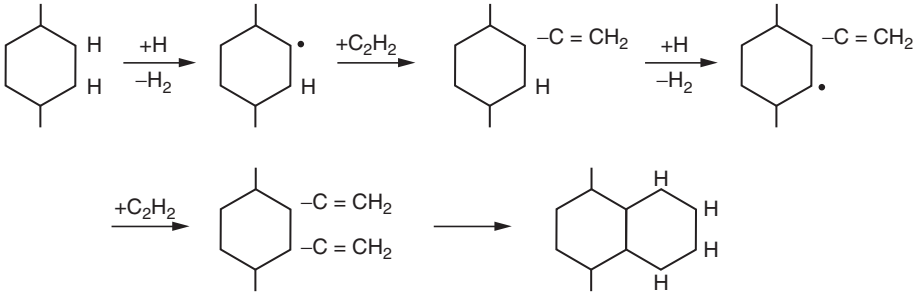

Figure 7.11 The sequence of hydrogen abstraction and acetylene addition reactions responsible for polycyclic aromatic hydrocarbon (PAH) growth in shells of carbon stars.

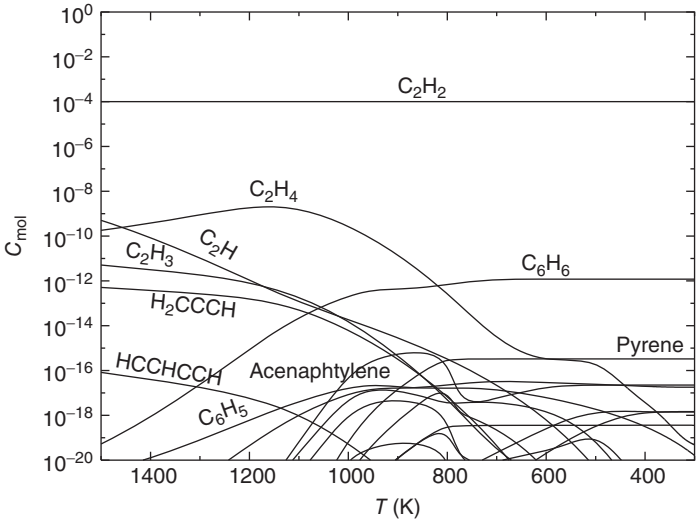

Figure 7.12 Concentrations of PAH molecules (relative to H) with up to 18 C atoms and some of their precursor molecules with 2–6 C atoms (acenaphthylene = $C_{12}H_8$, pyrene = $C_{16}H_{12}$).

growth [49]. It is not possible, however, to infer from this observation and from equilibrium condensation temperatures of C and TiC (Figure 7.5), for instance, pressures in the soot condensation zone, because soot formation occurs far below its stability limit.

For MgS, it has been argued that its formation requires another dust material as a growth substrate and that SiC dust grains are the likely candidate for this [58].

7.1.11 Concluding Remarks

In the preceding sections, we have discussed sites of cosmic dust formation and chemical pathways to circumstellar dust condensation. We showed that the conditions under which dust is formed restricts the number of possibilities for the actual condensation mechanism in the main dust-forming objects, the AGB stars:

1) pure SiO clustering in M stars where dust condenses at a gas temperature of $T < 1000$ K,
2) a mechanism for carbon stars for formation of the first six-carbon rings from propargyl followed by repeated steps of hydrogen abstraction and acetylene addition similar to the soot-formation process in laboratory acetylene flames.

Many problems, however, have not yet been solved: the formation of the less abundant dust species like Al/Ca compounds in M stars or carbides and sulfides in C stars and the condensation mechanisms in more exotic element mixtures, for example, in WN and WC stars. Thus, while currently we have some idea

about what is going on in dust-forming circumstellar shells, much future work is required to obtain a quantitative understanding of dust formation in such objects.

In the above discussions, two major classes of dust-forming objects were left out: novae and supernovae. The conditions encountered in ejected material following explosive events and in the more gentle outflows from highly evolved stars are very different, and the physics and chemistry of dust formation for both classes of objects have little in common. We have considered dust formation in stellar outflows and omitted dust formation following explosive events. For discussions on dust formation in SN ejecta, see Refs [59, 60] and for nova ejecta [61].

7.2
Laboratory Approach to Gas-Phase Condensation of Particles

Cornelia Jäger

7.2.1
Gas-Phase Condensation Methods in the Laboratory

Condensation of nanometer-sized silicates or carbonaceous grains in circumstellar environments is supposed to be a homogeneous nucleation process (see Sections 7.1.6 and 7.1.9). However, graphite spherules containing smaller grains of more resistant carbonaceous grains, such as TiC, have been found. They are supposed to condense at higher temperature than the pure carbonaceous component, but their role as nucleation seeds is still a matter of debate.

Laboratory gas-phase condensation techniques are used to mimic astrophysical condensation processes of cosmic dust grains in circumstellar environments or in supernovae and to produce cosmic dust analogs. However, in the laboratory, such processes need to be studied at higher pressures than prevailing under natural conditions due to the "system dimensions" which are much smaller than, for example, paths available to molecules or clusters in space (around 10 m for a pressure of 10^{-5} mbar). In the laboratory, we have to scale up the condensation pressure for grains at least by a factor of 10 or more. Second, a general problem is that temperatures and pressures in circumstellar condensation environments are uncertain since they depend on certain model assumptions, for instance, mass-loss rates, gas-density outflow velocity, and dust formation.

Homogeneous nucleation and particle growth is driven by the reduction of the Gibbs free energy, which can be achieved by a high supersaturation of the vapor phase [62, 63]. A freshly formed nucleus is stable only when its radius exceeds a critical value r^*. The relation between the size of the critical grains r^* and the Gibbs free energy is defined by $r^* = -2\gamma/\Delta G_v$, where γ stands for the surface energy of the condensed species [64]. The Gibbs free energy ΔG_v per unit volume of the solid phase is proportional to the temperature T and the supersaturation S via the relation $\Delta G_v = -kT/\Omega \ln(1 + S)$ (1) where k is the Boltzmann constant and Ω is the atomic volume. The supersaturation S can be defined as the ratio between the

partial pressure of the condensing species and the equilibrium pressure of the system. In order to reduce the critical size of stable nuclei in the condensation zone, which can be considered as the minimum size of the condensing particles required for the production of small nanometer-sized grains, one needs to increase the change of Gibbs free energy ΔG_v of nucleation per unit volume. Consequently, high supersaturation leads to small sizes of critical nuclei. However, the influence of experimental parameters on a homogeneous nucleation process is rather complex and difficult to interpret. In addition to the above-mentioned relation, the surface energy and supersaturation are also temperature-dependent.

Nanometer-sized dust particles can be produced by different gas-phase condensation techniques in two steps. The first step is the formation of atoms and clusters by evaporation or pyrolysis techniques. In the second step, the generated vapor is either deposited as a film on a substrate or is quenched in a cooling gas atmosphere. In this chapter, we will specify only a few examples out of the large number of gas-phase condensation techniques used to grow nanometer-sized grains in the laboratory.

Frequently employed methods of preparing cosmic dust grain analogs include laser-induced pyrolysis (LIP) of gaseous hydrocarbons [65–70], combustion of hydrocarbons in flames [71, 72], laser ablation of graphite [73–76], resistive heating [77, 78], and arc discharge of carbon electrodes [79, 80]. Reactive hydrocarbon plasmas were also used to produce carbonaceous cosmic dust analogs such as quenched carbonaceous composite (QCC) [81, 82], hydrogenated amorphous carbon (HAC) films [83], and plasma-polymerized dust grains [84].

Pulsed laser ablation is an efficient method of forming nanoparticles from most materials including solids with a very complex stoichiometry such as silicates. For applications of physical interest, pulsed laser ablation of solid targets in helium, helium/hydrogen, or helium/oxygen atmospheres has been frequently used to prepare carbon, silicate, and oxide grains (Figure 7.13). Solid graphite or amorphous carbon targets are employed to generate amorphous or HAC grains in helium or helium/hydrogen atmospheres. Silicate or oxide grains are produced from either pure metal or metal oxide targets condensed in a helium/oxygen or in a pure helium atmosphere, respectively.

Pulsed laser ablation is a complex nonequilibrium process. The individual steps involved, such as sublimation of the target material, ionization of the target species and the surrounding gas atoms and molecules, deceleration of gas and condensates, and, finally, particle aggregation, are difficult to describe.

The interaction of the laser photons with the solids induces electron transitions from the valence band and from occupied surface and defect states into the conduction band. The dominant absorption process depends on the photon energy and the electronic structure of the solid. If the photon energy is higher than the gap energy, high absorption coefficients in this wavelength range lead to strong heating. If the photon energy is lower than the gap energy, then multiphoton transitions or transitions from defect and surface states are the only means by which the solid can absorb the photon energy [86].

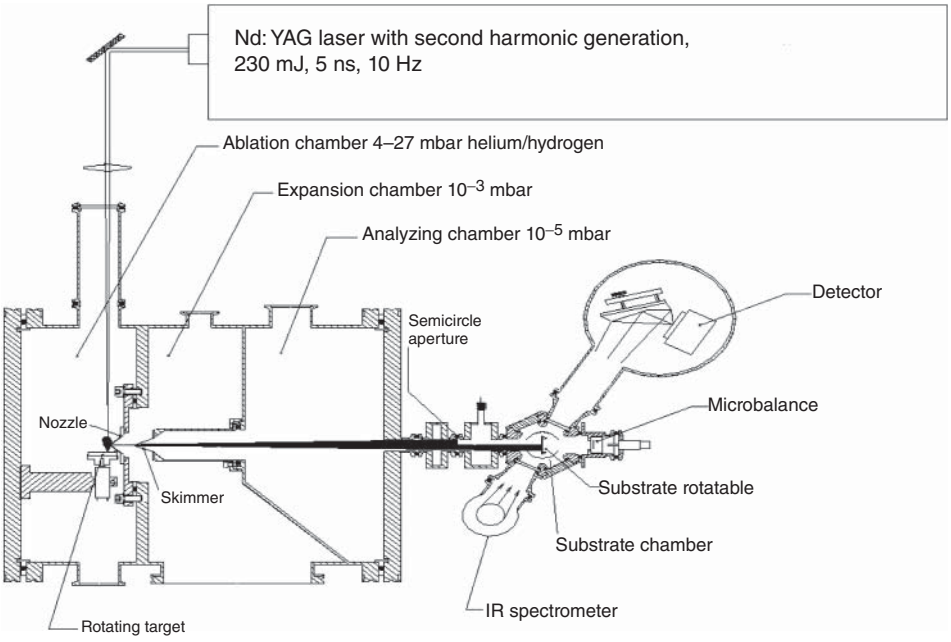

Figure 7.13 Laser ablation setup for gas-phase condensation experiments of carbonaceous, siliceous, and oxide grains. The laser is directed at a rotating target, and the ablated species condense in a quenching gas atmosphere. The condensing particles are extracted through a nozzle and a skimmer, and are deposited on the rotatable substrate. (Reproduced from Ref. [85] with permission of the AAS.)

Laser ablation of a target in a quenching gas atmosphere produces a shock wave. Its expansion velocity decreases with increasing distance from the target. The blast wave moves symmetrically, and its velocity depends on the pressure of the quenching gas [87]. The condensation of particles from the produced clusters and atoms occurs within a small zone located at the interface of the vapor plume and the quenching gas. Generally, cooling rates of the vapor are higher than 10 000 K s^{-1}. The choice of the quenching gas determines the size of the produced nanoparticles. The use of He compared to argon allows the condensation start earlier and the nanoparticle sizes are smaller compared to Ar [88]. This can be understood considering the higher heat conduction and diffusion properties (mass conductivity, viscosity) of the gas, leading to a faster cooling rate of the vapor plume which is related to a higher supersaturation and therefore smaller critical radius for homogeneous nucleation.

In addition, the laser energy (pulse energy) also influences the condensation process and particle sizes. When a laser hits a target and evaporates a certain amount of solid, the size of the vapor plume grows with increasing laser energy. The energy transfer from the vapor to the background or cooling gas is proportional to the surface area of the vapor plume r^2, and the cooling rate is proportional to r^{-1} [88]. The critical radius of the condensing particles and the time available

for the growth of grains are reduced in a smaller vapor plume with a higher cooling rate. This has been experimentally proven by measuring the average diameter of the condensing grains. More details on the influence of the laser ablation conditions can be found in Refs [88, 89].

In order to prevent further agglomeration of the condensing particles in the condensation zone, the gas–particle mix is extracted from it through a nozzle and a skimmer to form a molecular beam (Figure 7.13). The particles in the laser ablation chamber condense at low pressures between 1 and 25 mbar. The freshly condensed grains are extracted adiabatically through a nozzle (orifice 0.8 mm) into a second chamber which is held at a pressure of around 10^{-3} mbar. During this expansion, the particles decouple from the gas and the density of grains within a definite volume strongly decreases. Consequently, further particle growth due to reactions with reactive gas molecules and agglomeration processes is prevented. A second extraction is performed through a skimmer into a third chamber with a pressure of 10^{-6} mbar. The generated particle jet can be directed into the substrate chamber either to be deposited as a particle film onto a substrate suitable for spectroscopy or embedded into a cryogenic matrix (Ne or Ar) for spectroscopic measurements [77].

Another frequently used method to produce dust grains is LIP of gaseous hydrocarbons. This technique has been employed to produce silicon from silane (SiH_4) [67], silicon carbide from mixtures of silane and acetylene [90], and carbonaceous particles from diverse hydrocarbons [66, 70].

The general design of a flow reactor that can be used to produce carbonaceous or siliceous materials is sketched in Figure 7.14. Gaseous precursors can be directly introduced through two concentric tubes. Liquid precursors are introduced by

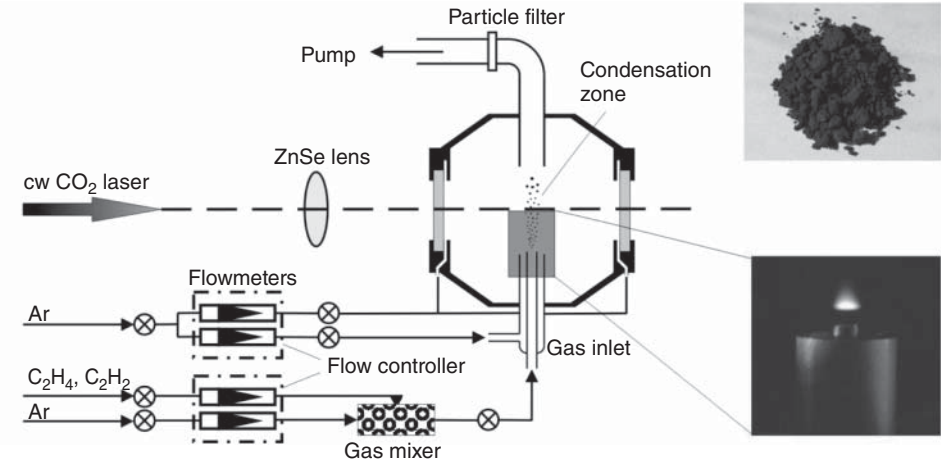

Figure 7.14 Schematic of the laser pyrolysis setup that is used for gas-phase condensation experiments of carbonaceous materials. Ethylene or ethylene/acetylene mixtures are used as precursors. The insets show a carbonaceous condensate collected in the particle filter and the flame formed under laser irradiation.

bubbling argon or helium gas through the precursor reservoir. The reaction gas enters the center of the flow reactor through the inner tube. Rare gas is flushed as a buffer gas through the outer tube in order to confine the reaction gas to the flow axis and to cool the reaction products. The beam of the pyrolyzing CO_2 laser ($\lambda = 10.6\,\mu m$) either pulsed or continuous wave (cw) is perpendicularly focused to a small diameter of only a few millimeters at the exit of the inner tube. This infrared (IR) laser radiation induces rapid heating and dissociation of the reaction gases. In order for the precursors to pyrolyze, they, of course, have to be able to strongly absorb at the laser wavelengths. Otherwise, a sensitizer such as SF_6 is necessary. In the dense and colder region between the dissociation zone and the buffer gas, in the outer zone of a small flame, formed a small distance away from the inlet tubes, the nanoparticles condense (Figure 7.14). The pressure in the flow reactor is kept constant between 250 and 750 mbar. The gas and solid reaction products are quickly extracted from the condensation zone by pumping them through a funnel-shaped tube facing the inlets. A filter in the pump line collects the particles produced during condensation. As in the laser ablation technique, laser pyrolysis can be combined with molecular beam extraction by introducing a conical nozzle into the reaction zone. The clusters, molecules, and condensed particles are released into free molecular flow and can be analyzed in a vacuum apparatus equipped with a time-of-flight (TOF) mass spectrometer or be deposited on a suitable substrate for spectroscopy [67, 70].

Another method that is used to prepare analogs of cosmic dust grains via gas-phase condensation is the combustion process. Here, soot grains are formed in flames of gaseous hydrocarbons that are mixed with oxygen. The soot formation threshold and efficiency in such flames strongly depend on the temperature, pressure, precursor gas, C/O ratio, and construction of the burner [91]. Various precursor hydrocarbons can be used for combustion in flames, including methane (CH_4, acetylene (C_2H_2), ethylene (C_2H_4), propylene (C_3H_6), and benzene mixed with oxygen, in a flat burner. For soot production, the C/O ratio can be varied in a wide range between 0.5 and more than 2. The temperature in a flame increases with distance from the burner and can reach more than 2500 K. Five groups of reaction products are observed in flames: polyynes, polycyclic aromatic hydrocarbons (PAHs), fullerenes, aromers (initial stages of fullerenes and soot particles), and soot particles [92]. Low pressure conditions are often used to expand the flame and, therefore, the condensation zone of the soot particles [71]. Quartz cones or nozzles are used to extract the reaction products from the condensation zone at specific distances from the burner surface [72].

Other important methods to mimic cosmic dust condensation processes are plasma based nucleation and condensation techniques. Nanoparticle formation is caused by ionization and dissociation of the precursor gas and subsequent condensation. For instance, the QCC condensate was prepared by hydrocarbon plasma deposition. The precursor gas (methane) was ionized by a microwave discharge and transferred into a vacuum chamber through a small nozzle. The adiabatically expanding plasma gas is efficiently quenched to generate solid material [81]. The same plasma-based condensation method was used for further

processing studies of carbonaceous dust analogs [82]. Spherical carbonaceous grains were polymerized in an acetylene plasma, with argon or nitrogen as the carrier gas [84].

7.2.2 Laboratory Tools for the Characterization of Condensation Products

The choice of the specific characterization method to use depends on the type of condensed material that is to be studied. The most important tools for the characterization of condensates are the transmission electron microscope (TEM) and the high-resolution transmission electron microscope (HRTEM). Information on the composition, structure, as well as the shape, size, and coagulation of nanometer-sized particles can be deduced. Crystalline phases can be identified by electron diffraction measurements. This method is able to distinguish between amorphous, partly amorphous, and crystalline (mono- or polycrystalline) phases. Crystalline phases can be identified, and information about the orientation of crystalline grains within an amorphous matrix can be obtained [93].

HRTEM allows a direct view inside the produced materials. One can easily distinguish between amorphous and crystalline structures. Amorphous materials show a variety of structural diversity described by the long-, medium-, and short-range order, which can be analyzed with HRTEM. The method is extremely helpful for the quantitative characterization of amorphous structures (see Section 7.4). For instance, the long-range order of amorphous carbonaceous grains describes the size and shape of the primary particles and their agglomeration state, whereas the medium-range order characterizes the arrangement, shape, and size of the so-called basic structural units (BSUs). In a carbonaceous material, these would be the subnanometer- or nanometer-sized graphitic crystallites or disturbed graphene layers, which can be randomly or concentrically arranged and linked by aliphatic bridges [76, 94]. The short-range order describes the direct vicinity of a carbon atom and the bonds between the carbon atoms. A quantitative description of these structural parameters is helpful for the understanding of the optical properties of carbonaceous cosmic dust. In addition, the amorphization and crystallization processes of different materials can be well monitored by imaging lattice fringes of the contained crystalline phases in the HRTEM [95, 96].

Energy-dispersive X-ray (EDX) analysis, an implementation of the electron microscope, can be used to analyze the composition of individual or coagulated grains qualitatively and quantitatively. The disadvantage of this method is that light elements, up to sodium, are difficult to study quantitatively and that the oxidation state of polyvalent metals cannot be easily determined. However, using standard materials with very similar composition and structure and well-known oxygen content allows the derivation of at least oxygen contents in the samples.

An electron energy loss (EEL) spectrometer can also be attached to an HRTEM to probe the composition of grains or the band structure of individual elements. While these methods require only small amounts of the sample, sample preparation and analysis can be very time consuming. However, EEL spectroscopy is very

helpful in analyzing the short-range order in carbonaceous materials. Two energy regions can be used for this analysis: the low-loss region up to 60 eV, where interband transitions and plasmon excitations can be seen; and the core loss region in the range 280–330 eV. The core loss spectra are characterized by the excitations of electrons from the carbon 1s orbital to states above the Fermi level. Ratios of sp^2- and sp^3-hybridized carbon atoms were derived for carbonaceous dust analogs from the carbon core loss spectra between 284 and 330 eV [77, 78, 97]. In silicates, the oxidation state of polyvalent ions, such as Fe^{2+}/Fe^{3+} ratios, can be derived from the energy-loss near-edge structure (ELNES) since the Fe $L_{2,3}$-edges between 707 and 730 eV of iron-bearing silicates are characterized by two white-line features characteristic of the Fe valence state [98].

X-ray absorption and scattering spectroscopy, such as extended X-ray absorption near edge fine structure (EXAFS) and X-ray absorption near edge structure (XANES), are additional methods to characterize the short- and medium-range order in amorphous and partially amorphous materials including carbon and silicates. EXAFS provides information about the coordination and distances between atoms. XANES spectra are sensitive to chemical properties such as the valence state of the absorber atom and the coordination numbers. For instance, the structural evolution of thermally processed amorphous magnesium and iron silicates was studied by using XANES and EXAFS [99]. The authors demonstrated that thermal annealing leads to the formation of an ordered arrangement of the SiO_4 tetrahedra and the requisite metal ions, but does not affect the bond lengths and angles within the SiO_4 units of silicates.

Table 7.5 provides an overview of characterization methods used in laboratory astrophysics to investigate siliceous and carbonaceous materials.

To learn about the short-range structure, spectroscopic and chromatographic methods can be employed. IR spectra are used to determine chemical composition and structure of condensed carbonaceous particles. When applied to carbonaceous grains, they can also be used to determine the content of given elements. For instance, the fraction of hydrogen in the carbon grains can be determined from the analysis of the C–H stretching bands at 3.3 μm (3060 cm^{-1}) and 3.4 μm (3000–2800 cm^{-1}) [100]. The derived information can be used to interpret the observed spectra of different astrophysical environments. For instance, a detailed analysis of the IR bands of the diffuse interstellar medium taken between 2.5 and 10 μm has been performed by Pendleton and Allamandola [101]. Interestingly, their analysis revealed that the interstellar carbon-bearing material is a HAC containing only little nitrogen or oxygen but composed of both aromatic and aliphatic structural areas. The presence and quantity of oxygen or nitrogen can be derived from vibrational modes of the corresponding functional groups such as C=O or CN. In the IR spectrum, a graphitization process of HACs, which may also occur in different astrophysical environments, is characterized by the decrease of absorption bands due to functional groups and by the general increase of the continuous absorption due to the formation of free charge carriers during the graphitization.

Very recently, gas chromatography (GC) and high-performance liquid chromatography (HPLC) combined with mass spectrometry and UV–vis spectroscopy

Table 7.5 Analytical tools that have been used to characterize cosmic dust analogs produced in the laboratory.

Method	Analysis	Comments
Carbonaceous materials		
HRTEM	Morphology, structure	Small sample mass, time consuming
EELS	sp^2/sp^3 ratios	Direct comparison to the HRTEM images
	structure	but difficult corrections
Raman	Structure, length of graphitic subunits	Fast, material processing during analysis is possible
^{13}C NMR	sp^2/sp^3 ratios functional groups	Accurate, large sample mass
IR spectroscopy	Functional groups hydrogen content aromatization degree	Adsorbed organic may adulterate the spectrum
UV–vis	Gap energy size of aromatic units	
MS	Mass of PAHs, fullerenes information on grain formation	Information on grains' intermediates
Chromatography	Separation of molecular components	
Siliceous materials		
HRTEM	Morphology, structure	Small sample mass
EDX	Composition, homogeneity	
IR spectroscopy	Polymerization of SiO_4, structure, homogeneity	
X-ray diffraction	Modification, structure	Large amount of sample
EELS	Valency of ions	Time consuming
Wet-chemical analysis	Composition, polyvalent ions	Very accurate, time consuming, large sample mass

were used to investigate the formation pathways of carbonaceous condensates. In these experiments, the soluble components were solvent-extracted from normal soot grains to identify precursors and intermediate products of the gas-phase condensation process.

Matrix-assisted laser desorption and ionization (MALDI) combined with a TOF mass spectrometer have also been employed to study the composition of the soluble components of gas-phase condensations. In the MALDI-TOF analysis, the role of the matrix is to absorb the laser's energy and transfer it to an embedded species of interest. In this way, its fragmentation is prevented. MALDI-TOF thus achieves a very soft desorption, allowing macromolecules to be detected as intact

ions with masses of up to a few hundred thousand daltons. Laser desorption mass spectrometry was used to analyze insoluble PAH samples with molecular weights up to 10 000 Da.

7.3
Gas-phase Condensation Experiments of Magnesium Iron Silicates

Frans J.M. Rietmeijer and Joseph A. Nuth

Few laboratory experiments can be done under natural astrophysical conditions, but well-conceived experimental data using simple analogs will often provide insights into astrophysical processes that are impossible to obtain through models, or even through observations, of natural systems. Experiments provide practical information that is otherwise unavailable: for example, information on the emergence of the smallest condensate grains from molecular clusters in condensing vapors and modifications of the smallest condensate grains that are potentially available in the grain size, and condensate grain size distributions produced in laboratory vapor phase condensation experiments conducted in contained environments. When condensation has ceased, there is still energy in the system that needs to be dissipated before opening the condensation chamber. During this auto-annealing period, subtle changes might occur, such as grain fusion and chemical homogenization [102], spinodal phase decomposition [103], and core–rim formation [104]. Once removed from the condensation chamber, a condensed sample (or smoke) can be heat-treated to study crystallization of amorphous smokes, the formation of nonequilibrium minerals [105, 106], and amorphization of metastable cristobalite [107]. The common magnesium iron silicate minerals on Earth, Moon, Mars, and asteroids are considered to have formed as equilibrium phases. These crystalline silicates are also identified in circumstellar disks around young stars [108, 109] such as the solar nebula. In the case of the solar nebula, we can study the Mg,Fe-silicates in the primitive carbonaceous chondrite meteorites [110] but there is no observational evidence that the Mg,Fe silicates olivine [$(Mg,Fe)_2SiO_4$; forsterite–fayalite] and pyroxene [$(Mg,Fe)_2Si_2O_6$; enstatite–ferrosilite] had formed by equilibrium condensation as was proposed by, among others, [111]. There is also no evidence that they did not. The matrix of primitive meteorites [112] and chondritic aggregate interplanetary dust particles (IDPs) [113] is a ferromagnesiosilica glass. Following astronomical convention, silicate minerals (olivine; pyroxene) are "crystalline silicates" and ferromagnesiosilica glass is "amorphous silicate." The latter is also present in the interstellar medium and circumstellar disks [108]. When crystalline magnesium iron silicates did not form by equilibrium condensation but were amorphous silicates that achieved chemical equilibrium at a particular set of state variables, it raises the question as to how amorphous Mg,Fe silicates were formed by either equilibrium or nonequilibrium vapor-phase condensation. Ostwald [114] proposed that the thermodynamically stable form of the bulk condensate never

nucleated directly from the vapor phase. Indeed, the surface energies of very tiny particles can potentially change the relative stabilities of specific mineral assemblages. Very high surface energies can ensure that condensates will nucleate as amorphous liquids at high levels of supersaturation and relatively low temperatures. However, the internal chemistry of such amorphous condensates might still be controlled to some degree by kinetic or thermodynamic factors and is always subject to thermal annealing at some later time to convert these amorphous grains to crystalline mineral assemblages. The higher the surface energy of the phase and the smaller the particle size, the more stringent are the limits placed on the severity of the environmental conditions experienced by the system since its formation.

7.3.1
Grain Production and Characterization

The condensation flow apparatus (CFA) (Figure 7.15) was designed to condense amorphous grains with chemical compositions determined stochastically by the composition of the vapor from which they formed. It produces gram quantities of

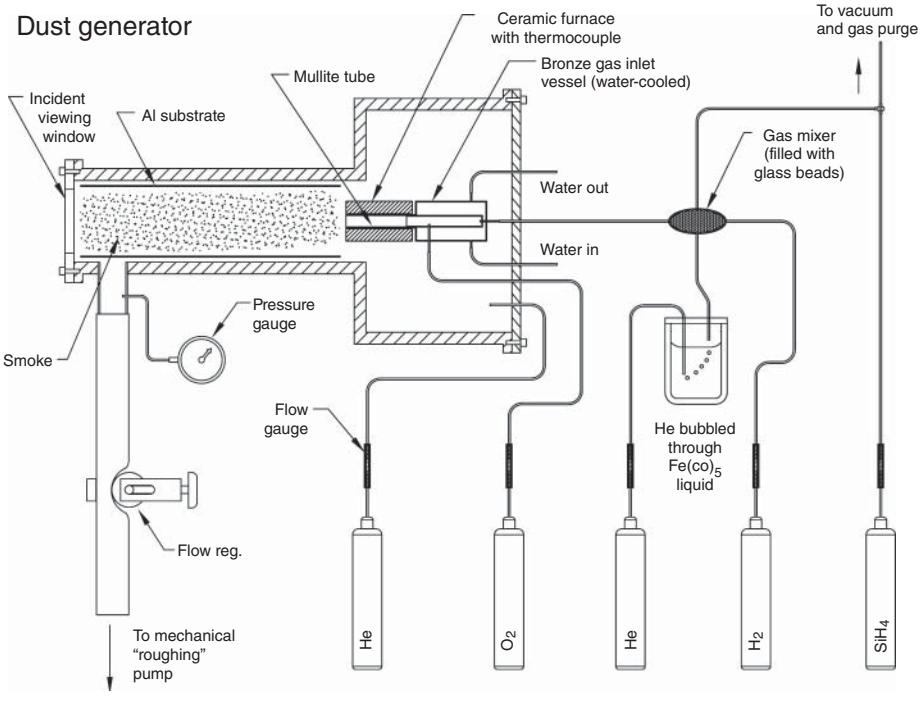

Figure 7.15 Schematic of the condensation flow apparatus used to manufacture nanometer-scale smoke particles via the combustion of hydrogen gas containing small amounts of silane, iron pentacarbonyl, and magnesium metal vapor.

aggregate samples of amorphous grains [115] by nonequilibrium gas-to-solid condensation in M–SiO–H_2–O_2 vapors (M: Mg, Fe, Al, Ca, or combinations thereof) [116, 117].

In this apparatus, there is no standard set of flow, temperature, or pressure settings, but the following conditions are all at least somewhat typical of an average experiment: the total pressure in the system is ∼100 Torr; the reaction occurs across a flame front within a resistively heated furnace at temperatures between 500 and 1500 K; the hydrogen flow rate is ∼1000 sccm (standard cubic centimeters per minute); the helium flow through the iron carbonyl is on the order of 250 sccm. We estimate that the iron pentacarbonyl [$Fe(CO)_5$] concentration is ∼10% of the total flow of helium. Magnesium metal is placed in a graphite boat inside the furnace. At the nominal 1000 K temperature of the furnace, magnesium metal has a vapor pressure of 5 Torr. The oxygen flow rate always equals or exceeds that of silane (SiH_4) but is usually within a factor of two of the silane setting. The silane flow rate is typically ∼100 sccm. As a result, the hydrogen/oxygen ratio is always >5 as some amount of hydrogen is also contributed by silane. The typical oxygen flow is sufficient to just balance the hydrogen contributed from the silane flow to produce water and Si^0 without affecting the bulk flow of hydrogen. In this system, the oxygen fugacity during condensation is a dynamic quantity that is dependent on reaction rates, rather than a thermodynamic quantity. The actual oxygen fugacity during condensation is conducive to the formation of iron oxides instead of Fe^0, to the formation of silicon oxides instead of Si^0, and to the formation of magnesium oxides rather than Mg^0. The hot gas and fresh grains are rapidly quenched as they flow into a larger stainless steel chamber. The condensates are collected on an aluminum substrate downstream of the furnace at temperatures below 350 K.

The size, morphology, and crystallographic properties (i.e., amorphous or crystalline) of individual grains (∼2 to ∼100 nm in diameter) in the samples were characterized by a 200 keV analytical and HRTEM (for details, see Ref. [118]). These HRTEM analyses showed that (i) the exact bulk composition of the condensing gas was unknown, though it was very close to the bulk composition of all solid grains in the resulting smoke [115, 117]; (ii) formation of hydrated condensate grains by transient water in the condensation chamber was extremely rare [119]; and (iii) formation of reduced condensates, for example, Mg metal [120] and Mg_2Si [121] could and did occur.

These condensation experiments typically produce mostly open aggregates which frequently consist of hundreds to thousands of individual grains, each connected to only two or three neighboring particles [122]. The majority of grains typically range from ∼2 to ∼100 nm in diameter (Figure 7.16) but there are many larger grains up to ∼500 nm [123]. They are mostly thin, plate-like grains with a (semi)rounded cross section or with a crystalline shape (Figure 7.17). A typical smoke is an open aggregate of interconnected strands of amorphous magnesiosilica and ferrosilica grains (∼2 to ∼100 nm) and amorphous or crystalline (tridymite) silica grains (∼20 to 60 nm). The presence of pure silica grains reflects the silica-saturated nature of the condensing metal–SiO–H_2–O_2 vapors.

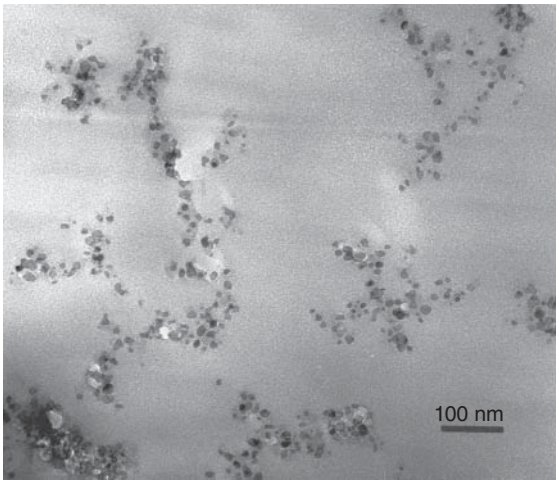

Figure 7.16 Low-magnification transmission electron micrograph of magnesiosilica (dark gray) and ferrosilica (black) grains condensed from a Mg–Fe–SiO–H_2–O_2 vapor using the condensation flow apparatus. For these analyses, the sample was embedded in an epoxy (gray background) to cut ultrathin (~70 nm) sections. (Image credit: Dr. James Karner (thesis research).)

Grain-to-grain collisions during settling in the condensing vapor or on the collector resulted in dumbbell-shaped grains or small clusters with an irregular circumference, but still showing the partial outlines of individual grains. This grain growth process, called *Ostwald ripening*, decreases the surface free energy and eventually leads to ever-larger spherical grains. As a result, the grains in the samples form two different log-normal size distributions with a transition that occurs between 25 and 30 nm. Grains smaller than 25 nm represent the condensation regime proper, and larger grains were generally formed during autoannealing.

7.3.2 Grain Compositions

Condensation of Mg–SiO–H_2–O_2 and Fe–SiO–H_2–O_2 vapors in the CFA produced two chemically distinct grain types: (i) mostly crystalline, metal oxides, namely MgO (periclase) (20–45 nm) [106, 124], Fe oxides (maghemite; magnetite) (~45 nm) [118, 125], and tridymite grains of a few nanometers up to 60 nm, and (ii) amorphous magnesiosilica and ferrosilica grains. Once formed, metal oxide nuclei could grow rapidly with no need of vapor mixing. Though some variation about an average grain composition was expected, it was not expected that any significant chemical processing could occur during the extremely rapid growth of the condensates. Yet, it did happen for magnesiosilica and ferrosilica grains. Grain formation is a stochastic, kinetically controlled process that occurs far from equilibrium, and phase changes are driven by the surface properties of the condensates. Prior to equalization of the gas and grain temperatures, the pre-equilibrium regime is

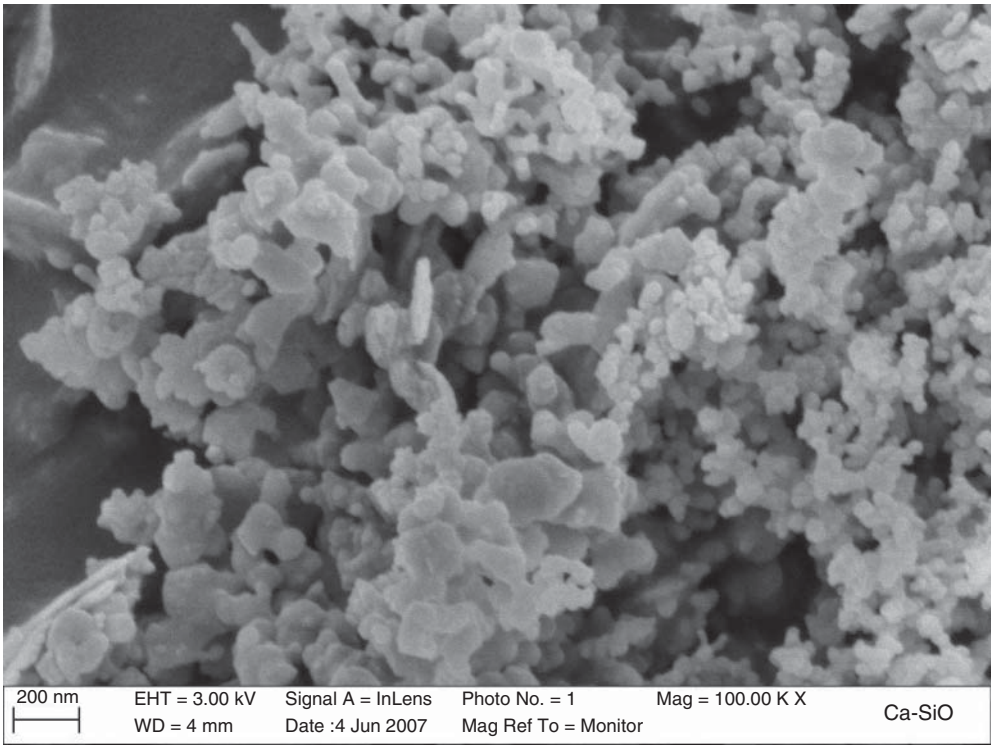

Figure 7.17 Scanning electron image of a Ca–SiO smoke with many plate-like grains >100 nm. Fine-grained smoke is visible near the right-hand side of this image. (Reproduced from Ref. [123]; image credit: Dr. Edith Hadamcik, UPMC Université Paris 06.)

characterized by cycles of condensation and evaporation [126] (Figure 7.18). The most abundant amorphous condensate grains of <25 nm that formed in this pre-equilibrium regime were dissipative structures wherein disequilibrium became a source of order [127].

The chemical compositions of the smallest magnesiosilica and ferrosilica condensate grains define three distinct Gaussian distributions: (i) magnesiosilica grains with 26 ± 7 wt% MgO, (ii) 46 ± 2 wt% MgO, and (iii) 87 ± 3.5 wt% MgO [124]; and ferrosilica grains with (i) ∼15 and ∼30 wt% FeO, (ii) ∼75 wt% FeO, and (iii) 97 wt% FeO [104, 125]. Subsequent condensation experiments occasionally showed slight shifts in these mean compositions, but they gave no cause to revise the original finding. Owing to variable oxidation states during vapor-phase condensation in the CFA, the smallest ferrosilica grains have variable FeO/Fe_2O_3 ratios which gave rise to two populations of low-Fe ferrosilica condensate grains. The population at ∼75 wt% FeO is rarely found, as it requires that only bivalent iron be present in the condensing vapor. These unique amorphous condensate grain compositions are reproducible, indicating that they are not a random phenomenon. These deep metastable eutectic (DME)

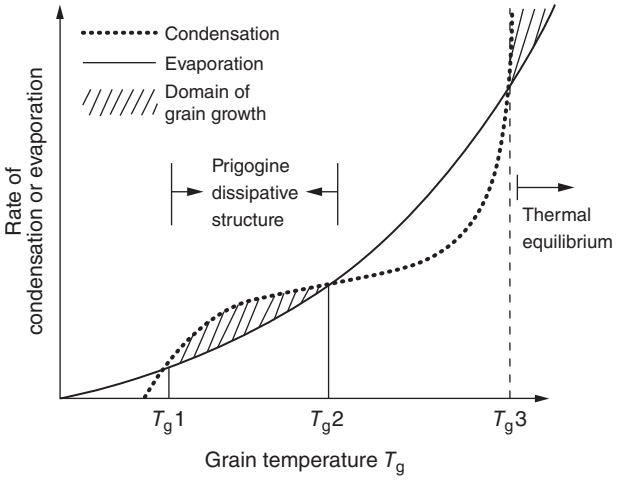

Figure 7.18 Condensation or evaporation rates as a function of grain temperature (T_g) in a nonequilibrium state prior to thermal equilibrium. (Reprinted from Ref. [126] with kind permission of Springer Science and Business Media and the author.)

condensate compositions in the MgO–SiO_2 and pseudo-binary FeO/Fe_2O_3-SiO_2 phase diagrams are shown in Figure 7.19.

A DME composition is possible in binary systems when the phase diagram has two stable eutectics, as is illustrated in the hypothetical A–B phase diagram with two eutectics (Figure 7.20). The extended liquidus boundaries from the eutectic points to lower temperatures eventually intersect at a DME point that is probably below the glass-transition temperature. Nanograins with a DME composition do not show the typical eutectic structure seen in ceramics and metals. The number of grain populations with a DME composition is determined not by the bulk composition of the condensing vapor but only by the number of eutectics in the phase diagram.

The DME compositions are (i) $Mg_3Si_2O_7$ and $Fe_3Si_2O_7$ serpentine dehydroxylate compounds, (ii) $Mg_6Si_8O_{22}$ and $Fe_6Si_8O_{22}$ smectite dehydroxylate compounds, and (iii) (unnamed) very low silicon MgSiO and low-silicon FeSiO compounds. The number of grains in the DME populations is a function of the bulk vapor composition [119]. As the condensing vapors are Si-rich, the number of condensate grains in the third DME population is typically very small. None of the amorphous DME magnesiosilica and ferrosilica grains has an olivine or pyroxene composition. Rare nanometer-scale crystalline forsterite in some magnesiosilica smokes [106] is possibly the result of a reaction between condensed Mg_2Si [121] and SiO vapor molecules [120, 128], namely, $Mg_2Si + 4SiO \Rightarrow Mg_2SiO_4 + 3Si^0$, due to variable oxidation states during condensation. It could also be the product of the reaction of condensed Mg_2Si with water vapor or atmospheric oxygen. While nonequilibrium condensation produces amorphous magnesiosilica and ferrosilica grains with very specific DME compositions, it

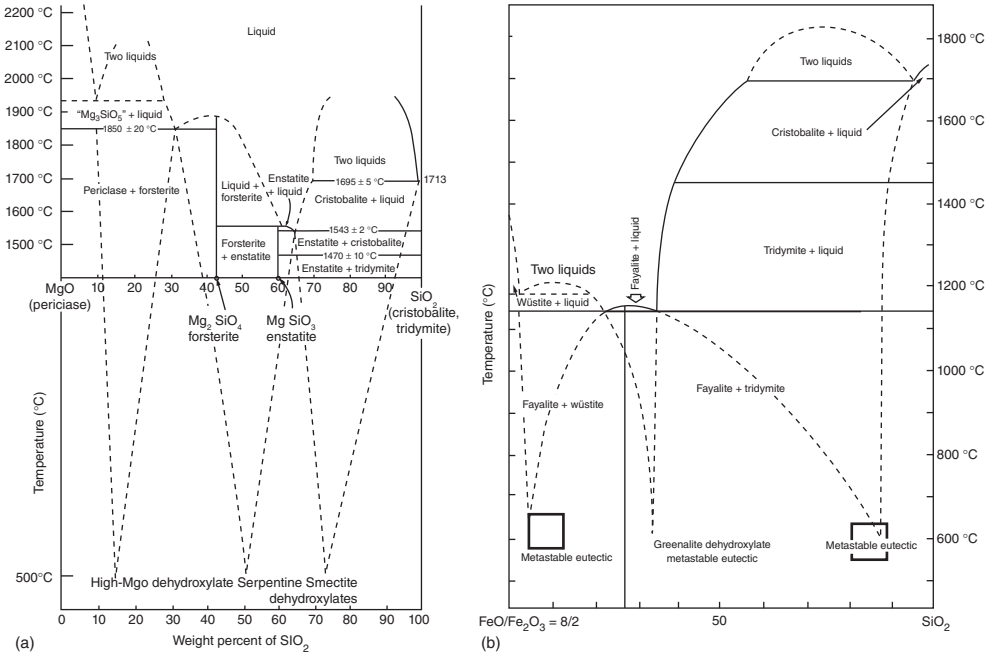

Figure 7.19 (a) Modified MgO–SiO_2 phase diagram showing the three deep metastable eutectic compositions (labeled) found in Mg–SiO–H_2–O_2 vapor phase condensation experiments. The metastable compound compositions cannot be fixed at a specific temperature in this diagram. The temperature refers to the quench temperature of the experiments and has no other significance. (b) The FeO/Fe_2O_3–SiO_2 phase diagram with both deep metastable eutectic compositions (open squares) found in Fe–SiO–H_2–O_2 vapor-phase condensation experiments at FeO/Fe_2O_3 = 8/2. The phase relationships in this diagram allow a third deep metastable compound. It is rarely found because it requires all iron to be in the ferrous state. (Reproduced from Ref. [125] with permission from the PCCP Owner Societies.) The same caveat as Figure 7.19 applies to the temperature.

does not yield amorphous olivine and pyroxene silicates. Thus, vapor-phase condensation experiments using Mg–Fe–SiO–H_2–O_2 vapors will be more realistic in constraining amorphous magnesium iron silicate formation in circumstellar disks around young stars.

7.3.3
Magnesium Iron Silicates

The Fe–Mg–SiO–H_2–O_2 vapor phase condensation experiments produced interconnected strands of magnesiosilica and ferrosilica grains that formed open aggregates [104]. The rounded and subhedral amorphous ferrosilica grains, ~10 to 30 nm in diameter (mean = 17 nm), have DME compositions: (i) ~10 wt% FeO and 22–30 wt% FeO (mean = 26 wt% FeO) of smectite dehydroxylate, (ii) serpentine dehydroxylate, 70–75 wt% FeO, and (iii) low-Si ferrosilica compounds.

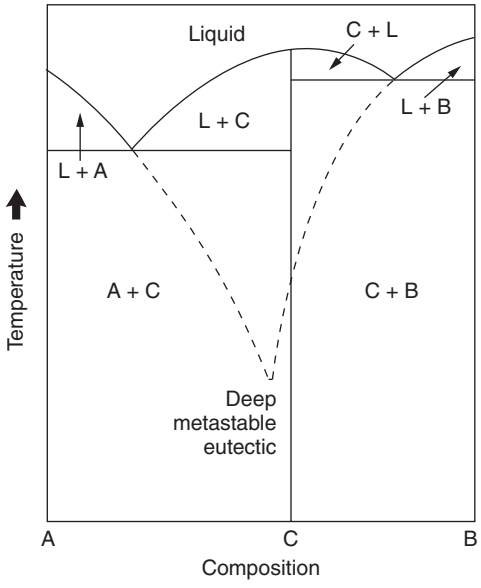

Figure 7.20 The hypothetical binary phase diagram with end-member compositions A and B showing the deep metastable eutectic that occurs at the intersection of the metastable extensions of the liquidus surface (dashed lines). The DME composition is between two eutectic compositions and below the glass-transition temperature.

Although the smallest magnesiosilica grains (40 nm in diameter) had experienced mild grain coarsening, their compositions still preserved the aforementioned magnesiosilica DME compositions, including the 48 wt% MgO serpentine dehydroxylate, $Mg_3Si_2O_7$ (Figure 7.21). The small grains that condensed in Mg–Fe–SiO–H_2–O_2 vapors mimicked the condensation behavior observed in the MgO–SiO_2 and FeO/Fe_2O_3–SiO_2 systems. There is a complete lack of condensate grains with variable Mg/Fe/Si ratios, and there are no condensates with preferred MgO–FeO/Fe_2O_3 compositions (Figure 7.21).

The MgO–Fe_2O_3 and MgO–FeO phase diagrams [129, 130] show complete solid solution, which means there is no opportunity to form metastable eutectic Mg,Fe oxides. Since none was produced, their absence is consistent with the hypothesis that grains with DME compositions due to nonequilibrium vapor phase condensation occur only in binary systems with at least two stable eutectics. It follows that nonequilibrium vapor-phase condensation cannot directly yield amorphous silicates (olivine and pyroxene) and will never yield amorphous Mg,Fe silicates.

Is it possible that amorphous magnesium iron silicates could be formed by reactions between condensed amorphous Mg and Fe silicates? Given their nanometer-scale size, amorphous structure, and highly metastable nature, DME compositions will be prone to equilibration reactions, especially those that reduce the surface-to-volume ratio of the grains. The resulting larger but still amorphous grains will

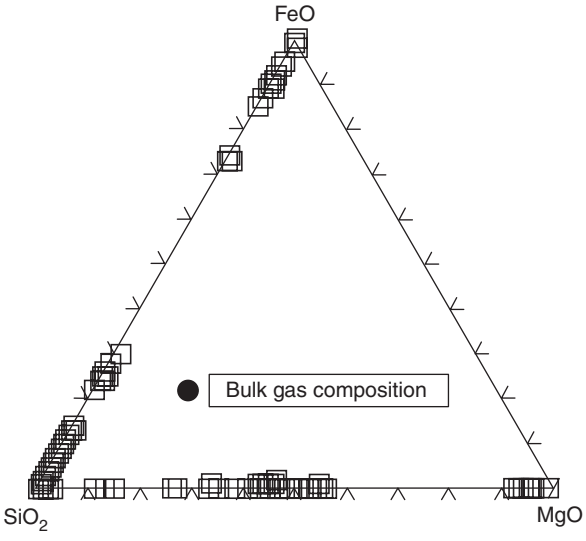

Figure 7.21 A MgO–FeO–SiO_2 diagram with the magnesiosilica and ferrosilica compositions of the smallest grains produced during condensation of a Mg–Fe–SiO–H_2–O_2 vapor [104]. (Reproduced from Ref. [113].) Present in the sample, but not shown in the figure, were periclase (MgO grains (70–140 nm), magnetite (Fe_3O_4) and maghémite (γ-Fe_2O_3) grains (30–350 nm), and SiO_2 (tridymite) grains 10 nm in size).

have Mg,Fe silicate compositions that evolved along the tie lines and between the DME compositions connecting the Mg–Si and Fe–Si joints of the diagram (Figure 7.22). They also evolve along the tie line between the very low Si MgSiO and low Si FeSiO DME compounds that typically occur in low abundances. They will not make a significant contribution during this chemical evolution. Most of the smallest condensate grains are expected to evolve along the tie lines connecting serpentine dehydroxylate (S-d) and smectite dehydroxylate (Sm-d) DME compositions. The Sm-d compositions on the Si–Fe joint of the diagram reflect the different iron oxide states of the DME ferrosilica grains. The ferrosilica S-d DME composition is $Fe_3Si_2O_7$ with ferrous iron only. They reflect the variable Fe oxidation states during condensation in the CFA.

Similar chemical evolution was observed among the DME Al,Fe silica grains that formed during condensation of Al–Fe–SiO–H_2–O_2 vapors. In these vapor-phase condensation experiments, this process led to the formation of amorphous Fe–Al silicate grains of up to 450 nm in diameter that had a stoichiometric Fe-cordierite composition [118]. It seems possible that amorphous magnesium iron silicates could also evolve from very small amorphous Mg and Fe silicates from nonequilibrium vapor-phase condensation. Assuming that intersections of tie lines are loci for preferred Mg,Fe silicate compositions, these larger amorphous silicates will be Mg-rich with Mg/(Mg + Fe) ~0.6 (Figure 7.22). These magnesium iron silicate compositions do not include stoichiometric silicate compositions except

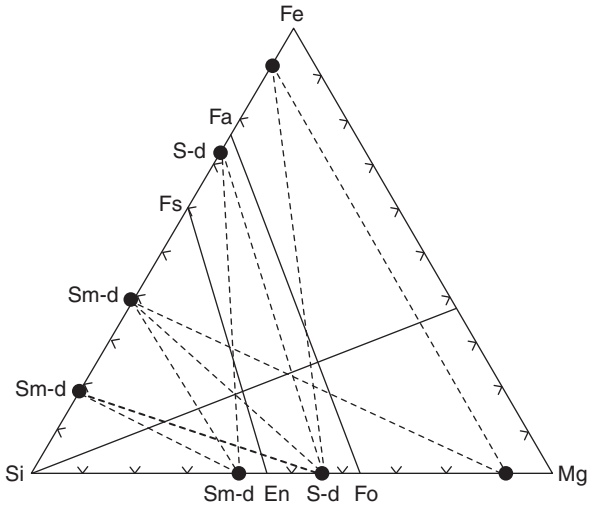

Figure 7.22 Deep metastable eutectic compositions of amorphous Mg and Fe silicates (dots) formed by nonequilibrium vapor-phase condensation of Mg–Fe–SiO–H_2–O_2 vapors and connected by tie lines (dashed) across the Si–Mg–Fe (el %) diagram, Sm-d; S-d. To avoid clutter, the diagram does not show all possible tie lines between the less abundant very low Si MgSiO and low-Si FeSiO DME compounds. The upper limit, Mg/(Mg + Fe) ~0.6, of amorphous magnesium iron silicates is indicated by the thin line from the Si corner to the Mg–Fe joint.

amorphous pyroxene, Mg/(Mg + Fe) ~0.6. Should conditions allow, it becomes crystalline Mg-rich Mg,Fe pyroxene.

7.3.4
Time Versus Temperature

The condensed samples are porous aggregates. Such open structures are not conducive to post-condensation thermal annealing. Annealing of porous magnesiosilica smokes initially showed changes in chemical bonds but no mineralogical adjustments. At higher temperatures and/or longer times, no detectable chemical and crystallographic changes were detected and sample development appeared to have stalled [131] except for pervasive grain growth and formation of contiguous amorphous domains [106]. With continued heat treatment entering the post-stall phase, silicate crystallization occurred with the formation first of forsterite olivine plus tridymite (SiO_2) and followed by enstatite pyroxene [106]. The time–temperature relationship of entering and exiting the stall phase of the porous smoke samples reached reasonable times only above 1050 K. By contrast, crystallization of the same metastable crystalline silicates in a nonporous, amorphous magnesiosilica smoke bypassed the stall phase entirely [105] (Figure 7.23).

Ultimately, thermal annealing yields various predictable mixtures of forsterite, enstatite, crystalline SiO_2, amorphous magnesiosilica grains with stoichiometric

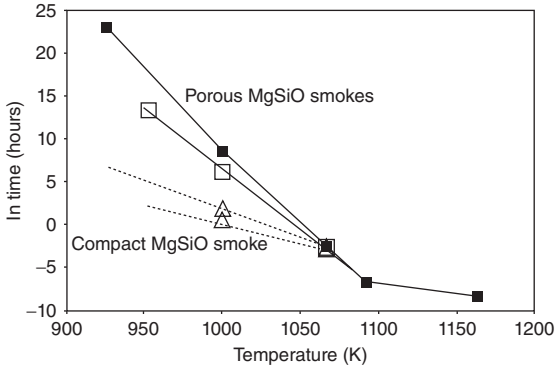

Figure 7.23 Time–temperature relationship for textural, chemical, and mineralogical evolution of amorphous magnesiosilica. The porous magnesiosilica smoke enters (open squares) and exits (solid squares) the stall phase much more slowly [106, 131] as a function of temperature than the compact MgSiO smoke (open triangles) [105]). (Modified after Ref. [132].)

olivine or pyroxene composition, and amorphous magnesiosilica grains with a serpentine or smectite dehydroxylate composition. Combinations of these amorphous and crystalline grains match those observed around Herbig Ae/Be stars wherein they constrain the Mg silicate mineralogical processes and the possible geological environments around these young stars [133].

The formation on geologically reasonable short timescales of crystalline olivine and pyroxene silicates from evolved amorphous magnesium iron silicate precursors after significant textural readjustments is possible. This can be achieved by thermal annealing alone and does not necessarily require a primitive parent body. These resulting crystalline silicates will be Mg-rich Mg,Fe olivine and pyroxene plus silica. Is there any evidence for such silicates? Chondritic aggregate IDPs are still the best resource to study the chemical and mineralogical properties of the least modified solar nebula dust. Many of these IDPs contain isolated grains that consist of a single olivine crystal, a single pyroxene crystal, and an amorphous silica grain, and the crystalline silicates have Fe-rich Mg,Fe silicate compositions (Figure 7.24). These composite grains in the matrix of aggregate IDPs match the predicted properties of the crystalline Fe-rich Mg,Fe olivine and pyroxene silicates [113, 134].

Unambiguous evidence for either equilibrium or nonequilibrium vapor-phase condensation origins of amorphous or crystalline magnesium iron silicates still remains to be found in these IDPs. These high-Mg magnesium iron silicates in chondritic aggregate IDPs may be end products of a process that began with nonequilibrium condensation of amorphous DME Mg silicate and Fe silicate grains in circumstellar or protostellar environments. They evolved chemically to amorphous Mg-rich magnesium iron silicates that ultimately underwent devitrification. Neither amorphous nor crystalline magnesium iron silicates form directly by nonequilibrium vapor-phase condensation.

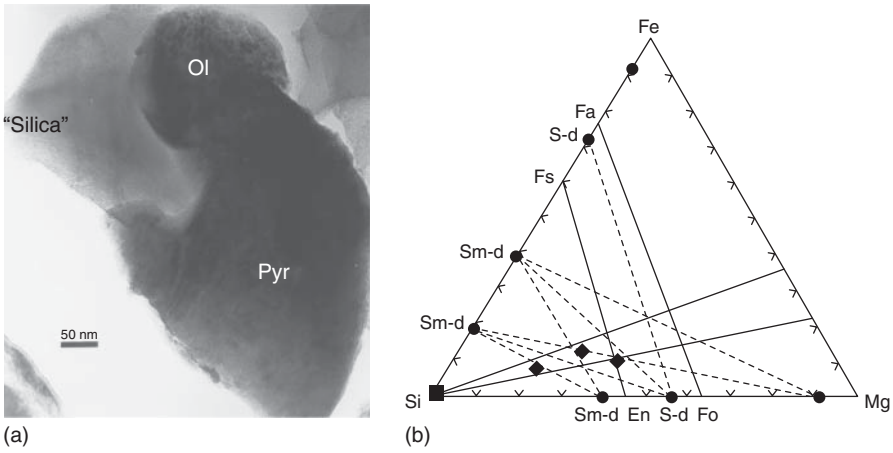

Figure 7.24 Transmission electron micrograph of a typical composite ferromagnesiosilica grain (a) found in the matrix of chondritic aggregate IDPs. They consist of coexisting crystalline olivine (ol) and pyroxene (pyr) crystals and amorphous silica. Its bulk composition, along with two other grains, is shown in the Si–Mg–Fe (el%) diagram (b) wherein they are found on the tie lines connecting the compositions of DME condensates. (Reproduced from Ref. [134] by courtesy of the Mineralogical Society of America and Ref. [113] by courtesy of Urban & Fischer Verlag.)

Despite showing evidence for nonequilibrium vapor-phase condensation and a multistep scenario to evolve crystalline magnesium iron silicates, one must not lose sight that the very nature of laboratory vapor-phase condensation experiments might affect our interpretations of the results. In the CFA, the condensing species, namely Mg, Fe, and Si, were introduced from different precursor materials. This is fundamentally different from condensation experiments wherein vapors are created by ablation or evaporation of crystalline silicates. It is possible that nanometer-scale fragments of these materials become the seeds for vapor-phase condensation. For example, powders of natural (terrestrial) low-Fe olivine (Fo84 and Fo92) produced condensates with almost identical compositions [135]. Interestingly, these experiments produced Mg–Fe–Si condensate compositions that are almost identical to the $MgO–FeO–SiO_2$ condensate compositions in the CFA condensation experiments (Figure 7.21) and those predicted along the tie lines of Figure 7.22, including the absence of Mg,Fe oxides. But whereas Nagahara *et al.* [135] concluded that crystalline forsterite, enstatite, and tridymite condensed directly from the gas phase, experiments using the CFA with newly created $Mg–SiO–H_2–O_2$, $Fe–SiO–H_2–O_2$, and $Fe–Mg–SiO–H_2–O_2$ vapors concluded that nonequilibrium condensation yielded amorphous magnesiosilica and ferrosilica compositions with specific DME compositions instead of crystalline silicates. Both conclusions are valid, but which one is correct? Perhaps the differences in the methods used to generate condensing vapors will show the condensation behavior that is observably different in different astronomical environments or can be observed as part of an evolving environment.

7.4
Gas-Phase Condensation of Carbonaceous Particles in the Laboratory

Cornelia Jäger, Harald Mutschke

Circumstellar shells of carbon-rich late-type stars are well-known factories of carbonaceous cosmic dust grains. It is imperatively assumed that the formation pathway of carbon determines the resulting structure, chemical composition, and morphology of the condensing grains and therefore also determines the spectral properties of these grains. The knowledge of the formation process, possible precursors, and/or intermediates such as polycyclic aromatic hydrocarbons (PAHs), fullerenes, or polyyne carbon chains, or other types of carbon are indispensable for the definition of the initial dust structure and composition and the understanding of the carbon dust cycle in different astrophysical environments.

Most experimental data on the kinetics of soot formation were obtained in flames and shock waves [136]. Generally, one distinguishes three main steps of soot formation: the formation of the molecular precursors of soot; the particle inception or nucleation, where the transition from a molecular to a particulate regime happens; and the final particle growth step, which can be subdivided again into the growth of particles by addition of gas-phase molecules, such as PAHs, and coagulation via reactive particle–particle collisions, a process which significantly increases particle sizes. The most controversially discussed phase is the nucleation process. So far, this transition is not understood. Soot formation in flames is complicated by temperature inhomogeneities however, which are not a problem in the isothermal gas-phase condensation techniques discussed in this section.

7.4.1
Condensation Pathways of Carbon Nanograins at Different Temperatures

Carbon-rich Asymptotic Giant Branch (AGB) stars are considered to be the most efficient sources for carbon soot production. Pulsations of the helium-burning shells in the AGB stars affect the atmospheres and cause shock fronts, which result in density/pressure fluctuations [137]. For AGB stars with an effective temperature of 2500 and 4000 K, pressure ranges of 3×10^{-5} to 0.1 mbar (0.03–100 dyn cm^{-2}) and $1{\times}10^{-3}$ to 0.8 mbar (1–800 dyn cm^{-2}) have been computed, respectively [138]. However, during pulsation, the pressure can rise by two orders of magnitude, resulting in a strong increase of the dust fraction in the shells [139–141].

Another source for carbonaceous dust grains is the hydrogen-poor Wolf–Rayet (WR) stars with effective temperatures between 20 000 and 90 000 K, running through the WC phase where carbon dust condensation is supposed to start with small carbon chains, which are possible precursors for fullerenes or fullerene fragments that finally form the amorphous carbon (AC) grains [142]. In this scenario, PAHs are completely ruled out as possible intermediates.

Of course, the spectral properties of the condensed carbon particles are affected by their internal structure, chemical composition, and morphology. These properties, in turn, are controlled by the formation pathway of the carbon condensation. Therefore, it is important to know the formation process of cosmic dust grains and possible precursors and/or intermediates such as PAHs, fullerenes, or polyyne carbon chains in order to understand their spectral properties in different astrophysical environments.

Gas-phase condensation experiments have been employed to produce nanometer- and subnanometer-sized carbonaceous particles within two different temperature regimes, a high-temperature (HT) and low-temperature (LT) condensation regime, which come close to the grain formation process suggested to occur in astrophysical environments. More experimental details on the techniques described here can be found in Refs [69, 76, 143, 144].

In HT condensations, either laser ablation of graphite with subsequent condensation of carbonaceous matter in quenching gas atmospheres of He or He/H_2 mixtures at low pressures, or laser-induced pyrolysis (LIP) of gas-phase hydrocarbon precursors (ethylene, acetylene, and benzene) using a pulsed CO_2 laser has been carried out. The laser power density varied between 1×10^7 and 9×10^9 W cm^{-2}, which correlates with the temperature in the condensation zone. Because, however, the laser ablation results in a plasma that is not in thermal equilibrium, the temperature of the electrons, ions, and neutrals are different in the ablation plume. The derived temperature of $\geq$3500 K in the condensation zone is only a lower limit. It is found on the basis of the following observations: High-resolution transmission electron microscope (HRTEM) images of the condensates shows no fractionalization of graphite or ablation of graphene layers. The temperature is high enough to completely evaporate graphite and ignite a plasma. In addition, the vibrational temperature of the plasma generated by laser evaporation of a graphite target in 10 mbar He is between 4000 and 6000 K at power densities of $0.5–2\times10^9$ W cm^{-2} [145].

LT condensation experiments were conducted by LIP of gas-phase hydrocarbon precursors comprising ethylene, acetylene, and benzene. A continuous-wave (cw) CO_2 laser was employed to dissociate the gaseous precursors. In these experiments, the laser power densities varied between 850 and 6400 W cm^{-2}, corresponding to temperatures between 1000 and 1700 K.

The formation pathways were studied by analytical characterization of all the carbonaceous condensates under the assumption that some fractions of the precursor molecules and intermediate products are preserved in the final condensate by efficient and rapid quenching of the condensed carbon materials after their formation. From the nature and composition of precursors and intermediates, formation pathways of solid condensates were construed. The internal structures of the condensed carbon particles were investigated with a HRTEM operating at an acceleration voltage of 300 kV. Soluble components of the condensates were removed by soxhlet extraction with toluene, or with methanol and dichloromethane. The extracts and condensates were characterized by gas chromatography and mass spectrometry (GC–MS), high-performance liquid

chromatography (HPLC) combined with a UV–vis diode array detector, and matrix-assisted laser desorption/ionization in combination with time-of-flight mass spectrometry (MALDI-TOF).

7.4.2 Characterization of the Condensation Products

Particulate carbon can be described on different length scales (Section 7.2). The term *medium-range order* characterizes the arrangement, shape, and size of the structural subunits or building blocks of carbonaceous grains. The hybridization state of carbon and the nature of the bonds between carbon atoms are specified by the short-range order of the material [68, 78]. Both the short- and medium-range orders of carbon structures or grains can be well described by the terms *amorphous carbon* (*AC*) or *hydrogenated amorphous carbon* (*HAC*). Both carbonaceous materials are characterized by aromatic islands of different sizes that are linked by aliphatic structures including sp, sp^2, and sp^3 carbon atoms. Note that an "aliphatic link" can be made of unsaturated and saturated sp, sp^2, and sp^3 hybridized carbons. Carbon dust components in astrophysical environments are often generally described as HACs [73, 101, 146, 147].

Micrographs of the condensed grains formed in the HT condensation regime reveal very small fullerene-like soot structures. These particles are composed of strongly bent graphene layers of varying lengths and distances between the layers. In addition, individual fullerenes, marked by arrows in Figure 7.25a, are produced. Soot condensates containing low amounts of hydrogen show more ordered and frequently closed fullerene cages (Figure 7.25c), whereas condensates with higher hydrogen contents are less ordered and do not show completely closed cages (Figure 7.25b,d). The cage fragments stick together by van der Waals forces or are linked by aliphatic $-CH_x$ groups (Figure 7.25d).

Symmetric and elongated cage molecules of different sizes between 0.5 and 1.03 nm corresponding to fullerenes from C_{36} up to C_{130} [148] are clearly detectable in the HRTEM micrographs. Soot formation via polyyne chains,

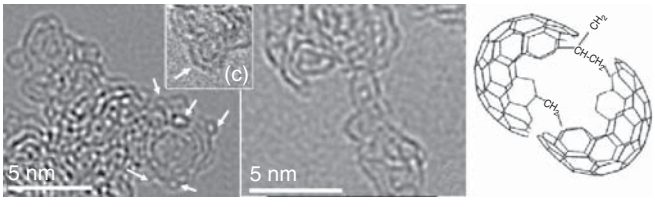

Figure 7.25 HRTEM images of fullerene-like nanoparticles generated in an HT condensation process. Fullerene and elongated fullerene molecules are marked by arrows in (a). Images (b) and (c) present a typical fullerene cage fragment and a bucky onion with two interleaved fullerene cages of 1.7 nm size, respectively. The model in (d) shows the supposed links between fullerene fragments in the grains.

fullerenes, and fullerene snatches has been proposed by Kroto and McKay [149]. MALDI-TOF studies of the HT condensate have shown that no PAHs are formed as intermediates. Quantum chemical molecular dynamics simulations have confirmed that high carbon densities are essential for such processes. Zheng *et al.* [150] found that C_2 molecules quickly react to form long and branched carbon macromolecules at temperatures above 2000 K. The macromolecules form small cyclic structures with attached carbon chains (nucleation). Further ring condensation, for example, between two linear chains, may occur and, consequently, fullerene fragments of bowl shape with side chains are formed [151]. Further, coalescence reactions of small fullerenes [152] can result in the formation of larger and elongated fullerene cages, which have also been observed by HRTEM.

In LT condensation processes, composites consisting of soot grains and PAHs are found. The lower the temperature in the condensation zone, the higher is the content of PAHs. The internal structure of the solid grains can be described by a concentric arrangement of well-developed planar graphene layers surrounding a disordered core (Figure 7.26). Obviously, large aromatic molecules form the particles in such processes. A detailed analysis of the HRTEM micrographs revealed a mean length of the graphene sheets inside the particles of around 2 nm. The largest graphene layers have extensions of about 3 nm, corresponding to the highest mass PAHs detected with mass spectrometry.

Because PAHs are soluble, we soxhlet-extracted them. Infrared (IR) spectroscopy of the PAH mixtures was performed to learn more about the composition of the extracted materials. Figure 7.27 shows a representative spectrum of this material. Aliphatic $-CH_2$ groups can account for the two strong bands at 2923 and 2853 cm^{-1} (3.4 μm (asymmetric and symmetric stretching

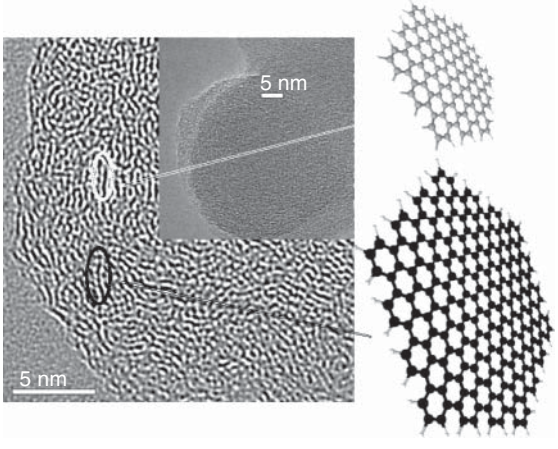

Figure 7.26 HRTEM image of a magnified section of a carbon nanoparticle formed in an LT condensation process. The average length of graphene layers is around 2 nm, which corresponds to PAHs with masses of around 1300 Da (smaller PAH molecule). The largest layers have a size of 3 nm, which correlates with PAHs of about 2700 Da (large molecule).

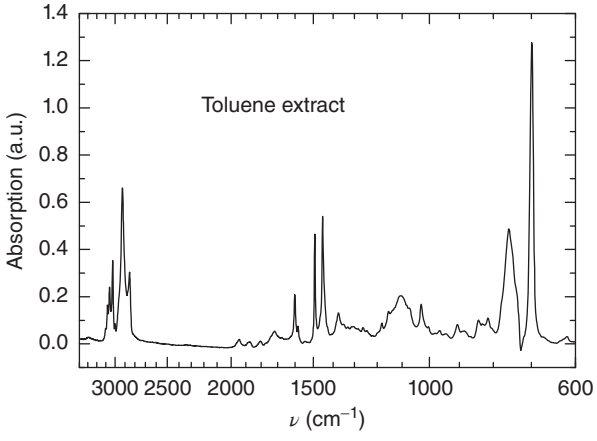

Figure 7.27 IR spectrum of the toluene extract of an LT carbonaceous condensate consisting of 33% PAHs and 67% soot. (Reproduced from Ref. [69] with permission.)

vibrations of $-CH_2$ groups). Thus, the PAHs are partially hydrogenated at the periphery of the molecules and may contain aliphatic side chains containing $-CH_2$ groups such as ethyl groups. The asymmetric and symmetric stretching vibrations of saturated $-CH_3$ groups appear as two weak shoulders at the blue tail of these two bands. A ratio of aromatic =C–H to non-aromatic –C–H groups of around 5 has been derived from the ratio of the bands assuming a 10 times stronger oscillator strength of the saturated –C–H vibrations compared to the aromatic =C–H groups [100]. A much more detailed analysis of the aliphatic groups in the PAH extract and a quantitative comparison with the observed interstellar C–H stretching bands at 3.4 μm based on quantitatively determined oscillator strengths of the –C–H bands are presented in Steglich *et al.* [153].

All the observed IR features in carbonaceous condensates are typical for both nonsubstituted PAHs or PAHs containing methyl or methylene groups, as well as for carbonaceous grains containing aromatic and aliphatic structures.

PAH mixtures were also studied by application of MALDI-TOF mass spectrometry described in Section 7.2. PAHs of up to 3000 Da and more were found (Figure 7.28). The variety of PAHs that are formed in LT condensation is extremely high. All possible isomers of PAHs were seen, but no saturated hydrocarbon molecules could be identified. For comparison, the largest PAH molecule synthesized in a chemical laboratory is of comparable mass and consists of 91 condensed aromatic rings.

7.4.3
Formation Pathways of Carbon Grains and Astrophysical Discussion

The pathways of forming carbonaceous grains are independent of the applied experimental method. Both laser ablation and LIP of hydrocarbons provide the same results in the same temperature regime.

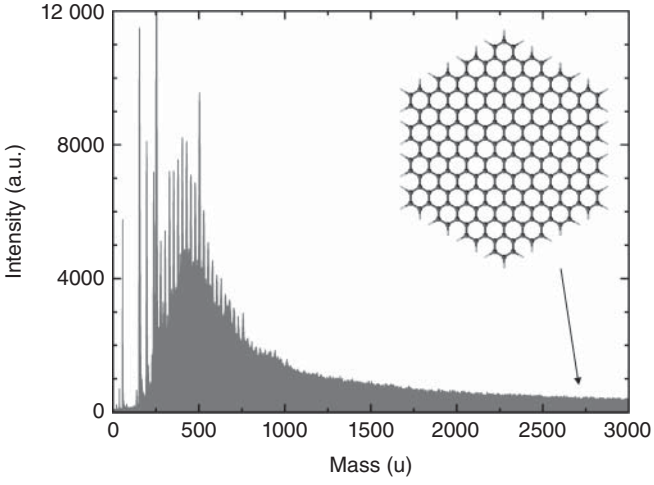

Figure 7.28 MALDI-TOF spectrum of an LT soot sample showing PAHs with masses up to 3000 Da. As an illustration, the inset shows a typical PAH of mass 2700 Da comprising 91 condensed rings (size ~3 nm). (Reproduced from Ref. [144] with permission of the AAS.)

In laboratory simulation experiments, the total pressure is not comparable to those in the atmospheres of dust-forming shells because we use a quenching gas to concentrate the condensation within a relatively small volume. The lower pressure in circumstellar condensation zones means that condensation takes place over longer distances and timescales compared to laboratory experiments. However, this does not mean that this results in a change of the condensate structure. HT condensation experiments performed over different pressure ranges (at ~3 and ~300 mbar) show no difference in the structures of the condensing species. Furthermore, the condensation of graphite is found to be pressure-independent and much more sensitive to the C/O ratio in dust-forming shells [154]. In addition, pulsations of the stellar interior can intermittently increase the pressure and the degree of dust condensation in the dust-forming zones of AGB stars [137, 139].

Carbon grains formed in HT condensation processes are characterized by small fullerene-like particles with sizes up to 3–4 nm and fullerenes of different sizes. The derived formation pathway of the soot particles is characterized by the formation of carbon chains that can form fullerene fragments of bowl shape with side chains. This type of condensation process of carbonaceous nanoparticles is expected to occur in supernovae [155] or in the hot circumstellar environments of carbon-rich stars, such as WR stars [142].

LT condensation starts with the formation of PAHs that are the precursors to particles, which condense on the surface of carbonaceous seeds via physisorption and chemisorption. Large PAHs have a lower volatility compared to the smaller ones. Therefore, a preferred accumulation of large molecules during the surface growth of particles can be observed. The accumulation of large molecules on the surfaces of seeds can be confirmed by a detailed analysis of HRTEM micrographs

(Figure 7.26), which reveal a mean length of the graphene sheets inside the particles of around 2 nm corresponding to PAHs with masses of around 1300 Da. The largest graphene layers determined in the soot particles have extensions of about 3 nm corresponding to biggest PAHs detected. The nature of the seeds is not yet completely understood. Either PAH clusters or large three-dimensional molecules with HAC-like structures may act as seeds in such condensation processes. Large grains are formed, with well-developed planar and slightly bent graphene layers in their interior. LT condensates are composed of soot grains and mixtures of PAHs that show a large variety of sizes, structures, and degrees of hydrogenation.

The experimental conditions are closely comparable to those encountered in circumstellar environments around AGB stars, suggesting that in these environments soot formation is governed by the synthesis of PAHs and their condensation on the surface of grains. Condensation temperatures in our laboratory studies were found to be very similar to the temperature range for carbon dust condensation in carbon-rich AGB stars, as predicted by Cherchneff and Cau [156] to start at a temperature of 1700 K. Carbonaceous condensates consisting of grain/PAH blends show a strong similarity to the IR spectral properties of post-AGB stars and protoplanetary nebulae (PPNs) [157] (Figure 7.30).

7.4.4
Spectral Properties of the HT and LT Condensates

In the UV absorption model developed by Robertson and O'Reilly [158], the band structure is determined by the size distribution of the condensed aromatic islands in the carbonaceous structure and can be expressed by the gap energy E_g. This gap energy can be derived from the optical spectra by means of the Tauc relation $\sqrt{\epsilon_2 E} = B(E - E_g)$ [159], which describes the energy dependence of the imaginary part of the dielectric function $\epsilon_2 = 2nk$ above $\kappa\rho = 10^4\ \mathrm{cm}^{-1}$. Instead of ϵ_2, one can also apply the absorption coefficient α to derive the gap energy, which is a very frequently applied method. However, we should stress that the absorption coefficient is proportional only for a constant refractive index n, which is not completely correct for carbonaceous material.

For the fullerene-like condensate produced in an HT condensation, we have found E_g values between 1.03 and 1.23 eV for the condensates with the lowest (H/C = 0.14) and the highest H content (H/C = 0.57), respectively. According to the relation $E_g = 2\beta M^{-1/2}$ derived by Robertson and O'Reilly [158], where β represents a quantum chemically estimated overlapping energy between two adjacent p_z orbitals and has an empirical value of 2.9 eV, the optical gap energy of soot is related to the number M of condensed rings in the graphene layers. Employing this relation, E_g values between 1.03 and 1.23 eV correspond to 32 to 22 condensed aromatic rings in a graphene layer or to diameters of the graphene layers between 2.8 and 1.7 nm (with the diameter of a single ring being ~0.24 nm).

The calculated lengths of the graphene layers, L_a, are not in agreement with the mean L_a values, but they agree approximately with the maximum L_a values measured by HRTEM. These largest L_a values are representative of only a few

strongly bent larger graphene layers seen as parts of the outer shells of a number of fullerene-like soot particles. The Gaussian contribution at the smallest wavenumbers in the UV–vis spectrum (Figure 7.29), probably caused by plasmon excitation in these few larger graphene layers, can also contribute to the gap energy to a certain extent.

We should note that the discrepancies between the calculated and measured lengths of the graphene layers can either originate from the fact that the calculated E_g values are inaccurate, or the applied model $E_g = 2\beta M^{-1/2}$ is valid only for plane aromatic units and not for bent layers and closed fullerene-like structures. More recent models and actual measurements of gap energies of large PAHs provide much higher values for E_g than calculated by the Tauc relation [160, 161]. The energy gap of PAHs depends not only on the size of the molecules but also on their structure, such as the nature of the periphery [162]. In any case, this investigation demonstrates that, in the case of a soot material with a wide variation of graphene layer sizes and curvatures, the optical gap energy may be of limited value as a structural parameter because it may not reflect the properties of the dominating structural units.

The UV–vis spectral properties of the HT and LT condensates differ considerably. Even though the HT soot grains contain around 50% sp^2-hybridized carbon atoms, the UV spectra do not show clearly distinct UV absorption bands (Figure 7.29). A deconvolution of the absorption band with Gaussian profiles

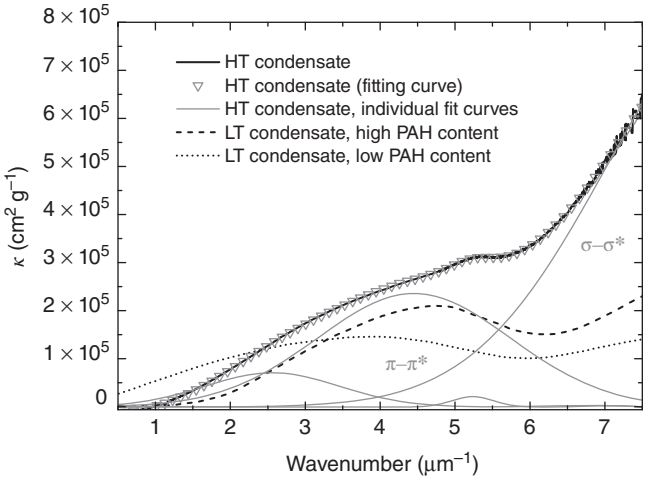

Figure 7.29 UV–vis spectra of selected LT and HT condensate samples. The high-temperature soot sample (thick black curve) has been prepared in a 6 mbar He/H_2 atmosphere by laser ablation (H/C = 0.52). Four individual Gaussian profiles (gray curves) were used to fit the absorption profile, and their sum is indicated by the inverted triangles superimposed on the thick black curve. The dashed and dotted black curves show the UV–vis spectra of two LT condensates containing high and low amounts of the soluble organic component, respectively. (Reproduced from Ref. [144] with permission of the AAS.)

reveals weak and broad bands due to the π–π* transitions between 4.45 and 3.84 μm^{-1}. The exact position of the electronic π–π* transition depends on the hydrogen content and the size of the aromatic clusters [76]. The width of the π–π* main band and the appearance of a plasmon band around 2.5 μm^{-1} (400 nm) result from the structural variety in the carbon particles (distribution of curvatures and lengths of bent graphene layers). A very weak band around 5.2 μm^{-1} (190 nm) can be attributed to the absorption of –C=O groups.

The carbonaceous grains generated in LT condensations have much higher content of sp^2-hybridized carbon atoms, which was found to range between 80% and 92%. The sp^2/sp^3 ratios were determined by near-edge X-ray absorption fine structure spectroscopy and electron energy loss spectroscopy (EELS) [76, 144, 163]. The UV spectra of LT condensates with very similar grain structure and composition (soot and PAH mixtures), produced by propane combustion [164, 165], are shown in Figure 7.29. The typical π–π* transitions ranging between 3.6 and 4.9 μm^{-1} (204 and 256 nm) are clearly visible. As for the HT soot grains, the UV band position is defined by the structure of the soot grains (sp^2 content) and the content and composition of the soluble PAH component, which also contributes to the spectrum. The spectrum with the band position at 3.6 μm^{-1} belongs to a condensate consisting of more than 90% soot. Here, the band position is dominated by the soot fraction and shows a strongly enhanced absorption in the visible range. The second LT spectrum is typical for a composite consisting of a high amount of PAHs (around 50%) and a smaller fraction of soot grains. Since the sizes and structure (sp^2/sp^3 ratios) of the grains are comparable in both condensates, the difference in the positions of the π–π* transitions is mainly due to the difference in the PAH content.

Generally, the mid-IR spectrum of carbonaceous materials is characterized by modes due to the fundamental vibrations of so-called functional groups such as –C=C–, –C–H_x, –C=O, –C–OH, –CHO, –COOH, and –C–N (among others), the position of which in the IR range is affected by adjacent atoms. In contrast, a carbon material without a relevant amount of hydrogen or other heteroatoms and with large aromatic subunits will be dominated by the continuous absorption of free charge carriers (see Section 6.6).

The mid-infrared (MIR) spectra of these gas-phase condensed carbonaceous solids produced in HT and LT condensation show aromatic infrared bands (AIBs) as well as aliphatic IR bands, partly superimposed on broad plateau features around 8 and 12 μm (Figure 7.30) and on the continuous absorption of free charge carriers. The appearance of broad plateaus is related to the spectral characteristics of solid carbonaceous material. Typical saturated aliphatic –CH_x absorption bands are the features at 3.4 μm (ν_{as} and ν_s of –CH, –CH_2, and –CH_3 groups), 6.8, and 7.25 μm (δ_{as} and δ_s) of the latter groups), and a few structures in between 7.4 and ~10 μm. In the HT-produced fullerene-like carbonaceous grains, saturated aliphatic –CH_x groups are mainly responsible for the links between the fullerene fragments [85]. The formation of carbon chains (polyynes) containing –C≡C– triple bonds and ≡C–H as intermediates on the way to fullerenes or fullerene snatches can be verified by the presence of bands at 4.7 and 3.0 μm in

in situ recorded IR spectra. Bands due to –C–C– stretching, –C–H, and –C–C– twisting, wagging, and rocking bands are expected in the range between 7.4 and 10 μm. They may overlap and merge to form broad plateau features. The assignment of these bands is almost impossible because of the occurrence of a multitude of different bands. In the 11–15 μm range, out-of-plane –C–H bending bands can be observed caused by –C–H groups at the periphery of the fullerene snatches. Oxygen-containing functional groups such as –C=O (carbonyl group) can also be incorporated into carbonaceous structures and can be identified at wavelengths between 5.8 and 6.0 μm. However, higher fullerenes can show vibrational modes in this range [94].

The more aromatic carbonaceous material produced by LT condensation of hydrocarbons in LIP [144] shows a series of aromatic bands including 3.3, 6.3, 8.6, 11.3, 12.3, and 13.3 μm as well as aliphatic IR bands at 3.4, 6.8, and 7.25 μm (–C–H stretching and deformation bands). For more detailed information, see Table 7.6. Most of the observed bands are typical of carbonaceous grains and PAHs. After the solvent extraction of the condensate, many IR bands become weaker, or they disappear. Bands of more diagnostic relevance can be found at wavelengths larger than 11 μm, which can be assigned to aromatic =C–H out-of-plane bending vibrations (see Table 7.6 and Figure 7.30).

Carbonaceous condensates consisting of grain/PAH blends show spectral characteristics that are comparable to the observed IR spectra of post-AGB stars and

Table 7.6 IR bands of carbonaceous material before and after the removal of soluble components. Most of the IR bands become weaker after the extraction. Exceptions are the bands at 1600 and 880 cm^{-1}, which became stronger and broader or kept the same intensity, respectively.

Before extraction		After extraction		Band attribution
(cm^{-1})	(μm)	(cm^{-1})	(μm)	
3046	3.3	3046	3.3	Aromatic =C–H stretching vibration
1711	5.84	1716	5.82	–C=O stretching vibration
1595	6.26	1600	6.25	–C=C stretching vibration
1575	6.35	—	—	–C=C stretching vibration
1482	6.74	—	—	–C–H deformation, –C=C stretching vibration
1452	6.88	—	—	–C–H deformation
1440	6.94	1439	6.95	–C–H deformation
1426	7.01	—	—	–C–H deformation
1385	7.22	—	—	–C–H deformation
879	11.15	879	11.37	Aromatic =C-H out-of-plane (1H)
841	11.89	835	11.98	Aromatic =C–H out-of-plane (1H, 2 adjacent H)
829	12.06	822	12.16	Aromatic =C–H out-of-plane (1H, 2 adjacent H)
817	12.23	817	12.23	Aromatic =C–H out-of-plane (1H, 2 adjacent H)
812	12.31	—	—	Aromatic =C–H out-of-plane (2 or 3 adjacent H)
753	13.28	754	13.26	Aromatic =C–H out-of-plane (3 or 4 adjacent H)
737	13.57	731	13.68	Aromatic =C–H out-of-plane (4 or 5 adjacent H)
699	14.30	695	14.39	Aromatic =C–H out-of-plane (5 adjacent H)

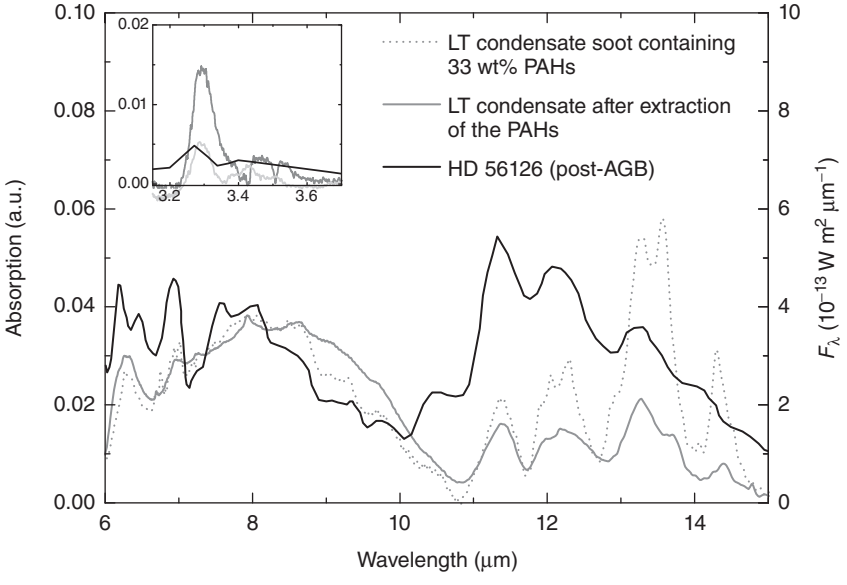

Figure 7.30 Comparison between the IR spectral properties of a carbonaceous condensate that consists of a mixture of solid carbon particles and PAHs and the observed spectrum of a post-AGB star. Adapted from Ref. [157]. (Reproduced from Ref. [144] with permission of the AAS.)

PPNs [157, 166, 167]. A comparison shown in Figure 7.30 demonstrates that nearly all the IR bands observed in the spectrum of the post-AGB star HD 56126 are also present in the spectrum of the laboratory LT condensate. The differences in band ratios, apparent for the =C–H out-of-plane bands between 11 and 14 μm, are due to a higher abundance of small PAHs or to larger PAHs containing outer rings with up to 3–4 H atoms compared to larger compactly condensed species which are thought to be very stable under astrophysical conditions. Spectra of carbonaceous particles built up by large PAHs in the growth process and purified from the adsorbed smaller PAHs by extraction show a better coincidence with the observed bands (gray solid curve in Figure 7.30). However, in order to obtain a dominance of the 11.3 μm out-of-plane band due to solo =C–H frequently observed in (PPNs and planetary nebulae (PNs), very large ($N_C \geq 100$) and rather elongated, ribbon-like PAH molecules are required [168]. Apart from differences in intensities and band ratios, the comparison reveals that the LT condensate is a promising dust analog for carbonaceous materials produced in carbon-rich AGB stars.

7.5
Processing of Silicates

Cornelia Jäger

Circumstellar shells represent the major dust factories, contributing about 85% to the entire dust budget (see Section 7.1) [169]. Strong stellar winds and shock waves

distribute the cosmic dust into the interstellar medium (ISM) where it is subjected to chemical and structural alteration as a result of harsh UV irradiation, ion bombardment, and destructive processes including erosion by sputtering processes, grain shattering, heating, and evaporation by shock waves.

According to Draine [170], only 4–6% of the circumstellar dust survives in the ISM. The destruction rate of dust was found to be faster than the stardust injection rate. On the other hand, measurements of the interstellar depletion [171] make clear that 99.9% of all refractory materials reside in solid grains in the ISM. Therefore, besides the UV- and ion-induced processing of cosmic grains, a recondensation of dust in the ISM is required. Very recently, the condensation of silicates at conditions prevailing in molecular clouds – which means temperatures of about 10 K – by the accretion of molecular silicon-bearing species on cold surfaces was studied in the laboratory [172, 173]. An efficient silicate formation at low temperature was experimentally proven.

Cosmic dust processing in various astrophysical environments is responsible for the continuous structural and chemical modifications of dust grains. It is indispensable to study these processes in the laboratory and to monitor these changes with respect to the spectral data over a broad wavelength range.

7.5.1 Thermal Annealing

Annealing of cosmic dust grains in different astrophysical environments is a major form of dust processing. The annealing of freshly formed dust grains may happen in the envelopes around Asymptotic Giant Branch (AGB) stars [174, 175], in the ISM due to annealing by high-energy photons and partly by shock waves, and in protoplanetary disks. One of the most exciting results of satellite-borne infrared (IR) observations was the detection of a fraction of crystalline silicates among the amorphous phases in circumstellar environments and around young stellar objects. This raised the question of under what conditions can such crystalline phases be formed in astrophysical environments. Therefore, quite a number of laboratory groups are working on annealing experiments of silicate dusts to see at what temperature the crystallization can be triggered and what timescales are necessary to crystallize silicates.

In a study of the modification of stoichiometry upon annealing of tridymite and forsterite nanocrystals (at 1000 K up to 4 h), the authors saw that nanocrystalline phases of forsterite and tridymite are not thermodynamically stable at that high temperature and evolve into enstatite crystals [105]. Such solid–solid reactions may be responsible for the formation of new stoichiometric compounds under certain conditions.

The spectral development of the 10 μm IR band of amorphous magnesium silicate and magnesium iron silicate smoke in a temperature range between 1000 and 1200 K has also been studied [176]. The authors observed clear signs of crystallization after annealing for 10.5 h at a temperature of 1027 K, and determined an activation energy for crystallization of E_a/k of 45 500 K for Mg_2SiO_4

smoke (see Section 7.3). The activation energy was calculated according to the equation $\tau^{-1} = \nu_0 e^{-E_a/kT}$, where ν_0 represents a constant proportional to the mean vibrational frequency of the silicate lattice $\nu_0 = 2.0 \times 10^{13}$ s^{-1} [174, 177]. During the annealing, there appeared a pause in the spectral evolution. The duration of the spectral "stall" was found to be highly dependent on the temperature. A possible reason of this stall phase is the inhomogeneity and porosity of the grains (see Section 7.3). The grains later developed into a structural order and formed pure forsterite phases. Olivine and forsterite are minerals that are frequently observed as cosmic dust components in different astrophysical environments (see Section 7.1 and Chapter 6).

The structural and spectral evolution of the silicate materials depends strongly on the composition and homogeneity of the amorphous precursor materials. For comparison, other experiments provided lower values of activation energy, and could not detect the spectral stall phase for more homogeneous material [178–181]. The final crystallized phase corresponds to the initial amorphous phase that was annealed; that is, amorphous silicate of pyroxene stoichiometry produces an ordered material belonging to the pyroxene minerals whereas olivine-like amorphous silicates form olivine minerals. For comparison, the derived activation energies of crystallization for differently produced silicate materials and the calculated time scales for crystallization are presented in Table 7.7.

Studies by Jäger *et al.* [180] showed that the incorporation of chemically bound (non-associated) OH^- or Fe^{2+} ions (both are network modifiers in amorphous silicates) decreases the viscosity of the material at elevated temperatures and, therefore, strongly decreases the activation energy for crystallization. This results in a drastic reduction of the timescales for crystallization. The incorporation of OH^- into the silicate structure can be frequently observed in sol–gel-produced magnesium silicates in the course of chemical condensation in water/alcohol mixtures. In fact, the formation of magnesium silicates with a small content of isolated Si–OH or Mg–OH bonds in astrophysical condensation zones can be considered to

Table 7.7 Activation energies of crystallization E_a/k determined for differently produced magnesium silicates.

Composition	Production method	E_a/k (K)	Time scale for crystallization
Mg_2SiO_4	Gas-phase condensation	45 500[a)]	300,000 a (750 K)
Mg_2SiO_4	Laser ablation	39 100[b)]	102 h (900 K) 70 a (750 K)
$Mg_{0.95}Fe_{0.05}SiO_3$	Glass	38 500[b)]	30 a
Mg_xSiO_{2+x} $x = 0.7–2.4$	Sol–gel process	26 600, ..., 31 700[c)] dependent on Si-OH content	Minutes to hours (750 K)

[a)] Hallenbeck *et al.* [176].
[b)] Fabian *et al.* [179].
[c)] Jäger *et al.* [180].

be highly probable, since H_2O, the most abundant oxygen-bearing molecule, participates in the formation of olivine- and pyroxene-type silicates [174].

These studies demonstrated that the relevant timescales for certain temperatures are short enough to match the residence time of amorphous silicates in circumstellar shells and thus to produce a fraction of crystalline silicates from amorphous ones by thermal annealing in the condensation zone of these shells.

7.5.2 Ion Bombardment

Dust in astrophysical environments is permanently subjected to energetic ionizing particle irradiation which affects the composition, structure, and morphology of dust gains. The source of such ions can be cosmic rays, ions accelerated in shock waves, or stellar winds. To understand the effects of ion bombardment on cosmic dust, we need to understand the interaction between the incident ions and solid matter, as well as the processing and damage caused by the ions in the cosmic dust grains. Potential consequences in the solid grains could be ionization of atoms, destruction of chemical bonds, electronic excitations, activations of phonons, displacements of atoms, and sputtering. When an ion penetrates a solid target, it suffers an energy loss until it is finally stopped. The stopping power S is composed of a nuclear (S_N) and an electronic energy loss (S_E) and refers to an energy deposited per unit length. The stopping power, the number of displacements per incident ion and unit length N_{displ}, the collision cascades, and the penetration depth of the ions can be simulated by a standard numerical code called SRIM (Stopping and Range of Ions in Matter) [182], which is based on Monte Carlo calculations.

Nuclear energy losses comprise the collisions of ions with atoms in the target in an elastic regime causing atom displacements (knock-on processes) and the formation of point defects. A primary knock-on process can produce a number of further atom displacements, resulting in the formation of a collision cascade, that is, a zone where many displacements produce an amorphous structure without long-range order. The overlapping of these cascades is responsible for the amorphization of crystalline targets.

Sputtering is caused either by the ejection of surface atoms by an incident ion or by collision cascades close to the surface of the target. To eject an atom, the deposited energy has to exceed the binding energy of the surface atoms. Sputtering is mainly responsible for complete grain erosion in shock waves [183] or depletion of particular atoms in the outer layers of interstellar dust or solar grains (rim formation) [184]. Sputtering yields and threshold energies for astrophysically relevant materials (silicates, amorphous carbon, ices) using H^+ and He^+ ions are discussed in the literature [185, 186].

Electronic energy loss is responsible for ionization, bond-breaking, and heating of the target. The strong heating of the target material competes with the structural damage by atomic displacements and cascades, allowing defects to be healed out immediately. This process strongly depends on the ratio between the nuclear and electronic stopping power. In some cases, electronic energy

deposition can also cause amorphization of a crystalline target material, at least along the ion tracks [187].

Most of the ion bombardment experiments in laboratory astrophysics were dedicated to understanding the lack of crystalline silicates in the ISM. First experiments on the ion bombardment of olivine and enstatite with 1.5–2 MeV H^+ ions at fluences of 5×10^{15}–7×10^{17} ions cm^{-2} [188] did not show changes in the IR spectral properties and structure. However, two years later, olivine exposed to a fluence of 5×10^{16} ions cm^{-2} of 1.5 MeV Ne^+ did clearly show an amorphization of the mineral [189]. In order to understand the ion-induced processing and amorphization of silicates in the ISM and in protoplanetary disks, more laboratory data were required.

Detailed studies of the amorphization efficiency of astrophysically most abundant He^+ and H^+ ions have been performed by different authors [96, 190–193]. The amorphization process of the crystalline grains can be well monitored either by electron diffraction or by high-resolution transmission electron microscope (HRTEM) analysis which is able to image lattice fringes of crystalline grains [96]. Another frequently used method is IR spectroscopy. The narrow IR bands characteristic of crystalline materials disappear upon the amorphization process, and broad bands typical for amorphous silicates evolve [191]. The experiments have shown that the light He^+ ion is not able to induce amorphization at much more than 50 keV impact energy [96, 191]. The crucial parameter for amorphization to occur is the ratio between the nuclear and electronic energy loss, which increases with the mass of the ions and decreases with acceleration energy. This can be understood if one compares the displacements per atom (dpa), which can be calculated from the employed ion fluences N_I according to the equation $\text{dpa} = N_{\text{displ}} \cdot N_I/N_0$, with N_0 the atomic density of the crystalline target ($MgSiO_3$). According to numerical and experimental results, 50 keV He^+ ions can amorphize crystalline enstatite grains up to a penetration depth of 360 nm at a fluence of 9×10^{16} ions cm^{-2} (corresponding to 5.24 dpa). This means that 5.2 dpa are necessary to induce the amorphization of enstatite grains. Ar^+ ions of 400 keV can amorphize at a fluence of 3×10^{14} ions cm^{-2} corresponding to 0.32 dpa. This dpa value is much lower because of competition of the amorphization caused by displacements and annealing via electronic energy deposition. Ions with $S_N/S_E \geq 0.4$ (50 keV He^+, 400 keV Ar^+, 1.5 MeV Xe^+ ions [194]) are able to amorphize a target efficiently [96] (Figure 7.31). The narrow bands of the crystalline silicate vanish but the 10 μm band does not shift its center of gravity, which means that the stoichiometry of the silicate does not change during the ion bombardment. At these ion energies, the amorphization occurs without changes of the chemical composition of the grains, which was also confirmed by other authors [193].

Grains with pyroxene and olivine stoichiometry bombarded with 20 keV protons (total dose, 1×10^{18} ions cm^{-2}) [184] showed the amorphization of grains accompanied by a depletion of MgO. At <20 keV, He ions selectively sputter Mg and O, depleting MgO [190, 192]. Amorphization of forsterite associated with a chemical change from olivine to pyroxene stoichiometry has been seen to occur

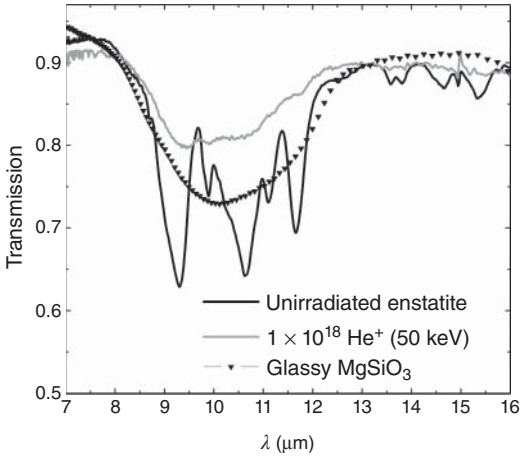

Figure 7.31 IR transmission spectra of nonirradiated and irradiated clino-enstatite compared to a glassy $MgSiO_3$ sample produced by melting and quenching. (Reproduced from Ref. [195] with permission.)

with 4 and 10 keV He^+ ions at a fluence of 1×10^{18} ions cm^{-2} which corresponds to the fluence expected for one shock wave.

In addition to amorphization and chemical erosion, changes in the morphology have also been observed (Figure 7.32), for example, the formation of pores and/or He bubbles, and the erosion of grain edges. The degree of the damage depends on the applied ion fluence [96, 191].

The experimental results on the ion bombardment of silicates finally suggest that one high-velocity shock wave is sufficient to amorphize most crystalline silicate grains [96, 190, 191] and that ion-induced processing is responsible for the absence of crystalline silicates in the ISM.

Solar wind bombardment of olivine was simulated with 1 and 4 keV He^+ ions, which showed the reduction of ferrous iron and even Si^{4+} in the grains [196]. This is due to selective sputtering processes of oxygen by the low-energy ions.

High-energy heavy ions interact with target atoms in the electronic energy loss regime. Consequently, ionization and destruction of bonds along their trajectories can occur within the target, corresponding to a high energy deposition rate. For heavy ions with very high energy, for example, larger than 1 MeV, the energy deposition melts a portion of the target material around the ion track. Amorphization due to heating and melting of the target material is seen in a cylinder of the material, which is followed by a rapid quenching process [197]. Eventually, a liquid-like amorphous structure can be observed. If the density of such tracks is high enough, this mechanism may account for the amorphization process of cosmic dust grains as well. Recently, the amorphization of forsterite bombarded by 10 MeV Xe ions was studied [187]. The authors have extrapolated their experimental results to predict the effects of heavy cosmic ray ions with energies between 0.1 and 5 GeV. They claimed that crystalline silicates can be amorphized on a timescale of around 70

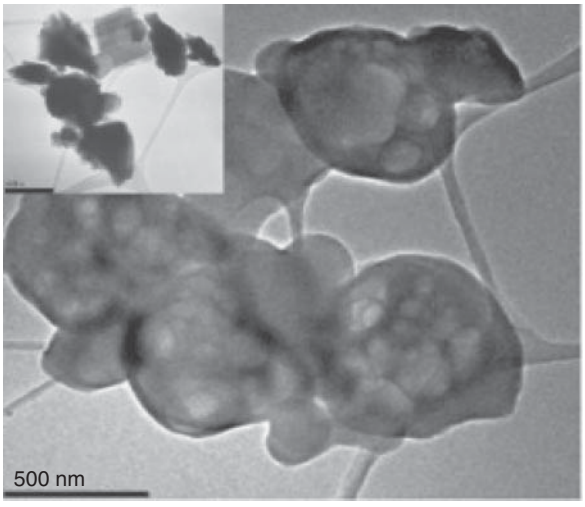

Figure 7.32 Transmission electron microscope (TEM) image of grains before (inset) and after bombardment with 50 keV He^+ at 1×10^{18} ions cm^{-2}. Morphological changes of the grains triggered by ion irradiation are clearly visible. (Reproduced from Ref. [195] with permission.)

Myr, which is shorter than the expected lifetime of interstellar silicates of around 400 Myr [183].

Sputtering, which is expected to occur in interstellar shocks [183, 198], is another important process that may change the composition and cause erosion of cosmic dust grains in interstellar environments. Atoms near the grain surface can be ejected from the surface either by an incident energetic particle or by a collision cascade from within the grain that reaches the surface. The sputtering yield depends on the energy and the angle of the incident ion. The energy that is transferred to the surface atoms has to be higher than the binding energy of the surface atoms. Generally, surface atoms are less strongly bound than bulk atoms, resulting in lower energy thresholds for sputtering processes compared to displacement or amorphization processes. Consequently, the sputtering yield is the highest for low-energy ions having energies between 0.1 and 10 keV. Sputtering yields of different cosmic grain materials have been provided by different authors [199, 200].

Besides the above-mentioned processes, ions can be implanted into dust grains, either in the form of gaseous species in bubbles and pores [190] or as interstitials between regular grain atoms. Subsequent annealing of the implanted materials can lead to the formation of new phases in the matrix.

All the presented laboratory experiments have demonstrated that ion bombardment is one of the most efficient means of modifying the structure, morphology, and composition of cosmic dust grains. However, further experimental work is necessary to fully understand cosmic dust cycles.

7.6 Carbon Dust Modifications under Thermal Annealing and Irradiation by UV Photons, Ions, and H Atoms

Vito Mennella

Carbon grains are an important component of interstellar dust and play a basic role in many interstellar processes. Evidence for their presence in the interstellar medium (ISM) dates back to more than 40 years, when the strongest extinction feature at 217.5 nm was first detected [201]. The band peak position is very stable for different lines of sight, while the width varies by about 25%. The UV bump has been attributed to many carbonaceous materials, spanning from graphite to polycyclic aromatic hydrocarbons (PAHs) molecules (e.g., Refs [202–204]). Nanosized carbon grains containing hydrogen and with a disordered structure are the most promising candidates as carriers of the UV bump [74, 77, 80, 205]. Carbon onions and fullerenes have also been proposed [206–209].

The presence of an aliphatic carbon component in the diffuse regions of the ISM is indicated by the 3.4 μm absorption band, produced by the C–H stretching vibrations of the aliphatic CH_2 and CH_3 functional groups [210]. The C–H bending bands at 6.85 and 7.25 μm have also been observed [211]. Although the carrier of the feature is a widespread component of the diffuse dust, it is absent in dense clouds [212–214]. At least 55% of C–H bonds seen in the diffuse medium are lacking in dense clouds [215]. This difference places severe constraints on models of the formation and evolution of the interstellar aliphatic component [216].

Nearly 30 analog materials have been proposed as carriers of the 3.4 μm absorption band. A thorough comparative analysis suggests that the interstellar carrier contains small amounts of oxygen and nitrogen and is much more similar to plasma-processed hydrocarbon materials than energetically processed ice residues [101]. Any material proposed as component of interstellar dust should be compatible with the physical conditions present in the ISM and with a reliable scenario for its formation and evolution. Heating and interaction with UV photons, cosmic rays, and gas are all processes that modify the composition and structure of cosmic dust. In cold, dense clouds, cosmic rays and UV photons deposit a comparable amount of energy in solids, about 300 and 400 eV per molecule in 10^9 years, respectively [217]. Energy deposition by UV photons dominates in diffuse interstellar clouds, where grains also interact with H atoms with a temperature of 100 K (8×10^{21} H atoms cm^{-2} in the cloud lifetime of 3×10^7 years). In dense clouds, the fluence of H atoms and their temperature are lower, namely 9×10^{19} H atoms cm^{-2} and 10 K, respectively.

Processing assumes particular importance in the case of carbon grains, whose optical properties depend on the structure and the presence of heteroatoms [218, 219]. In fact, the present understanding of hydrogenated carbon materials relies on structural descriptions that imply heterogeneity at the nanometric scale due to the possibility of carbon atoms to have different bonding configurations sp, sp^2, sp^3, which determine the type of bonding between C atoms and heteroatoms such

as hydrogen and oxygen. The electronic density of states and, consequently, the UV–vis optical properties depend on the size of sp^2 clusters and/or the state of bending of graphene layers, as well as on the presence of H atoms which favor sp^3 carbon hybridization [78, 218].

Laboratory simulations that are aimed at studying the spectroscopic modifications of analog materials under processing expected in space play a crucial role for a more realistic description of interstellar carbon dust properties and evolution.

7.6.1 Thermal Annealing

Thermal annealing causes structural changes and variations of the optical properties of hydrogenated carbon materials because of hydrogen effusion. Infrared (IR) spectroscopy has been used to study the evolution of carbon materials with annealing temperature, including different kinds of a-C:H films [220–222], hydrogenated carbon nanoparticles [223], and quenched carbonaceous composites (QCCs) produced by hydrocarbon plasma [82]. Although the details depend on the specific material, there is a general transformation of the C bonds from aliphatic to aromatic. The C–H stretching modes at 2955, 2925, and 2870 cm^{-1} in the CH_2 and CH_3 groups and the corresponding deformation modes near 1460 and 1380 cm^{-1} decrease in intensity with increasing temperature, while, on the contrary, the aromatic C–H stretching mode at 3050 cm^{-1} and the bending modes at ∼820, 750, and 700 cm^{-1} become more intense (Figure 7.33). Moreover, an increase of the band at ∼1600 cm^{-1} due to C–C skeleton vibrations in disordered carbons is observed, indicating an increase in the fraction of sp^2 sites and more ordering in the graphitic clusters. High resolution scanning tunneling microscopy (HRSTM) analysis showed the growth of graphitic clusters as hydrogen and the volatile hydrocarbons were removed from the film [221].

Thermal annealing at moderate temperatures (300–400 °C) activates the $\pi - \pi^*$ UV band in nano-sized hydrogenated carbon grains produced by arc discharge in a H_2 atmosphere [224]. After activation, the $\pi - \pi^*$ resonance becomes more and more intense and shifts toward longer wavelengths with increasing annealing temperature, up to 259 nm at 800 °C. The position of the $\sigma - \sigma^*$ band remains stable at ∼90 nm [225]. A similar intensity increase and wavelength shift, from 242 up to 253 nm at 800 °C, of the UV band has also been observed in more ordered carbon grains [226]. The UV spectral changes of carbon particles are accompanied by the evolution of the absorption edge, with an increase of the absorption in the vis–NIR (near-infrared) range and optical gap closure at ∼600 °C, as well as by changes in the Raman activity [227]. A similar spectral evolution upon heat treatment has been reported for QCCs. QCC films show a wavelength shift, from 204 to 221 nm in the range 180–700 °C, and an intensity decrease of the UV extinction band. These variations are correlated with changes in the sample structure: the amorphous starting material is grainy at 650 °C. A shift of up to 243 nm at 700 °C and intensity reduction have also been reported for dark QCC [206]. In this case, however, high resolution transmission electron microscope (HRTEM) shows that

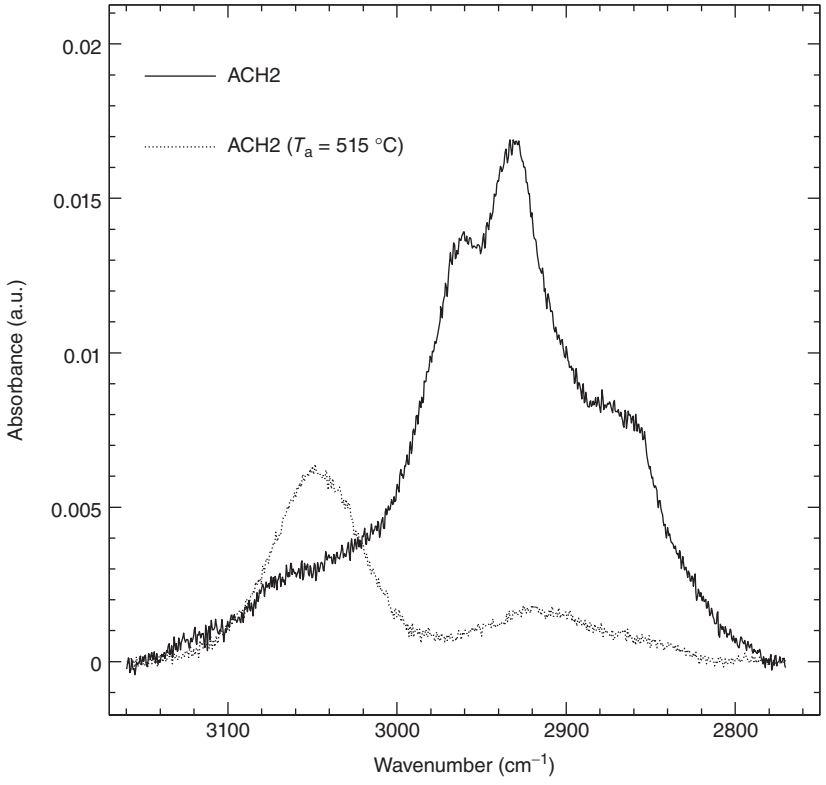

Figure 7.33 Evolution of the C–H stretching band in hydrogenated carbon grains (ACH2) with temperature. Aliphatic sp^3 C–H bonds are predominant before annealing. The overall decrease of the band intensity with temperature indicates hydrogen effusion from the grains. The intensity increase of the band at 3050 cm^{-1} shows that at 515 °C the remaining hydrogen atoms are mainly bonded to sp^2 aromatic sites.

the material is a coagulate of onion-like particles consisting of multiple shells with defects and with a void at the center.

Thermal treatment at higher temperatures produces allotropic changes: the transformation of nanodiamonds (3–6 nm in diameter) into onion-like graphitic particles takes place in the range 1100–1500 °C [228]. The transformation proceeds from the surface to the center in each diamond particle, and at intermediate temperatures the particles have a core–shell structure. Spherical onions without a diamond core are formed at 1700 °C [207]. The structural changes are accompanied by UV–vis spectral variations.

7.6.2 UV Irradiation

Relatively little laboratory data is available for UV and ion irradiation of astrophysically relevant refractory carbonaceous materials. UV irradiation of a-C:H films

induces changes of the absorption edge, with a decrease of the optical gap from 2.2 to 2 eV and a reduction of the 3.4 μm band intensity by ∼10% [229]. No variation of the 3.4 μm band has been reported for a-C:H film after exposure for several hours to the full light from a deuterium lamp [230]. Irradiation experiments of hydrogenated carbon particles were performed under simulated diffuse (i.e., bare grains) and dense (i.e., grains covered with water ice and/or ice mixture at 12 K) ISM conditions [231]. In both cases, UV photon irradiation leads to a reduction of the aliphatic 3.4 μm band intensity. When a water ice layer is present on the carbon grains, this reduction is accompanied by the formation of CO and CO_2 molecules (Figure 7.34) [232]. UV photons transform 6% and 5% of the C atoms of grains to CO and CO_2 molecules, respectively. The production of CO and CO_2 has also been observed with ion bombardment of similar samples [233]. This production mechanism can give a significant contribution to the column densities of CO and CO_2 molecules observed in dense clouds. Irradiation by UV photons

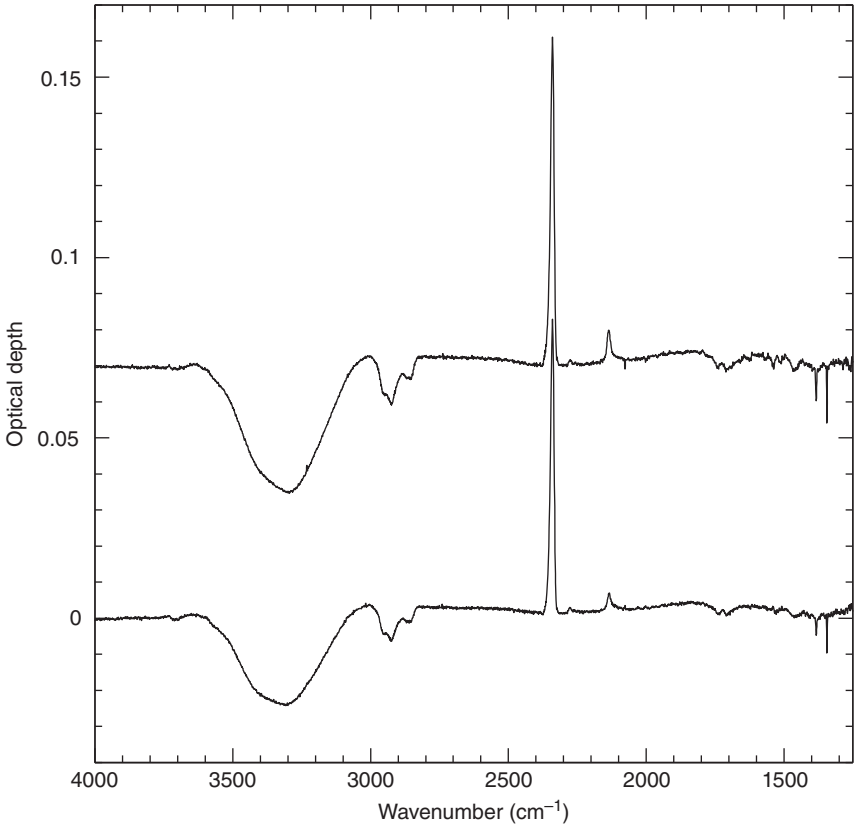

Figure 7.34 Spectra of hydrogenated carbon grains covered with a water ice layer after UV irradiation at fluences of 5×10^{18} (bottom) and 1×10^{19} photons cm^{-2} (top). The spectra are normalized to that before irradiation and are offset for clarity. (Reproduced from Ref. [232] with permission of the AAS.)

and cosmic rays determines a link between the properties of grains and those of their ice mantles. For carbon particles, the chemical composition of the mantle is modified by the formation of CO and CO_2 molecules. This process, in turn, represents a chemical erosion of carbon particles. When grains covered by ice enter into diffuse regions, desorption of the mantles returns the carbon locked in these molecules into the gas phase. UV photons and cosmic rays convert about 55% of C of carbonaceous particles to CO and CO_2 during the grain's lifetime.

Considering the C–H bond photodissociation cross section estimated from the decrease of the C–H stretching band intensity with UV fluence and the interstellar UV flux, one can conclude that the complete destruction of aliphatic C–H bonds by UV photons takes place in about 10^4 years, a time interval that is three orders of magnitude smaller than the typical diffuse cloud life time (3×10^7 years). It is evident that we will not be able to observe the 3.4 μm interstellar feature without a mechanism that is able to counteract the UV photodestruction of C–H bonds and form C–H bond *in situ*.

Unlike for thermal annealing, the conversion of aliphatic C–H bonds into aromatic C–H bonds is not observed during UV processing of hydrogenated carbon grains. The difference between the two processes is confirmed by the changes observed in the UV–vis spectrum of the same material. The evolution of the UV spectrum with the UV fluence is characterized by the activation of the $\pi - \pi^*$ band at 215 nm. The band does not shift, but its intensity increases with the UV fluence [80]. The highest fluence, F_{UV}, tested corresponds to about 13% of the value expected during a typical diffuse cloud timescale. The UV spectral variations are accompanied by a slight decrease of the optical gap. A model based on the results of UV processing of hydrogenated carbon grains has been proposed to reproduce the UV interstellar extinction bump [205]. The interstellar feature is attributed to a linear combination of absorptions of a class of carbon nanoparticles, whose UV extinction profiles vary according to the degree of UV processing along different lines of sight. For UV fluences higher than the maximum laboratory fluence, the UV profiles have been computed by extrapolating the experimental trend of the optical properties up to F_{UV}. The model reproduces the average interstellar UV bump and the observed profiles, with extreme deviations in peak position and width. Recently, UV irradiation experiments of hydrogenated carbon materials confirmed the activation of a UV band [234]. The position of the band shifts from 213 to 217.5 nm with increasing the UV fluence from 21% to 33% of F_{UV}. These experimental peak positions are very close to the predicted values [205]. HRTEM studies indicate that UV irradiation increases the size of the graphene layers (graphitization) in hydrogenated carbon materials [234].

7.6.3 Ion Bombardment

The interaction of a fast ion with a solid target produces several effects, such as sputtering, changes of the chemical properties, and structural modifications due to the ion energy loss through elastic collisions with nuclei and inelastic

collisions with electrons [235]. The effects of ion irradiation in carbon materials have been discussed in Ref. [236]. Many interesting allotropic changes have been observed. Carbon soot transforms into carbon onions under intense electron irradiation [237]. In turn, when such particles are heated at 700 °C and irradiated with electrons, their cores can be transformed to diamond [238]. The production of spherical carbon onions by irradiation of graphitic carbon soot with 3 MeV Ne^+ ions as well as the transformation of their cores to cubic diamond crystals has been reported [239]. A polymer-like refractory organic residue evolving, at higher doses, toward hydrogenated amorphous carbon is formed by ion irradiation of carbon-based ice mixtures at low temperature [240]. The formation of C–C triple bonds is also observed after ion bombardment of different carbon materials [241 – 244].

Spectroscopic studies have shown significant changes of the UV–vis spectrum of hydrogenated and hydrogen-free nano-sized carbon grains after bombardment with 3 keV He^+ ions [245]. In the first case, the UV peak shifts toward longer wavelengths, up to 215 nm, and the optical gap decreases from 1.32 to 0.69 eV. This indicates changes in the π electronic structure due to graphitization of hydrogenated carbon particles. In contrast, ion bombardment of more ordered hydrogen-free carbon particles induces the opposite effect: the UV band shifts from 240 nm to shorter wavelengths, down to 218 nm, and the optical gap slightly increases up to 0.62 eV for a dose of 660 eV per C atom. Similar behavior has been observed in carbon grains after exposure to 20 keV Ne^+ [246]. Amorphization takes place in materials with relatively high degree of sp^2 clustering. This interpretation is supported by the behavior of the G and D first-order Raman bands as a function of exposure [247]. Carbon materials with different starting properties tend to have similar values of the UV peak position (215 and 218 nm) and of the optical gap (0.62 and 0.69 eV) at high irradiation doses. Thus, two opposing processes, namely graphitization and amorphization, can occur when fast colliding ions interact with carbon grains. The prevailing process depends on the properties of the material [236]. However, at high doses, a stable microstructure is attained as a consequence of the competition between the two processes.

Ion beam and residual gas analyses have also shown that hydrogen loss takes place during ion bombardment of hydrogenated carbon films. This is confirmed by IR spectroscopic studies showing a reduction of the aliphatic and aromatic C–H bonds [241]. The cross section of C–H bond dissociation by 1 MeV protons (9.4×10^{-16} cm^2) has been derived by a systematic study of different types of hydrogenated carbon particles bombarded with 30 keV He^+ ions [243]. Although this quantity is about 10^4 times higher than the UV photodissociation cross section of C–H bonds, the high UV photon flux in the diffuse ISM determines a dissociation rate more than three orders of magnitude higher than that of cosmic rays. On the contrary, the dissociation rate by cosmic rays is more than a factor of 2 larger in dense regions.

7.6.4 H-Atom Irradiation

Interstellar gas, in particular H atoms, can induce important changes in refractory carbon grains in space. Atomic hydrogen activates the photoluminescence in non-photoluminescent a-C films and restores the photoluminescence of a-C:H films, previously reduced by irradiation with 250 nm photons. The hydrogenation of pure carbon films is greatly enhanced by the presence of UV irradiation [248].

The interaction of H atoms with hydrogen-free carbon particles determines the formation of C–H bonds [249, 250]. After H-atom irradiation, the C–H stretching vibrations in the aliphatic CH_2 and CH_3 groups at 2955, 2930, and 2870 cm^{-1} and the corresponding deformation modes at 1457 and 1378 cm^{-1} are observed. No formation of aromatic C–H bonds takes place. The C–H stretching and bending bands are strikingly similar, in terms of intensity and wavelength position, to those associated with diffuse interstellar dust (Figure 7.35). The mass absorption coefficient at 3.4 μm is rather high. For such a material, around 60 ppm is required to reproduce the intensity of the 3.4 μm interstellar band. From the increase of the integrated optical depth of the C–H stretching band with H-atom fluence, the cross section for C–H bond formation can be estimated. It decreases with H-atom temperature, indicating that there is an activation energy of about 70 K for the formation of the aliphatic C–H bonds [251]. A different behavior is observed under simulated dense medium conditions. Irradiation of hydrogen-free carbon grain samples covered with a water ice layer at 12 K with atomic hydrogen at 80 K does not activate the aliphatic C–H bonds, while the activation of a band at 2883 cm^{-1} (3.47 μm) takes place (Figure 7.35). The band has been attributed to C–H vibrations of hydrogen solo-bonded to tertiary sp^3 carbon atoms [212, 252]. The different behavior of the two types of C–H bonds has been interpreted in terms of different activation energies for C–H bond formation in aliphatic and tertiary sp^3 carbon sites [252]. The presence of the ice mantle has two effects: it determines adsorption of part of H atoms impinging on the sample, and lowers (down to 12 K) the temperature of atoms reaching carbon grains.

A clear result emerges from the experimental activity aimed at studying UV and cosmic ray irradiation of hydrogenated carbon particles under simulated diffuse and dense ISM conditions: in both environments, energetic processing easily destroys C–H bonds and we should not observe the 3.4 μm band in diffuse regions and the 3.47 μm feature in dense clouds. The key process that is able to counteract C–H bond destruction is the interaction of H atoms with carbon grains. This conclusion is supported by modeling of the evolution of carbon grains based on the experimental cross sections of C–H bond destruction by UV photons and ions and C–H bond formation by H atoms. The model not only gives a solid interpretation of the long-lasting enigmatic difference of the aliphatic feature between diffuse and dense clouds but also indicates a link between the two features (Figure 7.35). Carbon grains, which are responsible for the 3.4 μm in the diffuse regions of the ISM, can contribute to the absorption at 3.47 μm in dense clouds as a consequence of evolutionary transformations caused by processing. A

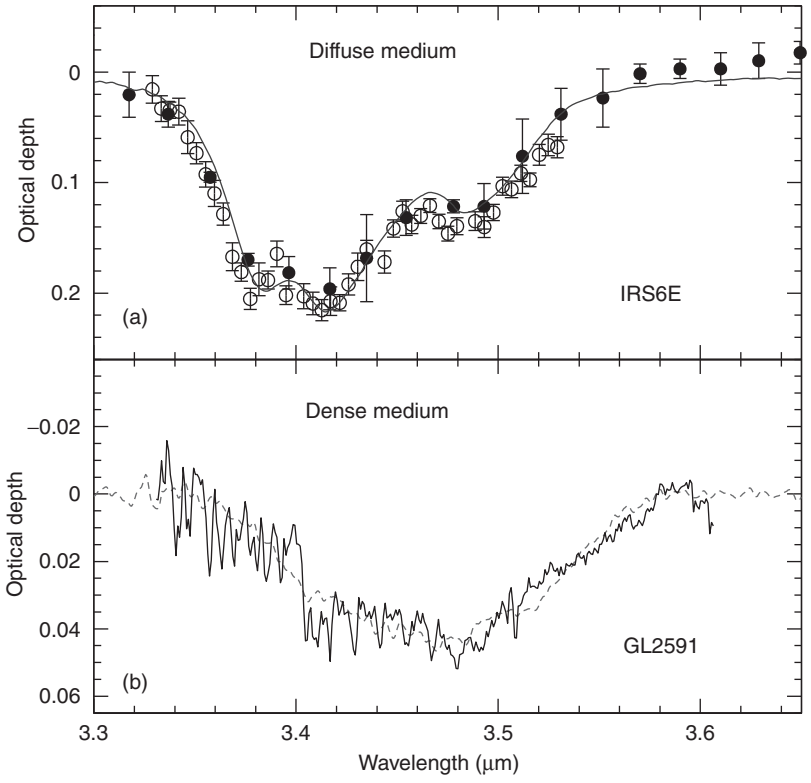

Figure 7.35 (a) The C–H stretching 3.4 μm band of H-processed carbon grains (continuous line) compared to that of diffuse dust observed toward the Galactic center source IRS6E (circles). (b) Comparison of the 3.47 μm band activated by H-atom exposure in carbon grains covered with a water ice layer (dashed lines) with that observed in a dense cloud (continuous lines). The laboratory spectra have been scaled to match the peak optical depth of the interstellar bands.

connection between the interstellar carbon component and the organics observed in interplanetary dust particles (IDPs) and cometary stardust grains has also been proposed [253]. Laboratory simulation has shown that, at the end of H-atom irradiation of carbon grains covered with a water ice layer at 12 K, which determines the formation of the 3.47 μm band, the CH_2 and CH_3 groups form after sample warm-up at room temperature. Therefore, the carbon material absorbing at 3.47 μm in dense clouds/protostars, included in a comet during the formation process in the outer edge of the solar nebula, may thermally evolve to develop the CH_2 and CH_3 groups. The previous results provide a unifying interpretation of how the aliphatic component appears in the main phases of its evolution in space.

Another interesting phenomenon is observed when H atoms interact with hydrogenated carbon grains: the formation of H_2 molecules by abstraction of H chemisorbed in aliphatic sites [254]. Fully hydrogenated carbon grains have been exposed to D atoms, and deuterated carbon grains to H atoms. The spectral

effects induced by atoms at 300 K in carbon grains at room temperature are shown in Figure 7.36. On increasing the D atom fluence, the C–H stretching feature of hydrogenated carbon grains decreases and the corresponding C–D feature increases. On the contrary, the C–D feature decreases and the C–H band increases when deuterated carbon grains are exposed to H atoms. The isotope exchange takes place through the following reaction sequence: (i) abstraction of chemisorbed H/D by impinging D/H, with the production of HD molecules; (ii) addition of D/H in the chemisorption sites. The abstraction and addition cross sections show that there is no isotope effect and that abstraction is the rate-limiting step of the reaction sequence. The formation of HD takes place

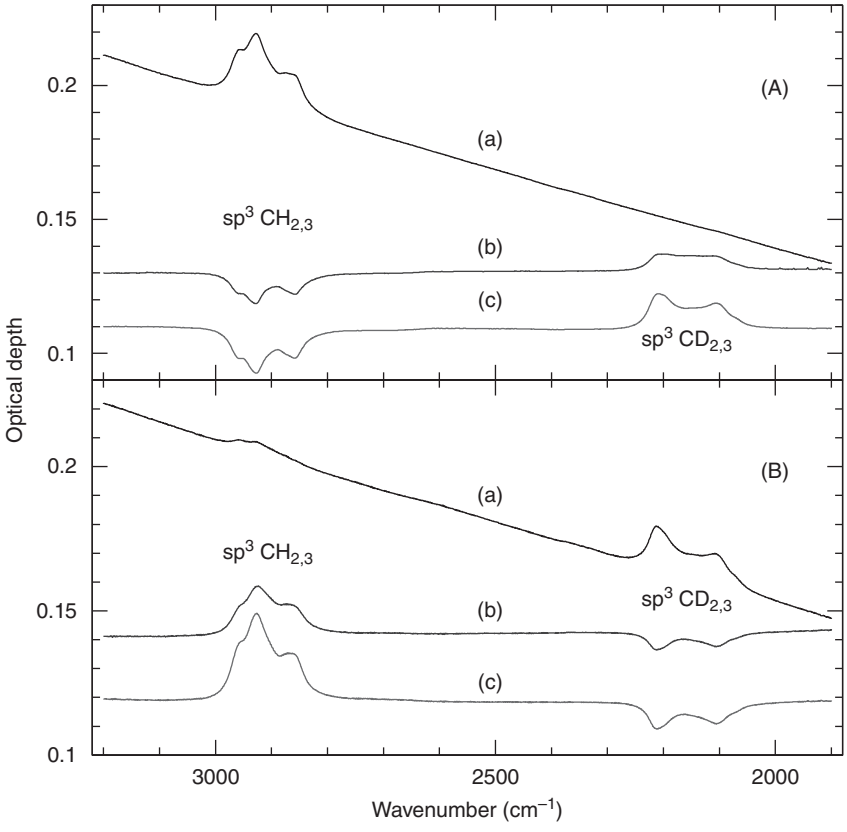

Figure 7.36 Evolution of the C–H and C–D stretching bands during D irradiation of hydrogenated carbon grains (A) and H irradiation of deuterated carbon grains (B). In both panels, the initial spectrum (a) and those after irradiation (shown after subtraction of the initial spectrum) of 6 $\times 10^{17}$ (b) and 1 $\times 10^{19}$ atoms cm^{-2} (c) are plotted. The difference spectra are offset for clarity. The weak sp^3 $CH_{2,3}$ band present in the spectrum of deuterated carbon grains is due to the small fraction (2%) of H_2 present in the D_2 gas used to produce the grains. (Reproduced from Ref. [254] with permission of the AAS.)

through an Eley–Rideal process as indicated by the small value of the abstraction cross section.

Mass spectroscopy measurements carried out during H-atom irradiation of deuterated carbon grains confirm HD production. The HD desorption signal decreases with grain temperature, while it does not vary by lowering the H-atom temperature from 300 to 80 K. The independence of the desorption rate on the H-atom temperature indicates that there is no barrier for abstraction of D atoms. At present, this mechanism represents the only viable route for the H_2 formation at grain temperatures prevailing in photodissociation regions, where the residence time of H atoms in physisorption sites is too short for recombination to take place. More generally, the abstraction experiments show that reactions involving H atoms can take place as chemical exchanges, rather than with physically adsorbed species.

7.6.5 Conclusions

Laboratory studies of the effects induced in carbon materials by energetic processing, thermal annealing, and atomic hydrogen have considerably improved our understanding of many aspects of the complex relations between the structure, composition, and optical properties of interstellar carbon particles. The properties of these particles vary by their interaction with gas, UV photons, and cosmic rays. It has been possible to outline, to a good degree of accuracy, the evolution of these particles in the interstellar environment, reconciling the observed spectral variations with environment with changes in the grain properties produced by processing. Moreover, these experiments have shown that carbon particles play an active role in astrochemistry through the formation of molecular hydrogen and other carbon-based molecules on their surface.

Acknowledgments

F.J.M.R. was supported by grants NNX07AI39G and NNX10AK28G from the NASA Cosmochemistry Program. J.A.N. is grateful for the support received from the Cosmochemistry Program at NASA Headquarters. V.M. has been supported by ASI and INAF research contracts.

References

1. Molster, F.J., Waters, L.B.F.M., and Kemper, F. (2010) in *Lecture Notes in Physics*, Vol. 815 (ed. T. Henning), Springer-Verlag, Berlin, pp. 143–201.
2. Lodders, K., Palme, H., and Gail, H.-P. (2009) *Landolt Börnstein*, p. 44.
3. Asplund, M., Grevesse, N., Sauval, A.J., and Scott, P. (2009) *Ann. Rev. Astron. Astrophys.*, **47**, 481–522.
4. Gail, H.-P., Zhukovska, S.V., Hoppe, P., and Trieloff, M. (2009) *Astrophys. J.*, **698**, 1136–1154.

5. Ferrarotti, A.S. and Gail, H.-P. (2006) *Astron. Astrophys.*, **447**, 553–576.
6. Zuckerman, B. and Aller, L.H. (1986) *Astrophys. J.*, **301**, 772–789.
7. Schaller, G., Schaerer, D., Meynet, G., and Maeder, A. (1992) *Astron. Astrophys. Suppl.*, **96**, 269–331.
8. Gilman, R.C. (1969) *Astrophys. J.*, **155**, L185.
9. Salpeter, E.E. (1977) *Ann. Rev. Astron. Astrophys.*, **15**, 267–293.
10. Lattimer, J.M., Schramm, D.N., and Grossman, L. (1978) *Astrophys. J.*, **219**, 230–249.
11. Lodders, K. and Fegley, B. (1997) in *American Institute of Physics Conference Series*, Vol. 402 (eds T.J. Bernatowicz and E. Zinner), pp. 391–423.
12. Smith, A. and Missen, R.W. (1982) *Chemical Reaction Equilibrium Analysis: Theory and Algorithms*, John Wiley & Sons, Inc., New York.
13. Saxena, S.K. and Eriksson, G. (1986) in *Chemistry and Physics of Terrestrial Planets* (ed. S.K. Saxena), p. 30.
14. Putnis, A. (2001) *Introduction to Mineral Sciences*, Cambridge University Press, Cambridge.
15. White, W.M. (2009) *Geochemistry, www.imwa.info/white-geochemistry.html.*
16. Smith, N. (2009) *ArXiv e-prints*.
17. Mitchell, R.M. and Robinson, G. (1978) *Astrophys. J.*, **220**, 841–852.
18. Bose, M., Floss, C., and Stadermann, F.J. (2010) *Astrophys. J.*, **714**, 1624–1636.
19. Nguyen, A.N., Nittler, L.R., Stadermann, F.J., Stroud, R.M., and Alexander, C.M.O. (2010) *Astrophys. J.*, **719**, 166–189.
20. Vollmer, C., Brenker, F.E., Hoppe, P., and Stroud, R.M. (2009) *Lunar and Planetary Institute Science Conference Abstracts*, Vol. 40, p. 1262.
21. Gail, H.-P. (2010) in *Astromineralogy*, Lecture Notes in Physics, Vol. 815 (ed. Th. Henning), Springer-Verlag, Berlin, Heidelberg, pp. 61.
22. Vollmer, C., Hoppe, P., Stadermann, F.J., Floss, C., and Brenker, F.E. (2009) *Geochem. Cosmochem. Acta*, **73**, 7127–7149.
23. Gail, H.-P. and Sedlmayr, E. (1988) *Astron. Astrophys.*, **206**, 153–168.
24. Danchi, W.C., Bester, M., Degiacomi, C.G., Greenhill, L.J., and Townes, C.H. (1994) *Astron. J.*, **107**, 1469–1513.
25. Groenewegen, M.A.T., Sloan, G.C., Soszyński, I., and Petersen, E.A. (2009) *Astron. Astrophys.*, **506**, 1277–1296.
26. Alexander, D.R. and Ferguson, J.W. (1994) *Astrophys. J.*, **437**, 879–891.
27. Agúndez, M. and Cernicharo, J. (2006) *Astrophys. J.*, **650**, 374–393.
28. Beck, H.K.B., Gail, H.-P., Henkel, R., and Sedlmayr, E. (1992) *Astron. Astrophys.*, **265**, 626–642.
29. Cherchneff, I. (2006) *Astron. Astrophys.*, **456**, 1001–1012.
30. Willacy, K. and Cherchneff, I. (1998) *Astron. Astrophys.*, **330**, 676–684.
31. Glassgold, A.E. (1999) in *Asymptotic Giant Branch Stars*, IAU Symposium, Vol. 191 (eds T. Le Bertre, A. Lebre, and C. Waelkens), p. 337.
32. Miller, T.A., Wooldridge, J.W., and Bozzelli, M.S. (2005) *Combust. Flame*, **137**, 73.
33. Suh, S.-M., Zachariah, M.R., and Girshick, S.L. (2001) *J. Vac. Sci. Technol.*, **19**, 940–951.
34. Koehler, T.M., Gail, H.-P., and Sedlmayr, E. (1997) *Astron. Astrophys.*, **320**, 553–567.
35. Nuth, J.A. and Donn, B. (1981) *Astrophys. J.*, **247**, 925–935.
36. Nuth, J.A. and Donn, B. (1982) *J. Chem. Phys.*, **77**, 2639–2646.
37. Gail, H.-P. and Sedlmayr, E. (1986) *Astron. Astrophys.*, **166**, 225–236.
38. Nuth, J.A. III and Ferguson, F.T. (2006) *Astrophys. J.*, **649**, 1178–1183.
39. Wetzel, S., Klevenz, M., Pucci, A., and Gail, H.-P. (2012) *Appl. Spectrosc.*, **66**, 1061–1066.
40. Reber, A.C., Paranthaman, S., Clayborne, P.A., Khanna, S.N., and Castleman, A.W. Jr. (2008) *ACS Nano*, **2**, 1729–1–37.
41. Reber, A.C., Clayborne, P.A., Reveles, J.U. *et al.* (2008) *Nano Lett.*, **6**, 1190.
42. Gail, H.-P., Wetzel, S., Pucci, A., and Tamanai, A. (2013) *Astron. Astrophys.*, **555**, A119.
43. Gail, H.-P. and Sedlmayr, E. (1998) *Faraday Discuss.*, **109**, 303.

44. Jeong, S.-J. (2000) Digital Repository of Technische Universität Berlin. PhD thesis, Technical University of Berlin, *http://opus.kobv.de/tuberlin/volltexte/2000/136/pdf/jeong kyung.pdf* (accessed 21 June 2014).
45. Jeong, K.S., Winters, J.M., Le Bertre, T., and Sedlmayr, E. (2003) *Astron. Astrophys.*, **407**, 191–206.
46. Sloan, G.C., Kraemer, K.E., Wood, P.R. *et al.* (2008) *Astrophys. J.*, **686**, 1056–1081.
47. Crowther, P.A. (2007) *Ann. Rev. Astron. Astrophys.*, **45**, 177–219.
48. Hoppe, P., Strebel, R., Eberhardt, P., Amari, S., and Lewis, R.S. (1996) *Geochem. Cosmochem. Acta*, **60**, 883–907.
49. Bernatowicz, T.J., Cowsik, R., Gibbons, P.C. *et al.* (1996) *Astrophys. J.*, **472**, 760.
50. Croat, T.K., Stadermann, F.J., and Bernatowicz, T.J. (2005) *Astrophys. J.*, **631**, 976–987.
51. Kimura, Y. and Kaito, C. (2003) *Mon. Not. R. Astron. Soc.*, **343**, 385–389.
52. Croat, T.K., Jadhav, M., Lebsack, E., and Bernatowicz, T.J. (2011) *Meteorit. Planet. Sci. Suppl.*, **74**, 5228.
53. Marinov, N.M., Pitz, W., Westbrook, C.K., Castaldi, M.J., and Senkan, S.M. (1996) *Combust. Sci. Technol.*, **116**, 211.
54. Frenklach, M. and Feigelson, E.D. (1989) *Astrophys. J.*, **341**, 372–384.
55. Cherchneff, I. and Barker, J.R. (1992) *Astrophys. J.*, **394**, 703–716.
56. Cherchneff, I., Barker, J.R., and Tielens, A.G.G.M. (1992) *Astrophys. J.*, **401** (1), 269–287.
57. Frenklach, M. (2002) *Phys. Chem. Chem. Phys. (Incorporating Faraday Transactions)*, **4**, 2028–2037.
58. Zhukovska, S. and Gail, H.-P. (2008) *Astron. Astrophys.*, **486**, 229–237.
59. Bianchi, S., Schneider, R., and Valiante, R. (2009) in *Cosmic Dust - Near and Far*, Astronomical Society of the Pacific Conference Series, Vol. 414 (eds T. Henning, E. Grun, and J. Steinacker), p. 65.
60. Kozasa, T., Nozawa, T., Tominaga, N. *et al.* (2009) *Cosmic Dust - Near and Far*, Astronomical Society of the Pacific Conference Series, Vol. 414 (eds T. Henning, E. Grun, and J. Steinacker), p. 43.
61. Starrfield, S., Gehrz, R.D., and Truran, J.W. (1997) in *American Institute of Physics Conference Series*, Vol. 402 (eds T.J. Bernatowicz and E. Zinner), pp. 203–234.
62. Granquist, C.G. and Buhrman, R.A. (1976) *J. Appl. Phys.*, **47**, 2200.
63. Heidenreich, S., Büttner, H., and Ebert, F. (2003) *Chem. Ing. Tech.*, **75**, 1787.
64. Cao, G. (2004) *Nanostructures and Nanomaterials-Synthesis, Properties and Applications*, Imperial College Press.
65. Buerki, P.R. and Leutwyler, S. (1991) *J. Appl. Phys.*, **69**, 3739–3744.
66. Herlin, N., Bohn, I., Reynaud, C. *et al.* (1998) *Astron. Astrophys.*, **330**, 1127.
67. Ledoux, G., Ehbrecht, M., Guillois, O. *et al.* (1998) *Astron. Astrophys.*, **333**, L39–L42.
68. Schnaiter, M., Henning, Th., Mutschke, H. *et al.* (1998) *Astrophys. J.*, **519**, 687.
69. Jäger, C., Mutschke, H., Huisken, F. *et al.* (2007) *Carbon*, **45**, 2981–2994.
70. Llamas Jansa, I., Jäger, C., Mutschke, H., and Henning, Th. (2007) *Carbon*, **45**, 1542–1557.
71. Schnaiter, M., Mutschke, H., Henning, Th. *et al.* (1996) *Astrophys. J.*, **464**, L187–L190.
72. Pino, T., Dartois, E., Cao, A.-T. *et al.* (2008) *Astron. Astrophys.*, **490**, 665–672.
73. Duley, W.W. (1994) *Astrophys. J.*, **430**, L133.
74. Duley, W.W. and Seahra, S. (1998) *Astrophys. J.*, **507**, 874.
75. Grishko, V.I. and Duley, W.W. (2002) *Astrophys. J.*, **568**, 448.
76. Jäger, C., Mutschke, H., Llamas-Jansa, I., Henning, Th., and Huisken, F. (2008) in *Organic Matter in Space; Proceedings of the IAU Symposium 251, Held in Hong Kong 2008* (eds S. Kwok and S. Sandford), SAO/NASA Astrophysics Data System.
77. Schnaiter, M., Mutschke, H., Dorschner, J., Henning, Th., and Salama, F. (1998) *Astrophys. J.*, **498**, 486–496.

78. Jäger, C., Henning, Th., Spillecke, N., and Schlögl, R. (1999) *J. Non-Cryst. Solids*, **258**, 161–179.
79. Colangeli, L., Mennella, V., Palumbo, P., Rotundi, A., and Bussoletti, E. (1995) *Astron. Astrophys. Suppl. Ser.*, **113**, 561.
80. Mennella, V., Colangeli, L., Palumbo, P. *et al.* (1996) *Astrophys.J.*, **464**, L191.
81. Sakata, A., Wada, S., Okutso, Y., Shintani, H., and Nakada, Y. (1983) *Nature*, **301**, 493.
82. Goto, M., Maihara, T., Terada, H. *et al.* (2000) *Astron. Astrophys. Suppl.*, **141**, 149–156.
83. Furton, D.G., Laiho, J.W., and Witt, A.N. (1999) *Astrophys. J.*, **526**, 752–763.
84. Kovačević, E., Stefanović, I., Berndt, J., Pendleton, Y.J., and Winter, J. (2005) *Astrophys. J.*, **623**, 242–251.
85. Jäger, C., Mutschke, H., Henning, Th., and Huisken, F. (2008) *Astrophys. J.*, **689**, 249.
86. Haglund, R.F. Jr. and Itoh, N. (1994) in *Laser Ablation* (ed. J.C. Miller), Springer-Verlag, Berlin, Heidelberg, p. 11.
87. Dyer, P.E. and Sidhu, J. (1988) *J. Appl. Phys.*, **64**, 4657.
88. Wen, S.-B., Mao, X., Greif, R., and Russo, R.E. (2007) *J. Appl. Phys.*, **101**, 123105.
89. Wen, S.-B., Mao, X., Greif, R., and Russo, R.E. (2007) *J. Appl. Phys.*, **101**, 023114.
90. Clément, D., Mutschke, H., Klein, R., and Henning, Th. (2003) *Astrophys. J.*, **594**, 642.
91. Mansurov, Z.A. (2005) *Combust. Explos. Shock Waves*, **41**, 727–744.
92. Homann, K.-H. (1998) *Angew. Chem.*, **110**, 2572.
93. Suzuki, N., Kimura, S., Nakada, T. *et al.* (2000) *Meteorit. Planet. Sci.*, **35**, 1269.
94. Mordkovich, V.Z. (2000) *Chem. Mater.*, **12**, 2813.
95. Hofmeister, H., Huisken, F., and Kohn, B. (1999) *Eur. Phys. J. D*, **9**, 137–140.
96. Jäger, C., Fabian, D., Schrempel, F. *et al.* (2003) *Astron. Astrophys.*, **401**, 57.
97. Fink, J., Müller-Heinzerling, T., Bubenzer, A., Koidl, P., and Crecelius, G. (1983) *Solid State Commun.*, **47**, 687.
98. van Aken, P.A., Liebscher, B., and Styrsa, V.J. (1998) *Phys. Chem. Miner.*, **25**, 323–327.
99. Thompson, S.P., Evans, A., and Jones, A.P. (1996) *Astron. Astrophys.*, **308**, 309.
100. Jacob, W. and Unger, M. (1996) *Appl. Phys. Lett.*, **68**, 475–477.
101. Pendleton, Y.J. and Allamandola, L.J. (2002) *Astrophys. J. Suppl. Ser.*, **138**, 75–98.
102. Rietmeijer, F.J.M., Pun, A., and Nuth, J.A. III (2009) *Mon. Not. R. Astron. Soc.*, **396**, 402–408.
103. Rietmeijer, F.J.M. and Nuth, J.A. III (1991) in *Lunar and Planetary Science Conference Proceedings*, Vol. 21 (eds G. Ryder and V.L. Sharpton), pp. 591–599.
104. Rietmeijer, F.J.M., Nuth, J.A. III, and Karner, J.M. (1999) *Astrophys. J.*, **527**, 395–404.
105. Rietmeijer, F.J.M., Nuth, J.A., and MacKinnon, I.D.R. (1986) *Icarus*, **66**, 211–222.
106. Rietmeijer, F.J.M., Hallenbeck, S.L., Nuth, J.A., and Karner, J.M. (2002) *Icarus*, **156**, 269–286.
107. Karner, J.M., Rietmeijer, F.J.M., and Janeczek, J. (1996) *Meteorit. Planet. Sci. Suppl.*, **31**, 69.
108. Molster, F.J. and Waters, L.B.F.M. (2003) in *Astromineralogy*, Lecture Notes in Physics, Vol. 609 (ed. T.K. Henning), Springer-Verlag, Berlin, pp. 121–170.
109. Molster, F. and Kemper, C. (2005) *Space Sci. Rev.*, **119**, 3–28.
110. Kerridge, J.F. and Matthews, M.S. (1988) *Meteorites and the Early Solar System* Tucson, Ariz. University of Arizona Press.
111. Grossman, L. and Larimer, J.W. (1974) *Rev. Geophys. Space Phys.*, **12**, 71–101.
112. Brearley, A.J. and Jones, R.H. (1998) in *Planetary Materials, Reviews in Mineralogy*, Vol. 36 (ed. J.J. Papike), Mineralogical Society of America, Chantilly, VA, pp. 3–1–398.
113. Rietmeijer, F.J.M. and Nuth, J.A. III (2002) in *IAU Colloq. 181: Dust in*

the Solar System and Other Planetary Systems (eds S.F. Green, I.P. Williams, J.A.M. McDonnell, and N. McBride), Elsevier Science Serials p. 333.

114. Ostwald, W. (1896) *Lehrbuch der Allgemeinen Chemie*, Leipzig. Veit. 1896 Vol. 2, Part 1, Leipzig.

115. Nuth, J.A., Hallenbeck, S.L., and Rietmeijer, F.J.M. (2000) *J. Geophys. Res.*, **105**, 10387–10396.

116. Nuth, J.A., Rietmeijer, F.J.M., Hallenbeck, S.L., Withey, P.A., and Ferguson, F. (2000) Astronomical Society of the Pacific Conference Series. *Thermal Emission Spectroscopy and Analysis of Dust, Disks, and Regoliths*, Vol. 196, pp. 313–332.

117. Nuth, J.A. III, Rietmeijer, F.J.M., and Hill, H.G.M. (2002) *Meteorit. Planet. Sci.*, **37**, 1579–1590.

118. Rietmeijer, F.J.M., Nuth, J.A., Rochette, P., Pun, A., and Karner, J.M. (2006) *Am. Mineral.*, **91**, 1688.

119. Rietmeijer, F.J.M., Nuth, J.A. III, and Nelson, R.N. (2004) *Meteorit. Planet. Sci.*, **39**, 723–746.

120. Nuth, J.A. and Donn, B. (1983) *J. Chem. Phys.*, **78**, 1618.

121. Kimura, Y. and Nuth, J.A. (2009) *Astrophys. J. Lett.*, **697**, L10–L13.

122. Hadamcik, E., Renard, J.-B., Rietmeijer, F.J.M. *et al.* (2007) *Icarus*, **190**, 660–671.

123. Rietmeijer, F.J.M., Hadamcik, E., Pun, A. *et al.* (2009) *Lunar and Planetary Institute Science Conference Abstracts*, Vol. 40, p. 1742.

124. Rietmeijer, F.J.M., Nuth, J.A. III, Karner, J.M., and Hallenbeck, S.L. (2002) *Phys. Chem. Chem. Phys. (Incorporating Faraday Transactions)*, **4**, 546–551.

125. Rietmeijer, F.J.M., Nuth, J.A. III, and Karner, J.M. (1999) *Phys. Chem. Chem. Phys. (Incorporating Faraday Transactions)*, **1**, 1511–1516.

126. De, B.R. (1979) *Astrophys. Space Sci.*, **65**, 191–198.

127. Prigogine, I. (1979) *Astrophys. Space Sci.*, **65**, 371–381.

128. Nuth, J.A. and Donn, B. (1984) *J. Geophys. Res.*, **89**, 657.

129. Phillips, B., Somiya, S., and Muan, A. (1961) *J. Am. Ceram. Soc.*, **44**, 167–169.

130. Muan, A. (1958) *Am. J. Sci.*, **256**, 171–207.

131. Hallenbeck, S.L., Nuth, J.A. III, and Nelson, R.N. (2000) *Astrophys. J.*, **535**, 247–255.

132. Helling, C. and Rietmeijer, F.J.M. (2009) *Int. J. Astrobiol.*, **8**, 3–8.

133. Rietmeijer, F.J.M. and Nuth, J.A. (2013) *Astrophys. J.*, **771**, 34.

134. Rietmeijer, F.J.M. (1998) in *Planetary Materials, Reviews in Mineralogy*, Vol. 36 (ed. J.J. Papike), Mineralogical Society of America, Chantilly, pp. 2–1–2–95.

135. Nagahara, H., Kushiro, I., Mysen, B.O., and Mori, H. (1988) *Nature*, **331**, 516.

136. Richter, H. and Howard, J.B. (2000) *Prog. Energy Combust. Sci.*, **26**, 565.

137. Nowotny, W., Aringer, B., Höfner, S., Gautschy-Loidl, R., and Windsteig, W. (2005) *Astron. Astrophys.*, **437**, 273.

138. Lederer, M.T., Lebzelter, T., Aringer, B. *et al.* (2006) *Mem. S.A.It.*, **77**, 1008.

139. Winters, J.M., Fleischer, A.J., Gauger, A., and Sedlmayr, E. (1994) *Astron. Astrophys.*, **290**, 623–633.

140. Hoefner, S., Feuchtinger, M.U., and Dorfi, E.A. (1995) *Astron. Astrophys.*, **297**, 815.

141. Nowotny, W., Aringer, B., Höfner, S., and Eriksson, K. (2013) *Astron. Astrophys.*, **552**, A20.

142. Cherchneff, I., Le Teuff, Y.H., Williams, P.M., and Tielens, A.G.G.M. (2000) *Astron. Astrophys.*, **357**, 572.

143. Jäger, C., Mutschke, H., Huisken, F. *et al.* (2006) *Astrophys. J. Suppl. Ser.*, **166**, 557–566.

144. Jäger, C., Huisken, F., Mutschke, H., Llamas Jansa, I., and Henning, Th. (2008) *Astrophys. J.*, **696**, 706–712.

145. Iida, Y. and Yeung, E. (1994) *Appl. Spectrosc.*, **48**, 945.

146. Jones, A.P., Duley, W.W., and Williams, D.A. (1990) *Q. J. R. Astron. Soc.*, **31**, 567–582.

147. Dartois, E. (2011) in *EAS Publications Series*, Vol. 46 (eds C. Joblin and A.G.G.M. Tielens), Cambridge University Press, pp. 381–391.

148. Goel, A., Howard, J.B., and Vander Sande, J.B. (2004) *Carbon*, **42**, 1907.
149. Kroto, H.W. and McKay, K. (1988) *Nature*, **331**, 328.
150. Zheng, G., Irle, S., and Morokuma, K. (2005) *J. Chem. Phys.*, **122**, 014708.
151. Irle, S., Zheng, G., Elstner, M., and Morokuma, K. (2003) *Nano Lett.*, **3**, 1657.
152. Yeretzian, Ch., Hansen, F., Diederich, K., and Whetten, R.L. (1993) *Suppl. Z. Phys. D*, **26**, 300.
153. Steglich, M., Jäger, C., Huisken, F. *et al.* (2013) *Astrophys. J. Suppl.*, **208**, 26.
154. Lodders, K. and Fegley, B. Jr. (1999) in *Asymptotic Giant Branch Stars; Proceedings of the IAU Symposium 191* (eds T. Le Bertre, A. Lebre, and C. Waelkens), SAO/NASA Astrophysics Data System, p. 279.
155. Clayton, D.D., Deneault, E.A.-N., and Meyer, B.S. (2001) *Astrophys. J.*, **562**, 480.
156. Cherchneff, I. and Cau, P. (1999) in *Asymptotic Giant Branch Stars; Proceedings of the IAU Symposium 191* (eds T. Le Betre, A. Lgraveebre, and C. Waelkens), ASP, San Francisco, CA, p. 251.
157. Hony, S., Tielens, A.G.G.M., Waters, L.B.F.M., and de Koter, A. (2003) *Astron. Astrophys.*, **402**, 211.
158. Robertson, J. and O'Reilly, E.P. (1987) *Phys. Rev. B*, **35**, 2946–2957.
159. Tauc, J., Grigorovici, R., and Vancu, A. (1966) *Phys. Status Solidi B*, **15**, 627.
160. Tyutyulkov, N., Ivanov, N., Müllen, K., Staykov, A., and Dietz, F. (2004) *J. Phys. Chem.*, **108**, 4275.
161. Yang, L., Park, C.-H., Son, Y.-W., Cohen, M.L., and Louie, S.G. (2007) *Phys. Rev. Lett.*, **99**, 186801.
162. Watson, M.D., Fechtenkötter, A., and Müllen, K. (2001) *Chem. Rev.*, **101**, 1267.
163. Lenardi, C., Piseri, P., Briois, V. *et al.* (1999) *J. Appl. Phys.*, **85**, 7159–7167.
164. Schnaiter, M., Gimmler, M., Llamas, I. *et al.* (2006) *Atmos. Chem. Phys.*, **6**, 2981–2990, *http://www.atmos-chem-phys.net/6/2981/2006/.*
165. Llamas Jansa, I. (2007) *Dissertation*, Friedrich-Schiller-Universität, Jena.
166. Kwok, S., Volk, K., and Bernath, P. (2001) *Astrophys. J.*, **554**, L87.
167. Hrivnak, B.J., Geballe, T.R., and Kwok, S. (2007) *Astrophys. J.*, **662**, 1059.
168. Hony, S., Van Kerckhoven, C., Peeters, E. *et al.* (2001) *Astron. Astrophys.*, **370**, 1030–1043.
169. Hoppe, P. (2009) in *Cosmic Dust - Near and Far*, Astronomical Society of the Pacific Conference Series, Vol. 414 (eds T. Henning, E. Grun, and J. Steinacker), Astron. Soc. Pacific, San Francisco, USA, p. 148.
170. Draine, B.T. (2009) in *Cosmic Dust - Near and Far*, Astronomical Society of the Pacific Conference Series, Vol. 414 (eds J. Steinacker, T. Henning, and E. Grun), Astron. Soc. Pacific, San Francisco, USA, p. 453.
171. Sandford, S.A. (1996) in *Polarimetry of the Interstellar Medium*, Astronomical Society of the Pacific Conference Series, Vol. 97 (eds W.G. Roberge and D.C.B. Whittet), Astron. Soc. Pacific, San Francisco, USA, p. 29.
172. Krasnokutski, S.A., Rouillé, G., Jäger, C. *et al.* (2014) *Astrophys. J.*, **782**, 15.
173. Rouillé, G., Jäger, C., Krasnokutski, S.A. *et al.* (2014) *Faraday Discuss.*, **168**, 449.
174. Gail, H.P. and Sedlmayr, E. (1998) in *The Molecular Astrophysics of Stars and Galaxies* (eds T.W. Hartquist and D.A. Williams), Oxford University Press, Oxford, pp. 285.
175. Sogawa, H. and Kozasa, T. (1999) *Astrophys. J.*, **516**, L33–L36.
176. Hallenbeck, S.L., Nuth, J.A., and Daukantas, P.L. (1998) *Icarus*, **131**, 198–209.
177. Lenzuni, P., Gail, H.P., and Henning, Th. (1995) *Astrophys. J.*, **447**, 848.
178. Brucato, J.R., Colangeli, L., Menella, V., Palumbo, P., and Busoletti, E. (1999) *Astron. Astrophys.*, **348**, 1012–1019.
179. Fabian, D., Jäger, C., Mutschke, H., Dorschner, J., and Henning, Th. (2000) *Astron. Astrophys.*, **364**, 282–292.
180. Jäger, C., Dorschner, J., Mutschke, H., Posch, Th., and Henning, Th. (2003) *Astron. Astrophys.*, **408**, 193.
181. Thompson, S.P. (2008) *Astron. Astrophys.*, **484**, 251.

182. Ziegler, J.F. (1996) *SRIM: The Stopping Power and Range of Ions in Matter*, IBM Publications, New York.
183. Jones, A.P., Tielens, A.G.G.M., and Hollenbach, D.J. (1996) *Astrophys. J.*, **469**, 740.
184. Bradley, J.P. (1994) *Science*, **265**, 925.
185. Tielens, A.G.G.M. (2005) *The Physics and Chemistry of the Interstellar Medium*, Cambridge University Press, Cambridge.
186. Baragiola, R.A., Vidal, R.A., Svendsen, W. *et al.* (2003) *Nucl. Instrum. Methods Phys. Res., Sect. B*, **209**, 294–303.
187. Bringa, E.M., Kucheyev, S.O., Loeffler, M.J. *et al.* (2007) *Astrophys. J.*, **662**, 372–378.
188. Day, K.L. (1977) *Mon. Not. R. Astron. Soc.*, **178**, 49P.
189. Krätschmer, W. and Huffman, D.R. (1979) *Astrophys. Space Sci.*, **61**, 195.
190. Demyk, K., Carrez, P., Leroux, H. *et al.* (2001) *Astron. Astrophys.*, **368**, L38–L41.
191. Demyk, K., d'Hendecourt, L., Leroux, H., Jones, A.P., and Borg, J. (2004) *Astron. Astrophys.*, **420**, 233.
192. Carrez, Ph., Demyk, K., Cordier, P. *et al.* (2002) *Meteorit. Planet. Sci.*, **37**, 1599.
193. Brucato, J.R., Strazzulla, G., Baratta, G., and Colangeli, L. (2004) *Astron. Astrophys.*, **413**, 395.
194. Wang, S.X., Wang, L.M., Ewing, R.C., and Doremus, R.H. (1998) *J. Non-Cryst. Solids*, **238**, 198–213.
195. Jäger, C., Mutschke, H., Henning, Th., and Huisken, F. (2009) in *Cosmic Dust - Near and Far*, Astronomical Society of the Pacific Conference Series, Vol. 414 (eds J. Steinacker, T. Henning, and E. Grun), Astron. Soc. Pacific, San Francisco, USA, p. 319.
196. Dukes, C.A., Baragiola, R.A., and McFadden, L.A. (1999) *J. Geophys. Res.*, **104**, 1865.
197. Bringa, E.M. and Johnson, R.E. (2004) *Astrophys. J.*, **603**, 159–164.
198. Dwek, E., Foster, S.M., and Vancura, O. (1996) *Astrophys. J.*, **457**, 244.
199. Baragiola, R.A. (2004) *Philos. Trans. R. Soc. London, Ser. A*, **362**, 29–53.
200. May, P.W., Pineau des Forêts, G., Flower, D.R. *et al.* (2000) *Mon. Not. R. Astron. Soc.*, **318**, 809–816.
201. Stecher, T. and Donn, B. (1965) *Astrophys. J.*, **142**, 1681.
202. Draine, B.T. and Lee., H.M. (1984) *Astrophys. J.*, **285**, 89.
203. Mathis, J.S. (1994) *Astrophys. J.*, **422**, 176.
204. Joblin, Ch., Leger, A., and Martin, P. (1992) *Astrophys. J.*, **393**, L79.
205. Mennella, V., Colangeli, L., Bussoletti, E., Palumbo, P., and Rotundi, A. (1998) *Astrophys. J.*, **507**, L177.
206. Wada, S., Kaito, Ch., Kimura, S., Ono, H., and Tokunaga, A.T. (1999) *Astron. Astrophys.*, **345**, 259.
207. Tomita, S., Fujii, M., and Hayashi, S. (2002) *Phys. Rev. B*, **66**, 245424.
208. Chhowalla, M., Wang, H., Sano, N. *et al.* (2003) *Phys. Rev. Lett.*, **90**, 155504.
209. Iglesias-Groth, S. (2004) *Astrophys. J.*, **608**, L37.
210. Pendleton, Y.J., Sandford, S.A., Allamandola, L.J., Tielens, A.G.G.M., and Sellgren, K. (1994) *Astrophys. J.*, **437**, 683–696.
211. Chiar, J.E., Tielens, A.G.G.M., Whittet, D.C.B. *et al.* (2000) *Astrophys. J.*, **537**, 749.
212. Allamandola, L.J., Sandford, S.A., and Tielens, A.G.G.M. (1992) *Astrophys. J.*, **399**, 134–146.
213. Brooke, T.Y., Sellgren, K., and Geballe, T.R. (1999) *Astrophys. J.*, **517**, 883–900.
214. Chiar, J.E., Adamson, A.J., and Whittet, D.C.B. (1996) *Astrophys. J.*, **472**, 665.
215. Mu noz Caro, G.M., Ruiterkamp, R., Schutte, W.A., Greenberg, J.M., and Mennella, V. (2001) *Astron. Astrophys.*, **367**, 347–354.
216. Allamandola, L.J., Sandford, S.A., Tielens, A.G.G.M., and Herbst, T.M. (1993) *Science*, **260**, 64–66.
217. Moore, M.H. (1999) in *Solid Interstellar Matter: The ISO Revolution* (eds L. d Hendecourt, C. Joblin, and A. Jones), Springer-Verlag, Berlin, pp. 199–218.
218. Robertson, J. (1991) *Prog. Solid State Chem.*, **21**, 199–333.

219. Papoular, R., Conard, J., Guillois, O. *et al.* (1996) *Astron. Astrophys.*, **315**, 222–236.
220. Dischler, B. (1983) *Solid State Commun.*, **48**, 105–108.
221. Scott, A. and Duley, W.W. (1996) *Astrophys. J. Lett.*, **472**, L123–L125.
222. Bounouh, Y., Thèye, M.L., Dehbi-Alaoui, A., Matthews, A., and Stoquert, J.P. (1995) *Phys. Rev. B*, **51**, 9597–9605.
223. Mennella, V., Colangeli, L., Pestellini, C.C. *et al.* (1996) in *NASA Conference Publication*, Vol. 3339 (eds M.E. Kress, A.G.G.M. Tielens, and Y.J. Pendleton), pp. 109–112.
224. Blanco, A., Bussoletti, E., Colangeli, L. *et al.* (1993) *Astrophys. J.*, **406**, 739–741.
225. Mennella, V., Colangeli, L., Blanco, A. *et al.* (1995) *Astrophys. J.*, **444**, 288–292.
226. Mennella, V., Colangeli, L., Bussoletti, E. *et al.* (1995) *Planet. Space Sci.*, **43**, 1217–1221.
227. Mennella, V., Colangeli, L., Bussoletti, E. *et al.* (1995) *Astrophys. J. Suppl. Ser.*, **100**, 149.
228. Kuznetsov, V.L., Chuvilin, A.L., Butenko, Y.V., Mal'Kov, I.Y., and Titov, V.M. (1994) *Chem. Phys. Lett.*, **222**, 343–348.
229. Iida, S., Ohtaki, T., and Seki, T. (1984) *American Institute of Physics Conference Series*, Vol. 120, pp. 258–265.
230. Ogmen, M. and Duley, W.W. (1988) *Astrophys. J.*, **334**, L117.
231. Mennella, V., Mu noz Caro, G.M., Ruiterkamp, R. *et al.* (2001) *Astron. Astrophys.*, **367**, 355–361.
232. Mennella, V., Baratta, G.A., Palumbo, M.E., and Bergin, E.A. (2006) *Astrophys. J.*, **643**, 923–931.
233. Mennella, V., Palumbo, M.E., and Baratta, G.A. (2004) *Astrophys. J.*, **615**, 1073–1080.
234. Gadallah, K.A.K., Mutschke, H., and Jäger, C. (2011) *Astron. Astrophys.*, **528**, A56.
235. Leroux, H. (2009) in *EAS Publications Series*, Vol. 35 (eds F. Boulanger, C. Joblin, A. Jones, and S. Madden), Cambridge University Press, pp. 153–169.
236. Compagnini, G. and Calcagno, L. (1994) *Mater. Sci. Eng.*, **13**, 193–263.
237. Ugarte, D. (1992) *Nature*, **359**, 707–709.
238. Banhart, F. and Ajayan, P.M. (1996) *Nature*, **382**, 433–435.
239. Wesolowski, P., Lyutovich, Y., Banhart, F., Carstanjen, H.D., and Kronmüller, H. (1997) *Appl. Phys. Lett.*, **71**, 1948–1950.
240. Strazzulla, G., Baratta, G.A., and Palumbo, M.E. (2001) *Spectrochim. Acta*, **57**, 825–842.
241. Reynaud, C., Guillois, O., Herlin-Boime, N., and Rouzaud, J.-N. (2001) *Spectrochim. Acta*, **57**, 797–814.
242. Strazzulla, G. and Moroz, L. (2005) *Astron. Astrophys.*, **434**, 593–598.
243. Mennella, V., Baratta, G.A., Esposito, A., Ferini, G., and Pendleton, Y. (2003) *Astrophys. J.*, **587**, 727.
244. Compagnini, G., D'Urso, L., Puglisi, O., Baratta, G.-A., and Strazzulla, G. (2009) *Carbon*, **47**, 1605–1607.
245. Mennella, V., Baratta, G.A., Colangeli, L. *et al.* (1997) *Astrophys. J.*, **481**, 545.
246. Henning, T. (1999) in *Solid Interstellar Matter: The ISO Revolution* (eds L.D. Hendecourt, C. Joblin, and A. Jones), EDP Sciences and Springer-Verlag, p. 247.
247. Baratta, G.A., Arena, M.M., Strazzulla, G., Mennella, V., and Bussoletti, E. (1996) *Nucl. Instrum. Methods Phys. Res., Sect. B*, **116**, 195–199.
248. Furton, D.G. and Witt, A.N. (1993) *Astrophys. J. Lett.*, **415**, L51–L54.
249. Mennella, V., Brucato, J.R., Colangeli, L., and Palumbo, P. (1999) *Astrophys. J.*, **524**, L71.
250. Mennella, V., Brucato, J.R., Colangeli, L., and Palumbo, P. (2002) *Astrophys. J.*, **569**, 531–540.
251. Mennella, V. (2006) *Astrophys. J. Lett.*, **647**, L49–L52.
252. Mennella, V. (2008) *Astrophys. J. Lett.*, **682**, L101–L104.
253. Mennella, V. (2010) *Astrophys. J.*, **718**, 867–875.
254. Mennella, V. (2008) *Astrophys. J. Lett.*, **684**, L25–L28.

Index

Laboratory Astrochemistry: From Molecules through Nanoparticles to Grains, First Edition.
Edited by Stephan Schlemmer, Thomas Giesen, Harald Mutschke and Cornelia Jäger.

WILEY END USER LICENSE AGREEMENT

Go to www.wiley.com/go/eula to access Wiley's ebook EULA.